PROCEEDINGS

TWENTIETH WORKSHOP GEOTHERMAL RESERVOIR ENGINEERING

January 24-26, 1995

Stanford Geothermal Program
Workshop Report SGP-TR-150

Library of Congress Catalog Card No. 86-643338
ISSN 1058-2525

TABLE OF CONTENTS

PREFACE

The Twentieth Workshop on Geothermal Reservoir Engineering, dedicated to the memory of Professor Hank Ramey, was held at Stanford University on January 24-26, 1995. There were ninety-five registered participants. Participants came from six foreign countries: Japan, Mexico, England, Italy, New Zealand and Iceland. The performance of many geothermal reservoirs outside the United States was described in several of the papers.

Professor Roland N. Horne opened the meeting and welcomed visitors to the campus. The key note speaker was Marshall Reed, who gave a brief overview of the Department of Energy's current plan.

Thirty-two papers were presented in the technical sessions of the workshop. Technical papers were organized into eleven sessions concerning: field development, modeling, well test/bore, injection, geoscience, geochemistry and field operations. Session chairmen were major contributors to the workshop, and we thank: Ben Barker, Bob Fournier, Mark Walters, John Counsil, Marcelo Lippmann, Keshav Goyal, Joel Renner and Mike Shook.

In addition to the technical sessions, a panel discussion was held on "What have we learned in 20 years?" Panel speakers included Patrick Muffler, George Frye, Alfred Truesdell and John Pritchett. The subject was further discussed by Subir Sanyal, who gave the post-dinner speech at the banquet.

The Workshop was organized by the Stanford Geothermal Program faculty, staff, and graduate students. We wish to thank our students who operated the audiovisual equipment.

Shaun D. Fitzgerald
Program Manager

PROCEEDINGS, Twentieth Workshop on Geothermal Reservoir Engineering
Stanford University, Stanford, California, January 24-26 1995
SGP-TR-150

GEOTHERMAL PROGRAM ACTIVITIES OF THE DEPARTMENT OF CONSERVATION DIVISION OF OIL, GAS, AND GEOTHERMAL RESOURCES

William F. Guerard, Jr.

Department of Conservation
Division of Oil, Gas, and Geothermal Resources
801 K Street, MS 20-20
Sacramento, California 95814-3530

HISTORY

Thank you very much for the opportunity to address this, the 20th Annual Workshop on Geothermal Reservoir Engineering. It is a pleasure to be here. A great deal of invaluable information has been brought forward through the Annual Workshops, and I give the Stanford University Petroleum Engineering Department a tremendous amount of credit for having the foresight 20 years ago to recognize the need for such an endeavor.

While preparing for this talk, I realized it was nearly 30 years ago, this year, that the Department of Conservation's Division of Oil, Gas, and Geothermal Resources, then called the Division of Oil and Gas, began regulating geothermal development in California. Although many of you are familiar with our geothermal program, in general, you may not be familiar with the history of the program and some of the special projects with which we are involved. Therefore, I would like to take this opportunity to briefly describe our history and a few of our special projects before I discuss the theme of this conference, what we have learned in the last 20 years.

California's oil and gas industry began when the first commercial well was completed in 1876. The industry grew rapidly, and it became apparent in the early Twentieth Century that some controls were necessary to protect hydrocarbon resources, groundwater, and the environment. Recognizing the shortcomings of the local regulatory efforts that were in place, the State Legislature created what is now the Division in 1915. The Division's basic mandate was to prevent damage to oil and gas deposits from infiltrating groundwater and other causes. The charge was later expanded to encourage the wise development of oil and gas resources through good conservation and engineering practices.

Although geothermal resources were also first exploited in the Nineteenth Century, it wasn't until development began in earnest in the early 1960s that the Legislature turned to the Division to establish a geothermal program similar to the oil and gas regulatory program. The enabling legislation, which was the first geothermal law in the Nation, was passed in 1965. Afterwards, as the industry grew, the Division created a Geothermal Unit to deal with the unique characteristics of the resource.

In fact, Dave Anderson, whom you know, and who is the Executive Director of the Geothermal Resources Council, was our first Geothermal Officer. Marshall Reed, now with the U.S. Department of Energy's Geothermal Reservoir Technology Program, was one of his first assistants.

From these early beginnings, our current program has evolved.

SUBSIDENCE PROTECTION

By the 1970s, experience gained in the developed geothermal regions of the world indicated subsidence was possible in the Imperial Valley as a result of geothermal development. Subsidence was a special concern because of the irrigation systems that crisscross the Salton Sea and Heber Geothermal fields. The Division, with primary responsibility for subsidence detection and abatement in that area, began working closely with the Imperial County Surveyor to record data, maintain the integrity of the monitoring network, and review annual leveling-survey data required as a condition of injection project permits.

Currently, Division staff are working with the Lawrence Berkeley Laboratory to develop a reservoir model of the Heber Geothermal field that will include

subsidence prediction capabilities. The techniques developed with this project should be applicable in other geothermal fields.

To date, significant subsidence has been observed at only one geothermal site in the State, the Amedee Geothermal field in northeastern California, where two production wells are located near a fault that serves as a conduit for hot water. In addition to the localized subsidence that has occurred, surface fractures have also developed in the dry lake sediments along the vertically displaced fault trace.

SLOPE STABILITY MONITORING

Slope stability is monitored at The Geysers Geothermal field, which is known both for its steep, rugged, and landslide-prone terrain, and incompetent rock types. A wellsite location can present a hazard if there is a potential for a poor cement job and ground movement that can result in wellbore shear. Both conditions existed in the 1950s when well "Thermal" 4 was drilled and later blew out. Although the initial blowout was eventually controlled, total plugging has never been achieved and venting continues today.

After several more expensive blowouts occurred, the Division instituted a wellsite stability program. Now, when a new well is planned in The Geysers, the operator must submit a geological and engineering report on the proposed site. After reviewing the report, a Division engineer visits the site, conducts an onsite investigation, issues a permit (if conditions are satisfactory), and visits the site during the construction phase. The program has worked so well that no blowouts have occurred at The Geysers since the slope-stability program was initiated.

UNDERGROUND INJECTION

The Division also regulates the injection of geothermal fluids to enforce State statutes and an agreement with the U.S. Environmental Protection Agency, which administers the Safe Drinking Water Act. Project proposals are reviewed, permitted, and monitored to ensure injected fluids are confined to the intended zone(s) and the groundwater resources are protected.

WELL AND PIPELINE CORROSION MONITORING

Due to the high temperature and acidic nature of some of California's geothermal resources, steel casings, wellheads, and pipelines have a potential to fail from corrosion, which can lead to serious injury and environmental damage.

Currently, Division engineers inspect pipelines visually; however, we are beginning a program to electronically monitor the thickness of wellheads and exposed casings of idle wells to determine how much corrosion may have occurred.

INTERAGENCY CONSULTING

The Division is frequently asked to provide its expertise to other governmental agencies. For example, the California Energy Commission asks the Division to review the adequacy of geothermal resources before permitting construction of new geothermal power plants.

In addition, Division staff have participated in advisory committees that review geothermal issues, and have assisted the State of Hawaii and the Government of Peru in evaluating the adequacy of drilling regulations.

PRODUCTION/INJECTION STATISTICS AND PUBLIC RECORDS

The Division also maintains a large library of data that can be invaluable in geothermal resource evaluations. Reservoir engineers are especially interested in the computerized database of virtually all geothermal production and injection records in the State. Hardcopy well histories, well logs, and other records of all nonfederal geothermal wells in California are also available to the public.

PUBLICATIONS

The Division also publishes geothermal information in many forms, for both technical and nontechnical audiences. In addition, we provide statistical, general, and technical data and publish maps that show the State's known high-temperature geothermal

wells. We have also worked with our sister agency, the Division of Mines and Geology, to prepare a map of California's known thermal sources.

WHAT HAVE WE LEARNED?

So what have we learned in the last 20 years? For one thing, the failure of a few projects has shown that lawyers, politicians, and accountants do not make good reservoir engineers. Also, the unexpected, accelerated production decline at The Geysers Geothermal field indicates geothermal reservoirs are subject to overdevelopment and excessive production. Therefore, if we are going to exploit our resources properly, decisions regarding production rates and development should be left to the reservoir experts. Also, no two geothermal fields are alike. No drilling, workover, or plugging operations go exactly as planned. Therefore, an effective regulatory program must have the flexibility to deal with a variety of situations. As regulators, we must keep an open mind and be open to new ideas and procedures.

As in our oil and gas program, we, at the Division, have found it far more productive to work with the industry to reach desired goals, than to fall back on a rigid set of rules and regulations that prove to be self-defeating. I feel we have accomplished that goal during the past 30 years, and I hope we continue in that direction in the future. Thank you.

PROCEEDINGS, Twentieth Workshop on Geothermal Reservoir Engineering
Stanford University, Stanford, California, January 24-26 1995
SGP-TR-150

PUBLIC INFORMATION PROJECTS OF THE GEOTHERMAL RESOURCES COUNCIL AND THE GEOTHERMAL ENERGY ASSOCIATION

David N. Anderson and Estela Smith

Geothermal Resources Council
P.O. Box 1350, Davis, California 95617-1350

ABSTRACT

During the past 20 years the Geothermal Resources Council (GRC), has grown and changed dramatically. An educational organization, the GRC sponsors an annual scientific meeting, and short courses, workshops, and symposia. Meetings and workshops typically are held at locations where members can also attend field trips. The GRC also publishes special reports, a monthly magazine, the GRC *BULLETIN*, and annual meeting transactions. The GRC On-line Information System, a relatively new service, is a library containing over 20,000 technical geothermal papers, articles, maps and periodicals. Presently, citations for 10,000 of these library materials are stored on computer and available via modem to users anywhere in the world. New citations are added to the library frequently.

The GRC's sister association, the Geothermal Energy Association (GEA), collaborates with the GRC on educational programs.

DISCUSSION

Education and dissemination of geothermal-related information are the GRC's primary mission and purpose for existence. In 1972, when GRC began, the emphasis was on educational programs in exploration, drilling, well testing, reservoir engineering and economics. Over the years, the emphasis has shifted. Today, GRC education programs focus on reservoir management, power generation, plant maintenance, project financing, and export of U.S. goods and services.

Although the content of the educational program has changed, the basic format has changed very little. As always, prices for meetings, courses, workshops, and educational materials are held as low as possible to allow all members to take advantage of the program.

The GRC and its sister association, the GEA, formerly the recently-merged National Geothermal Association (NGA) and the Geothermal Resources Association (GRA), share the same staff, offices, and office equipment, and occasionally are involved in the same projects. Although the GRC is an educational organization and the GEA is a trade association, their relationship is productive and beneficial to the geothermal community. Because of this close involvement, their information projects will also be discussed in context in this paper.

The predecessors of the GEA were founded in 1986 and 87 to develop representation in Washington, D.C. and to promote exports for U.S. companies. Although the GEA is a trade association, it features a significant educational program. Much of its program is designed to acquaint persons in other countries with the value of U.S. geothermal expertise.

The GRC and GEA presently offer the following information/educational programs:

ANNUAL MEETING

The GRC and GEA annual meetings are usually held in a western U.S. city in a hotel that meets criteria developed over the years by the GRC's meetings group. These meetings provide a wide range of general and theoretical information on all aspects of geothermal exploration, development and production. They normally feature 8 to 10 technical sessions and a trade show with 45 to 50 exhibitors. Two or three short courses or workshops are usually offered just prior to the meeting.

The opening session features knowledgeable keynote speakers discussing pertinent problems facing geothermal developers. Two or three field trips are usually scheduled after the meeting, along with several concurrent social events that allow attendees to exchange information, make contacts and consummate deals.

All of the technical papers submitted at an annual meeting are offset printed and hardbound into single volumes or sometimes in two volumes. Although these papers are not peer reviewed for absolute accuracy, they are reviewed for content, grammar and spelling by the Technical Program Committee of the Annual Meeting Committee. They are available for purchase at the meeting and after the meeting. The annual meeting policy of the GRC is to provide as much information as possible in the shortest amount of time.

SHORT COURSES AND WORKSHOPS

Next in importance to the annual meeting are the courses and workshops that are convened throughout the year. Including those convened at the annual meeting, the GRC and GEA together offer six to eight of these functions per year. The courses and workshops usually are held within the U.S.; however, both the GRC and the GEA are offering more and more of their courses and workshops in other countries.

Subjects of the courses and workshops over the years have included: introduction to geothermal resources; exploration; drilling; well testing; reservoir engineering; power plant design and construction; power plant maintenance; environmental aspects; financing, legal and other related subjects. Most courses and workshops last from one to four days, with two and one-half days as the average. The courses and workshops have been a prime source of information for a large number of U.S. geothermists over the last 20 years. Usually, these functions are also attended by a few international attendees, which adds to their appeal and importance.

All speakers at courses and workshops are asked to submit expanded outlines or copies of the papers(s) that they present. These are duplicated and inserted into binders (study guides) that are given to attendees when they register. In most cases, the study guides from courses also are available after the function to persons who did not attend.

SYMPOSIA

Occasionally, the GRC holds a symposium on a subject that is of high importance to the geothermal community. Symposia are usually offered at convenient locations in close proximity to the origin of the subject matter. For example, a symposium on the geothermal potential of the Cascade Mountain Range would be held in Portland, Oregon. The primary reason for locating a symposium near the subject area is that field trips to areas discussed are easily developed and attended. Topics for these functions are usually obvious and are generally of great interest to the geothermal community. Speakers usually are asked to produce papers, but sometimes this is not done due to time constraints. There is usually a set of papers produced for each function; however, some of the papers consist only of expanded outlines and copies of overhead transparencies. The papers and transparencies are duplicated, inserted into binders, and made available to the attendees. In some cases, these binders are made available for sale after the symposium to persons who did not attend.

In March of 1994, the GRC held two special symposia on subjects that are critical to the long range development of geothermal resources in the U.S. The titles were: "Sustainability of Geothermal Resources" and "Basin and Range Development." Both were two days in length, but they differed from the normal format in that all the invited speakers were asked to make 20-minute presentations concerning a common subject on the first day and, through discussions, arrive at some consensus on various problems on the subject on the second day. Both of these symposia were pointed directly at the solution of long time problems, and both were very successful. This format will be used again in the future, to help solve major problems and to clear the way for development of geothermal resources in areas plagued by show-stopping problems.

SPECIAL PUBLICATIONS

From time-to-time, GRC publishes special reports on topics that are pertinent to geothermal development. Seventeen special reports have been completed, and two new ones are now under development. Following is a selected list of titles:

- **Special Report No. 3** — *Geothermal Exploration in the First Quarter Century.*
- **Special Report No. 9** — *Commercial Uses of Geothermal Heat.*
- **Special Report No. 13** — *Role of Heat in the Development of Energy & Mineral Resources in the Northern Basin & Range Province.*
- **Special Report No. 17**— *Monograph on The Geysers Geothermal Field.*

Because of the success of these publications, the GRC will continue to publish special reports on any aspect of geothermal development and production that is of high interest to the geothermal community.

GRC ON-LINE INFORMATION SYSTEM

In 1992, the GRC began cataloging its in-house library. This collection of documents comprises 20,000 separate technical papers, articles, maps and periodicals. Most of the library materials were collected over a period of 20-plus years. In addition, the library was augmented by the addition of three major libraries that were donated to the GRC during the past 5 years.

With the help of the Department of Energy, funds for cataloging the library materials are now being used to maintain a full-time librarian and several students to assign keywords and sort publications. Five on-line data bases have been completed and made available to GRC members and the public via subscriptions. The data bases are described below:

Geothermal Data Base

Over 6,000 citations (titles, author(s), name of journal, publisher and page numbers) are now on-line; 50 percent of them have keywords assigned. By the end of 1994 over 10,000 citations should be available and the assignment of keywords to these citations should follow within six months. An additional 6,000 to 8,000 documents will be keyboarded during the next few years. Even in its present incomplete form, this on-line information system is the most comprehensive, pure geothermal library available to industry and the general public. In the years to come it likely will emerge as the single largest source of information on geothermal energy anywhere.

Geothermal Resources Council ***BULLETIN*** Data Base

The GRC publishes a monthly magazine, the GRC *BULLETIN*. It includes feature articles, announcements, and news about geothermal energy development around the world. There are 23 volumes and 199 issues, from 1972 to 1994. This GRC *BULLETIN* On-line data base is maintained on a monthly basis and it is an excellent historical reference journal. A description of the color photos used on the covers has also been included.

Heat Pump/Direct-Use and OIT Bulletin Data Base

The Geo-Heat Center at the Oregon Institute of Technology (OIT), using the same library software program and format as the GRC, has cataloged their library. It contains mostly direct-use and heat pump publications. The citations in this collection number over 3,400 and it has become an excellent adjunct to the GRC library. This data base is now part of the GRC on-line information system. Note that the GRC in-house library does not have hard copies of all OIT citations. If OIT library materials are not available in the GRC library, it will be noted on the citation that copies can be obtained through the Geo-Heat Center at OIT. OIT also has Bulletin, which contains news about technical advances in the industry. Citations for articles in OIT's Bulletin are included in the OIT data base.

Power Plant Data Base

In 1992, the GRC contracted to have a list compiled of all the geothermal power plants throughout the world and to display this material in a standard outline format. This data base, which numbers 228 power plants, was updated in late 1993 and early 1994 and a new, easier-to-read format was developed. This data base is unique in that the information it contains is not available in any other single place. A subscriber is able to search and print on his printer a detailed outline on any power station in the world in a matter of minutes. This data base will undergo continuous updating as new information is gathered. Country maps showing power plant locations are also available upon request from the GRC office.

U.S. Vendors of Geothermal Goods and Services

In 1993, the GRC contracted to have a list of the U.S. Vendors of Geothermal Goods and Services compiled into a single usable document. This list was subsequently keyboarded on to the library software and entered as one of the on-line data bases. This data base contains information on 168 U.S. vendors.

The GRC plans to add additional data bases over the next few years. Some of the proposed on-line data bases are:

- **Geothermal Standards** — Standards on all aspects of geothermal development are important and can save a considerable amount of time and money during design and construction of projects.
- **Statistics** — Statistics on all aspects of geothermal development since about 1960 will be compiled for geothermal resources in the U.S. This data base will include annually recorded items such as wells drilled, megawatts produced, power generation capacity installed, and other important data.
- **Well Data** — A great deal of well information exists for wells constructed in the U.S. — for example, locations, depths, lithology, tests, and well status. These data eventually will be keyboarded and offered as a data base for geothermal developers.

The library went on-line January 1, 1994; and by April 1 of the same year 10 companies had subscribed to the service. This is one third of the estimated 30 subscribers projected for 1994.

If information in the GRC library is needed quickly, it can be faxed or sent by express mail. There is a nominal charge for faxing up to six or eight sheets; however, a larger fee will be charged for extensive searches, copying, mailing, and express mail.

GENERAL INFORMATION

Through its staff, the GRC dispenses information on all aspects of geothermal exploration, development and production throughout the U.S.A. and the world. Information dispensed is in the form of brochures, flyers, maps, copied articles and data sheets. Data packets generally are mailed free of charge; however, if a request involves lengthy searches for articles or copying and mailing of heavy packages, a nominal labor charge plus mailing fee is imposed.

For additional information, contact the GRC office in Davis, California (916) 758-2360.

PROCEEDINGS, Twentieth Workshop on Geothermal Reservoir Engineering
Stanford University, Stanford, California, January 24-26 1995
SGP-TR-150

ARE THERE SIGNIFICANT HYDROTHERMAL RESOURCES IN THE U.S. PART OF THE CASCADE RANGE?

L.J. Patrick Muffler[1] and Marianne Guffanti[2]

[1]US Geological Survey, MS 910, Menlo Park, CA 94025
[2]US Geological Survey, MS 922, Reston, VA 22092

ABSTRACT

The Cascade Range is a geothermal dichotomy. On the one hand, it is an active volcanic arc above a subducting plate and is demonstrably an area of high heat flow. On the other hand, the distribution of hydrothermal manifestations compared to other volcanic arcs is sparse, and the hydrothermal outflow calculated from stream chemistry is low.

Several large estimates of undiscovered geothermal resources in the U.S. part of the Cascade Range prepared in the 1970s and early 1980s were based fundamentally on two models of the upper crust. One model assumed that large, partly molten, intrusive bodies exist in the upper 10 km beneath major volcanic centers and serve as the thermal engines driving overlying hydrothermal systems. The other model interpreted the coincident heat-flow and gravity gradients west of the Cascade crest in central Oregon to indicate a partly molten heat source at 10 ± 2 km depth extending $\approx$30 km west from the axis of the range. Investigations of the past ten years have called both models into question.

Large long-lived high-temperature hydrothermal systems at depths <3 km in the U.S. part of the Cascade Range appear to be restricted to silicic domefields at the Lassen volcanic center, Medicine Lake volcano, Newberry volcano, and possibly the Three Sisters. Federal land-use restrictions further reduce this list to Medicine Lake and Newberry. Dominantly andesitic stratocones appear to support only small transitory hydrothermal systems related to small intrusive bodies along the volcanic conduits. The only young caldera, at Crater Lake, supports only low- to intermediate-temperature hydrothermal systems. Most of the Cascade Range comprises basaltic andesites and has little likelihood for high-level silicic intrusions and virtually no potential for resultant large high-temperature hydrothermal systems. Undiscovered hydrothermal resources of the Cascade Range of the United States are substantially lower than previous estimates. The range does have potential for intermediate-temperature hot dry rock and localized low- to intermediate-temperature hydrothermal systems.

INTRODUCTION

This paper presents preliminary conclusions from a multi-year effort of the U.S. Geological Survey to evaluate the geothermal potential of the Cascade Range. A detailed assessment will be published as a Bulletin of the U.S. Geological Survey (Muffler and Guffanti, in preparation). Here we draw heavily on a manuscript (Guffanti and Muffler, 1995) submitted to the May 1995 World Geothermal Congress in Florence, Italy, as well as several recent publications of our USGS colleagues, particularly Ingebritsen *et al.* (1989, 1992, 1994), Mariner *et al.* (1990), and Blakely (1994).

TECTONIC AND VOLCANIC SETTING

The Cascade volcanic arc lies above the Cascadia subduction zone along which the small Gorda, Juan de Fuca, and Explorer plates are being subducted eastward under the large North American plate. The Cascade volcanic arc consists of two physiographic and geologic provinces (Peck *et al.*, 1964; Duncan and Kulm, 1989): the 42–10 Ma Western Cascades, and the 10–0 Ma High Cascades. Just east of the High Cascades are two large, essentially bimodal, basalt-rhyolite volcanoes: Newberry volcano in Oregon, and Medicine Lake volcano in northern California.

Major composite volcanoes that have erupted andesites, dacites, and even rhyolites occur at intervals of $\approx$100 km along the Cascade Range (Figure 1). In addition, there are several thousand smaller, discrete volcanoes that over the past five million years have erupted only once, or at most a few times, producing primarily basaltic andesite (see Guffanti and Weaver, 1988).

Sherrod and Smith (1990) estimated the following extrusion rates since 2 Ma in km^3 per km of arc length per million years:

- north of Mount Rainier: 0.21
- southern Washington and northern Oregon: 1.6
- central Oregon: 3–6
- northern California: 3.2.

The high extrusion rates for Oregon and northern California are determined in great part by the large volumes of basaltic andesite in Oregon and in the Lassen region of California (See Figure 3 of Sherrod and Smith, 1990).

The major Cascade volcanic centers are of four main types (Guffanti and Muffler, 1995):

Stratovolcanoes. These comprise the most common type, ranging in composition from predominantly andesitic (Mount Baker, Mount Adams, Mount Rainier, and Mount Hood) to more dacitic (Glacier Peak, Mount St. Helens, and Mount Shasta). Of these, Mount Shasta is the largest, having an extruded volume of 400 km^3, and the most silicic.

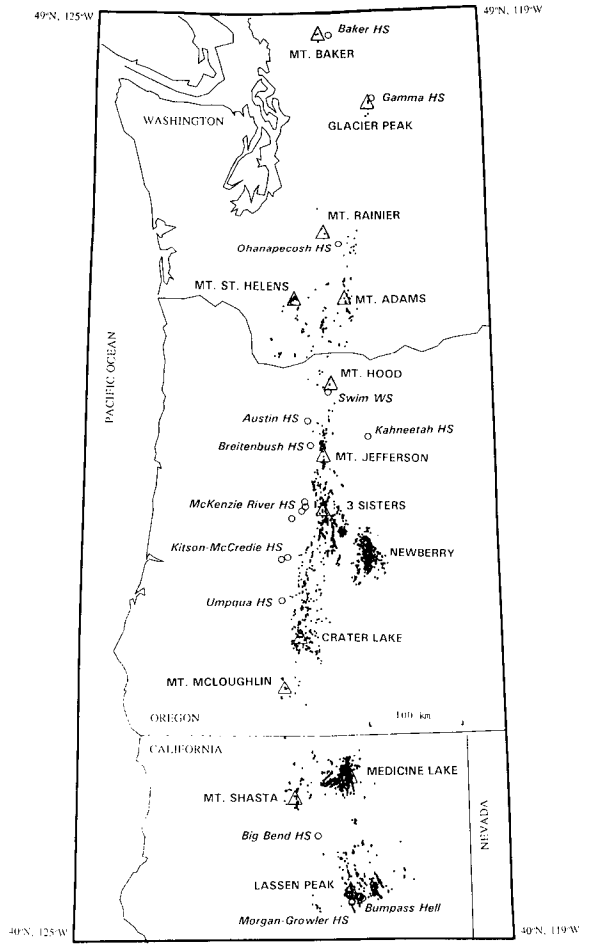

Figure 1. Volcanic setting of the Cascade Range, USA. Large triangles are major Quaternary volcanic centers. Small dots are individual volcanic vents younger than 730,000 years. Open circles are hot springs associated with known hydrothermal systems having subsurface temperatures ≥90°C. From Guffanti and Muffler (1995).

Composite centers. These are andesitic strato-volcanoes combined with silicic domefields and are exemplified by the Lassen volcanic center and the Three Sisters volcanic center.

Shield complexes. Two large shield complexes, Newberry volcano and Medicine Lake volcano, have developed on the east side of the Cascade Range where extensional tectonism of the back-arc-like Basin and Range province impinges on the Cascade Range. Both volcanoes are dominantly mafic, with silicic domes and flows of dacitic to rhyolitic composition typically found on the higher parts of the volcanic edifices. Both volcanoes have erupted numerous times during the past 10,000 years (MacLeod and Sherrod, 1988; Donnelly-Nolan, 1988).

Collapse caldera. The only large young collapse caldera is at Crater Lake, Oregon, where a catastrophic eruption of ≈50 km^3 of andesitic to dacitic magma occurred at Mount Mazama 7700 years ago (Bacon and Druitt, 1988).

The Cascade Range is characterized by a positive, conductive heat-flow anomaly (Blackwell and Steele, 1992). This anomaly has been investigated in detail in central Oregon, where the regional conductive heat flow of 100 mW m^{-2} of the Cascade Range is more than twice that of the Willamette Valley and Coast Range to the west; an abrupt heat-flow gradient separates the two regions (Blackwell *et al.*, 1990a).

Mariner *et al.* (1990), using a chloride-inventory method that detects both thermal water discharged in springs and thermal water discharged into streams, estimated that the total discharge of thermal springs in the Cascade Range of California, Oregon, and Washington was 340 L s^{-1}, corresponding to ≈82 MW_t. This value is approximately 5% of that estimated from Sumi (1980) for the minimum discharge of hot springs of the Tohoku volcanic arc (Muffler and Tamanyu, 1995). This difference in hydrothermal discharge between the two arcs also correlates qualitatively with the far greater number of thermal springs in the Tohoku arc (compare Sumi, 1975, with Figure 1a of Mariner *et al.*, 1990).

PREVIOUS GEOTHERMAL RESOURCE ASSESSMENTS OF THE CASCADE RANGE

Identified Geothermal Resources

Brook *et al.* (1979) identified seventeen geothermal systems ≥90°C in the Cascade Range (as used here to include Newberry, Kahneetah, Klamath Falls, and Klamath Hills). The sum of the individual energy figures given by Brook *et al.* (1979) for these systems is 118×10^{18} J (Table 1), with most of the energy residing in three major systems (Lassen at 42×10^{18} J, Newberry at 27×10^{18} J, and Klamath Falls at 30×10^{18} J).

Resources (identified thermal energy that can be extracted legally and used at some future time under reasonable economics) are even less. Laws and regulations prohibit geothermal development in National Parks and Wilderness Areas, where some of the most attractive targets exist. Accordingly, Brook *et al.* (1979) did not calculate geothermal resources in Lassen Volcanic National Park or at Ohanapecosh Hot Springs (in Mount Rainier National Park). Recoverable thermal energy from identified >150°C reservoirs totaled 8.3×10^{18} J, equivalent to 880 MW_e for 30 years. Of this, 740 MW_e was from Newberry and 116 MW_e from Morgan-Growler (probably southerly outflow from the large geothermal system centered in Lassen Volcanic National Park). Recoverable thermal energy from identified 90°–150°C reservoirs totaled 10.4×10^{18} J, with beneficial heat of 2600 MW_t for 30 years. These figures are dominated by Klamath Falls (resource = 7.4×10^{18} J; beneficial heat = 1890 MW_t for 30 years).

Reed *et al.* (1983) estimated reservoir energy for 36 low-temperature (<90°C) spring systems in the Cascade Range and calculated the mean resource (using a recovery factor of 0.25) and beneficial heat. The total reservoir energy of these systems is 3.5×10^{18} J (Mariner *et al.*, 1983, Table 5), and the total beneficial heat is 390 MW_t for 30 years

Wright (1991, 1992) estimated that the Cascades region may be capable of producing 750 MW_e of electrical power from geothermal generation in the next two decades, with most of this coming from Medicine Lake. No data were given to back up this estimate.

Undiscovered Geothermal Resources

The range of estimates of undiscovered geothermal resources in the Cascade Range (Table 1) is great, reflecting in great part the sparsity of drillhole information. An additional factor, however, is a profound geothermal dichotomy—*i.e.*, the existence of Quaternary volcanism and high regional heat flow opposed to the sparsity of hot springs and identified hydrothermal reservoirs of geothermal energy. Many workers have suggested that substantial quantities of geothermal energy are masked by cool, near-surface groundwater. This interpretation was encouraged by the discovery of 265°C temperatures at 930 m depth beneath Newberry volcano (Sammel, 1981), effectively masked by a surficial zone greater than 300 m thick at less than 100°C (Swanberg *et al.*, 1988). Optimism for the High Cascades, however, was balanced by Benoit (1983), who concluded that several geological, geochemical, and geophysical factors severely limit the chances of discovering and developing high-temperature geothermal reservoirs in the High Cascades of Oregon (excluding Newberry volcano).

Brook *et al.* (1979), on the basis of the favorable volcano-tectonic setting, multiplied the identified reservoir energy of the Cascade Range (including National Parks and Wilderness Areas) by a subjective factor of 20 to give an estimate of 1140×10^{18} J for the undiscovered accessible resource base to a depth of 3 km. Newberry volcano and Kahneetah were considered by Brook *et al.* (1979) to be part of the Oregon Plateaus geologic province, and Klamath Falls and Klamath Hills to be part of the northwestern Basin and Range province; in both these provinces, the undiscovered accessible resource base was estimated to be five times the identified. Thus the total undiscovered accessible geothermal resource base for the Cascade Range (as considered in this paper) can be estimated from the figures and assumptions of Brook *et al.* (1979) to be 1440×10^{18} J.

Mariner *et al.* (1983) estimated that the undiscovered accessible resource base <90°C was 10.5×10^{18} J, three times the thermal energy in identified low-temperature reservoirs. Corresponding figures for the resource and the beneficial heat would be 2.5×10^{18} J and 1170 MW_t for 30 years.

Black *et al.* (1983) calculated an accessible resource base for the Oregon Cascade Range of 105×10^{18} J to $16{,}000\times10^{18}$ J, with the corresponding range in electrical energy being 2500–370,000 MW_e for 30 years (excluding National Parks, etc.). The high figure assumed that most of the range is underlain at 1.75–3.0 km by a hydrothermal reservoir at 190°C. The low figure assumed permeability only in 100-m-wide fracture zones between 1.75 and 3.0 km depth. Black *et al.* (1983) stated that these estimates "***are based solely upon the conductive heat-flow anomaly underlying the Cascade Range east of the transition zone. Estimates for known (e.g., Austin and Breitenbush Hot Springs) or undiscovered hydrothermal systems masked by cool groundwater are not included, nor are estimates of residual heat remaining in igneous related systems ***."

Another large estimate of undiscovered geothermal resources in the Cascade Range was given by Bloomquist *et al.* (1985) for the Cascade Range in Oregon and Washington. Basing their calculations on the temperature-depth model of Blackwell *et al.* (1982), Bloomquist *et al.* (1985) inferred a geothermal reservoir 40–60 km wide with a reservoir thickness of 1.25 km in the southern part and 0.5 km in the northern part. Mean reservoir temperature in the southern part was estimated to be 190°C, and in the northern part, 165°C. Bloomquist *et al.* (1985) used these volumes in the accepted volumetric heat equation (Brook *et al.*, 1979, equation 1) to give a stored reservoir thermal energy between the 150°C isotherm and at depth of 3 km of 11,800–$17{,}600\times10^{18}$ J.

Bloomquist *et al.* (1985) also calculated thermal energy for individual geothermal systems in the Cascade Range. The total of these estimates (2400×10^{18} J) is heavily weighted by Mount McLoughlin and Crater Lake (500×10^{18} J and 1630×10^{18} J, respectively). Reservoir thicknesses and temperatures for these regions were based on the modeled crustal temperatures of Blackwell *et al.* (1982), and the areas were taken from associated Curie Point isotherm anomalies.

Table 1: *Estimates of geothermal energy in Cascade Range of USA. Numbers rounded to 2 significant figures.*

Temperature range (°C)	Accessible resource base (10^{18} J)	Resource (10^{18} J)	Electrical Energy (MW_e for 30 y)	Beneficial Heat (MW_t for 30 y)
Brook *et al.* (1979) identified (including Newberry, Kahneetah, Klamath Falls, & Klamath Hills)				
>150		8.3	880	
90–150		10.4		2600
≥90	118	18.7		
Reed *et al.* (1983) identified <90°C (all of Cascade Range				
	3.5	0.84		390
Wright (1992) (all of Cascade Range)				
			750 MW_e[a]	
Brook *et al.* (1979) undiscovered ≥90°C (including Newberry, Kahneetah, Klamath Falls, & Klamath Hills)				
>150	550–890[b]	138–220[b]	14,000–22,000[b]	
90–150	550–890[b]	138–220[b]		35,000–56,000[b]
≥90	1440	360		
Reed *et al.* (1983) undiscovered <90°C (all of Cascade Range)				
	10.5	2.5		1170
Black *et al.* (1983) (Cascade Range in Oregon; conductive regimes only)				
	105–16,000		2500–370,000	
Bloomquist *et al.* (1985) (Cascade Range in Oregon and Washington)				
	11,800–17,600		185,000–280,000	
Black (1994) (Cascade Range in Oregon, including Newberry; conductive regimes only)				
	2900		580–5800	

[a] Electrical capacity (time not specified)

[b] Range depends on whether one assumes constant reservoir volume *vs.* temperature or whether one assumes increase of reservoir volume with temperature of the line in figure 13 of Brook *et al.* (1979)

The large amounts of thermal energy calculated by Bloomquist *et al.* (1985) and by Black *et al.* (1983) at depths <3 km do not necessarily imply a large amount of recoverable geothermal energy. Much of the calculated thermal energy may be tied up in rock of low porosity and permeability ("hot dry rock") and thus be unavailable for conventional recovery as from a hydrothermal reservoir. Specifically, the recovery factor of 0.25 is far too high, perhaps by several orders of magnitude, for use throughout a geological province. Accordingly, the figures given by Bloomquist *et al.* (1985, p. 75) are probably two orders of magnitude too high.

Black (1994) presented an estimate of the geothermal power potential of the Cascade Range in Oregon, including Newberry volcano, based on a systematic calculation of thermal energy in each township at depths between the 150°C isotherm and a depth of 3 km, assuming a totally conductive thermal regime. Electrical energy for each block was calculated using a utilization factor of 0.4 and a range of recovery factors. The results were corrected to include only the part of each block not in a National Park or a Wilderness Area. The summary ranges (Table 1) reflect recovery factors of 0.25 and 0.025 for Newberry volcano and 0.025 and 0.0025 for the rest of the Cascade Range in Oregon, under the assumption that recovery factors for Newberry volcano are likely to be higher than for the rest of the Cascade Range in Oregon (Black, 1994, p. 9).

The implications of this analysis are not clear, primarily because of the lack of any specific criteria for choosing among the 10^3 range of recovery factors presented. Given that this analysis is based solely on conductive heat transfer (hydrothermal systems are specifically excluded), the analysis falls under the broad category of "hot dry rock", with any recovery factor being based upon the specific technology and economics anticipated.

UNDERLYING EARTH-SCIENCE MODELS

The optimism of the geothermal-resource assessments described above was predicated primarily on three factors: (1) the minimal amount of exploration and deep drilling carried out in the Cascade Range, (2) the large amounts of thermal energy estimated by Smith and Shaw (1975, 1979) to be in igneous-related systems to a depth of 10 km,

and (3) the heat-flow interpretation of Blackwell *et al.* (1982) and Blackwell and Steele (1983, 1985) that invoked an extensive upper-crustal heat source underlying both the Quaternary rock and adjacent older rocks. The first factor has not changed very much—geothermal exploration in the Cascade Range (with the exception of Newberry and Medicine Lake volcanoes) has been minimal, and there still are few deep drill holes. Factors 2 and 3, however, are amenable to re-analysis in the light of geological, geophysical, and geochemical data accumulated over the past two decades.

Geothermal resources related to crustal magmatism

The association of volcanic rocks with high- and intermediate-temperature geothermal systems has been noted for over three decades (e.g., Muffler, 1976). Accordingly, identification of the Cascade Range as a geothermal target was hardly surprising. The fact that High Cascade volcanism has persisted for ≈10 m.y. and is still continuing indicates that substantial mass and heat have been transmitted from the mantle through the crust, providing the potential for igneous heat sources that could support substantial overlying hydrothermal systems.

For such igneous activity to support a hydrothermal system, however, igneous rock must lodge in the upper crust at depths of 3–10 km. Smith and Shaw (1975) emphasized that "***basic rocks (basalts, andesite, and comparable magmas) are formed in the mantle and/or lower crust and rise to the surface through narrow pipes and fissures; the individual magma pulses are volumetrically small, and such systems contribute little stored heat to the upper crust until magma chambers begin to form at high levels. With the exception of large oceanic volcanoes, basic magmas do not form high-level storage chambers out of context with derivative silicic magmas (dacites, rhyolites, and comparable derivative magmas). On the other hand, we think that silicic magmas are always erupted from high-level storage chambers, probably in the upper 10 km of the crust".

The significance of the estimates of Smith and Shaw (1975, 1979) for "igneous-related geothermal systems" is in the role that young, still hot, silicic intrusions can play in supporting overlying hydrothermal systems in the upper crust. If the volume of young magma chambers (whether still molten or already partially cooled) in the upper crust is substantial, there ought to be substantial overlying hydrothermal systems. But if the volume of young intrusive material in the upper crust is small, the heat sources to support overlying convection of meteoric water are doomed to be few and impotent.

The tables of Smith and Shaw (1975, 1979) presented estimates of thermal energy still remaining in silicic intrusions and adjacent country rock, calculated by conductive cooling models using estimates of the size and age of intrusions (these estimates are critically dependent on the volumes assumed). Smith and Shaw (1979) estimated that roughly $3{,}900\times10^{18}$ J remain today to depths of 10 km in eleven igneous-related systems in the Cascade Range (including Medicine Lake and Newberry volcanoes) for which data available in 1978 allowed such calculations. They further noted that additional igneous-related energy resides in systems not evaluated because of insufficient data. They gave no estimate specific to the Cascade Range, but for the entire United States they estimated that the unevaluated geothermal energy in igneous-related geothermal systems is perhaps 10 times that which could be evaluated in 1978. If this ratio applies to the Cascade Range, the implication is that greater than $40{,}000\times10^{18}$ J remain today in volcanic areas of the Cascade Range, to a depth of 10 km. It is this figure that had major influence upon the estimate of Brook et *al.* (1979) that the undiscovered hydrothermal resource to depths of 3 km beneath the Cascade Range was 20 times the identified resource. It did not appear unreasonable that the hydrothermal resource at depths <3 km could be ≈4% of the igneous-related thermal energy.

Extensive mid-crustal heat source beneath the Cascade Range

High heat flow measured in the Cascade Range has also been used to suggest a substantial volume of molten or still high-temperature igneous rock at depths of 10±2 km beneath the Cascade Range (Blackwell *et al.*, 1982, 1990b). Heat flow in the Cascade Range is undeniably high, ≈100 mW m^{-2}, contrasting with heat flow of 40–50 mW m^{-2} to the west (Blackwell *et al.*, 1982, 1990a, 1990b; Blackwell and Steele, 1992). Blackwell *et al.* (1982, figure 8) converted the heat-flow data in central Oregon to a set of isotherms in the crust. The solution is not unique—any one of these isotherms can explain the heat-flow data. The choice that Blackwell *et al.* (1982) made among the isotherms was based on comparison with regional Bouguer gravity data, under the fundamental assumption that the change in Bouguer gravity along this cross section "is directly associated with the same phenomenon which causes the change in heat flow" (Blackwell *et al.*, 1982, p. 8,749). They argued that the observed gravity anomaly is much too great to be explained by simple thermal expansion of rock at any of the subsolidus temperatures of their Figure 8. Accordingly, they concluded that partial melting is required, with partial melting at a depth of 6 to 10 km giving the best correspondence to the observed gravity data. Although Blackwell *et al.* (1982, Figure 10) presented several other models to explain the heat-flow data, they preferred "the model that relates the gravity and heat flow data to a (large) zone of hot, low-density (partially molten) material in the upper part of the crust (10±2 km) beneath the High Cascade Range and extending about 10 km west of the High Cascade Range boundary." (p. 8750 of Blackwell *et al.*, 1982; see also Blackwell and Steele, 1985, Figure 3, and Blackwell *et al.*, 1990a, 1990b).

Blackwell *et al.* (1982) projected the thermal and gravity cross sections to the north and to the south from central Oregon, based upon the uniformity of the heat-flow and Bouguer gravity transition zones. The resultant geometry—a uniform heat source 40-60 km wide (Blackwell and Steele, 1983) at temperatures of 600–800°C extending under the entire Cascade Range—became the philosophical basis for the estimates of Black *et al.* (1983), Bloomquist *et al.* (1985), and Black (1994).

Blakely (1994), however, has used ideal-body analysis to show that the gravity gradient must be caused by density variations in the upper 2.5 km of the crust, most likely a relict boundary between a pre-Oligocene extensional trough to the east and oceanic crust to the west. Blakely's conclusion precludes interpretation of the gravity and heat-flow gradients as caused by the same hot mid-crustal mass. Consequently, the gravity data can not be used to choose between the thermal models presented by Blackwell *et al.* (1982, Figure 10).

In addition, Blakely (1994, figure 9) compared the observed heat flow in central Oregon (from Blackwell, 1982) with the conductive heat flow expected above semi-infinite heat sources located at various depths (from Lachenbruch *et al.*, 1976). This comparison demonstrates that the heat-flow gradient is too abrupt to be explained by conductive heat sources deeper than 5 km.

Ingebritsen *et al.* (1989, 1992, 1994) recontoured the heat-flow data in central Oregon and presented a map displaying significant complexity, in contrast to the simple, linear north-south contours of Blackwell *et al.* (1982, 1990b) and Blackwell and Steele (1993). On the basis of this map, isotopic studies, and hydrologic modeling, Ingebritsen *et al.* (1989, 1992, 1994) argued that high heat-flow values west of the Cascade crest are due to lateral outflow of water heated by discrete igneous centers along a relatively narrow zone of magmatism along the Cascade crest.

LOCALIZED MAGMATIC HEAT SOURCES

The composition, depth, and configuration of possible magmatic heat sources in the US part of the Cascade Range were analyzed by Guffanti and Muffler (1995) and by Muffler and Guffanti (in preparation), on the basis of extensive investigations of the USGS in the Cascade Range during the past two decades. They concluded that large, silicic, upper-crustal intrusions capable of supporting major, high-temperature, hydrothermal systems occur only in some of the major volcanic centers. At the thousands of smaller short-lived mafic volcanoes of the Cascade Range in Oregon and northern California, mafic magma is stored deeper than 10 km and is transported to the surface quickly in only narrow conduits. Only small volumes of magma are stored in the upper crust at any time, there is little likelihood for sizable high-level intrusions, and resultant long-lived, high-temperature hydrothermal systems are unlikely.

Furthermore, even the major volcanic centers display widely differing hydrothermal potential (Guffanti and Muffler, 1995; Muffler and Guffanti, in preparation). At predominantly andesitic stratovolcanoes (Mount Baker, Mount Adams, Mount Rainier, and Mount Hood), hydrothermal activity occurs primarily in the vicinity of the narrow, still-warm magmatic conduit within the volcanic cone and is transitory, as shown by Shevenell (1990) and Shevenell and Goff (1993) at Mount St. Helens. In addition, lateral transport of thermal fluids away from the cone involves substantial mixing with cold groundwater flowing within the volcanic edifice. Geothermal potential at stratovolcanoes appears to be modest, although deep undiscovered hydrothermal resources can not be precluded, particularly at the more dacitic stratocones (Mount Shasta, Mount St. Helens, and Glacier Peak). At composite centers (Lassen; Three Sisters), shallow intrusions related to young silicic domes appear to be effective heat sources for hydrothermal circulation. At the only young explosive caldera (Crater Lake), a catastrophic eruption of the shallowest and most silicic part of the magma chamber 7700 years ago removed a potent heat source from the upper crust. A viable heat source may remain, however, as the deeper (>7.5 km) andesitic portion of the magma chamber, and discrete intrusive bodies associated with pre-caldera dome eruptions may act as effective shallow heat sources for hydrothermal systems of modest temperature. Indeed, the chemistry of the large-volume, 5–10°C, Wood River group of springs south of Crater Lake has been interpreted by Nathenson *et al.* (1994) to indicate a heat discharge of 87 MW_t. Finally, the shield complexes of Newberry volcano and Medicine Lake volcano, along the boundary with the Basin and Range province, have high geothermal potential. The shallow intrusive plexuses of sills and dikes that underlie the centers apparently provide favorably configured heat sources for hydrothermal circulation, although no single mafic or silicic intrusion is large.

Known high-temperature hydrothermal systems in the U.S. Cascade Range are associated with silicic domefields at Medicine Lake volcano, Newberry volcano, Lassen volcanic center, and perhaps in north-central Oregon in the vicinity of Mt. Jefferson and Three Sisters. It appears significant that these sites are in extensional settings where the southern Cascades adjoins the Basin and Range province.

LAND-USE CONSIDERATIONS

Any evaluation of hydrothermal potential of the Cascade Range must take into account the spatial relationship between volcanic centers likely to have upper-crustal intrusions capable of supporting major high-temperature hydrothermal systems and areas subject to land-use restrictions. For example, hydrothermal systems in National Parks (most conspicuously the Lassen hydrothermal system) are not available for any geothermal development. Similar restrictions apply to hydrothermal systems in Wilderness Areas, thus eliminating virtually all of the

volcanic centers in the High Cascades. Development of hydrothermal systems adjacent to a National Park (e.g., Crater Lake caldera) is likely only if it can be convincingly demonstrated that there will be no adverse effect on hydrothermal phenomena or other protected aspects of the Park.

CONCLUSIONS

Newberry and Medicine Lake volcanoes are the main (and possibly the only) high-temperature geothermal targets in the Cascade Range. Newberry was included in identified resources by Brook *et al.* (1979), whereas Medicine Lake was included with undiscovered resources by Brook *et al.* (1979) but certainly now should be considered an identified resource. Klamath Falls remains the major identified intermediate-temperature hydrothermal system. The Cascade Range does have significant additional potential for localized low- to intermediate-temperature hydrothermal systems and for intermediate-temperature hot dry rock. Deep (>2 km) cryptic high-temperature hydrothermal systems at the major volcanic centers cannot be precluded, but their reservoir characteristics and resource potential cannot be evaluated without deep drilling data. Overall, undiscovered hydrothermal resources of the Cascade Range of the United States appear to be substantially less than published numerical estimates, a conclusion presaged by Benoit (1983).

REFERENCES CITED

Bacon, C.R., and Druitt, T.H., 1988, Compositional evolution of the zoned calcalkaline magma chamber of Mount Mazama, Crater Lake, Oregon: Contributions to Mineralogy and Petrology, Vol. 98, p. 224–256.

Benoit, W.R., 1983, An explorationist viewpoint of the high-temperature geothermal potential of the Cascade Range in Oregon: Geothermal Resources Council Transactions, v. 7, p. 227–232.

Black, G.L., 1994, Geothermal electrical power generation potential of Newberry Volcano and the Oregon Cascade Range: Oregon Department of Geology and Mineral Industries Open-File Report O-94-07, pp. 1–74.

Black, G.L., Blackwell, D.D., and Steele, J.L., 1983, Heat flow in the Oregon Cascades, in Priest, G.R., and Vogt, B.F., eds., Geology and geothermal resources of the central Oregon Cascade Range: Oregon Department of Geology and Mineral Industries Special Paper 15, p. 69–76.

Blackwell, D.D., Bowen, R.G., Riccio, Joseph, and Steele, J.L., 1982, Heat flow, arc volcanism, and subduction in northern Oregon: Journal of Geophysical Research, v. 87, p. 8735–8754.

Blackwell, D.D., and Steele, J.L., 1983, A summary of heat flow studies in the Cascade Range: Geothermal Resources Council, v. 7, p. 233–236.

Blackwell, D.D., and Steele, J.L., 1985, Heat flow of the Cascade Range, in Guffanti, Marianne, and Muffler, L.J.P., eds., Proceedings of the Workshop on Geothermal Resources of the Cascade Range, May 22–23, 1985, Menlo Park, California: U.S. Geological Survey Open-File Report 85-521, p. 20–23.

Blackwell, D.D., and Steele, J.L., 1992, Geothermal map of North America: Geological Society of America, DNAG Neotectonics Series, scale 1,500,000, 4 sheets.

Blackwell, D.D., Steele, J.L., Frohme, M.K., Murphey, C.F., Priest, G.R., and Black, G.L., 1990a, Heat flow in the Oregon Cascade Range and its correlation with regional gravity, Curie point depths, and geology: Journal of Geophysical Research, v. 95, p. 19,475–19,493.

Blackwell, D.D., Steele, J.L., Kelley, S., and Korosec, M.A., 1990b, Heat flow in the state of Washington and thermal conditions in the Cascade Range: Journal of Geophysical Research, v. 95, p. 19,495–19,516.

Blakely, R.J., 1994, Extent of partial melting beneath the Cascade Range, Oregon: constraints from gravity anomalies and ideal-body theory: Journal of Geophysical Research, v. 99, p. 2757–2773.

Bloomquist, R.G., Black. G.L., Parker, D.S., Sifford, A., Simpson, S.J., and Street, L.V., 1985, Evaluation and ranking of geothermal resources for electrical generation or electrical offset in Idaho, Montana, Oregon and Washington: Bonneville Power Administration, DOE/BP-13609-1, v. 1, 504 p.

Brook, C.A., Mariner, R.H., Mabey, D.R., Swanson, J.R., Guffanti, Marianne, and Muffler, L.J.P., 1979, Hydrothermal convection systems with reservoir temperatures ≥90°C, in Muffler, L.J.P., ed., Assessment of Geothermal Resources of the United States--1978: U.S. Geological Survey Circular 790, p. 18–85.

Donnelly-Nolan, J.M., 1988, A magmatic model of Medicine Lake volcano, California: Journal of Geophysical Research, v. 93, p. 4412–4420.

Duncan, R.A., and Kulm, L.D., 1989, Plate tectonic evolution of the Cascades arc-subduction complex: Geological Society of America, The Geology of North America, v. N, p. 413–438.

Guffanti, Marianne, and Muffler, L.J.P., 1995, Geothermal potential of diverse volcanotectonic settings of the Cascade Range, USA: Proceedings of the World Geothermal Congress, Florence, Italy, May 1995, International Geothermal Association (in press).

Guffanti, Marianne, and Weaver, C.S., 1988, Distribution of late Cenozoic volcanic vents in the Cascade Range: volcanic arc segmentation and regional tectonic considerations: Journal of Geophysical Research, v. 93, p. 6513–6529.

Ingebritsen, S.E., Mariner, R.H., and Sherrod, D.R., 1994, Hydrothermal systems of the Cascade Range, north-central Oregon: U.S. Geological

Survey Professional Paper 1044-L, 86 p.

Ingebritsen, S.E., Sherrod, D.R., and Mariner, R.H., 1989, Heat flow and hydrothermal circulation in the Cascade Range, north-central Oregon: Science, v. 243, p. 1458–1462.

Ingebritsen, S.E., Sherrod, D.R., and Mariner, R.H., 1992, Rates and patterns of groundwater flow in the Cascade Range volcanic arc, and the effect on subsurface temperatures: Journal of Geophysical Research, v. 97, p. 4599–4627.

Lachenbruch, A.H., Sass, J.H., Munroe, R.J., and Moses, T.H., Jr., 1976, Geothermal setting and simple heat conduction models for the Long Valley caldera: Journal of Geophysical Research, v. 81, p. 769–784.

MacLeod, N.S., and Sherrod, D.R., 1988, Geologic evidence for a magma chamber beneath Newberry volcano, Oregon: Journal of Geophysical Research, v. 93, p. 10,067–10,079.

Mariner, R.H., Brook, C.A., Reed, M.J., Bliss, J.D., Rapport, A.L., and Lieb, R.J., 1983, Low-temperature geothermal resources in the western United States, in Reed, M.J., ed., Assessment of low-temperature geothermal resources of the United States—1982: U. S. Geological Survey Circular 892, p. 31–50.

Mariner, R.H., Presser, T.S., Evans, W.C. and Pringle, M.K.W., 1990, Discharge rates of fluid and heat by thermal springs of the Cascade Range, Washington, Oregon, and Northern California: Journal of Geophysical Research, v. 95, p. 19,517–19,531.

Muffler, L.J.P., 1976, Tectonic and hydrologic control of the nature and distribution of geothermal resources: Proceedings of the Second United Nations Symposium on the Development and Use of Geothermal Resources, San Francisco, 1975, v. 1, p. 499-507.

Muffler, L.J.P., and Guffanti, Marianne, Geothermal resource assessment of the Cascade Range of California, Oregon, and Washington: U.S. Geological Survey Bulletin (in preparation).

Muffler, L.J.P., and Tamanyu, Shiro, 1995, Tectonic, volcanic, and geothermal comparison of the Tohoku volcanic arc (Japan) and the Cascade volcanic arc (USA): Proceedings of the World Geothermal Congress, Florence, Italy, May 1995, International Geothermal Association (in press).

Nathenson, Manuel, R.H. Mariner, and J.M. Thompson, 1994, Convective heat discharge of Wood River group of springs in the vicinity of Crater lake, Oregon: Geothermal Resources Council Transactions, v. 18, p. 229–236.

Peck, D.L., Griggs, A.B., Schlicker, H.H., Wells, F.G., and Dole, H.M., 1964, Geology of the central and northern parts of the western Cascade Range in Oregon: U.S. Geological Survey Professional Paper 449, 56 p.

Reed, M.J., R.H. Mariner, C.A. Brook, and M.L. Sorey, 1983, Selected data for low-temperature (less than 90°C) geothermal systems in the United States; reference data for U. S. Geological Survey Circular 892: U. S. Geological Survey Open-File Report 83-250, 129 p

Riddihough, R.P., 1984, Recent movements of the Juan de Fuca plate system: Journal of Geophysical Research, v. 89, p. 6980–6994.

Sammel, E.A., 1981, Results of test drilling at Newberry volcano, Oregon—and some implications for geothermal prospects in the Cascades: Geothermal Resources Council Bulletin, v. 10, no. 11, p. 3–8.

Sherrod, D.S., and Smith, J.H., 1990, Quaternary extrusion rates of the Cascade Range, northwestern United States and southern British Columbia: Journal of Geophysical Research, v. 95, p. 19,465–19,474.

Shevenell, L., 1990, Chemical and isotopic investigation of the new hydrothermal system at Mount St. Helens, Washington, University of Nevada, Reno, Ph.D. dissertation, 282 p.

Shevenell, L., and Goff, F., 1993, Addition of magmatic volatiles into hot spring waters of Loowit Canyon, Mount St. Helens, Washington, USA: Bulletin of Volcanology, v. 55, p. 489–503.

Smith, R.L., and Shaw, H.R., 1975, Igneous-related geothermal systems, in White, D. E., and Williams, D. L., eds., Assessment of geothermal resources of the United States--1975: U. S. Geological Survey Circular 726, p. 58–83.

Smith, R.L., and Shaw, H.R., 1979, Igneous-related geothermal systems, in Muffler, L. J. P., ed., Assessment of geothermal resources of the United States--1978: U. S. Geological Survey Circular 790, p. 12–17.

Sumi, Kiyoshi, 1975, Distribution map of hot springs in Japan (2nd edition): Geological Survey of Japan, 1:2,000,000 Map Series, No. 8.

Sumi, Kiyoshi, 1980. Distribution map of heat discharge by hot springs in Japan: Geological Survey of Japan, 1:2,000,000 Map Series, No. 21.

Swanberg, C.A., Walkey, W.C., and Combs, Jim, 1988, Core hole drilling and the "rain curtain" phenomenon at Newberry volcano, Oregon: Journal of Geophysical Research, v. 93, p. 10,163–10,173.

Wright, P.M., 1991, Exploration potential for new hydrothermal resources for electrical power generation in the 48 contiguous United States: Geothermal Resources Council Transactions, v. 15, p. 217–228.

Wright, P.M., 1992, Exploration potential for new hydrothermal resources for electrical power generation in the 48 contiguous United States: Geothermal Resources Council Bulletin, v. 21, no. 2, p. 31–43.

PROCEEDINGS, Twentieth Workshop on Geothermal Reservoir Engineering
Stanford University, Stanford, California, January 24-26 1995
SGP-TR-150

THERMAL EXTRACTION ANALYSIS OF FIVE LOS AZUFRES PRODUCTION WELLS

Paul Kruger
SGP
Stanford University
Stanford, CA

Luis Quijano
GPG
Com. Fed. de Elec.
Morelia, Mich.

ABSTRACT

Thermal energy extraction from five wells supplying 5-MWe wellhead generators in three zones of the Los Azufres geothermal field has been examined from production and chemical data compiled over 14-years of operation. The data, as annual means, are useful in observing small-scale changes in reservoir performance with continuous production. The chemical components are chloride for quality control and the geothermometer elements for reservoir temperatures. The flowrate and fluid enthalpy data are used to calculate the thermal extraction rates. Integration of these data provides an estimate of the total energy extracted from the zone surrounding the well. The combined production and chemical geothermometer data are used to model the produced fluid as coming from just-penetrating wells for which the annual produced mass originates from a series of concentric hemispheric shells moving out into the reservoir. Estimates are made of the drawdown distance into the reservoir and the far-field conditions.

INTRODUCTION

The Los Azufres geothermal field, located 100 miles west of Mexico City, has produced electricity since August, 1982 with the installation of five 5-MWe backpressure wellhead units. The capacity of the field has since grown to 98 MWe (Quijano and Sanchez, 1993) which includes another four 5-MWe units. The field is characterized by a series of east-west faults with two areas of intense fracturing: (1) Tejamaniles-Agua Fria to the south and (2) El Chino-Maritaro to the north. The location of the five study wells with respect to the faulting system is shown in Figure 1.

With the initiation of operations in 1982, an extensive database has been compiled by CFE to monitor the properties of the total Los Azufres geothermal field. One aspect of the overall program has been a joint project between CFE and the Stanford Geothermal Program to evaluate the extent of changes observable by operation of small (5-MWe) generating units in a potentially large (> 200 MWe) geothermal field. The joint project consisted of three study phases:

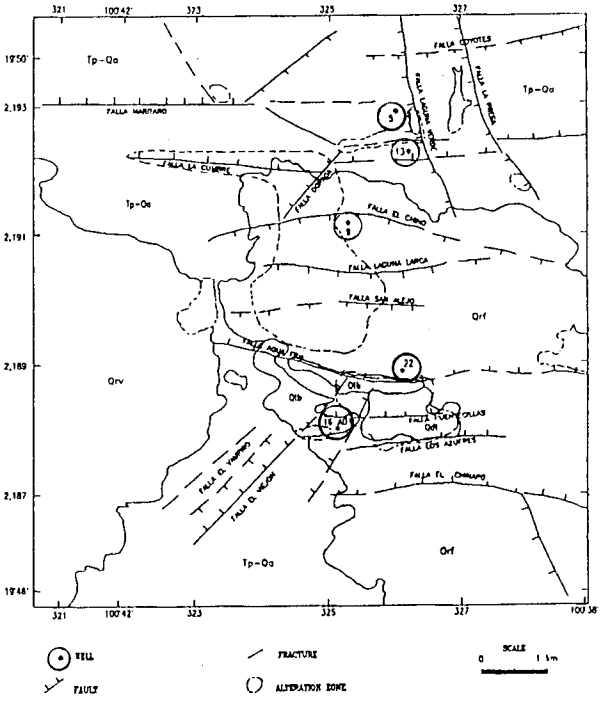

Fig.1. The Los Azufres geothermal field showing the location of the five study wells in relation to the main faulting system.

(1) data reduction and trend analysis of the production and chemical data for selected wells in the major production zones of the field; (2) evaluation of the combined data in relation to reservoir thermodynamic conditions: and (3) analysis of thermal extraction with respect to deliverability, longevity, and reservoir volume.

In the initial study, the wells selected were the wells supplying steam to the original five generating units. The results of the study after 2 and 2.5 years of operation of these wells were reported by Kruger, et al (1985a,b) and after 4 years by Kruger, et al (1987). Results after 5 years of operation with changes in the well-generator couplings were reported by Kruger, Sanchez, and Ortiz (1989). Analysis of the compiled

Table 1
Well Production History

Zone	Well No.	Startup Year		Years
		Well	Unit	Prodn
Maritaro	Az-5	1979	1982	14
	Az-13	1980	1982	14
El Chino	Az-9	1987	1988	7
Tejamaniles	Az-16AD	1983	1984	11
	Az-22	1981	1987	13

data for 5 wells covering three major production zones continued by Kruger and Gutierrez (unpublished) until 1991 when it was determined that the production and chemical data for these wells prior to generation of electricity had not been included in the joint study. Re-analysis of the database for the five wells is examined in this report.

Table 1 lists the five Los Azufres wells in the Maritaro, El Chino, and Tejamaniles production zones and the startup dates for the wells and generators. Since an important part of the well production history occurs in the early years of its life, attempt was made to obtain all available pre-generation data. The production data for the wells consisted of semester and annual means of the wellhead and separator pressures, the liquid- and steam-phase flowrates, and wellhead enthalpy. The chemical data consisted of chloride concentration for quality control, sodium-potassium-calcium concentrations for far-field temperatures (Fournier and Truesdell, 1973), and silica concentration for near-field temperature (Fournier and Potter, 1982). The individual data were evaluated for short-term by the Student t-test and for long-term small changes in reservoir characteristics by trend analysis. The combined data were used to estimate the thermal extraction rate and cumulative thermal energy extraction. The volummetric behavior of the reservoir was examined as "just-penetrating" wells in a large well-fractured medium by the method of Muskat (1937).

MODEL OF "JUST-PENETRATING" WELLS

The wells drilled into the Los Azufres geothermal reservoir may be visualized (as shown in Figure 2) as "just-penetrating" wells, in which drilling stops when a zone of well-fractured, fluid-bearing, permeable rock is encountered. The "just-penetrating" well was described by Muskat (1937) for porous media in which production over time is given as concentric hemispherical volumes moving out into the reservoir. Since the Los Azufres geothermal field consists of a dense network of fracturing between major E-W faults, the application of the model for porous media should be sufficiently sensitive for examining drawdown around the well-fractured wellbore zones.

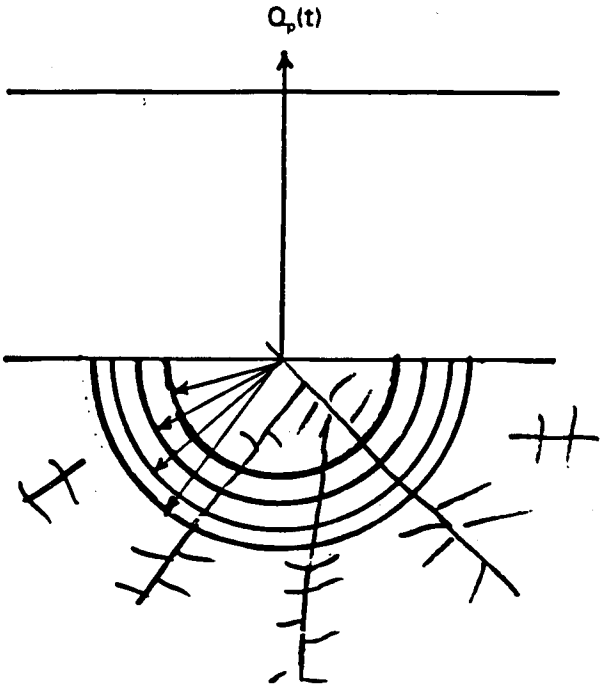

Fig. 2. Schematic of a "just-penetrating" well with concentric hemispherical zones over well-fractured media around the wellbore.

Muskat (1937) noted that the potential, Φ, for a "just-penetrating" well is given by

$$\Phi = - k/\mu \, (p - \rho g z) \qquad (1)$$

where k = permeability
μ = viscosity
p = pressure
$\rho g z$ = hydrostatic head

The "just-penetrating" well differs from the line-source well in that the relationship between flowrate and potential is linear rather than logarithmic and is given by

$$Q = 2\pi(\phi_e - \phi_w) \,/\, (1/r_w - 1/r_e) \qquad (2)$$

where ϕ_e = far-field potential
r_e = far-field radius
ϕ_w = well-bottom potential
r_w = well radius

To examine the extent of the Los Azufres wells as "just-penetrating" into a well-fractured reservoir, it was assumed that the reservoir pressure is much greater than the hydrostatic pressure ($p \gg \rho g z$) and that the pressure in the i^{th} concentric hemisphere is approximated by the far-field pressure ($p_o \approx p_e$). Thus,

Table 2
Annual Averaged Production Data
Well: Az-5 1979-93

Year No.	P(wh) (MPa)	T(wh) (C)	P(sp) (MPa)	Q(v) (kg/s)	X(v) (%)	Q(t) (kg/s)	Mass (Mt)	H(wh) (kJ/kg	TER (MJ/s)	FT (%)	HE (PJ)
1'79	2.62	219	0.07	14.2	61.6	23.0	0.598	1739	40.0	91.7	1.160
2'80	2.64	221	0.07	13.9	64.8	21.5	0.620	1820	39.0	100.0	1.234
3'81	3.21	237	0.07	9.3	61.5	15.1	0.447	1711	25.8	100.0	0.814
4'82	2.70	228	0.85	17.5	65.3	26.8	0.799	2008	53.7	91.7	1.556
5'83	2.81	230	0.94	16.6	62.0	26.8	0.850	2005	53.8	100.0	1.699
6'84	2.49	224	1.01	17.8	61.5	29.0	0.902	1988	57.6	100.0	1.821
7'85	2.58	225	0.99	18.0	61.5	29.2	0.797	1987	58.1	83.3	1.530
8'86	2.42	222	0.98	18.0	63.1	28.5	0.872	2039	58.2	100.0	1.838
9'87	2.37	221	0.92	17.5	63.1	27.8	0.845	2009	55.8	91.7	1.615
10'88	2.12	214	0.92	17.8	59.1	30.1	0.962	1926	58.0	100.0	1.834
11'89	2.17	217	0.98	17.5	57.5	30.4	0.941	1919	58.3	100.0	1.843
12'90	2.08	215	1.00	18.2	56.2	32.3	1.018	1893	61.2	100.0	1.933
13'91	1.70	204	0.81	18.3	59.9	30.6	0.810	1960	60.0	100.0	1.895
14'92	1.34	193	1.00	18.9	66.4	28.5	0.884	2100	59.8	100.0	1.890
Total							11.35				22.66
Avg.	2.38	219		16.7	61.7	27.1		1936	52.8		

the mean pressure in hemispherical shell i is given by

$$\overline{p}_o = \mu\overline{Q}/2\pi k\ (1/r_w - 1/R_e) + \overline{p}_w \qquad (3)$$

where R_o is the radius of shell i. If it is further assumed that parameters μ, k, r_w, Q, and p_w do not change appreciably with production time, the hemispherical shell pressure is given by the linear relationship

$$p_o = a + b/R_o \qquad (4)$$

in which a and b are given by the quasi-constant parameters:

$$a = \mu\overline{Q}/2\pi k r_w + \overline{p}_w \qquad b = \mu\overline{Q}/2\pi k \qquad (5)$$

The value for pressure in shell i is obtained as the saturation temperature for that shell, estimated from the Na-K-Ca geothermometer described by Fournier and Truesdell (1973).

DATA ANALYSIS

Preparation of the data for analysis consisted of converting each measurement in the CFE database to a consistent set of S.I. units, pressure adjusted to MPa-absolute, flowrate to kg/s, enthalpy to kJ/kg, and thermal extraction rate to MJ/s. To maintain an even distribution of measurements by time, individual measurements were averaged over each month. Thus some months with 6 or 7 measurements were given the same weight in the semester or annual average as months with only 1 or 2 measurements, although the latter had larger standard deviations. The smoothing by longer-period averages provides more readily observable small changes over long periods.

An example of the resulting averaged production data (for well Az-5) is given in Table 2. The cumulative mass for the three plus years of flow before generation is about 18 percent of the 14-year total of 11.35 Mt. The cumulative heat extracted is also about 18 percent of the total. The data were corrected for shut-in times, estimated in weeks, in the fractional time (FT) column. An overview summary of the thermal production data for the five selected wells in the three production zones is given in Table 3.

An example of the trends of the chemical data (for well Az-5) is given in Table 4. with the resulting geothermometer temperatures. A summary of the mean chloride concentration for the total production period for each of the five wells is given in Table 5. The uncertainty in chloride measurements derived from sampling and analytical procedures is estimated by the Los Azufres staff as less than ±5 %. Therefore, the

Table 3
Summary of Thermal Production

	Production Zone				
	Maritaro		El Chino	Tejamaniles	
Well Number Az:	5	13	9	16AD	22
Years of Production	14	14	7	11	13
Mean T(wh) (°C)	219	189	171	179	225
Mean Enthalpy(kJ/kg)	1936	1909	1703	224	1633
Mean TER (MJ/s)	52.8	47.5	34.3	19.6	61.4
Mass Extracted (Mt)	11.4	9.49	3.91	2.69	12.7
Heat Extracted (PJ)	22.7	17.4	6.68	6.21	22.7

Table 4
Annual Averaged Chemical Data
Well: Az-5 1979-93

Year No.	Dates	[Na] (mg/l)	[K] (mg/l)	[Ca] (mg/l)	[Cl] (mg/l)	[SiO2] (mg/l)	T(Na/K) (C)	T(Si) (C)	H(Si) (kJ/kg)
1	79-80	1775	469.1	12.0	3163	1247	309.9	307	1375
2	80-81	1740	485.3	8.6	3163	1303	318.0	315	1422
3	81-82	1656	420.1	7.8	3044	1159	308.6	302	1350
4	82-83	1677	421.8	9.1	2997	1129	308.6	297	1325
5	83-84	1689	447.4	9.1	3044	1085	312.5	293	1304
6	84-85	1644	459.1	7.3	3073	966	318.7	281	1245
7	85-86	1701	464.3	7.1	3044	1091	318.0	294	1307
8	86-87	1632	453.4	7.5	3006	1126	317.4	297	1324
9	87-88	1672	438.1	8.4	3037	1041	311.3	291	1291
10	88-89	1717	452.2	9.5	3141	1037	310.5	291	1289
11	89-90	1588	414.5	9.6	3107	1047	308.4	291	1293
12	90-91	1597	423.2	9.4	3029	1096	309.1	296	1319
13	91-92	1641	435.6	10.0	3059	1268	309.1	311	1405
14	92-93	1634	439.8	9.9	--	1098	310.4	296	1320

changes in chloride concentration seen in Figure 3 for wells Az-9, 16AD, and 22 are due to processes in the reservoir. The marked increase in chloride concentration exhibited by well 16AD is caused by local boiling and recycling of reinjected brine. The data for well Az-9, where the chloride concentration shows a continuous decrease, is more difficult to explain. The data suggest that there is an inflow of less saline water, but with similar geochemical temperature as noted by the constant temperature given by the Na-K-Ca geothermometer.

Table 6 lists the data for the hemispherical drawdown for well Az-5. The Na-K-Ca geotemperature is a key parameter in estimating the reservoir pressure in the hemisphere and the fluid density in the annual production shell. The weakest link in the analysis is the mean reservoir porosity. Available data for a few wells at Los Azufres consist of laboratory measurements of core porosity, which range from 4 to 10 percent. Based on discussions with several Los Azufres staff over the years, an average value of 8 percent is used in this analysis.

An example of a drawdown history (for well Az-5) is shown in Figure 4. Evaluation of the drawdown trend is conveniently made by type-curve matching of the infinite radius of the regression line and its slope by the matching parameters in Equ.(5). Figure 5 shows a set of curves for intercept p = 10 MPa. A summary of the hemispherical drawdown analysis is given in Table 7. The essentially zero regression coefficients for the three two-phase wells in the northern zones indicate that the reservoir pressure has been essentially independent of the fluid and thermal extraction over the first decade of production. The regression coefficients of 50 percent for the two wells in the steam-dominant Tejamaniles zone indicate significant dependence of reservoir pressure on fluid extraction. It is noted that the extent of pressure drawdown exhibited in the model agrees well with the observed pressure drawdown of about 1 to 1.5 MPa for these wells (Quijano and Sanchez, 1994). Efforts are currently underway to obtain estimated values for the quasi-constant parameters in the intercept and slope type-match parameters a and b, and to evaluate the extent of the model to predict longer-term behavior of continued production. One result of the model output is the estimate of drawdown radius of about 300-500 m into the fractured reservoir, which for a hemisphere is the minimum horizontal distance. It sets a reasonable minimum-distance value for drilling additional wells to avoid interference problems.

Table 5
Mean Chloride Concentration

Well	t (yrs)	[Cl] ± σ (mg/kg)	σ (%)
Az-5	14	3070 ± 56	± 1.8
Az-13	14	2839 ± 146	± 5.1
Az-9	7	3542 ± 412	± 11.6
Az-16AD	11	4970 ± 1494	± 30.0
Az-22	13	3828 ± 310	± 8.1

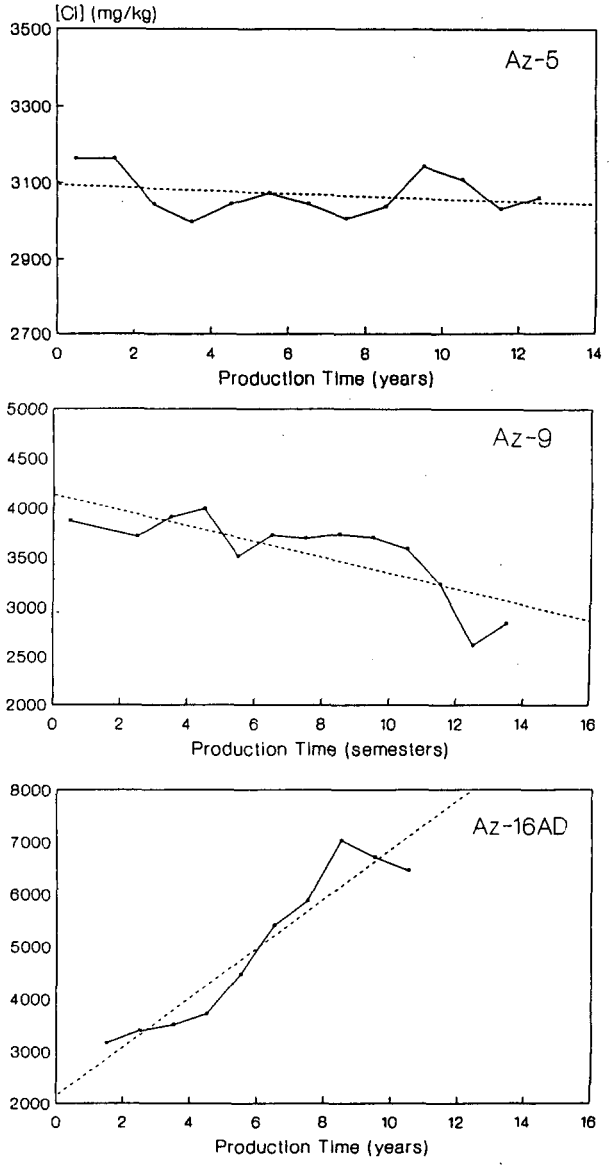

Fig. 3. Change of chloride concentration with production time for three wells: (a) Az-5; (b) Az-9; and (c) Az-16AD.

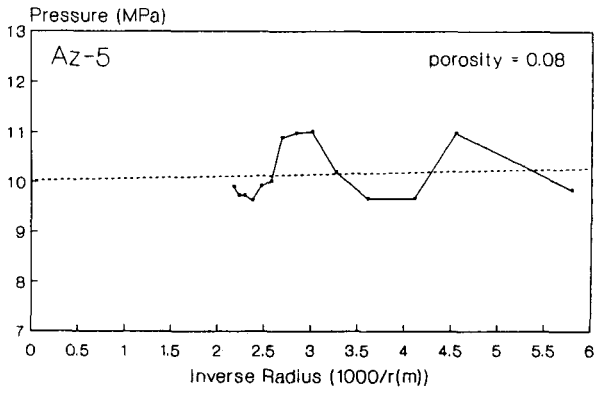

Fig. 4. Hemispherical drawdown history for well Az-5.

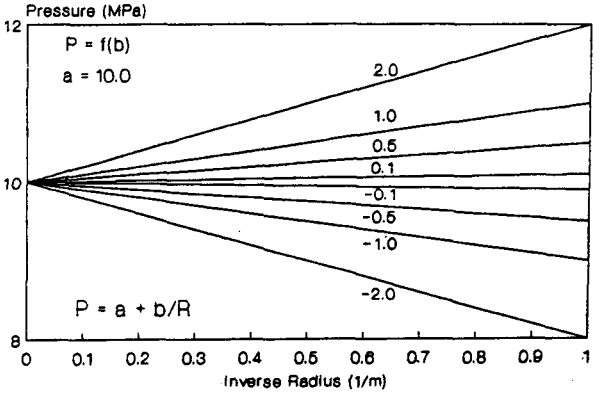

Fig. 5. Drawdown type curves for the slope of the outer-shell pressure as a function of the outer-shell inverse radius for pressure intercept of 10 MPa.

Table 7
Hemispherical Drawdown Analysis

Well	t (yrs)	R(t) (m)	P(o) (MPa)	Slope (MPa.m)	Regr. Coeff.
Az-5	14	462	10.04	0.038	0.005
Az-13	14	430	8.73	-0.057	0.027
Az-9	7	328	11.46	-0.011	0.001
Az-16AD	11	277	3.58	0.457	0.519
Az-22	13	479	8.97	0.352	0.542

Table 6
Hemispherical Drawdown
Well Az-5

Yr (t)	Year	Mass (Gg)	T(r) (C)	ρ(T) (kg/m3)	V(t) (Mm3)	V(Tot) (Mm3))	r(t) (m)	P(T) (MPa)	1000/r (1/m)
1	'79-80	598.0	309.9	691.1	10.82	10.82	172.9	9.84	5.785
2	'80-81	620.0	318.0	672.1	11.53	22.35	220.2	10.98	4.542
3	'81-82	447.0	308.6	694.0	8.05	30.40	243.9	9.67	4.100
4	'82-83	799.0	308.6	694.0	14.39	44.79	277.6	9.67	3.603
5	'83-84	850.0	312.5	685.2	15.51	60.30	306.5	10.20	3.263
6	'84-85	902.0	318.7	670.4	16.82	77.11	332.7	11.01	3.006
7	'85-86	797.0	318.0	672.1	14.82	91.94	352.8	10.98	2.835
8	'86-87	872.0	317.4	673.6	16.18	108.12	372.3	10.89	2.686
9	'87-88	845.0	311.3	687.9	15.35	123.47	389.2	10.03	2.569
10	'88-89	962.0	310.5	689.8	17.43	140.91	406.7	9.92	2.459
11	'89-90	941.0	308.4	694.5	16.94	157.84	422.4	9.64	2.367
12	'90-91	1018.0	309.1	692.9	18.36	176.21	438.2	9.74	2.282
13	'91-92	810.0	309.1	692.9	14.61	190.82	450.0	9.74	2.222
14	'92-93	884.0	310.4	690.0	16.01	206.83	462.2	9.91	2.163

REFERENCES

Fournier, R.O. and R.W. Potter, "A Revised and Expanded Silica (Quartz) Geothermometer, Geoth.Res.Counc.Bull. 11, 3-12, November, 1982

Fournier, R.O. and A.H. Truesdell, "An Empirical Na-K-Ca Geothermometer for Natural Waters", Geochim. et Cosmochim. Acta 37, 1255-1275 (1973).

Kruger, P., L. Semprini, S. Verma, R. Barragan, R. Molinar, A. Aragon, J. Ortiz, C. Miranda, A. Garfias, and M. Gallardo, "Initial Chemical and Reservoir Conditions at Los Azufres Wellhead Power Plant Startups", Proceedings, Tenth Workshop on Geothermal Reservoir Engineering, Stanford University Report SGP-TR-84, 219-226, January, 1985a.

Kruger, P., L. Semprini, D. Nieva, S. Verma, R. Barragan, R. Molinar, A. Aragon, J. Ortiz, C. Miranda, A. Garfias, and M. Gallardo, "Analysis of Reservoir Conditions during Startup at the Los Azufres Geothermal Field", Trans.Geoth.Res.Counc., 9, Part II, 527-532, August, 1985b.

Kruger, P., J. Ortiz, C. Miranda, and M. Gallardo, "Response of the Los Azufres Geothermal Field to Four Years of 25-MW Wellhead Generation", Proceedings, Twelth Workshop on Geothermal Reservoir Engineering, Stanford University Report SGP-TR-109, 181-187, January, 1987.

Kruger, P., P. Sanchez, and J. Ortiz, "Startup Analysis of Wellhead Unit Production Well", Proceedings, Symposium in the Field of Geothermal Energy", pp. 149-160, Final Symposium, DOE-CFE Geothermal Agreement, San Diego, CA, April, 1989.

Muskat, M., "The Flow of Homogeneous Fluids through Porous Media" (Mc-Graw Hill, New York, 1937).

Quijano, J.L. and R. Sanchez, "Expansion Possibilities of the Los Azufres Geothermal Field", Trans.Geoth.Res.Counc. 18, 281-282, 1994.

PROCEEDINGS, Twentieth Workshop on Geothermal Reservoir Engineering
Stanford University, Stanford, California, January 24-26 1995
SGP-TR-150

EVALUATION OF THE CURVE-FITTING METHOD AND THE HORNER-PLOT METHOD FOR ESTIMATION OF THE TRUE FORMATION TEMPERATURE USING TEMPERATURE RECOVERY LOGGING DATA

Masami Hyodo and Shinji Takasugi

Geothermal Energy Research and Development Co., Ltd., Tokyo 103, Japan

ABSTRACT

This paper describes the method to estimate the true formation temperature using temperature recovery logging data after the well reach to total depth (T.D.). The method designated as "Curve-fitting method (CFM)" is based on mathematical model proposed by Middleton (1979, 1982). The accuracy and applicability of this method are evaluated with several field data and compared advantageously with the Horner-plot method.

Then, real-time data acquisition system including interpretation software has also been successfully developed.

As a conclusion, the followings are confirmed:

1) The developed CFM can be applicable to the estimation of the true formation temperature even using 24 hours temperature recovery data, although the Horner-plot method might need up to 120 hours recovery data, usually.

2) Though depending upon the quality of the data and/or number of the temperature recovery logging data, it might be possible to estimate the true formation temperature using less than 24 hours recovery data. Because, the computer program of this system has the function to decide when the measurement of temperature recovery logging should be finished.

1. INTRODUCTION

The true formation temperature is one of the important parameter for geothermal reservoir evaluation and it will be used if drilling of the well will be made complete or not when the well is reached to planned T.D. In order to obtain the true formation temperature, temperature recovery logs are most often carried out. Also, another important information of the fluid entry depth in the well will be obtained by these logs. If we could estimate the formation temperature using short period of logging data, it is very preferable to save the rig time and logging cost.

The Horner-plot method has been popularly used for estimating the formation temperature (Dowdle and Cobb, 1975). This method is easy to utilize even in the field, however on the other hand, it requires relatively long period of temperature recover data up to 120 hours to estimate correctly. It is also pointed out that the fluid circulation time as the Horner-time is very critical to the estimated result, therefore the Horner-time must be decided carefully.

Mathematical models for borehole temperature stabilization were proposed to estimate the true formation temperature. In this paper, these models were evaluated for the applicability to the estimation of the true formation temperature and the recovery temperature.

2. ESTIMATION OF THE TRUE FORMATION TEMPERATURE

2.1 Horner-Plot Method

The Horner-plot method as a formation temperature estimation which is based on an empirical analysis method that the phenomenon of temperature recovery after circulation has ceased in heat conductive geothermal well, is similar to the pressure build-up behavior of geothermal reservoir. The Horner-plot method proposed by Dowdle and Cobb (1975) gives a reliable static formation temperature in region of low geothermal gradient, and can be expressed the following formula:

$$BHTh = Tf + C \log\{(t+dt)/dt\} \quad (1)$$

Tf is the true formation temperature; t is the circulation time; dt is the elapsed time after circulation has ceased.

According to Dowdle and Cobb, comparative and analytical studies of the temperature build-up and pressure build-up using the diffusibility equation showed that the two methods are not completely analogous and Equ. (1) is not correct theoretically. Therefore, the method required long period of temperature recover time.

2.2 Curve-Fitting Method

(1) Curve-fitting method

The analytical CFM based on mathematical temperature stabilization has been proposed to calculate the true formation temperature with better accuracy even from shorter period of temperature recovery data by Luikov (1968), Carslaw and Jaeger (1959), and Middleton (1979, 1982). CFM calculates a static temperature of the equilibrium formation by mathematically represented the physical well model for temperature recover. Proposed mathematical model by Middleton was the temperature distribution in the center of the well with a vertical cylinder of infinite length, after circulation of drilling mud has ceased; BHTc(t) can be expressed the following formula:

$$BHTc(t) = Tini + (Tf - Tini) \times \left\{ erfc\left(\frac{R}{(4Kt)^{1/2}}\right) \right\}^2 \quad (2)$$

t is the elapsed time after circulation has ceased; Tini is the initial temperature in the borehole at t = 0; Tf is the true formation temperature; R is the effective radius of the region affected by drilling; K is the thermal diffusibility of the well contents.

Fluid circulation time in drilling, which is required for the Horner-plot method and also is a little uncertainty about adequate number, is not necessary in this model.

(2) Mathematical well models

Proposed several physical well models to analyze the behavior of wellbore temperature recovery after circulation has ceased are examined. The "Circular model" proposed by Luikov is assuming the physical well model as a circular cylinder (Fig. 1 (a)). The "Square model" proposed by Carslaw and Jaeger is assuming that a well can be approximated by a square cylinder as a physical well model (Fig. 1 (b)). Middleton proposed that a conductive heat transfer into a vertical, approximately cylindrical region of small diameter in rectangular coordinates leads to an expression for temperature which is very much simpler than the corresponding expression in cylindrical coordinates (Fig. 1 (c)). Through case studies of these models using non-linear least squares fitting, results of calculated formation temperature from the model proposed by Middleton are evaluated more reliable and more accurate in comparison with field data. The reason why the most unreal Middleton's well model in three models calculates most reliable and accurate results is expected that the Middleton's model may be expressed realistic wellbore such as very rough shape and not gauged (Fig. 2).

(3) Inversion for CFM

Forward and inverse techniques as fitting method are examined. In forward technique, the formation temperature can be obtained by superimposing a set of master curve, based on Equ. (2), on observed temperature data plotted at the same scale (similar to type-curve matching). However, many master curves are necessary to obtain accurate result, and it is very complicated work of trial and error, and also it's takes time.

Then, inverse technique which is non-liner least squares fitting method expressed in Equ. (3) is applied to obtain the formation temperature.

$$S = \sum_{i=1}^{n} \{BHTo(ti) - BHTc(Ti)\}^2 = Minimum \quad (3)$$

BHTo(ti) is the observed temperature at a time; BHTc(ti) is the calculated temperature at a time from Equ. (3); n is number of measured data. Where the effective radius; R and thermal diffusibility; K are expressed simply assumption following value α;

$$\alpha = \frac{R}{\sqrt{K}} \quad (4)$$

$$K = \frac{\lambda}{\rho c} \quad (5)$$

λ is the thermal conductivity; ρ is the density; c is the specific heat capacity. Therefore, in inverse technique, estimated true formation temperature can be obtained by iterate to minimize the sum of squares between BHTo and BHTc at a time. Features of a non-liner least squares method, in comparison with type-curve matching, are in its rapidity and objectivity. Therefore, we call this inverse method as CFM. Figure 3 illustrates an example of the non-liner least squares fitting result by inversion.

3. EVALUATION OF METHODS FOR ESTIMATING THE TRUE FORMATION TEMPERATURE

3.1 Estimated Formation Temperature by the Horner-Plot Method

Estimation of the true formation temperature by the Horner-plot method using experimental temperature recovery logging data which was performed at the LC-1 well in Kyushu, Japan is shown in Fig. 4. This graph shows that the Horner-plot method needs the temperature recovery logging data at least up to 48 hours, usually 120 hours of elapsed time to obtain the liner region in the Horner-plot. It is also confirmed that the value of circulation time is very essential to estimate correctly, otherwise it is very easily to miss-estimate 20-50°C.

3.2 Estimated Formation Temperature by Curve-Fitting Method (CFM)

Evaluation of CFM was performed using experimental temperature recovery data (Takai et al., 1994). Reliability and accuracy were exhaustively evaluated using elapsed time of temperature recovery log versus number of data and time interval as explained in Table 1. Through these case studies, it is verified that CFM can be suitable to estimate the formation temperature. That is, the accuracy of the estimated formation temperature using until 24.5 hours data is at most 5°C, and even using until 12.5 hours data, is at most 10°C. The computation time for CFM is less than 10 seconds using recent lap-top PC.

3.3 Comparison of Estimated Temperature

Figure 5 shows the cross plot of estimated formation temperature by the Horner-plot method (Tfbuild) and by CFM (Tffit) using 31 temperature recovery logs at 13 experimental wells in eight geothermal areas. Figure 5 (a) illustrates the cross-plot with the temperature recovery data up to 120 hours of elapsed time after the circulation ceased. The average error between both methods (Tffit - Tfbuild) is about -8.6°C (standard variation; σ = 7.0). Figure 5 (b) illustrates the cross-plot with the temperature recovery until eight hours. The average error of Tffit - Tfbuild is approximately -13.7°C (σ = 9.4). As shown in Fig. 5, the error becomes bigger in region where geothermal gradient is higher.

4. QUALIFICATION OF THE METHODS

Through the case studies, qualification of the methods can be concluded as follows.

4.1 Horner-Plot Method

One of the reason of difference between estimated temperatures by both methods shown in Fig. 5 can be understood that a main cause for the error in estimated temperatures by the Horner-plot method is insufficient temperature recovery log data and inexact circulation time. Therefore, it is possible to derive that bigger errors in estimated temperature by the Horner-plot method are the defect of this method for estimation of the true formation temperature in geothermal area where geothermal gradients are relatively high.

4.2 Curve-Fitting Method (CFM)

The mathematical model for CFM is based on the heat conductive formation model, therefore CFM cannot be applied to estimate formation temperature in non-conductive temperature distribution zone. From the same reason, CFM also cannot estimate the true formation temperature at lost circulation zone. If it is important to estimate the temperature in this zone, we need more study.

However, estimated temperature is not sensitive to the circulation time, therefore it is easier to use in the field and more accurate than the Horner-plot method.

5. SYSTEM DEVELOPMENT FOR FIELD APPLICATION

In order to apply CFM as a method for the true formation temperature estimation and/or recover temperature estimation at any elapsed time during temperature recovery logging in the field, real-time data acquisition system has been developed. Acquired data on field computer are processed almost real-timely, accordingly the estimated temperature can be calculated at every depth just after the temperature recovery log has been run.

This computer program has the function for evaluation of the reliability of the estimated temperature. Then, the engineer can use this information for his decision making when temperature recovery logs shall be finished. This function will help to keep the accuracy of the measurement, and to save the rig time and logging cost. As a function to decide termination of temperature recovery log, the following parameters are calculated and plotted;

1) standard deviation,
2) transition of difference of the estimated temperature (Tffit(n) – Tffit(n–1)),
3) standardized sum of squares by number of data, and
4) transition of the estimated true formation temperature.

Figure 6 illustrates examples of these features.

Also, using continuous temperature logging data in depth, this program can estimate the formation temperature and/or recovery temperature at any elapsed time versus depth continuously. This means the true formation temperature profile and its reliability are plotted just after temperature recovery log has been run.

6. CONCLUSIONS

The true formation temperature is essentially important value for geothermal reservoir evaluation. Estimation of the true formation temperature with good accuracy using short period of logging time is preferable economically and help to make a quick decision, that is very important for the well drilling. Through these studies, we can conclude as follows:

1) The Curve-fitting method (CFM) as an estimation method of the true formation temperature has been successfully developed. CFM is based on mathematical model for temperature recovery and includes the inversion scheme with the non-liner least squares method. Because of these schemes, estimated temperature can be computed immediately after the temperature recovery log has been done.

2) In comparison with the Horner-plot method, CFM is more reliable and useful for the temperature recovery and the true formation temperature estimation.

3) The accuracy for the true formation temperature estimation is less than 5°C even using 24 hours temperature recovery data, according to our case studies.

4) Developed data acquisition system can give various parameters for decision making when the measurement of temperature recovery should be finished.

5) Through these case studies, it is expected to reduce the logging and rig costs using CFM as an estimation method of the true formation temperature and recovery temperature.

ACKNOWLEDGMENTS

The authors express their appreciation of the New Energy and Industrial Technology Development Organization (NEDO) for giving us permission to present the results obtained in the "Development of Geothermal Hot Water Power Generation Plant" in MITI's the Sunshine Project, Japan.

REFERENCES

Carslaw, H.S. and Jaeger, J.C. (1959), "Conduction of heat in solids," Oxford University Press.

Chiba, M., Takasugi, S., Hachino, Y., and Muramatsu, S. (1988), "Estimating of equilibrium formation temperature by curve fitting method," Proceedings of the International Symposium on Geothermal Energy, 383–386.

Dowdle, W.L. and Cobb, W.M. (1975), "Static formation temperature from well logs – an empirical method," J. Petrol. Tech., 27, 1326–1330.

Hyodo, M., Takai, K., and Takasugi, S. (1994), "Evaluation of curve-fitting method for estimating the formation temperature from logging data," Proceedings of the 90th SEGJ Conference, 285-289.

Luikov, A.V. (1968), "Analytical heat diffusion theory," Academic Press Inc.

Middleton, M.F. (1979), "A model for bottom-hole temperature stabilization," Geophysics, 44, 1458-1462.

Middleton, M.F. (1982), "Bottom-hole temperature stabilization with continued circulation of drilling mud," Geophysics, 47, 1716-1723.

New Energy Industrial Technology Development Organization (1992), "Summary of development of techniques to control lost circulation in geothermal wells," 18-27.

Takai, K., Hyodo, M., and Takasugi, S. (1994), "Estimating of equilibrium formation temperature by curve fitting method and its problems," Stanford Nineteenth Annual Workshop on Geothermal Reservoir Engineering.

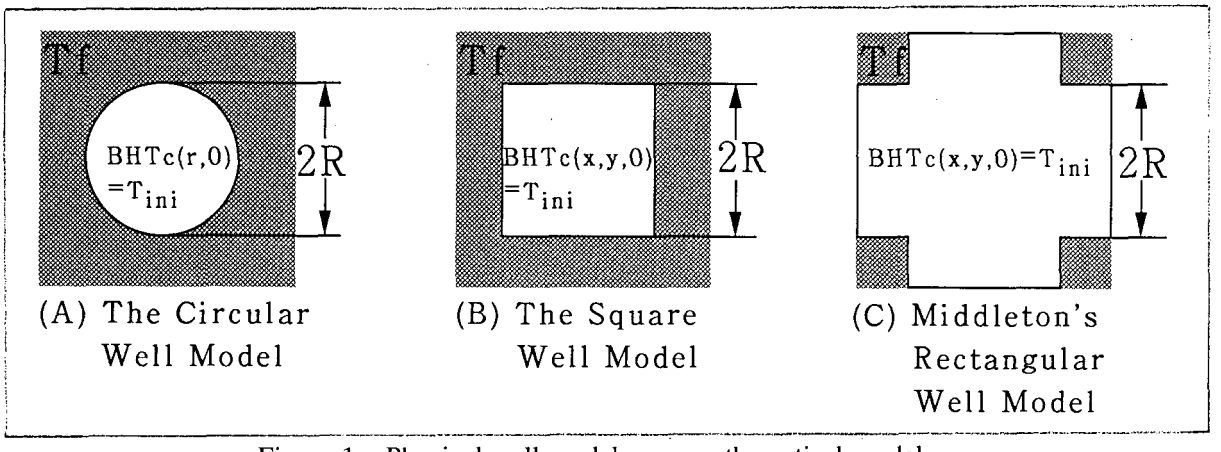

Figure 1. Physical well models as a mathematical model.

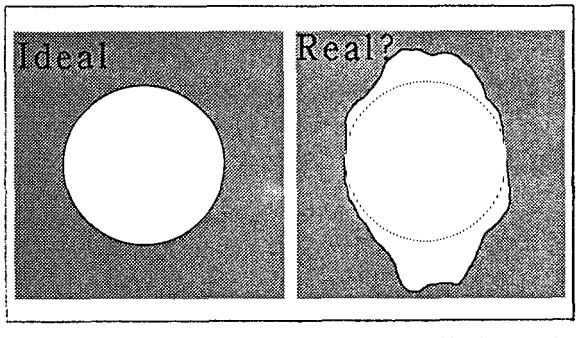

Figure 2. Schematic ideal and realistic wellbore configuration.

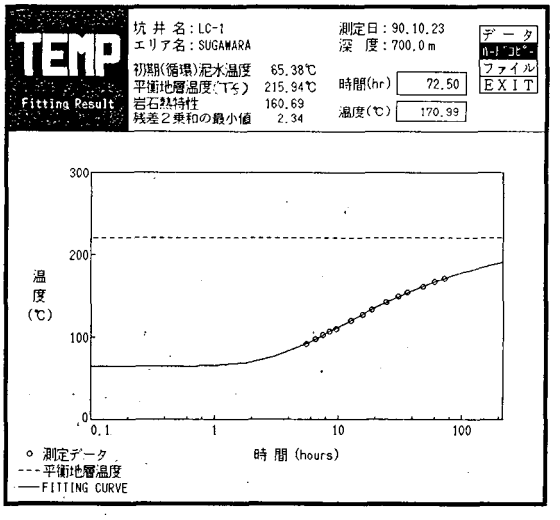

Figure 3. Example of curve-fitting with field data by the Curve-fitting method at 700 m depth of the LC-1 well.

Table 1. Accuracy of the Curve-fitting method depending upon number of data and log interval.

Elapsed Time (Hours)	①	②	③	④	⑤ − 1	⑤ − 2	⑤ − 3	⑤ − 4	⑥	⑦	⑧	⑨
5.5	92.0	92.0	92.0	92.0	92.0	92.0		92.0	92.0	92.0	92.0	92.0
6.5	98.5					98.5		98.5			98.5	
7.5	103.0	103.0	103.0	103.0	103.0	103.0					103.0	
8.5	107.4	107.4				107.4					107.4	107.4
9.5	110.4	110.4	110.4	110.4	110.4		110.4		110.4	110.4	110.4	
12.5	119.6	119.6	119.6				119.6				119.6	119.6
15.5	126.6	126.6	126.6	126.6	126.6		126.6	126.6	126.6		−	−
18.5	132.8	132.8	132.8	132.8			132.8	132.8			−	−
24.5	142.4	142.4	142.4	142.4	142.4	142.4	142.4	142.4	142.4	142.4	−	−
No. of Data	9	8	7	6	5	5	5	5	4	3	6	3
E.F.T(℃) for 72.5 hrs	170.5	170.4	171.2	170.7	171.2	169.1	174.9	172.4	172.0	171.5	159.7	160.9
E.F.T - TRUE for 72.5 hrs	− 0.5	− 0.6	+ 0.2	− 0.3	+ 0.2	− 1.9	+ 3.9	+ 1.4	+ 1.0	+ 0.5	-11.3	-10.1

E.F.T : Estimated Formation Temperature by Curve-Fitting Method
TRUE : Measured Temperature by Logging at 72.5 hours(170.9 degree C)

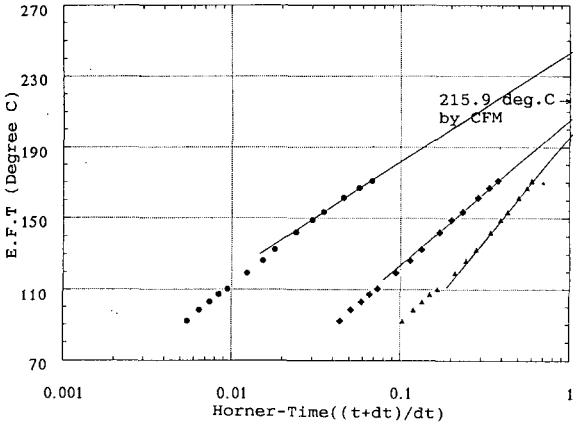

Figure 4. Example of estimation of the true formation temperature by the Horner-plot method.
These graphs show effects between the various circulation time at 700 m depth of the LC-1 well (Tffit = 215°C). C: Assumed circulation time is 40 days (Tfbuild = 243°C). S: Assumed circulation time is five days (Tfbuild = 205°C). T: Assumed circulation time is two days (Tfbuild = 196°C).

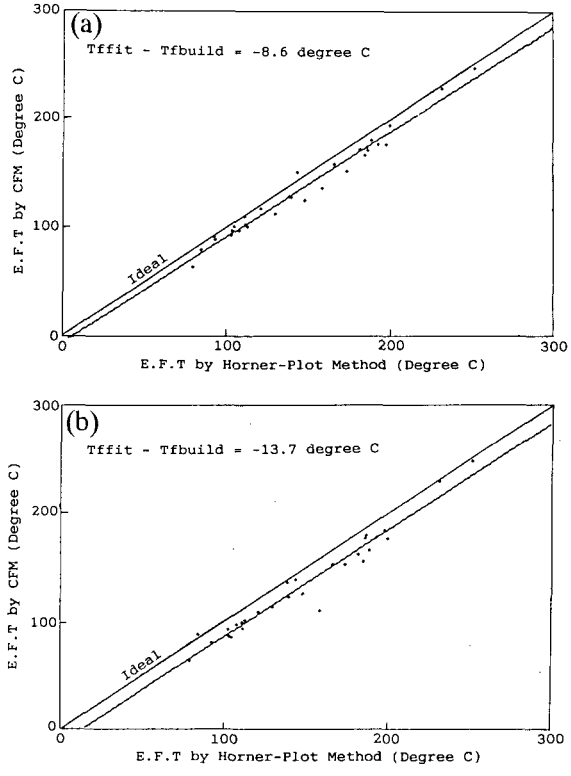

Figure 5. Cross-plot of estimated true temperature by the Horner-plot method versus CFM (a) using elapsed time of 120 hours and (b) using elapsed time of eight hours.

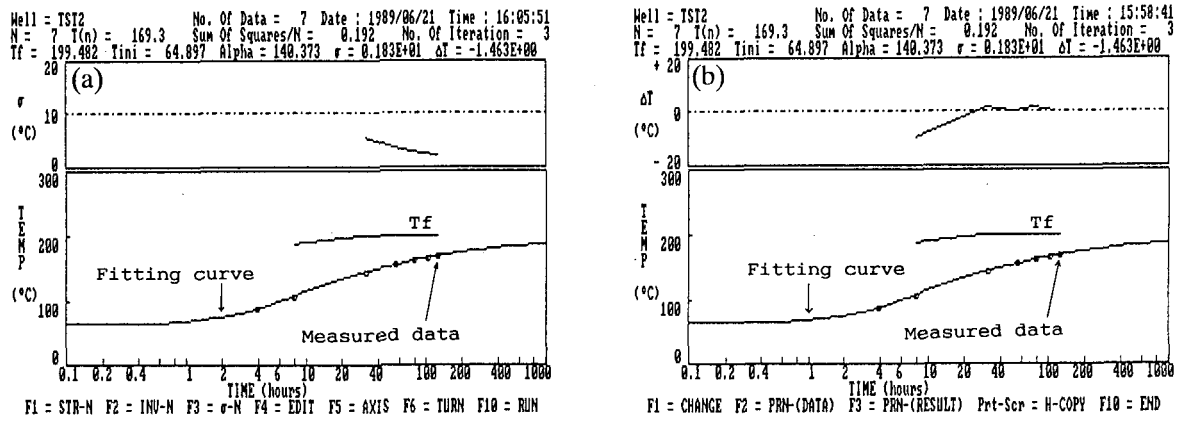

Figure 6. Example of parameters for evaluation of reliability of estimated temperatures. (a) Example of standard deviation of estimated temperatures. (b) Example of transition of estimated temperatures.

PROCEEDINGS, Twentieth Workshop on Geothermal Reservoir Engineering
Stanford University, Stanford, California, January 24-26 1995
SGP-TR-150

PRODUCTION/INJECTION CHARACTERISTICS OF SLIM HOLES AND LARGE-DIAMETER WELLS AT THE SUMIKAWA GEOTHERMAL FIELD, JAPAN

Sabodh K. Garg
S-Cubed
La Jolla, California

Jim Combs
Geo Hills Associates
Los Altos Hills, California

ABSTRACT

Production and injection data from slim holes and large-diameter wells at the Sumikawa Geothermal Field, Japan, were analyzed to determine the effect of wellbore diameter on (1) the productivity/injectivity indices, and (2) on the discharge rate. The injectivity indices for Sumikawa boreholes do not depend on borehole diameter in any systematic manner; furthermore, the productivity indices (for boreholes with liquid feeds) are more or less equal to the injectivity indices. For boreholes with liquid feed zones, discharge rates scale with diameter according to a relationship previously presented by Pritchett. Pritchett's scaling rule does not appear to apply to discharge data from boreholes with two-phase feed zones; however, discharge characteristics of slim holes with two-phase feed zones can be used to infer production rates from large-diameter two-phase geothermal wells.

1. INTRODUCTION

Under its drilling research program, the U.S. Department of Energy (DOE) through Sandia National Laboratories (Sandia) has initiated a research effort to demonstrate that slim holes can be used (1) to provide reliable geothermal reservoir parameter estimates comparable to those obtained from large-diameter wells, and (2) to predict the behavior of large-diameter wells (Combs and Dunn, 1992). DOE/Sandia plan to drill and test pairs of small-diameter slim holes with large-diameter production wells in several geothermal fields in the western United States; the first of these tests was completed in mid-1993 at the Steamboat Hills Geothermal Field, Nevada (Finger, *et al.*, 1994). In addition, DOE/Sandia are supporting the examination of existing Japanese data on the use of slim holes in geothermal exploration and reservoir assessment; in the first of these studies, Garg, *et al.* (1994) analyzed production and injection data from the Oguni Geothermal Field, Japan. In this paper, we examine the existing production and injection flow test data for both small-diameter slim holes and large-diameter production wells at the Sumikawa Geothermal Field.

A brief overview of the Sumikawa Geothermal Field is presented in Section 2. This section also gives the feedzone location, temperature, and pressure for eighteen Sumikawa boreholes for which some production or injection data are available. Injection and production data from both slim holes and large-diameter production wells are analyzed in Section 3 to determine injectivity/productivity indices. In Section 4, the injectivity/productivity indices for Sumikawa boreholes are compared with those for the Oguni Geothermal Field boreholes. The variation of discharge rate with borehole diameter is discussed in Section 5.

2. SUMIKAWA GEOTHERMAL FIELD

The Sumikawa Geothermal Field is located in the Hachimantai volcanic area in northern Honshu, Japan, about 1.5 kilometers to the west of Ohnuma geothermal power station operated by Mitsubishi Materials Corporation (MMC). The Hachimantai area also includes the Matsukawa and Kakkonda Geothermal Fields. An extensive well drilling and testing program was initiated in October 1981 with the spudding of boreholes S-1 and S-2 by MMC and the Mitsubishi Gas Chemical Corporation (MGC). The New Energy and Industrial Technology Development Organization (NEDO) became involved in the field characterization effort with the drilling of borehole N59-SN-5 (~ 2 km west of S-1 and S-2) in 1984–1985. The field exploration and characterization program at Sumikawa was successfully concluded in 1990 with a decision to build a 50 MWe power plant. The Sumikawa geothermal power plant is expected to be commissioned some time in 1995.

The Sumikawa/Ohnuma geothermal area is shown in Figure 1. The Sumikawa Geothermal Field lies in the western part of the area. Mt. Yake lies to the southwest of the Sumikawa area, and Mt. Hachimantai is just to the southeast (outside the area illustrated in Figure 1). Between the Sumikawa prospect (which may be regarded as centered in the neighborhood of the S-series boreholes, S-1, S-2, S-3, and S-4) and the Ohnuma borefield is a north-south region of relatively low ground surface elevation where natural hot springs and fumaroles are found. The Sumikawa/Ohnuma area lies within a north-south oriented regional graben structure which extends many kilometers both north and south of the Sumikawa area. Indeed, the Sumikawa field itself appears to be located along the western edge of the graben.

An east-west cross section corresponding to line A-A′ is depicted in Figure 2. Extensive faulting has rendered the detailed geological structure at Sumikawa somewhat obscure, but the abundance of drilling logs from the various boreholes in the area has revealed the following geological sequence: (1) *ST formation*—Surficial andesitic tuffs, lavas, and pyroclastics of recent origin (from Mt. Yake); (2) *LS formation*—Lake sediments, Pleistocene tuffs, sandstones, siltstones, and mudstones; (3) *DA formation*—Pliocene dacites, dacitic tuffs, and breccias, (4) *MV formation*—"Marine/volcanic complex" containing interbedded Miocene dacitic volcanic rocks and "black-shale" oxygen-poor marine shales and sediments; (5) *AA formation*—Altered andesitic rocks that apparently are extensively fractured, and (6) *BA formation*—

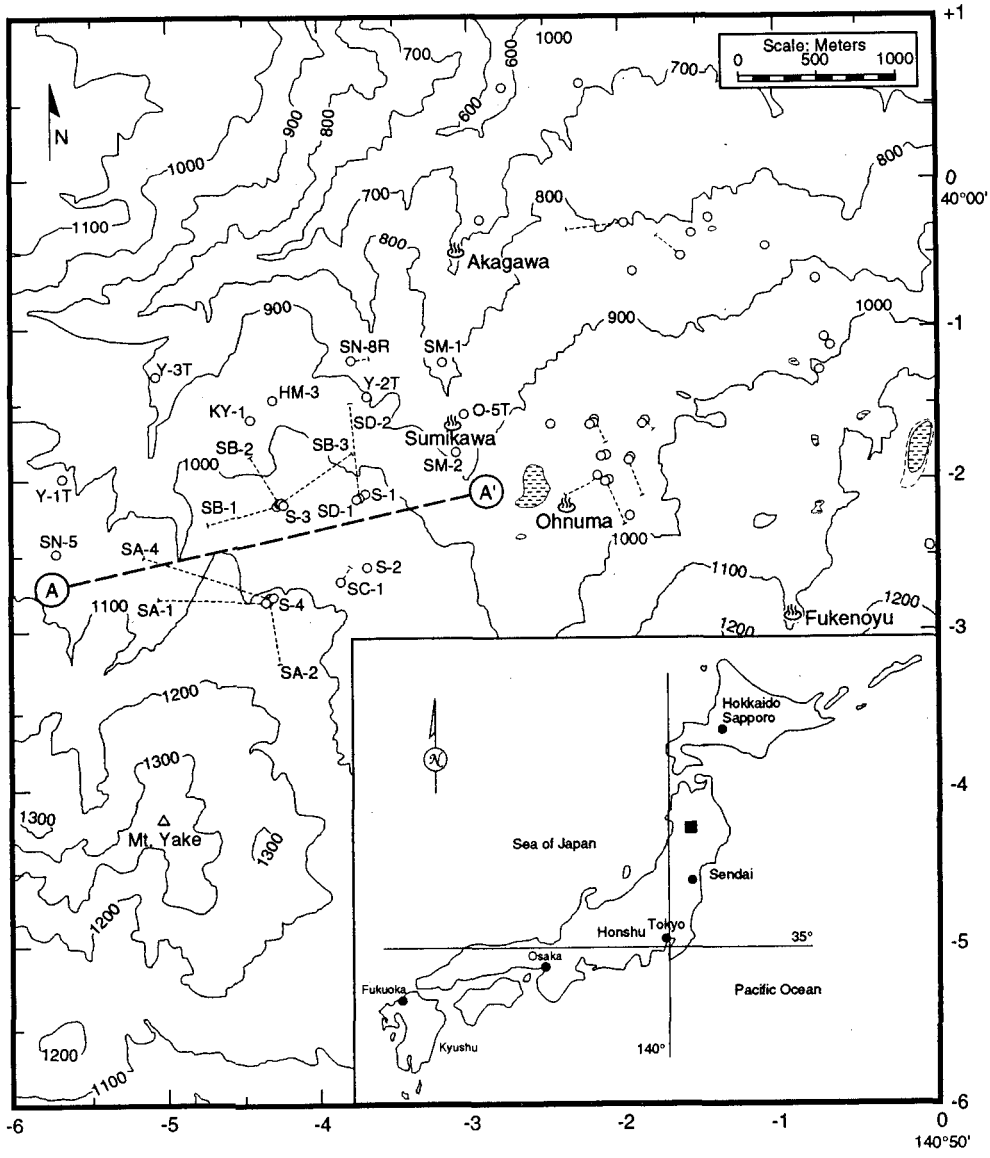

Figure 1. The Sumikawa/Ohnuma area, showing locations of wells and cross-section A–A′. The origin of the local co-ordinate system is 40°N latitude and 140°50′E longitude. The inset map of Japan shows the location of the Sumikawa/Ohnuma Area (dark retangle).

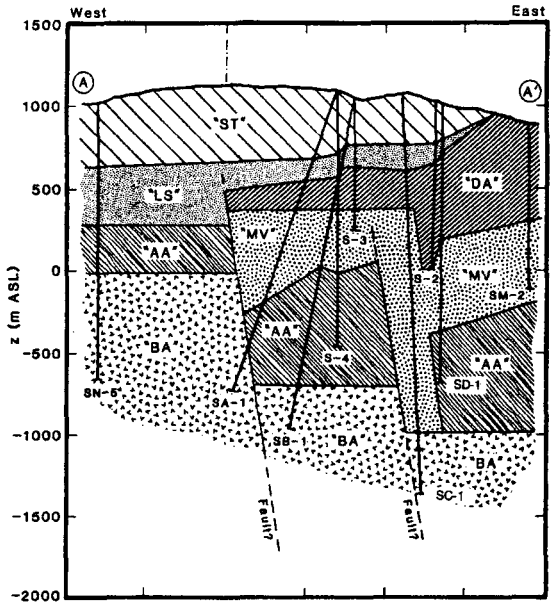

Figure 2. East-west A–A′ (total length = 3 km) geological cross-section through the Sumikawa area.

Crystalline rocks (mainly granodiorite and diorite). The BA formation is the deepest so far encountered by drilling (well SC-1 bottomed in this formation at 2486 m depth), but the pre-Tertiary basement, which presumably underlies the above sequence, has not yet been reached.

At Sumikawa, underground temperatures are highest to the south and decline to the north and northwest. The estimated temperatures at sea level (~700–1100 m depth) in the area (based mainly on temperature surveys in shut-in boreholes) are shown in Figure 3. The highest temperature so far measured in the field is at the bottom of well SA-2 (320°C at 840 m below sea level); this is also the southernmost deep borehole at Sumikawa. Temperatures are significantly higher at Sumikawa (near the S-series boreholes) than at the nearby operating Ohnuma borefield. On the whole, temperatures appear to increase monotonically with depth; large-scale temperature inversions (with the exception of well SC-1) are not observed.

Pritchett, *et al.* (1990) have examined the various downhole feedpoint pressure determinations available from boreholes in the Sumikawa/Ohnuma area in detail. The reservoir pressures are surprisingly uniform throughout the area; apart from a small region immediately adjacent to the Ohnuma power station, deep shut-in pressures may be determined from the empirical correlation

$$P(\text{bars}) = 61.170 - 79.985\,Z - 6.492\,Z^2$$

where Z is elevation, measured in kilometers with respect to sea level (km ASL). The pressure data from several boreholes in the Ohnuma borefield (0-1R, 0-2R, 0-3R-a, 0-3R-b), obtained prior to the startup of Ohnuma power plant, are also in good agreement with the deep correlation obtained above (see Figure 4). The Ohnuma geothermal power plant started producing electric power in 1973. The sparse pressure data available for the Ohnuma boreholes suggest that the pressures at Ohnuma have fallen by several bars during the last 20 years. Since the pressure measurements upon which the deep pressure correlation is based were made between 1968 and 1988 (average date = 1980), it is apparent that any pressure disturbance induced by operations associated with the Ohnuma power station must be of limited areal extent.

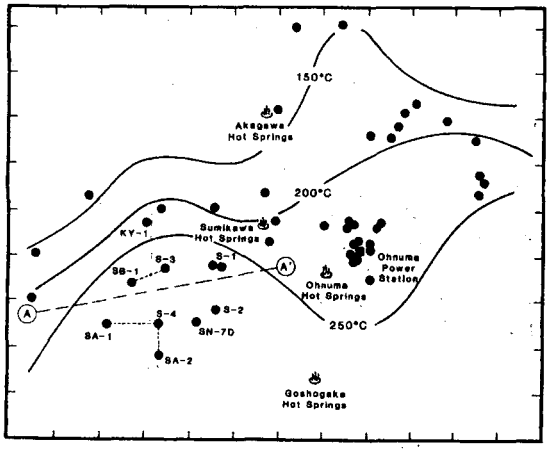

Figure 3. Temperatures at sea-level elevation in the Sumikawa/Ohnuma area (adapted from Kubota 1988).

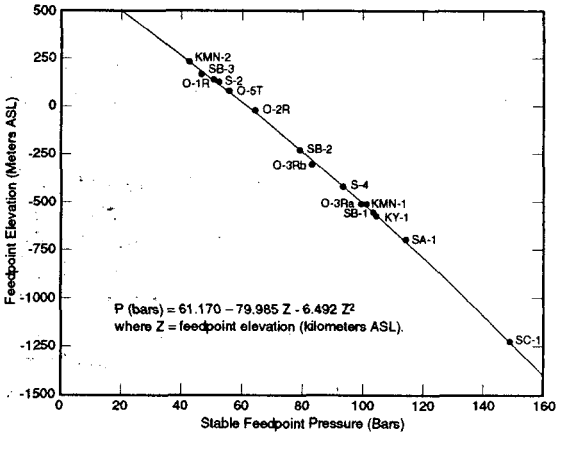

Figure 4. Selected deep feedpoint pressures and algebraic fit. (from Pritchett, *et al.* 1990).

Samples collected from discharging Sumikawa boreholes indicate that the reservoir fluid is of low salinity (<3000 ppm) and that the noncondensible gas content is very low (typically < 0.1 percent by volume of the steam). The reservoir fluids are mainly of the Na-Cl type with a near neutral pH.

It is virtually certain that a two-phase (water and steam) flow region is present in the southern part of the reservoir system at depth, extending from the lower part of the lake sediment layer (600 m ASL to 800 m ASL) down to a considerable depth. Slim hole S-1 (feedpoint elevation ~ 580 m ASL) discharged nothing but dry steam. Furthermore, it appears that the two-phase region in the neighborhood of slim hole S-3 extends at least as deep as +400 m ASL. Since temperatures generally increase to the south in the Sumikawa area, it would appear that the depth of the bottom of the two-phase zone will likewise increase to the south.

The vertical permeabilities at Sumikawa are small in comparison with horizontal permeabilities. Permeability in the field is due primarily to the pervasive network of fractures. Both the volcanic and sedimentary country rocks between the fractures appear to be essentially impermeable. The lake sediments are nearly impermeable and act as a caprock for the underlying geothermal reservoirs. Pressure transient tests have been interpreted (see *e.g.*, Pritchett, *et al.*, 1990; Garg, *et al.*, 1991) to imply the presence of two high-transmissivity geothermal aquifers within the "altered andesite" and the deeper "granodiorite" formations. The shallower of these two reservoirs (in the andesite formation) is usually encountered between 1000 and 1800 meters depth, and has been penetrated by several wells. At present, only well SC-1 produces a substantial quantity of hot fluid from a permeable horizon in the "granodiorite" formation. Pressure interference data have also been used to confirm the presence of a moderately transmissive layer in the "marine-volcanic complex" formation. Because of its low vertical permeability, the "marine-volcanic complex" formation will be used for injecting waste brine.

As of early-1990, MMC and NEDO had drilled and tested thirteen slim holes (diameter ≤ 15 cm) and eleven large-diameter (diameter > 15 cm) wells. With the exception of four slim holes (0-3T, Y-1T, Y-2T, and Y-3T) and two large-diameter wells (SD-2, SN-8R), some injection and/or production data are available for all of the Sumikawa boreholes. The authors have analyzed drilling data (circulation losses, well completion and geologic data) and downhole PTS (*i.e.*, pressure/temperature/spinner) surveys for the eighteen boreholes for which some production and/or injection data are available. The feedzone depth, final borehole diameter and feedzone temperature are listed in Table 1.

Table 1. Sumikawa boreholes with production or injection data

Borehole Name	Measured Depth (meters)	Vertical Depth (m TVD)	Feedzone Depth (m TVD)	Final Diameter (mm)	Feedzone Temperature (°C)	Production/ Injection Data
50-HM-3	501	501	460?	79	—	I
N60-KY-1	1604	1604	1560	101	205	I
O-5T	749	749	747?	64	>210	I
S-1	448	448	436	143	—	P,I
S-2*	905	905	900	101	>225	P,I
S-2	1065	1065	940	101	240	P,I
S-3	805	805	700	101	240	P,I
S-4	1552	1552	1520	159	295	P,I
SA-1	2001	1832	1800	216	305	P,I
SA-2	2005	1943	1450	216	≥300	P,I
SA-4	2009	1739	1240	216	≥290	P,I
SB-1	2086	2006	1600	216	>260	P,I
SB-2	1384	1308	1270	216	~250	I
SB-3	1542	1366	880	216	~210	I
SC-1	2486	2472	2310	216	246	P,I
SD-1	1704	1691	1550	216	250	P,I
52E-SM-1	1003	1003	730?	79	—	I
52E-SM-2*	803	803	550	101	>170	P,I
52E-SM-2	1001	1001	980	79	>230	P
N59-SN-5	1701	1701	1600	101	>260	I

*Partially-drilled hole

3. INJECTION AND PRODUCTION TESTS

Injection tests have been performed on eighteen Sumikawa boreholes. It is a standard practice at Sumikawa to perform a short (a few hours) injection test soon after (usually within a few days) the drilling and completion of a borehole. In an effort to improve the productivity and injectivity of wells SA-1, SA-2, SA-4, S-4, SB-1, SB-2 and SB-3, MMC injected large amounts of cold river water in these wells in April and May 1989; step-rate injection tests were performed (with downhole pressure gauges) both prior to (wells SA-1, SA-2, and SA-4 only) and subsequent to (all seven wells) the river water injection. A typical injection test at Sumikawa consists of injecting cold water into a borehole at several different rates and simultaneously monitoring pressure (and temperature) downhole. While exceptions do exist, in most of the tests, the pressure tool was placed substantially above the feedzone depth. Because of wellbore cooling, the measured change in pressure at the gauge depth (gauge depth << feedzone depth) will underestimate the change in pressure at the feedzone depth. The discrepancy in rates of change at the gauge and feedzone depths will decline with continued injection. After the injection of a few wellbore volumes (say 2 or 3), the rates of pressure change at the two depths should be similar. Since in most of the Sumikawa injection tests several wellbore volumes of cold water were injected, the measured pressures can be used to infer the injectivity index (II). The injectivity index (II) is defined as follows:

$$II = \frac{\Delta M}{\Delta P}$$

Here $\Delta M/\Delta P$ is the slope of the straight-line fit to the multi-step injection rate versus injection pressure (at gauge depth) data.

Measurements taken during a typical Sumikawa injection test are shown in Figure 5. Well SC-1 was injection tested on November 15, 1987 soon after well drilling and completion. The pressure gauge in this test was set fairly close to the principal feedzone at 2310 m TVD; the slope of the straight line in Figure 5 implies an injectivity index of 5.5 kg/s-bar. The available injectivity data for the various Sumikawa boreholes are summarized in Table 2.

A total of eleven Sumikawa boreholes (slim holes S-1, S-2, S-3, and 52E-SM-2; production wells S-4, SA-1, SA-2, SA-4, SB-1 and SC-1; injection well SD-1) have been discharged at one time or another. In addition, two partially-drilled slim holes (S-2 and 52E-SM-2) were discharged for brief periods. The discharge test data are needed to define the characteristic output curves (*i.e.*, mass and enthalpy versus wellhead pressure). Wellhead enthalpy measurements suggest that slim holes S-2 (final completion), S-3 and 52E-SM-2 (final completion), and production wells SB-1 and SC-1 produce from

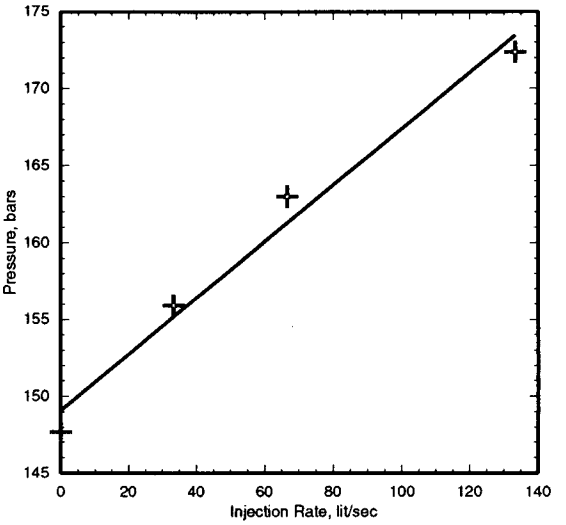

Figure 5. Injectivity test for production well SC-1 performed on November 15, 1987. The pressure gauge was set at 2300 m MD (2290 m TVD).

Table 2. Injectivity indices for Sumikawa boreholes.

Borehole Name	Final Diameter (mm)	Feedzone Depth (m TVD)	Test Date	Pressure Gauge Depth (m TVD)	Injectivity Index (kg/s-bar)	Remarks
50-HM-3	79	460	12-02-75	0	0.016	After well completion
N60-KY-1	101	1560	08-07-86	1177	0.012	After well completion
O-5T	64	747	09-22-78	280	0.28	
S-1	143	436	05-20-82	250	1.3	Injection into a shallow horizon (70–100
			05-26-82	300	6.8	meters) through a casing break
S-2	101	900	06-23-82	400	0.76	Partially-drilled, hole depth = 904.6 m
		900	07-16-82	500	0.76	Partially-drilled, hole depth = 904.6 m
		?	10-04-82	450	0.52	Partially-drilled, hole depth = ?
		940	10-16-82	500	1.62	After well completion
		940	10-23-82	500	1.76	After well completion
S-3	101	?	09-02-82	400	0.79	Partially-drilled, hole depth = 603 m?
		?	10-06-82	300	0.43	Partially-drilled, hole depth = 603 m?
		?	05-16-83	600	0.25	Partially-drilled, hole depth = 656 m
		700	06-12-83	600	1.4	After well completion
S-4	159	1520	11-06-83	700	1.4	After well completion
			11-07-83	700	1.4	After well completion
			05-19-89	700	4.9	After 1989 injection
SA-1	216	1800	10-11-86	1057	1.5	After well completion
			04-16-89	1726	0.90	Before 1989 injection
			05-16-89	1726	2.0	After 1989 injection
SA-2	216	1450	09-22-87	968	1.0	After well completion
			09-22-87	968	1.2	After well completion
			04-16-89	1062	1.3	Before 1989 injection
			05-17-89	1061	1.7	After 1989 injection
SA-4	216	1240	05-30-88	1127	0.31	After well completion
			04-17-89	1262	0.88	Before 1989 injection
			05-18-89	1262	1.0	After 1989 injection
SB-1	216	1600	10-25-87	0	0.98	After well completion
			10-26-87	0	1.5	After well completion
			11-08-87	965	0.37	After well completion
			05-27-88	965	0.49	
			08-15-88	1665	0.44	
			05-28-89	1626	2.0	After 1989 injection
SB-2	216	1270	06-22-88	674	1.8	After well completion
			05-29-89	684	1.6	After 1989 injection
SB-3	216	880	08-05-88	678	0.41	After well completion
			05-30-89	678	1.5	After 1989 injection
SC-1	216	2310	11-15-87	2290	5.5	After well completion
			06-07-88	2329	4.9	
SD-1	216	?	09-04-86	387	2.7	Partially-drilled; hole depth = 396 m
		1550	10-12-86	700	0.65	After well completion
		1550	10-17-86	799	0.92	After well completion
52E-SM-1	79	730	09-30-78	0	0.002	After well completion
52E-SM-2	101	550	08-26-78	0	0.068	Partially-drilled; hole depth = 803 m
N59-SN-5	101	1600	11-12-85	0	0.068	After well completion

Notes: 1. After well completion ≡ within 1 month of drilling and well completion.
2. 1989 injection test: cold river water was injected into SA-1, SA-2, SA-4, S-4, SB-1, SB-2 and SB-3 during April and May 1989.

all liquid feedzones with little or no *in situ* boiling. Production from all the other Sumikawa boreholes is accompanied by *in situ* boiling. Slim hole S-1 and production wells SA-2 and SA-4 discharge only steam. A typical mass output curve for a Sumikawa borehole is shown in Figure 6. Interestingly, production from partially-drilled slim holes S-2 and 52E-SM-2 causes *in situ* boiling; final completions of these slim holes discharge fluid with an enthalpy equal to that of liquid water in the reservoir. In an attempt to stimulate well productivity, cold river water was injected into wells S-4, SA-1, SA-2, SA-4 and SB-1 in April and May 1989. Cold water injection was ineffective in raising the productivity of wells S-4 and SA-2. Production from well SA-1 nearly doubled and that from SA-4 increased by about 25 percent. In as much as SB-1 was not discharged prior to cold river water injection, it is impossible to evaluate the efficacy of cold water injection for this well.

Figure 6. Discharge rate versus wellhead pressure for production well S-4 (1984, 1985, 1986, and 1988).

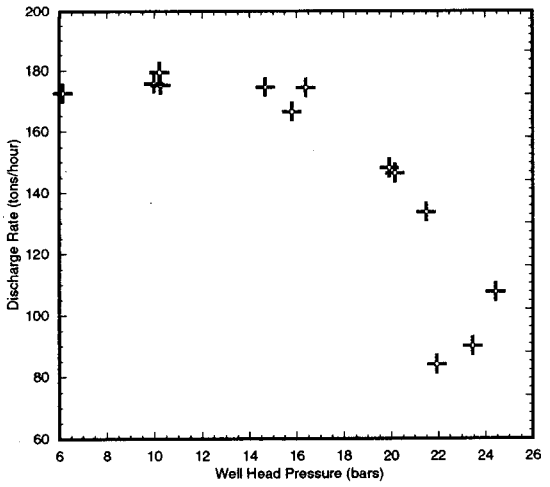

The measured maximum mass discharge rates for the various Sumikawa boreholes are presented in Table 3. It is apparent from Table 3 that the maximum discharge for Sumikawa production wells varies over a wide range (from 28 tons/hour for SA-2 to 490 tons/hour for SC-1). Even for wells with liquid feeds and/or wells with limited *in situ* boiling, the discharge rate varies widely (from < 100 tons/hour for SD-1 to 490 tons/hour for SC-1). This large variation in discharge rates underscores the heterogeneous character of formation permeability at Sumikawa.

During the discharge tests of seven boreholes (slim hole S-2, partially-drilled slim hole S-2, large-diameter wells S-4, SA-1, SA-4, SC-1 and SD-1), pressure and temperature (or pressure, temperature

Table 3. Measured and predicted discharge rates for Sumikawa boreholes.

Borehole Name	Final Diameter (mm)	Measured Discharge Rate (tons/hour)	Area-Scaled Discharge* (tons/hour)	Scaled Maximum Discharge** (tons/hour)	Remarks
(A) Boreholes with liquid feeds and no *in situ* boiling					
52-E-SM-2	79	27	202	355	Final completion
S-2	101	52	238	364	Final completion
S-3	101	16	73	112	
SB-1	216	105			
SC-1	216	490			
(B) Boreholes with limited *in situ* boiling					
S-4	159	180	332	394	
SD-1	216	100			
(C) Boreholes with extensive *in situ* boiling					
52E-SM-2	101	5.1	23	36	Partially-drilled
S-2	101	4.1	19	29	Partially-drilled
S-1	143	35	80	101	
SA-1	216	62			
SA-2	216	28			
SA-4	216	30			

* Area Scaled Discharge Rate = Measured Discharge Rate × (216/well dia. in mm)^2

** Scaled Maximum Discharge Rate = Measured Discharge Rate × (216/well dia. in mm)$^{2.56}$

and spinner) surveys were run. These pressure/temperature surveys were used to calculate the productivity indices for the Sumikawa boreholes. Productivity index, PI, is defined as follows:

$$PI = \frac{M}{P_{ns} - P_{fp}}$$

where M is the mass discharge rate, P_{ns} is the stable (static) feedzone (or gauge depth) pressure, and P_{fp} is the flowing feedzone (or gauge depth) pressure. The static feedzone (or gauge depth) pressure was estimated from shutin pressure surveys. The pressure surveys in the discharging boreholes were used to obtain the flowing pressures.

As an example, consider production well SC-1. The well produces liquid water from several feedzones between 1950 m MD (temperature = 307°C) and 2320 m MD (temperature = 246°C). Over 60 percent of the production is derived from the feedzone at 2320 m MD (2310 m TVD). The stable pressure at 2310 m TVD is 149.0 bars. During a discharge test in November 1988, three downhole pressure/temperature/spinner surveys were run. Using the flowing pressures measured in the latter surveys, the productivity index for SC-1 is estimated to be 5.7 (±0.5) kg/s-bar. The productivity indices for individual Sumikawa wells are summarized in Table 4.

4. COMPARISON OF PRODUCTIVITY AND INJECTIVITY INDICES

Apart from transient effects associated with the initiation of production (or injection) from a borehole, the flow resistance (*i.e.*, pressure losses) of the reservoir rocks can be represented by the productivity (or injectivity) index. Injectivity indices are available for eighteen Sumikawa boreholes (see Table 2). Five of the boreholes listed in Table 2 (50-HM-3, O-5T, 52E-SM-1, 52E-SM-2, and N59-SN-5) are located outside the permeable zone of the Sumikawa field. Slim hole N60-KY-1 within the

Table 4. Productivity indices for Sumikawa boreholes.

Borehole Name	Final Diameter (mm)	Feedzone Depth (m TVD)	Test Date	Total Flow Rate (kg/s)	Static Pressure (bars)	Flowing Pressure (bars)	Productivity Index kg/s-bar)	Remarks
S-1	143	436	04-25-82 04-27-82 04-30-82	—	—	—	0.86	Produced dry-steam. PI estimated from mass flow rate and wellhead pressure (see text).
S-2	101	900	07-11-82	1.10	47.3*	7.26	0.027	Partially-drilled, hole depth = 904.6 m Two-phase feed
	101	940	11-10-82	13.4	51.0	40.5	1.3	Liquid feed
S-4	159	1520	10-04-84 10-31-84 10-12-85	37.5 39.1 35.1	93.0	51.3 49.4 58.2	0.90 0.90 1.01	Two-phase feed. Flowing pressure extrapolated from pressure surveys to 1050, 1050 and 1070 meters depth (see text).
SA-1	216	1800	09-21-89 09-22-89	13.6 13.7	114.0	26.5 34.6	0.16 0.17	Well produces mostly steam Two-Phase feed
SA-4	216	1240	09-23-89	8.06	81.0	10.8	0.11	Well produces dry steam from a two-phase feed
SC-1	216	2310	11-04-88 11-06-88 11-07-88	48.1 55.2 86.1	149.0	139.7 140.1 133.6	5.2 6.2 5.6	Liquid feeds (several entries)
SD-1	216	1200 (middle of permeable interval)	09-18-89 09-19-89	23.5 17.4	77.0	23.8 47.0	0.44 0.58	Several entries. Shallowest (800–900 m) two-phase; deeper entries liquid.

*Estimated from a fit to feedzone pressures for Sumikawa wells

Sumikawa field displays excellent pressure communication with several Sumikawa wells (S-4, SB-1, and SB-2); this slim hole has, however, very limited injectivity (see Table 2). Slim hole N60-KY-1 was injection tested only once (shortly after drilling); it is likely that the permeable fractures at the time of the test were laden with drilling mud and/or rock flour. In the following discussion, we will not further consider injectivity data for the aforementioned six boreholes. Of the remaining twelve boreholes (S-1, S-2, S-3, S-4, SA-1, SA-2, SA-4, SB-1, SB-2, SB-3, SC-1, SD-1), productivity indices (Table 4) are available for seven boreholes (S-1, S-2, S-4, SA-1, SA-4, SC-1, SD-1). The productivity and injectivity indices for the latter seven boreholes are compared in Table 5.

Table 5. Comparison of productivity and injectivity indices for Sumikawa boreholes.

Borehole Name	Final Diameter (mm)	Feedzone Depth (m TVD)	Injectvity Index (kg/s-bar)	Productivity Index (kg/s-bar)	Remarks
S-1	143	436	1.3–6.8	0.86	Borehole produces dry steam. Injection and production depths are different.
S-2	101	900	0.76	0.027	Partially-drilled, hole depth = 904.6 m. *In situ* boiling on discharge.
	101	940	1.7	1.3	Liquid feed.
S-4	159	1520	1.4	0.94	*In situ* boiling on discharge; 1983 Injectivity Index
SA-1	216	1800	1.5	0.16	*In situ* boiling on discharge; 1989 Injectivity Index
SA-4	216	1240	0.94	0.11	1989 Injectivity Index; *in situ* boiling on discharge.
SC-1	216	2310	5.2	5.7	Liquid feeds.
SD-1	216	1200 (middle of permeable interval)	0.78	0.51	Shallowest feedzone two-phase; deeper feeds liquiid.

The injectivity indices for ten of the twelve boreholes (the two exceptions are S-1 and SC-1) are all of the order of unity. Injectivity index for SC-1 is significantly larger than that for other Sumikawa boreholes. Apparently, the injected fluid in S-1 enters the formation through a casing break at 70–100 meters; thus the injectivity index for S-1 is not representative of conditions at depth. The injectivity indices for Sumikawa boreholes do not depend in any systematic manner on the borehole diameter. This result is in agreement with theoretical results of Pritchett (1993) and of Hadgu, *et al.*, (1994). Both of these authors have suggested that apart from any differences associated with differences in wellbore skin (*i.e.*, near wellbore formation damage or stimulation), the productivity (or injectivity) should exhibit only a weak dependence on borehole diameter. The Sumikawa results are, however, at variance with results for the Oguni Geothermal Field (Garg, *et al.*, 1994). Both the productivity and injectivity indices for the Oguni wells display a strong dependence on borehole diameter. We suggest that the difference between the Oguni and Sumikawa results is due to the differences in drilling practice at the two fields. At Oguni, most of the slim holes were drilled with a complete loss of circulation; the drilling mud and/or rock flour apparently plugged some of the permeable fractures. In the case of Sumikawa slim holes, no blind drilling was necessary. Rotary drilling—employed to drill large-diameter holes in both the Sumikawa and Oguni Geothermal Fields—is rarely carried out with complete loss of circulation. Thus, it is likely that formation plugging is responsible for the apparent variation of productivity/injectivity indices with diameter at Oguni; apparently, formation plugging does not vary

with diameter at Sumikawa. Data from other geothermal fields should be examined to determine the frequency of the occurrence of excess formation plugging with core drilling.

The injectivity indices for Sumikawa boreholes (~0(1)) are significantly smaller than productivity/ injectivity indices for Oguni production wells (productivity indices for Oguni wells range from 4 kg/s-bar to 15 kg/s-bar). Liquid conditions prevail at the feedzone depth during production from Sumikawa boreholes S-2 (completed hole only) and SC-1; the productivity indices for these boreholes are more or less the same as the corresponding injectivity indices. The latter conclusions are in accord with results from the Oguni boreholes (Garg, *et al.*, 1994). Production from Sumikawa boreholes other than S-2 (completed hole only) and SC-1 is accompanied by *in situ* boiling. Low formation permeability and high formation temperatures ($250°C < T < 320°C$) are responsible for *in situ* boiling on discharge. The formation transmissivity for two-phase flow is always smaller than that for liquid flow. For Sumikawa boreholes with *in situ* boiling (S-1, S-4, SA-1, SA-4 and SD-1), the productivity index is, as expected, smaller than the corresponding injectivity index.

5. EFFECT OF BOREHOLE DIAMETER ON DISCHARGE RATE

Discharge characteristics of a geothermal borehole are principally controlled by (1) pressure losses associated with flow in reservoir rocks, and (2) pipe friction and heat losses in the wellbore. At Sumikawa, pressure losses in the reservoir constitute the bulk of pressure losses in boreholes for which discharge is accompanied by *in situ* boiling. Even for boreholes with liquid conditions at the feedzone depth, the pressure loss in the formation exceeds 10 bars (see Table 4 for boreholes S-2 and SC-1). This situation is quite different from that prevailing in the case of the Oguni Geothermal Field. At Oguni, the formation permeability is sufficiently high such that the pressure losses in the reservoir are insignificant compared to pressure losses in the borehole. The discharge behavior of an Oguni borehole is principally determined by pipe friction and heat losses in the wellbore. Pressure losses in the formation cannot, however, be neglected in the case of Sumikawa boreholes.

Pritchett (1993) employed numerical simulation to investigate the fluid-carrying capacity of boreholes of varying size. In the work by Pritchett (1993), the pressure losses in the formation were assumed to be negligible. Furthermore, the feedzone was assumed to contain single-phase liquid. Based on numerical simulations, Pritchett (1993) suggests that the maximum discharge rate M_{max} will increase at a rate somewhat greater than the square of borehole diameter.

$$M_{\max} = M_o\left(d/d_o\right)^{2+n}, \quad n>0$$

where M_o is the actual borehole discharge rate, and d and d_o are the internal borehole diameters (mm). The exact value of n will most likely vary with feedzone conditions (depth, pressure, enthalpy, and gas content). For the conditions assumed by Pritchett (depth = 1500 m, pressure 80 bars, single phase liquid at 250°C, uniform borehole diameter), n is approximately equal to 0.56. The conditions assumed in Pritchett's work do not hold for Sumikawa boreholes. There is a need to extend Pritchett's work to investigate the effects of pressure losses in the reservoir and of *in situ* boiling on the flow capacity of geothermal boreholes.

The "area-scaled discharge rate" M^* is defined as follows:

$$M^* = M_o\left(d/d_o\right)^2$$

The "area scaled" and "scaled maximum ($n=0.56$)" discharge rates for the Sumikawa slim holes are compared with measured discharge rates from large-diameter Sumikawa production wells in Table 3. The discharge rates for wells SB-1 (liquid feed) and SD-1 (limited boiling) are approximately equal to the scaled maximum discharge rate for slim hole S-3. The discharge rates for wells SB-1, SD-1 and S-3 (scaled maximum discharge rate) are unusually small for wells with liquid feedzones; the discharge rate in this case is limited by low formation permeability and not by pressure losses in the borehole. The scaled maximum discharge rates for slim holes S-2 and 52E-SM-2 (liquid feeds) provide an adequate prediction for discharge from well S-4 (limited *in situ* boiling). The measured discharge rate for well SC-1 (liquid feeds), however, exceeds the scaled maximum discharge rate for slim holes S-2 and 52E-SM-2 by about 25 percent. The maximum discharge (scaled to a nominal 216 mm diameter) rates for Sumikawa boreholes with little or no *in situ* boiling (52E-SM-2, S-2, S-3, SB-1, SC-1, S-4, SD-1) range from 100 tons/hour (well SD-1) to 490 tons/hour (well SC-1). The comparable range for Oguni wells extends from 227 ton/hour (slim hole GH-7) to 488 ton/hour (slim hole GH-8). The upper limit for the discharge rates is about the same for both the Sumikawa and Oguni boreholes. The Sumikawa boreholes do, however, display considerably more variability in discharge rates than the Oguni boreholes. In any event, the above-discussed data for Sumikawa boreholes taken in conjunction with Oguni data (Garg, *et al.*, 1994), imply that the "scaled-maximum discharge rate"

provides a reasonable first prediction of the discharge performance of large-diameter geothermal wells (with little or no *in situ* boiling).

The measured maximum discharge rates for Sumikawa boreholes with extensive *in situ* boiling are substantially lower than for boreholes with liquid feedzones. The average scaled maximum discharge rate for slim holes 52E-SM-2, S-2, and S-1 is 55 tons/hour. By comparison, the average measured discharge rate for production wells SA-1, SA-2 and SA-4 is 40 tons/hour. The latter value for discharge rate (40 tons/hour) is not too different from that for Oguni well GH-15 (36 tons/hour). Oguni slim hole HH-2 has a scaled maximum discharge rate of 72 tons/hour. Based upon the available data from Oguni and Sumikawa boreholes (four slim holes, four large-diameter wells) with extensive *in situ* boiling, it appears that the "scaled maximum discharge rate" provides too high a prediction for the discharge rate of large-diameter wells. In all likelihood, the scaling rule (n = 0.56) derived for boreholes with liquid feeds and with little or no pressure loss in the formation, is not applicable to boreholes with two-phase feeds. Additional theoretical work is needed to examine the scalability (or lack thereof) of discharge data from slim holes to predict the performance of large-diameter wells.

The Sumikawa and Oguni borehole data (especially for boreholes with liquid feeds) provide support for the premise that the discharge performance of large-diameter production wells may be forecast using production/injection data from slim holes. The utility (and applicability) of any prediction scheme can only be established by examining actual discharge data from a statistically significant number of slim holes and production wells from several geothermal fields. The set of geothermal fields should include both single and two-phase reservoirs. A wide range of permeabilities is also needed to delineate the effect of pressure losses in the reservoir on the discharge performance of boreholes.

6. ACKNOWLEDGMENTS

We express our sincere appreciation to the Mitsubishi Materials Corporation, Tokyo, Japan (MMC) for their kind cooperation in making their proprietary data for the Sumikawa Geothermal Field available for the present study. This work was supported under contract AG-4387 from Sandia National Laboratories.

7. REFERENCES

Combs, J. and J. C. Dunn (1992), "Geothermal Exploration and Reservoir Assessment: The Need for a U.S. Department of Energy Slim-Hole Drilling R&D Program in the 1990s", *Geothermal Resources Council Bulletin, Vol. 21, No. 10,* pp. 329–337.

Finger, J. T., C. E. Hickox, R. R. Eaton, and R. D. Jacobson (1994), "Slim-hole Exploration at Steamboat Hills Geothermal Field," *Geothermal Resources Council Bulletin, Vol. 23, No. 3,* pp. 97-104.

Garg, S. K., J. Combs and M. Abe (1994), "A Study of Production/Injection Data from Slim Holes and Production Wells at the Oguni Geothermal Field, Japan," *Proceedings Nineteenth Workshop on Geothermal Reservoir Engineering*, Stanford University, Stanford, California, January 18–20, in press.

Garg, S. K., J. W. Pritchett, K. Ariki, and Y. Kawano (1991), "Pressure-Interference Testing of the Sumikawa Geothermal Field," *Proceedings Sixteenth Workshop on Geothermal Reservoir Engineering*, Stanford University, Stanford, California, January 23–25, pp. 221–229.

Hadgu, T., R. W. Zimmermann and G. S. Bodvarsson (1994), "Comparison of Output from Slim Holes and Production-Size Wells," *Proceedings Nineteenth Workshop on Geothermal Reservoir Engineering*, Stanford University, Stanford, California, January 18–20, in press.

Kubota, Y. (1988), "Natural Convection System at the Ohnuma-Sumikawa Geothermal Field, Northeast Japan," *Proceedings Tenth New Zealand Geothermal Workshop*, Auckland, New Zealand, pp. 73–78.

Pritchett, J. W. (1993), "Preliminary Study of Discharge Characteristics of Slim Holes Compared to Production Wells in Liquid-Dominated Geothermal Reservoirs, *Proceedings Eighteenth Workshop on Geothermal Reservoir Engineering,* Stanford University, Stanford, California, January 26–28, pp. 181–187.

Pritchett, J. W., S. K. Garg, T. G. Barker and A. H. Truesdell (1990), Case Study of a Two-Phase Reservoir, Sumikawa Geothermal Field (Phase 5)," Report Number SSS-FR-90-11401, S-Cubed, La Jolla, California.

PROCEEDINGS, Twentieth Workshop on Geothermal Reservoir Engineering
Stanford University, Stanford, California, January 24-26 1995
SGP-TR-150

PRELIMINARY ESTIMATES OF ELECTRICAL GENERATING CAPACITY OF SLIM HOLES—A THEORETICAL APPROACH

John W. Pritchett
S-Cubed, P.O. Box 1620
La Jolla, California 92038-1620

ABSTRACT

The feasibility of using small geothermal generators (< 1 MWe) for off-grid electrical power in remote areas or for rural electrification in developing nations would be enhanced if drilling costs could be reduced. This paper examines the electrical generating capacity of fluids which can be produced from typical slim holes (six-inch diameter or less), both by binary techniques (with downhole pumps) and, for hotter reservoir fluids, by conventional spontaneous-discharge flash-steam methods. Depending mainly on reservoir temperature, electrical capacities from a few hundred kilowatts to over one megawatt per slim hole appear to be possible.

1. BACKGROUND

Small geothermal generators (from 100 to 1000 kilowatts capacity) have considerable promise for off-grid electrification around the world. Areas of particular interest include the more remote parts of Latin America, the Philippines and Indonesia, as well as numerous islands around the Pacific Rim. Entingh, *et. al.* (1994) examined the economic feasibility of such projects and concluded that small single-well plants of this type can compete favorably with existing off-grid electrification techniques in this capacity range (mainly diesel generators, which typically cost around one U.S. dollar per kilowatt-hour).

For projects in the 100–1000 kWe range, however, the costs of drilling and completing the production well dominate the economics. Entingh, *et. al.* assumed that the well would be drilled using conventional techniques (13-$^5/_8$ inch casing to 750 feet, 9-$^5/_8$ inch below that depth). If a slim hole could be used instead (herein defined as a well with inside diameter of six inches or less), considerable savings in drilling costs and final electricity price would be realized. Slim-hole drilling costs are typically only about one-third (per foot) of those of conventional drilling practice in the geothermal industry (Combs and Dunn, 1992).

The main drawbacks of using slim holes are (1) the capacity of a slim hole to produce fluid is substantially less than that of a conventional production well (Pritchett, 1993) and (2) if a downhole pump is required, small-diameter downhole pumps suitable for high-temperature operation are not presently commercially available. The absence of a suitable downhole pump mostly reflects lack of demand; no major technical obstacles exist in principle to scaling down designs for existing driveline pumps to fit into wells as small as four inches inside diameter (Gonzalez, 1994).

The remaining problem is to establish whether or not slim holes can deliver enough hot brine to the wellhead to be of practical interest for off-grid electrification projects. A preliminary examination of this question is presented in this paper. In view of the exploratory character of this study, numerous simplifying assumptions were made which could be relaxed in future work and examined in a properly funded sensitivity analysis. The main objective of the present study was simply to establish whether or not slim holes are practical for fueling small scale (< 1 MWe) geothermal power plants. Two situations were considered: (1) small backpressure and condensing steam-turbine geothermal plants powered by spontaneously discharging wells, and (2) small binary geothermal plants using wells with downhole pumps.

The present study is not exhaustive; in fact, only a single well feedpoint depth was considered (600 meters). The stable reservoir pressure at this depth was likewise fixed at 40 bars (absolute) for all cases considered. The reservoir fluid was treated as pure H_2O, even though substantial amounts of dissolved CO_2 gas are often present, which can have significant effects (both positive and negative) on power production. All wells considered have uniform inside diameter: either four inches (10.16 cm), five inches (12.70 cm) or six inches (15.24 cm). Three different values of borehole productivity index were likewise considered: 2 kg/second/bar, 4 kg/second/bar and infinity. Reservoir temperatures considered range from 100°C to 240°C. In all cases, the reservoir fluid is single-phase liquid.

2. FLASH-STEAM TURBOGENERATORS / UNPUMPED SLIM HOLES

Small backpressure steam turbines are the simplest geothermal generators available. Their main disadvantages are high steam consumption and potential air pollution problems. Skid-mounted backpressure units have been available commercially for many years, with capacities ranging from 200 kWe to 5,000 kWe. Typically, the inlet pressure for these units is about 50 psig (4.46 absolute bars). At that pressure, steam consumption ranges from 5 to 8 kilograms of 50 psig steam per second per megawatt of electricity generated. It was conservatively estimated, for modeling purposes, that a "typical" backpressure turbine requires 7 kg/s/MWe of steam at 50 psig.

Small condensing steam turbines, while more complex and costly, produce substantially more power for a fixed steam supply and can be equipped to minimize air pollution. Unfortunately, such units are not yet readily available on a production-line basis at commercially acceptable terms. Condensing steam turbines can be designed to operate at much lower inlet pressures than backpressure units (sub-atmospheric inlet pressures are even possible), and thereby can exploit lower-temperature reservoirs. For the present study, however, it was assumed that a "typical" small condensing steam turbogenerator would also require a 50 psig steam supply, and that the specific steam consumption would be one-half of that of the backpressure turbine (3.5 kg/s/MWe). This estimate is probably conservative.

Although it is likely that the generating unit will be located very near the wellhead, a 0.5 bar pressure drop was assumed to occur between the wellhead and the turbine inlet. Thus, in all cases considered, the wellhead pressure was fixed at 4.96 bars (57.3 psig). A series of calculations was then carried out of the flow in uniform-diameter vertical wells to establish the total flow rate available as a function of hole diameter, productivity index, and reservoir temperature. The feedpoint depth was fixed at 600 meters where the assumed stable reservoir pressure is 40 bars. The vertical pressure gradient at a point in a flowing geothermal borehole consists of three components—hydrostatic head, an acceleration term which is small for single-phase flow but may be substantial in the two-phase region, and pipe friction. For friction, the formulation of Dukler, *et. al.* (1964) was employed. The general numerical approach is described by Pritchett (1985); for simplicity, a no-slip condition was assumed between the liquid and vapor phases in the two-phase region and lateral conductive heat losses to the formation through the casing were neglected.

Figure 1 shows the result of a typical calculation. In this case, the borehole diameter is five inches and the "intermediate" (4 kg/s/bar) productivity index was used. The reservoir temperature is 210°C. The stable reservoir pressure is 40 bars, but flow resistance in the formation (expressed by the productivity index) reduces the bottomhole flowing pressure to 35.8 bars. Below 400 meters depth the flow is essentially isothermal, but above that level the liquid boils and two-phase flow occurs. The total discharge rate is 16.8 kilograms of fluid per second which, if separated at 50 psig, yields 2.23 kg/s of steam. Note that, at 7 kg/s/MWe specific steam consumption, this borehole would produce steam capable of generating 320 kWe from a backpressure unit. At 3.5 kg/s/MWe, a condensing turbogenerator unit could deliver 640 kWe from this slim hole.

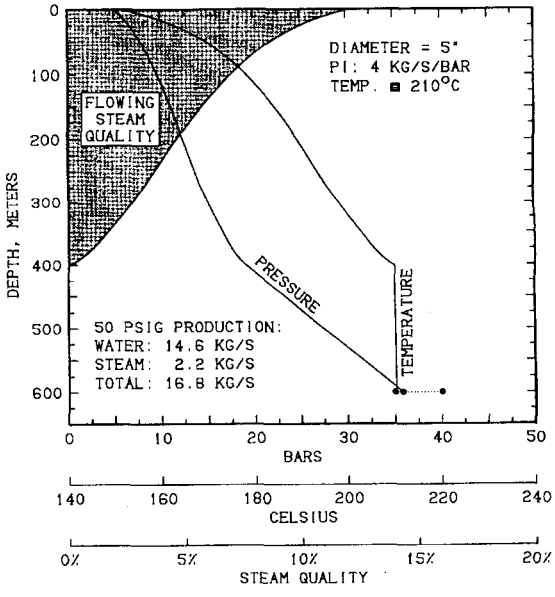

Figure 1. Computed downhole profiles in a discharging slim hole.

Calculations were carried out for 4", 5" and 6" inside diameter and for productivity indices of 2 kg/s/bar, 4 kg/s/bar, and infinity. Figure 2 summarizes the results in terms of mass flow rate of steam separated at 50 psig as a function of reservoir temperature, and also in terms of generating capacity from a small condensing turbogenerator operating at 3.5 kg/s/MWe. For a backpressure unit, these electrical capacity values should be reduced by a factor of two. Note that, at higher temperatures, capacities can significantly exceed 1000 kWe. The width of the shaded band for each hole diameter reflects the effect of varying the productivity index.

These results also indicate that reservoir temperatures of at least 180°C–190°C are required to

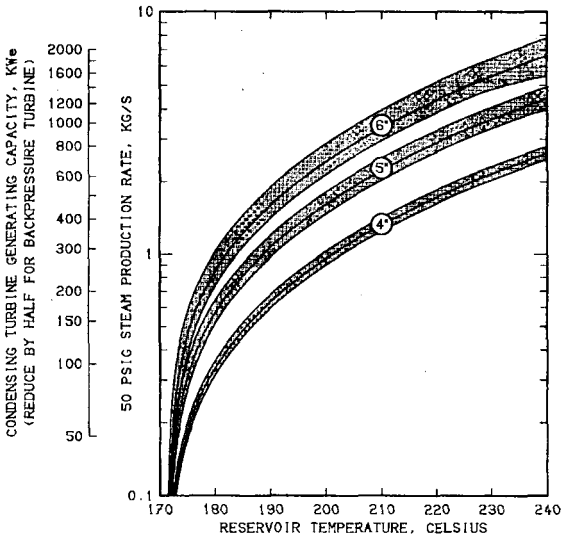

Figure 2. Steam production rate (separated at 50 psig) and available electrical generating capacity using flash-steam techniques from slim holes of various diameters as functions of reservoir temperature. Ranges are due to variations in downhole productivity index assumed.

produce useful amounts of power using these techniques. If, however, steam turbines with lower inlet pressures had been incorporated in the study (in addition to the 50 psig units), this temperature limitation would be less severe (at the cost of higher specific steam consumption). Using turbine entry pressure as an independent parameter and optimizing the system for maximum power production for each (reservoir temperature) / (productivity index) / (wellhead pressure) combination would increase the available power and extend the useful temperature range to lower values. In any event, it seems clear that if reservoir temperatures are sufficient, slim holes can provide enough steam for the desired applications using small conventional steam turbogenerators.

3. BINARY SYSTEMS / DOWNHOLE PUMPS

Binary generators have historically been the preferred technique for obtaining electricity from low- and moderate-temperature geothermal resources. Brine is brought to the surface with the help of a downhole pump, then circulated through a heat exchanger and reinjected. A low boiling-point secondary working fluid (such as isobutane or freon) flows in a closed loop from the heat exchanger (where it is vaporized) through a gas turbogenerator to a condenser, then back to the heat exchanger. The principal disadvantages of binary units are relatively high initial capital cost, mechanical complexity, and (for higher reservoir temperatures) reduced efficiency compared to condensing steam turbines.

Downhole pumps are required because reservoir temperatures are usually too low in typical binary applications for spontaneous discharge, and because it is important to maintain the geothermal brine in an all-liquid condition to maximize heat transfer and avoid scaling and corrosion in the heat exchanger (which is one of the most expensive components of the system). Conventional practice is to use driveline pumps, with an electric motor at the wellhead driving a multi-stage downhole pump through a gearbox by means of a long downhole vertical driveshaft. "Submersible" pumps (in which the electric motor is also downhole) have been under development for a number of years, but with limited success. For the present study, it was assumed that driveline pumps would be employed. One important limitation of driveline pumps is that the maximum practical pump depth is around 500 meters (Gonzalez, 1994).

The hot fluid requirements of binary generating systems depend upon numerous design parameters. For the present preliminary study, however, it was simply assumed that the amount of electrical power obtainable from such a power plant per kilogram of hot supply brine per second depends only on the plant inlet brine temperature (thereby neglecting differences in heat exchanger design, working fluid properties, *etc.*). Figure 3 shows the relationship between the plant efficiency (expressed as output

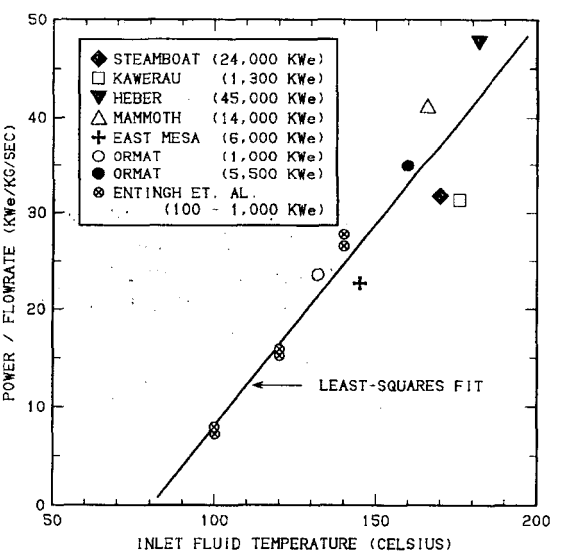

Figure 3. Gross electrical generating capacity (normalized to inlet brine mass flow rate) of various binary geothermal power stations as functions of brine inlet temperature.

electrical power relative to inlet brine flow rate) and plant inlet temperature for a variety of systems, including both actual field experience (Steamboat, Kawerau in New Zealand, Heber, Mammoth and the old East Mesa facility) and design estimates (Ormat, Entingh, *et. al.*). Somewhat surprisingly, despite variations in secondary loop fluid characteristics and other design parameters, all the data in Figure 3 are reasonably well represented by a simple linear function of inlet temperature:

$$\dot{E}_{gross} = 0.415\dot{M}(T - 80.6) \qquad (1)$$

where $\dot{E}_{gross}$ is the electrical power available from the generator, $\dot{M}$ is the inlet plant brine flow rate in kilograms per second and T is the brine inlet temperature (Celsius). A more detailed investigation would doubtless reveal important dependences upon other aspects of plant design, but for the present preliminary study the above correlation suffices.

As will be seen, the electrical power demands of the downhole pump have a major influence upon the net generating capacity of the binary systems considered in this study. Essentially, a downhole pump is a device for raising the flowing pressure of the upflowing fluid as it passes through the pump. The hydraulic power delivered by the pump is given simply by:

$$\dot{E}_{hyd} = \Delta P \times \dot{V} \qquad (2)$$

where ΔP is the pressure increase induced by the operation of the pump and $\dot{V}$ is the volumetric flow rate of the liquid through the pump. The hydraulic power $\dot{E}_{hyd}$ is related to the mechanical power delivered to the downhole pump by the driveline $\left(\dot{E}_{mech}\right)$ by the "mechanical/hydraulic efficiency", which depends upon a variety of factors including pump design, diameter, and flow rate. The mechanical power $\dot{E}_{mech}$ is related in turn to the electrical power consumed by the wellhead motor $\left(\dot{E}_{motor}\right)$ by the "electrical/mechanical efficiency" which incorporates losses in the motor, the gearbox, the downhole shaft bearings, etc. In the present study, it was assumed that the "electrical/mechanical efficiency" is 85 percent, based on informal discussions with various field operators:

$$\dot{E}_{mech}/\dot{E}_{motor} = 0.85 \qquad (3)$$

The "mechanical/hydraulic efficiency" $\left(\dot{E}_{hyd}/\dot{E}_{mech}\right)$ depends, for a particular pump, on the volumetric flow rate passing through the pump. The efficiency is zero at zero flow rate, but increases with increasing flow rate to a maximum value, then decreases again with further flow rate increase. For typical geothermal driveline pumps, the maximum efficiency is around 70 percent to 80 percent. Smaller diameter pumps exhibit similar behavior, but the maximum efficiency will usually be somewhat lower and will be realized at a much lower flow rate.

Figure 4 shows measured mechanical/hydraulic efficiency data for several downhole pumps, including four different pumps of 33 cm diameter and one of only 9 cm diameter (the 9 cm diameter pump is similar in basic design to the 33 cm geothermal pumps, but was not intended for high-temperature applications). In Figure 4, the efficiency data are plotted as functions of volumetric flow rate per unit cross-section area (of the smallest pipe within which the pump will fit), which amounts to the average upward fluid velocity just below the pump. Evidently, maximum efficiency is achieved when this average velocity is around 0.8 to 1.0 meters per second for pumps of this type. As shown, these data are adequately represented by the following expression:

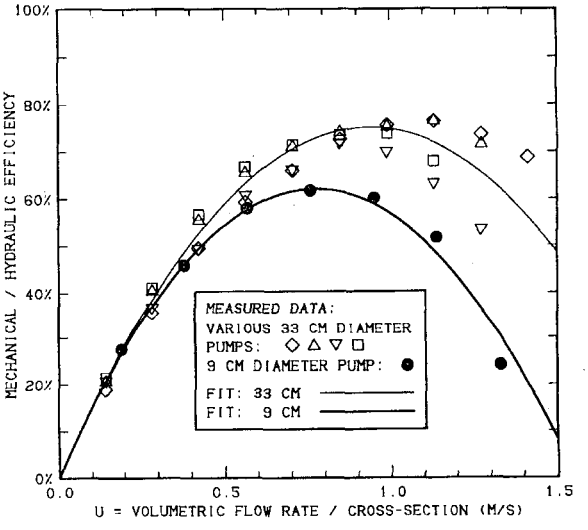

Figure 4. Mechanical/hydraulic efficiency of various driveline-type downhole pumps.

$$\dot{E}_{hyd}/\dot{E}_{mech} = 1.60\,U - \left(0.784 + \frac{2.22}{D}\right)U^2 \qquad (4)$$

where U is the above average velocity (m/s) and D is the pump (pipe) diameter in centimeters. This expression was used to estimate the pump efficiency available from the (hypothetical) downhole pumps in the slim holes considered in this study. For various inside diameters of interest, the fit yields for the

maximum efficiency and the corresponding volumetric flow rate:

Diameter	Maximum Efficiency	Corresponding Velocity	Corresponding Flow Rate
4" (10.16 cm)	63.9%	0.798 m/s	0.0065 m^3/s
5" (12.70 cm)	66.8%	0.834 m/s	0.0106 m^3/s
6" (15.24 cm)	68.8%	0.860 m/s	0.0157 m^3/s
13" (33.00 cm)	75.2%	0.939 m/s	0.0803 m^3/s

These pumps are only effective for single-phase liquid flow. To avoid pump cavitation, the minimum pump depth was required to be 20 meters below that depth within the well where the fluid would otherwise begin to boil.

Since all flow within the well for these binary cases is by definition single-phase, the calculation of the flow within the well is somewhat simplified as compared to the flash-steam cases. In the binary case, however, lateral heat losses to the formation were taken into account using a heat loss formulation (see Pritchett, 1985) derivable from the work of Minkowycz and Cheng (1976), assuming a fairly high average formation thermal conductivity (3 W/m/°C) and that the formation temperature distribution is linear with depth between 10°C at the ground surface and reservoir temperature at the feedpoint (600 meters). This will usually overestimate heat losses somewhat. The Dukler, *et. al.* (1964) friction correlation was also employed in the binary cases.

The general approach is as follows. For specified values of reservoir temperature, well diameter and productivity index, at any particular mass flow rate the pump is placed 20 meters below the bubble-point depth, and the pump-induced pressure increase (ΔP) is adjusted so as to just maintain single-phase liquid conditions at the wellhead. As a practical matter, the necessary number of downhole pump stages is dictated by the above value of ΔP. The volumetric flow rate at the pump is computed based on the pipe diameter, the specified mass flow rate, and the steam-table density of water at the local temperature. This permits the calculation of the hydraulic power required (Eqn. 2) and the power required by the electric motor (using Eqns. 3 and 4). The gross electric power available from the generator is given by Eqn. 1 (where T is the computed wellhead brine temperature); the net exportable electrical power available from the system is therefore:

$$\dot{E}_{net} = \dot{E}_{gross} - \dot{E}_{motor} \qquad (5)$$

This procedure is repeated for various assumed mass flow rates until a value is found which maximizes $\dot{E}_{net}$ (the maximum power available from the binary system for the selected values of well diameter, productivity index, and reservoir temperature).

Figure 5 (upper) shows the ratio $\dot{E}_{motor}/\dot{E}_{gross}$ as a function of reservoir temperature for these calculations; the width of the band reflects the variability due to variations in well diameter (4" to 6") and productivity index (2 kg/s/bar to infinity). At low temperatures, the downhole pumping burden can consume over half the gross electricity generated. Even at high temperatures, the burden exceeds 20%. The reservoir considered in these calculations is relatively low-pressure (40 bars at 600 meters depth), which contributes to the high pumping power requirements. The lower part of Figure 5 similarly shows the range of "minimum pump depth" as a function of reservoir temperature for these calculations. At 200°C, required pump depths are approaching 500 meters, which is the probable practical depth limit for driveline pumps. For this reason, calculations were not carried out for higher reservoir temperatures.

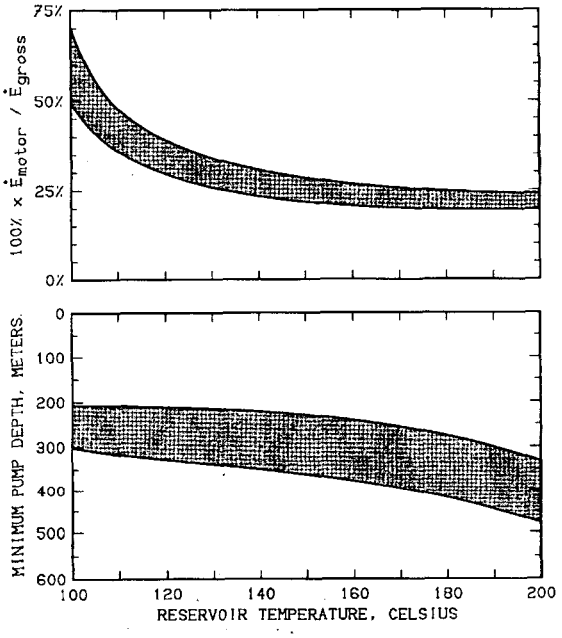

Figure 5. Electrical burden imposed by downhole pump (upper) and minimum permissible pump depth (lower) as functions of reservoir temperature. Ranges due to variations in well diameter (4" to 6") and productivity index assumed (2 kg/s/bar to infinity).

Figure 6 shows how the maximum value of the net export power $\dot{E}_{net}$ varies with reservoir temperature for each well diameter considered (4", 5" and 6"). The width of each band reflects the effects of varying the productivity index. Even for the smallest hole diameter considered (4"), 100 kWe or more

can be generated so long as the reservoir temperature exceeds 125°C or so, and for higher temperatures the capacity of a six-inch slim hole approaches 1000 kWe.

4. SUMMARY AND CONCLUSIONS

Substantial improvements are obviously required to transform the present preliminary "quick-look" into a comprehensive study of the generating

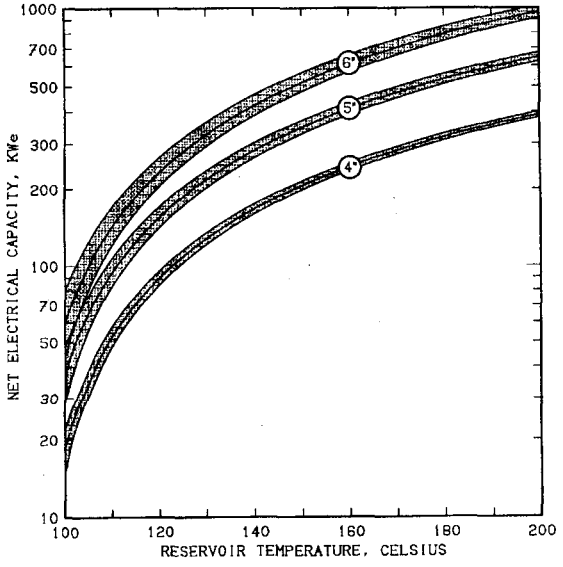

Figure 6. Net electrical generating capacity using binary techniques available from slim holes of various diameters as functions of reservoir temperature. Ranges are due to variations in downhole productivity index.

capacity of slim hole completions. These include increasing the sophistication of the powerplant models employed (both flash-steam and binary), improving the characterization of the downhole pump (and perhaps considering alternatives to driveline pumps), and improving the borehole brine flow description (in particular, incorporating liquid/vapor slip and lateral heat losses in the flash-plant model). Consideration should also be given to varying the inlet turbine pressure for the condensing flash-steam case to optimize performance. For low inlet pressures and low reservoir temperatures, downhole pumps may be required in the flash-steam case as well. Furthermore, the effects of varying the borehole feedpoint depth (fixed at 600 meters in the present work) and the reservoir pressure relative to depth (40 bars at 600 meters herein), as well as possible effects of non-condensables such as CO_2 need to be taken into account.

Despite these limitations, the present study clearly demonstrates that slim-hole completions have considerable potential for satisfying the brine requirements of small off-grid power stations in the 100–1000 kilowatt range. The initial capital cost savings available using slim-hole drilling techniques could substantially reduce the final cost per kilowatt-hour of such geothermal projects.

5. ACKNOWLEDGEMENTS

The author deeply appreciates the technical advice he received from Jim Combs, Jim Dunn, Sabodh Garg, Jorge Gonzalez and Colin Goranson. Without their cooperation and expertise, this study would not have been possible.

6. REFERENCES

Combs, J. and J. C. Dunn (1992), "Geothermal Exploration and Reservoir Assessment: The Need for a U. S. Department of Energy Slim-Hole Drilling R&D Program in the 1990's", Geothermal Resources Council Bulletin, v. 21, No. 10, pp. 329-337.

Dukler, A. E., M. Wicks III and R. G. Cleveland (1964), "Frictional Pressure Drop in Two-Phase Flow — B. An Approach Through Similarity Analysis", A. I. Ch. E. J., v. 10, p. 44.

Entingh, D. J., E. Easwaran and L. McLarty (1994), "Small Geothermal Electric Systems for Remote Powering", Geothermal Program Review XII: Geothermal Energy and the President's Climate Change Action Plan, U. S. Department of Energy, San Francisco.

Gonzalez, J. (1994), Johnston Pump Co., personal communication.

Minkowycz, W. J. and P. Cheng (1976), "Free Convection about a Circular Cylinder Embedded in a Porous Medium", Int. J. Heat and Mass Transfer, v. 19, p. 805.

Pritchett, J. W. (1985), "WELBOR: A Computer Program for Calculating Flow in a Producing Geothermal Well", S-Cubed Report Number SSS-R-85-7283.

Pritchett , J. W. (1993), "Preliminary Study of Discharge Characteristics of Slim Holes Compared to Production Wells in Liquid-Dominated Geothermal Reservoirs", Proc. Eighteenth Workshop on Geothermal Reservoir Engineering, Stanford University, Stanford, California, January 26–28, pp. 181–187.

PROCEEDINGS, Twentieth Workshop on Geothermal Reservoir Engineering
Stanford University, Stanford, California, January 24-26 1995
SGP-TR-150

CHARACTERIZATION OF INJECTION WELLS IN A FRACTURED RESERVOIR USING PTS LOGS, STEAMBOAT HILLS GEOTHERMAL FIELD, NEVADA, USA

Colin Goranson
Geological Engineering Consultant, Richmond, CA 94805, USA

Jim Combs
Geo Hills Associates, Los Altos Hills, CA 94022, USA

ABSTRACT

The Steamboat Hills Geothermal Field in northwestern Nevada, about 15 km south of Reno, is a shallow (150m to 825m) moderate temperature (155°C to 168°C) liquid-dominated geothermal reservoir situated in highly-fractured granodiorite. Three injection wells were drilled and completed in granodiorite to dispose of spent geothermal fluids from the Steamboat II and III power plants (a 30 MW air-cooled binary-type facility). Injection wells were targeted to depths below 300m to inject spent fluids below producing fractures. First, quasi-static downhole pressure-temperature-spinner (PTS) logs were obtained. Then, the three wells were injection-tested using fluids between 80°C and 106°C at rates from 70 kg/s to 200 kg/s. PTS logs were run both up and down the wells during these injection tests. These PTS surveys have delineated the subsurface fracture zones which will accept fluid. The relative injectivity of the wells was also established. Shut-in interzonal flow within the wells was identified and characterized.

INTRODUCTION

The Steamboat Hills Geothermal System is part of the Steamboat Springs Geothermal Area which was classified as a Known Geothermal Resource Area ("KGRA") by the United States Geological Survey. The KGRA is located on the eastern flank of the Sierra Nevada Mountains about 15 km south of Reno, Nevada along Highway 395 (see Figure 1). The Steamboat Hills geothermal reservoir is a fracture-controlled geothermal resource hosted in granitic rocks. The first geothermal well was drilled in 1920, located at a site about one mile south of the Far West Capital, Inc. ("FWC") geothermal electric power development area. A chronological account of the commercial development of geothermal power plant facilities at the Steamboat Hills Geothermal Area was presented by Combs and Goranson (1994) based primarily on earlier work by Goranson and coworkers (1990, 1991).

Injection is the necessary and acceptable disposal method for handling spent geothermal fluids. Thus, the effects of injection must be understood, with respect to the geothermal and surrounding hydrologic system. The geothermal and surrounding hydrologic system are monitored at Steamboat Hills to ascertain effects of geothermal power plant operations. Specifically, the geothermal/hydrologic system is monitored to determine any thermal, hydrologic or geochemical changes. Of direct concern, with respect

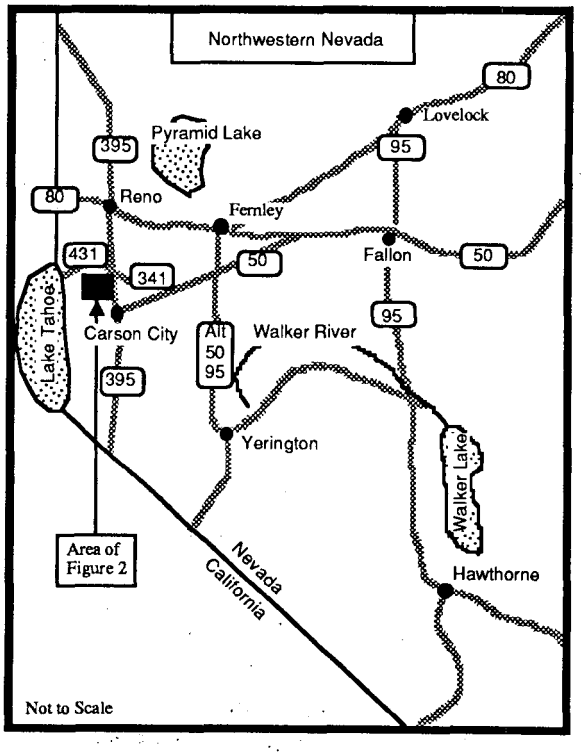

Figure 1. Regional location map of the Steamboat Hills Geothermal System.

to sustainable reservoir management, is thermal breakthrough of cooled injected fluids to production wells. Therefore, injection of spent geothermal fluids must be matched to reservoir geology, subsurface fracture zones and reservoir fluid circulation patterns.

Three injection wells; IW-1, IW-4, and IW-5, were drilled and completed in granodiorite to dispose of spent geothermal fluids from FWC Steamboat II and III (SB II&III) power plants; a 30 MW air-cooled binary-type facility (see Figure 2).

During October, 1992, with financial support from the U.S. Department of Energy through Sandia National Laboratories, injection tests were conducted on the three injection wells IW-1, IW-4 and IW-5. The injection well testing program was designed (i) to identify subsurface fracture zones accepting fluids using PTS logs, (ii) to examine the relative injectivity of the wells, and (iii) to document whether there was interzonal flow within the injection wells.

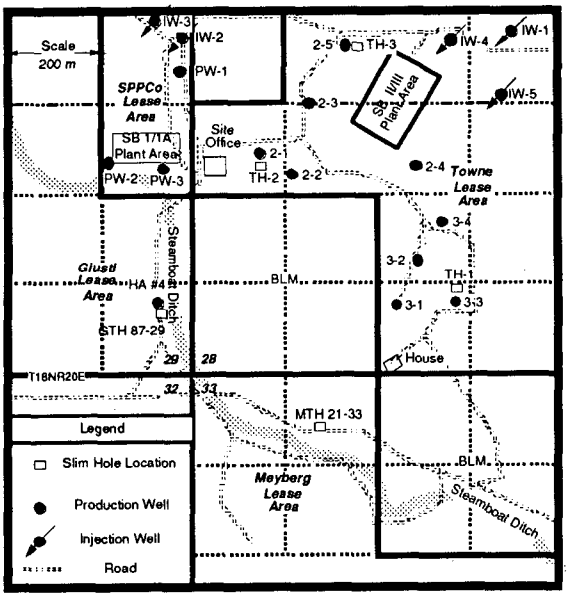

Figure 2. Location map of FWC Steamboat Hills power plants, production and injection wells.

GEOLOGICAL AND STRUCTURAL SETTING

A detailed description of the geology, hydrology, and hydrothermal alteration is beyond the scope of this paper, but a general description of the geology and structure of the Steamboat Hills Geothermal Area is provided based on the work of van de Kamp (1991). The geology of the Steamboat Springs area was initially mapped in detail by Thompson and White (1964) and White, et al. (1964). These two publications formed the basis for the geological evaluation of the geothermal system beneath the FWC leases. The moderate-temperature geothermal system covers about 6.5 km^2, including hot springs and numerous fumaroles associated with siliceous sinter surface deposits. The geothermal fluid in the reservoir has a chlorinity and temperature of approximately 800 ppm and 165°C, respectively. The fluid is produced from fractured granodiorite at a depth of approximately 300m. All of the produced fluid is injected back into the geothermal reservoir.

The oldest rock unit present in the northeast Steamboat Hills, and the geothermal reservoir host, is granodiorite of Mesozoic age (estimated as 150 to 80 mya, Silberman, et al., 1979). Younger Tertiary sediments, volcanic rocks and alluvial deposits overlie the granodiorite. In outcrops, it is apparent that there has been fracturing and faulting in the granodiorite. A fine- to medium-grained granodiorite is the major portion of the rocks penetrated by the injection wells. Additionally, the granodiorite has no intrinsic permeability, nor is there any appreciable rock matrix porosity. Therefore, the granodiorite has essentially no fluid storage capacity and all fluid flow within the granodiorite is confined to fractures. The rock is generally hard and only slightly altered to chlorite and clay minerals with abundant minute pyrite crystals located within fracture zones. Apparently, there was an early stage of chloritic alteration and fracturing in the granodiorite, followed much later by fracturing related to geothermal processes. In the later stage of fracturing, there was also chloritic alteration and filling of fractures with calcite, chlorite, silica, and minor amounts of heavy-metal mineralization.

The structural setting of the northeastern Steamboat Hills, which is part of the larger Steamboat Hills structural block, has been described in detail by van de Kamp (1991). The Steamboat Hills were uplifted relative to areas to the east, north, and west in late Tertiary and Recent times. The uplift is bounded by steep dipping north-northeast and east-northeast trending normal faults with displacement of tens to hundreds of meters or more. Fault and fracture strikes range from northeast to northwest, with measured dips ranging from 45° to 90°. Cenozoic warping and block faulting are responsible for the present mountainous topography in the Steamboat Hills area.

Three systems of faulting have been recognized in the Steamboat Hills (van de Kamp, 1991). One set strikes northeast, parallel to the axis of the Steamboat Hills. A second set, essentially at right angles to the first, strikes northwest. The third set of faults strike north-northeast and are prominent on the sinter terrace associated with dormant hot springs. In the distant past, this fault zone issued geothermal fluids to the surface, where active hot springs and associated siliceous sinter precipitation occurred, similar to the modern situation at the Steamboat Hot Springs located east of the FWC leases. Additionally, based on the results of a tracer test (Adams, et al., 1993), there is clear evidence of anisotropy within the

reservoir. The primary faults controlling fluid circulation in the geothermal reservoir appear to be the northeast trending series of steep normal faults. The abundance of fractures appears to increase with depth. Near-vertical, open fractures in the granodiorite control movement of geothermal fluids.

DRILLING AND COMPLETION DATA

Three injection wells, IW-1, IW-4 and IW-5, are located on the northeast side of the Steamboat Hills SB II&III well field (see Figure 2). The injection wells were drilled and completed deeper than producing wells. The injection well locations and design were based on three main criteria: (i) injection wells should be situated on a set of surface lineaments that strike northeast, parallel to the axis of the Steamboat Hills, within the known reservoir to provide pressure support; (ii) the injectors should be completed at depths greater than production wells to avoid thermal breakthrough, which could decrease the temperature of produced geothermal fluids (however, the possibility of lower permeability at greater depths was also of concern); and (iii) since injection wells

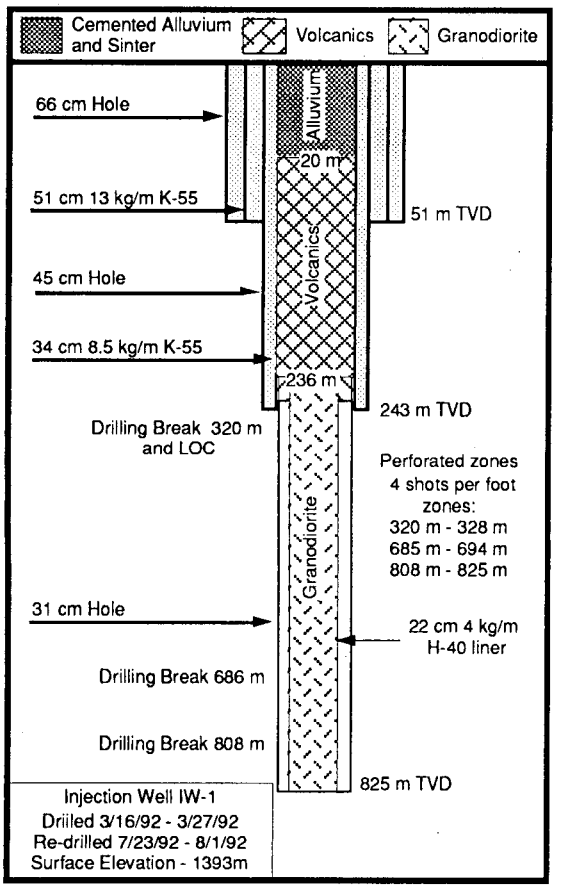

Figure 3. Geology and well completion schematic of injection well IW-1.

were located at the outer margin of the geothermal field, it was thought that they could possibly be deepened later to reach hotter fluids and converted into production wells.

All nine of the SB II&III production wells were completed into the granodiorite formation. Production well depths vary between 180m and 670m, with the majority completed to less than 300m. Injection wells were also completed into the granodiorite formation. In order to inject the spent fluids at depths below the producing fractures, and due to down dropping of the granodiorite reservoir formation with distance from Steamboat Hills, (as was expected prior to drilling), the depths and completion programs for the injection wells were designed to encounter fracture sets at subsurface depths greater than 300m.

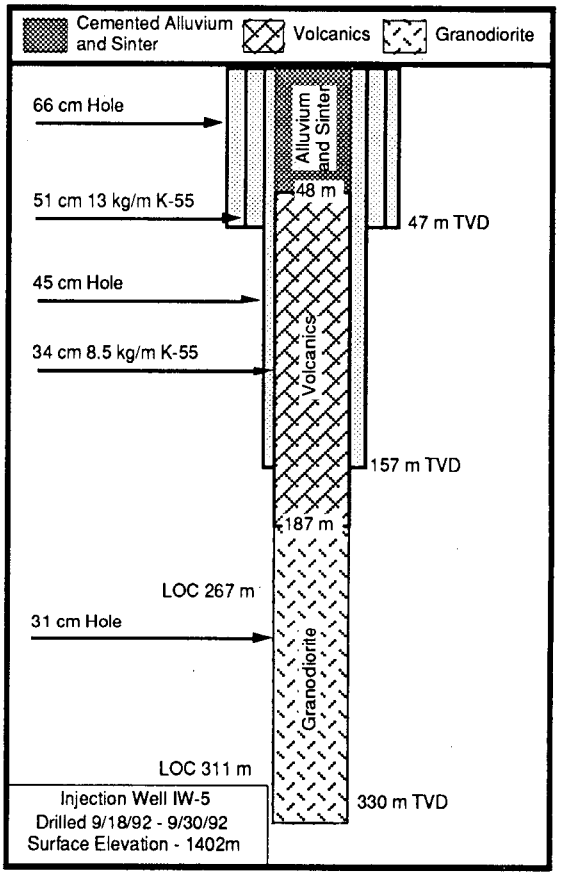

Figure 4. Geology and well completion schematic of injection well IW-5.

Injection wells, IW-1, IW-4 and IW-5, were cased to 243m, 238m, and 157m, respectively, in order to eliminate interzonal flow from the fractures above these depths. Total depths of the injectors are 825m, 550m and 330m with bottom-hole diameters of 31-cm. Each of the injection wells was drilled through a

sequence of alluvium and sinter, volcaniclastic materials, and granodiorite (see Figure 3 and Figure 4). Injection well completions consisted of a surface casing of 51-cm diameter, an intermediate casing of 34-cm diameter and a 31-cm open-hole section to total depth. Injection well IW-1, to reduce sloughing problems encountered at the contact between the volcanics and granodiorite formations, was completed with a 22-cm liner perforated over three depth intervals, corresponding to drilling breaks (see Figure 3). IW-4 and IW-5 were completed open-hole to total depth, similar to SB II&III production well completions. No circulation-loss zones were encountered above the granodiorite formation in these wells. Within the granodiorite formation circulation losses occurred; these, together with drilling breaks (with drilling rates increasing from 1.5 m/hr to >15 m/hr) serve to identify permeable subsurface fracture zones.

INJECTION AND DISCHARGE TESTING

Initial injection well testing consisted of discharging the well to an atmospheric flash tank attached to a weir box (water flow measurement device) while measuring downhole pressures with the drilling rig still in place. Well discharge was initiated by injecting air through open-ended drill pipe. Drill pipe was, typically, set at 180 m during discharge test operations.

The total discharge rate was estimated based on (1) the measured water rate through the weir box and (2) a steam flow rate, estimated based on the known reservoir temperature, one-atmosphere enthalpies of saturated water and steam and an assumption of isenthalpic flow up the well. Downhole pressures were measured with a gauge attached to the drill pipe. Based on the results of downhole pressure versus discharge rate behavior of production wells, it was determined that sufficient well injectivity existed when downhole pressure changes between static (maximum pressure measured during air injection and before initiation of discharge) and flowing downhole pressure (drill pipe pressure measured without air injection) were less than 7 kPa at a total discharge rate of 65 kg/s.

During October 1992, injection tests were conducted on the three injection wells in the Steamboat Hills reservoir associated with the SB II&III power plants. The purpose of the present injection testing program was (i) to determine the location of subsurface fracture zones accepting fluids using PTS logs, (ii) to examine the relative injectivity of the wells, and (iii) to document whether interzonal flow existed within the individual injection wells. The injection tests were carried out during the 30-day power plant acceptance test, which somewhat inhibited test operations. PTS logs were conducted under quasi-static conditions, during injection and following shut-in (fall-off). In addition, downhole pressure, temperature and spinner behavior during injection was also obtained at particular depths. From injectivity tests, spinner data and PTS log evaluation, an understanding of subsurface injection characteristics of the wells was obtained.

RESULTS AND DISCUSSION

Pressure, temperature and spinner survey data obtained during the injection test of well IW-1 are shown in Figure 5 (well completion shown in Figure 3). Fluid was injected at a rate of 75 kg/s. Initial injection fluid temperature was 83°C. Injection fluid temperature increased during the test, due to power plant operations, to a maximum of 106°C. The data shown in Figure 5 indicate that several reservoir zones are accepting the injected fluid. These zones correspond with drilling breaks encountered during drilling. The granodiorite formation has a high compressive strength, and, within the granodiorite, drilling breaks are assumed to occur only in fractured/altered sections.

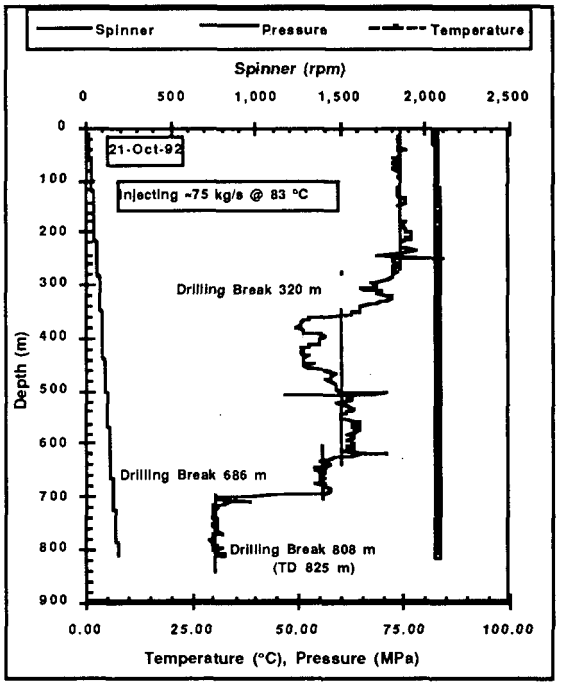

Figure 5. PTS survey plot for IW-1 during injection of 75 kg/s of 83°C water.

Pressure fall-off data were also obtained for IW-1. The data are plotted in Figure 6 and Figure 7. The spinner data shown in Figure 6 indicate that it took

approximately 10 minutes to shut-in the well. This is due partly to the power plant operations, which limit abrupt line pressure changes, and the fact that 41-cm valves are used on the injection lines. These valves require ≈220 turns for full valve closure. Also noted in Figure 6 is that the spinner tool did not return to a zero read-out after injection shut-in, indicating that flow was still occurring within the well; whereas, visual inspection and the surface pipeline flow meter indicated zero injection rate. The downhole PTS tool

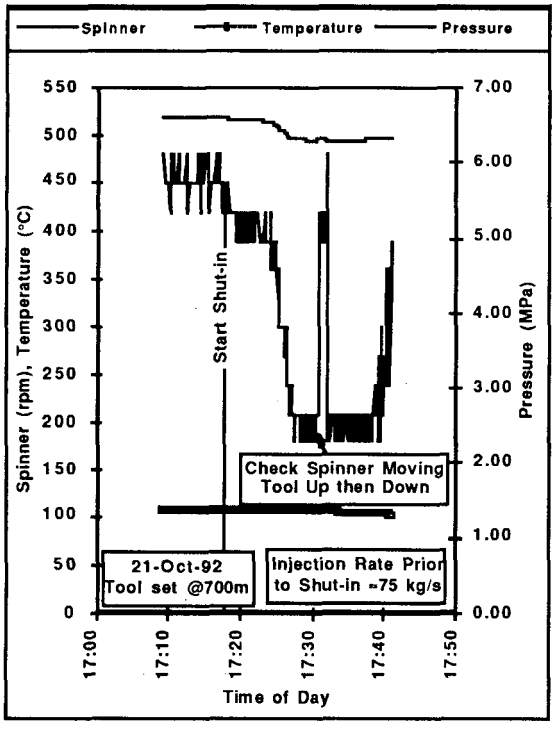

Figure 6. PTS plot for IW-1 during fall-off with tool set at 700m.

was moved to ensure proper operation. The tool was moved upwards and downward to the original position (700m). These data indicate that interzonal flow was downwards (note that movement of the tool in an upwards direction caused an increase in spinner output). In addition to the interzonal flow within the wellbore, the data shown in Figure 7 indicate a pressure fall-off of ≈0.3 MPa and a temperature decrease of ≈3°C.

It should be noted that permeability of a particular fracture zone depends on the square of fracture aperture. The amount of fluid accepted by a particular fracture zone is proportional to transmissivity, (permeability-thickness product), and therefore, approximately depends on the cube of the fracture aperture. However, The number of the fractures within a particular zone, and their individual apertures, control the Reynolds number. The Reynolds number, in turn, controls the measured downhole pressure drop incurred from injection (or production) of fluids in fractured reservoirs. In other words, the larger the fracture aperture, the larger the Reynolds number, the greater the chance that turbulent flow will occur.

Since interzonal flow within the wellbore existed, and the fact that wellbore pressure drop may be proportional to flow rate squared during turbulent flow conditions, rather than being directly proportional to flow rate under Darcy conditions, detailed pressure transient analyses were not carried out on the data. Nevertheless, simple analyses of the data suggests that the Steamboat geothermal reservoir has a relatively high permeability (i.e., 25 kg/s per MPa, or 10 gpm per psi).

Downhole PTS survey data and fall-off data were obtained for injection well IW-5 (well completion shown in Figure 4). The injection rate was 70 kg/s at 80°C. A quasi-static PTS survey was run prior to injection. PTS survey data during injection are shown in Figure 8. The spinner data indicate that a large portion of the injected fluid is exiting directly below the cased portion of the hole. In addition, the spinner and temperature data indicate that fluid is exiting the

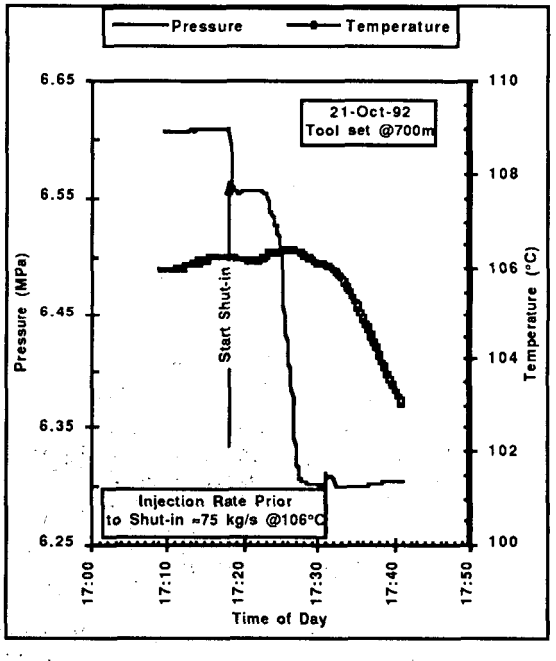

Figure 7. Pressure and temperature data for well IW-1 during fall-off with tool set at 700m.

lowest portion of the wellbore. Compare Figure 8 with Figure 9 and note the difference in spinner

output and temperature versus depth during the injection period and during static conditions directly after injection.

A static PTS survey was run after fall-off data were obtained (≈20 minutes after injection). These data are shown in Figure 9. A temperature spike is noted between 215m and 240m. This corresponds to an area of zero spinner output measured during the injection PTS survey (see Figure 8). The static survey data after injection suggests that fluid is flowing through the reservoir and past the wellbore at this depth.

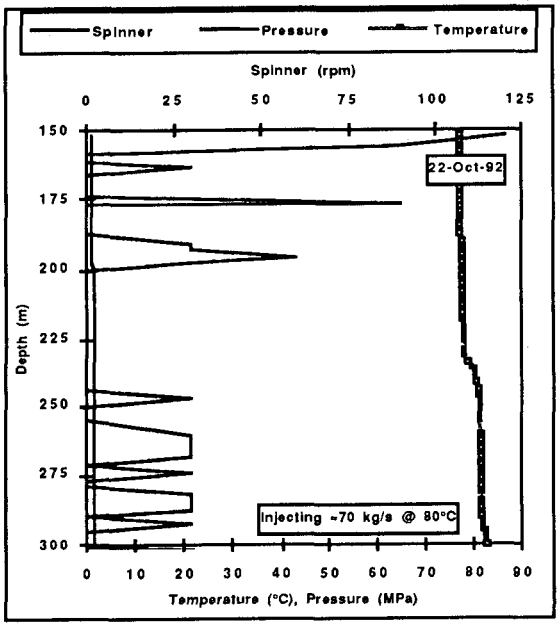

Figure 8. PTS survey plot for IW-5 during injection of 70 kg/s of 80°C water.

Pressure transient test analyses were not carried out on the IW-5 injection data. Maximum pressure change was ≈0.07 kPa during fall-off. There was no distinct pressure trend versus time. The reason for the erratic behavior of the spinner tool (±25 rpm) is unknown, but was noted during both injection and static surveys.

INJECTION TRACER TESTING

In order to gain additional experience and information about reservoir flow paths and possible injection fluid breakthrough to the production wells during long-term injection, a tracer test was conducted in the Steamboat Hills Geothermal Field. Rhodamine WT was used in conjunction with Fluorescein (Adams, et al., 1993). The two fluorescent dyes were injected simultaneously in injection well IW-4 (see Figure 2.) at a weight ratio of 1:2 (Rhodamine WT:Fluorescein). Fluid was simultaneously injected into IW-1 and IW-5. Injection rates were approximately equal for all of the three wells. Tracers analyses indicated recovery of dyes from the nine production wells (see Figure 2) over a period of approximately 330 days. The tracer peaks were detected in one production well (2-4) at 15 days, two wells (2-2 and 2-4) at 50 days, three wells (2-5, 3-3, and 3-4) at 77 days, and four wells (2-1, 2-3, 3-1, and 3-2) at 92 days. During the sampling period, ≈109%

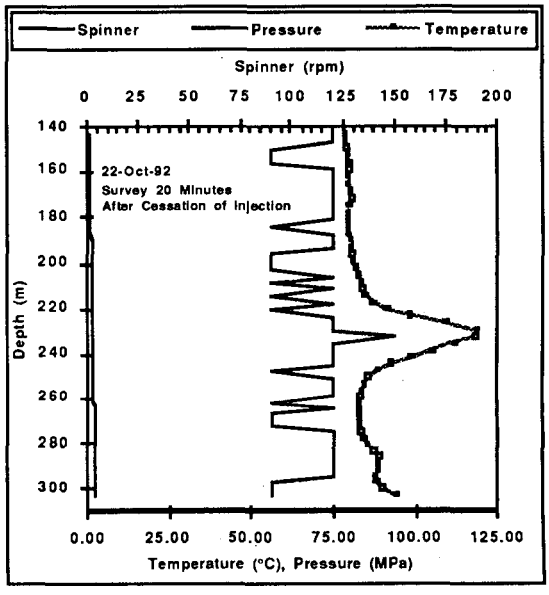

Figure 9. PTS survey plot in well IW-5 about 20 minutes after cessation of injection .

of the Fluorescein and 65% of the injected Rhodamine WT were recovered within 200 days, suggesting that 35% of the Rhodamine WT was adsorbed, absorbed, transformed or un-accounted for during the tracer test.

Using the decay kinetics obtained from buffer-solution laboratory testing, and, the reported well temperatures, Rose and Adams (1994) predicted the ratio of Rhodamine WT to Fluorescein for the nine production wells. The predicted (laboratory) ratios correlated with the measured ratios for all nine wells. In turn, the measured data documented that injected fluids are returned through the fractured geothermal reservoir from IW-4 to all of the production wells. Additionally, the tracer test results suggest permeability anisotropy within the geothermal system.

CONCLUSIONS

Data from injection testing of these wells support the premise that it is possible to obtain definitive reservoir parameters, define subsurface injection zones and provide a cost effective initial geothermal reservoir assessment using injection wells. In addition, PTS logging and analyses during static conditions and while injecting fluids can document interzonal flow between subsurface fractures.

Test data from injection wells can be used to predict the discharge performance of geothermal production wells. The injection pressure data versus time obtained for these wells suggest, essentially, infinite reservoir permeability. It should be noted that injection wells IW-4 and IW-5 can each, individually, accept 100% of the power plant injected fluid (1050 kg/s), which is equivalent to the output of nine pumped production wells.

Finally, the results of the tracer test suggest permeability anisotropy within the reservoir. Furthermore, the variation of tracer peak arrival times seems to reflect the importance of northeasterly trending fractures.

ACKNOWLEDGMENTS

We thank the management of Far West Capital, Inc. for permission to use their unpublished proprietary data for this study. In addition, we also thank Sabodh Garg, John Pritchett and Peter van de Kamp for their review of this manuscript. This work was partially supported through Geo Hills Associates under Contracts AA-7144 and AK-0472 from Sandia National Laboratories.

REFERENCES

Adams, M.C., J.N. Moore, P.C. van de Kamp and C. Goranson (1993), "Rhodamine WT as a Geothermal Tracer - A Field Test at Steamboat Hills, Nevada," *Geothermal Resources Council 1993 Annual Meeting*, Burlingame, California, 10-13 October, poster presentation.

Combs, J. and C. Goranson (1994), "Use of Slim Holes for Reservoir Evaluation at the Steamboat Hills Geothermal Field, Nevada, U.S.A.," *Proceedings Nineteenth Workshop on Geothermal Reservoir Engineering*, Stanford University, Stanford, California, 18-20 January, 8pp., in press.

Goranson, C., P.C. van de Kamp, and T. DeLong (1990), "Geothermal Injection and Monitoring Program History at the Caithness Power, Inc. Flash Steam Power Plant Steamboat Springs," Nevada: *Proceedings of the Symposium on Subsurface Injection of Geothermal Fluids*, Santa Rosa, CA , 29-30 October, pp. 101-124.

Goranson, C., P.C. van de Kamp, and E. Call (1991), "Summary and Interpretation of Six Years of Groundwater Monitoring Data at the SB GEO, Inc. Geothermal Power Plant Steamboat Springs," NV: *Proceedings of the Underground Injection Practices Council Meeting*, Reno, NV, 28-31 July, pp. 77-94.

Silberman, M.L., D.E. White, T.E.C. Keith, and R.D. Docker (1979), "Duration of Hydrothermal Activity at Steamboat Springs, Nevada, from Ages of Spatially Associated Volcanic Rocks," *U. S. Geol. Survey Prof. Paper 458-D*, 14pp.

Thompson, G.A., and D.E. White (1964), "Regional Geology of the Steamboat Springs area, Washoe County, Nevada," *U.S. Geol. Survey Prof. Paper 458-A*, 52pp.

van de Kamp, P.C. (1991), "Geothermal Geology of the Northern Steamboat Hills, Nevada," report submitted to Far West Capital, Inc., Salt Lake City, Utah, August, 5pp and 9 plates.

White, D.E., G.A. Thompson, and G.A. Sanberg (1964), "Rocks, Structure, and Geologic History of the Steamboat Springs Thermal Area, Washoe County, Nevada," *U.S. Geol. Survey Prof. Paper 458-B*, 63pp.

PROCEEDINGS, Twentieth Workshop on Geothermal Reservoir Engineering
Stanford University, Stanford, California, January 24-26 1995
SGP-TR-150

INTERPRETATION OF PRE- AND POST-FRACTURING WELL TESTS IN A GEOTHERMAL RESERVOIR

Norio Arihara[1], Hiroshi Fukagawa[1], Masami Hyodo[2] and Maghsood Abbaszadeh[3]

1. Waseda University, Tokyo 169, Japan
2. Geothermal Energy Research and Development Co., Ltd, Tokyo 103, Japan
3. Japan National Oil Corporation, Chiba 260, Japan

ABSTRACT

Pre- and post-fracturing well tests in TG-2 well drilled next to the Matsukawa field are interpreted for evaluating effects of a massive hydraulic fracturing treatment. The interpreted data include multiple-step rate tests, a two-step rate test, and falloff tests. Pressure behaviors of massive hydraulic fracturing are matched by a simulator of dynamic fracture option.

Fracture parting pressures can be evaluated from the multiple-step rate test data. The multiple-step rates during the massive hydraulic fracturing treatment show that multiple fractures have been induced in sequence. Although the pre-fracturing falloff tests are too short, fracture propagation can be evaluated qualitatively from the falloff data. Interpretation of the falloff test immediately after the MHF suggests that extensive fractures have benn created by the MHF, which is verified by simulation. The post-fracturing falloff tests show that the fractures created by the MHF have closed to a great degree.

INTRODUCTION

Hydraulic fracturing is an effective way of well stimulation in tight oil and gas reservoirs. Development of geothermal systems including hot dry rock reservoirs also employs this technology (Wright et al., Tester et al.). Design and evaluation of a field operation of hydraulic fracturing are important and difficult tasks particularly for geothermal reservoirs, because fluid flow is predominantly controlled by natural fractures.

Well testing either by producing or by injecting fluid is normally conducted before and after hydraulic fracturing in order to obtain data for reservoir evaluation. Injection and falloff tests in water injection wells are common practices of the pressure transient test in oil fields under waterflooding. Analysis of injection and falloff tests can be complicated by two important effects: the multiphase effect and temperature effect.

If the injected fluid is different from the reservoir fluid, a saturation front propagates into the reservoir, and a saturation gradient is established in the reservoir because of differences in fluid properties. In case of water injection into an oil reservoir at the connate stage, the oil bank with initial water saturation is located ahead of the injection front. Abbaszadeh and Kamal (1989) presented an interpretation method for injectivity and falloff testing considering saturation gradients. They prepared type curves for falloff tests.

In a water injection well test, the injected fluid usually has a temperature different from the initial reservoir temperature. A temperature front also propagates into the reservoir. As viscosity is a temperature-dependent parameter, the well test interpretation has to account for this effect. Bratvold and Horne (1990) presented generalized procedures to interpret pressure injection and falloff data following cold-water injection into a hot oil reservoir. They showed that type-curve matching provides estimates of parameters such as the temperature-dependent mobilities of the flooded and uninvaded regions, the size of the invaded region, and the distance to the temperature discontinuity.

Another complexity in injection and falloff tests is caused by dynamic fractures. Several authors reported on pressure transient analysis for fractured water injection wells. Larsen and Bratvold (1994) analysed effects of propagating fractures on pressure-transient injection and falloff data. They modified the previous solutions of the cold-water injection and falloff (Bratvold and Horne) to cover flow in elliptic systems and to account for the propagating fracture. By matching pressure-transient data and analytical solutions, key parameters such as fracture propagation, reservoir and fluid parameters, and temperature and saturation profiles can be determined.

In well testing at geothermal reservoirs, the temperature of a injected fluid can be much lower than the reservoir temperature. As a possible injection rate is quite high in geothermal well testing, dynamic fractures also can be easily induced being initiated from natural fractures.

The principal objectives of this paper are to interpret pre- and post-fracturing well tests, and to evaluate physical mechanisms of hydraulic fracturing in a geothermal reservoir.

DISCUSSIONS

Background

The tested well TG-2 was drilled next to the Matsukawa geothermal field under a plan to produce steam after creating communication with the Matsukawa reservoir by hydraulic fracturing. This was a part of the "Technology for Increasing Geothermal Energy Recovery" project of the New Energy and Industrial Technology Development Organization. The well is deviated and of the open hole interval 710 - 1,298 m depth. The target zone for hydraulic fracturing consists mainly of naturally fractured silt and tuff formations (Shinohara and Takasugi). Mutiple-step rate tests by fresh water and injection tests by different gels were first carried out to choose an injection fluid and to evaluate reservoir properties for hydraulic fracturing.

After having decided to use fresh water for testing and fracturing, pre-fracturing well tests, a massive hydraulic fracturing (MHF) treatment, and post-fracturing well tests were performed sequentially. All the well tests accomplished were injection and falloff tests. In all the tests except the multi-step rate and gel injection tests, and the MHF, production logging was run to survey injection profiles, and pressure and temperature gradients during the injection period, and then the tool was stationed at a fixed depth to monitor falloff pressures (Ujo et al.).

Test Procedure

Testing and operation consist of four parts:

(1) Two multiple step rate tests (MSRT-1, and MSRT-2) with fresh water and three gel injection tests, conducted on January 23 through 26, 1992, to choose a fracturing fluid and to evaluate formation properties;

Pressure and rate data of MSRT-1 and MSRT-2 are shown in Fig. 1. In MSRT-1, the rate was increased by ten steps from 0 to 12 BPM for 54.5 minutes. In MSRT-2, the rate was increased by nine steps from 0 to 16 BPM for 50.0 minutes. Three gel injection tests were performed with YF-650, YF-660 and PSS polymers respectively, each at about 10 BPM for about 50 minutes.

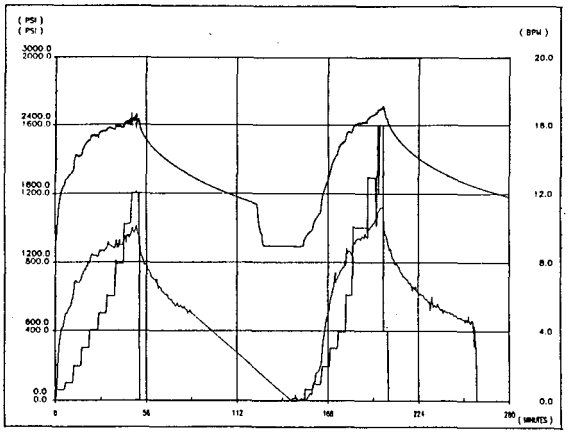

Fig. 1 - Multiple-step rate tests MSRT-1 and -2 and falloff tests

(2) Two injection-falloff tests with fresh water conducted in sequence on September 22, 1992, to evaluate pre-frac properties of formation;

As shown in Fig. 2, the first injection (IT-1) continued at about 0.88 BPM (1261 BPD) for 48 min. and was followed by a falloff test FOT-1. The second injection test (IT-2) was at about 9.42 BPM (13562 BPD) for 75 min. and a longer falloff test (FOT-2) followed immediately after injection.

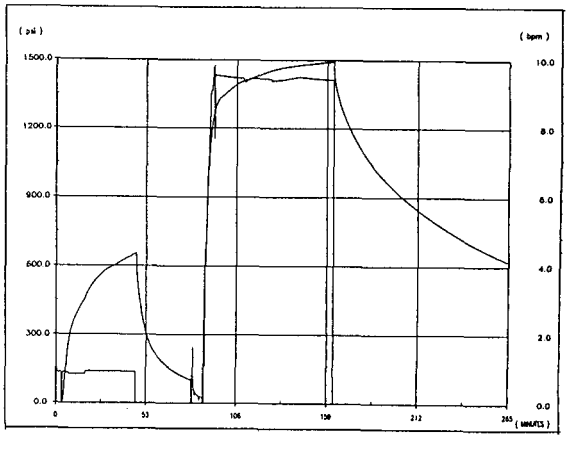

Fig. 2 - Two-step rate tests

(3) MHF operated with fresh water on November 24 and 25, 1992 (Hyodo et al., Wright et al.);

Pressure and rate records are shown in Fig. 3. The injection rate was initially increased stepwise to a maximum rate 25.4 BPM and kept between 25.4 and 24.5 BPM. Injection was interrupted four times, each time for about 30 min. Total injected water amounts to 27,400 Bbls. A pressure falloff test followed 24 hours injection.

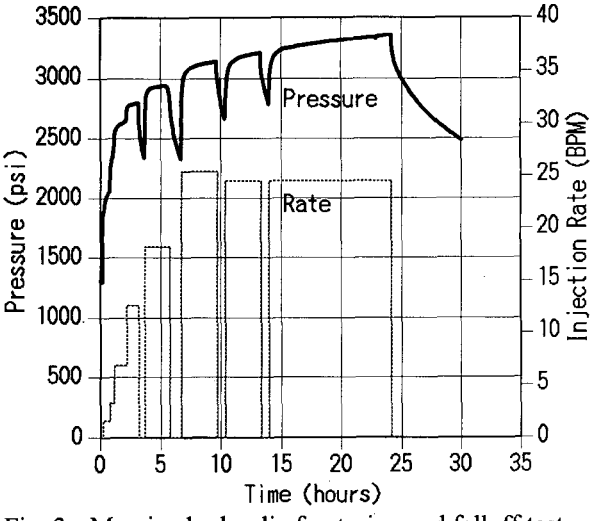

Fig. 3 - Massive hydraulic fracturing and falloff test

(4) Two post-frac injection-falloff tests conducted on November 27 and 29, 1992, respectively;
Fresh water was injected at a rate of 9.44 BPM for 4.14 hours and 1.87 hours before the November 27 falloff test (FOT-3) and the November 29 falloff test (FOT-4), respectively.

Analysis of Step Rate Tests

Bottom-hole flowing pressures of MSRT-1 and MSRT-2 are graphed against injection rate as shown in Fig. 4. The plotted pressures are taken at the end of each rate step. Fig. 4 shows that linear increases in pressure break twice at about 2,000 and 2,250 psia in both tests as injection rate increases. A fracture started parting at 2,000 psia and another fracture was induced at 2,250 psia, and both kept propagating above 2,250 psia.

Fig. 5 shows also bottom-hole flowing pressures vs. injection rate for the first five step rates of the MHF. Although conclusive interpretation is not allowed because of scarce data points, the pressure does not break sharply but gradually bend between about 2,200 and 2,700 psia. This suggests that multiple fractures were induced sequentially. Another observation is that the parting and propagating pressures are much higher than those of MSRT-1 and MSRT-2, which

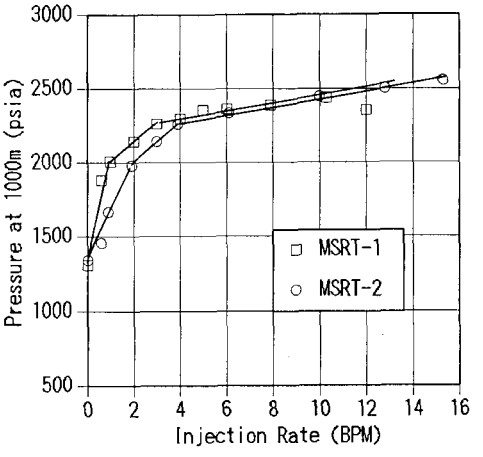

Fig. 4 - Pressure vs. rate plot for step rate analysis

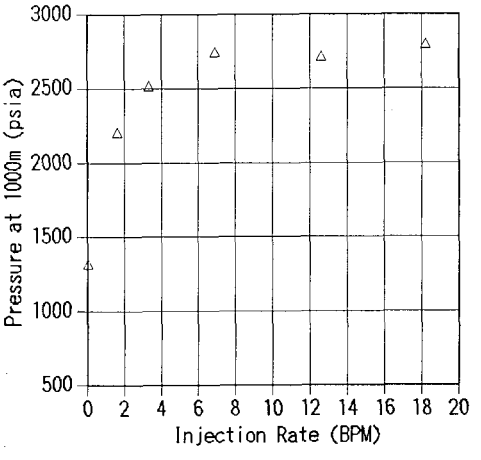

Fig. 5 - Pressure vs. rate plot for step rate analysis

means that the fractures created by the MHF propagate into zones of different rock properties.

Injection pressures of IT-1 and IT-2 are interpreted by the method proposed by Singh and Agarwal (1990). Figs. 6 and 7 plot the pressure function $\Delta p/\Delta q$ against the multirate equivalent time assuming radial flow and linear flow, respectively, where $\Delta p = p_{wf_n}(\Delta t) - p_{wf_{n-1}}(t_{n-1})$ and $\Delta q = q_{n-1} - q_n$. Here, pressures of IT-1 are well below an estimated fracture parting pressure, and therefore can be taken as the baseline data. Data for the two steps coincide as long as the fracture parting pressure (FPP) is not exceeded. When the FPP is exceeded during the second step IT-2, the IT-2 data beyond this time will deviate from the baseline IT-1 data with a smaller slope. From Figs. 6 and 7, the FPP is estimated to be 2,038 psia at an equivalent time of about 0.014 hours.

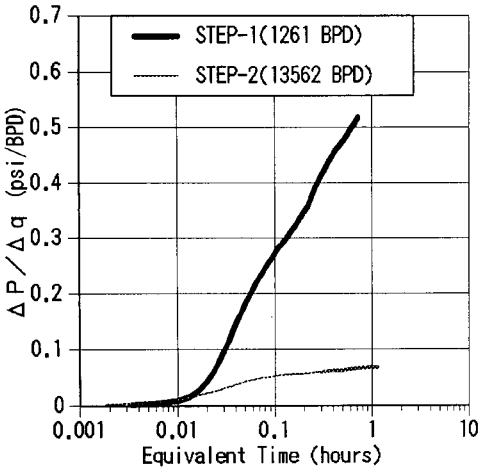

Fig. 6 - Radial-flow multirate equivalent-time analysis for 2-step rate test

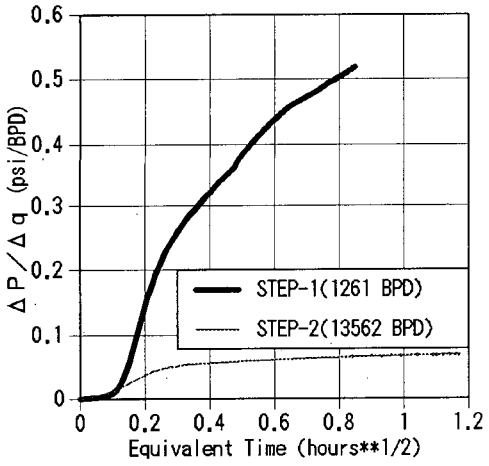

Fig. 7 - Linear-flow multirate equivalent-time analysis for 2-step rate test

Analysis of Pre-Fracturing Falloff Tests

The falloff tests after MSRT-1 and MSRT-2, and falloff tests FOT-1 and FOT-2 were interpreted without considering effects of propagating fractures. As the multiple-step rate tests MSRT-1 and MSRT-2, and the injection test IT-2 definitely reflect fracture propagation, meaningful interpretation is to be attempted by an appropriate method (Larsen and Bratvold).

All the pre-frac falloff data turned out to be too short to obtain full reservoir information. Figs. 8 and 9 are the pressure and derivative plots of the falloff tests after MSRT-1 and MSRT-2, respectively. The falloff test after MSRT-1 shows only a behavior of linear flow into infinite conductivity fracture. Effective (or equivalent) fracture half-length x_f can be estimated

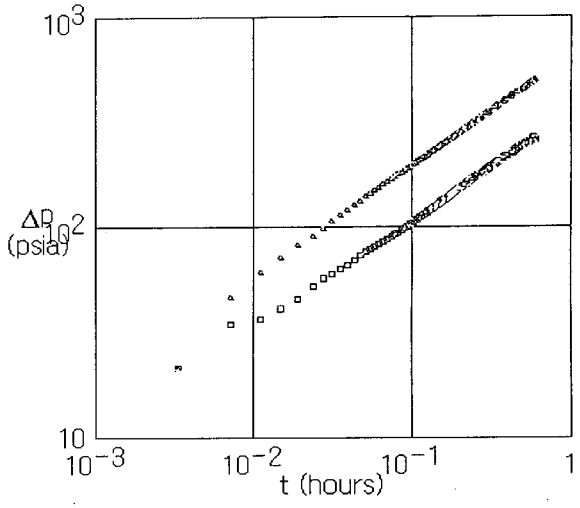

Fig. 8 - Log-log plot of falloff data after MSRT-1

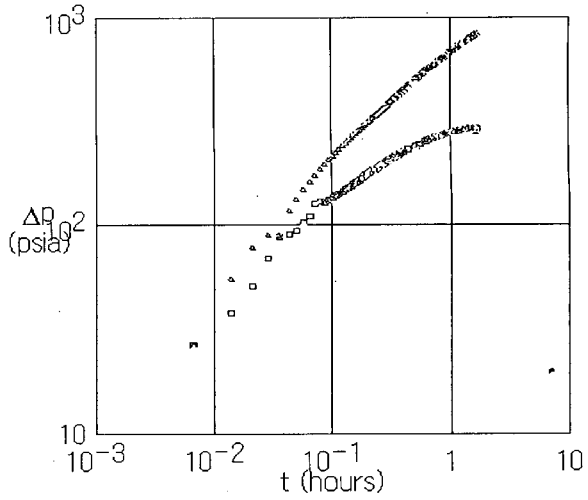

Fig. 9 - Log-log plot of falloff data after MSRT-2

from the slope of pressure vs. $\sqrt{t}$ plot, knowing permeability-thickness product kh of formation. Estimating a kh value is not correctly done, however, as the duration of the falloff time is too short to obtain radial flow information. The falloff test after MSRT-2 shows a fractured well behavior as indicated by the half slope on the derivative curve. This has a longer duration, but has not reached radial flow either as seen in Fig. 9. $x_f h^{1/2}$ is evaluated to be 1,840 $ft^{3/2}$ if a kh value 725 md·ft calculated by the last part of the data is used.

FOT-1 and FOT-2 are plotted as Figs. 10 and 11, respectively. FOT-1 has not quite reached radial flow yet, but is slowly approaching there. Thus an

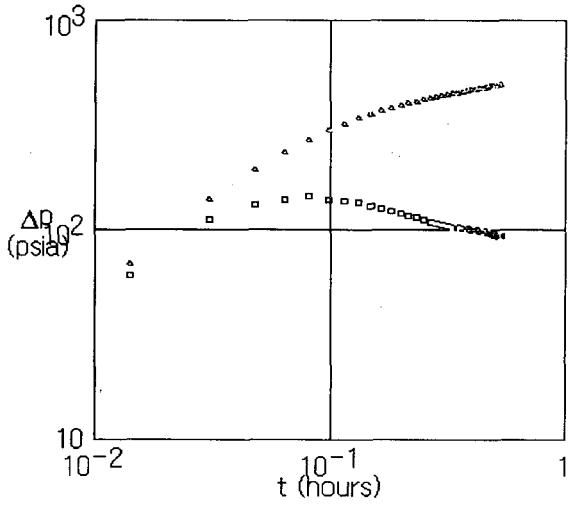

Fig. 10 - Log-log plot of falloff test FOT-1

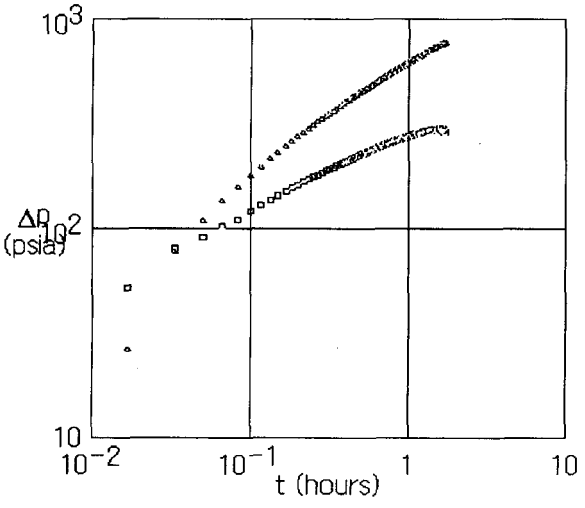

Fig. 11 - Log-log plot of falloff test FOT-2

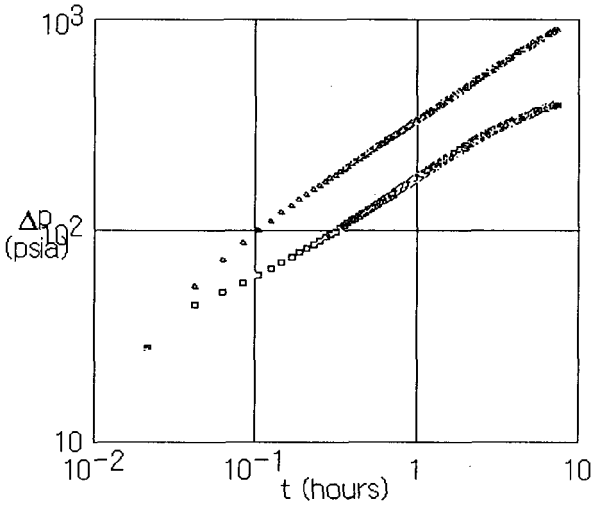

Fig. 12 - Log-log plot of falloff data following MHF

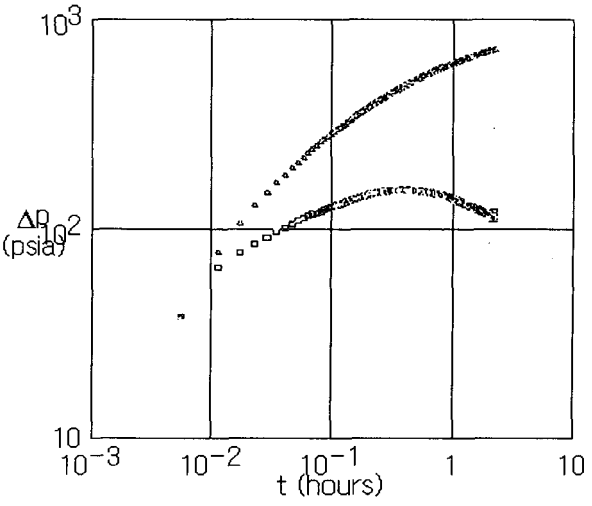

Fig. 13 - Log-log plot of falloff test FOT-3

estimated kh value 122 md·ft is considered to be the lower bound. This low kh value may represent a small net thickness h before fracturing as testing pressures are lower than the fracture parting pressure. FOT-2 is similar to the falloff test after MSRT-2. $x_f h^{1/2}$ is calculated as 1,750 $ft^{3/2}$ with a kh of 430 md·ft estimated from the slope of the last portion of the data.

Analysis of Post-Fracturing Falloff Tests

The falloff test immediately after the MHF clearly shows a behavior of infinite conductivity fracture as seen in Fig. 12. All the pressure data are still in the linear flow region and radial flow has not been reached yet. If the kh value 430 md·ft obtained by FOT-2 is assumed, an effective value of $x_f h^{1/2}$ is estimated to be 8,380 $ft^{3/2}$ which proves that extensive fracturing has been accomplished.

Fig. 13 shows the falloff test FOT-3 on November 27, two days after the MHF. Figs. 14 and 15 plot the falloff test FOT-4 on November 29, four days after the MHF. These two tests show very similar transient behaviors such that FOT-3 is shorter and only an early part of FOT-4. These plots seem to indicate two zone behavior by two constant derivatives, the inner zone with a lower kh and the outer zone with a higher kh. It is not clearly understood what causes the inner zone, but the outer zone properties dominate the late radial flow from which kh is estimated as 2,045 md·ft. Using this kh value and the slope of pressure vs. $\sqrt{t}$

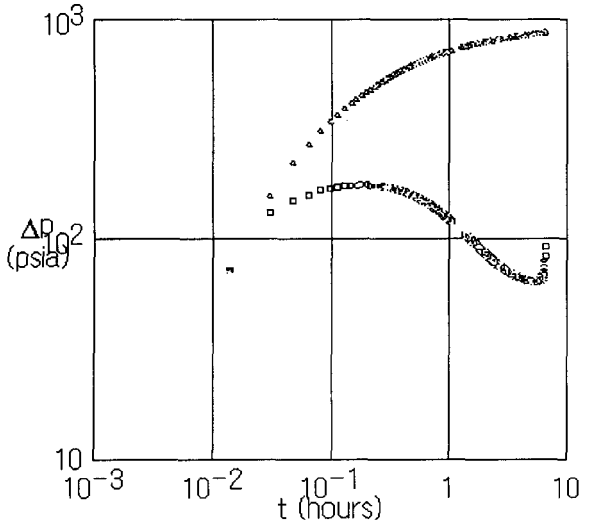

Fig. 14 - Log-log plot of falloff test FOT-4

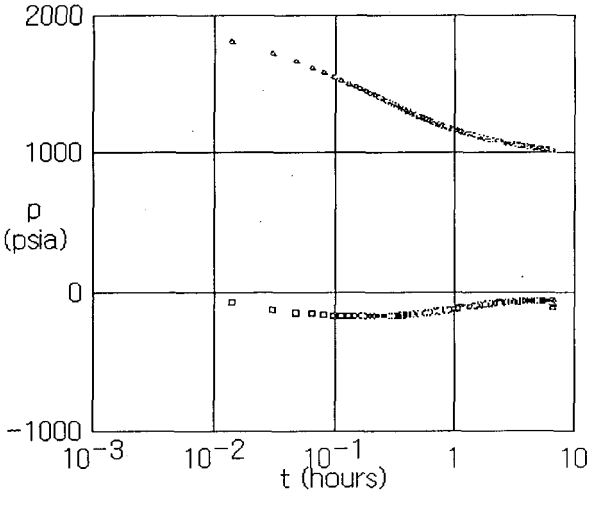

Fig. 15 - Semi-log plot of falloff test FOT-4

plot, $x_f h^{1/2}$ is estimated to be 390 $ft^{3/2}$. The high kh value may most likely be caused by the fact that network of fractures has extended both vertically and laterally, giving an effectively large thickness h to the system. The injection profiles measured by production logging before and after the MHF support this interpretation (Shinohara and Takasugi). The effective fracture half-length has decreased remarkably, however, which proves that the initial goal of establishing communication with the Matsukawa reservoir cannot be achieved.

Simulation of MSRT-1 and MHF

MSRT-1 including the pressure falloff immediately

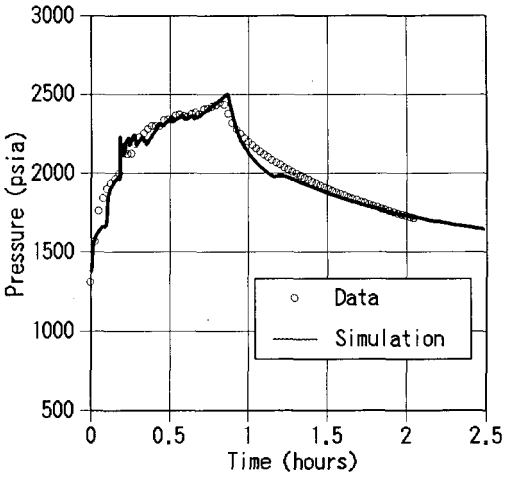

Fig. 16 - Simulation of MSRT-1 and falloff data

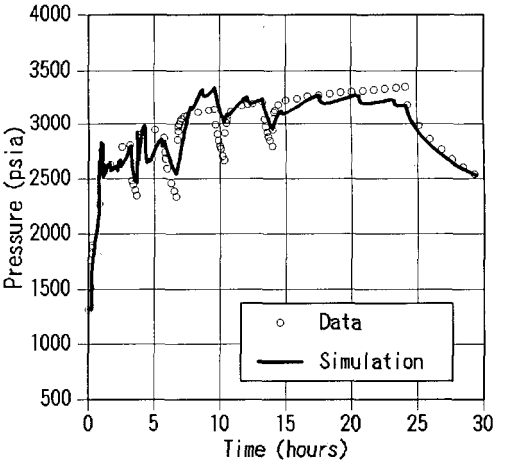

Fig. 17 - Simulation of MHF and falloff data

after it and the MHF have been simulated by STARS, a thermal oil recovery simulator which has a dynamic fracture option. This option was enabled essentially by four parameters; (a) fracture opening pressure, (b) a range of pressure over which fracture opens, (c) maximum transmissibility multiplier to be applied for fully open fracture, and (d) location of fracture.

Fig. 16 is a matching result by a 2D areal model for which the parameter values as shown in Table 1 were used. The gradual increase in pressure during injection could be reasonably matched by assuming that the well rows and columns are dynamically fractured up to 80 feet away from the well. Formation permeability is assumed to be 0.9 md except the row blocks dynamically fractured are assigned 5 md initially.

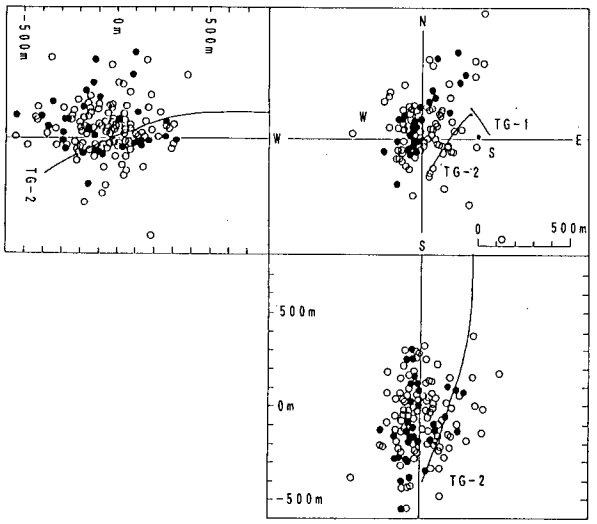

Fig. 18 - Epicenter plot of AE events during MHF (• : AE of S/N bigger than 45dB)

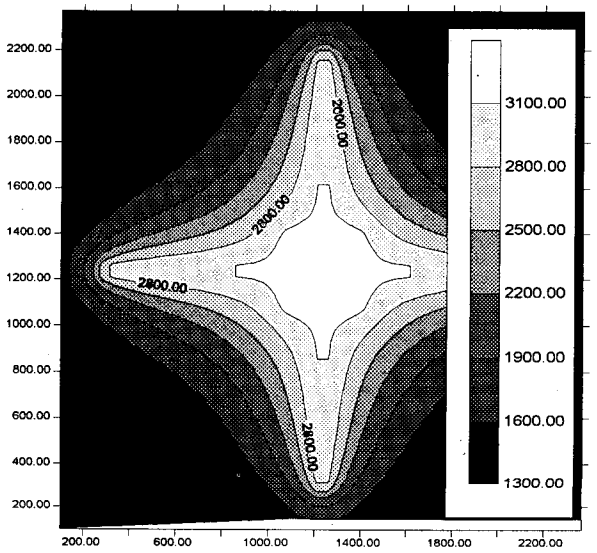

Fig. 19 - Simulated pressure distribution at the end of MHF

Simulation of the MHF was also made by a 2D areal model of the parameters as shown in Table 1. In order to reproduce the pressure behavior as shown in Fig. 17, extensive dynamic fracturing needs to be assumed, i.e. areal propagation for the 410 ft x 410 ft square zone with the well at center as well as linear propagation along the well rows and columns up to 980 ft away from the well. Fig. 18 shows the acoustic emission recorded during the MHF, which can be referred to for qualitative verification of the geometry

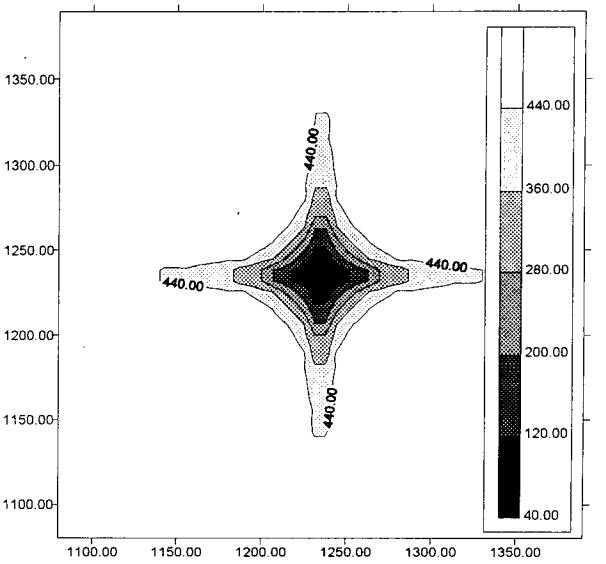

Fig. 20 - Simulated temperature distribution at the end of MHF

	MSRT-1 model	MHF model
Matrix porosity	0.1	0.1
Matrix perm., md	two 80' rows: 5. others: 0.9	two 980' rows, col's: 20. others: 0.9
Frac open press., psi	2,000	2,500
Press. range to full open frac	100	100
Max frac trans. multiplier	10,000	10,000
Frac location	two 80' rows & columns	two 980' rows & col's, 410'x410' area

Table 1 - Parameters for dynamic fracture simulation

and dimension of fracture propagation. As seen in the planview plot, the acoustic emission events are dense within about 200 m distance from the well. Figs. 19 and 20 shows the simulated pressure and temperature distributions at the end of the MHF injection.

CONCLUSIONS

1. Two values of the fracture parting pressure (FPP) can be detected from the multiple-step rate test data. The multiple-step rates during the massive hydraulic fracturing treatment also show multiple FPP's.
2. The pre-fracturing falloff tests are too short in time

to obtain the true formation kh. Evaluation of $x_f h^{1/2}$ may be possible from the falloff data, however, by assuming a kh calculated from the last part of the falloff data.

3. Interpretation of the falloff test immediately after the MHF gives a large effective value of $x_f h^{1/2}$ which suggests that extensive fractures have been created by the MHF. Simulation of the MHF also requires an extensive three-dimensional fracture network to reproduce the observed pressure behavior.

4. The post-fracturing falloff tests show that the fractures created by the MHF have closed to a great degree.

ACKOWLEDGMENTS

The field data and information used in this study were obtained in the "Technology for Increasing Geothermal Energy Recovery" project of the New Energy and Industrial Technology Development Organization (NEDO). The authors would like to thank NEDO for permission to present this paper.

Well test analysis was accomplished by AutoWIN, the well test interpretation system developed by Petroway, Inc. in Palo Alto, California.

The simulation model used is STARS developed by Computer Modelling Group in Calgary, Canada.

REFERENCES

1. Abbaszadeh, M. and Kamal, M.: "Pressure-Transient Testing of Water-Injection Wells", *SPE Reservoir Engineering*, (Feb. 1989), 115-124.

2. Bratvold, R.B. and Horne, R.N.: "Analysis of Pressure-Falloff Tests Following Cold-Water Injection", *SPE Formation Evaluation*, (Sept. 1990), 293-302.

3. Hyodo, M., Shinohara, N. and Takasugi, S.: "Hydraulic Fracturing Test and Pressure Behavior Analysis at the TG-2 Well", Preprints, SEG Japan, June 1993.

4. Koning, E.J.L. and Niko, H.: "Fractured Water-Injection Wells: A Pressure Falloff Test for Determining Fracture Dimensions", paper *SPE 14458* presented at the 1985 SPE Annual Technical Conference and Exhibition, Las Vegas, Sept. 22-25.

5. Larsen, L. and Bratvold, R.B.: "Effects of Propagating Fractures on Pressure-Transient Injection and falloff Data", *SPE Formation Evaluation*, (June 1994), 105-114.

6. Peng, C.P., Singh, P.K., Halvorsen, H. and York, S.D.: "Fractured Reservoir Characterization Through Injection, Falloff, and Flowback Tests", *SPE Formation Evaluation*, (Sep. 1992), 241-246.

7. Shinohara, N. and Takasugi, S.: "Fracture Design and the Result of Mini Hydraulic Fracturing, Employed for the TIGER Project", Preprints, SEG Japan, June 1993.

8. Singh, P. and Agarwal, R.G.: "Two-Step Rate Test: New Procedure for Determining Formation Parting Pressure", *J. Pet. Eng.*, (Jan. 1990), 84-90.

9. Tateno, M., Wei, Q. and Hanano, M.: "Evaluation of Fracture Extension Created by Hydraulic Fracturing using AE measurement, employed for TIGER Project", Preprints, SEG Japan, June 1993.

10. Tester, J.W., Murphy, H.D., Grigsby, C.O., Potter, R.M. and Robinson, B.A.: "Fractured Geothermal Reservoir Growth Induced by Heat Extraction", *SPE Reservoir Engineering*, (Feb. 1989), 97-104.

11. Ujo, S., Shinohara, N. and Takasugi, S.: "Evaluation of Productivity Improvement by Hydraulic Fracturing Using PTS Logging at the TG-2 Well", Preprints, SEG Japan, June 1993.

12. Wright, C.A., Tanigawa, J.J., Hyodo, M. and Takasugi, S.: "Real-Time and Post-Frac' #-D Analysis of Hydraulic Fracture Treatments in Geothermal Reservoirs", Preprints, Nineteenth Annual Workshop Geothermal Reservoir Engineering, January 1994.

PROCEEDINGS, Twentieth Workshop on Geothermal Reservoir Engineering
Stanford University, Stanford, California, January 24-26 1995
SGP-TR-150

MODELING DISCHARGE REQUIREMENTS FOR DEEP GEOTHERMAL WELLS AT THE CERRO PRIETO GEOTHERMAL FIELD, MEXICO

Anthony J. Menzies[1], Eduardo E. Granados[1], Hector Gutierrez Puente[2] and Luis Ortega Pierres[3]

[1]GeothermEx, Inc., 5221 Central Ave. #201, Richmond, CA 94804
[2]Comisión Federal de Electricidad, Residencia de Estudios, Cerro Prieto
[3]Comisión Federal de Electricidad, Gerencia de Proyectos Geotermoelectricos, Morelia

ABSTRACT

During the mid-1980's, Comisión Federal de Electricidad (CFE) drilled a number of deep wells (M-200 series) at the Cerro Prieto geothermal field, Baja California, Mexico to investigate the continuation of the geothermal reservoir to the east of the Cerro Prieto-II and III production areas. The wells encountered permeability at depths ranging from 2,800 to 4,400 m but due to the reservoir depth and the relatively cold temperatures encountered in the upper 1,000 to 2,000 m of the wells, it was not possible to discharge some of the wells.

The wells at Cerro Prieto are generally discharged by injecting compressed air below the water level using 2-3/8-inch tubing installed with either a crane or workover rig. The objective of this technique is to lift sufficient water out of the well to stimulate flow from the reservoir into the wellbore. However, in the case of the M-200 series wells, the temperatures in the upper 1,000 to 2,000 m are generally below 50°C and the heat loss to the formation is therefore significant. The impact of heat loss on the stimulation process was evaluated using both a numerical model of the reservoir/wellbore system and steady-state wellbore modeling.

The results from the study indicate that if a flow rate of at least 300 liters/minute can be sustained, the well can probably be successfully stimulated. This is consistent with the flow rates obtained during the successful stimulations of wells M-202 and M-203. If the flow rate is closer to 60 liters/minute, the heat loss is significant and it is unlikely that the well can be successfully discharged. These results are consistent with the unsuccessful discharge attempts in wells M-201 and M-205.

INTRODUCTION

The Cerro Prieto geothermal field is located in Baja California, Mexico approximately 30 km SE of Mexicali and was the first geothermal field in Mexico to be developed on a commercial scale. The field development was undertaken by Comisión Federal de Electricidad (CFE) and production began in April 1973, with the start-up of the Cerro Prieto-I (CP-I) power plant which was initially equipped with two turbine-generators of 37.5 MW capacity each. In 1977 construction began on the second stage of the CP-I development and two additional turbine-generators, identical to the first two, began operations in April 1979, bringing the total installed capacity to 150 MW. In 1982, a fifth generating unit was placed into service with a capacity of 30 MW, increasing the total installed capacity to 180 MW.

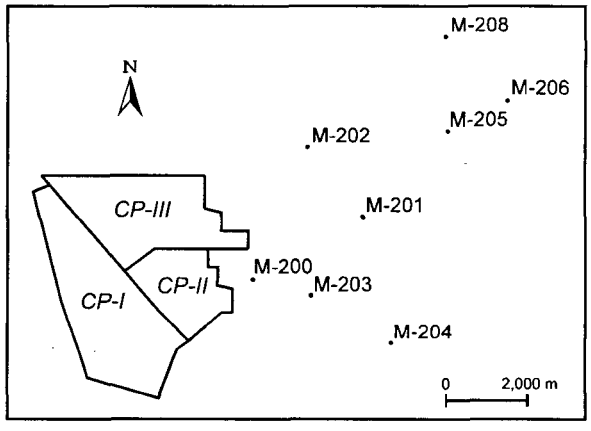

Figure 1: Series M-200 well location map

In 1980, CFE began field development planning and drilling for the CP-II and CP-III power plants. The production areas for these plants, as well as the CP-I production area, are shown in figure 1. CFE decided to proceed with the installation of 220 MW generating capacity at each site, in part due to the signing of two long-term power purchase contracts with Southern California Edison (SCE) and San Diego Gas & Electric Company (SDG&E) for a total of 220 MW. Construction began in 1982 and by September 1986 CFE brought on line three generating units of 110 MW each. The fourth unit

Well	Completion Date	Open Interval (m)	Temperature (°C)	Status
M-200	Feb. 5, 1984	2,482-2,834	>320	Flowed 1985/1986; well open
M-201	Sep. 24, 1985	3,600-3,816	≈350	Blocked @ 7-inch liner (2,340 m)
M-202	June 7, 1984	3,700-3,987	>330	Flowed during 1984; killed by cool inflow from 7-inch liner lap; drillpipe lost in well in 1985
M-203	July 26, 1984	3,538-3,993	285+	Flowed 1984-1986; blocked @ 3,710 m
M-205	Aug. 30, 1985	3,766-3,909 4,209-4,389	>350	Blocked @ 780 m

Table 1: Basic information from completed M-200 series wells

was operational in 1987, bringing the total installed capacity at Cerro Prieto to 620 MW. In recent years, CFE have maintained an overall capacity factor at Cerro Prieto in excess of 90%.

In addition to drilling wells for the CP-II and CP-III developments, CFE also completed a number of deep wells (the M-200 series wells) to investigate the continuation of the geothermal reservoir to the east of the CP-II and CP-III production areas. A total of eight wells (M-200, M-201, M-202, M-203, M-204, M-205, M-206 and M-208) were drilled from 1983 through 1986; well locations are shown in figure 1. Of the eight wells drilled, five were completed for possible production (M-200, M-201, M-202, M-203 and M-205), two were suspended without running 7-inch cemented liner (M-204 and M-206) and well M-208 was abandoned at 2,406 m. Basic well information for the five completed wells is summarized in table 1.

The five completed wells encountered permeability at depths ranging from 2,800 m to 4,400 m and temperatures generally greater than 300°C. The depth to the reservoir increases towards the east; this trend is consistent with data from the CP-II and CP-III production wells. Attempts were made to flow the wells using air injection and this was successful in wells M-200, M-202 and M-203; however, discharge attempts were not successful in wells M-201 and M-205 which are located further to the east. It is believed that the lack of success was due to a number of possible factors, including well blockages, low productivity, high heat loss due to cold casing (<50°C) in the upper 1,000 to 2,000 m of the wells and difficulty in maintaining continuous air injection.

CFE are now considering adding additional capacity at Cerro Prieto, including an 80 MW development in the area of the M-200 series wells (Hiriart-LeBert and Gutiérrez-Negrin, 1994). However, due to limited flow data that was collected from the wells during the 1980's, further flow testing is required to determine the commercial viability of new wells that would be drilled in this area of the field, particularly in view of the significant cost that would be involved in drilling to the required depths. The available well data were therefore reviewed and, based on the data summarized in table 1, it was recommended that well M-203 be cleaned out and used for additional testing, including a six month flow test. The results from the flow testing would then be used to design new wells to maximize well productivity. The present wells, except for M-200, were completed with 6-inch open hole and 4-1/2-inch slotted liner and their productivity is therefore restricted.

The study also included an evaluation of the requirements for a successful well discharge as it is likely that difficulties will be encountered in stimulating the existing wells to flow in addition to any new wells that may be drilled in the future. It was recommended that CFE consider using nitrogen injection with a coiled tubing unit for well stimulation rather than their present technique of injecting compressed air below the water level through 2-3/8-inch tubing installed with either a crane or workover rig. Both techniques are similar but the use of nitrogen and a coiled tubing unit would allow for greater flexibility and control during the stimulation process which should reduce the possibility of casing damage caused by thermal shock. The coiled tubing unit can also be used to clean-out the wells, assuming

the blockages are due to scale or sand; at present CFE use a rig to clean out scale from their wells.

The stimulation process was investigated using both a numerical model of the reservoir/wellbore system and by running a series of steady state wellbore simulations. The temperature and pressure conditions used in both the numerical model and the wellbore simulation model were based on measured data from well M-201.

WELL M-201 HISTORY

Well M-201 is located approximately 3.5 kms east of the CP-III production area (figure 1). The well was initially completed to 3,617 m on January 29, 1984 and was later deepened to 3,817 m. At this depth, a total loss of circulation occurred and the well was finally completed on September 24, 1985, with 4-1/2-inch liner from 3,570 to 3,816 m; the liner was cemented from 3,570 to 3,600 m and slotted from 3,600 to 3,816 m (figure 2).

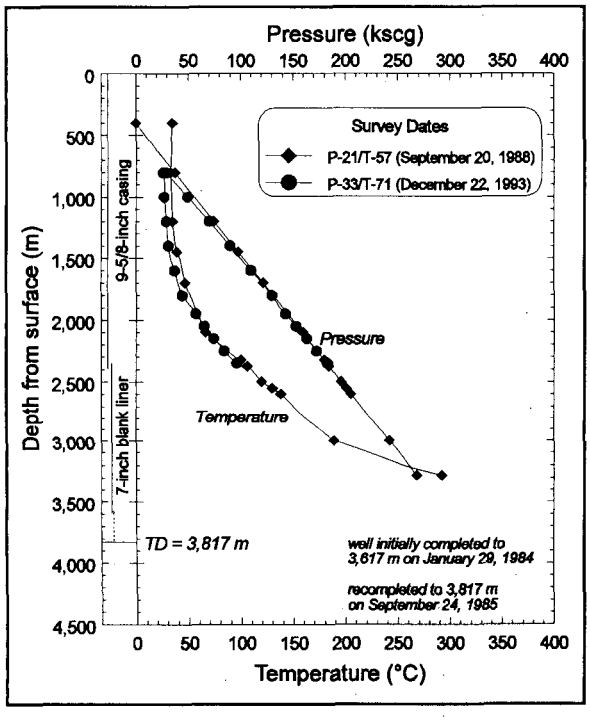

Figure 2: Downhole summary plot, Well M-201

After completion, the well was allowed to heat-up and downhole surveys were run at regular intervals. Unfortunately, the well was found to be blocked above the 4-1/-2-inch liner and it was not possible to measure the true reservoir temperatures; the available data (figure 2) suggest that the bottomhole temperatures are close to 350°C. There is also a significant length of the well (1,900 m) where temperatures are less than 50°C.

An attempt was made to flow M-201 from October 4 to 9, 1991 using air injection through 2-3/8-inch tubing that was lowered down the well from 550 m to 1,120 m. The attempt was not successful as the flow of water from the well was less than 33 liters/ minute. The temperature of the discharge water varied from 23°C to a maximum temperature of only 36°C. Over the six day period, the total volume extracted was only 11.5 m^3; equivalent to only 280 m of the wellbore.

After the tubing was retrieved, a 3-3/4-inch gauge ring was lowered into the well but was unable to pass the 9-5/8-inch:7-inch liner hanger. Water was injected to try and wash out the blockage but the operation was not successful. During injection, the wellhead pressure rose to 77 ksc and the falloff in water level after injection was relatively slow (from 78 to 246 m in nine hours). These results suggest either that the reservoir transmissivity in the vicinity of well M-201 is very low or that the blockage at the hanger has significantly reduced the degree of communication with the reservoir. Because the well has been blocked above the 4-1/2-inch liner virtually since completion, it is possible that this blockage is having a significant impact on the well characteristics.

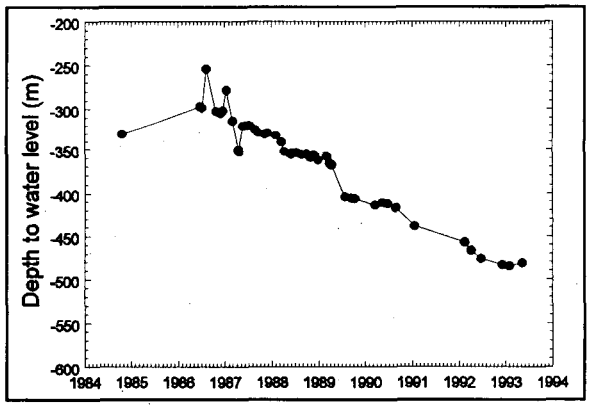

Figure 3: Water level changes, Well M-201

Since the discharge attempt, gauge ring surveys and downhole survey data continue to show that the well is blocked at the 9-5/8-inch:7-inch liner hanger. However, the blockage is not total as the well has been used successfully as an observation well from 1986 to the present time (figure 3); the measured

decline in water level indicates that there is still communication between the wellbore and the reservoir.

MODELING THE STIMULATION PROCESS

As discussed above, the requirements for successful well stimulation were evaluated by constructing a numerical model of the reservoir/wellbore system and by using a wellbore simulator. A numerical model was used as it can include the transient effects of fluid flow within the wellbore and heat transfer to the surrounding cold formation. Wellbore simulation can also include heat transfer but generally assumes steady state flow conditions. It is therefore necessary to run a series of steady state simulations in time to obtain information on the transient effects.

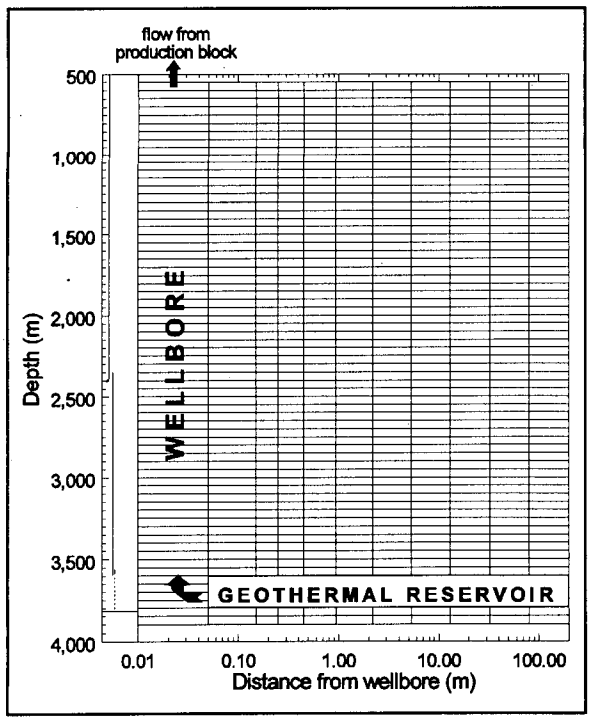

Figure 4: Numerical model grid layout

Numerical Model Results

In the numerical model, a radial grid was constructed which included the reservoir, wellbore and allowed for heat transfer from the wellbore to the surrounding rock (figure 4). The grid extends from 550 to 3,900 m in the vertical direction and from the wellbore to 200 m in the radial direction, with a total of 670 grid blocks. In figure 4, the radial grid is shown on a logarithmic axis to show the number of grid blocks more clearly. To model the wellbore, a very high vertical permeability (1 m^2) was specified and the porosity was set to 100% in the wellbore blocks. The horizontal permeability within the wellbore blocks and the blocks above and below the geothermal reservoir blocks was set to zero permeability. Within the reservoir blocks and the wellbore blocks opposite the reservoir, the horizontal permeability was set to 10^{-14} m^2; this is equivalent to a reservoir transmissivity of 2 Darcy meters, which is reasonable for the deep wells based on available data.

The temperatures and pressures used in the model were based on the measured data from well M-201 (figure 3); this well has the greatest length of casing under 50°C (1,900 m) and therefore reflects the most difficult conditions for well stimulation.

The simulation runs were made by setting a constant rate fluid extraction from the upper wellbore grid block. Four runs were made at flow rates of 60, 300, 600 and 1,200 liters/minute. The lower flow rate of 60 liters/minute is similar to the fluid extraction rates obtained during the unsuccessful stimulation attempts at wells M-201 and M-205 while the 300 liters/minute flow rate is similar to the fluid extraction rates obtained during the successful stimulations of wells M-202 and M-203.

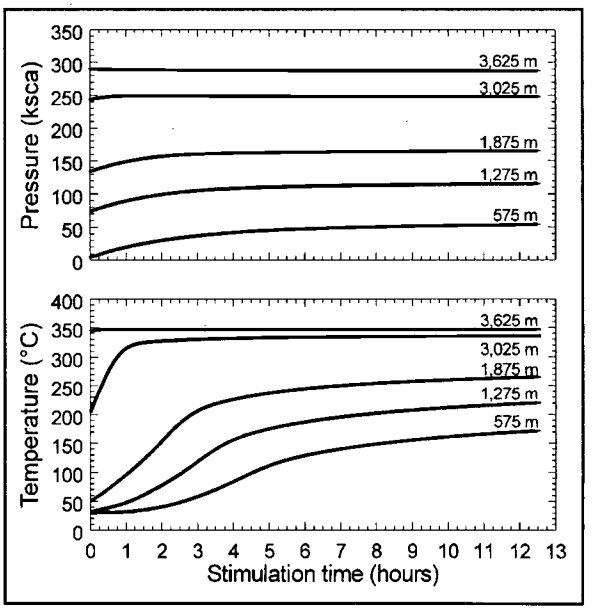

Figure 5: Simulation results for 300 liters/minute

The model required a significant run time as the maximum time step size never exceeded 13 secs which limited the overall simulation time to only a

few hours. This limited the amount of information that could be obtained and for the 60 liters/minute run, the simulated time of 1 to 2 hours was too short to provide useful results. For the other runs, however, the simulated time was long enough to provide some interesting insights into the stimulation process; the results from the 300 liter/minute run are presented as changes in pressure and temperature at various wellbore depths in figure 5. The changes in pressure and temperature in the production block at the top of the wellbore for the three different extraction rates are compared in figure 6.

The results in figure 5 show that in the deep wellbore block at 3,625 m, pressure decline occurs as expected but in the upper part of the wellbore, a significant pressure ***increase*** occurs with time during the stimulation process. The large pressure increase is due to the replacement of the long column of initially cold water with hot, less dense water from the reservoir, as shown by the increasing temperature with time.

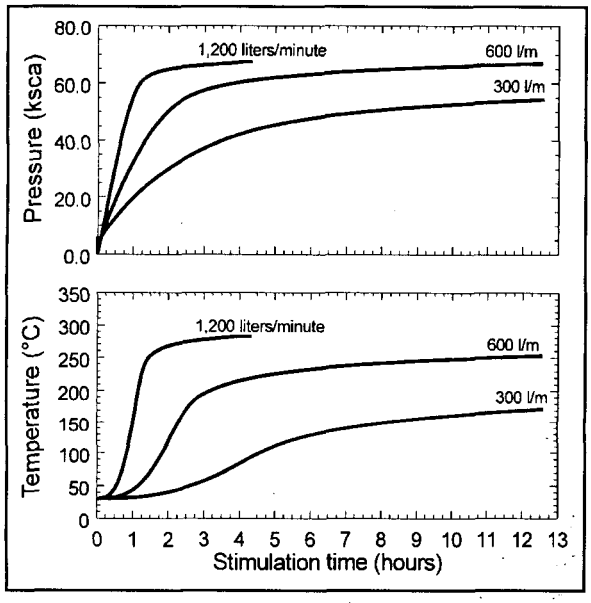

Figure 6: Results from production block

Assuming an average temperature of 100°C in the upper 575 m of the wellbore, the well should start to flow without the need for stimulation when the pressure in the production block reaches 55 ksca. The results in figure 6 indicate that this condition is reached after 1 hour at 1,200 liters/minute, after 2.5 hours at 600 liters/minute and at greater than 13 hours at 300 liters/minute. As expected, there is a significant reduction in the required stimulation time at higher flow rates. The model results also show that when the well starts to flow by itself, it will be flowing single phase water under artesian conditions. This is consistent with data available from the successful stimulations of wells M-202 and M-203. It was reported that both wells produced single phase water at positive wellhead pressures and temperatures of between 86°C and 90°C after air injection had stopped and prior to the onset of flashing flow.

As mentioned above, the successful stimulations of wells M-202 and M-203 occurred at induced flow rates close to 300 liters/minute but a stimulation time of several days was required instead of the several hours suggested by the numerical model results. This may be due in part to the assumption of continuous flow in the numerical model whereas in the field situation, air injection was not continuous and the discharge water flow rates were probably not constant. The model also does not account for any cooling of the fluid column due to the air injection and it is also possible that the heat transfer parameters are not correctly specified.

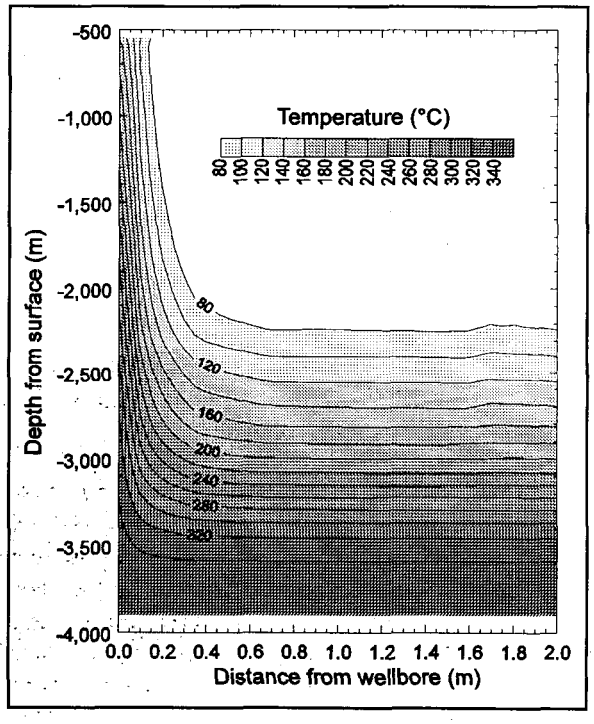

Figure 7: Model temperature distribution after 13 hours flow at 300 liters/minute

Figure 7 presents the calculated temperature distribution within a 2 m radius around the wellbore at the end of the 300 liter/minute run. The contours

show that after approximately 13 hours, the flow within the wellbore has only affected the rock temperatures within a 0.4 to 0.6 m radius from the wellbore.

Wellbore Simulation Results

A series of wellbore simulation runs were also conducted to provide additional information on the discharge process. For these runs, the static conditions from M-201 were again used as the initial conditions and runs were made after flow times of 0.1, 1, 5 and 20 days for extraction rates of 60, 300, 600 and 1,200 liters/minute.

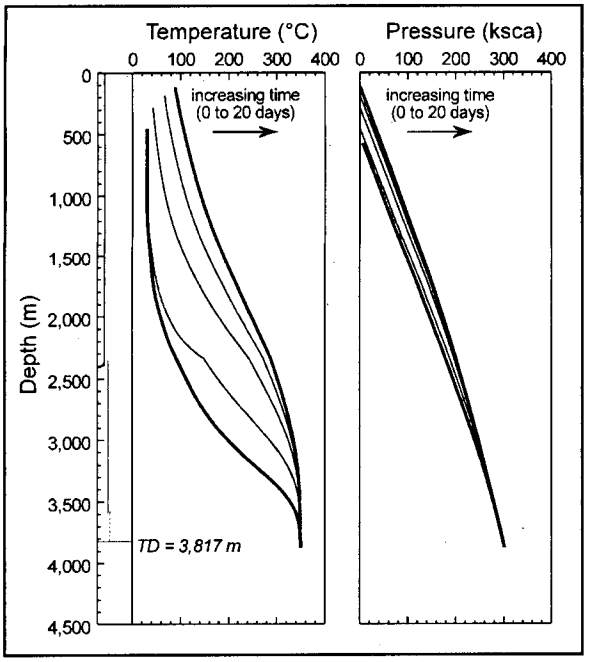

Figure 8: Wellbore simulation results; flow from well = 60 liters/minute

The results from the wellbore simulation runs at 60 and 300 liters/minute are presented in figures 8 and 9. These cases approximate the conditions during the previous stimulation attempts of the deep wells. The initial static conditions are also included on the plots. The results show that a flow rate of 60 liters/minute is not sufficient to stimulate the well to flow, even after 20 days of flow time, due to heat loss to the cold casing in the upper 1,900 m of the well. These results are consistent with the unsuccessful attempts to flow wells M-201 and M-205. At the higher flow rate of 300 liters/minute, the results show that successful discharge should occur in less than 1 day. These results are consistent with the numerical model results; however, as noted above, the estimates of stimulation time are significantly shorter than has been found in the field situation.

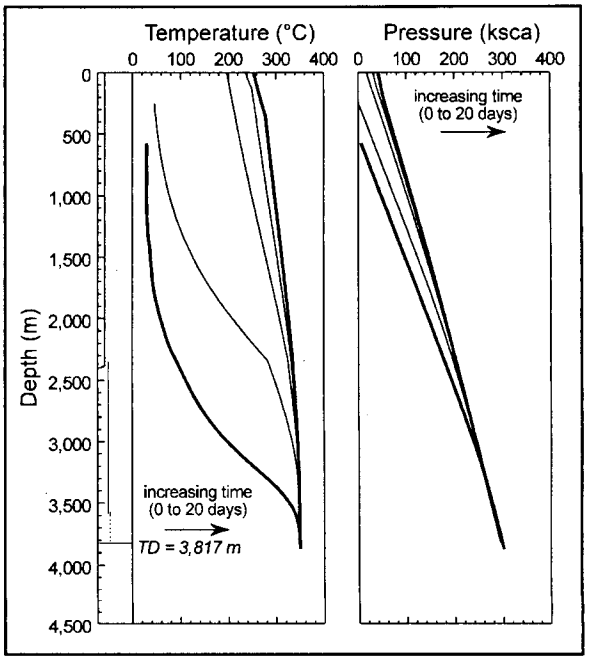

Figure 9: Wellbore simulation results; flow from well = 300 liters/minute

The calculated profiles plotted in figures 8 and 9 clearly show that as the hot water moves up the wellbore, the increase in temperature has a dramatic impact on wellbore pressures. The increase in pressure helps considerably in stimulating the well to flow.

CONCLUSIONS

From the results of the modeling study of well discharge requirements at Cerro Prieto, it is apparent that the deep wells can probably be successfully stimulated if a discharge rate of at least 300 liters/minute can be sustained. This is consistent with the previous successful stimulations of wells M-202 and M-203. If the sustainable flow rate from the well is closer to 60 liters/minute, then it is unlikely that the well can be successfully stimulated in a reasonable time. These results are consistent with the unsuccessful attempts in wells M-201 and M-205.

The model results also suggest that stimulation times of less than one day should be required, assuming a fluid discharge rate of greater than 300 liters/minute can be sustained. These times are significantly less

than noted in actual field operations, where stimulation times of up to 11 days have been required. This suggests that the ideal conditions assumed in the model runs probably deviate significantly from actual field conditions.

One of the reasons for the difference between estimated and observed stimulation time is probably the assumption of continuous flow. In practice, it is not possible to maintain continuous flow with air injection due to the need to change tubing depth or to service the compressors. It is therefore recommended that CFE consider using nitrogen injection with a coiled tubing unit for future discharge attempts on the M-200 series wells. This will allow for significantly more flexibility and control over the stimulation process which will also lessen the risk of casing damage associated with thermal shock.

One of the more interesting observations from the model study was the significant increase in pressure that occurs in the wellbore due to the replacement of the cold water column with hot water from the reservoir; an overall increase of up to 50 ksc was calculated near the top of the well. This helps the stimulation process considerably and allows the well to initially flow under artesian conditions. It is also probably one of the factors that explains the very high productivity of the production wells within the Cerro Prieto field.

ACKNOWLEDGEMENTS

We are very grateful to the management of Comisión Federal de Electricidad (CFE) for permission to present this paper. The study was undertaken as part of a contract between CFE and GeothermEx, Inc. and involved the review of a significant number of internal CFE documents and reports at the Cerro Prieto geothermal field. We would therefore like to thank the staff of the Residencia de Estudios at Cerro Prieto, in particular Ing. Miguel O. Ribó Muñoz and Ing. Jesus S. De León Vivar, for their assistance.

REFERENCES

Hiriart-LeBert, G. and L.C.A. Gutiérrez-Negrin (1994), "Geothermal Development in Mexico", Geothermal Resources Council TRANSACTIONS, Vol. 18, October 1994, pp 269-274.

PROCEEDINGS, Twentieth Workshop on Geothermal Reservoir Engineering
Stanford University, Stanford, California, January 24-26 1995
SGP-TR-150

APPLICATION OF MAGNETIC METHOD TO ASSESS THE EXTENT OF HIGH TEMPERATURE GEOTHERMAL RESERVOIRS

S. Soengkono and M.P. Hochstein

Geothermal Institute, The University of Auckland,
Private Bag 92019, Auckland, New Zealand

Key words - geophysical exploration, airborne and ground magnetic surveys, volcanic reservoir rocks, hydrothermal demagnetization, near surface alteration, high temperature reservoirs.

ABSTRACT

The extent of thermally altered rocks in high temperature geothermal reservoirs hosted by young volcanic rocks can be assessed from magnetic surveys. Magnetic anomalies associated with many geothermal field in New Zealand and Indonesia can be interpreted in terms of thick (up to 1 km) demagnetized reservoir rocks. Demagnetization of these rocks has been confirmed by core studies and is caused by hydrothermal alteration produced from fluid/rock interactions. Models of the demagnetized Wairakei (NZ) and Kamojang (Indonesia) reservoirs are presented which include the productive areas.

Magnetic surveys give fast and economical investigations of high temperature prospects if measurements are made from the air. The magnetic interpretation models can provide important constraints for reservoir models. Magnetic ground surveys can also be used to assess the extent of concealed near surface alteration which can be used in site selection of engineering structures.

INTRODUCTION

Almost all geophysical methods have been used to assess geothermal systems, the success (or failure) of each method depends on the geological and hydrological setting as well as the type of the geothermal system. This paper reviews application of the magnetic method for study of high temperature (high T) geothermal systems in young (Quaternary) volcanic rocks. Investigation techniques that can be used to estimate reservoir extent and for mapping surface hydrothermal alteration are discussed with reference to case histories. Application of the magnetic method to assess crustal temperature structures, i.e. Curie point depths (e.g. Laughlin, 1982), is not discussed here.

The size of a geothermal reservoir is an important constraint for any conceptual model of a geothermal prospect and for resource assessment. The likely lateral extent of a geothermal reservoir can usually be assessed in moderately steep terrain from geophysical surveys, since significant contrast in physical parameters exist between reservoir rocks and the surrounding country rocks as a result of fluid/rock interactions. In many geothermal prospects, fluids also affect the ground surface. For such prospects, the size of a geothermal field can often be obtained from a study of surface manifestations, including mapping of altered ground. However, in most volcanic settings, hydrothermally altered rocks are hidden by vegetation or a weathered layer, or else covered by younger deposits of tephra and alluvium. Since thermally altered ground also exhibits physical parameters which differ with respect to those of unaltered ground, geophysical investigation methods can be used to detect such ground even where concealed.

HIGH-T GEOTHERMAL RESERVOIRS HOSTED BY YOUNG VOLCANIC ROCKS

Almost all volcanic rocks are magnetic because they contain small amounts of primary magnetic minerals (mainly magnetite and titanomagnetite). The total magnetization of volcanic rocks (in the range of 0.5 to 10 A/m) is given by the vector sum of induced and remanent magnetization. Induced magnetization depends on the magnetic susceptibility of the rocks (which is proportional to the volume fraction of magnetic minerals present) and the magnitude of the earth's magnetizing field. Remanent magnetization is the result of a complex unbalanced domain structure within the magnetic minerals and exists even where the magnetizing field is absent; rocks with remanent magnetization in the opposite direction to the present day earth's magnetic field are termed "reversely magnetized" rocks. In many liquid dominated geothermal fields, hydrothermal processes alter magnetite and titanomagnetite to almost non-magnetic minerals, such as pyrite, leucoxene, or hematite (Browne, 1994). Such processes cause the volcanic rocks to become partly or completely demagnetized and a significant magnetization contrast exists between the reservoir rocks and the unaltered volcanic rocks outside it.

Residual magnetic anomalies associated with a thick layer (0.5-1 km) of demagnetized rocks in the upper part of high T reservoir can usually be recognised from airborne magnetic data if larger areas surrounding the geothermal prospect are also covered by the survey and no reversely magnetized rocks (age ≥0.7 M yr) occur inside and outside the reservoir. Algorithms suitable for 3-D magnetic modelling of hydrothermal demagnetization zones are available (for example, Barnett, 1976). In large volcanic fields associated with so-called "active margins", regional effects of deeper seated magnetic bodies can cause a shift of residual magnetic anomalies. Assessment of such a regional field is required to obtain a representative "zero level" value for the residual bipolar anomalies; this can be obtained from the analysis of pronounced, isolated "topographic anomalies" outside the prospect, or by simultaneous analysis of first order residual anomalies observed at a higher level and extended to non-magnetic basement rocks (Hochstein and Soengkono, 1994).

Demagnetization of volcanic rocks by fluid/rock interaction is a complex process which depends on parameters controlling the stability of the primary magnetic minerals, like pH and temperature of fluids, joint permeability, fluid movement, etc. In an oxidizing environment, magnetite can be stable which explains why volcanic rocks on top of a high T reservoir and at levels above shallow boiling can retain their magnetization (Hochstein and Soengkono, 1994). Elsewhere the same rocks forming pronounced topographic highs (volcanic domes) may be completely demagnetized by interaction with shallow, acid condensates as hematite and limonite replace primary magnetic minerals.

Demagnetization by hot fluid/rock interaction is cumulative and irreversible. Demagnetized rocks therefore occur in extinct geothermal systems, a phenomenon now used to explore for epithermal mineral deposits. Cumulative demagnetization of active systems may also reflect the control of paleo-permeability and paleo- subsurface fluid flow patterns. In some cases demagnetization can affect large areas outside the present day high T reservoir, thus causing some rather indistinct magnetic anomaly patterns (Hochstein and Soengkono, 1994). In the following two case histories, demagnetization is clearly restricted to the productive area of high T reservoir and where the geometry of the demagnetized reservoir can be used for modelling it.

Kamojang Geothermal Field

The Kamojang Geothermal Field is located in West Java, Indonesia. It is a vapour dominated system hosted by a sequence of young, dominantly andesitic volcanic rocks (e.g. Hochstein, 1976; Dench, 1980; Grant *et al.*, 1982). The reservoir is capped by a thick (about 300-350m) condensate layer in which temperature increases from about 100° C at the top to about 235° C at the bottom.

An airborne magnetic survey was conducted in 1986 at 2500m asl altitude (about 900m above mean terrain), covering the Kamojang and the nearby Darajat fields. A representative "zero level" value of the residual anomalies was obtained from topographic modelling (Suranto, 1987). The residual magnetic anomalies over the Kamojang field are presented in Figure 1 which shows a magnetic low centred on the field as delineated by DC-resistivity surveys. At Kamojang, where the magnetic inclination is about -35°, the centre of the magnetic low has been shifted north of the centre of the anomalous body. There is no evidence that rocks within or outside the Kamojang reservoir are reversely magnetized. The residual anomalies were interpreted using 3-D magnetic modelling (Soengkono *et al.*, 1988). The interpretation shows that the magnetic low can be explained by a thick demagnetized volcanic body in the southern part of the Kamojang field (see Figure 1) at depths below 300m (Figure 2). This is supported by core studies (Figure 3) which show that between about 300 and 1000m depth most cores are significantly demagnetized. The demagnetized rocks lie now within the vapour dominated reservoir below the condensate layer. However, the widespread occurrence of replacement and vein calc-silicates in the vapour dominated reservoir indicates that demagnetization took place when Kamojang was a liquid-dominated system (Hochstein and Soengkono, 1994). Cores taken from the surface to 300m depth and below 900m depth are still magnetic.

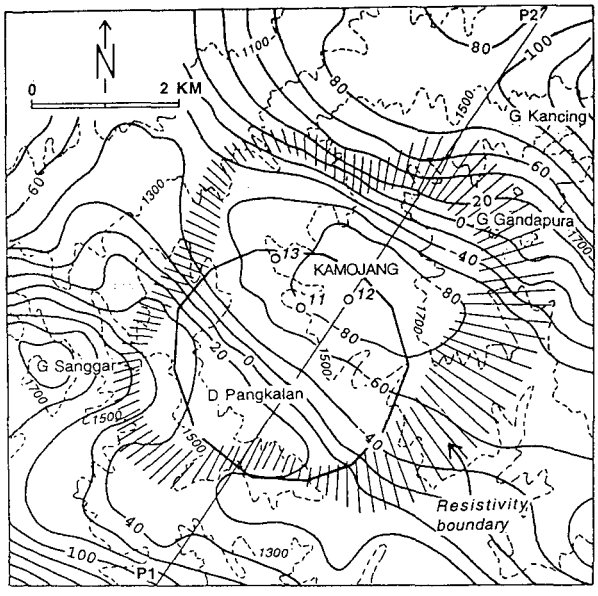

Figure 1. Residual total force anomaly (solid contours, 20 nT interval) at 2500m asl over the Kamojang Geothermal Field, West Java, Indonesia. The topography is shown by broken contours (interval 200m). The demagnetized body below 300m depth is outlined by the polygon. Numbered circles are wells referred to in Figure 3 (from Soengkono *et al.*, 1988).

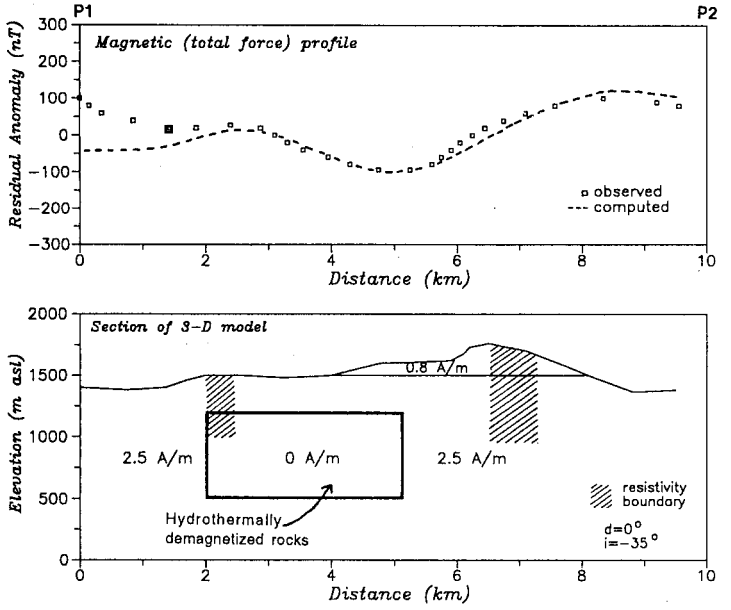

Figure 2. Observed and computed anomalies of profile P1-P2 (see Figure 1) together with interpreted cross section (taken from Soengkono *et al.*, 1988).

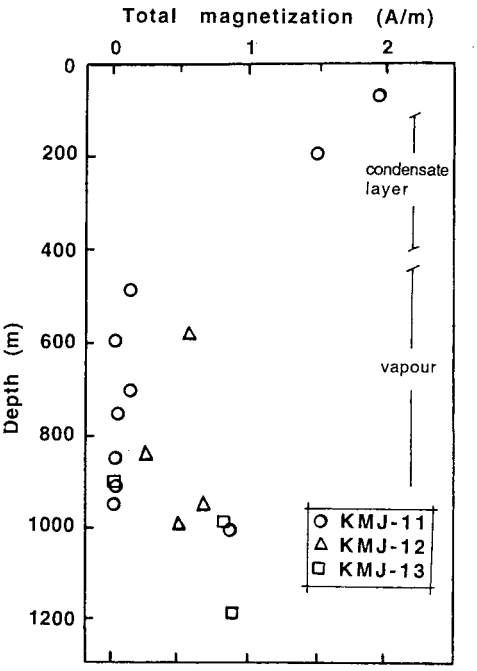

Figure 3. Plot of total magnetization of cores from Kamojang wells against depth (modified from Soengkono *et al.*, 1988). Well localities are shown in Figure 1.

Assuming that fluid characteristics remain about constant at the same level throughout the reservoir, it can be inferred that demagnetization has been controlled by the (paleo-) permeability of the rocks. Based on this inference, Soengkono *et al.* (1988) suggested that parts of the Kamojang reservoir which lie outside the demagnetized body, but still within the resistivity boundary, should exhibit a lower permeability. Figure 4 shows that the demagnetized reservoir encompasses the Kamojang borefield and wells with low productivity (i.e. KMJ- 9, 13, 25, 12, 7, 20 and 32) are indeed located close to the boundary of the magnetic model. Reservoir modelling by Saptadji (1987) also indicates that the permeability of volcanic rocks outside the Kamojang borefield is low.

Wairakei Geothermal Field

The Wairakei Geothermal Field is part of the large Wairakei-Tauhara hot water dominated system in the Taupo Volcanic Zone (TVZ), Central North Island, New Zealand. The geothermal reservoir stands in a sequence of young, dominantly rhyolitic volcanic rocks (Steiner, 1977). The Wairakei field has been exploited since 1950s and is now probably one of the best studied geothermal systems in the world.

The Wairakei Field was covered by a low level (760m asl; about 300m above mean terrain) airborne magnetic survey conducted in 1984 by staff of the Geothermal Institute. Residual anomalies were computed by removing the normal field, defined by the International Geomagnetic Reference Field (IGRF) of Malin and Barraclough (1981), and reducing the regional field

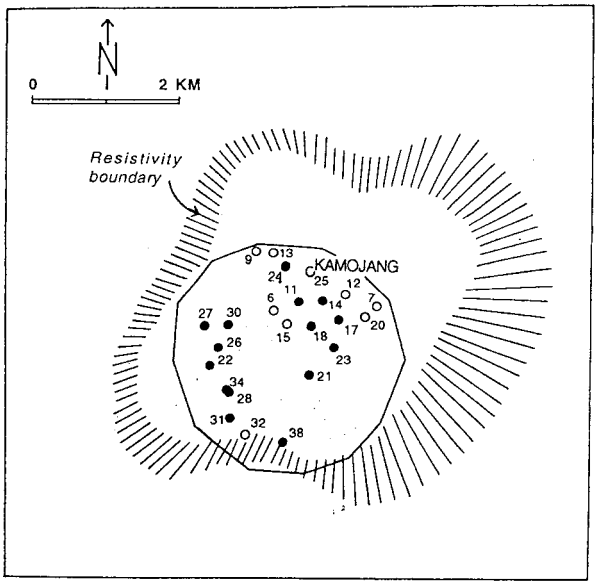

Figure 4. Map showing the extent of demagnetized rocks (thick polygon) and locality of Kamojang production wells with mass flowrate ≥30 t/h (solid circle) and ≤30 t/h (open circle).

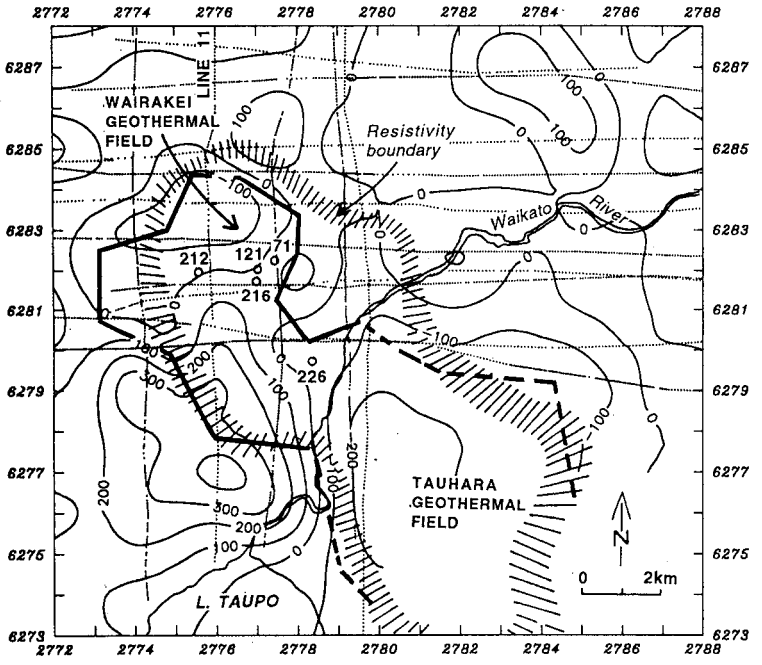

Figure 5. Residual total force anomaly (solid contours, 100 nT interval) at 760m asl over the Wairakei Geothermal Field, Central North Island, New Zealand (modified from Soengkono and Hochstein, 1992). The demagnetized body below sea level is outlined by the thick line. Numbered circles are wells referred to in Figure 6. Flight lines of the survey are shown by the dotted lines.

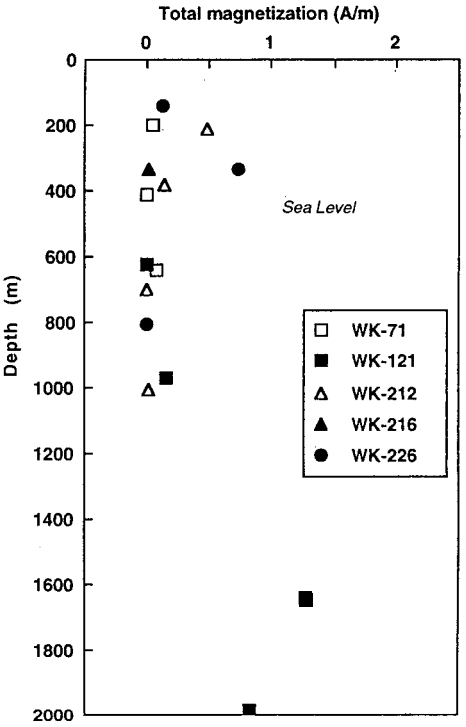

Figure 6. Plot of total magnetization of cores from Wairakei wells against depth. Well localities are shown in Figure 5.

caused by deeper seated magnetic bodies beneath the TVZ (Soengkono and Hochstein, 1992). Residual anomalies are presented in Figure 5 which shows the presence of a distinct magnetic low in the northwestern part of the Wairakei field as defined by the resistivity boundary. The data in Figure 5 also indicate a second magnetic low associated with the Tauhara Field, although this field is not fully covered by the survey. A large magnetic high (max. amplitude c.400 nT) occurs to the south-west of the field; its northeast extension separates the magnetic low in the northwestern part of the Wairakei Field from that over the Tauhara Field. There is no evidence of any reversely magnetized rocks in the Wairakei area.

A study of cores from several wells was conducted by Lampoonsub (1987). This (Figure 6) showed that cores taken from below sea level (c.450 m depth) are almost completely demagnetized. Some cores from higher levels are magnetic and not greatly affected by hydrothermal alteration; cores taken from below 1000m depth also have retained their magnetization. A similar pattern was found at Kamojang in West Java, Indonesia (see Figure 3) and in the Mokai geothermal field, about 25 km north-west of Wairakei (Soengkono, 1985).

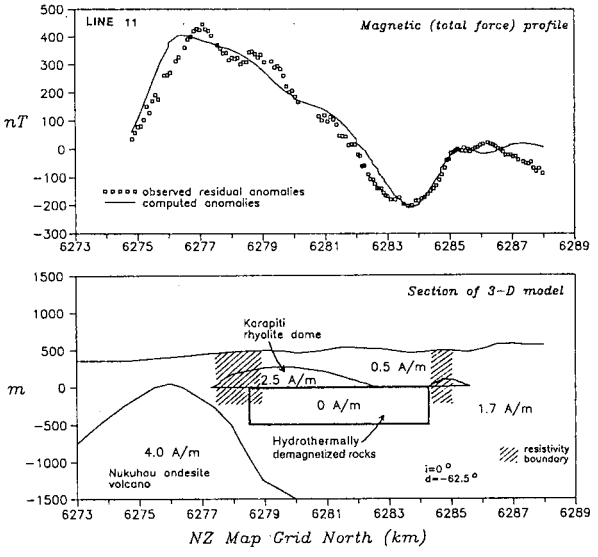

Figure 7. Observed and computed anomalies of line 11 (see Figure 5) together with interpreted cross section (taken from Soengkono and Hochstein, 1992).

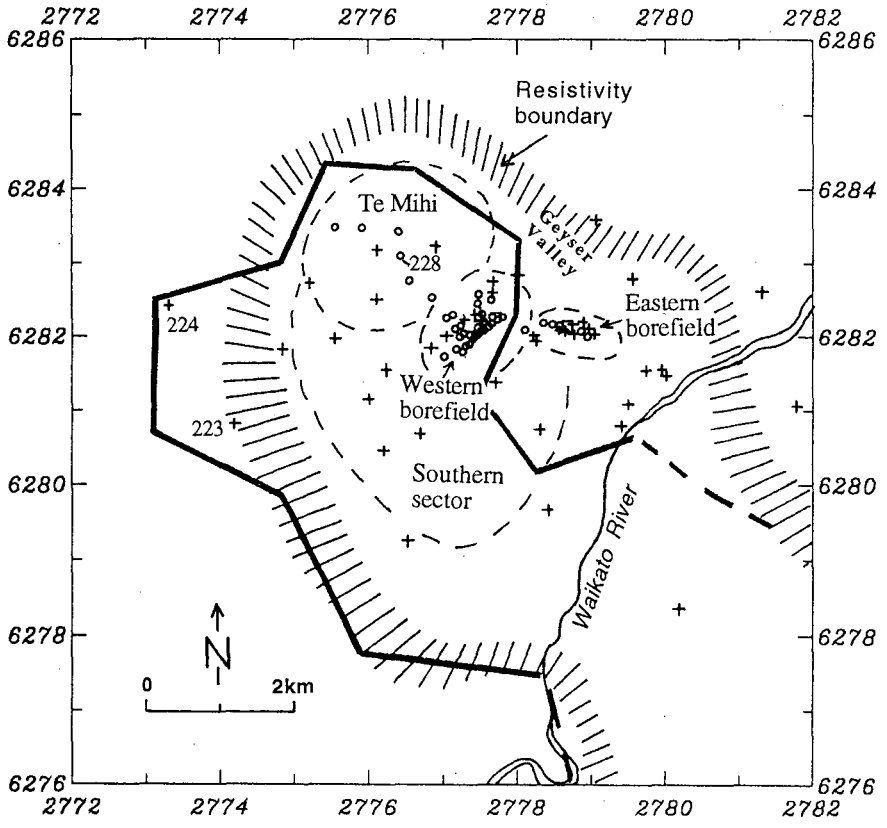

Figure 8. Map showing the extent of demagnetized rocks (thick line) and locality of Wairakei production wells (open circles) and investigation wells (crosses).

A 3-D magnetic model of the Wairakei geothermal field (see Figure 5 and 7) was constructed by Soengkono and Hochstein (1992) which includes hydrothermally demagnetized rocks to about -500m below sea level (450-950m depth from the surface). A concealed rhyolite dome (Karapiti Rhyolite) still retains its magnetization; a large concealed andesite strato volcano to the south-west of the Wairakei field (not reached in any drillholes) is also highly magnetic.

The magnetic model (Figure 8) shows that the demagnetized reservoir covers the Te Mihi sector, the main western bore field, and the southern sector of the Wairakei field, but not the smaller eastern borefield. Well 228 drilled in the Te Mihi area (Figure 8) is one of the large producing wells in this field, with a production of 90 t/h dry steam (Grindley, 1986). Based on pressures, temperatures and fluid constituents of wells drilled in the Te Mihi sector, Grant (1982) inferred that a major upflow occurs beneath this area. In the natural state hot fluids must have flowed laterally to the east of the area now occupied by the western and eastern borefields and towards Geyser Valley (now called Wairakei Valley). If this interpretation is true, we can explain the lack of demagnetization in the eastern part of the Wairakei field in terms of this being a very young outflow region.

The demagnetized rocks extend also outside the western resistivity boundary of the Wairakei Field. Well 223 lies over this extension and has temperatures up to 100° C at 600m depth. Well 224, which is located outside the resistivity boundary but still within the extension of demagnetized body, is cold; core studies (Lampoonsub, 1987) show that the rocks from well 224 are not greatly altered, but they have relatively low remanent magnetization. The cause of this primary low remanent magnetization is still unknown.

MAPPING OF CONCEALED SHALLOW ALTERATION

For detection of shallow hydrothermal demagnetization patterns, airborne magnetic data are usually not very useful, since the magnetic signal associated with such rather thin near-surface anomalous bodies is rapidly attenuated with height. However, near surface alteration zones can often be detected by ground magnetic surveys, particularly when the gradient of magnetic field components is measured during the survey.

The phenomenon that volcanic rocks at the top of some high T systems have been partially demagnetized is a recent discovery. No systematic studies of shallow cores and outcrops have been made yet. If magnetite were stable in an oxidizing environment, such shallow demagnetization should not occur. However, the two case histories presented below show that demagnetization of

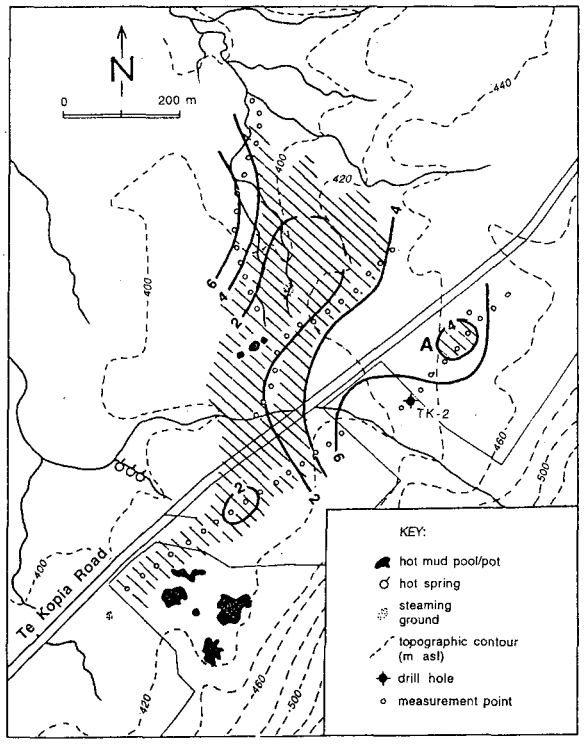

Figure 9a. Horizontal magnetic gradient (solid, thick contours) over the northern part of Te Kopia geothermal field, Central North Island, New Zealand; contour values are in nT/m (modified from Nguyen Hong Bang (1993) and Perez-Ramos (1993)). Areas where the gradient is ≤4 nT/m (zones of near surface alteration) are hatched .

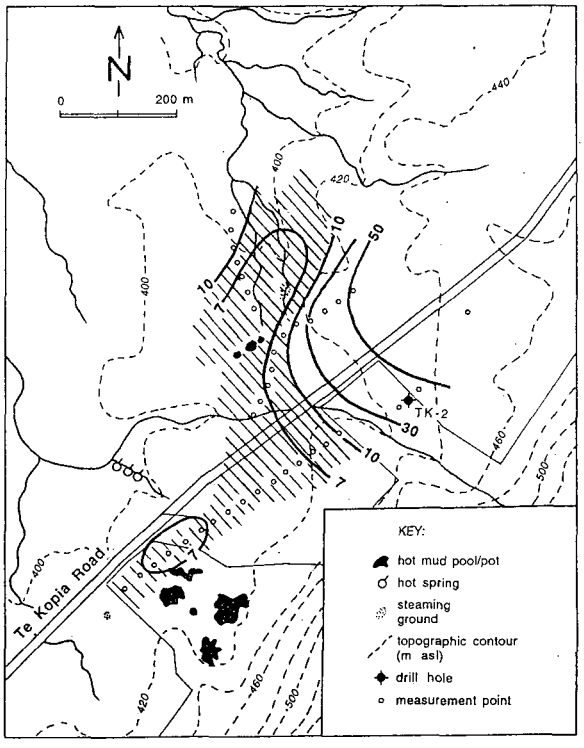

Figure 9b. Apparent resistivity measured using a Schlumberger array with AB/2=60m (solid, thick contours) over the same area shown in Figure 9b; contour values are in Ω-m (modified from Nguyen Hong Bang (1993) and Perez Ramos (1993)). Area where the apparent resistivity is ≤10 Ω-m (zones of near surface alteration) is hatched.

shallow rocks is common. At present we believe that the phenomenon is caused mainly by the same process which causes demagnetization of high standing surface extrusions, namely demagnetization induced by acid steam condensates.

Northern Te Kopia Geothermal Field

The Te Kopia Field lies about 25 km north east of the Wairakei Geothermal Field. Present day thermal activity consists of fumaroles, mud pools, steaming ground and some hot springs. Two deep exploratory wells have been drilled which show that the geothermal reservoir lies in a sequence of rhyolitic pyroclastics and lavas (Bignall, 1991) which outcrop in places.

Ground magnetic gradient measurement together with Schlumberger resistivity traversing (AB/2 spacing of 30 and 60m) were conducted in 1993 in the northern part of the Te Kopia field (Nguyen Hong Bang, 1993; Perez-Ramos, 1993). Results of these surveys are presented in Figures 9a and 9b. The figures show that low apparent resistivity values (≤10 Ω-m for AB/2=60m), which indicate the presence of electrically conductive altered ground, are clearly associated with low values of the horizontal magnetic gradient (≤ 4 nT/m). In Figures 9a and 9b, the hatched pattern indicates the likely extent of the altered ground which is now covered by soils or thin layers of pumice; samples taken from 1 m depth show that hydrothermal alteration indeed occurs beneath a thin unaltered cover. A small area with low magnetic gradient to the north of well TK-2 (indicated by A in Figure 9a) coincides with a zone of high apparent resistivity values (Figure 9b). A similar phenomenon occurs in the Northern Tokaanu-Waihi field and a possible explanation is given in the following section.

Northern Tokaanu-Waihi Geothermal Field

The Tokaanu-Waihi prospect is an undeveloped geothermal field located near the southern shore of Lake Taupo, about 45 km southwest of the Wairakei Geothermal Field. The area is mainly covered by young andesite flows of the Tongariro Volcanic Centre (Grindley, 1960). Two larger areas with hydrothermal activity occur in this field - the Tokaanu thermal reserve near Tokaanu village and the Hipaua thermal area in a rugged area in the north. In addition, several discharges of hot water occur along Lake Taupo shore line near the Waihi village.

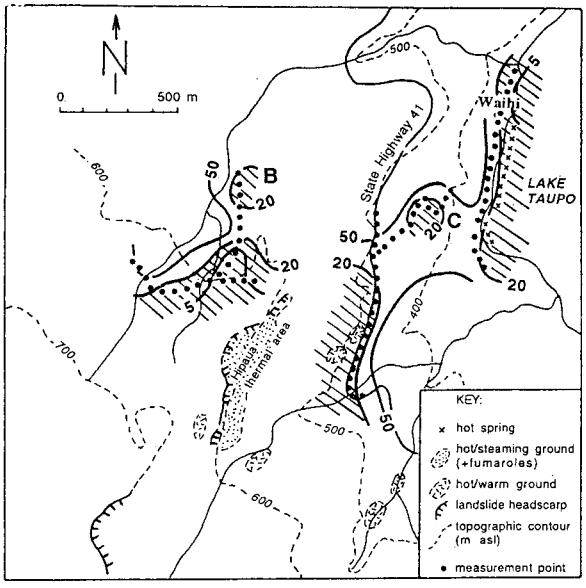

Figure 10a. Horizontal magnetic gradient (solid, thick contours) over the northern part of Waihi-Tokaanu geothermal field, Central North Island, New Zealand; contour values are in nT/m (modified from Siripongsatian, 1994). Areas where the gradient is ≤20 nT/m (zones of shallow alteration) are hatched.

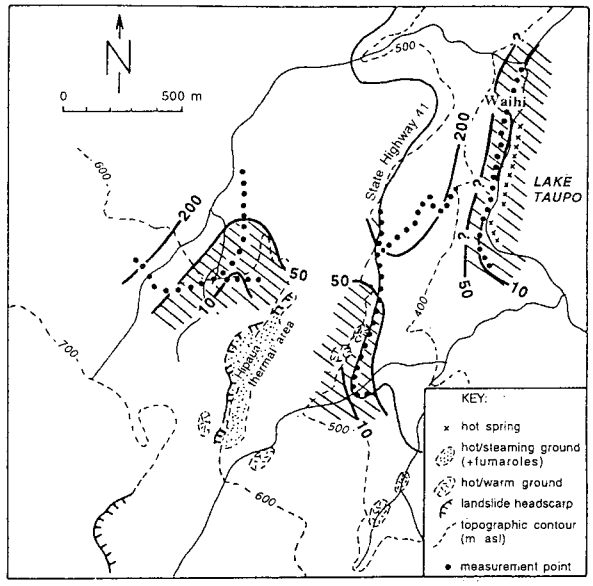

Figure 10b. Apparent resistivity measured using the Schlumberger array with AB/2=60m (solid, thick contours) over the same area shown in Figure 10a; contour values are in Ω-m (modified from Munyithya, 1994). Area where the apparent resistivity is ≤50 Ω-m (zones of shallow alteration) is shown hatched.

Ground magnetic gradient measurements and resistivity traversing using AB/2 spacing of 50 and 100m were conducted in the northern part of the Tokaanu-Waihi geothermal field in 1994 (Munyithya, 1994; Siripongsatian, 1994). Correlation between apparent resistivity and magnetic gradient values (Figures 10a and 10b) shows a pattern similar to that observed at Te Kopia (discussed in the previous section). However, the interpreted near surface alteration zones (Figures 10a and 10b) appear to be associated with higher values of both magnetic gradient and apparent resistivity in comparison to those at Te Kopia. At Tokaanu-Waihi, areas with near-surface alteration are marked by a magnetic gradient ≤20 nT/m and an apparent resistivity ≤50 Ω-m. It is possible that the difference in magnitude of magnetic gradient and shallow apparent resistivity in both areas reflect the level of boiling. At Te Kopia boiling temperatures occur at shallow depths (probably 10 to 30m) whereas beneath the highstanding Hipaua area at Tokaanu-Waihi boiling occurs at depths >100m (Severne and Hochstein, 1994).

There are two small areas (B and C in Figure 10a) with magnetic gradient values ≤20 nT/m which are not associated with low apparent resistivity values. As mentioned in the previous section, one such area also occurs at Te Kopia. As magnetite and titanomagnetite are the first minerals to be altered in NZ prospects by hydrothermal activity (Browne, 1994), it is possible that a shallow hydrothermal alteration process has started in these areas, which has altered the magnetic to non-magnetic minerals, but which has not produced a sufficient amount of clay minerals to cause the rocks to become electrically conductive. Thus, the phenomenon of smaller areas with low magnetic gradient but high apparent resistivity values may indicate an initial stage of alteration. An anomalous ground temperature at 1 m depth of more than 1° C above ambient also occurs in area B in Figure 10a (Munyithya, 1994).

SUMMARY AND DISCUSSION

Geophysical investigations using airborne magnetic surveys are useful to assess the lateral extent of many high temperature geothermal reservoirs in young volcanic rocks. Airborne magnetic surveys can be used to quickly investigate a large prospect area with access problems. Interpretation of residual airborne magnetic anomalies can often provide models that show the extent of hydrothermally demagnetized rocks and concealed paleo-permeability structures. In active geothermal fields, the presence of thick and extensive demagnetized rocks can indicate areas of high reservoir permeability and upflow regions, as shown by the discussion of two high T reservoirs which are presently exploited (Wairakei and Kamojang). However, hydrothermal

demagnetization is an irreversible process and demagnetized bodies interpreted from the residual magnetic data also reflect hydrothermal past activity.

Studies of two NZ geothermal prospects (Te Kopia and Tokaanu-Waihi) show that ground magnetic surveys can be used to detect and map the distribution of concealed near-surface alteration. At Tokaanu-Waihi, thermally altered ground beneath steeper terrain is unstable (Severne and Hochstein, 1994) and should be avoided by construction site.

Acknowledgements

The authors thank A/Prof P.R.L. Browne (Geothermal Institute) for his valuable comments to the final draft of this paper.

REFERENCES

Barnett, C.T. (1976). "Theoretical modeling of the magnetic and gravitational fields of an arbitrarily shaped three-dimensional body." Geophysics, vol 41, no 6, 1353-1364.

Bignall, G. (1991). "Subsurface stratigraphy and hydrothermal alteration at Orakeikorako and Te Kopia geothermal systems, New Zealand." Proc. 13th NZ Geothermal Workshop, 199-201.

Browne, P.R.L. (1994). "86.101 Geology Lecture Notes." Geothermal Institute, The University of Auckland, NZ.

Dench, N.D. (1980). "Interpretation of fluid pressure measurements in geothermal wells." Proc. 2nd NZ Geothermal Workshop, 55-59.

Grant, M.A. (1982). "The recharge to the Wairakei reservoir." Proc. 4th NZ Geothermal Workshop, 33-37.

Grant, M.A., Donaldson, I.G. and Bixley, P.F. (1982). "Geothermal Reservoir Engineering." Academic Press, New York, 369 pp.

Grindley, G.W. (1960). "Sheet 8 Taupo - Geological Map of New Zealand 1:250,000." Department of Scientific and Industrial Research, Wellington, New Zealand.

Grindley, G.W. (1986). "Te Mihi steam reservoir, Wairakei - An exploitable geothermal resource." Proc. 8th NZ Geothermal Workshop, 165-170.

Healy, J. (1984). "Wairakei geothermal field review". Unpublished geothermal circular JH/10. NZ Geological Survey, Lower Hutt, New Zealand.

Hochstein, M.P. (1976). "Geophysical exploration of the Kawah Kamojang Geothermal Field, West Java." Proc. of the 2nd Symposium on the development and use of geothermal resources (San Fransisco), 1049-1058.

Hochstein, M.P. and Soengkono, S. (1994). "Magnetic anomalies associated with high temperature reservoirs in the Taupo Volcanic Zone (New Zealand)". Submitted to the World Geothermal Congress 1995, Florence, Italy.

Lampoonsub, K. (1987). "Magnetic properties from Wairakei, Orakeikorako, Te Kopia and Reporoa geothermal fields." Geothermal Institute Report 87.13, The University of Auckland, NZ.

Laughlin, W. (1982). "Exploration for Geothermal Energy." In: Edwards, L.M., Chilingar, G.V., Rieke III, H.H. and Fertl, W.H. (Eds): Handbook of Geothermal Energy, 218-242. Gulf Publishing Company, Book Division, Houston, London, Paris, 613 pages.

Malin, S.R.C. and Barraclough, D.R. (1981). "An algorithm for synthesizing the geomagnetic field." Computers and Geosciences, vol 7, no 4, 401-405.

Munyithya, J.M. (1994). "Surface alteration study in the northern part of Tokaanu-Waihi geothermal field using shallow resistivity survey and soil temperature measurement." Geothermal Institute Report 94.14, The University of Auckland, NZ.

Nguyen Hong Bang. (1993). "Surface alteration study in the northern part of Te Kopia geothermal area using shallow resistivity techniques, measurement of magnetic gradient and soil temperatures." Geothermal Institute Report 93.17, University of Auckland, NZ.

Perez-Ramos, S.G. (1993). "Surface alteration study in the northern part of Te Kopia geothermal area using XRD analysis, soil temperature and magnetic measurements, and resistivity investigation." Geothermal Institute Report 93.19, The University of Auckland, NZ.

Saptadji, N.M. (1987). "Reservoir simulation of Kamojang Field." Geothermal Institute Report 87.19, The University of Auckland, NZ.

Severne, C.M. and Hochstein, M.P. (1994). "Heat and mass transfer of the Hipaua thermal area (Tokaanu-Waihi geothermal field), Lake Taupo, New Zealand." Proc. 16th NZ Geothermal Workshop, 209-214.

Siripongsatian, S. (1994). "Surface alteration study in the northern part of Tokaanu-Waihi geothermal field using measurement of magnetic gradient and soil temperature, and XRD analysis." Geothermal Institute Report 94.23, The University of Auckland, NZ.

Soengkono, S. (1985). "Magnetic study of the Mokai geothermal field." Proc. 7th NZ Geothermal Workshop, 25-30.

Soengkono, S., Hochstein, M.P. and Suranto (1988). "Magnetic anomalies over the Kamojang geothermal field (West Java, Indonesia)." Proc. 10th NZ Geothermal Workshop, 129-132.

Soengkono, S. and Hochstein, M.P. (1992). "Magnetic anomalies over the Wairakei geothermal field, Central North Island, New Zealand." Geothermal Resources Council Trans., vol 16, 273-278.

Steiner, A. (1977). "The Wairakei geothermal area, North Island, New Zealand." New Zealand Geological Survey Bulletin 90, 136 pp.

Suranto (1987). "Interpretation of airborne magnetic anomalies at Kamojang, West Java, Indonesia." Geothermal Institute Report 87.21, The University of Auckland, NZ.

PROCEEDINGS, Twentieth Workshop on Geothermal Reservoir Engineering
Stanford University, Stanford, California, January 24-26 1995
SGP-TR-150

MICROEARTHQUAKE MONITORING AT THE SOUTHEAST GEYSERS USING A HIGH-RESOLUTION DIGITAL ARRAY

Ann Kirkpatrick, John E. Peterson, Jr., and Ernie L. Majer

Earth Sciences Division
Lawrence Berkeley Laboratory
Berkeley, California 94720

ABSTRACT

Microearthquake activity at the Southeast Geysers, California, geothermal field is monitored with a high-resolution digital seismic network. Hypocenters are spatially clustered in both injection and production areas, but also occur in more diffuse patterns, mostly at depths from 1 to 2.8 km. Hypocenters near the injection well DV-11 exhibit a striking correlation with movement of injectate and injectate-derived steam. Preliminary moment tensor results show promise to provide information on the differing source mechanisms resulting from fluid injection and steam extraction.

INTRODUCTION

Over the last several years, Lawrence Berkeley Laboratory (LBL) has been monitoring microearthquake (MEQ) activity at the Southeast (SE) Geysers, California, using a high-resolution, high-frequency digital array. The original array consisted of eight three-component stations operated by LBL, and five three-component stations operated by Lawrence Livermore National Laboratory (LLNL). A re-configured array of 13 stations telemetered to a central site went on-line in January 1994. From these new data we have been able to determine a three-dimensional (3-D), P- and S-wave velocity model for the SE Geysers, and to utilize this model to obtain high-quality MEQ hypocenters. We have also inverted the data for moment tensors, providing information on event size and source characteristics.

One of the main objectives of the project is to evaluate the utility of high-resolution MEQ monitoring as a geothermal reservoir management tool. Specifically, we wish to determine what kind of hypocentral accuracy can be obtained with this type of network, what kind of analysis can be performed with such hypocentral data, and whether the results of such analysis are of use to reservoir managers. To this end, we report here on the MEQ locations we have obtained in the SE Geysers, and compare them to those determined using the lower-resolution, analog MEQ network operated at the Geysers by the Unocal-NEC-Thermal (U-N-T) partnership. We discuss the seismicity associated with the Unit 18 Cooperative Injection Project, and its relation to the effects of the injection on nearby production wells. We also discuss the seismicity associated with steam extraction in a production well, and compare it with injection-related seismicity.

Another objective of the project is to use the seismic velocity structure obtained from the MEQ data to infer the physical conditions and properties of the reservoir. In this report, however, the velocity structure is discussed only in relation to its use in determining hypocenters.

NETWORK AND DATA

The LBL array consists of 13 high-frequency (4.5 Hz), digital (480 samples/s), three-component stations deployed on the surface, in portions of the Calpine, U-N-T, and Northern California Power Agency (NCPA) leases. U-N-T has monitored seismicity of portions of the Geysers since 1985 (Stark, 1992). Their network consists of mostly vertical, 4.5-Hz seismometers, with some three-component stations. The data are recorded in analog form, but later digitized at 100 samples/s. Both the LBL and the U-N-T arrays are shown in Figure 1. The U-N-T network covers a larger area and has a larger station spacing.

The LBL network records regional and teleseismic events as well as those from the Geysers area. To avoid processing these extraneous events, U-N-T provides us with a list of events which they have located in the SE Geysers. We use this list to identify and extract the events of interest from our data for processing. Because of the greater sensitivity of the LBL network, this means that many of the smaller events recorded at the SE Geysers by the LBL array,

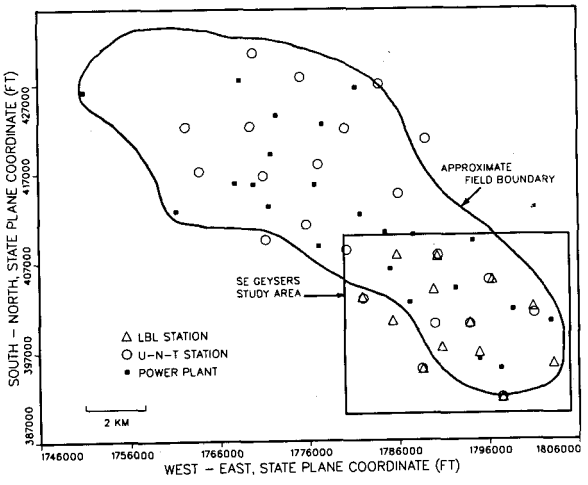

Figure 1. Location of LBL and U-N-T MEQ networks at The Geysers, California.

but not by the U-N-T array, remain unprocessed. Also, because of down-time of the LBL array due to operating problems, some events that were located by U-N-T were not recorded by LBL.

Once the events are identified, the P- and S-wave arrival times for each event at each station are picked manually. The uncertainty in the P arrival time is estimated at 0 to 3 samples, or up to 0.006 s, and the uncertainty in the S arrival time is estimated at 2 to 6 samples, or 0.004 to 0.012 s. These arrival times provide the data set for the velocity model and hypocentral location inversions. The moment tensor inversion models the amplitude (obtained by integration over the pulse width) and polarity of the P-wave pulses.

From January 1994 through July 1994, 930 "U-N-T events" were processed and located using LBL data. In June, we processed all of the LBL data, and located an additional 139 events within the area defined by U-N-T as the SE Geysers (as well as others outside this area that we wished to use in the velocity inversion). Since U-N-T located 225 events in June, it appears that the LBL network is capable of locating some additional 50% of events.

THREE-DIMENSIONAL SEISMIC VELOCITY INVERSION

In order to determine high-quality hypocenters, an accurate model of the seismic velocity is needed. We chose approximately 300 events from the January to June 1994 time period to use in an inversion for three-dimensional P- and S-wave velocity structure. The events were selected to maximize ray coverage of the imaged volume. The final data set consisted of 2731 P arrival times, and 1578 S arrival times from 295 events.

The joint hypocenter-velocity inversion method of Thurber (1983), as modified by Michelini and McEvilly (1991) was used. Initial velocity values are assigned to nodes on a 3-D grid, and are adjusted in an iterative procedure that minimizes the travel-time residuals using damped least squares. The initial velocity model was an average of the 1-D, P velocity model obtained by O'Connell and Johnson (1991) for the central portion of the Geysers field, and the 1-D P model used by U-N-T (M. A. Stark, pers. comm.), which is based on that obtained by Eberhart-Phillips and Oppenheimer (1984). The initial S model was calculated from the P model using an assumed Vp/Vs of 1.7.

A 7 km by 4 km area bounded by the stations was imaged to a depth of 2.5 km. The horizontal node spacing was 1.0 km and the vertical node spacing was 0.5 km. The inversion resulted in a 52% weighted root mean square residual reduction over the 1-D starting model, and a 59% weighted variance reduction.

MICROEARTHQUAKE LOCATION RESULTS

The new 3-D, P- and S-wave velocity model was used to relocate the SE Geysers events. The hypocenters for the January to July 1994 time period are shown in Figure 2. They can be compared with the U-N-T hypocenters for the January to June 1994 period shown in Figure 3.

The uncertainty of the hypocenter locations arises primarily from two factors, errors in the arrival times, and inaccuracy of the velocity model. We estimate the uncertainty in locations arising from error in arrival times as less than 30 m. The uncertainties arising from inaccuracy of the velocity model are more difficult to assess. We plane to estimate them by perturbing the velocity values, then relocating the events to see how much the locations change.

Distinct spatial patterns of seismicity are evident on the LBL map (Figure 2). The seismicity on the U-N-T map (Figure 3) appears much more diffuse; the use of the LBL data and the 3-D model results in much tighter clustering of events. Also, absolute locations of many events and clusters differ between the two

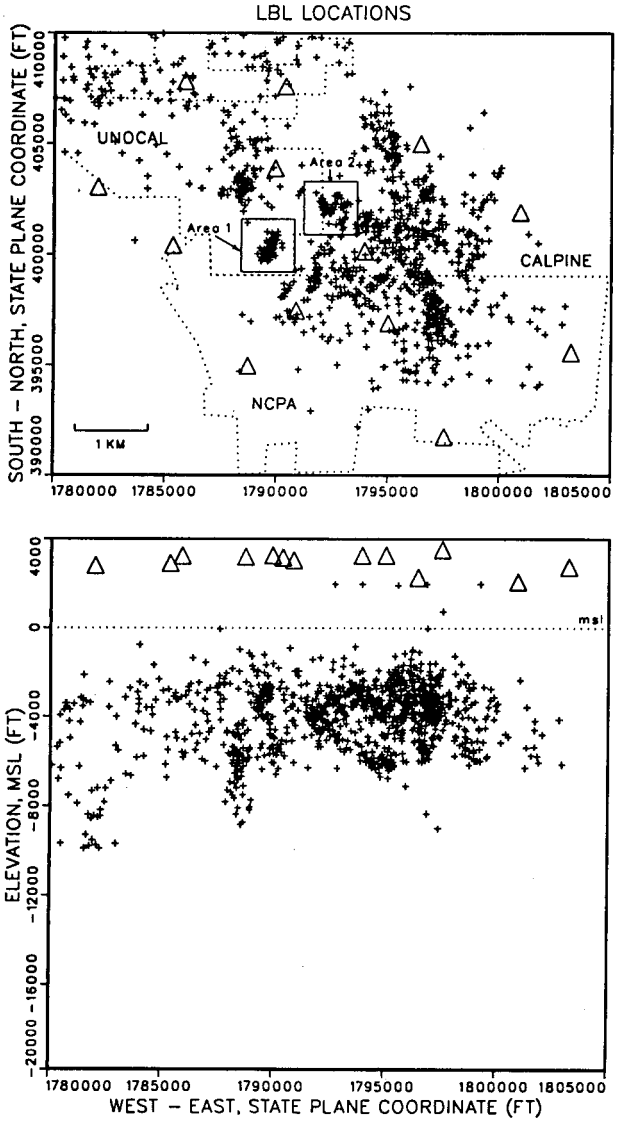

Figure 2. MEQ hypocenters at the SE Geysers for January to July 1994, obtained using the LBL array and a 3-D, P- and S- wave velocity model. Plan view and projection onto east-west plane shown. Areas 1 and 2 are shown in detail in Figures 5 to 8. Triangles represent LBL stations. Note: events north of 407500 and west of 1785000 are from June 1994 only and are additional to the U-N-T events.

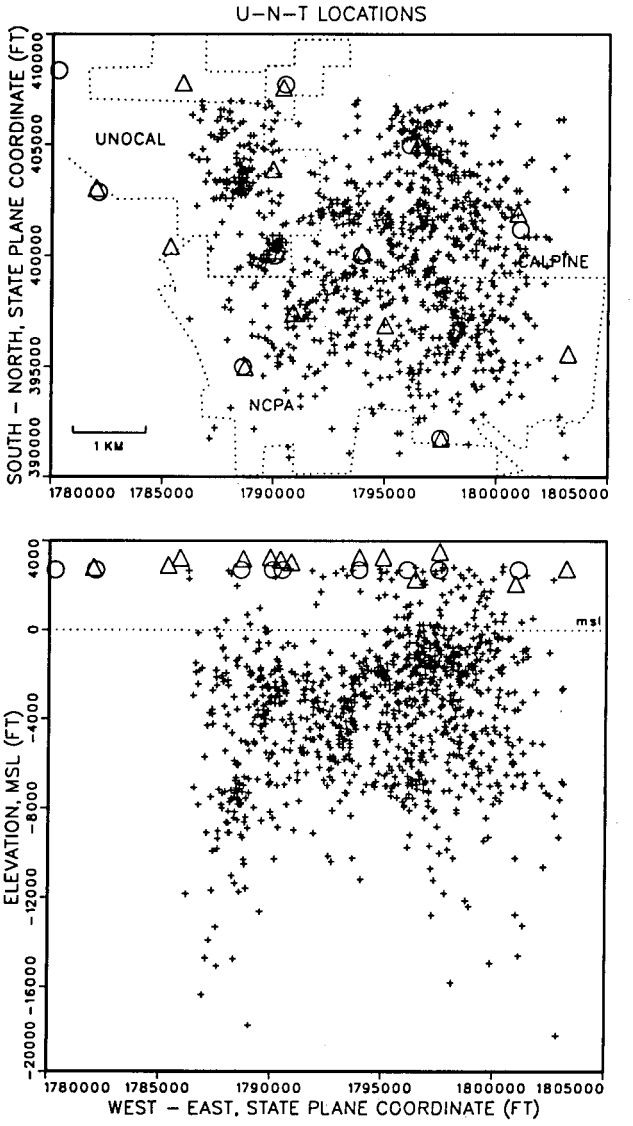

Figure 3. MEQ hypocenters at the SE Geysers from January to June 1994, obtained using the U-N-T array and a 1-D velocity model. Plan view and projection onto east-west plane shown. Circles represent U-N-T stations; LBL stations also shown for reference (triangles). Compare with Figure 2.

figures. Several of the clusters are known to correlate with injection wells, while at least one of the clusters is associated with a production well. Two of these clusters (the boxed areas in Figure 2) are discussed in detail in the following sections. The rest of the seismicity has not yet been studied for detailed correlation with injection and production activities.

The depth distribution of the LBL hypocenters is also less diffuse than the U-N-T hypocenters. The LBL hypocenters locate in a much more limited depth range, between –1000 and –7000 ft msl (–0.3 to –2.1 km msl, or a depth of 1.0 to 2.8 km, using an average surface elevation of 0.7 km msl), with several localized MEQ "stringers" extending below the base of the main zone of seismicity. This result is similar to that found at the NW Geysers by Romero et al. (1994). Using a similar array, they identified a shallow zone of microseismicity between 1 and 3 km in depth, and a more limited zone from 3.5 to 5 km in depth.

The observation that few events occur above –1000 ft (–0.3 km) msl is interesting in that the elevation of the top of the steam reservoir ranges from 1000 ft to –3000 ft (0.3 to –0.9 km) msl in the area that is seismically active (Field Operators, 1992). The top of the steam is above the –1000 ft (–0.3 km) level over approximately one-half of the seismic area. Thus, it appears that the portion of the steam reservoir between 1000 and –1000 ft (0.3 and –0.3 km) msl is relatively aseismic.

More detailed study will be conducted to determine the relation of the base of the seismicity with the bottom of the reservoir. The depths of the deeper events are less well constrained than the shallower events due to poorer resolution of the velocity model with depth. In general, producing wells in this area extend down to elevations of –5000 to –6000 ft (–1.5 to –1.8 km) msl, roughly coincident with the base of the primary zone of seismicity. Clearly, however, some MEQs do occur below the maximum depth that the steam reservoir is currently being exploited.

It would be desirable to know which components of the LBL monitoring process contribute to the differences between the LBL and U-N-T hypocenter results. If, for example, it were determined that the inclusion of S-wave data did not contribute appreciably to improved accuracy, it would be much cheaper to operate a high-resolution network since horizontal components would not be required. Therefore, we conducted several tests to separate the effects of the use of P- and S-wave data vs. the use of P-wave data only, and also the use of a 1-D vs. a 3-D model.

First, the events were relocated using the 3-D, P velocity model, excluding S-wave arrival times. Locations shifted an average of 240 ft (73 m) horizontally, and in a random pattern. The clustered patterns of seismicity were still quite evident, and the depth distribution of events did not differ significantly from the 3-D, P and S case, although depths of many of the individual events shifted appreciably.

Next, the events were relocated using a 1-D, P- and S-wave velocity model. In this case, the clustering of events still occurred, but the locations of the clusters shifted appreciably, up to 1500 ft (0.45 km). The base of the main seismicity zone extended to –9000 ft (–2.7 km) msl. Relocations using a 1-D model without S-waves were also performed. The results are similar to the 1-D, P and S case, although some clusters were not as tight.

We conclude that the high-resolution data and/or the increased density of the LBL array results in more clustered event locations compared to the U-N-T data, and that use of a 3-D velocity model significantly affects the absolute locations of the events and clusters. S-wave data may be of limited usefulness for hypocentral locations of SE Geysers MEQs with this particular array. Because the large amount of energy in the P-wave coda in these seismograms tends to obscure the S-wave arrivals, their arrival times are fewer and less accurate than those of the P waves, and therefore may not contribute appreciably to the inversion. We plan to test the effect of the high-resolution data by adding random noise to the arrival times and relocating the events. This should indicate how much picking error is needed to make the LBL locations as diffuse as the U-N-T locations.

SEISMICITY ASSOCIATED WITH AN INJECTION WELL

The cluster of seismicity associated with the injection well DV-11 was investigated in detail ("Area 1" in Figure 2). Injection in DV-11 began in late December 1993 as part of The Geysers Unit 18 Cooperative Injection Project, a three-year cooperative program between the U.S. Department of Energy (DOE) and U-N-T, Calpine, NCPA, and Pacific Gas and Electric, to increase the

understanding of injection into known productive intervals at The Geysers (Voge et al. 1994).

Analysis of 1993 and 1994 data shows that the DV-11 area was seismically quiescent prior to February 1994. During that month, five MEQs occurred near DV-11. By June 1994, they occurred at a rate of 21 events per month. The injection rate and the seismicity rate are compared in Figure 4. There is a lag time of approximately one month between initiation of continuous injection and the onset of seismicity. A similar lag time is observed between the cessation of injection in late May and the drop in seismicity in July. In contrast, only seven days after the January 7 injection start, enhanced steam production began to occur from the five producing wells on the injection well pad (Voge et al., 1994).

The DV-11 study area and the wells being monitored for physical and chemical parameters during the injection test are shown in Figure 5. Posted next to each well is the nominal flowrate difference in kph (thousand pounds per hour) between 12/1/93 and 4/30/94, four months after injection began (data from Voge et al., 1994). Note that the largest increases in steam production are seen in the wells with steam entries to the west and south of the injector.

The LBL hypocenter locations in the DV-11 injection area are shown in detail in Figure 6. The MEQs are located near and below the bottom of the injection well (from 400 ft above [120 m] to 3500 ft [1070 m] below the well TD), and distances up to 400 ft

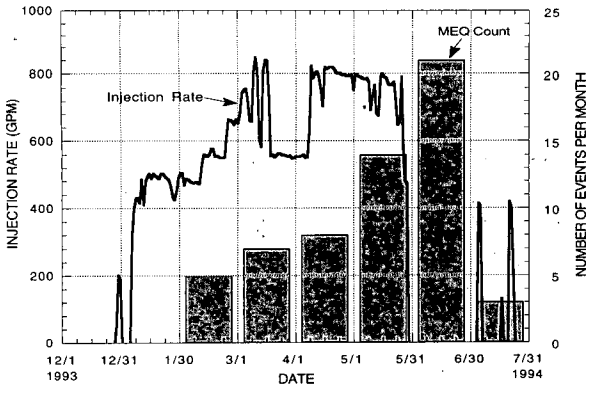

Figure 4. Comparison of DV-11 injection rate and seismicity in the surrounding 2400- × 2400-ft (0.73- × 0.73 km) area. MEQ count is based on U-N-T data, because of some down-time of the LBL network during the period shown.

(120 m) north, 1000 ft (300 m) west, and 1000 ft (300 m) south. This trend in event locations is toward the wells that showed the largest increases in production (wells DV-1, DV-6, DV-15, DV-16, and DV-17; see Figure 5). There are few events to the east of DV-11; likewise, well DV-24-RD, whose steam entries are directly east of DV-11, showed only one-half to one-third the nominal flowrate increase of these other five wells. The maximum depth of the MEQs is similar to the depth of the deepest production wells in this area.

Most of the flowrate increase in DV-6 did not occur until April 1994, while the other increases were seen almost immediately. Voge et al. (1994) suggest that the delayed increase was due to the time necessary for expansion of the boiling front from the injected liquid to reach the deep DV-6 steam entries. This interpretation may be supported by the observation that the deepest MEQs in Figure 6 (those below –4000 ft [–1.2 km] msl) all occurred in June, with the exception of one each in March, April and May. The distribution of the shallower events do not show a temporal pattern.

It has been suggested that MEQs indicate the presence of injectate, but also that conversely, the absence of MEQs cannot be taken to mean its absence. There has been at least one case of injection with no clear increase in seismicity detected (M. A. Stark, pers. comm.), and preliminary correlation of LBL hypocenters with injection wells in the NCPA lease area indicates that seismicity can decrease or even stop around injectors active for long periods of time. Likewise, the absence of MEQs above –2500 ft (–7.6 km) msl in Figure 5 cannot be taken to show that injectate is not leaving the well above that elevation, because the mechanisms by which injection induces MEQs are not known. We have already discussed the existence of a relatively aseismic zone within the reservoir above –1000 ft (–0.3 km) msl over other areas of the SE Geysers.

The top of the felsite intrusion is also shown in Figure 6, and it is seen that the located MEQs occur within the felsite. This observation should be compared with the felsite-dependence of other injection-related MEQs as well as production-related MEQs to evaluate its significance. Much of the Geysers is underlain by this northwest-trending intrusive body, and in the SE Geysers, the productive reservoir is found in both the felsite and the overlying greywacke unit.

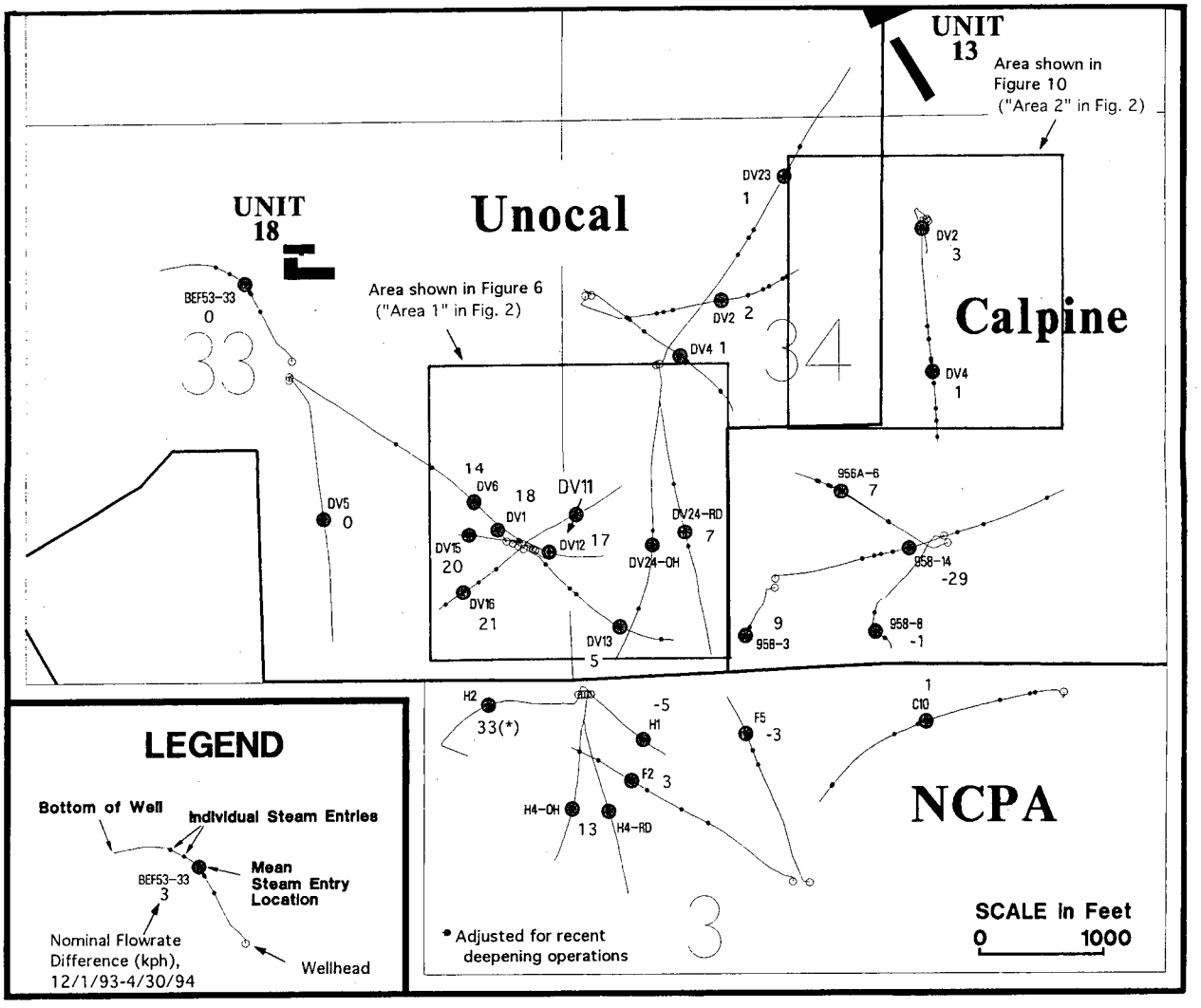

Figure 5. Unit 18 Cooperative Injection Project study area, showing monitored U-N-T, Calpine, and NCPA wells. Base map provided by NCPA.

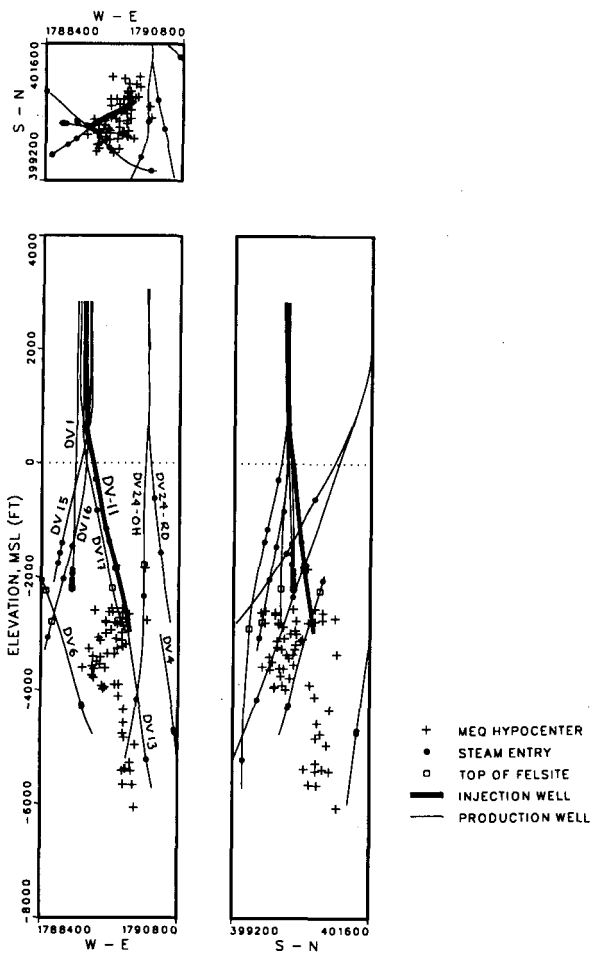

Figure 6. Plan view and east-west and north-south cross sections of seismicity for January to July 1994 near injection well DV-11, obtained using LBL data and 3-D P- and S-wave velocity model. Location of area indicated by boxes on Figures 2 ("Area 1") and 5.

In summary, the data do suggest that the MEQ distribution can be interpreted as a rough indication of the pathway of injectate and/or injection-derived steam, and further, of the existence of fractures or high-permeability pathways. While it is possible that the larger number of wells extracting steam to the west and south of DV-11 influenced preferential fluid movement in that direction and the corresponding seismicity, this would not explain the seismicity to the north of DV-11. If the locations of the hypocenters are accurate, they could indicate the movement of some injectate to the north, and consequently that deep drilling in this area could increase fluid recovery. Voge et al. (1994) estimated for April 1994 a 40.7% near-term recovery of injectate as produced steam in the existing nearby wells, primarily to the south and west.

Presented in Figure 7 are plots of the DV-11 seismicity determined using different data and velocity models. They demonstrate that in doing the above type of analysis, confidence is increased by the use of a 3-D model and LBL-type network data, and to a lesser extent, S-wave data. The U-N-T locations (Figure 7a) are more diffuse, both laterally and vertically, than the LBL locations. The trend towards the wells showing increased flowrate is not as defined, and many events locate to the east of DV-11. Events also locate above the felsite, and below the TD of the deepest wells.

Figure 7b shows the hypocenters obtained using LBL data, but with a 1-D model. The events are clustered, but are shifted to the southeast, towards wells that showed low flowrate increases. Some events also locate much deeper than in Figure 6, below the TD of the deepest production wells in this area.

Figure 7c presents the hypocenters obtained with LBL data and a 3-D model, but without using S-wave data. The MEQ distribution is very similar to that in Figure 6, and all of the same conclusions could be drawn from this data. However, elimination of S-wave data has resulted here in more events located to the north of DV-11, making a stronger case for infill well drilling in that area than might be warranted from the 3-D, P- and S-wave results.

SEISMICITY ASSOCIATED WITH A PRODUCTION WELL

A tight cluster of seismicity occurring around the Calpine production wells DV-2 and DV-4 was also studied in detail ("Area 2" in Figure 2). A detailed plan view and cross-section is shown in Figure 8, and Figure 5 shows the area in relation to the DV-11 injection test. Although Calpine DV-2 and DV-4 are being monitored as part of the DV-11 injection project, we do not believe the seismicity associated with these two wells is related to the DV-11 injection, because the rate of seismicity in this area has not increased appreciably since the injection began. Both LBL and U-N-T data show a cluster of events in this area in 1993. Also, flowrates in Calpine DV-2 and DV-4 have shown almost no response to DV-11 injection, although small amounts of tracers injected into DV-11 have been recovered. They may, however, be influenced by injection in two nearby Calpine wells. One injection wellhead is located just to the east of the area shown, with the well course deviated to the southeast. The other injection

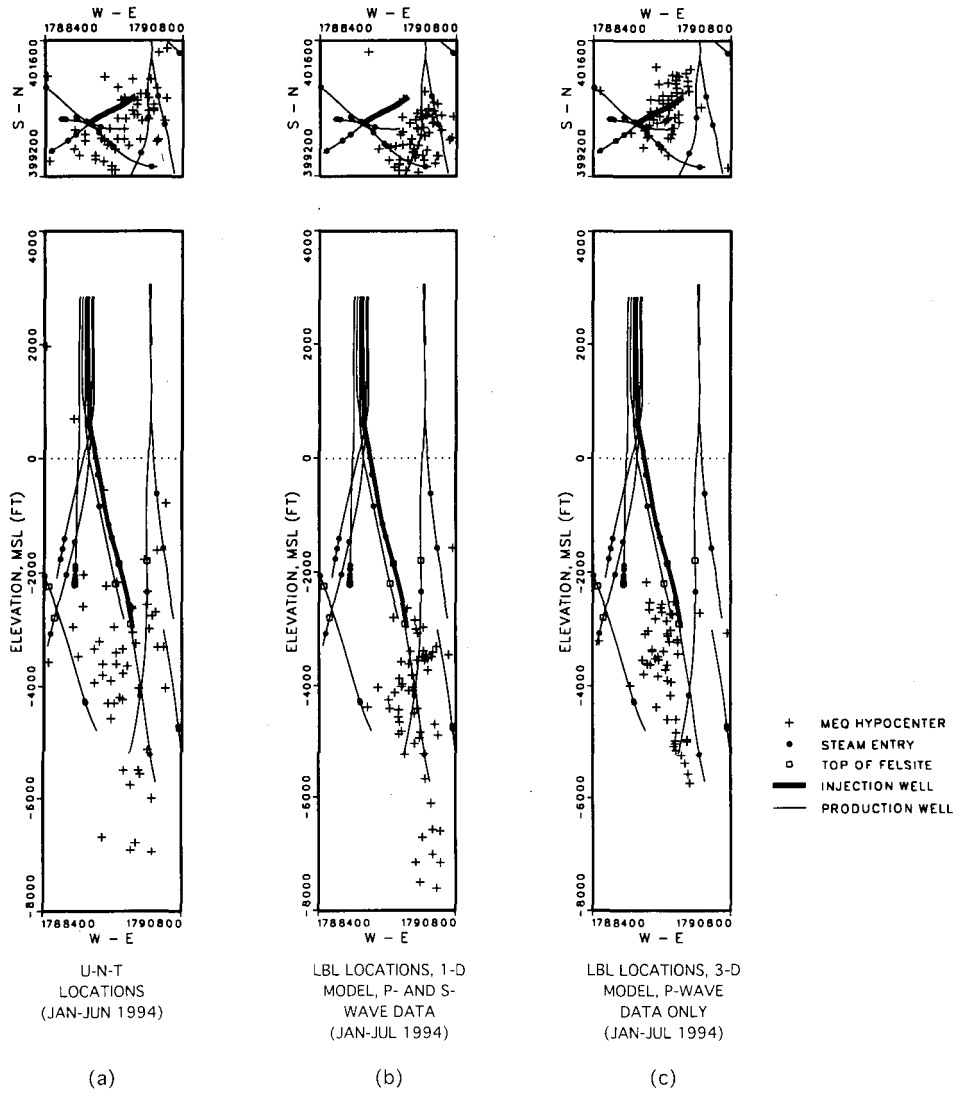

Figure 7. Plan views and east-west cross sections of seismicity near injection well DV-11, obtained using differing data and velocity models. Compare with Figure 6.

wellhead is on the same pad as 956A-6 and 958-8, shown in Figure 5, and the well course is nearly vertical. Both DV-2 and DV-4 produce at a rate around 70 kph (Voge et al, 1994).

The MEQs occur mostly near and below the bottom of well DV-2, and within the felsite, similar to the seismicity near the injection well DV-11. Again, it appears that the upper portion of the steam reservoir is relatively aseismic here. The events are also displaced laterally from the DV-2 well course, or to its projection downward in the case of those events located below the well's TD. The seismicity nearest to DV-4 is also displaced by about 300 ft (90 m) east. Differences in source characteristics between these events and those near DV-11 are discussed in the next section.

SOURCE MECHANISM STUDIES

In order to obtain information on the size and source characteristics of the MEQs, the LBL data were inverted for moment tensors. The procedure yielded a scalar moment and an orientation of the maximum compressive and tensional stresses (P and T axes) for each event. Because the procedure takes both amplitude and polarity of P waves into account, the results are better constrained than the standard fault plane solutions, which are often ambiguous. High-resolution data is required for this method because

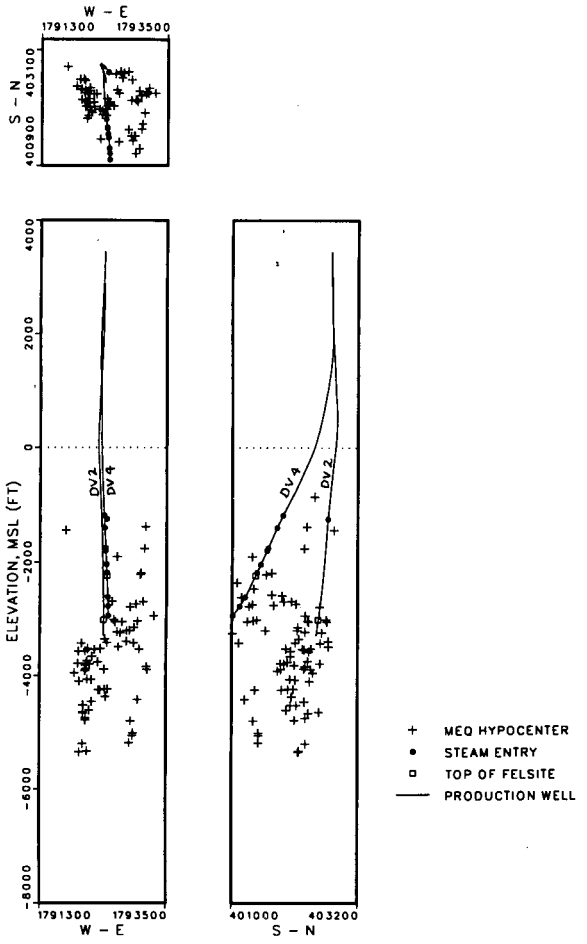

Figure 8. Plan view and east-west and north-south cross sections of seismicity near the Calpine production wells DV-2 and DV-4. Location of area indicated by boxes on Figures 2 ("Area 2") and 5.

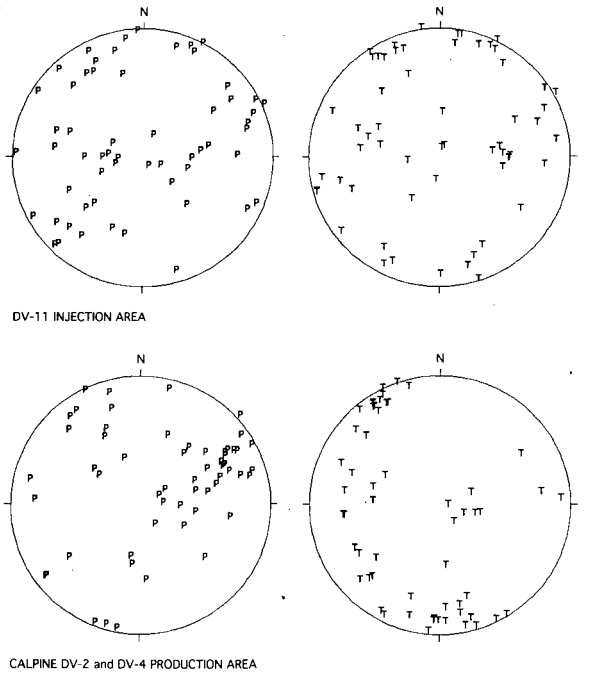

Figure 9. Orientation of P and T axes obtained by moment tensor inversion of the LBL data, for the events for January to August 1994, from the areas shown in Figures 6 and 8. Lower hemisphere equal area projection.

the amplitudes are obtained by integration over the pulse width; therefore the uncertainty in arrival time must be small compared to the pulse width. The method is also capable of using S-wave data; however, because of the high uncertainty of the LBL S-wave arrival times, we were not able to do so.

Although the method is still in the development stages, preliminary orientations of the P and T axes of the events in the DV-11 injection area and the Calpine DV-2 and DV-4 production area are shown in Figure 9. While there is a great deal of scatter in the orientations in both areas, it does appear that there are some differences. The axes in the injection area are more randomly oriented while in the production area there is a cluster of P axes oriented in a NE-SW direction, and alignment of many T axes in a NW-SE direction. The production area axes are consistent with the orientation of the regional strain field from geodetic measurements, of approximately N79W extension and N11E contraction (Prescott and Yu, 1986), and with many of the P and T axes obtained by Oppenheimer (1986) for The Geysers from fault plane solutions on USGS data.

If this difference in focal mechanisms between one injection and one production area were found for all injection- vs. production-related events at the SE Geysers, it would have important implications for different earthquake-inducing mechanisms. As pointed out by Oppenheimer (1986), agreement between the orientation of the production-related earthquake stress axes with the regional strain rate axes would indicate that the stress perturbations resulting from extraction are small compared to the regional tectonic stress field. On the other hand, the lack of such correlation for the injection-related events would indicate that the local stress perturbations induced by injection dominate.

The scalar moments of the SE Geysers MEQs are shown in a standard "b-value" plot in Figure 10. The

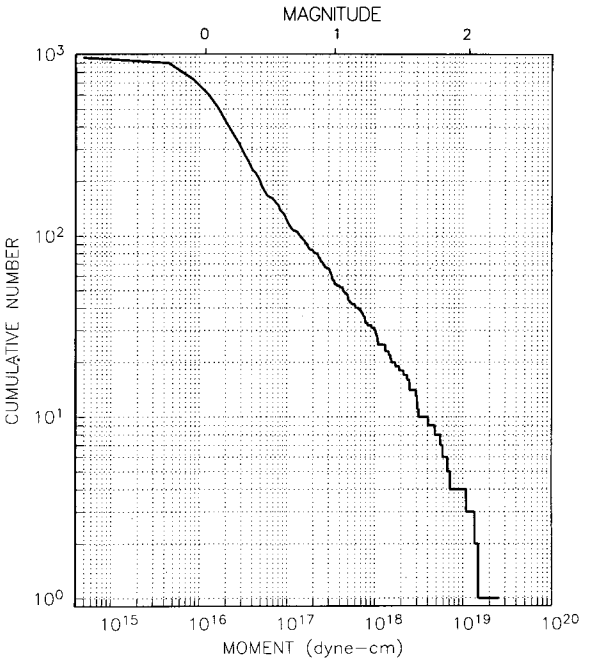

Figure 10. SE Geysers B-value plot, showing cumulative number of events above given moment vs. moment for January to August 1994. Slope of line corresponding to moments less than 3×10^{18} is 0.68; slope of line for greater moments is approximately 1.0.

different slope of the line for moments above and below 3×10^{18} dyn-cm may indicate differing mechanisms for the events above and below this value. One possible explanation is that the larger events have causes related to tectonic stresses, while the mechanism of the smaller events are related to production, resulting in a different frequency distribution.

The moments (M_o) were converted to magnitude (M_w) using the relationship

$$M_w = \frac{2}{3} \log M_o - 10.7$$

(Hanks and Kanamori, 1979). The equivalent magnitudes are shown on the upper x axis of the b-value plot. The size of the events at the SE Geysers are quite small. For the time period January to July 1994, the largest event recorded by the LBL array had a moment of 2×10^{19} dyn-cm, or a magnitude of about 2.2.

The results presented above indicate that further investigation of moment tensors is warranted and may provide important information regarding the mechanisms inducing MEQs at the SE Geysers. It may also be possible to infer additional source characteristics such as energy release, size of rupture surface, and source duration from the moment tensor results.

CONCLUSIONS

High-quality MEQ hypocenter locations have been obtained at the SE Geysers using a high-resolution digital array operated by LBL and have been compared with those obtained from the U-N-T array. The use of a 3-D seismic-velocity model is important for obtaining accurate absolute locations, while either the high sample rate or the tight array configuration, or both, is required for accurate relative locations.

Use of the new array reveals that MEQs at the SE Geysers occur in spatial clusters which can be associated with both injection and production activities, as well as in a more diffusely scattered pattern. Elevations of most of the events are between −1000 and −7000 ft msl, or depths of 1 to 2.8 km. The base of this primary seismicity zone is approximately coincident with the maximum depth from which the steam reservoir is currently being produced. The portion of the steam reservoir from 1000 to −1000 ft (0.3 to −0.3 km) msl is relatively aseismic. The seismic moments of the events recorded have been under 2×10^{19} dyn-cm, or a magnitude of about 2.2.

MEQs appear to have been induced by injection of water into well DV-11. The LBL data showed that the lateral, vertical, and temporal distribution of seismicity was towards the production wells responding most favorably to the injection, adding credibility to the use of MEQs to track injectate or to infer the location of high-permeability pathways. MEQs also spread north from DV-11 towards an unexploited area of the field, which, using this principle, indicates that recovery of injectate might increase with drilling in this area.

Orientations of P and T axes of moment tensors of events near the injection well DV-11 differ from those of events near the Calpine production wells DV-2 and DV-4. The source mechanism studies are in a preliminary stage, but show promise for

providing information on the mechanisms by which water injection and steam extraction induce MEQs. High-resolution data are required for the moment tensor analysis.

ACKNOWLEDGEMENTS

This work was supported by the Assistant Secretary for Energy Efficiency and Renewable Energy, Geothermal Division, of the U.S. Department of Energy under contract No. DE-AC03-76SF00098. The authors would like to thank U-N-T, NCPA, and Calpine for their cooperation in this project. In particular, we express our gratitude to Mitchel Stark, Bill Smith, and Joe Beall for their comments and interaction. Thanks are also given to Robert Nadeau for many helpful discussions, and to Lane Johnson for the moment tensor inversion code.

REFERENCES

Eberhart-Phillips, D., and D. H. Oppenheimer (1984), "Induced seismicity in The Geysers geothermal area, California," J. Geophys. Res. 89, 1191–1207.

Field Operators (1992), "Map of the top of the steam reservoir at The Geysers," Geotherm. Resour. Counc. Special Report No. 17, back cover pocket.

Hanks, T. C., and H. Kanamori (1979), "A moment magnitude scale," J. Geophys. Res. 84, 2348–2350.

Michelini, A., and T. V. McEvilly (1991), "Seismological studies at Parkfield: I. Simultaneous inversion for velocity structure and hypocenters using cubic b-splines parameterization," Bull. Seismol. Soc. Am. 81, 524–552.

O'Connell, D. R., and L. R. Johnson (1991), "Progressive inversion for hypocenters and P wave and S wave velocity structure: Application to The Geysers, California, geothermal field," J. Geophys. Res. 96, 6623–6236.

Oppenheimer, D. H. (1986), "Extensional tectonics at The Geysers geothermal area, California," J. Geophys. Res. 91, 11463–11476.

Prescott, W. H., and S. Yu (1986), "Geodetic measurement of horizontal deformation in the northern San Francisco Bay region, California," J. Geophys. Res. 91, 7475–7484.

Romero, A. E., A. Kirkpatrick, E. L. Majer, and J. E. Peterson (1994), "Seismic monitoring at The Geysers geothermal field," Geotherm. Resour. Counc. Trans. 18, 331–338.

Stark, M. A. (1992), "Microearthquakes—a tool to track injected water in The Geysers reservoir," Geotherm. Resour. Counc. Special Report No. 17, 111–117.

Thurber, D. H. (1983), "Earthquake locations and three-dimensional crustal structure in the Coyote Lake area, Central California," J. Geophys. Res. 88, 8826–8236.

Voge, E., B. Koenig, J. L. Smith, S. Enedy, J. J. Beall, M. C. Adams, and J. Haizlip (1994), "Initial findings of The Geysers Unit 18 Cooperative Injection Project," Geotherm. Resour. Counc. Trans. 18, 353–357.

PROCEEDINGS, Twentieth Workshop on Geothermal Reservoir Engineering
Stanford University, Stanford, California, January 24-26 1995
SGP-TR-150

HYDROTHERMAL FACTORS IN POROSITY EVOLUTION AND CAPROCK FORMATION AT THE GEYSERS STEAM FIELD, CALIFORNIA — INSIGHT FROM THE GEYSERS CORING PROJECT

Jeffrey B. Hulen and Dennis L. Nielson

Earth Sciences and Resources Institute,
Department of Civil Engineering, University of Utah,
Salt Lake City, Utah 84112

ABSTRACT

The Department of Energy (DOE)/geothermal industry-sponsored Geysers Coring Project (GCP) has yielded 236.8 m of continuous core apparently spanning the transition between the uppermost Geysers steam reservoir and its caprock. Both zones in the corehole are developed in superficially similar, fractured, complexly veined and locally sericitized, Franciscan (late Mesozoic) graywacke-argillite sequences. However, whereas the reservoir rocks host two major fluid conduits (potential steam entries), the caprock is only sparingly permeable. This discrepancy appears to reflect principally vein texture and mineralogy. Two types of veins are common in the core — randomly-oriented, Franciscan metamorphic quartz-calcite veins; and high-angle, late Cenozoic veins deposited by The Geysers hydrothermal system. The older veins locally contain hydrothermal carbonate-dissolution vugs, which, although concentrated at the larger fluid conduit, are scattered throughout the core. The younger veins, commonly with intercrystalline vugs, consist dominantly of euhedral quartz, calcite, K-feldspar, wairakite, and pyrite — those in the reservoir rock also contain minor epidote and illite. The corresponding caprock veins are devoid of epidote but contain abundant, late-stage, mixed-layer illite/smecite (5-18% smectite interlayers) with minor chlorite/smectite (40-45% smectite interlayers). We suggest that clots of these two expandable clays in the caprock clog otherwise permeable veins and carbonate-dissolution networks at strategic sites to produce or enhance the seal on the underlying steam reservoir. Illite/smectite geothermometry indicates that the SB-15-D caprock clays were precipitated in the approximate temperature range 180-218°C, and those in the reservoir at about 218-238°C. These temperatures, along with occurrence of the clays on commonly etched calcite, K-feldspar, or wairakite, suggest that the clays were precipitated from mildly acidic steam condensate under conditions similar to those now prevailing.

INTRODUCTION

The GCP is a geothermal industry/DOE collaboration aimed at improving understanding of porosity, permeability, and remaining fluid saturation in The Geysers vapor-dominated geothermal system (Fig. 1; Hulen et al., 1995).

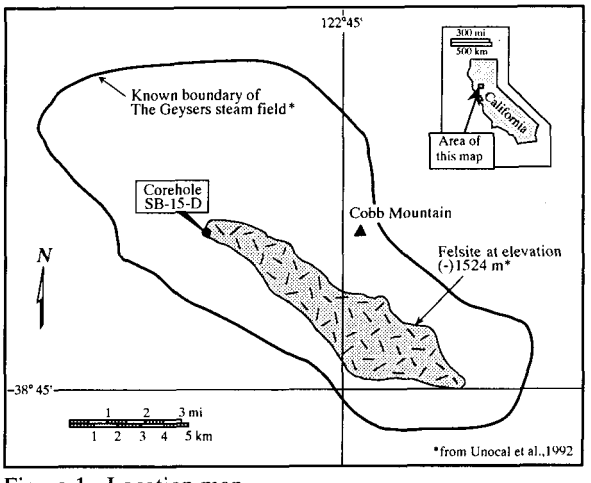

Figure 1. Location map

Gaining that understanding requires core, which, prior to the GCP, was a scarce commodity here. At the time the project was initiated, only 24 short (<8 m) cores <90 m in combined length had been collected from the field. The drilling phase of the GCP, completed late in 1994, yielded 236.8 m of additional continuous core, spanning the depth interval 251.4-488.3 m, from a newly-created sidetrack (SB-15-D) to an existing Unocal Corporation production well (Fig. 1).

Detailed characterization and precise quantification of porosity, permeability, and fluid saturation in this new core must await the results of focused investigations now in progress by the GCP's collaborating investigators (e.g. Bonner et al., 1995). However, our own baseline geologic studies in support of these efforts have begun to reveal significant differences between core from the relatively impermeable upper 70% of SB-15-D (above a depth of 417.3m) and the lower 30%, in which two prominent fluid conduits (potential steam entries) were penetrated (Hulen et al., 1995). Chief among these differences are the types, distributions, and abundances of vein-hosted hydrothermal clays. This paper discusses the implications of these differences — with emphasis on the clays — for evolution of reservoir porosity and formation of the caprock above the modern Geysers steam field.

GEOLOGIC AND HYDROTHERMAL SETTING

The Geysers geothermal system occurs principally in subduction-trench-related Franciscan (Late Mesozoic) metagraywacke, metashale, and metasiltstone, hereinafter referred to as "graywacke" and "argillite" (McLaughlin, 1978, 1981; Sternfeld, 1981, 1989). These rocks are intruded by a large (>100 km^3), composite, late Cenozoic felsic pluton (the felsite; Fig. 1) which has produced a thick, contact-metamorphic aureole in the enveloping older lithologies (Schriener and Suemnicht, 1982; Thompson, 1992; Dalrymple, 1992; Hulen and Nielson, 1993). The intrusive and contact-metamorphic rocks also host a significant portion of the steam field. Mapped faults at The Geysers include high-angle, northwest-trending, dextral strike-slip faults related to the San Andreas system, and low- to high-angle, also commonly northwest-trending thrust faults of probable Franciscan age (McLaughlin, 1978, 1981; Oppenheimer, 1986; Thompson and Gunderson, 1992). Faults and fractures controlling major steam conduits tend to be high-angle in the felsite (Thompson and Gunderson, 1992) and low- to moderate-angle in the Franciscan rocks (Beall and Box, 1992; Thompson and Gunderson, 1992).

The Geysers steam field is divisible into a so-called "normal" reservoir, with a pre-exploitation temperature of about 235°C at a pressure of about 3.3 MPa (White et al., 1971) and, principally in the northwest Geysers, a deeper, "high-temperature" reservoir (Walters et al., 1992) with rock temperatures locally exceeding 300°C. Although now vapor-dominated, The Geysers hydrothermal system was initially hot-water dominated, with deeper temperatures probably as high as 400°C (Moore, 1992; Gunderson and Moore, 1994). While in this earlier stage, the system created significant secondary porosity by dissolving calcite from Franciscan metamorphic quartz-calcite veins (Hulen et al., 1991, 1992; Thompson and Gunderson, 1992; Gunderson, 1992). The system also precipitated a well-zoned suite of hydrothermal vein minerals including tourmaline at deeper levels, epidote throughout most of the future steam reservoir, and commonly bladed calcite at higher elevations (McLaughlin et al., 1983; Hulen et al., 1991, 1992; Moore, 1992). The bladed calcite has been cited as an important porosity-sealing phase in The Geysers' caprock (Hulen et al., 1991, 1992; Moore, 1992).

The existence of such a caprock is necessary to "...inhibit the free escape of rising vapor" from the underlying steam reservoir (White et al., 1971). As we will argue, corehole SB-15-D apparently penetrates the transition zone between the basal portion of this caprock and the upper portion of the subjacent reservoir. This penetration provides an opportunity to investigate the means by which this essential seal was formed.

LITHOLOGY, FRACTURING, ALTERATION, VEIN MINERALIZATION, AND THE NATURE OF POROSITY

The GCP corehole encountered a sequence of interbedded Franciscan graywackes and argillites, with the graywackes strongly predominant (Fig. 2). These rocks were deposited as turbidites. The generally fine- to medium-grained graywackes show graded bedding and load casts, and the argillites, prominent flame structures (see also Sternfeld, 1989). Prevailing dip angles in these strata (relative to a plane normal to the core axis, itself inclined 83° from horizontal) range from 40-65°. The argillites at deeper levels, below a depth of about 375 m, appear slightly more indurated and competent than their higher-level counterparts (Hulen et al., 1995).

Although the SB-15-D core was highly fractured throughout (Hulen et al., 1995), losses of the water- and polymer-based drilling fluid to the formation were only 10-25% to a depth of 417.3 m. At this depth, a total loss of circulation occurred (Fig. 2), and the remainder of the hole was cored without drilling-fluid returns. A second major fluid conduit, somewhere between 472.4 m and 488.3 m (Fig. 2), was detected by a post-drilling Sandia National Laboratories temperature survey conducted immediately following injection of cool water into the partially thermally reequilibrated corehole (Brian Koenig, pers. communication, 1994). Both this deeper conduit and the one at 417.3 m almost certainly would have been steam entries had SB-15-D been air-drilled.

The lack of an obvious correlation between fracture type or density (not illustrated on Figure 2) and the fluid conduits noted above suggests to us that many of the penetrated fractures were induced or enhanced during drilling and core recovery. Probable causes for this artificial fracturing include relief of overburden pressure (formation of hackly disk-like fractures) and core contraction accompanying cooling (enlargement of existing fractures; "pull-apart" of weakly cemented veins). There are, however, numerous, clearly natural, high-angle (typically >65°), slickensided fractures (principally in argillites) along the entire length of the core. The slickensides are commonly subhorizontal features, recording strike-slip to low-angle oblique-slip displacement.

Hydrothermal alteration of the core is typically minimal and confined to thin (less than a few mm) selvages on the Geysers hydrothermal veinlets described immediately below. However, scattered zones of intense alteration up to a meter or more in length occur locally (for example, around the major fluid conduit at 417.3 m). Sericitization, the principal alteration type, is characterized by replacement of susceptible original clastic components of the rock (especially albite and volcanic rock grains) by white to greenish-white illite (or phengite). The illite throughout the core generally contains <5% smectite interlayers, as determined by X-ray diffraction (XRD) analysis. Other alteration minerals occurring both

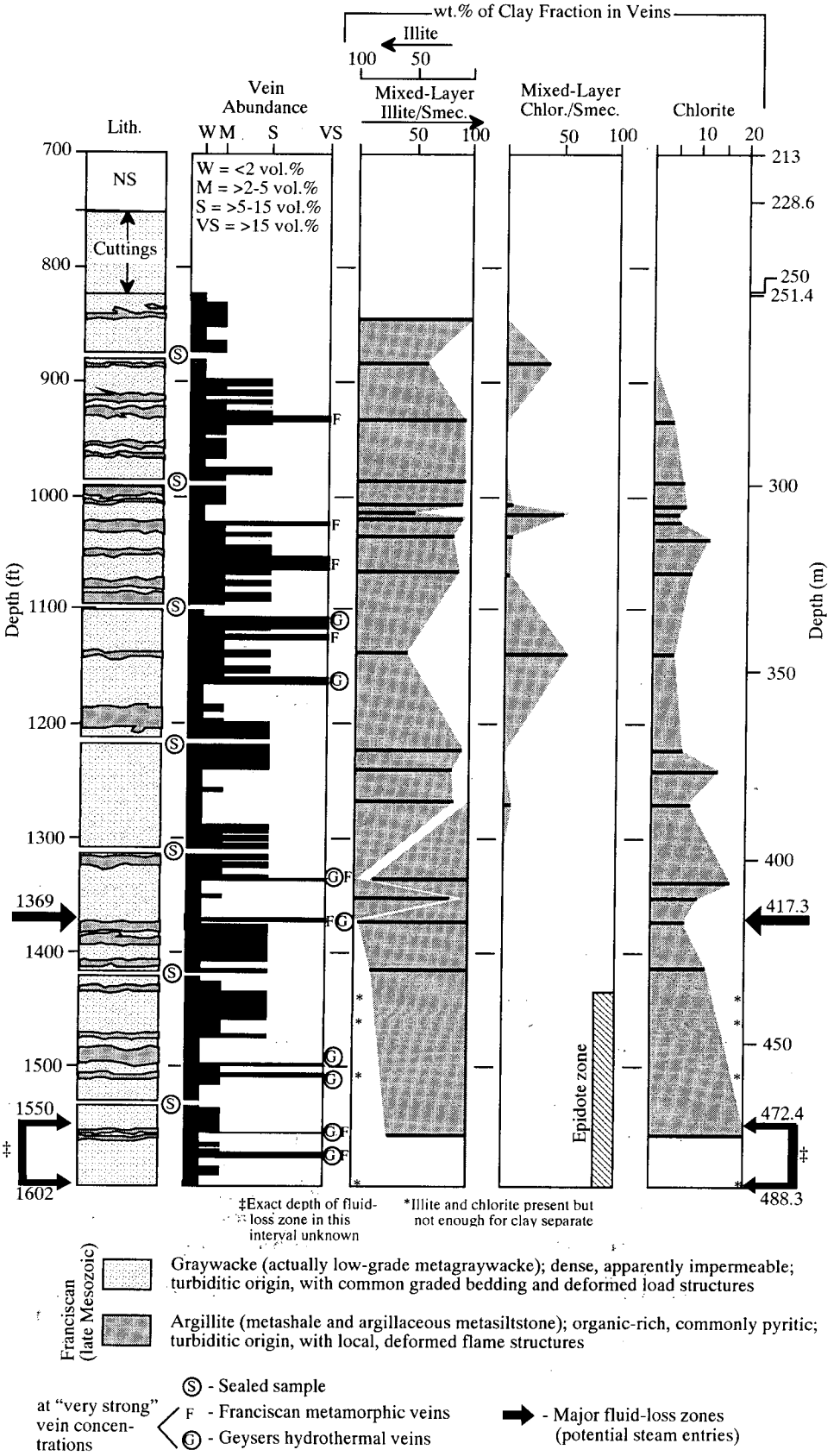

Figure 2. Corehole SB-15-D — Simplified log of lithology, vein distribution, and clay mineralogy of hydrothermal veins.

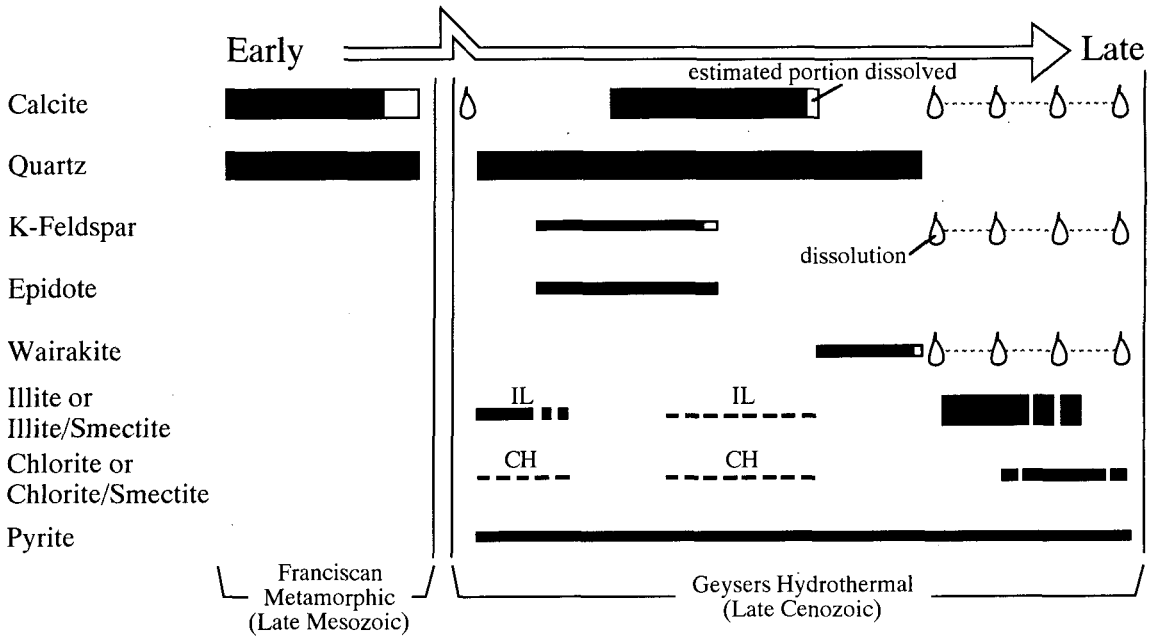

Figure 3. Corehole SB-15-D — Generalized vein–mineral paragenetic sequence. Bar widths denote relative abundances of minerals. IL = illite only. CH = chlorite only.

with the sericite and in separate selvages include K-feldspar, quartz, chlorite, and pyrite.

Metamorphic and hydrothermal veins are abundant in the SB-15-D core (Figs. 2 and 3). The metamorphic veins are Franciscan in age, randomly oriented, of variable shape, and consist exclusively of turbid white calcite and quartz. Hydrothermal veins, deposited during the hot-water-dominated stage of the Geysers geothermal system, are texturally distinctive from the Franciscan varieties. They tend to be high-angle (>65°), straight-sided, and uniform in width (typically 0.5-1.5 mm). Their fillings are also readily detachable from the veinlet walls, whereas the Franciscan veins are "frozen" to their wallrocks. The hydrothermal veinlets contain colorless to translucent white, euhedral prismatic quartz, bladed calcite, and (locally) K-feldspar, with minor pyrite, wairakite, illite, chlorite, mixed-layer clays, epidote (below a depth of 435.8 m), and scattered traces of sphalerite, galena, and chalcopyrite. The calcite is the bladed variety, indicating precipitation from a boiling hydrothermal solution (Tulloch, 1982).

Both types of veins in the GCP core are locally vuggy, especially in the vicinity of the upper major fluid conduit at 417.3 m. Here, the vugs are clearly an important element of porosity and permeability, but such cavities are present to a lesser extent even in the tight overlying strata. The vugs are of two origins. Some Franciscan veins contain amoeboid to irregular voids believed on textural evidence to represent hydrothermal dissolution of metamorphic calcite. These dissolution voids are commonly lined by the same assemblage of secondary minerals found in the younger veins. Larger vugs in these Geysers hydrothermal veins are intercrystalline, the result of incomplete filling of the initially available open space. Both types of vugs are generally <1 cm in diameter but a few (for example in the fluid-conduit zone at 417.3 m) reach diameters or lengths of up to 5 cm. In addition to these major vug types, there are also small-scale (<1-50 micron), surficial dissolution pits and scours locally present on hydrothermal calcite, K-feldspar, and wairakite crystals.

CLAY MINERALOGY OF HYDROTHERMAL VEINS

The vein-hosted clays in the SB-15-D core are principally late-stage minerals (Fig. 3), commonly precipitated on weakly etched wairakite, K-feldspar, and (especially) bladed calcite. Some illite and chlorite also occur both in early bands precipitated on vein walls and in multiple zones of solid inclusions in euhedral quartz crystals. The late-stage clay minerals show a distinct vertical zonation (Fig. 2). Illite occurs in veins below a depth of 406 m, and mixed-layer clays are found in those above 410 m, with minor amounts of chlorite nearly ubiquitous (Fig. 2). (We define discrete illite and chlorite for this study arbitrarily as having <5% expandable interlayers as determined by XRD). Clays are also much more abundant in veins at and above the major fluid-loss zone at 417.3 m than in those below this depth. The higher-level veins commonly contain up to 10% late-stage clay, whereas most of their deeper counterparts are essentially clay-free.

Mixed-layer illite/smectite (IL/SM) occurring in these veins (Figs. 3-5) is a brilliant white to greenish-white, pearlescent variety. As determined from XRD scans of

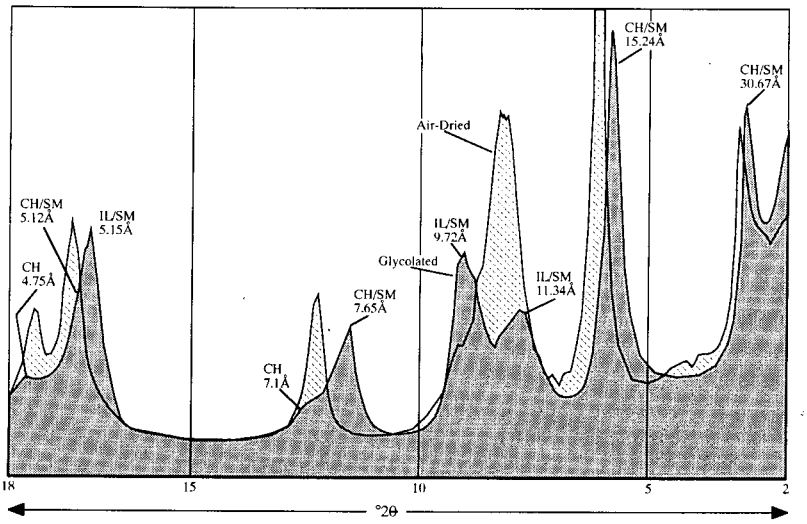

Figure 4. Corehole SB-15-D — X–ray diffractogram of clay (<5 micron) fraction extracted from hydrothermal vein at depth of 346.2 m. IL/SM = mixed-layer illite/smectite. CH/SM = mixed-layer chlorite/smectite. CH = chlorite.

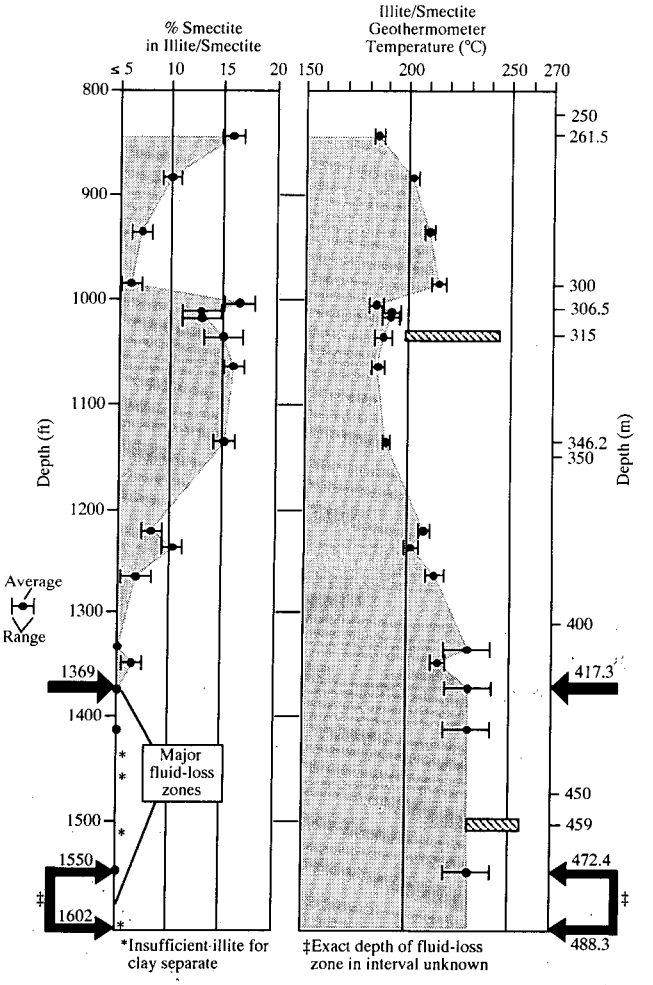

Figure 5. Corehole SB-15-D — Illite/smectite expandability and geothermometer temperatures for hydrothermal veins. Hachured horizontal bars denote ranges, in two selected hydrothermal veins, of primary and pseudosecondary fluid-inclusion homogenization temperatures for earlier-stage euhedral quartz (courtesy of Joseph Moore, pers. communication, 1995).

<5μ separates of the veins, using the methods of Środoń (1980), it is an R3-ordered variety containing 5-18% smectite interlayers (Fig. 5). There are two smectite-interlayer maxima, one at a depth of 261.5 m, the other at 306.5 m. Below each of these maxima, smectite percentage in general decreases with depth (Fig. 5). The upper major fluid conduit in SB-15-D occurs at about the point in the corehole where expandable interlayers in IL/SM diminish to <5% (Fig. 5).

The pale greenish-gray mixed-layer chlorite/smectite occurring with IL/SM in these veins (Figs. 3 and 4) is the variety corrensite, an R1-ordered clay with a distinct superlattice peak at about 30.7A. According to methods outlined in Moore and Reynolds (1989), the corrensite in the SB-15-D veins contains 40-45% smectite interlayers. At this stage of our investigation, we cannot explain the discrepancy in ordering and interlayer smectite content between the corrensite and coexisting IL/SM.

Vein-Mineral Illite/Smectite Geothermometry

The smectite-interlayer content of IL/SM (especially hydrothermal varieties) is a sensitive indicator of depositional temperature — in general, as this temperature rises, fewer smectite interlayers are formed, and those which do form attain a higher degree of ordering with illite interlayers (Steiner, 1968; Henley and Ellis, 1983; Browne, 1984; Hedenquist and Houghton, 1988; Moore and Reynolds, 1989; Pollastro, 1991). A widely used IL/SM geothermometer is the one calibrated for active New Zealand geothermal systems by C.P. Wood (personal communication reported in Hedenquist and Houghton, 1988). According to this geothermometer, an IL/SM precipitated at 187°C would have a smectite interlayer content of 15%, whereas one formed at 238°C would have no smectite interlayers (and by the definition given above would actually be an illite).

The smectite interlayer content of the SB-15-D IL/SM above a depth of 410 m varies from 5% to 18%, corresponding to a geothermometer temperature range of 180-218°C (Fig. 5). The illites below 406 m contain <5% expandable interlayers and indicate a depositional temperature range of 218-238°C. This reservoir paleotemperature range corresponds well with the reported pre-exploitation temperature of about 235°C for The Geysers steam reservoir as a whole (White et al., 1971), and with the estimated initial reservoir temperature (about 230°C) encountered in the upper reaches of production well SB-15 (Brian Koenig, pers. communication, 1994). It is interesting to note, however, that both the modern and clay-mineral geothermometer temperatures are slightly lower than those indicated by preliminary fluid-inclusion microthermometry of pre-clay hydrothermal quartz in veins at depths of 315 m and 459 m (Fig. 5; Joseph Moore, pers. communication, 1995). This relationship suggests that the clays were precipitated after The Geysers hydrothermal system at these depths had cooled slightly from its thermal maximum.

DISCUSSION AND CONCLUSIONS

The nature and distribution of late-stage clay minerals in hydrothermal veins in the SB-15-D core, when considered along with (1) the downhole locations of major fluid conduits (potential steam entries) and (2) the depth range of vein epidote, now suggest to us that the corehole penetrates the transition zone between the uppermost Geysers steam reservoir and its largely impermeable caprock. Below the upper fluid conduit at 417.3 m (Figs. 2 and 5), epidote is present, vein-hosted clay minerals are minor constituents, and mixed-layering in these clay minerals is minimal. By contrast, in veins above the 417.3 m fluid channel, epidote is absent, clay minerals are common, and mixed-layering is prevalent. In support of this caprock-reservoir zoning model is the subtle apparent textural difference between less competent argillites at upper levels in the corehole and brittler, more competent argillites at deeper levels.

The vein- (and vug-) hosted mixed-layer clays are the most distinguishing features of what we have interpreted as the caprock in SB-15-D. The reservoir and caprock lithologies (apart from the slightly different argillite textures) are very similar, and they are cut by similar types and abundances of fractures and veinlets. Carbonate-dissolution and intercrystalline vugs in the veins are locally present throughout the core, although the largest and most interconnected of these vugs are certainly found at the 417.3 m fluid conduit (Hulen et al., 1995).

Gunderson (1992) and Williamson (1992) have presented evidence that much of the matrix rock at The Geysers is only weakly porous and permeable, with fractures, breccias, and open veins in this matrix providing the reservoir's major steam-bearing conduits. The corollary to this suggestion is that a zone of such rock without these conduits, or with the conduits sealed at strategic sites, would be an effective hydrologic barrier — a caprock if positioned above the reservoir. We contend that the SB-15-D mixed-layer clays would function as effective vein seals, particularly the corrensite, with up to 45% smectite interlayers. Clots of these expandable clays, if kept moistened (most likely by steam condensate) would choke off otherwise open channels. Furthermore, unlike brittle vein minerals (for example calcite), the clays would tend to absorb tectonic stresses plastically rather than breaking to create new porosity.

It must be noted that steam entries were encountered in the original production well, SB-15, at depths as shallow as 330.7 m (Hulen et al., 1995), well within the zone in SB-15-D we have characterized as caprock. One possible explanation for this discrepancy is that the controlling conduits for these original steam entries are steeply-inclined, and either miss SB-15-D entirely or intersect the corehole below 417.3 m. This would imply that the caprock-reservoir interface is complex and irregular, with salients of each zone locally projecting deeply into the other.

The physical/chemical conditions prevailing during precipitation of these vein-hosted mixed-layer clays and illite remain to be fully understood. White et al. (1971) speculated that pore-clogging smectite and kaolin above the steam reservoir could form by reaction of (acidic) CO_2-saturated steam condensate with rock- (and by extension, vein-) forming silicates. Although these lower-temperature minerals (e.g. Browne, 1984) might be expected to develop at higher elevations than those tested by SB-15-D, the same mechanisms at deeper levels and higher temperatures might readily form the smectite-interlayered clays and illite encountered by the corehole.

The layer silicates in the SB-15-D veins commonly occur on slightly corroded calcite blades as well as etched K-feldpar and wairakite (Hulen et al., 1995). This relationship supports the concept of clay precipitation from a late-stage acidic condensate. Since (1) inferred modern temperatures and vein IL/SM geothermometer temperatures are comparable for the SB-15-D steam-reservoir interval (417.3-488.3 m); and (2) fluid-inclusion temperatures for pre-IL/SM quartz in selected reservoir and caprock veins are up to 26-53°C higher than the IL/SM temperatures (Fig. 5), we suggest that the clay-precipitating condensate developed under similar-to-modern vapor-dominated conditions rather than in the precursor hot-water-dominated hydrothermal system.

ACKNOWLEDGEMENTS

Funding for the drilling phase of the GCP was provided jointly by DOE (Geothermal Division; GD) and Unocal Corporation. Our baseline geologic studies of the core are sponsored by DOE-GD under contract DE/AC07/90ID12929. Said support does not necessarily constitute a DOE endorsement of the views expressed in this paper. We are grateful to our colleagues at Unocal Corporation (particularly Brian Koenig) for their essential role in making the GCP a reality. Discussions with Joe Moore were helpful for understanding this shallow caprock/reservoir transition zone in the context of his comprehensive model for evolution of The Geysers hydrothermal system. Louise Spann prepared clay separates and completed corresponding XRD scans. Graphic artist Bob Turner produced the illustrations.

REFERENCES

Beall, J.J., and Box, W.T., 1992, The nature of steam-bearing fractures in the south Geysers reservoir *in* Monograph on The Geysers geothermal field (C. Stone, ed.): Geothermal Resources Council, Special Report 17, p. 69-77.

Bonner, B.P., Roberts, J.J., Schneberk, D., Marsh, A., and Ruddel, C., 1995, X-ray tomography of preserved core from The Geysers scientific corehole: Stanford, California, Stanford University, 20th Annual Workshop on Geothermal Reservoir Engineering, preprint, 8 p.

Browne, P., 1984, Lectures on geothermal geology and petrology: Reykjavik, Iceland, United Nations University, Geothermal Training Program, Course Notes, 92 p.

Dalrymple, G.B., 1992, Preliminary report on $^{40}Ar/^{39}Ar$ incremental heating experiments on feldspar samples from the felsite unit, Geysers geothermal field, California: U.S. Geological Survey, Open-File Report 92-407, 15 p.

Gunderson, R.P., 1992, Porosity of reservoir graywacke at The Geysers *in* Monograph on The Geysers geothermal field (C. Stone, ed.): Geothermal Resources Council, Special Report 17, p. 89-96.

Gunderson, R.P., and Moore, J.N., 1994, Oxygen isotope geochemistry of The Geysers reservoir rocks, California: Stanford, California, Stanford University, 19th Annual Workshop on Geothermal Reservoir Engineering, preprint, 8 p.

Hedenquist, J.W., and Houghton, B.F., 1988, Epithermal gold mineralization and its volcanic environments: Kelian, Kelimantan, Short Course Notes, 416 p.

Henley, R.W., and Ellis, A.J., 1983, Geothermal systems, ancient and modern: Earth Science Reviews, v. 19, p. 1-50.

Hulen, J.B., and Nielson, D.L., 1993, Interim report on geology of The Geysers felsite: Geothermal Resources Council, Transactions, v. 17, p. 249-258.

Hulen, J.B., Walters, M.A., and Nielson, D.L., 1991, Comparison of reservoir and caprock core from the northwest Geysers steam field, California — Implications for development of reservoir porosity: Geothermal Resources Council, Transactions, v. 15, p. 11-17.

Hulen, J.B., Nielson, D.L., and Martin, W., 1992, Early calcite dissolution as a major control on porosity development in The Geysers steam field, California — Additional evidence in core from Unocal well NEGU-17: Geothermal Resources Council, Transactions, v. 16, p. 167-174.

Hulen, J.B., Koenig, B.A., and Nielson, D.L., 1994, The Geysers coring project — A cooperative investigation of reservoir controls in a vapor-dominated geothermal system: Geothermal Resources Council, Transactions, v. 18, p. 317-323.

Hulen, J.B., Koenig, B.A., and Nielson, D.L., 1995, The Geysers coring project, Sonoma County, California, USA — Summary and initial results: Florence, Italy, World Geothermal Congress, Transactions, 6 p. (in press).

McLaughlin, R.J., 1978, Preliminary geologic map and structural sections of the central Mayacmas Mountains and The Geysers steam field, Sonoma, Lake, and Mendocino Counties, California: U.S. Geological Survey, Open-File Map 78-389, scale 1:24,000.

McLaughlin, R.J., 1981, Tectonic setting of pre-Tertiary rocks and its relation to geothermal resources in the Geysers-Clear Lake area, California: U.S. Geological Survey, Professional Paper 1141, p. 3-23.

McLaughlin, R.J., Moore, D.E., Sorg, D.H., and McKee, E.H., 1983, Multiple episodes of hydrothermal circulation, thermal metamorphism, and magma injection beneath The Geysers steam field, California: Geological Society of America, Abstracts with Programs, v. 15, p. 417.

Pollastro, R.M., 1991, The illite/smectite geothermometer — Concepts, methodology, and application to basin history and hydrocarbon generation *in* Applications of thermal maturity studies to energy exploration (V.F. Nuccio, C.E. Barker, and S.J. Dyson, eds.): Society of Economic Paleontologists and Mineralogists, Rocky Mountain Section, p. 1-18.

Moore, J.N., 1992, Thermal and chemical evolution of The Geysers geothermal system, California: Stanford, California, Stanford University, 17th Workshop on Geothermal Reservoir Engineering, p. 121-126.

Moore, D.M., and Reynolds, C.R., Jr., 1989, X-ray diffraction and the identification and analysis of clay minerals: New York City, Oxford University Press, 332 p.

Oppenheimer, D.H., 1986, Extensional tectonics at The Geysers geothermal system, California: Journal of Geophysical Research, v. 91, p. 7475-7484.

Schriener, A., Jr., and Suemnicht, G.A., 1981, Subsurface intrusive rocks at The Geysers geothermal area, California *in* Proceedings of the symposium on mineral deposits of the Pacific Northwest (M.L. Silberman, C.W. Field, and A.L. Berry, eds.): U.S. Geological Survey, Open- File Report 81-355, p. 295-302.

Środoń, J., 1980, Precise identification of illite/smectite interstratifications by X-ray powder diffraction: Clays and clay minerals, v. 28, p. 401-411.

Steiner, A., 1968, Clay minerals in hydrothermally altered rocks at Wairakei, New Zealand: Clays and clay minerals, v. 16, p. 193-213.

Sternfeld, J.N., 1981, The hydrothermal petrology and stable-isotope geochemistry of two wells in The Geysers geothermal field, Sonoma County, California: Riverside, California, University of California at Riverside, M.S. Thesis (also Report UCR/IGPP 81-27), 202 p.

Sternfeld, J.N., 1989, Lithologic influences on fracture permeability and the distribution of steam in the northwest Geysers steam field, Sonoma County, California: Geothermal Resources Council, Transactions, v. 13, p. 473-479.

Thompson, R.C., 1992, Structural stratigraphy and intrusive rocks at The Geysers geothermal field *in* Monograph on The Geysers geothermal field (C. Stone, ed.): Geothermal Resources Council, Special Report 17, p. 59-64.

Thompson, R.C., and Gunderson, R.P., 1992, The orientation of steam-bearing fractures at The Geysers geothermal field *in* Monograph on The Geysers geothermal field (C. Stone, ed.): Geothermal Resources Council, Special Report 17, p. 65-68.

Tulloch, A.J., 1982, Mineralogical observations on carbonate scaling in geothermal wells at Kawerau and Broadlands: Pacific Geothermal Conference, Proceedings, v. 1, p. 131-134.

Unocal Corporation, Geysers Geothermal Company, NCPA, GEO Operator Corporation, Santa Fe Geothermal, and Department of Water Resources, 1992, Geysers (geothermal field) top-of-reservoir and top-of-felsite maps *in* Monograph on The Geysers geothermal field (C. Stone, ed.): Geothermal Resources Council, Special Report 17, scale 1:98,182.

Walters, M.A., Sternfeld, J.N., Haizlip, J.R., Drenick, A.F., and Combs, J., 1992, A vapor-dominated, high-temperature reservoir at The Geysers, California *in* Monograph on The Geysers geothermal field (C. Stone, ed.): Geothermal Resources Council, Special Report 17, p. 43-53.

White, D.E., Muffler, L.J.P., and Truesdell, A.H., 1971, Vapor-dominated geothermal systems compared with hot-water systems: Economic Geology, v. 66, p. 75-97.

Williamson, K.H., 1992, Development of a reservoir model for The Geysers geothermal field *in* Monograph on The Geysers geothermal field (C.Stone, ed.): Geothermal Resources Council, Special Report 17, p. 179-188.

PROCEEDINGS, Twentieth Workshop on Geothermal Reservoir Engineering
Stanford University, Stanford, California, January 24-26 1995
SGP-TR-150

X-RAY TOMOGRAPHY OF PRESERVED SAMPLES FROM THE GEYSERS SCIENTIFIC COREHOLE

B. P. Bonner,(1) J. J. Roberts,(1) D. J. Schneberk,(2) A. Marsh,(1) C. Ruddle,(1) and E. Updike(2)

(1)Earth Science Division, (2)Nondestructive Evaluation Section
Lawrence Livermore National Laboratory
Livermore, CA, 94550

ABSTRACT

Approximately 800 ft. of continuous core was recovered from borehole SB-15 D (on unit 15, near the site of the abandoned Geysers Resort) during a recently completed drilling operation funded by the USDOE. Sections of this core were collected at 50 ft intervals for subsequent examination as drilling proceeded. Five foot sections were not removed at the drill site, but were sealed in the innermost sleeve of a triple tube coring system to minimize drying and disturbance of the core.

All cores remained sealed and were radiographed within 72 hours of drilling: the five foot core from near 1400 ft. was scanned within 18 hours of drilling. A third generation x-ray scanner, which uses high energy radiation to penetrate the aluminum sleeve and 3.5 inch cores, was used to make preliminary radiographs and to collect multiple views of the sample as the core is rotated in front of the beam. True three dimensional tomographs are then reconstructed from the data. At present, the images have a spatial resolution of approximately 140 micrometers and can resolve contrast differences of 0.2%. The tomographs clearly show differences in lithology with depth in the reservoir. Partially filled fractures, vein selvage and vuggy porosity are all evident in parts of the core.

A principle goal of the imaging effort is to help determine the fluid content of the reservoir. Important questions to investigate include water loss during core recovery, infiltration of drilling fluid, and the heterogeneous distribution of pore fluid. Images show that radial gradients in x-ray attenuation commonly occur in jacketed cores. Regions of excess attenuation extend about halfway into the 3.5 in. core, and are probably caused by mud invasion induced by capillarity of the small scale porosity of the graywacke matrix. X-ray measurements will be coordinated with other independent measurements of fluid content underway in separate studies, particularly NMR spectroscopy of frozen 'pressure core,' and compressional velocity and electrical resistivity measurements.

INTRODUCTION

The successful completion of The Geysers scientific corehole at the site of SB-15 (near the abandoned Geysers resort) provides an unprecedented opportunity to study rocks from the upper regions of The Geysers steam reservoir. High quality core was recovered starting near 800 ft extending to ~1600 ft depth from a sidetrack starting from the former production well, SB-15. The rock was characterized at the drill site by Hulen and Nielson as "highly fractured, heavily veined, but weakly altered Franciscan graywacke with minor argillite." The graywacke's origin appears to be turbiditic as indicated by the graded beds, load structures and the interbedded argillite, a dark organic-rich shale which exhibits flame structures into the graywacke. Details of the drilling operation and a first analysis of the rocks encountered are given by Hulen et al., 1994. Sections of this core were collected at 50 ft intervals for subsequent examination at Lawrence Livermore National, Laboratory. At alternating intervals, either 1.5 ft of core was selected and sealed, or a 5 ft section was preserved. The five foot sections were not removed from the core tubes, but were sealed at the drill site with caps fitted with 'o' rings to minimize drying and disturbance of the core.

The jacketed cores are examined with a third generation x-ray scanner, which uses high energy radiation to penetrate the aluminum sleeve and three inch cores. Two types of data are collected: digital radiographs and tomographs. Radiographs are made by collecting two dimensional projections of x-ray transmission through the sample on high resolution film. Tomographs are produced by collecting multiple views of the sample as the core is rotated in front of the beam, and then reconstructing true three dimensional images using computational techniques. Both types of images are useful for locating highly fractured regions, for detecting structural features such as filled veins and folds and for detecting changes in lithology. Improved estimates of the amount of stored water at The Geysers are also of interest because these data are critical for predicting the performance and lifetime of the reservoir. Water

content can in principle be determined by weighing recovered core as it dries under controlled conditions. However, water content estimates can be biased either by invasion of drilling mud or by fluid loss as the core cools and depressurizes on its way to the surface. High resolution x-ray methods have potential for evaluating the importance of these artifacts. Scoping tests of tomographic methods for small, unjacketed cores of graywacke from deep in the reservoir in the northeast Geysers (Bonner, Roberts and Schneberk, 1994) determined that pore fluid could be detected. However, changes in x-ray attenuation caused by saturation were comparable to fluctuations resulting from grain scale heterogeneity. Measured porosities for that graywacke, cored at ~8400 ft in NEGU-17, are ~1%, near the low end reported for the Geysers reservoir (Gunderson, 1990). Porosity is not yet known for the relatively shallow SB-15 rocks, but may well be higher than for the NEGU-17 samples. Therefore, changes in x-ray attenuation associated with pore fluids should be easier to detect than for the NEGU-17 core.

EXERIMENTAL APPARATUS AND METHODS

The x-ray imaging system used here has several advantages as compared to systems typically used for studies of rocks, which are usually adaptations of medical systems. These include higher energy x-rays, better spatial and contrast resolution, and specialized reconstruction software. Both film radiography and CT were performed with a PHILLIPS 450 kVp source. Radiographs were taken with single m film with a source to film distance of 53 in. at an energy of 125 kVp. Imaging was performed with the PCAT scanner which uses a cone shaped beam of x-radiation to illuminate the object and a two dimensional detector to collect the transmitted radiation. This system includes a variable integration rate CCD camera, lens-coupled to a piece of scintillator glass. A 1024 by 1024 CCD chip with a dynamic range of 14 bits detects the output of the glass. A rotational stage spins the sample to obtain third generation (rotation-only) scans - a 2D radiograph is acquired at each rotational angle, and reconstructed directly into a 3D volume. To minimize the impact of source unsharpness the magnification was kept at 1.04 with a source to detector distance of 134 cm. This configuration results in a cone angle of 2.2 degrees requiring the use of the Feldkamp code for image reconstruction. The 10.16 cm field of view was employed for each of the scans which results in a pixel size of 97 micrometers and an effective spatial resolution of approximately 140 micrometers (as measured by the ASTM Full Width Half Maximum technique). Contrast sensitivity of this scanner was measured at 0.2% with aluminum penetrameters. The most extensive scans, which inspected 4 in. sections of core took 8 hrs to complete. All radiographic data were processed and reconstructed with software developed at LLNL. Additional discussion is given by Bonner, Roberts and Schneberk, 1994.

RESULTS AND DISCUSSION

Test of Core Sealing Method–A primary goal of the scientific coring project was to retrieve material with the in-situ water content as well preserved as possible (Hulen and Nielson, 1994). A triple tube coring system was used for the LLNL samples to maximize the possibility of recovering representative core from depth. Separate attempts to 'pressure core' while the hole was sealed and pressurized from the surface, which minimized the loss of steam during retrieval, were also made by Withjack and colleagues. The triple tube coring system had not previously been used in a geothermal field. Therefore, a test was devised to verify that the tube had been successfully sealed. Since the laboratory air in which the core was stored ranges in relative humidity from 20 to 30%, values lower than 100% inside the core tube would indicate that the atmosphere had exchanged with the ambient atmosphere subsequent to capping the tube at the drill site. First, a plastic tube was glued to the end cap of the core and a hole was drilled inside the tube through the end cap. A humidity sensor, which very nearly fills the plastic tube, was then inserted to sample the internal atmosphere for one week. The humidity increased rapidly at first and then steadily increased until it reached 100% after several days. Although only a single 1.5 ft core from 918.9 ft has been tested to date, and loss of fluid while the core barrel is on the wireline must be considered, the methods for sealing the tubes on site appear to be reliable.

Radiographs–Radiographs are taken as soon as possible of all received core to make a preliminary judgment of core quality and locate regions of interest for further study. Radiographs are x-ray shadowgraphs of an object, with denser regions producing less exposure on the film or detector collecting the image. Exposures of the entire core can be obtained rapidly, usually within a few minutes. Two examples of radiographs taken of 5 ft core from coring run 7, 875 ft and run 68, 1415 ft, are shown as Figure 1 a, b. Brighter regions absorb more of the illuminating radiation; numerals seen on the radiograph are lead markers placed outside the core tube before the exposure to locate points on the image as the source is moved relative to the core. These images have been filtered to enhance edges by locally increasing the contrast. The shallower core is less competent and more highly fractured than the core from 1415 ft. Linear features approximately normal to the core axis, such as those just above the 3 and midway between 6 and 5 in Figure 1a and near 3 in Figure 1b, are very likely drilling induced discing

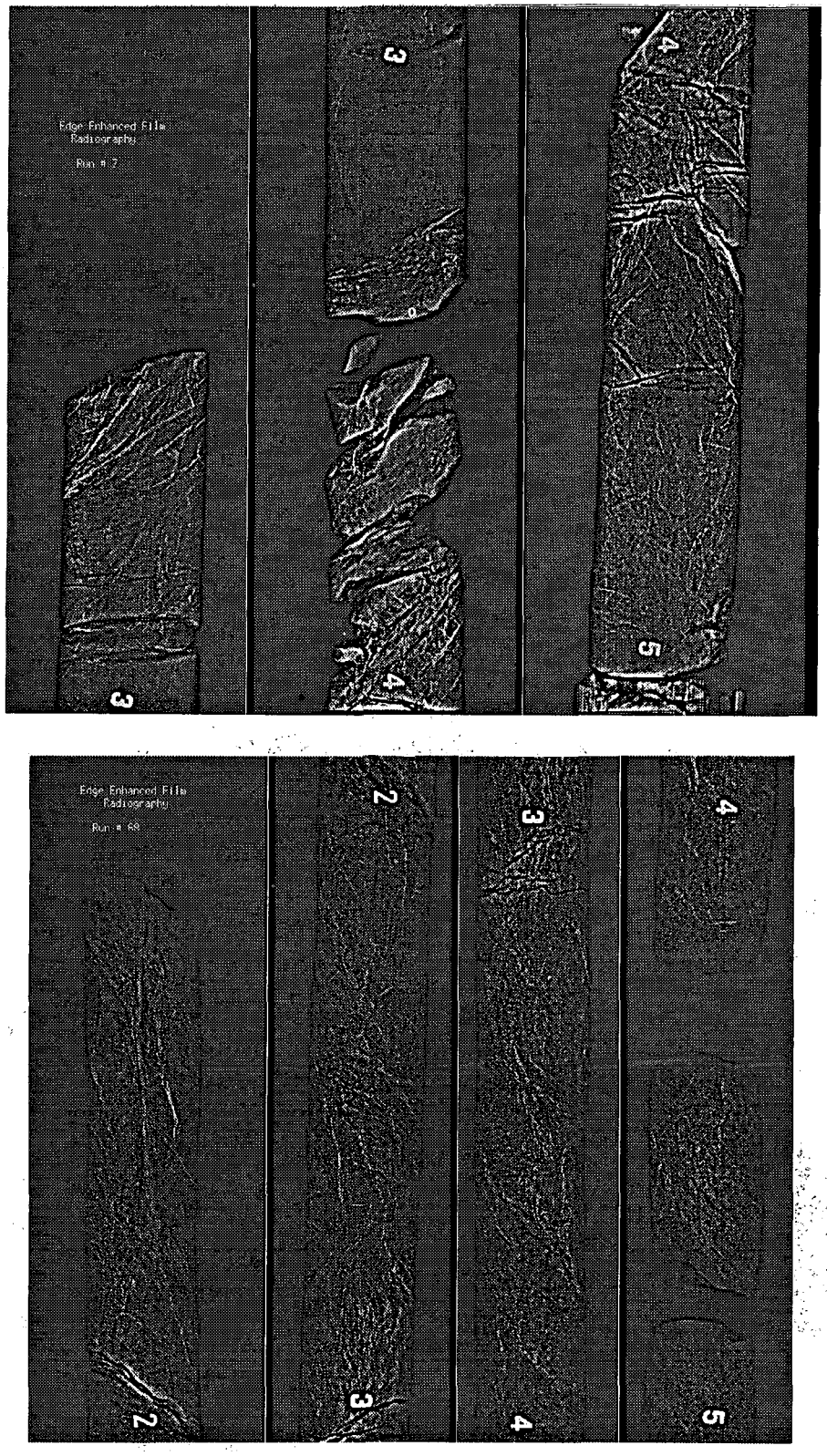

Fig. 1. Radiographs of five ft core lengths within sealed aluminum coring tubes. Core is ~3.4 inches in diameter. Images have been filtered to enhance edges. Brighter regions indicate higher x-ray attenuation, darker areas less x-ray attenuation. Numerals are lead markers placed on the outside of the cores for reference. a) Run 7, 875 ft depth. b) Run 68, 1415 ft depth.

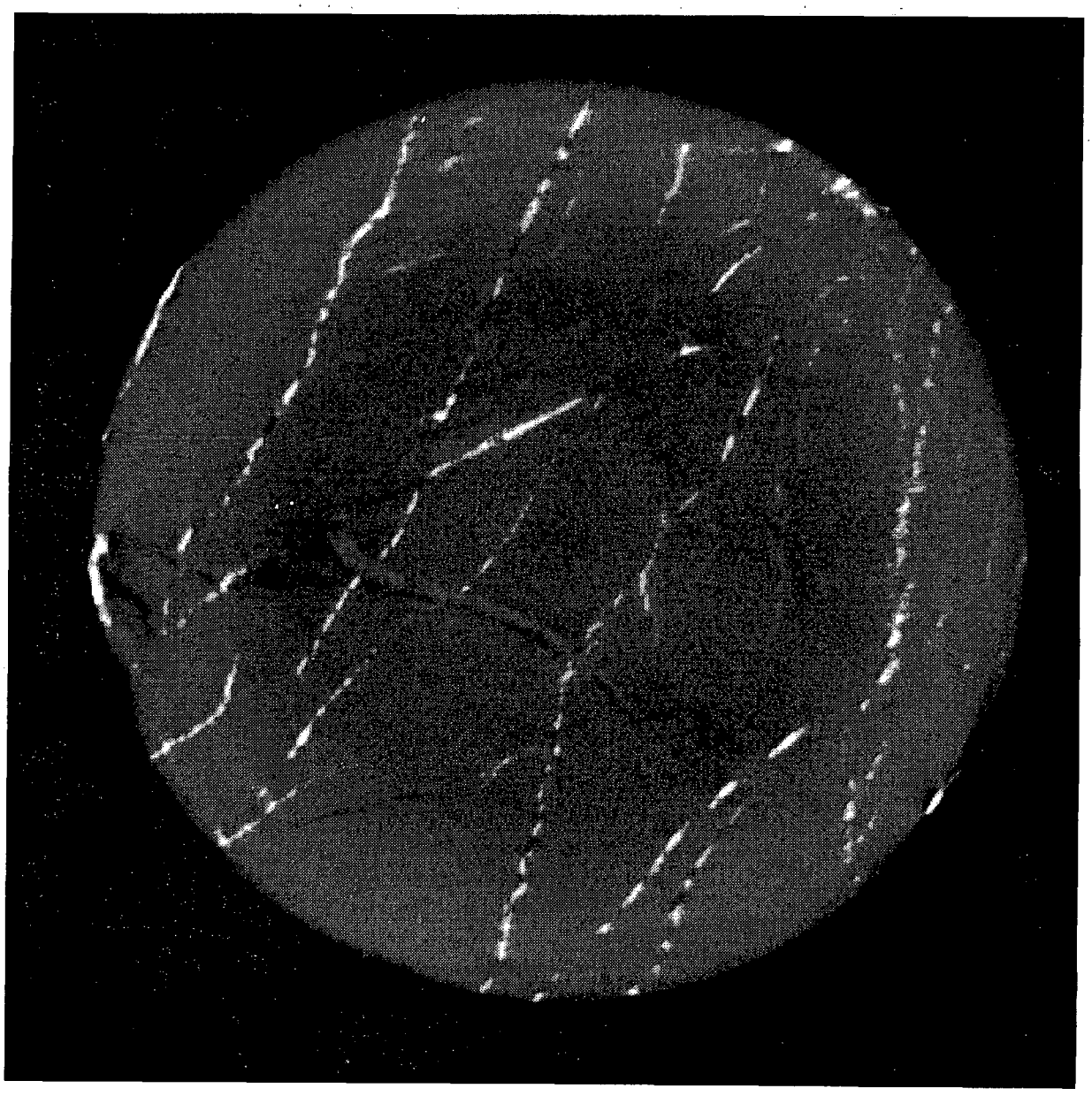

Fig. 2. X-ray tomograph of run 7, 875 ft depth. This is a radial cross section taken between locations 4 and 5 (Fig. 1a). Pixel size is 97 μm, core is ~3.4 in. in diameter. The outer ring is the aluminum tube. Partially filled veins are readily visible.

fractures. These images were produced by digitizing the film negative with an imaging system limited to eight bits of dynamic range in brightness, considerably less than the original. Drop outs in the core section may not necessarily be real, and are primarily an artifact of the imaging method.

Tomographs–An example of a high resolution tomograph is given in Figure 2. This is a radial cross section of the 875 ft core shown in the radiograph of Figure 1a, scanned between locations 4 and 5 and high pass filtered to enhance contrast. Brighter areas indicate higher x-ray attenuation. The narrow ring surrounding the core is the aluminum core tube. Bright linear sub- parallel features are partially mineralized veins which appear to be discontinuous at high resolution. Conspicuous gaps in the mineralization are characteristic at this depth, and seem to indicate vuggy porosity. Another feature, roughly perpendicular to the filled veins, appears to be a fracture crossing the core at a high angle.

Four radial sections are shown as Figure 3 to illustrate the range of structural features that can be resolved in the tomographs and to show the effect of depth in the reservoir. Figure 3b is of a relatively shallow core, taken at 918 ft. The missing material in the upper left may be associated with a large mineralized vein and will be examined in detail. A ring like region of higher attenuation extending inward from the outer boundary in all cores differs in detail in each case but is a common feature at all depths.

It appears that the gradient in x-ray attenuation can be related to invasion of the core by drilling mud. An enlargement of the radial tomograph taken of core from run 68, depth 1420 ft, Figure 4a, shows an invasion front similar to that seen to varying degree in the radial tomographs made at all depths. A region of excess attenuation beginning at the outer radius extends into the interior. The invasion front is not completely axisymmetric, but changes character in the northeast quadrant. This section of the core contains a contact between heterogeneous, coarser grained rock and fine grained material, possibly argillite. The mud invasion is less extensive in this area. It should be noted that beam hardening artifacts, which occur in tomographic reconstructions as a result of preferential radiation at lower energies, appear as radially symmetric rings starting at the outer edge of a sample. The asymmetry of the 'c like' feature coupled with the observation that the heterogeneous and fine grained sections have similar average density, e.g., x-ray attenuation, suggests that the beam hardening correction applied to all data is adequate.

The second part of the Figure, 4b, plots relative attenuation along the lines crossing Figure 4a. The first profile, labeled as s1, crosses the annular ring of high attenuation at both ends of the traverse. The second profile, s2, crosses the argillite and shows that attenuation is lower at this end of the traverse, consistent with less mud invasion in the region.

Radiographs of the deepest 5 ft core recovered for x-ray inspection, run 81, reveal a vuggy section near 1531 ft. The radial tomograph, Figure 5a, shows a slice through this structure, a complicated partially mineralized vein. Note also the fresh fracture near the bottom of the slice. Vertical slices through the central region of the core were examined to investigate the three dimensional character of the vuggy region. The vertical slices are ~0.7 in high, extending upward into the core from the radial slice. The slices are taken across the core progressing from the top to bottom of the radial section according to the index numbers shown next to the mineralized region. The slices show that this feature is not planar, but extends upward and to the left as a system of loosely connected stringers.

CONCLUSION

Images of sealed cores clearly resolve major structural features, changes in lithology, vuggy porosity, and other features with sufficient detail to draw conclusions about processes which have occurred in the reservoir. For example, cores from 820 ft contain intermittent veins suggesting that fluids undersaturated in the vein filling minerals have circulated through this region, dissolving material and leaving vuggy porosity. Tomography has sufficient spatial and contrast resolution to detect the prominent features of the lost circulation zone encountered in SB-15 D at 1396 ft. Features such as interconnected vugs in the metamorphic Franciscan vein, and large bladed calcite crystals, as described by Hulen et al., 1994, can probably be detected. None of the 5 ft cores sealed for x-ray inspection are close enough to the lost circulation zone at 1396 ft to sample it, but detailed inspections of the core from 1308 ft will be made to search for related features.

With further refinements, it may be possible to make quantitative measurements of mineralogy, porosity and water content and distribution. Preliminary measurements indicate that quantitative measurements of water content are possible if cores can be scanned as drying proceeds, but this depends on our ability to relocate points in the core in successive scans. It is also necessary to calibrate the effect of pore fluid on x-ray attenuation against measurements on fully saturated material, or independent measurements such as NMR, which is directly sensitive to hydrogen content. Another possibility for future work is to

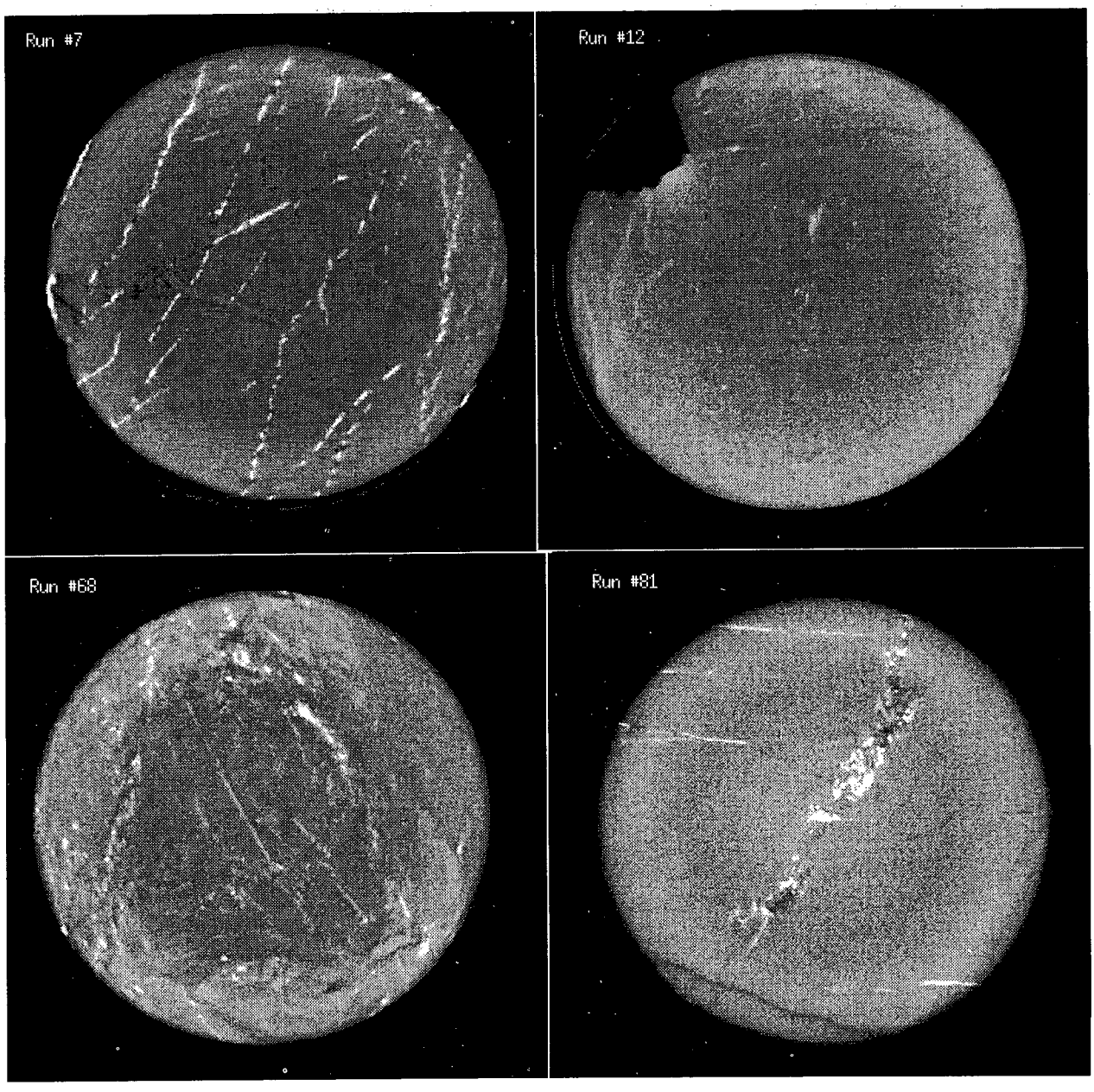

Fig. 3. Four radial tomographs taken at different depths to illustrate variability in texture, fracturing, and degree of mineralization. Core diameters are ~3.4 in. a) Run 7, 875 ft depth; b) run 12, 918 ft depth; c) run 68, 1420 ft depth; d) run 81, 1531 ft depth.

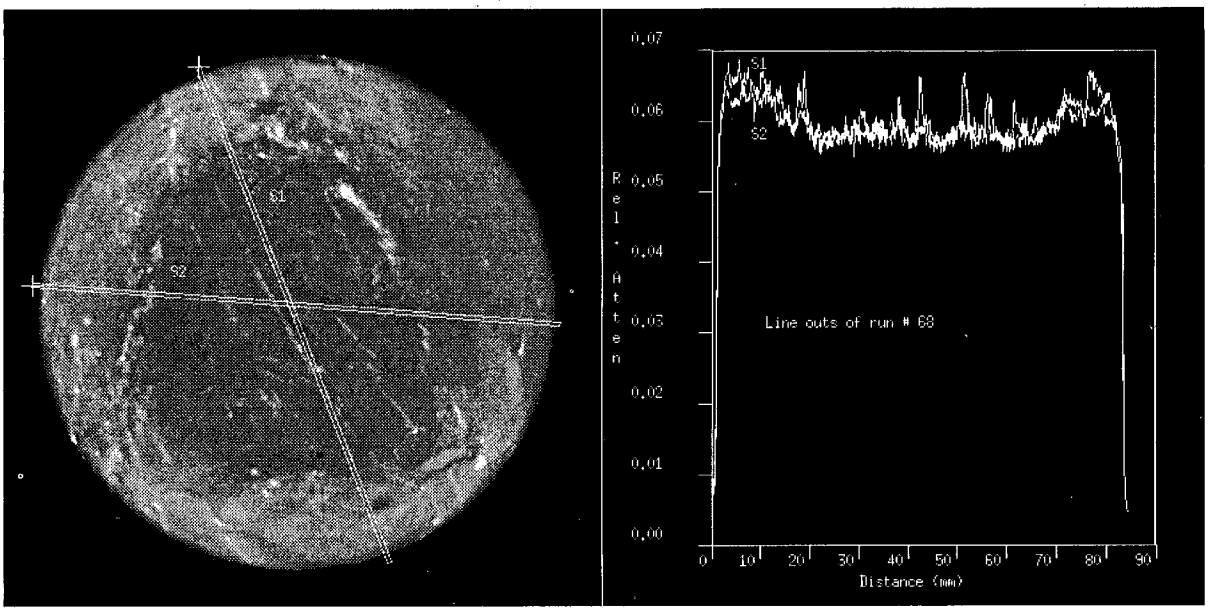

Fig. 4. a) Radial tomograph of run 68, 1420 ft depth, with enhanced contrast. Core is ~3.4 in. in diameter. Note the brighter (more highly attenuating) region around the perimeter of the sample. This is interpreted as evidence for mud infiltration during the drilling process. All the radial tomographs display this feature to some degree. In this sample the more highly attenuating region is not continuous, but is less pronounced in the northeast corner. The lines crossing the figure are plotted in b as relative attenuation versus distance. Both lines show higher attenuation near the edges of the core, however, S2 is less attenuating than S1 on the right hand edge, the area of decreased infiltration.

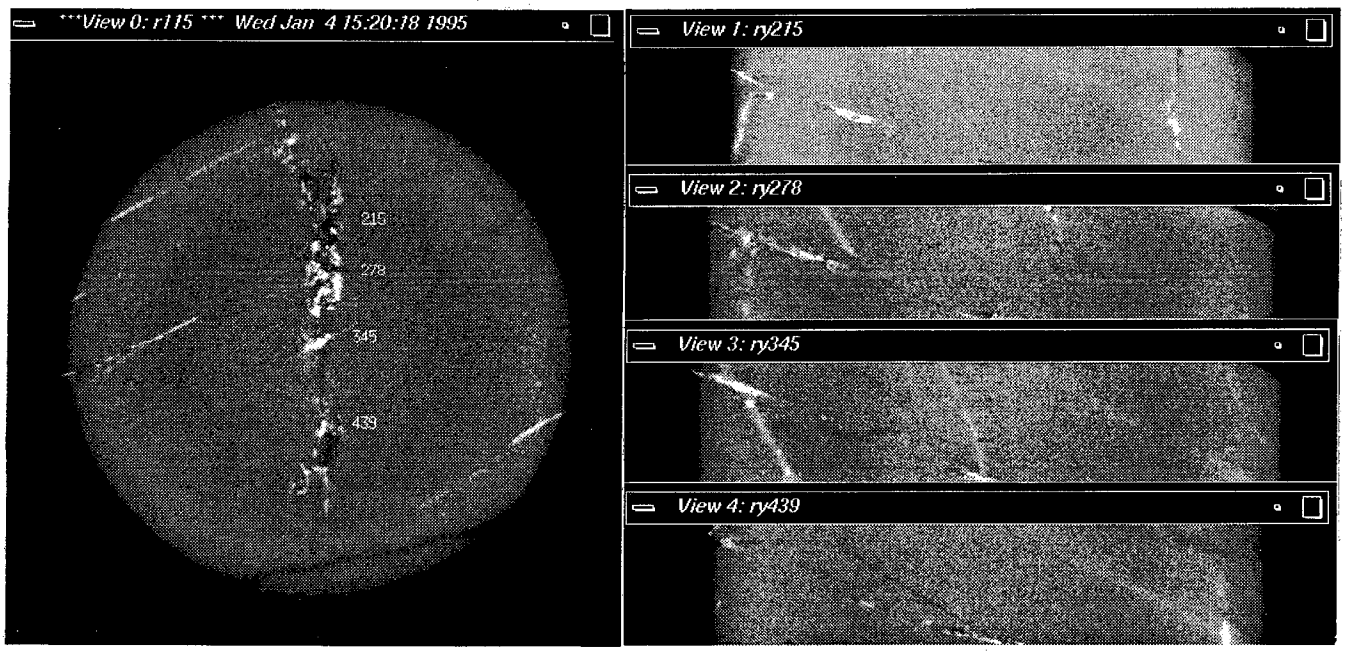

Fig. 5. Tomographs of run 81, 1531 ft depth, the deepest core examined using x-ray methods. a) Radial tomograph showing a partially mineralized vein, open fracture, and parallel filled fractures. Core diameter is ~3.4 in. The numerals indicate approximate locations where vertical tomographs have been reconstructed (b). Vertical slices are ~0.7 in. high.

extract estimates of fluid diffusivity at reservoir conditions by searching for variations of mud invasion along the core. Sections at the top or beginning of a coring run are exposed to the drilling fluid for a longer time allowing for greater penetration. Alternatively, mud invasion may be useful for correlating changes of fluid diffusivity with depth or lithology. Chemical analysis of the mud and the outer sections of the core will be performed to determine if the attenuation contrast apparently caused by mud infiltration was enhanced by contamination by materials with high atomic number, that increase x-ray attenuation relative to pure water. It is also worth noting that areas near the core edges consistently show higher attenuation, opposite from the effect expected if fluid is lost during core recovery. However, it is possible that changes caused by fluid loss might be masked by mud infiltration. Time lapse tomography will prove useful for determining drying rates of recovered core, and the influence of fractures on imbibition and drying.

Studies of recovered core are indispensable for understanding The Geysers reservoir, but are inherently limited to sampling a small fraction of the reservoir volume. A principle long term goal of this x-ray scanning program is to provide basic data for determining water content in-situ. Geophysical properties, such as seismic velocity and electrical conductivity, depend on water saturation. If the relationships between these quantities and water content can be calibrated reliably, borehole and field scale measurements of seismic and electrical properties could provide measures of water saturation in-situ at scales ranging to several kilometers.

ACKNOWLEDGMENTS

Prompt examination of this core would not have been possible without the extraordinary efforts of J. Hulen, D. Nielson, A. Satler and B. Koenig at the drill site. This research was sponsored by the Geothermal Division of the USDOE and performed under the auspices of the U. S. Department of Energy under contract No. W-7405-ENG-48.

REFERENCES

Bonner, Brian P., J. J. Roberts and D. L. Schneberk, "Determining water content and distribution in reservoir graywacke from the northeast Geysers with x-ray computed tomography," Trans. Geothermal Resources Council, 18, 305-310, 1994.

Gunderson, Richard P., "Reservoir Matrix Porosity at the Geysers from Core Measurements," *Trans. Geothermal Resources Council*, **14**, PART II, 1661-1665, 1990.

Hulen, J. B. and D. L. Nielson, "Sample handling, field procedures, and curation guidelines for The Geysers Coring Project," University of Utah Research Institute Report, ESL-94002-TR,1994.

Hulen, J. B., B. A. Koenig, and D. L. Nielson, "The Geysers coring project–summary and initial results," *World Geothermal Congress*, Florence Italy, in review, 1994.

PROCEEDINGS, Twentieth Workshop on Geothermal Reservoir Engineering
Stanford University, Stanford, California, January 24-26 1995
SGP-TR-150

LABORATORY MEASUREMENTS ON RESERVOIR ROCKS FROM THE GEYSERS GEOTHERMAL FIELD

G. N. Boitnott
New England Research, Inc.
76 Olcott Drive
White River Junction, VT, 05001

ABSTRACT

A suite of laboratory measurements have been conducted on Geysers metagraywacke and metashale recovered from a drilled depth of 2599 to 2602 meters in NEGU-17. The tests have been designed to constrain the mechanical and water-storage properties of the matrix material. Various measurements have been made at a variety of pressures and at varying degrees of saturation.

Both compressional and shear velocities exhibit relatively little change with effective confining pressure. In all of the samples, water saturation causes an increase in the compressional velocity. In some samples, saturation results in a moderate decrease in shear velocity greater in magnitude than would be expected based on the slight increase in bulk density. It is found that the effect of saturation on the velocities can be quantitatively modeled through a modification of Biot-Gassmann theory to include weakening of the shear modulus with saturation. The decrease is attributed to chemo-mechanical weakening caused by the presence of water. The degree of frame weakening of the shear modulus is variable between samples, and appears correlated with petrographic features of the cores.

Two related models are presented through which we can study the importance of saturation effects on field-scale velocity variations. The model results indicate that the saturation effects within the matrix are significant and may contribute to previously observed field anomalies. The results help to define ways in which we may be able to separate the effects of variations in rock properties, caused by phenomena such as degree of fracturing, from similar effects caused by variations in matrix saturation. The need for both compressional and shear velocity data in order to interpret field anomalies is illustrated through comparisons of model results with the field observations.

I. INTRODUCTION

Results of field seismic experiments by *O'Connell and Johnson,* [1991] and *Zucca et al.,* [1994] have identified anomalies which have been interpreted to reflect variations in the degree of fluid saturation associated with the water/steam transition. However, these interpretations have been based on laboratory data on other rock-types and field data from other geologic settings. The purpose of this project is to provide direct measurements on reservoir material from The Geysers to assess and constrain these interpretations.

Over the last 18 months, a suite of measurements have been conducted on Geysers rocks recovered from reservoir depths in NEGU-17. The tests have focused on studying the physical properties of the matrix and their relationship to the degree of saturation. Ultrasonic velocity data has demonstrated that the V_p/V_s signature of saturation is quantitatively similar to anomalies observed in field data. However the interpretation is complicated by a number of factors concerning the extrapolation of laboratory scale velocity measurements to field scales, since velocities at the field scale are considerably lower than the matrix velocities measured in the laboratory.

In this work, we are emphasizing measurements required to enable the extrapolation of laboratory data to field scales. Models are being developed to better understand the importance of matrix properties in influencing field scale observations. In order to have confidence in extrapolating from laboratory measurements to field observations, a physical understanding of the influence of saturation on matrix properties is required.

II. SAMPLE SELECTION AND DESCRIPTION

The results of tests performed on 8 plugs from 4 core samples of NEGU-17 material are reported here. The samples were selected to obtain representative and uniform pieces of the intact matrix material, as well as to represent the range of lithologies prevalent in the reservoir. Table I provides a summary of the hand samples from which the plugs were taken and a brief description of the individual plugs which were tested. A detailed discussion of the petrography of the NEGU-17 core and its geologic context has been given by *Hulen et al.* [1992].

Table I

Sample Description

Sample	Depth (m)	Sample Description	Plug	Plug Description
2	2598.82-2598.91	Massive metagraywacke, moderately veined with quartz, locally ferroaxinite and epidote. Abundant flakes and grain-sized inclusions of meta-shale. A highly altered portion with associated veining and enhanced porosity dominates in one corner of the sample.	2x	Massive metagraywacke, relatively unaltered, oriented parallel axis of NEGU-17 core.
			2y1	Massive metagraywacke, moderate to little alteration with some enhanced porosity in the form of macro-pores, oriented perpendicular to axis of NEGU-17 core.
			2y2	Massive metagraywacke, moderate to little alteration with some enhanced porosity in the form of macro-pores, oriented perpendicular to axis of NEGU-17 core.
			2u	Massive metagraywacke, highly altered with significantly enhanced porosity in the form of macro-pores, oriented parallel to axis of NEGU-17 core.
12	2599.64-2599.73	Metagraywacke with stringers of argillaceous graywacke metasiltstone; prominent quartz-ferroaxinite-epidote veinlets concentrated in the metagraywacke.	12u	Metagraywacke, darker and finer grained than samples 2 and 39, and with numerous fine stringers and grain-sized flakes of metashale.
21	2600.49-2600.55	Tectonically and chaotically admixed graywacke metasiltstone and argillite (metashale) with abundant, contorted quartz veinlets (most inherented from franciscan-vintage regional metamorphism.	21u	Dominantly argillite (metashale) with abundant, contorted quartz veinlets.
39	2602.08-2602.17	Massive metagraywacke, moderately veined with quartz, locally ferroaxinite and epidote. Less abundant grain-sized inclusions if metashale than as in sample 2.	39u	Massive metagraywacke with prominent quartz vein cutting through one corner of the plug.
			39u2	Massive metagraywacke.

Table II

Bulk Properties

Plug -	Dry Density g/cc	Saturated Density g/cc	Porosity %	Grain Density g/cc
2x	2.664	2.674	1.0	2.691
2y1	2.634	2.651	1.7	2.680
2y2	2.644	2.662	1.8	2.692
2u	2.506	2.584	7.8	2.718
12u	2.654	2.669	1.5	2.694
21u	2.736	2.752	1.6	2.780
39u	2.654	2.674	2.0	2.708
39u2	2.642	2.660	1.8	2.690
Westerly	2.646	2.652	0.6	2.662
Berea#1	2.134	2.319	18.8	2.628
Berea#2	2.141	2.329	18.9	2.640

In addition to the Geysers material, identical tests were performed on samples of Berea sandstone and Westerly granite. Berea and Westerly were chosen because they have been heavily studied, they have microstructures and petrographic characteristics which are different from the Geysers material, and they have been used in the past as material for studies of rock properties under hydrothermal conditions (see *Ito et al.* [1979], *DeVilbiss* [1980], and *Zucca et al.* [1994]).

Sample dimensions, bulk densities (dry and saturated), and inferred porosities and grain densities (based on dry and saturated densities) are given in Table II. For the NEGU-17 samples, porosities range from 1.0 to 2.0 percent with the exception of sample 2u, which was recovered from a highly altered piece of metagraywacke containing significantly enhanced porosity. Grain densities are confined to a limited range of 2.68 to 2.72 g/cc, with the exception of the metashale (21u) which exhibited a moderately higher density.

III. ULTRASONIC VELOCITIES

A variety of ultrasonic pulse propagation experiments have been conducted. The results of measured velocities versus pressure for the NEGU-17 samples and comparisons with field values are shown in Figure 1. The results illustrate that all samples exhibit relatively little pressure effect on velocities, even in the case of dry samples. This indicates that the matrix is very tight, an observation further supported by the high velocities and low acoustic attenuation characteristic of the samples. The comparisons with the field values illustrate that matrix values are consistent with the highest field velocities and asymptotically approached by the field velocities at depth, consistent with the notion that the field velocities are influenced (reduced) by field-scale features such as rock joints which are not sampled at the laboratory scale.

All samples exhibit some increase in compressional velocity with saturation, the effect being most notable at low pressures. Shear velocities are either not effected by saturation (i.e. samples 2u and 2y1), or more commonly exhibit some reduction with saturation. This behavior, which is uncommon in low porosity rocks, is thought to reflect the presence of chemo-mechanical weakening of the matrix material. The metashale sample (21u) exhibits a persistent shear velocity reduction with saturation, while some of the metagraywackes commonly exhibit a slight decrease in shear velocity with saturation which appears to increase with increasing effective confining pressure.

Table III summarizes the variations in velocities among samples at 30 MPa effective confining pressure. Despite the general lack of pressure effect on the velocities of the NEGU-17 matrix, the saturation effects are of similar relative magnitude as other rocks of diverse micro-structure (i.e. Berea sandstone and Westerly granite). Note that there is between 4 to 9% variation among the NEGU-17 samples in compressional velocities, shear velocities, and V_p/V_s ratios for both the dry and saturated results. Also of interest is the fact that sample 2u exhibited the highest velocities and the smallest effect of saturation of all the samples tested, despite its exceptionally high porosity and degree of alteration. In addition, the slowest velocities and one of the largest shear velocity reductions with saturation were recorded for sample 12u, which exhibited one of the lowest porosities. These observations serve to illustrate some of the odd behavior of the NEGU-17 material.

IV. MODELING THE DATA

The effects of saturation on acoustic velocities have been well studied, and are qualitatively understood to result from four basic mechanisms: "Biot-Gassmann stiffening" of the bulk modulus, "local flow stiffening of both the bulk and shear moduli; change in bulk density with saturation; and chemo-mechanical effects (usually weakening) (see *Murphy*, [1982], *Mavko and Jizba* [1991]).

In contrast to most other rocks, we have found that for the NEGU-17 matrix samples the dominant effect of saturation on the compressional velocities is quantitatively consistent with Biot-Gassmann poroelastic theory. The classically used Biot-Gassmann theory provides as simple relationship between the dry and saturated dynamic elastic moduli, resulting from changes in density with saturation as well as the increase in bulk modulus due to the finite bulk modulus of the saturating fluid. According to the low frequency version of the theory, the saturated bulk modulus (K_{sat}) is given by

$$K_{sat} = K_{dry} + \Delta K \qquad (1a)$$

where ΔK represents the increase in bulk modulus due to saturation and is given by

$$\Delta K = \frac{(K_{solid} - K_{dry})^2}{K_{solid}\left[1 - \phi - (K_{dry}/K_{solid}) + \phi(K_{solid}/K_f)\right]} \qquad (1b)$$

ΔK is a function of the porosity (ϕ), the bulk moduli of the fluid (K_f) and the solid (K_{solid}) comprising the matrix, and the bulk modulus of the dry matrix itself (K_{dry}) (see *Biot*, [1956]; *Winkler*, [1985]). The shear modulus G is assumed to be independent of saturation (i.e. $G_{dry} = G_{sat}$).

While the low frequency Biot-Gassmann theory does a reasonable job of being able to model the increase in compressional velocity with saturation

Table III									
Velocities @ 30 MPa Effective Pressure									
	Dry			Saturated			Effect of Saturation		
Plug	V_p m/s	V_s m/s	V_p/V_s	V_p m/s	V_s m/s	V_p/V_s	$\Delta V_p/V_p\|_{dry}$	$\Delta V_s/V_s\|_{dry}$	$\frac{\Delta(V_p/V_s)}{(V_p/V_s)_{dry}}$
2x	5593	3446	1.623	5770	3378	1.708	0.032	-0.020	0.052
2y1	5529	3421	1.616	5605	3431	1.634	0.014	0.002	0.011
2y2	5622	3467	1.621	5732	3424	1.674	0.020	-0.012	0.033
2u	5917	3573	1.656	6008	3586	1.675	0.015	0.004	0.011
12u	5370	3370	1.593	5668	3277	1.727	0.055	-0.028	0.084
21u	5650	3412	1.656	5799	3272	1.772	0.026	-0.041	0.070
39u	5458	3367	1.621	5598	3334	1.679	0.026	-0.010	0.034
39u2	5437	3362	1.617	5683	3329	1.707	0.045	-0.010	0.056
NEGU-17†	5574†	3427†	1.626‡	5733†	3379†	1.697‡	0.028‡	-0.014‡	0.044‡
Westerly	5577	3252	1.715	5908	3312	1.784	0.059	0.018	0.040
Berea#1	3908	2510	1.557	3989	2399	1.663	0.021	-0.044	0.068

† Average values of velocities of all NEGU-17 samples.

‡ Computed from average values of velocities of all NEGU-17 samples.

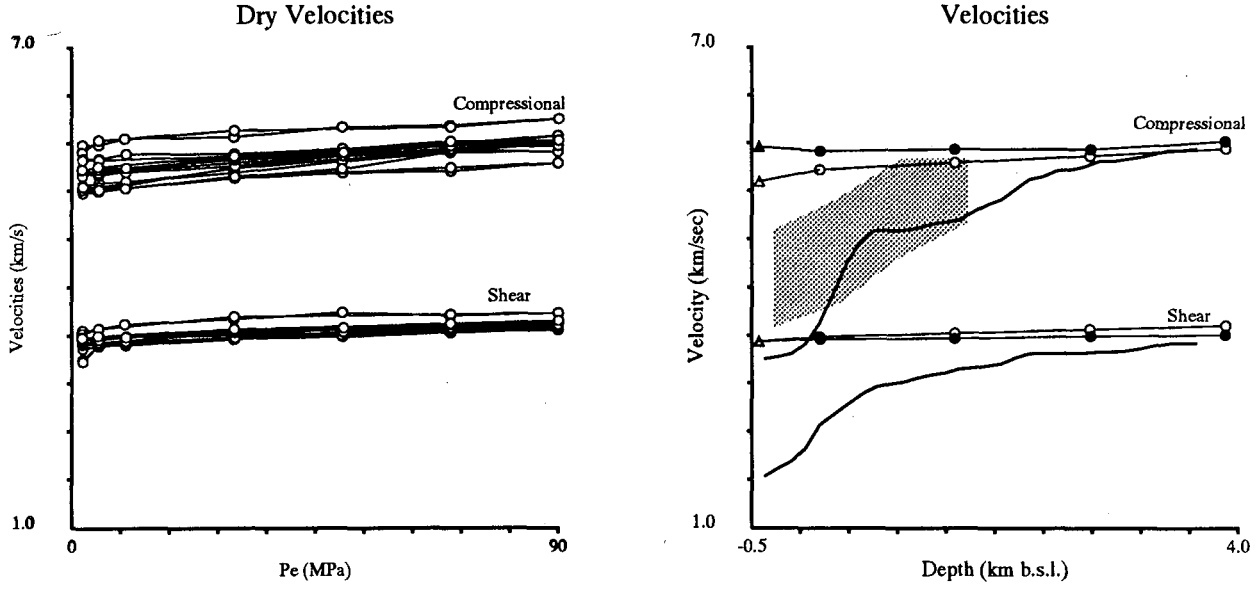

Figure 1:

a) Dry compressional and shear velocities as a function of confining pressure for the eight NEGU-17 plugs. Note the lack of a significant pressure effect, indicating the tight nature of the matrix material.

b) Comparison of laboratory velocity measurements on sample 2x with the results of field seismic inversions from the central Geysers. Ultrasonic velocity measurements were conducted on dry (open circles) and saturated (closed circles), and exhibit small but measurable saturation effects on both compressional and shear velocities. Solid lines are from *O'Connell and Johnson*, [1991] and the gray shaded region represents the variation in compressional velocities from the 3-D work of *Zucca et al.*, [1994].

exhibited by the NEGU-17 samples, many samples exhibit a shear velocity reduction with saturation which is far in excess of what can be explained by the theory. In the simplest case, the weakening effect can be modeled by assuming that the weakening effects the shear modulus but has little influence on the bulk modulus. Thus we replace the assumption that $G_{dry}=G_{sat}$ with a weakened shear modulus, where the weakening is a function of effective pressure.

$$G_{sat} = G_{dry} - \Delta G \qquad (1c)$$

Note that this weakening effects both the saturated shear and compressional velocities.

Applying the modified theory to the data at hand, we find that we have two free parameters, namely the bulk modulus of the solid material comprising the matrix (K_{solid}) and the shear weakening term ΔG. The value of K_{solid} is determined from equations 1a and 1b by first computing K_{dry} and K_{sat} from the high pressure dry and saturated compressional and shear velocities and using the bulk properties from Table II. Likewise, the values of ΔG are determined through use of the dry and saturated shear velocities as a function of effective pressure.

An example of comparisons of data and model are given in Figure 2. Note that both the reduction in shear velocity as well as second order effects of the shear weakening on compressional velocities are modeled by the theory. All of the NEGU-17 samples are modelable with this approach, with values of K_{solid} near 59 GPa, reasonable values for rocks of these compositions.

The modified Biot-Gassmann theory provides us with a theoretical foundation upon which to interpret field observations, develop models of wave propagation in partially saturated rock, and identify physical processes and phenomena which may be important to reservoir performance.

V. EXTRAPOLATING TO FIELD SCALES

Field seismic imaging experiments at The Geysers have indicated V_p, V_p/V_s, and attenuation anomalies associated with the dry steam reservoir [*O'Connell and Johnson*, 1991; *Zucca et al.*, 1994]. The observed anomalies have been interpreted as reflecting changes in the degree of saturation associated with the water/steam transition. It has been observed that the measured difference between V_p/V_s for dry and saturated matrix is quantitatively consistent with the observed anomaly reported by *O'Connell and Johnson* [1991], however the correlation is not straightforward since the average field scale velocities are significantly lower than the velocities measured in the laboratory on the reservoir matrix material (see Fig. 1).

The discrepancy between field and laboratory velocities is certainly not surprising, and is commonly attributed to the presence of joints and other large scale features not sampled in the laboratory specimens. In order to assess whether the matrix effects measured in the laboratory may be the cause of the field scale anomalies, two related models have been developed to incorporate the measured matrix properties with the expected properties of joints in order to predict the field scale properties. As a starting point, we would like to see if by adding sufficient number of joints to lower the lab velocities to field values, we can still preserve the V_p/V_s signature of saturation exhibited by the matrix.

For The Geysers rocks, there is little evidence of significant rate dependent phenomena (i.e. local flow), with the lab results being fairly easily modeled with the modified low-frequency Biot-Gassmann theory. Thus, we are left with dealing with field scale features such as joints and fractures, features which are well known to be ubiquitous within The Geysers reservoir. Because rock joints are compliant features, their presence within a matrix can significantly reduce the field-scale velocities. Here we present two simple models to include the effect of rock joints and use the models to test if the matrix properties are potentially important in controlling and/or influencing the observed field scale anomalies.

At the scale of the passing elastic wave, we assume that the stresses within the medium are continuous, while the displacements are discontinuous across the joints. We assume that the scale of deformation (i.e. the wavelength) is large enough that we can treat the deformation of the matrix as independent from that the joints. This is to say that the compliance of the jointed medium subject to a given stress is the sum of the compliances resulting from the elastic deformation of the matrix and that attributed to the compliance of the joints. For convenience, we parameterize field-scale (effective) bulk and shear moduli in terms of the moduli of the matrix (denoted by the subscript m) and the moduli associated with the presence of joints and fractures (denoted by the subscript f) :

$$\frac{1}{K_{eff}} = \frac{1}{K_m} + \frac{1}{K_f} \qquad (2a)$$

$$\frac{1}{G_{eff}} = \frac{1}{G_m} + \frac{1}{G_f} \qquad (2b)$$

From laboratory and theoretical studies of joints, we know that both the compressional (k_n) and shear (k_s) stiffnesses increase with normal load across the joint, and that for each the relationship is approximately linear with effective stress for a wide variety of joints. It follows that the ratio k_n/k_s is roughly independent of stress. As a result we might postulate

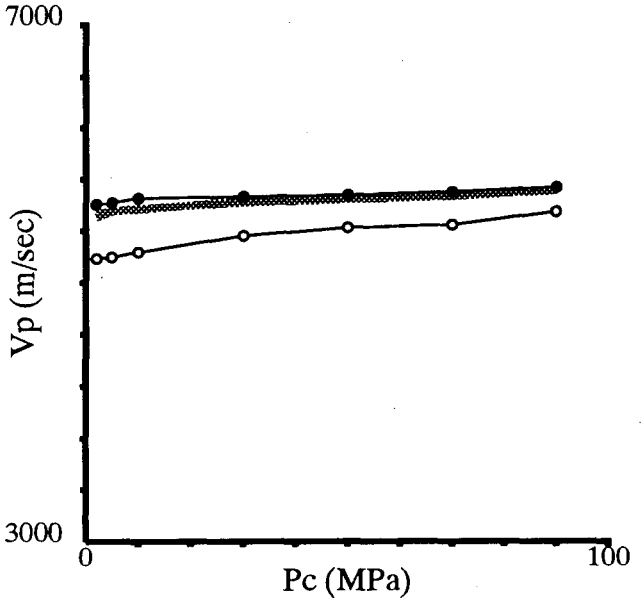

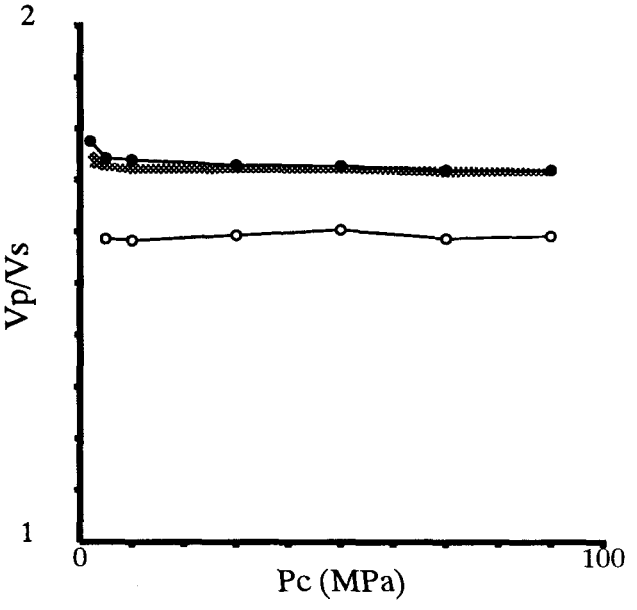

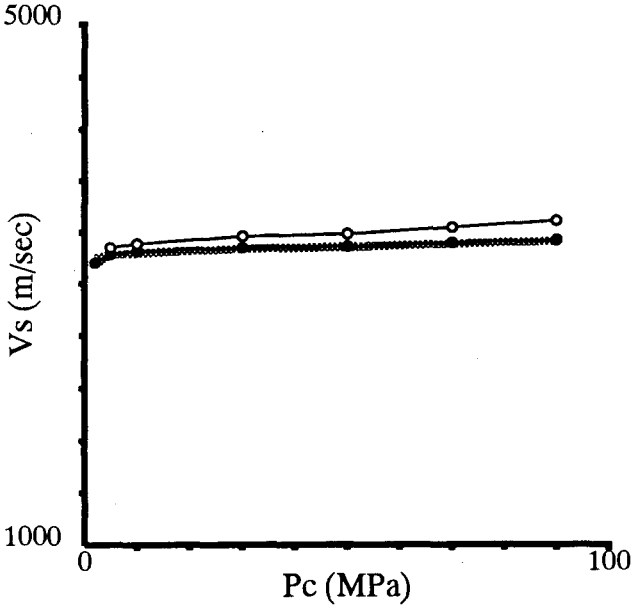

Figure 2: Dry (open circles) and saturated (closed circles) compressional velocities, shear velocities, and V_p/V_s ratios, as a function of effective confining pressure for sample 12u. The measurements compare vary favorably with the modified Biot-Gassmann model described by equations 1(a,b,c), in which the shear modulus is weakened by saturation. Model predictions of saturated velocities based on the dry measurements are shown with the gray shaded lines in each figure, indicating very good agreement with measured values. All of the NEGU-17 samples can be modeled with similar degree of accuracy using the same model.

that K_f/G_f will be insensitive to effective stress as well as fracture density, and thus treat it as a physical constant of the fractured rock mass.

Alternatively, we might adopt the parameterization of *Fossum* [1985] in which the effective elastic moduli are parameterized directly in terms of the normal and shear stiffnesses of the joints and the joint spacing (s). The model, which assumes a isotropic distribution of fractures, provides alternative estimates of K_{eff} and G_{eff} denoted schematically through functions $\kappa(\,)$ and $\gamma(\,)$ as follows:

$$K_{eff} = \kappa(K_m, G_m, k_n, k_s, s) \qquad (3a)$$

$$G_{eff} = \gamma(K_m, G_m, k_n, k_s, s) \qquad (3b)$$

Either model can be used to test to see if field data and laboratory data are internally consistent with such a simple fractured rock model. Working with the model as parameterized in equations 2(a,b), if we have estimates from field and laboratory shear velocities of G_{eff} and G_m, we can use equation 2b to compute G_f. Assuming K_f/G_f is constant, we then use equation 2a and laboratory measurements of K_m to estimate K_{eff}. Hence, we have a prediction of the field scale V_p.

A similar argument can be used in the context of equations 3(a,b). Again noting that k_n/k_s is roughly independent of stress, as well as the fact that functions $\kappa(\,)$ and $\gamma(\,)$ are such that the joint spacing (s) always appears as a product with k_n or k_s, we can use laboratory measurements of G_m, assume a value of k_n/k_s, and find $s \cdot k_s$ consistent with field measurements of G_{eff} through equation 3b. We then use laboratory measurements of K_m and G_m and equation 3a to predict K_{eff} and thus the field V_p.

These models are well suited for predicting the degree to which matrix saturation will effect field-scale velocities. It should be noted that both models outlined above contain only one free parameter which is assumed independent of depth and fracture density (i.e. the ratio K_f/G_f in equations 2a,b and the ratio k_n/k_s in equations 3a,b). Through use of matrix properties representative of dry and saturated conditions, we can use the models to test to see if field-scale V_p and V_s are compatible, thus indicating both the fracture properties and the state of saturation of the matrix.

VI. DISCUSSION

An example of such an exercise using the field data of *O'Connell and Johnson* [1991] is shown in Figure 3. The velocities at depth are assumed to represent the matrix values, being consistent with the laboratory values. The modified Biot-Gassmann theory is used, along with the laboratory values of velocities versus pressure, to constrain realistic dry and saturated matrix velocities. The shear velocity versus depth from *O'Connell and Johnson* [1991] is then combined with matrix values, and the contribution to the rock mass compliance attributed to the presence of joints is determined.

Using such a procedure, these models can be used to predict the sensitivity of the V_p/V_s signature in the fractured rock mass to the V_p/V_s signature of the matrix. Preliminary calculations as in Figure 3 illustrate that it is conceivable that the observed field scale anomalies may result in part from matrix effects. They also suggest that the overall velocity versus depth (as well as the spatial variations in velocity observed by *Zucca et al.* [1994]) are most likely controlled by fracture properties and/or fracture density.

Importantly, the model results illustrate that both saturation effects and the effects of joints can influence the compressional and shear velocities as well as V_p/V_s (see Fig. 3b). It appears dangerous to assume (as was done by *O'Connell and Johnson* [1991]) that some of the V_p/V_s variations with depth are not the result of joint density and/or the effects of pressure on joints. Thus V_p/V_s ratios alone should not be used to indicate saturation.

Similarly, assumptions that V_p variations reflect saturation effects, as postulated by *Zucca et al.* [1994], also appear dangerous in that the dominant cause of velocity variations appears associated with joints (i.e field scale features). While *Zucca et al.* [1994] noted that low compressional velocities corresponded to regions of the reservoir thought from other evidence to be the driest, this association may result from a correspondence between fracture density and reservoir depletion rather than being direct evidence of dry/depleted matrix. Without high resolution shear velocity information to compare with the compressional velocity variations, it is difficult to assess to what extent low compressional velocities are related to the saturation state of the matrix.

Through use of models as described above, one can begin to separate the two effects if both compressional and shear velocities are well constrained in the field. Using dry matrix values along with the models given by equations 2 and/or 3, correspondence between predicted and measured field-scale compressional velocities may be used to indicate dry reservoir. Likewise, using saturated matrix values, correspondence between predicted and measured compressional velocities can be used to indicate saturated reservoir. In so doing, the effect of fractures on the velocities, and hence V_p/V_s is removed and the fracture properties are constrained. With this accomplished, the effects of saturation within the matrix can then be assessed.

VII. ACKNOWLEDGMENTS

This work has been funded by the Geothermal Division of the U. S. Dept. of Energy through subcontract C93-134002 administered by INEL.

VIII. REFERENCES

Biot, M. A., Theory of propagation of elastic waves in a fluid-saturated porous solid: I. Low-frequency range, *J. Acous. Soc. Amer.*, 28, 168-178, 1956.

DeVilbiss-Munoz, J. W., Wave dispersion and Absorption in partially saturated rocks, Ph. D. Thesis, Stanford U. 1980.

Fossum, A. F., Effective elastic properties for a randomly jointed rock mass, *Int. J. Rock Mech. Mining Sci.*, v. 22, p. 467-470, 1985.

Hulen, J. B., D. L. Nielson, and W. Martin, Early calcite dissolution as a major control on porosity development in The Geysers steam field, California - Additional evidence in core from UNOCAL well NEGU-17, *Geothermal Resources Council, Trans.*, v. 16, p. 167-174, 1992.

Ito, H., J. DeVilbiss, and A. Nur, Compressional and shear waves in saturated rock during water-steam transition, *J. Geophys. Res.*, 84, 4731-4735, 1979.

Mavko, G. and D. Jizba, Estimating grain-scale fluid effects on velocity dispersion in rocks, *Geophysics*, 56, 1940-1949, 1991.

Murphy, W. F. III, Effects of microstructure and pore fluids on the acoustic properties of granular sedimentary materials, Ph. D. Thesis, Stanford U., 1982.

O'Connell, D. R. H., and L. R. Johnson, Progressive inversion for hypocenters and P wave and S wave velocity structure: Application to the Geysers, California, geothermal field, *J. Geophys. Res.*, 96, 6223-6236, 1991.

Winkler, K. W., Dispersion analysis of velocity and attenuation in Berea sandstone, *J. Geophys. Res.*, 90, 6793-6800, 1985.

Zucca, J. J., L. J. Hutchings, and P. W. Kasameyer, Seismic velocity and attenuation structure of the Geysers geothermal field, California, *Geothermics*, 1994.

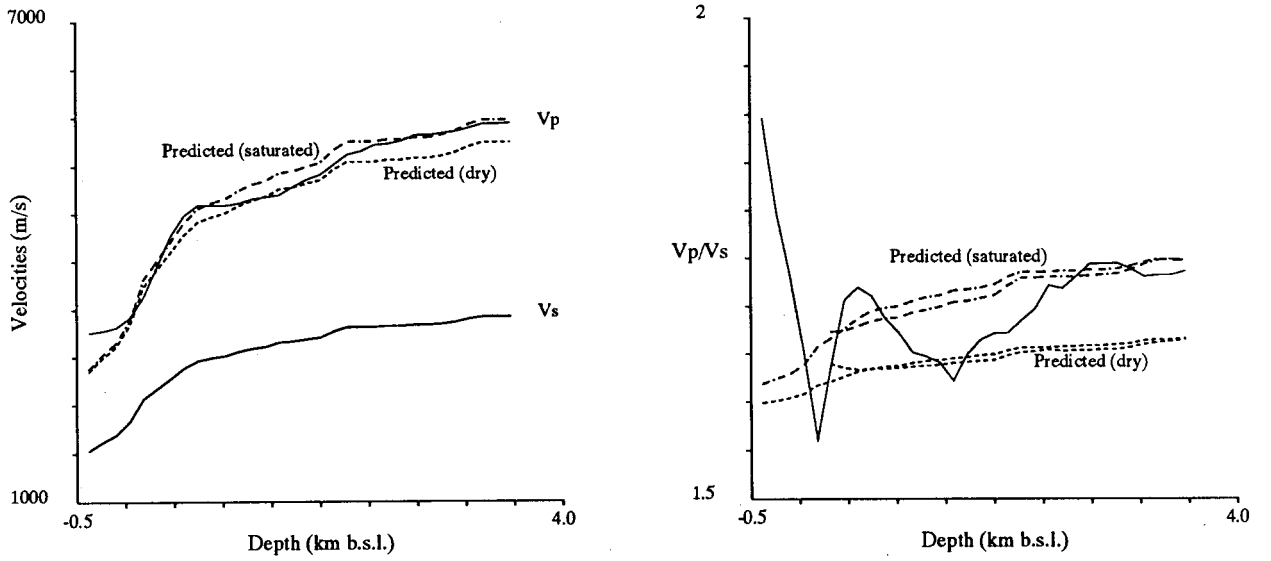

Figure 3: a) Comparison of predicted dry (dashed) and saturated (dot-dashed) compressional velocities with values from an field-seismic inversion of *O'Connell and Johnson* [1991] (solid lines). The model uses the difference between matrix shear velocities (measured in the laboratory) and field measurements of V_s from *O'Connell and Johnson* [1991] to infer shear modulus reduction due to the presence of joints and other field-scale features. Equations 2a,b were used, with a value of $K_f/G_f = 2.5$, for the predictions in Fig 3a. Similar results can be obtained using equations 3a,b and $k_n/k_s = 2.0$. Note the remarkable agreement over the entire depth range, indicating the appropriateness of assuming K_f/G_f is constant. The predictions are consistent with (and illustrate) an anomaly thought to reflect and understated region within the reservoir at a depth of approximately 1.8 km.

b) Comparison of predicted V_p/V_s ratios using equations 2a,b ($K_f/G_f = 2.5$) and equations 3a,b ($k_n/k_s = 2.0$) with values from a field-seismic inversion of *O'Connell and Johnson* [1991] (solid line). Dashed lines are the model results using dry matrix values while dot-dashed lines are for saturated matrix values. Note that both models produce nearly identical results. The anomaly between 1 and 2 km b.s.l. appears to be explainable by the matrix saturation effects, being consistent with a dry matrix.

PROCEEDINGS, Twentieth Workshop on Geothermal Reservoir Engineering
Stanford University, Stanford, California, January 24-26 1995
SGP-TR-150

LOCATING AN ACTIVE FAULT ZONE IN COSO GEOTHERMAL FIELD BY ANALYZING SEISMIC GUIDED WAVES FROM MICROEARTHQUAKE DATA

M. Lou[1], P.E. Malin[2] and J.A. Rial[1]

[1]Wave Propagation Lab, Department of Geology, University of North Carolina at Chapel Hill, NC27599-3315

[2]Department of Geology, Duke University, Durham, NC 27708-0235

ABSTRACT

Active fault systems usually provide high-permeability channels for hydrothermal outflow in geothermal fields. Locating such fault systems is of a vital importance to plan geothermal production and injection drilling, since an active fault zone often acts as a fracture-extensive low-velocity wave guide to seismic waves. We have located an active fault zone in the Coso geothermal field, California, by identifying and analyzing a fault-zone trapped Rayleigh-type guided wave from microearthquake data. The wavelet transform is employed to characterize guided-wave's velocity-frequency dispersion, and numerical methods are used to simulate the guided-wave propagation. The modeling calculation suggests that the fault zone is *~200m* wide, and has a P wave velocity of *4.80km/s* and a S wave velocity of *3.00km/s*, which is sandwiched between two half spaces with relatively higher velocities (P wave velocity *5.60km/s*, and S wave velocity *3.20km/s*).

(1) INTRODUCTION

To maintain high-permeability channels for hydrothermal outflow in geothermal fields, it is necessary to have active faults and fractures. In this context, "active" does not indicate that felt earthquakes associated with the fault are imminent, but that there has been enough seismic activity in the geologic past to maintain permeability along the fault plane. From a global survey of active hydrothermal systems, nearly all active venting is closely associated with faults (Aydin and Page 1984, Pollard 1987, Scholz et. al. 1993, Malin 1994). Locating active fault systems is of a vital importance to plan production and injection drilling in a geothermal field, and some major tectonically-controlled fault systems may be mapped directly by surface geological observation or subsurface drilling, or/and indirectly by geophysical methods such as reflection/refraction seismology. However, small to medium scale fault zones are difficult to delineate with traditional seismic reflection/refraction methods, and the surface seismic method is not effective to explore fault zones having vertical or nearly vertical dipping fault planes.

Fault zones usually act as low velocity seismic wave guides. These are energy-trapping, dispersion-inducing channels which make the observation of seismic guided waves an effective tool to delineate and monitor such fault zones. The Love-type fault-trapped seismic guided waves were first discovered in a three-dimensional vertical seismic profiling (VSP) experiment in the area surrounding a borehole drilled into fault zone of the Oroville, California, earthquake of 1975 by Li et. al.(1987). Similar trapped modes were also identified in some of the borehole seismograms obtained at the San Andreas fault near Parkfield (Li et. al. 1990), and at the fault zone of the Landers, California earthquake (Li et. al. 1994). In this paper, we describe how we located an active fault zone in the Coso geothermal field, California, by identifying and analyzing the Rayleigh-type guided waves from microearthquake seismograms recorded by a dense down-hole three-component seismographic network in the Coso area. As far as we know, this is the first report on Rayleigh-type guided waves ever observed in an active fault zone.

The trapped modes in a fault zone arise as a consequence of constructive interference of multiple reflections/ refractions at the boundaries between the low-velocity fault zone and high-velocity surrounding rocks. The waveforms of trapped waves (including features such as amplitude-space distribution and velocity-frequency dispersion) strongly depend on the fault zone geometry and its physical properties. We employed a guided wave modeling method to invert the fault zone width and rock velocity structure. In addition, we used the Wavelet Transform, a kind of time-varying Fourier Transform, to analyze the dispersion and frequency-content of guided wave modes.

(2) GEOLOGIC BACKGROUND AND THE COSO SEISMOGRAPHIC NETWORK

The Coso geothermal field lies to the east of the

Sierra Nevada Frontal Fault (SNFF) in southern Owens Valley, California. The field is covered locally by a thin, less than 100m layer of recent volcanics (Duffield et al. 1980). Geological maps (e.g. Figure 1) of the area (Duffield and Bacon 1981; Roquemore 1981) and recently acquired seismic reflection profiles (Monastero 1992, Malin 1994) delineate the general structure of the area. Although most major NW trending faults exposed on the surface have been detected, their extent below the surface, as well as other possible smaller scale faults systems, have yet to be determined.

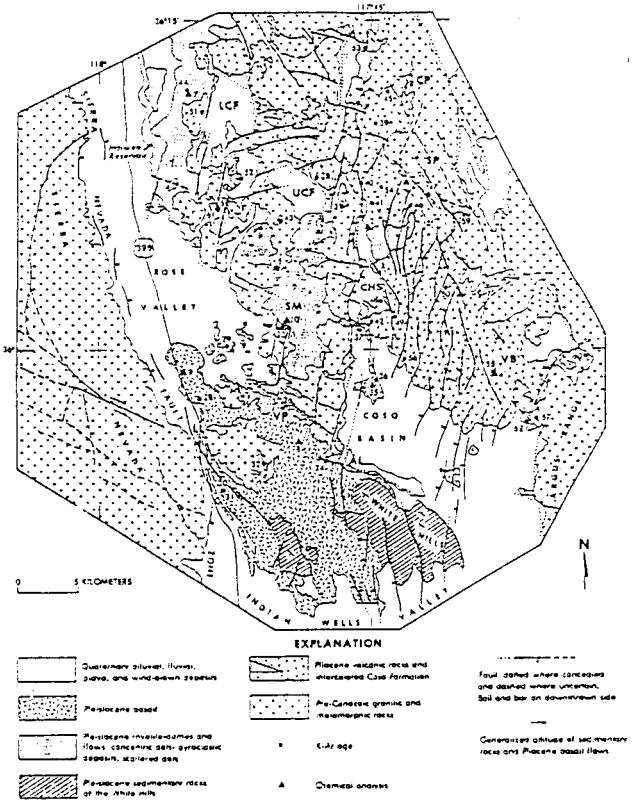

Figure 1. Generalized geological map of the Coso geothermal field and surrounding area (from Duffield and Bacon 1981).

The Coso geothermal area is a very active seismic zone with an average of 20 microearthquakes per day (Malin 1993). Starting in 1990, Duke University has operated a three-component downhole seismographic station network at the area. The network has 16 bit digital telemetry to an earthquake triggered central computer, which samples the signals at 480 Hz. The network sensors are in 100m or deeper boreholes, greatly reducing background noise and increasing the high-frequency band width of microearthquake observations. This downhole sensor environment is particularly useful to record any possible fault-trapped guided waves, since the downhole sensors would avoid the geological complexity of the near surface weathered layer which itself is a low velocity wave guide.

(3)GUIDED WAVE IDENTIFICATION AND ANALYSIS

Figure 2 shows 5 selected seismic stations, laid roughly along a north-south line, which recorded the reported guided waves. Careful inspection of the recently (since July of 1993) recorded events at the 5 stations of Figure 2, revealed that those seismograms recorded at station *S1* with source locations near the dashed line (a possible fault trace with orientation of $\sim N30^{o}W$) display some distinguishing guided-wave features on the components normal to the direction of wave propagation. Figure 3 shows three-component recordings at the same five stations from event *149*,

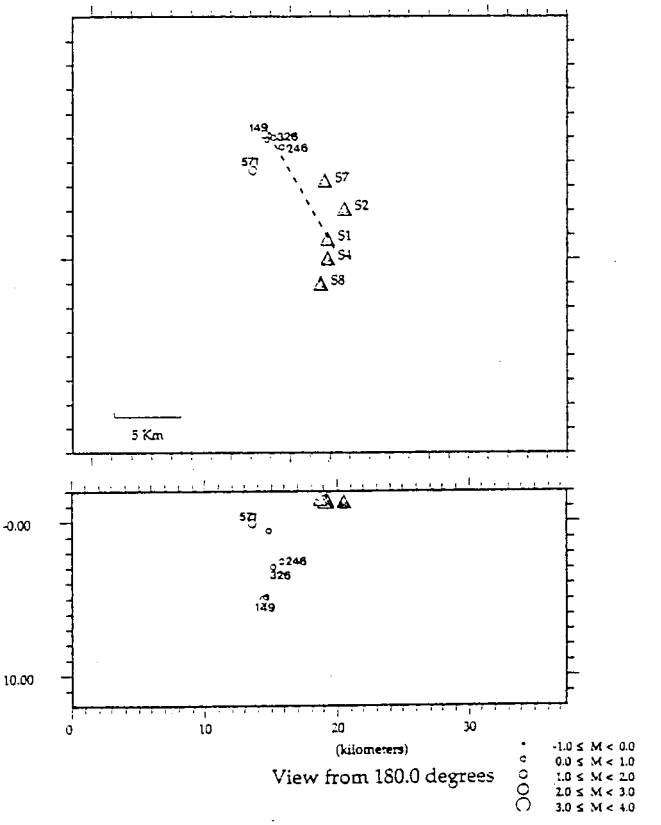

Figure 2. Five selected Coso seismographic network stations, microearthquake event locations, and orientation of a possible active fault zone (dashed line).

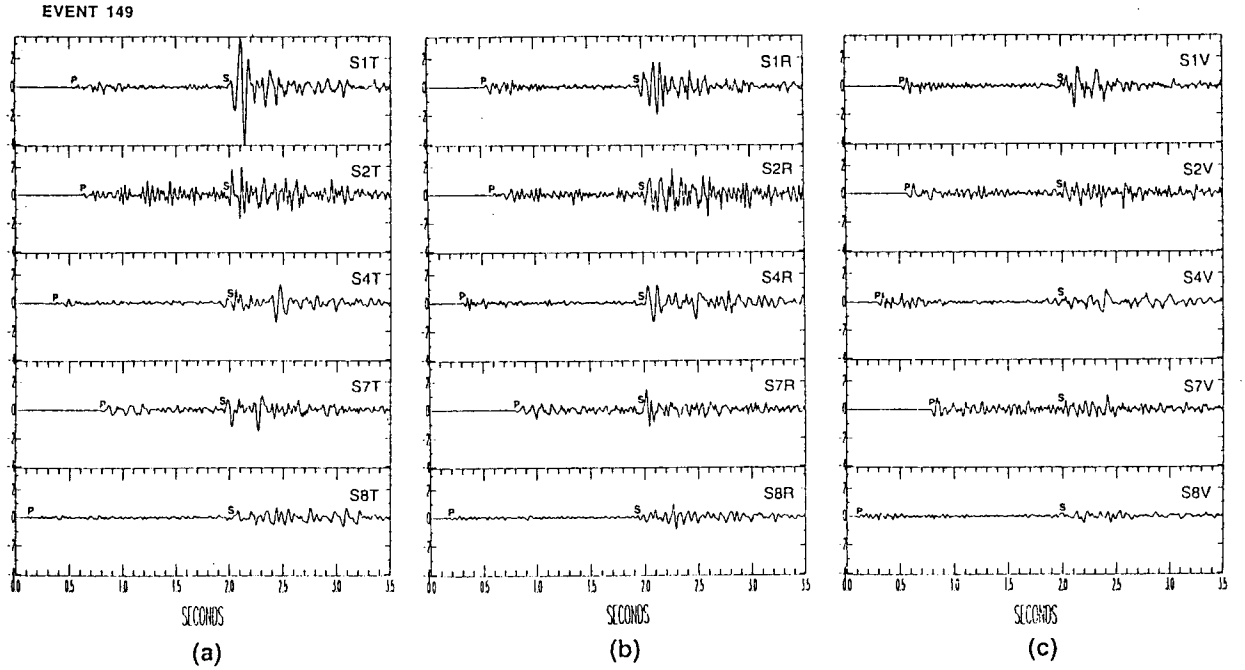

Figure 3. Three-component seismograms of event *149* (inside fault zone) recorded by the five selected stations: (a) the horizontal components normal to propagation direction*(T)* , (b) the horizontal components parallel to propagation direction*(R)* , and (c) the vertical components *(V)*. A large amplitude, dispersive Rayleigh guided wave is received by the two horizontal components of station *S1*, only.

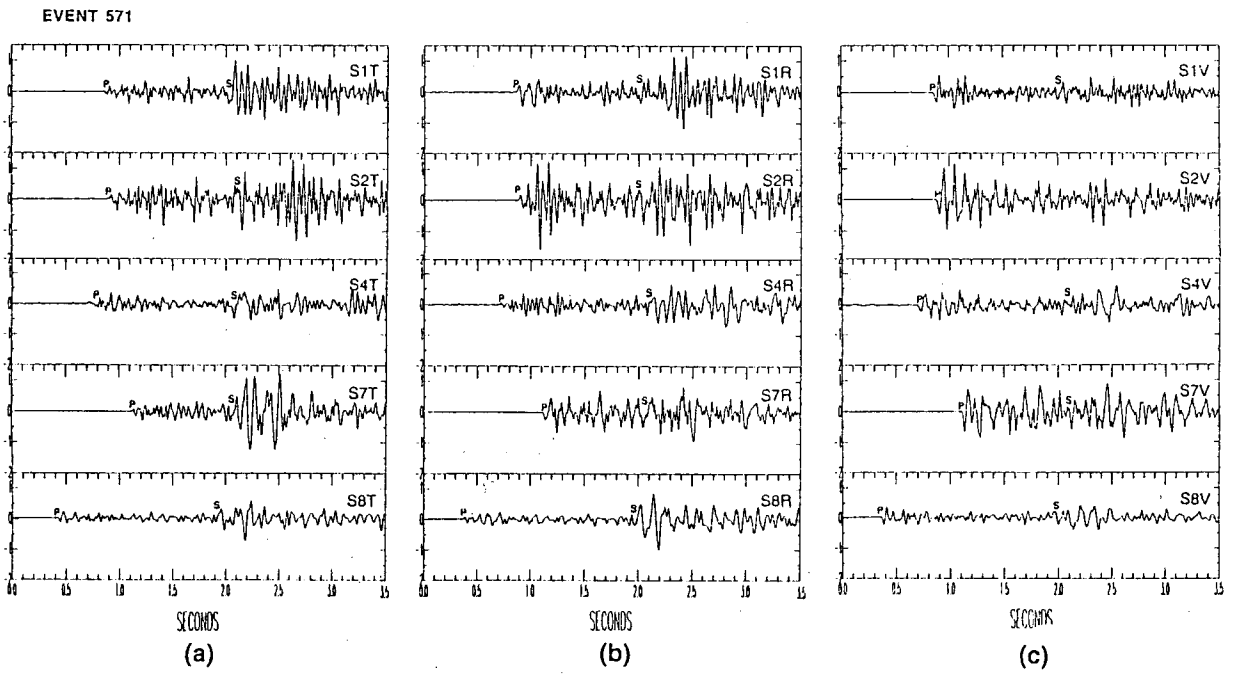

Figure 4. Three-component seismograms of event *571* (outside fault zone) recorded by the five selected stations. (a) the horizontal components normal to propagation direction*(T)*, (b) the horizontal components parallel to propagation direction*(R)*, and (c) the vertical components*(V)*. No guided waves similar to Figure 3 are received by any of the five stations.

which is located at *6.31 km* deep and is of magnitude *1.2*. The seismograms at station *S1*, particularly on the component normal to the direction of wave propagation *(S1T)*, show an abnormally large amplitude and a relatively long period wave train closely following the S wave arrival. The wave train disappears at other stations as located off the dashed line of Figure 2. For example, although station *S7* is at a closer distance(about *9.0km*) from the event than station *S1* (about *12.0km*), the amplitude ratio between components *S1T* and *S7T* is *4:1*. The wave train recorded by the two horizontal components of station *S1* also shows some normal dispersion, which is diagnostic of guided-wave modes. Comparing with the Love-type fault-trapped modes at vertical components observed by Li et. al. (1987, 1990, 1994), the wave train recorded by station *S1* is of Rayleigh type, since it is primarily polarized on the plane normal to a fault plane.

In contrast, the event *571* (*1.36km* deep, magnitude *1.1*) occurring outside the dashed line shows no evidence of a trapped mode at any of the five stations (Figure 4). This suggests that the abnormally large amplitude and relatively long period wave train seen at station *S1* (Figure 3a) is closely associated with the location of the event, rather than with any possible difference of station site effects.

Further evidence for identification of guided waves is shown in the seismograms from two additional fault-zone events *326* (Figure 5a) and *246* (Figure 5b), recorded at the *T*-component of three different stations (*S1, S2, S4*). The dispersion of guided waves can be easily displayed by a wavelet transform (see Lou and Rial 1995a) shown in Figure 6, for (a) the guided wave recorded by *S1*, and (b) non-guided wave recorded by *S4*, respectively. Typical normal dispersion is seen clearly in Figure 6a, while Figure 6b shows no evidence of dispersion (Indeed, a slightly abnormal dispersion is observed, which may be due to some high frequency attenuation of a body wave).

The source locations and magnitudes of all events showing similar guided-wave characteristics are plotted in Figure 2. The event location distribution suggests that the fault zone has a near vertical fault plane, with the depth extended at least *7 km* below the surface.

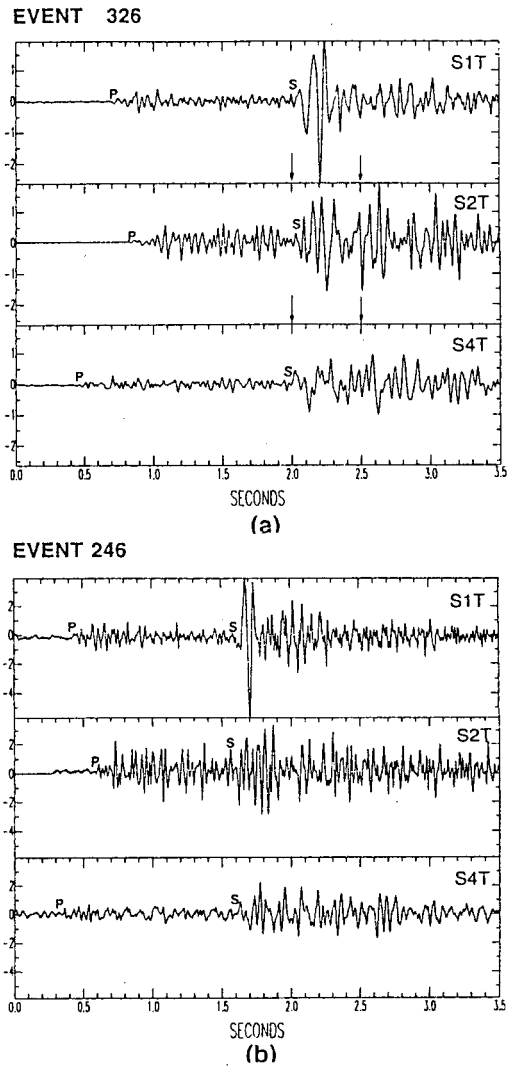

Figure 5. Seismograms of two additional fault-zone events (a) *326* and (b) *246*, recorded by the horizontal component normal to propagation direction of three different stations (*S1T, S2T,* and *S4T*). A large amplitude, and strong dispersive Rayleigh guided wave is observed by the station *S1* for both events.

(4) GUIDED-WAVE MODELING

To model the above observed seismic guided waves, we employed a Green's function method to compute the Rayleigh guided-wave propagation (Lou and Rial 1995b). Based on plausible seismic velocity structures in the Coso area (Malin 1993, 1994), we constructed a simple fault zone model composed of a low-velocity layer sandwiched between two half-spaces with relatively high P velocity, as shown in Figure 7. Because of the observed guided waves in Figures 3 and 5 have a relative simple, short wave train, we only considered the

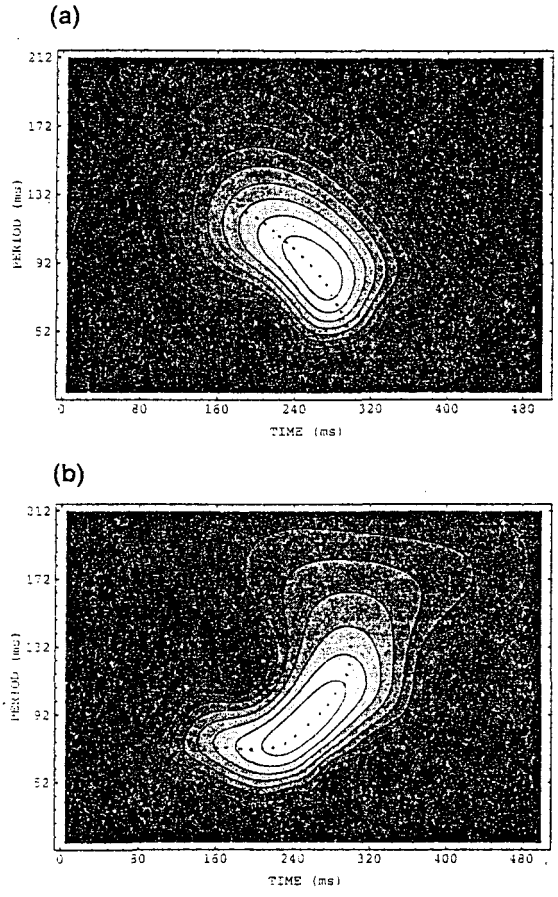

Figure 6. The amplitude spectral of the wavelet transform (a kind of Time-Varying Fourier Transform) to the windowed seismograms of Figure 5a (marked by arrows): (a) the spectrum of the guided wave recorded by the station *S1*, and (b) the spectrum of non-guided wave recorded by the station *S2*.

fundamental mode of Rayleigh-type guided waves. Figure 8 shows the phase-velocity (solid line) and group-velocity (dashed line) dispersion curves of the fundamental mode of Rayleigh guide wave for the fault-zone model of Figure 7. From the group-velocity dispersion curve, we see that the dispersion of the guided wave starts at about *5 Hz*, and is well developed at around *10 Hz*, which basically matches the wavelet transform plot of the observed guided wave in Figure 6a.

Figure 9 illustrates the synthetic results (*synS1T, synS1R, synS4T, and synS4R)* from the simulation of the two-horizontal component seismograms recorded at stations *S1* (inside fault zone) and *S4* (off fault zone) for event *149*. We tested a range of model parameters (fault zone width, P- and S wave velocities), we found the best match to observations with model parameters shown in Figure 7. Although these modeling parameters may not be unique, we think it is reasonable to constrain the velocities on the basis of observed P- and S arrival times, and the width on the period of dispersive trapped waveforms.

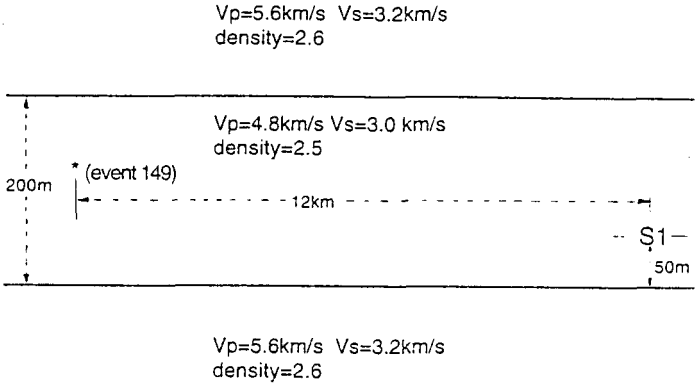

Figure 7. The fault zone model, showing source and station location used to compute the guided wave of event *149*.

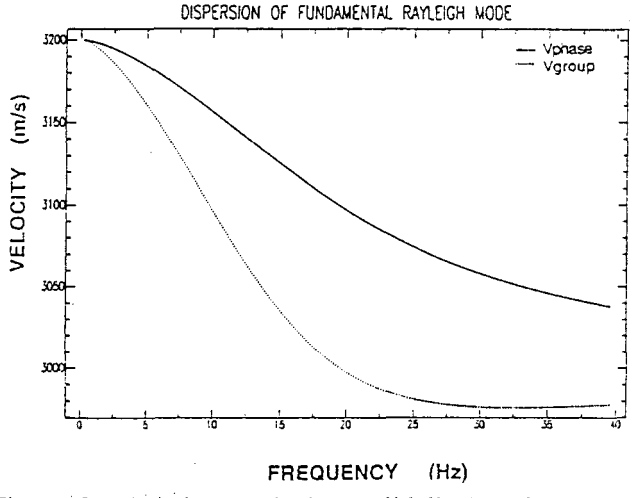

Figure 8. The phase velocity (solid line) and group velocity (dashed line) dispersion curves of the fundamental Rayleigh mode of the guided waves for the model of Figure 7.

We did not include an attenuation factor (internal friction) in the simulation, but simulated it by low-pass filtering (with *15 Hz* high cutoff) the synthetic guided waves. On the other hand, the modeling is somewhat restricted because we only simulated the trapped mode from one event, and we also assumed the fault zone to be a two dimensional infinite uniform waveguide. A more thorough modeling of trapped waves from more events with different locations would result

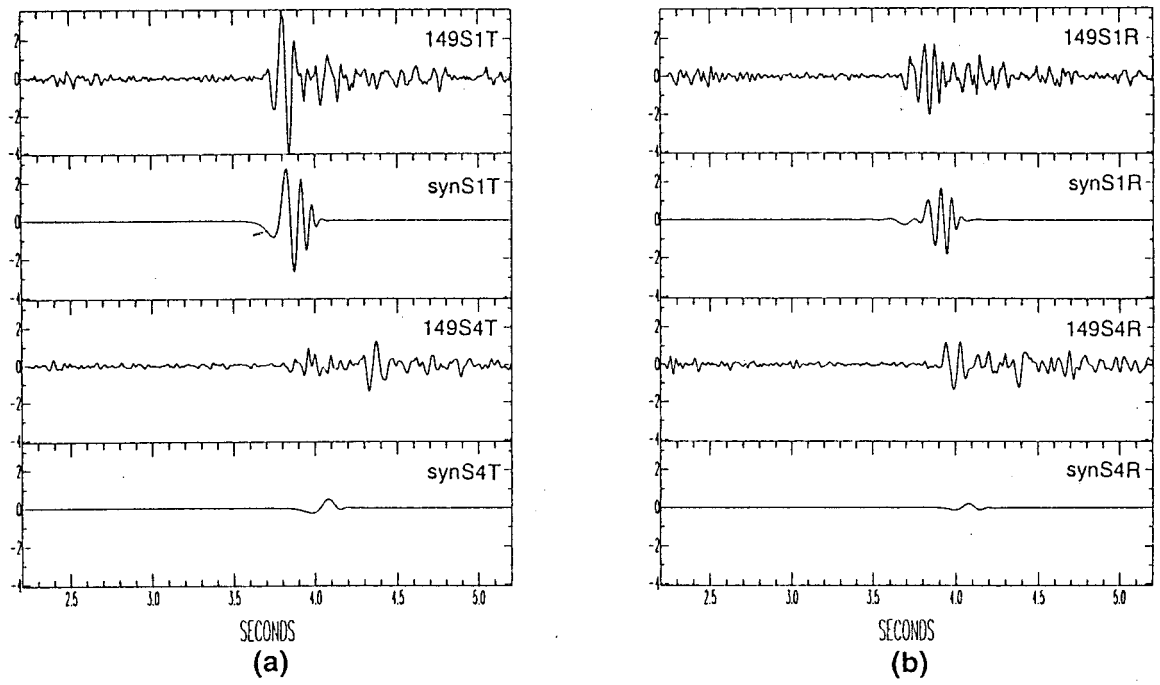

Figure 9. Synthetic guided waves and their comparison with real records of event *149* for two stations *S1* (inside fault zone) and *S4* (outside fault zone): (a) the horizontal component normal to propagation direction, and (b) the horizontal component parallel to propagation direction.

in a more detailed 3-D model of the fault zone. Numerical methods such as finite elements and finite differences, which allow to incorporate some inhomogeneity and intrinsic attenuation, may give more precise modeling results.

(5) DISCUSSION

We have clearly identified a fault-zone trapped Rayleigh-type guided wave from the microearthquake data recorded in the Coso geothermal field, California. As far as we know, this is the first report on a Rayleigh guided-wave ever observed in a fault zone. These trapped modes appear as wave trains of relatively large amplitude wave trains closely following S waves on seismograms recorded at stations close to fault trace for the events occurring within the fault zone. They are clearer on the components normal to fault plane than parallel to fault plane, which suggests the guided waves are of Rayleigh type. For the events occurring in a relatively shallow depth , we also observe strongly dispersive guided waves. From the spectral amplitude of the wavelet transform, we observed that the dominant frequency of trapped mode is lower *(~10Hz)* than the non-guided waves outside fault zone *(~12 Hz*), which is the phenomenon also found by Li et. al. (1987, 1990, 1994).

In order to define the fault zone revealed by those guided waves, we used a numerical method to calculate synthetic Rayleigh-type guided waves. By comparing the observed waveform with the synthetic calculated in a planar low-velocity zone, we estimate a fault zone width of *-200m*, a fault zone P wave velocity of *4.8 km/s* and S wave velocity of *3.0 km/s*, with surrounding rock P wave velocity of *5.6 km /s* and S wave velocity of *3.2km/s*. These parameters are generally consistent with the Coso geologic structure and previous seismic interpretation (Caruso and Malin 1994, Malin 1994). From the source location distribution of guided waves, we estimate the fault system has a near-vertical dip with the depth extended to at least *7 km* below surface.

An active fault system plays a very important role in the development and maintenance of fluid conduits in a geothermal field. Locating such fault system is critic to economically plan production and injection drilling for geothermal reservoirs. The seismic guided waves are very sensitive to the structure and material or fracture properties of an active fault zone. Our work suggests that careful analysis and modeling of such seismic guided

waves could provide a very effective method to locate and monitor active fault systems.

ACKNOWLEDGMENTS

This research is supported by the US Navy (Geothermal Program Office, Naval Air Weapons Station, China Lake), Idaho National Engineering Laboratory (EG&G), the California Energy Company, Inc. (CECI), and the Department of Energy (Geothermal Division), under subcontract No. C93-160437. Authors would like to thank John Copp, CECI for his valuable comments and suggestions to the manuscript.

REFERENCES

Aydin, A. and Page, B. M., 1984, Diverse Pliocence-Quaternary tectonics in a transform environment, San Franscisco Bay region, California: *Geological Society of America Bulletin*, **95**, 1303-1317.

Caruso, C.W. and Malin, P.E., 1994, Shallow structure of the Coso geothermal field, southern Owens Valley, California from high resolution seismic refraction data, *Geophysical Research Letter*, in review.

Duffield, W.A., Bacon, C.R. and Dalrymple, G.B., 1980, Late Cenozoic volcanism, geochronogy, and structure of the Coso Range, Inyo County, California: *Journal of Geophysical Research*, **85**, 2381-2404.

Duffied, W.A. and Bacon, C.R., 1981, Geological map of the Coso volcanic field and adjacent areas, Inyo County, California, *U.S. Geological Survey Miscellaneous Investigations* I -1200.

Li, Y.-G. and Leary, P.C., 1990, Fault zone trapped seismic waves, *Bulletin of Seismology Society of America*, **80**, 1254-1271.

Li, Y.-G., Leary, P.C., Aki, K. and Malin, P.E., 1990, Seismic trapped modes in the Oroville and San Andreas fault zones, *Science*, **249**, 763-766.

Li, Y.-G., Aki, K., Adams, D., Hasemi, A., and Lee, W.H., 1994, Seismic guided waves trapped in the fault zone of the Landers, California, earthquake of 1992, *Journal of Geophysical Research*, **99**, 11705-11722.

Lou, M. and Rial, J.A., 1995a, Application of the wavelet transform in detecting multievents of microearthquake, submitted to the *Geophysical Research Letters*.

Lou, M. and Rial, J.A., 1995b, A numerical method to simulate seismic guided waves, in preparation.

Malin, P.E., 1993, Report on workshop on extensional process in the Coso and Indian Wells Valley area, July 23, 1993, Duke University.

Malin, P.E., 1994, The seismology of extensional hydrothermal system, Geothermal Resources Council TRANSACTIONS, vol.18, 17-22.

Monastero, F.C., 1992, Tectonic influence on geothermal resources in the southwestern Basin and Range, U.S.A.: *China Lake Naval Weapons Center Miscellaneous Reports*.

Pollard, D.D., 1987, Elementary fracture mechanics applied to the structured interpretation of dikes, in Halls, H.C. and Fahrig, W.F., eds., Mafic Dyke Swarms: *Geological Association of Canada Special Paper*, 5-24.

Roquemore, G.R., 1981, Active faults and associated tectonic stress in the Coso Range, California, *Naval Weapons Center Technical Publication* 6270.

Scholz, C.H., Dawers, N.H., Yu, J.Z., Andrers, M.H. and Cowie,P.A., 1993, Fault growth and fault scaling laws: Preliminary results: *Journal of Geophysical Research*, **98**, 21951-21961.

PROCEEDINGS, Twentieth Workshop on Geothermal Reservoir Engineering
Stanford University, Stanford, California, January 24-26 1995
SGP-TR-150

Effect of Sorption/Curved Interface Thermodynamics on Pressure transient

K.T.Lim and K.Aziz
Stanford University

January 1995

Abstract

A simulation model capable of handling the effects of sorption was constructed. It accounts for the curved interface thermodynamics associated with adsorption and desorption. Data from several laboratory experiments were used to verify the model. The results indicated that simulation runs using sorption isotherms adequately model the pressure transient behavior observed in the laboratory experiments. Dry steam models severely underestimated the the effective compressibility. Models using flat-interface (steam table) thermodynamics over-estimated the compressibility of the system, indicated by slower than actual rate of pressure transient propagation.

1 Introduction

In a porous medium, the interface between different fluid phases is seldom flat, like the one that would occur when the fluid is placed in a large container. The phase occurring on the concave side of a curved interface can exist at a pressure lower than its corresponding saturation pressure. (Saturation pressure is defined as the equilibrium pressure with a flat interface.) For a vapor-liquid system in equilibrium this phenomenon explains the existence of the vapor phases at pressures lower than the saturation pressure, commonly known as the vapor pressure lowering effect. Other thermodynamic effects due to the presence of a curved interface are discussed in Section 2.

The objective of this work is to construct a numerical model that honors the thermodynamics of sorption in the presence of curved interfaces. This was achieved by treating laboratory measured sorption isotherms as the governing mass balance relationship, and accounting for the thermodynamic effects of curved interfaces in the mass and energy balance equations. The model also has a separate option of using flat-interface (steam table) thermodynamics for comparison. The flat-interface option of the simulator has been verified by successfully modeling all of the cases in the Stanford Geothermal Model Intercomparison Study (1980). The numerical model with sorption was verified by modeling various laboratory adsorption and desorption experiments. Comparisons were made against models with flat-interface thermodynamics and single-phase dry steam. The following discussions focus on the implementation of the sorption model.

2 Thermodynamic Effects of Curved Interface

Apart from the vapor-pressure lowering effect, the presence of a curved interface also causes an increase in the heat of vaporization compared to that with a flat interface. Equilibrium thermodynamics analyses also showed that curved interface causes both phases to exist in superheated states (Udell 1982). The thermodynamics relationships outlined in this section follow those of Defay and Prigogine (1966) and Kaviany (1991).

2.1 Vapor Pressure Lowering

Consider a liquid and a vapor phase in equilibrium in the presence of a curved interface. Starting with the Gibbs-Duhem equation for each phase, it can be shown that the presence of a curved interface implies the existence of a pressure difference between the liquid and vapor phases — the capillary pressure:

$$p_c = p_v - p_l \quad (1)$$

The phase occurring on the concave side of a curved interface can exist in equilibrium at a pressure lower than its corresponding saturation pressure by a quantity equal to the capillary pressure.

2.2 Liquid Superheat

The thermodynamics relationship for determining the amount of superheat in the liquid phase is:

$$\left(\frac{1}{T} - \frac{1}{T^o}\right) = \frac{R}{h_{fg}} \ln\left(\frac{p_v}{p_l}\right) \qquad (2)$$

The quantity $(T-T^o)$ is the degree of superheat in the liquid phase. By honoring Eq. 2 while solving for p_l as a secondary variable an input of p_c is unnecessary because it will overconstrain the solution.

2.3 Increase in Heat of Vaporization

The presence of curvature also causes an increase in the heat of vaporization in comparison with the corresponding value when a flat interface is present:

$$h_{fg} = h^\circ_{fg} + \left(v_l - T\left.\frac{\partial v_l}{\partial T}\right|_{p_l}\right)(p_c) \qquad (3)$$

where the superscript '°' refers to a case with flat-interface. In general (Kaviany, 1991),

$$v_l \gg T\left.\frac{\partial v_l}{\partial T}\right|_{p_l}$$

so that the last term in Eq. 3 can be ignored. In the model the heat of vaporization is computed as:

$$h_{fg} = h^\circ_{fg} + \left(\frac{p_v - p_l}{\rho_l}\right) \qquad (4)$$

3 Governing Equations

Mass, energy and momentum balances are the three governing equations of fluid flow. For a given component c in a multicomponent system the mass balance equation is:

$$\frac{\partial}{\partial t}\left[\sum_p y_{cp}\phi\rho_p S_p\right] + q^w_c - \sum_p \nabla\cdot[y_{cp}\rho_p\vec{v}_p] = 0 \qquad (5)$$

The terms in Eq. 5 are, respectively, rate of accumulation, source/sink term and net influx of component c. For a given phase p, the momentum balance in a porous media is governed by Darcy's Law:

$$\vec{v}_p = \frac{kk_{rp}}{\mu_p}(\nabla p_p - \rho_p\, g\nabla D) \qquad (6)$$

Eqs. 5 and 6 are combined to form a mass balance equation for each component.
The energy balance equation is:

$$\frac{\partial}{\partial t}\left[\sum_p \phi\rho_p S_p U_p + (1-\phi)\rho_r U_r\right] + q^w h^w - H$$

$$-\sum_p \nabla\cdot(\rho_p\vec{v}_p h_p) - \nabla\cdot(\lambda\nabla T) = 0 \qquad (7)$$

The physical meaning of the terms in Eq. 7 are, respectively, rate of accumulation of internal energy, heat production, specified heat influx, energy associated with fluid influx and heat conduction term.

3.1 Primary Variables

Each simulation gridblock has n_c mass balance equations and one energy balance equation. Therefore, the number of independent primary variables required is $n_c + 1$. The primary variables are chosen such that the variables are independent of one another over all physical regions of the fluid system. The primary variables chosen for this study are

- p_v (pressure in the vapor phase, 1 variable)
- z_c (overall mole fractions of component c, $n_c - 1$ variables)
- h (overall specific enthalpy of fluid, 1 variable)

For a single component system, the primary variables are p_v and h.

3.2 Secondary Variables

After the primary variables are obtained, the remaining variables can be determined using constitutive relationships and phase equilibrium calculations. The variables to be determined are temperature, liquid phase pressure and phase saturations. Flat-surface thermodynamics and regions with sorption (i.e. curved interface) are treated separately. The following discussion is limited to single component, two-phase systems.

3.2.1 Flat-Interface Thermodynamics

A flat interface between the liquid and vapor phases implies that both phases exist at the same pressure. Saturated steam (steam table) properties are applicable.

In the two phase region pressure and temperature are dependent on each other, and saturations can be easily determined from the primary unknowns. At a given temperature, mass transfer between the phases can occur without a change in pressure.

In the single phase (compressed water and superheated steam) regions fluid properties are functions of both pressure and temperature. The temperature is determined iteratively by satisfying all constitutive relations and equilibrium thermodynamics. Convergence can be easily obtained in very few iterations because the temperature of a reservoir does not vary much, with the probable exception around source or sink locations.

3.2.2 Sorption

In the sorption model the mass balance is influenced by the sorption isotherm. The isotherms relate the mass adsorbed to pressure and specified temperatures. Knowledge of the pressure and temperature would allow explicit determination of phase saturations. To account for temperature variations, mass-relative pressure isotherms are internally converted to mass-activity relationships (Hsieh and Ramey, 1983). For a given adsorbed mass (X, mass-of-water/mass-of-rock) the liquid saturation is:

$$S_l = \frac{1-\phi}{\phi} \frac{\rho_r}{\rho_l} X \qquad (8)$$

In this case the liquid phase pressure, p_l, becomes a secondary unknown instead of saturation. It is to be determined by satisfying all the thermodynamic effects described in section 2.

4 Verification

Results from three separate sets of laboratory pressure transient experiments were used to verify the numerical models. All numerical models are one-dimensional. Analyses were made for the case of a single component steam-water system. For comparison purposes, the corresponding cases assuming flat-interface thermodynamics and dry steam were also analyzed. The flat surface thermodynamics cases were initialized with the same liquid saturations as those in the corresponding cases with sorption. The dry-steam cases assumed zero liquid saturation and that the steam remained as single phase vapor at all times.

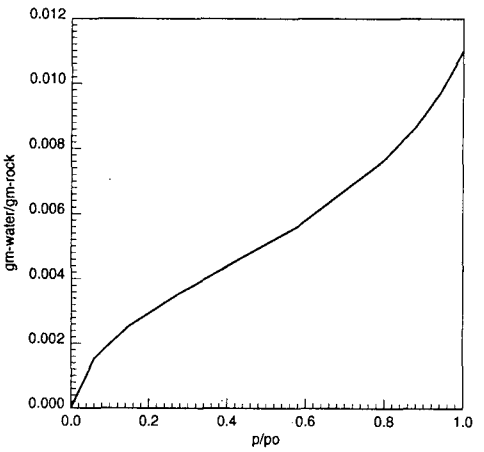

Figure 1: Isotherm for temperature of 146°C, from Herkelrath et al. (1983).

Analyses also showed that the results were not sensitive to the gridblock sizes, but are very sensitive to the sorption isotherms.

4.1 Adsorption: Data of Herkelrath et al. (1983)

Herkelrath et al. (1983) conducted a series experiments to study the transient steam flow in a uniform porous medium. A sample holder 61 cm long with an internal diameter of 5.04 cm was used. Transient, superheated steam flow experiments were run by first bringing the porous material to a uniform initial pressure. A step increase in pressure was imposed at one end of the sample by exposing it to a saturated steam reservoir while measuring the pressure at the other end. The experiments were conducted at 100°, 125° and 146°C. The corresponding adsorption isotherm was measured separately. Fig. 1 shows the isotherm for this study.

Laboratory data and simulation results for the experiment conducted at 146°C are shown in Fig. 2. Simulation results assuming gas flow theory (for the case labeled dry steam) and flat interface thermodynamics are also shown. The results showed that the transient pressure response could be adequately modeled with the sorption model using the measured adsorption isotherm. This observation was also made by Herkelrath et al. (1983). The sorption model takes

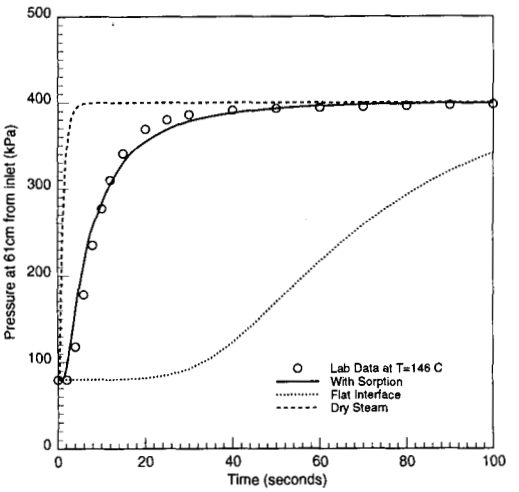

Figure 2: Transient flow experiment of Herkelrath et al. (1983) at 146°C.

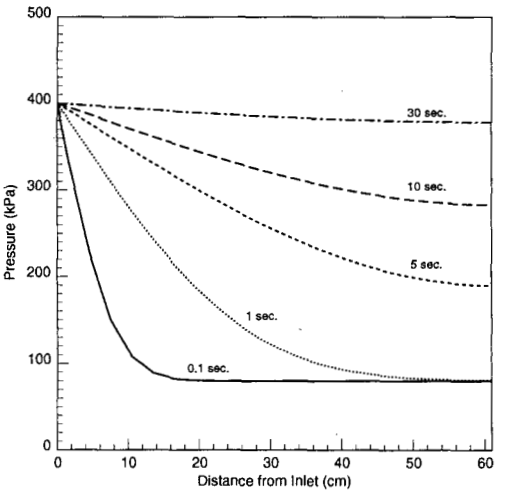

Figure 3: Pressure distributions for the 146°C case, sorption model.

into account the fact that there always exists a pressure difference between the vapor and liquid phases and can be adequately represented by the pressure-sorption relationship contained in the isotherm. The dry steam case severely underestimated the time required for the pressure at one end of the core to reach the pressure imposed at the other end. This is due to the absence of phase change associated with adsorption of steam on the rock surfaces, which would reduce the speed of pressure propagation. Assuming flat surface thermodynamics, on the other hand, caused a delay in pressure response compared to the experimental data. This is because the quantity $\frac{\partial V}{\partial p}$ at a given temperature is infinite in the two phase region. In each simulation gridblock this phenomenon results in steam condensation at an almost constant pressure. Pressure changed during condensation because the model was not isothermal, with the injected steam having a higher temperature than the initial conditions in the model. The is reflected in the simulation result as a model having very large apparent compressibility.

To illustrate the differences in pressure responses, the pressure distributions at various times for the sorption and flat-interface models are shown in Figs. 3 and 4, respectively. With flat surface thermodynamics, the speed of pressure propagation is almost an order of magnitude slower compared to that with sorption. Pressure distributions at 1 and 5 second for the sorption model resembles those at 10 and 50 seconds for the flat interface model.

Results of the 100° and 125°C cases showed essentially the same results as the 146°C case.

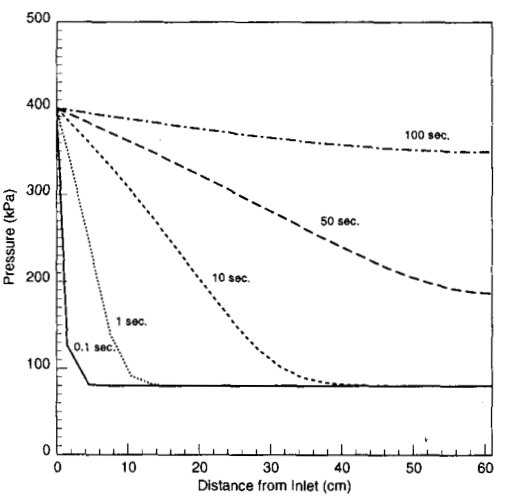

Figure 4: Pressure distributions for the 146°C case, with flat-interface thermodynamics.

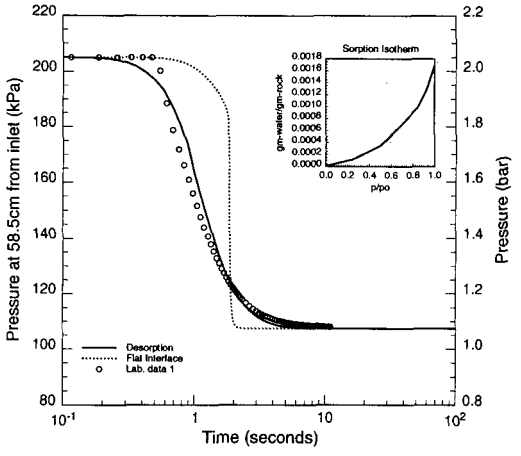

Figure 5: Desorption experiment of Palar and Horne (1994).

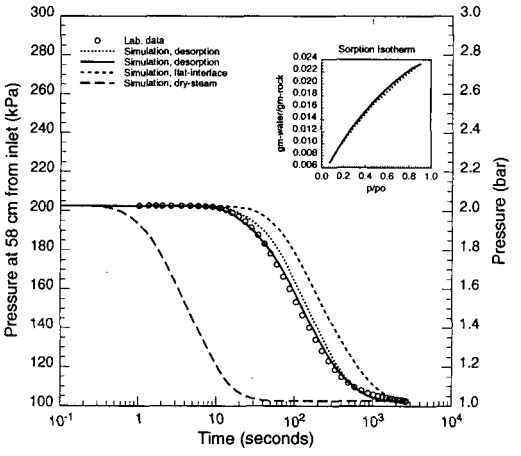

Figure 6: Desorption experiment of Herkelrath (1994)

4.2 Desorption: Data of Palar and Horne (1994)

Palar and Horne (1994) used equipments similar to that of Herkelrath et al. (1983) to conduct desorption experiments. A rock sample from the Geysers geothermal field was used. The sample was exposed to saturated steam at about 125°C and the corresponding saturation pressure. One end of the sample holder was exposed to the atmosphere while the pressure change at the other end was monitored. Fig. 5 shows the measured transient pressure decline against time. Due to the low level of adsorption (the estimated overall liquid saturation is less than 1 per cent), and high permeability of the sample (37.5 darcy) the pressure decline propagated to the closed end of the sample holder very rapidly. Also shown in Fig 5 are the simulated results with the sorption and flat-interface models. The sorption isotherm inset in Fig 5 is the isotherm used in the simulation model. The isotherm is a slight modification of that obtained by Palar and Horne (1994) using regression analysis. Again the sorption model gives a good match with the laboratory observations. The flat-interface model results implied a very large effective compressibility, as indicated by the delayed pressure drop.

4.3 Desorption: Data of Herkelrath (1994)

The experiment was run using a column packed with Tipperary Sand, a dune sand obtained near Fallon, Nevada. The samples contain only the less-than 106 micron fraction of the sand. The following are the sample data:

sample mass	1941 g
sample length	58 cm
sample diameter	5.2 cm
porosity	0.42
permeability	1.61E-08 cm**2

Steam pressure-drawdown experiment was run at 123°C. The sample was evacuated and then charged with steam until the steam pressure reached 2.026 bars, and the temperature stabilized. At time=0, the bottom of the sample was opened to the atmosphere, and the pressure at the top of the sample was monitored as a function of time. Sorption isotherm was measured in a separate equilibrium experiment using the same sample. Simulation results are shown in Fig. 6. The dotted line is the results obtained using sorption data of Herkelrath (1994). It gave a much better match to the laboratory data than either the dry-steam or the flat-interface case. An excellent match was obtained by modifying the sorption isotherm very slightly, as shown by the solid line in Fig. 6. Considering the fact that the same sample was used for two separate experiments with different packings, the differences between the isotherms shown in Fig. 6 are well within experimental accuracy.

5 Conclusions

From the preceding discussions the following conclusions can be made:

1. A numerical model capable of honoring the thermodynamics of sorption has been constructed and verified against laboratory experiments.
2. Pressure transient due to sorption could be adequately modeled using equilibrium sorption isotherms, and the results were in excellent agreement with experimental observations.
3. Sorption of steam on rock surfaces results in delayed transient pressure response and in a higher apparent compressibility compared to a dry steam case. However, the apparent compressibility due to sorption is much lower than that of a flat-interface model.
4. Direct application of steam table properties in the flat interface models resulted in very large apparent compressibilities and in delayed pressure transient propagation compared to those observed in experiments.

Nomenclature

h = specific enthalpy
H = heat influx
k = permeability
k_r = relative permeability
p = pressure
p_c = capillary pressure
R = universal gas constant
T = temperature
q = source/sink term
s = specific enthropy
S = saturation
t = time
T = temperature
U = specific internal energy
v = specific volume
$\vec{v}$ = velocity
X = adsorption, mass/mass-of-rock
y = mole fraction
z = overall mole fraction
λ = thermal conductivity
μ = viscosity, or chemical potential
ϕ = porosity
ρ = density

Subscripts

c = component
g = gas phase
l = liquid phase
r = rock
p = a given phase
v = vapor phase

Superscripts

$^\circ$ = saturated state
^{T} = total
^{w} = well

References

[1] Defay, R. and Prigogine, I.: *Surface Tension and Adsorption*, J. Wiley (1966).

[2] Herkelrath, W.N., Moench, A.F. and O'Neal, C.F. II.: "Laboratory Investigation of Steam Flow in a Porous Medium," *Water Resources Research, Vol* 19, No. 4, August 1983, 931-37.

[3] Herkelrath, W.N., personal communication, June 1994.

[4] Hsieh, C.H. and Ramey, H.J. Jr.: "Vapor-Pressure Lowering in Geothermal Systems," *SPEJ*, February 1983, 157-67.

[5] Kaviani, M.: *Principles of Heat Transfer in Porous Media*, Springer-Verlag (1991).

[6] Palar, S. and Horne, R.N.: "The Effect of CO_2 on Steam Adsorption," presented at the 19th Stanford Geothermal Workshop, Stanford CA., Jan. 18-20, 1994.

[7] Stanford Geothermal Program TR-42: "Proceedings, Special Panel on Geothermal Model Intercomparison Study," Stanford, CA., December 1980.

[8] Udell, K.S.: "The Thermodynamics of Evaporation and Condensation in Porous Media," SPE 10779 presented at the 1982 California Regional Meeting of SPE, San Francisco, CA., March 24-26, 1982.

PROCEEDINGS, Twentieth Workshop on Geothermal Reservoir Engineering
Stanford University, Stanford, California, January 24-26 1995
SGP-TR-150

A PORE NETWORK MODEL FOR ADSORPTION IN POROUS MEDIA

Cengiz Satik

Stanford Geothermal Program
Stanford University
Stanford, CA 94305-2220

and

Yanis C. Yortsos

Petroleum Engineering Program
Department of Chemical Engineering
University of Southern California
Los Angeles, CA 90089-1211

ABSTRACT

Using a pore network model to represent porous media we investigate adsorption-desorption processes over the entire range of the relative pressure, highlighting in particular capillary condensation. The model incorporates recent advances from density functional theory for adsorption-desorption in narrow pores (of order as low as 1 *nm*), which improve upon the traditional multi-layer adsorption and Kelvin's equation for phase change and provide for the dependence of the critical pore size on temperature. The limited accessibility of the pore network gives rise to hysteresis in the adsorption-desorption cycle. This is due to the blocking of larger pores, where adsorbed liquid is allowed to but cannot desorb, by smaller pores containing liquid that may not desorb. By allowing for the existence of supercritical liquid in pores in the *nm* range, it is found that the hysteresis area increases with an increase in temperature, in agreement with experiments of water adsorption-desorption in rock samples from The Geysers. It is also found that the hysteresis increases if the porous medium is represented as a fractured (dual porosity) system. The paper finds applications to general adsorption-desorption problems but it is illustrated here for geothermal applications in The Geysers.

INTRODUCTION

In sorption experiments, a condensible gas is introduced into a porous medium, which is initially evacuated. The gas pressure is then progressively increased at constant temperature until it reaches the saturation pressure value at the given temperature. Measuring the amount adsorbed at equilibrium as a function of the relative pressure constitutes the adsorption stage. Desorption is the reverse cycle, where the adsorbed phase desorbs by progressively decreasing the gas pressure. Information on the surface area, the pore size distribution and other properties can be obtained from an analysis of these cycles. Gas adsorption-desorption in porous media differs from adsorption on open surfaces due to two factors, the existence of curved surfaces or pores, where capillary condensation may occur, and possible accessibility or topological effects incurred by the porous medium.

In adsorption of gases over an unconstrained surface, at the early adsorption stage, corresponding to sufficiently small gas pressure, gas molecules are physically adsorbed on the solid surface owing to sorbent-solid molecular interactions. As the process continues, one and subsequently multiple layers of adsorbed fluid cover the solid surface. For larger values of pressure, the thickness of the adsorbed layer is sufficiently large so that the adsorbed fluid behaves as a continuum *liquid* film, at which point a distinct vapor-liquid interface exists. The thickness of the adsorbed layer depends on the gas pressure as well as other parameters that are gas and solid specific. Eventually, as the pressure approaches the saturation pressure, bulk condensation occurs.

In adsorption of gases in pores, the early part of adsorption is similar to the above. Because of the pore wall curvature, however, bulk condensation

occurs earlier (at a lower relative pressure) than over a flat surface. This capillary condensation is described by Kelvin's equation, to be discussed in detail below. Additionally, in narrow pores (of the order of a few nm), due to the proximity of solid surfaces, the growing film is subject to strong intermolecular forces. As a result, capillary condensation may occur earlier and at conditions different than predicted by Kelvin's equation. For sufficiently small pores, a phase change may actually not occur, and the fluid remains in a supercritical state, as discussed below.

LITERATURE REVIEW

Understanding adsorption-desorption in porous media requires first its understanding in single pores (slits, cylinders), and subsequently the understanding of the collective behavior of an ensemble (network) of pores. Below we briefly review the relevant literature in these two areas.

1. Single-pore models: The literature in this area can in turn be divided into two parts: (i) Surface (physical) adsorption in the absence of pores, where single- and multi-layer adsorption are emphasized. Clearly, no hysteresis in adsorption-desorption cycles is observed here. A comprehensive review of this subject can be found in Gregg and Sing (1982) and Adamson (1990). For the purposes of this paper we note that the thickness of the adsorbed layer can be expressed by various models, of which we shall make use of the following

$$t = \left(\frac{\epsilon_o}{RT \ln \frac{P_{V0}}{P_V}} \right)^{\frac{1}{\alpha}} \qquad (1)$$

where t is the thickness of the adsorbed layer, ϵ_o is the adsorption potential of the solid surface, $\frac{P_V}{P_{V0}}$ is the relative pressure, and α is an empirical parameter. This expression is derived from the Frankel-Halsey-Hill (FHH) equation [1]. Although used over the entire pressure range, the accuracy of the above equation is questionable at very small pressures. However, for the purposes of this study, we shall use the FHH equation over the entire pressure range.

(ii) Adsorption-desorption in pores. Following multi-layer adsorption, capillary condensation occurs. This is traditionally described by Kelvin's equation

$$\ln \left(\frac{P_V}{P_{V0}} \right) = -\frac{2\sigma V_L}{R_g T (R - t)}, \qquad (2)$$

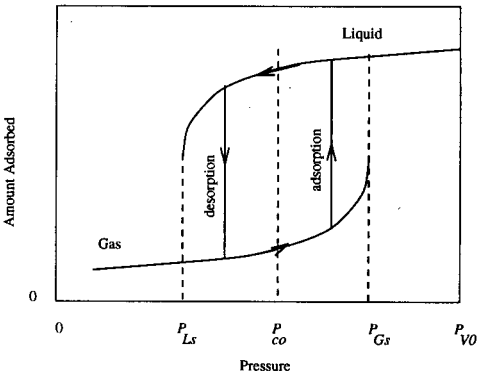

Figure 1: Schematic isotherms indicating single-pore hysteresis (from Liu et al. (1993)).

where $\sigma, V_L, R_g, T, P_V, P_{V0}$ and R are the surface tension, the liquid molar volume, the gas constant, the absolute temperature, the gas pressure, the saturation vapor pressure and the pore radius, respectively. Actually, the above is a modified form of Kelvin's equation, where the pore radius was appropriately reduced by the amount of the adsorbed film. In the standard approach, the onset of capillary condensation denotes an instability of the film (gas-liquid) interface due to the pore curvature. In fact, this mechanism is also responsible for a single-pore hysteresis, where the phase change (from liquid to vapor) during desorption occurs at a radius smaller by a factor of 2 than (2).

An explanation of single-pore hysteresis is given in Figure 1 which shows schematic isotherms for a single pore (from Liu et al. (1993)). Condensation or evaporation in a single pore is to take place at a pressure, P_{co}, at which liquid and gas coexist and the chemical potentials for liquid and gas phase are the same. However, it is possible for condensation and evaporation to be delayed until pressure values different than P_{co}. Now, adsorption and desorption follow the spinoidal branches shown in Figure 1. The onset of phase change may occur at pressure values between P_{co} and P_{Gs} (the spinoidal pressure for the gas phase), and between P_{co} and P_{Ls} (the spinoidal pressure for liquid phase) for condensation and evaporation, respectively. Kelvin's equation in the two different geometries accounts for these two different presures. The end result is that even for a single pore different paths can be followed depending on the direction (condensation or evaporation).

When the pores involved are narrow, fluid

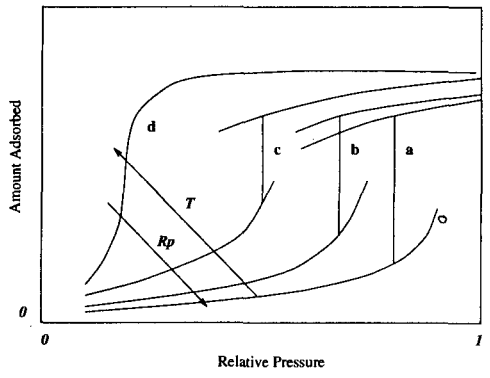

Figure 2: Schematic of adsorption-desorption isotherms in a narrow pore.

molecules interact with solid surfaces on either side of the pore (Evans et al. (1986) and Ball and Evans (1989)), thus adsorption and desorption are strongly affected. Consider, for example, the process in a narrow pore (Figure 2). As pressure increases, the usual adsorption behavior is followed. At low temperatures (and large radius values) the single-pore behavior is as shown in Figure 1. However, as the temperature increases (or the pore radius decreases), the isotherms shift towards the left, while the jumps between liquid and gas branches at the phase transition become smaller (curves a, b and c in Figure 2). Significantly, for a critical value of temperature or a critical size of the pore, the adsorbed fluid becomes supercritical and a clear transition is not observed (curve d in the Figure). Evans et al. (1986) defined this as the *capillary critical point*, beyond which a distinct vapor-liquid interface ceases to exist and the density increases monotonically over the whole range of pressure. Evidently, use of Kelvin's equation will be inappropriate in this range. We note that this behavior is reminiscent of the critical behavior in a bulk liquid. Evans et al. (1986) used a functional density approach to study the characteristics of adsorption in such pores. They obtained the following approximate expression for the critical capillary radius

$$R_{cr} \sim \frac{1}{\lambda} \frac{T_{cr}}{T_{cr} - T} \qquad (3)$$

where R_{cr}, λ and T_{cr} are the critical capillary radius, the decay length of solid-fluid potentials (a function of solid and liquid) and the critical temperature of the fluid, respectively. It should be noted that single-pore hysteresis is also predicted from the theory of Evans et al. (1986), as can be seen schematically in the Figure isotherms.

Along similar lines, but using Monte-Carlo computer simulations, adsorption in narrow pores was studied by Nicholson (1975), Seaton et al. (1989), Aukett et al. (1992) and Lastoskie et al. (1993).

2. Multiple-pore models: Early work on adsorption-desorption made use of the simple model of parallel capillaries (Everett and Haynes (1972)). Mason (1983) suggested that accessibility effects would be important in porous media and attempted to model adsorption-desorption hysteresis by a probabilistic approach. Parlar and Yortsos (1988) and (1989) realized that the process shares common aspects with percolation phenomena and proceeded to explain desorption-adsorption hysteresis, based on the lack of accessibility of liquid-containing pores to bulk (connected) vapor. The following rules were postulated: for phase change to occur in a pore (body or throat), the pore radius first must be consistent with Kelvin's equation (be allowed). At any capillary condensation (adsorption) stage R, given by an equilibrium pressure P_V (equation 2), vapor in all pore bodies with $R_P < R$ and all pore throats with $R_P < R/2$ is *allowed* to condense. Since vapor has access to all of the pores in the network during adsorption, condensation occurs in all pores that are *allowed*. On the other hand, for capillary evaporation (desorption) to take place in a pore with size R_P, the following two conditions must hold: (a) $R_P > R$ and (b) the pore (body or throat) must have access to vapor phase (either to bulk vapor or to a nucleation center). These two rules include the two plausible mechanisms of hysteresis behavior observed in adsorption experiments for porous solids, namely the local (or single-pore) hysteresis [3] and the network (or pore blocking) effect [17]. The first mechanism, reflected above as a difference of 1/2 between adsorption and desorption radii, may appear in pore throats due to the cylindrical geometry. The second mechanism may occur during desorption due to the necessity of having access to vapor. The origin of the second mechanism for hysteresis is due to the topology of the pore space. Depending on the geometry of pore network, evaporation in some large pores may not occur if they are surrounded by small pores that are not allowed to desorb at the particular pressure value.

Recently, the work of Parlar and Yortsos (1988) was expanded by Liu et al. (1993) .

3. Empirical approaches: In relation to the adsorption behavior of steam in The Geysers, many previous studies have been conducted, in-

cluding those by Hsieh (1980), Hsieh and Ramey (1983), Luetkehans (1988), Harr (1991), Hornbrook (1994) and Shang et al. (1994). A recent attempt was made by Correa and Ramey (1994) to explain experimental results with the use of some empirical models. Recent experiments by Satik and Horne (1995) have shown a dramatic temperature effect on hysteresis and the existence of a "residual" value in the amount of desorbed liquid. This cannot be explained convincingly by the work published so far. In this paper, we shall use a pore network model coupled with the theory of Evans et al. (1986) to propose a possible explanation of this effect. More generally, the paper develops a general pore network model for adsorption-desorption processes in porous media.

The paper is organized as follows: First, the pore network model is described. The model results are then compared with the experiments and the sensitivity to effects of temperature and mean pore size is described. Finally, we briefly examine the effect of correlated porespace on the adsorption-desorption behavior.

PORE NETWORK MODEL AND RESULTS

To simulate the process of sorption in porous media, we have made use of a pore network model. We represent the pore space by a 3-D lattice composed of pore bodies (sites) and connections between pore bodies (bonds or pore throats). In this approach, pore bodies and throats are approximated by spherical and cylindrical geometries, respectively. A simple cubic lattice, where six bonds emanate from a site, corresponding to a coordination number of six, is taken (although other lattice types can also be used). Radii for sites and bonds were randomly distributed from a truncated Gaussian random distribution with means 32.5 nm and 5.5 nm, respectively and standard deviations of 35 nm and 9 nm, respectively, while the bond length (l_b) was kept constant at 25 nm. Adsorption and desorption were modeled following the rules of Parlar and Yortsos (1988).

Adsorption proceeds by multi layer adsorption, modeled via the FHH equation, then capillary condensation in sufficiently large pores occurs. We used the modified Kelvin equation for its description. For desorption to occur, the given pore must have size sufficiently large, as predicted by Kelvin's equation or its modifications, but it must also be connected to the bulk vapor. Narrow pores containing supercritical liquid were not allowed to desorb. Owing to stability considerations [17], if a bond is occupied by vapor, the two adjacent sites are also occupied by vapor, while if a site is occupied by liquid, all bonds connected to it are also occupied by liquid.

As discussed above, during a typical sorption experiment for porous solids, a hysteresis behavior is commonly observed. Depending on the process parameters, different types of hysteresis can be expected. Although different in shape, in most cases adsorption and desorption isotherms coincide below a moderate pressure value, indicating the end of hysteretic behavior. However, a rather unusual hysteresis was observed in high temperature steam adsorption experiments conducted in samples obtained from The Geysers geothermal field (see Satik and Horne (1995)). These experiments showed that at higher temperatures, e.g. 120 °C, hysteresis persists down to very low pressures, of order 0.001 psia, while diminishing at lower temperatures. With the use of the pore network model, we have attempted to investigate this behavior and to interpret the effects of temperature. In all simulations presented the size of the network was taken to be 20x20x20, which was found to be sufficiently large to eliminate finite-size effects.

Figure 3 shows two sorption isotherms obtained from the numerical model at 80 and 120 °C. The figure shows a very good agreement with the experimental findings of Satik and Horne (1995). In particular, the two main experimental features are clearly observed in the simulations: A hysteresis persisting down to very small pressures, at high temperature values, and a diminishing of the hysteresis cycle at lower temperatures. Figure 4 shows a comparison of the simulation results with the experiments (for a sample from The Geysers) of Satik and Horne (1995). Figure 4a and 4b shows the experimental results, while Figure 4c and 4d contain the numerical results obtained at 120 and 80 °C, respectively. A very good agreement is shown, considering the experimental errors involved. Figure 5 shows the effect of the mean radius on the adsorption curves. We have examined three cases with mean radius corresponding to 5.5, 6 and 10.5 nm,respectively. As shown in the figure, the degree of hysteresis increases as the mean radius decreases. This is expected in view of both the Kelvin equation and the effects of the critical capillary radius. The implication is that the rock samples treated by Satik and Horne (1995) must contain pores of a narrow size (of order of a few

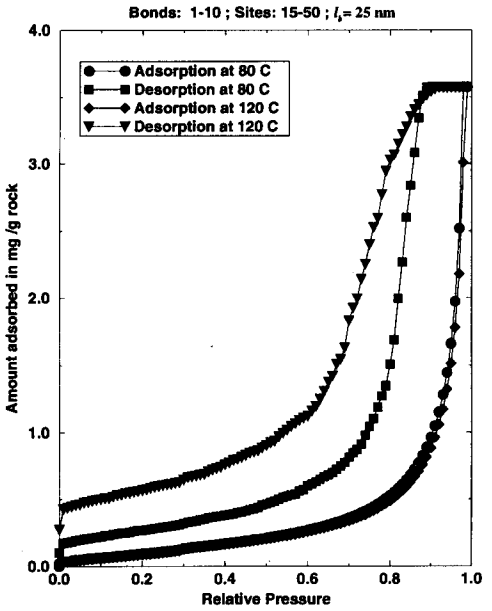

Figure 3: Sorption isotherms in pore networks at 80 and 120 °C.

nm).

Experimental and numerical results show that hysteresis diminishes as the temperature decreases, this is opposite to the trend in a single-pore. We explain this as follows: As temperature increases, the capillary critical radius, below which fluids occupying pore space are supercritical, also increases. This implies that a larger fraction of pores contain supercritical fluid. The fluid density in these pores decreases slowly and monotonically with pressure from an initial liquid-like density to a gas-like density at very small pressures (see curve d in Figure 2). In a pore network, these small pores eventually surround larger pores, preventing them from desorption due to the pore-blocking effect explained above. This behavior results in the hysteresis persisting until very small pressure values, and being a strong function of temperature.

Figure 6 shows a comparison of the sorption isotherms obtained for a fractured and an uncorrelated pore network. A fractured system was generated by assigning two very different average pore size values, with smaller values assigned to the "matrix" and larger values assigned to the "fracture" system. For the results shown in the figure, the fracture sysytem consisted of five orthogonal fracture planes parallel to the three coordinates of the cubic lattice (x=const,y,z), (x,y=const,z) and

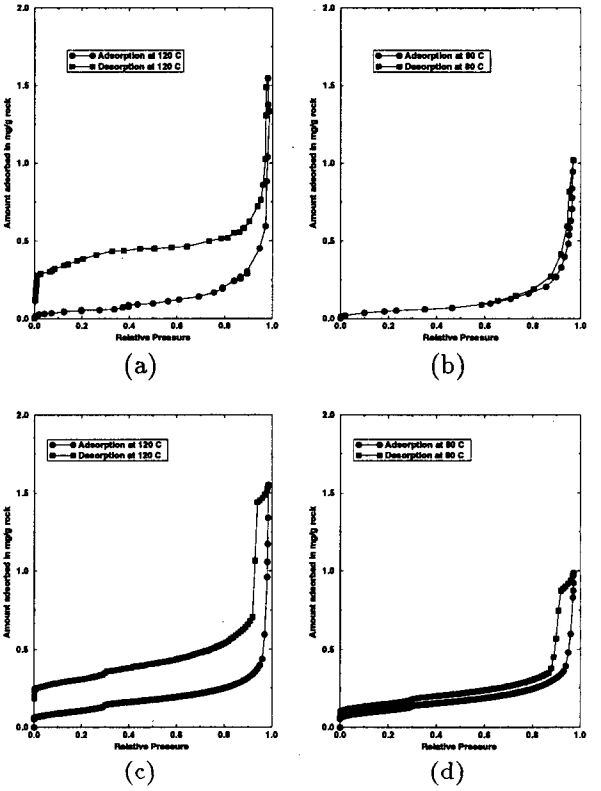

Figure 4: Comparison of the experimental sorption isotherms (a and b) obtained for a Geysers sample at 120 and 80 °C (from Satik and Horne (1995)) with the results from the pore network model (c and d).

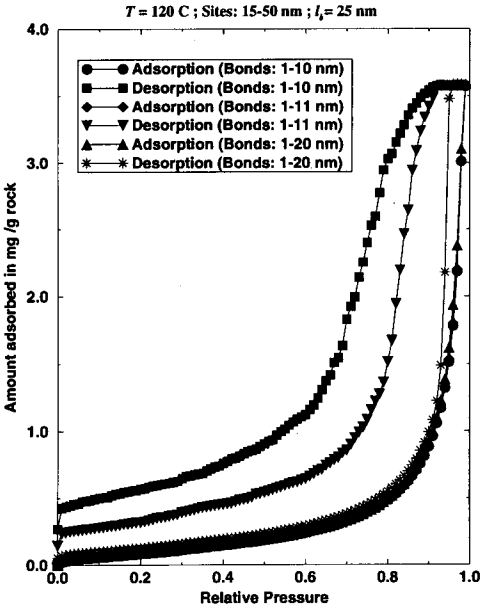

Figure 5: Effect of the mean radius on sorption isotherms in pore networks.

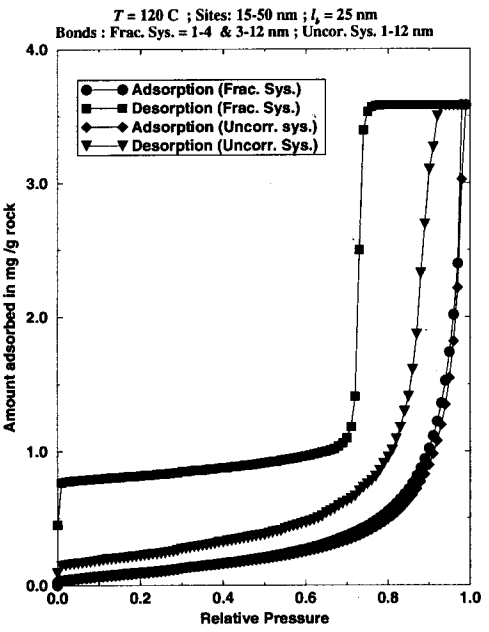

Figure 6: Comparison of sorption isotherms obtained for a fractured and an uncorrelated pore network.

(x,y,z=const), each spanning the whole network and intersecting each other. As shown in the figure, the fractured systems display a pronounced hysteresis behavior compared to uncorrelated systems. This is also due to the pore blocking effect. We must note, however, that the hysteresis behavior shown in Figure 6 will not depend on temperature, hence a fracture network itself would not be able to simulate the experimental results if the previous mechanism involving supercritical fluid is not accounted for.

CONCLUSIONS

We have presented a pore network model that incorporates improved single-pore pheneomena for adsorption and desorption in porous media, particularly the supercritical behavior at narrow pores. The latter accounts for substantial hysteresis which depends sensitively on temperature. The network model gives results in good agreement with the experiments. This hysteresis is attributed to a pore blocking mechanism, where narrow pores containing supercritical fluid prevent larger pores from desorbing, due to lack of access to bulk vapor. Hysteresis is also found to increase in a dual porosity (fracture) system.

ACKNOWLEDGEMENTS

The work of the first author CS was supported by DOE contract DE-FG07-90ID12934 through Stanford Geothermal Program. YCY was supported by DOE contract DE-FG22-90BC14600. The contribution of these sources is gratefully acknowledged.

References

[1] Adamson, A. W.: *Physical Chemistry of Surfaces*, John Wiley & Sons, New York (1990).

[2] Aukett, P., Quirke, N., Riddiford, S., and Tennison, S. R.: "Methane adsorption on microporous carbons-A comparison of experiment, theory and simulation," *Carbon* (1992) **30**, 913–924.

[3] Ball, P. C. and Evans, R.: "Temperature dependence of gas adsorption on a mesoporous solid: Capillary criticality and hysteresis," *Langmuir* (1989) **5**, 714–723.

[4] Correa, A. C. and Ramey, H. J., J.: "Theoretical Investigation of adsorption in Porous

media," Submitted to SPE Advanced Technology Series, 1994.

[5] Evans, R., Marconi, U. M. B., and Tarazona, P.: "Capillary condensation and adsorption in cylindrical and slit-like pores," *Chem. Soc. Faraday Trans. 2* (1986) **82**, 1763–1787.

[6] Everett, D. H. and Haynes, J. M.: "Model studies of capillary condensation: I. Cylindrical pore model with zero contact angle," *J. Colloid and Interface Science* (1972) **38(1)**, 125–137.

[7] Gregg, S. J. and Sing, K. S. W.: *Adsorption, Surface Area and Porosity*, Academic Press, London and New York (1982).

[8] Harr, M. S.: "Laboratory Measurements of Sorption in Porous Media," M.S Report, Stanford University, 1991.

[9] Hornbrook, J.: "The effects of adsorption on injection into and production from vapor dominated geothermal reservoirs," Ph.D. Thesis, Stanford University, 1994.

[10] Hsieh, C. H.: "Vapor Pressure Lowering in Porous Media," Ph.D. Thesis, Stanford University, 1980.

[11] Hsieh, C. H. and Ramey, H. J., J.: "Vapor Pressure Lowering in Geothermal Systems," *SPEJ*, Vol 23(1), pp. 157-167, 1983.

[12] Lastoskie, C., Gubbins, K. E., and Quirke, N.: "Pore Size Heterogeneity and the Carbon Slit Pore: A Density Functional Theory Model," *Langmuir* (1993) **9**, 2693–2702.

[13] Leutkehans, J.: "A Laboratory Investigation of Steam Adsorption in Geothermal Rocks," M.S Report, Stanford University, 1988.

[14] Liu, H., Zhang, L., and Seaton, N. A.: "Analysis of sorption hysteresis in mesoporous solids using a pore network model," *Chem. Eng. Sci.* (1993) 285–293.

[15] Mason, G.: "A model of adsorption-desorption hysteresis in which hysteresis is primarily developed by the interconnections in a network of pores," *Proc. R. Soc. London A* (1983) **390**, 47–72.

[16] Nicholson, D.: "Molecular Theory of Adsorption in Pore Spaces," *J. Chem. Soc. Faraday Trans. 1* (1975) **71**, 238–255.

[17] Parlar, M. and Yortsos, Y. C.: "Percolation theory of vapor adsorption-desorption processes in porous materials," *J. of Colloid and Int. Sci.* (1988) **124(1)**, 162–176.

[18] Parlar, M. and Yortsos, Y. C.: "Nucleation and Pore Geometry Effects in Capillary Desorption Processes in Porous Media," *J. of Colloid and Int. Sci.* (1989) **132(2)**, 425–443.

[19] Satik, C. and Horne, R. N.: "An experimental Study of Adsorption in vapor-dominated geothermal systems," To be presented at the Twentieth Stanford Geothermal Workshop 1995, Stanford, CA, Jan. 24-26 1995.

[20] Seaton, N. A., Walton, J. P. R. B., and Quirke, N.: "A new analysis method for the determination of the pore size distribution of porous carbons from nitrogen adsorption measurements," *Carbon* (1989) **27**, 853–861.

[21] Shang, S. B., Horne, R. N., and Ramey, H. J., J.: "Study of water adsorption on geothermal reservoir rocks," Submitted to *Geothermics*, 1994.

PROCEEDINGS, Twentieth Workshop on Geothermal Reservoir Engineering
Stanford University, Stanford, California, January 24-26 1995
SGP-TR-150

AN EXPERIMENTAL STUDY OF ADSORPTION IN VAPOR-DOMINATED GEOTHERMAL SYSTEMS

Cengiz Satik and Roland N. Horne

Stanford Geothermal Program
Stanford University
Stanford, CA 94305-2220

ABSTRACT

We report results of steam adsorption experiments conducted for rock samples from vapor-dominated geothermal reservoirs. We examine the effect of the temperature on the adsorption/desorption isotherms. We find that the temperature effect is only important on the desorption such that the hysteresis becomes more pronounced as the temperature increases. The scanning behavior within the steam sorption hysteresis loop is also studied to investigate the behavior during repressurization. Collection of sets of data on the sorption behavior of The Geysers geothermal field in California is presented.

INTRODUCTION

Geothermal systems can be classified into two categories: Liquid-dominated and vapor-dominated reservoirs. Liquid- and vapor-dominated geothermal reservoirs have large and small liquid saturations, respectively. Since the resident fluid is saturated or superheated steam, the vapor-dominated geothermal systems are among the most interesting commercially. In particular, we focus on The Geysers, CA, the world's largest vapor-dominated reservoir.

In the past, there have been some attempts to explain the recharge in The Geysers geothermal field. White (1973) speculated on the two plausible mechanisms: A separate external water source and adsorption of liquid water. The first mechanism has been ruled out since further research has been unsuccessful in proving any evidence of a hidden water source, leaving adsorption phenomena as the most plausible fluid storage mechanism in The Geysers field. Therefore, to improve efficiency during injection/production projects in The Geysers, the phenomena of adsorption and its effects on the fluid flow and storage processes in such geothermal systems must be further explored. To this end, a number of studies have been initiated at Stanford to measure the amount of water adsorbed and ultimately to construct an *adsorption map* of the field. Earlier attempts were reported by Hsieh (1980) and Leutkehans (1988). A BET type sorptometer equipment was constructed and used for high temperature adsorption measurements on Berea sandstone and unconsolidated silica sands, as well as on core samples from The Geysers, CA and Larderallo, Italy. However, the accuracy of these experimental results were questioned due to the excessive leaks from the sorptometer equipment at the elevated temperatures, mainly due to the long equilibrium times required when using very tight core samples. This problem was also acknowledged by Herkelrath and O'Neal (1985) in their experimental study of water adsorption in the context of disposal of nuclear wastes. Recently, Harr (1991) and Shang et al. (1994) made an advance and conducted more accurate steam adsorption measurements on tight core samples from The Geysers, CA, by using an improved, computer-automated, high temperature sorptometer equipment.

In this paper, we report on the continuing experimental effort to examine the effects of adsorption in vapor-dominated geothermal systems, particularly The Geysers, CA. First, we describe our experimental apparatus and procedure. Next, we discuss our experimental results and illustrate sorption isotherms for various Geysers' samples at different temperatures. Finally, we shall discuss *scanning curves*, which are adsorption isotherms that span only a partial range of pressure.

EXPERIMENTAL APPARATUS

Our experimental apparatus is a computer-automated, high temperature sorptometer (built

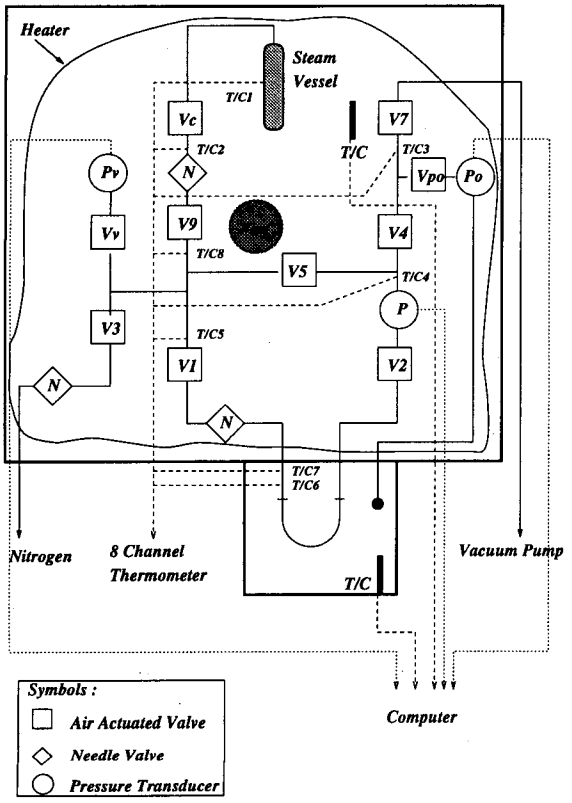

Figure 1: A schematic of the experimental apparatus.

by Porous Materials, Inc.). It consists of three isolated chambers (electronics, top and sample chambers), a computer system and a vacuum pump. All of the electronics that control the operation are located inside the electronics chamber, which is kept at room temperature. Control software loaded in the computer system is used to operate and carry out sorption experiments. A schematic of the top and the sample chambers is shown in Figure 1. As shown in the figure, the top chamber consists of a set of valves, transducers and thermocouples, a steam vessel, a heater and a fan. This chamber is kept at a temperature higher than the experiment temperature. At present, however, the temperature limitation on the equipment imposes a restriction on the maximum temperature (currently 150 °C) of this chamber. Finally, the third chamber is the sample chamber where a sample tube container is located. The sample chamber has a separate heating system such that it can be kept at the experiment temperature. Samples to be used for experiments are loaded into the sample cell (or tube). The sample cell is a stainless steel U-tube with inner diameter of 9.65 mm, restricting the size of the samples. Therefore, every core sample is crushed into smaller pieces that can fit to the sample cell. We must also note that breaking samples into smaller pieces might affect both adsorption and desorption results. However, Harr (1991) reported that the effect of crushing on the amount adsorbed is insignificant. On the other hand, considering the fact that the adsorption equilibrium time for tight core samples, such as The Geysers, with porosities of order of a few percent could be extremely long, using moderately crushed samples conveniently reduces the experiment run time and reduces the danger of leaks.

EXPERIMENTAL PROCEDURE

Since the equipment is computer-automated, the experimental procedure is simple. Normally, an operator only needs to load and start the control software. The remaining experimental procedure is carried out under computer control. Here we shall summarize the sequence. Before each experiment, a new sample is outgassed under vacuum for a sufficiently long time at an elevated temperature (normally at 180 °C). Then, the procedure followed to obtain a single point on an adsorption and a desorption isotherm is as follows: First, during adsorption, the sample cell is initially isolated from the reference volume, located inside the top chamber, by closing the valves V1 and V2 (see Figure 1). Steam is then introduced to the reference volume. Next, a pressure reading (p_i) is taken when the pressure is stabilized in the reference volume. Following this, steam in the reference cell is expanded into the sample cell by opening the valves V1 and V2 and another pressure reading (p_f) is taken when the pressure in the system is stabilized again, at which time the stage is completed by closing the valves V1 and V2. Thus, an adsorption isotherm over the entire pressure range can be obtained by repeating the above steps until the saturation pressure is reached, after which the direction of the experiment can be reversed to a desorption, if desired. During desorption, the reference and the sample cells are also initially isolated. The pressure in the reference volume is now reduced by producing a certain amount of steam. A stabilized pressure reading, again corresponding to p_i, is taken. Next is to open the valves V1 and V2 and to wait until an equilibrium pressure p_f is obtained. This gives a single point on the desorption curve. Repeating these steps until the minimum pressure value desired completes the desorption isotherm.

During an adsorption (or a desorption) stage,

the amount of water adsorbed (or desorbed) is calculated from the following equation

$$X^n = X^{n-1} + (p_i^n - p_f^n)\frac{V_r}{RT_r} - (p_f^n - p_f^{n-1})\frac{V_{SC} - V_S}{RT_t}, \quad (1)$$

where $X, p_i, p_f, Vr, V_{SC}, V_S, T_r, T_t$ and R are the amount adsorbed in moles, the initial and the equilibrium pressures, the reference, the sample cell and the sample volumes, the temperatures in the top and the sample chambers, respectively. Superscripts n and $n-1$ denote the parameter values corresponding to the current and the previous stages, respectively.

DISCUSSION OF RESULTS

We carried out a series of steam sorption experiments towards the final goal of constructing an *adsorption map* of The Geysers geothermal field. We also examined the effects of temperature on steam adsorption process, and finally investigated the behavior of *scanning curves* of steam adsorption hysteresis for The Geysers' samples. Adsorption experiments were carried out for samples from five different wells located in The Geysers field. Experiments for each sample were repeated at three different temperatures (80, 100 and 120 °C). Due to the temperature restriction mentioned earlier, we have not conducted tests at temperatures higher than 120 °C. In the future, however, higher temperature experiments are planned following modifications to the equipment.

In Figures 2, 3, 4, 5 and 6, we show results obtained in steam adsorption experiments for samples from NEGU-17, Calpine Co. MLM-3, Sulphur Bank 15-D, Cold Water Creek and CCPA Prati State 12 at 80, 100 and 120 °C, respectively. The location of these wells in the field is as follows: NEGU-17 (North East Geysers Unit 17) is in the north east, MLM-3 in the south east, Prati Sate-12 and Cold Water Creek in the north west and Sulphur Bank-15D in the central west Geysers. Significant differences in the adsorption behavior of the samples studied were observed. The shape of the curves as well as the magnitude of the adsorption are quite different. For the NEGU-17 sample (Figure 2), the curve remains almost flat until a very high relative pressure value, at which point it curves upward, while a different behavior is observed for the samples from the other four locations (Figures 3-6). These other isotherms show a monotonical increase as relative pressure increases. A previous Stanford study by Shang et al. (1994) showed that adsorption behavior may

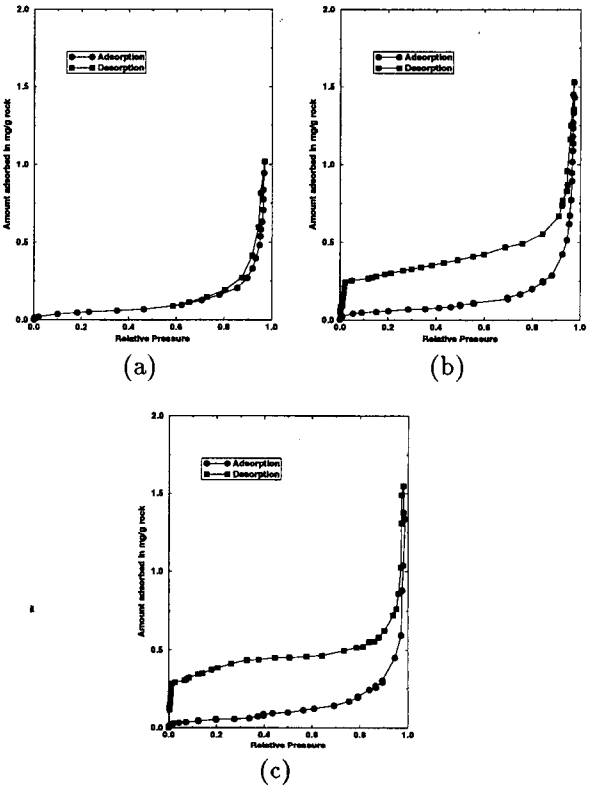

Figure 2: Results of adsorption experiments for NEGU-17 at (a) 80, (b) 100 and (c) 120 °C.

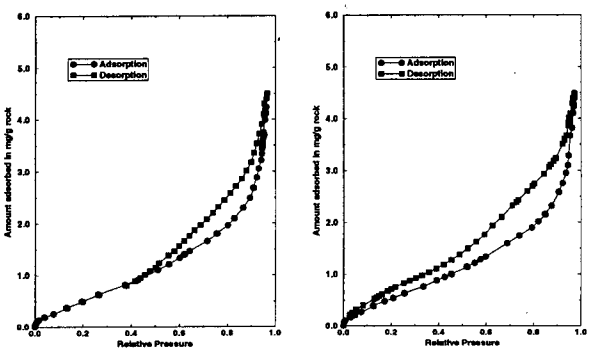

(a) (b)

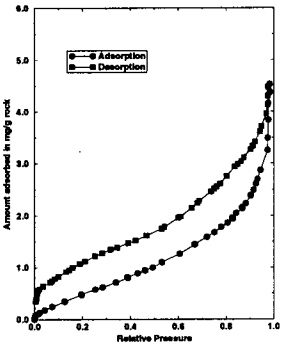

(c)

Figure 3: Results of adsorption experiments for Calpine Co. MLM-3 at (a) 80, (b) 100 and (c) 120 °C.

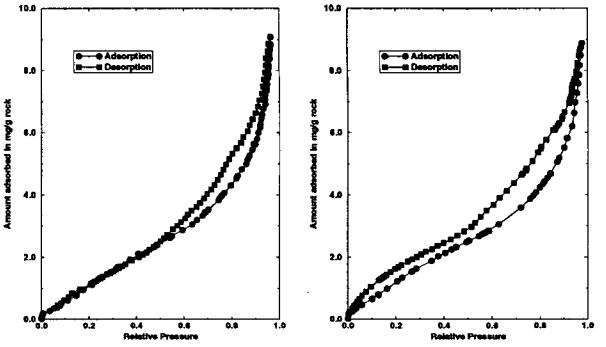

(a) (b)

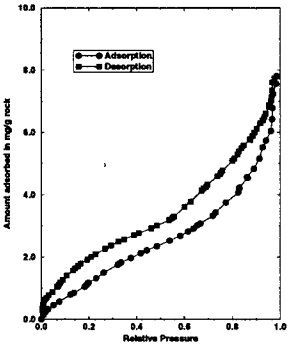

(c)

Figure 4: Results of adsorption experiments for Sulphur Bank 15-D at (a) 80, (b) 100 and (c) 120 °C.

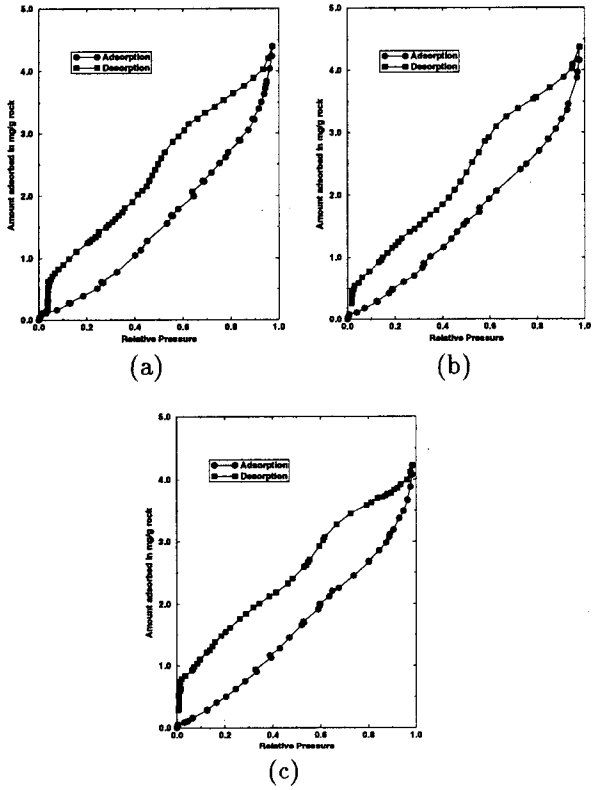

Figure 5: Results of adsorption experiments for Cold Water Creek at (a) 80, (b) 100 and (c) 120 °C.

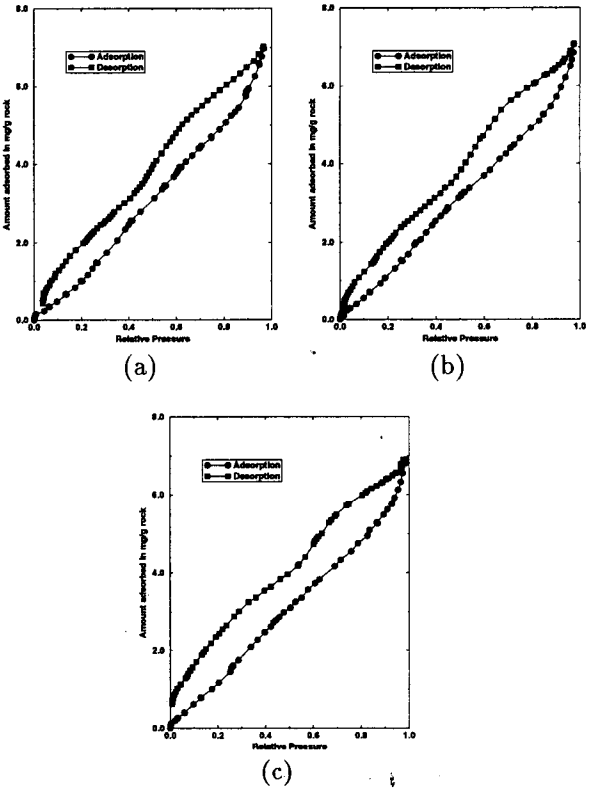

Figure 6: Results of adsorption experiments for CCPA Prati State 12 at (a) 80, (b) 100 and (c) 120 °C.

differ even for samples obtained at different elevations in the same well. At this point, our preliminary results are not conclusive since the experimental data do not cover the whole field. However, they indicate a need for further research in this area. Therefore, in order to have a better understanding of the adsorption behavior in The Geysers geothermal field, more adsorption experiments are required from additional locations.

An interesting and rather unusual feature observed in the results shown in Figures 2-6 is the temperature effect. The figures indicate that the temperature has a very important effect on the desorption curve while it has only a slight effect on the adsorption. The temperature effect on the desorption curve is such that the hysteresis loop becomes more pronounced (Figures 2-4) as temperature increases. Moreover, the shape of the adsorption-desorption loop is very different than that previously reported for other sorption experiments in other porous solids. The difference is that the hysteresis here persists until a very small pressure value (of order of 0.001 *psia*) leaving a residual amount adsorbed, whereas it is normal for hysteresis to cease at a moderate pressure value. Furthermore, experimental results for samples from Cold Water Creek (Figure 5) and Prati State 12 (Figure 6) show a different temperature effect, limited only to small pressure values. This effect is of importance because it controls the hysteresis loop. From our results, we conjecture that the temperature effect on the hysteresis will be even more pronounced at higher temperatures than those we studied. Recently, Satik and Yortsos (1995) have made an attempt to explain this effect by modelling the process with the use of a pore network model and combining it with the improved adsorption theory of Evans et al. (1986) for narrow pores and also with a model proposed by Parlar and Yortsos (1988). Satik and Yortsos (1995) compared their numerical simulation results with our experimental findings and found a good agreement. To explain the temperature effect observed in our experiments, their results suggested that, for adsorption in microporous solids, liquid occupying narrow pores (of order of 1 *nm*) can behave in a supercritical state as the temperature exceeds a critical value. Such fluids, depending on the topology of the porous medium, can actually prevent the liquid occupying larger pores from evaporating due to the lack of their accessibility to vapor, delaying evaporation (desorption) until very small presure values.

Finally, in Figure 7, we show *scanning curves* obtained for a sample from NEGU-17 at 120 °C. *Scanning curves* are obtained by changing the direction of the experiment from an adsorption to a desorption at an earlier pressure for each loop. As seen from the figure, the starting pressure value for each loop is the same, at a complete vacuum. Figure 7 also shows that hysteresis diminishes as the final pressure value for a loop decreases. A complement to this type of *scanning curve* is to start the adsorption part at larger pressure value for each loop and to finish it always at the saturation pressure. However, the second type of curve requires changing the direction of the experiment from a desorption to an adsorption at a larger pressure value for each loop. At present, only the first type of the curves can be obtained because our sorptometer equipment can not handle the sequence of steps required for the second type. With a further modification to the control software, we also expect to obtain the second type of curves in the near future. The two types of *scanning curves*, when combined together, should reveal information important to the optimization of injection-production strategies in The Geysers geothermal field.

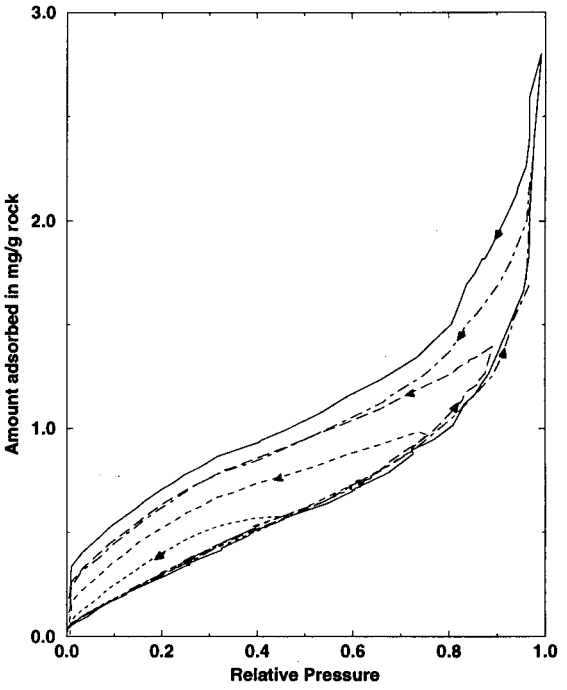

Figure 7: Scanning curves obtained for a sample from NEGU-17 at 120 °C.

CONCLUSIONS

In this paper, we have reported our results of sorption experiments conducted for samples from The Geysers geothermal reservoir, CA. We have studied the effect of the temperature on the adsorption/desorption cycle. Our results have shown that the effect of temperature is insignificant on the adsorption whereas it is very important on the desorption, therefore, a more pronounced hysteresis behavior is observed as the temperature inceases. We also conjectured that this effect can even be more pronounced at larger temperature values than we examined. To have a better understanding of the phenomena, however, more experiments at elevated temperatures are required. Finally, we studied the behavior of *scanning curves* and presented a family of *scanning curves* of the hyteresis for a sample from The Geysers field.

ACKNOWLEDGEMENTS

This work was supported by DOE contract DE-FG07-90ID12934, the contribution of which is gratefully acknowledged. The authors also would like to thank Willis Ambusso for his assistance in conducting experiments, Ron Webber for his help in resolving the problems encountered with the sorptometer equipment and Yanis C. Yortsos for his invaluable comments in analyzing our results.

References

[1] Evans, R., Marconi, U. M. B., and Tarazona, P.: "Capillary condensation and adsorption in cylindrical and slit-like pores," *Chem. Soc. Faraday Trans. 2* (1986) **82**, 1763–1787.

[2] Harr, M. S.: "Laboratory Measurements of Sorption in Porous Media," M.S Report, Stanford University, 1991.

[3] Herkelrath, W. N. and O'Neal II, C. F.: "Water Vapor Adsorption in Low-Permeability Rocks," *International Association of Hydrogeologists*, Memories Vol. XVII, Part I, 248-253, 1985.

[4] Hsieh, C. H.: "Vapor Pressure Lowering in Porous Media," Ph.D. Thesis, Stanford University, 1980.

[5] Leutkehans, J.: "A Laboratory Investigation of Steam Adsorption in Geothermal Rocks," M.S Report, Stanford University, 1988.

[6] Parlar, M. and Yortsos, Y. C.: "Percolation theory of vapor adsorption-desorption processes in porous materials," *J. of Colloid and Int. Sci.* (1988) **124(1)**, 162–176.

[7] Satik, C. and Yortsos, Y. C.: "A pore network Model for Adsorption in Porous Media," To be presented at the Twentieth Stanford Geothermal Workshop 1995, Stanford, CA, Jan. 24-26 1995.

[8] Shang, S. B., Horne, R. N., and Ramey, H. J.: "Measurement of surface area and water adsorption capacity of the Geysers Rocks," Paper presented at the 19th Stanford Geothermal Reservoir Engineering Workshop, January 18-20, 1994, Stanford, Ca.

[9] White, D. E.: *Geothermal Energy*, Stanford University Press (1973).

PROCEEDINGS, Twentieth Workshop on Geothermal Reservoir Engineering
Stanford University, Stanford, California, January 24-26 1995
SGP-TR-150

AN EXPERIMENTAL MEASUREMENT OF THE ADSORPTION OF SUPER-HEATED STEAM

Ruggero Bertani, Renato Perini, Bruno Tarquini.

ENEL SpA DPT/VDT/G Via Andrea Pisano, 120 - 56122 Pisa, Italy.

1. Introduction

The adsorption of liquid water in a vapour-dominated geothermal reservoir is one way the rocks hold fluids. The presence of this adsorbed water must be taken into account in the evaluation of the reservoir capacity.

A great number of papers have been published in the last ten years on this matter (see for instance [Hornbrook, 1994], and [Economides, 1985]); at Stanford University a big effort was carried out in experimental measurements of the adsorption/desorption from reservoir samples (see [Shang, 1994[1]]).

In Italy we have a new geothermal field not exploited yet, in the Monteverdi region (southern border of Larderello), where 16 productive wells were found, supplying two 20 MW geothermal units. All the wells produce superheated steam.

The effect of adsorbed water was simulated, and the results will be presented in WGC 95 [Bertani, 1995].

2. Adsorption Simulation

2.1. *Grid geometry and thermodynamic conditions*

A mathematical model of the field was developed in order to have a preliminary field evaluation, using the STAR [Pritchett 1992].

The reservoir area is a roughly rectangular shape of 4x8 km, and the reservoir elevation is from -1000 to -3500 m a.s.l.

The grid used for the simulation is rectangular, with all the cells 500x500 meters in each horizontal (XY) plane.

The number of cells is 8x15x12, covering a volume of 4000x7500x2500 m^3. The vertical thickness of the reservoir is from -3500 to -1000 m a.s.l. The grid orientation is north-west-south-east, as shown in Figure 1.

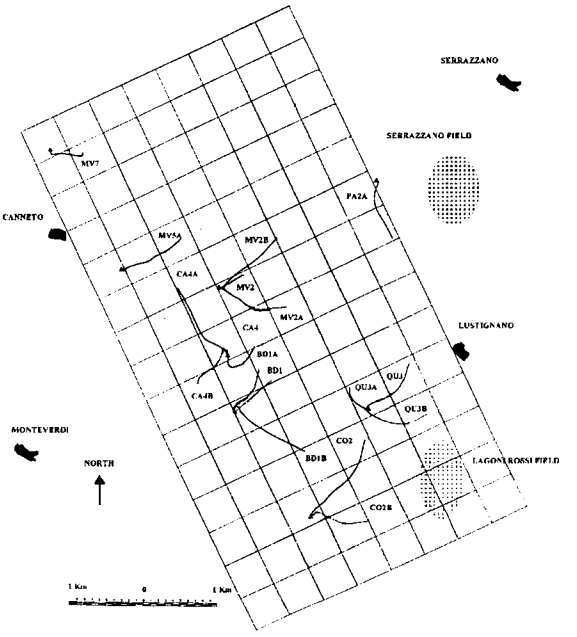

Figure 1: Monteverdi zone with the grid orientation.

The vertical (Z) cell distribution is irregular starting from 500 (at the bottom) to 100 meters (at the top).

Temperature and pressure indicate superheated conditions; the maximum degree of superheat is 70°C (7.5 MPa and 360°C). The initial temperature distribution was based upon extrapolated values taken *ad hoc* during drilling; the temperature distribution at -2500 has a maximum to the south-east (360°C) and a

minimum to the north-west (300°C), as shown in the contour plot given in Figure 2.

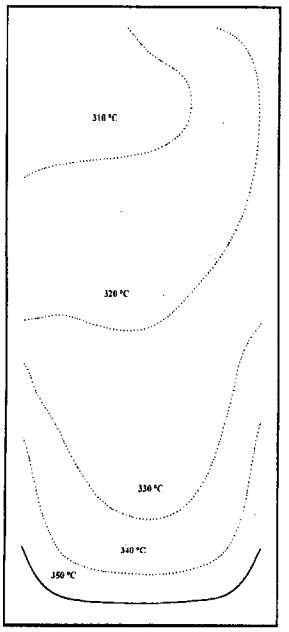

Figure 2: Isotherms at -2500 m a.s.l.

2.2. *Results of Simulation*

Available experimental data show that the amount of adsorbed water depends on the pressure, temperature and rock properties. Only a small fraction of the pore volume can be occupied by the adsorbed film, but the overall effect on the fluid density can be significant: for example, at 350°C and 7 MPa the steam density is 28 kg/m^3; we have, with 10% of the pore volume filled with liquid water, a change of the effective steam/water mixture density to 85 kg/m^3, with an increment of 200% in fluid storage.

We can define a global reservoir value of the amount of adsorbed liquid water per kg of rock (called ADS in the present paper).

We simulated the natural state with different values of ADS, with all the other rock parameters unchanged.

The results of the exploitation are illustrated in Figure 3. The average electrical power for 20 years roughly increases from 15 MW (ADS=0) to 35 MW in the two ADS runs.

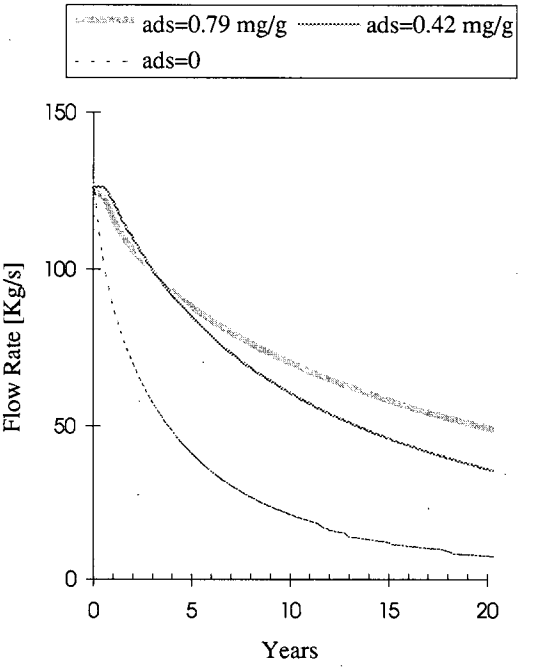

Figure 3: Simulated exploitation for different adsorption values.

The important effect of the value of ADS on the total electrical energy is evident. In any case, with the lowest value (ADS=0.42), we can exploit the reservoir for twenty years with adsorbed water still stored in the pore volume. For this reason, there is only a small difference between the two ADS values over practical industrial exploitation time scales.

On the other hand, in the two ADS cases, it is possible to exploit the reservoir with a different number of wells: it will give a greater difference of extracted mass in the same time.

3. Experimental measuraments

Unfortunately, there is a lack of measurements of the adsorption parameters in the high temperature region, where our reservoir is located.

The experimental data available for Monteverdi are shown in Figure 4 from [Shang, 1994[1]].

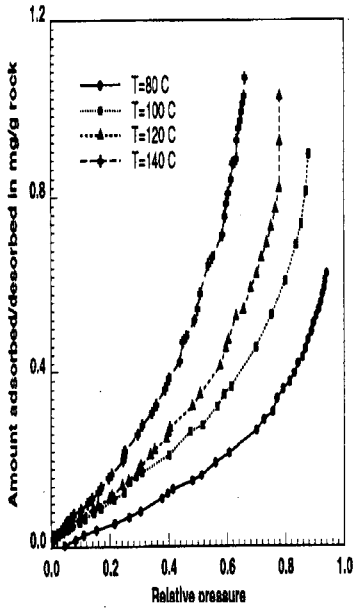

Figure 4: Stanford measuraments on Monteverdi sample.

For this reason, we have planned an experiment, on the basis of the Stanford ones, in order to measure the Desorption versus Pressure curve with the Monteverdi sample.

3.1. Apparatus

The experimental apparatus is shown in Figure 5.

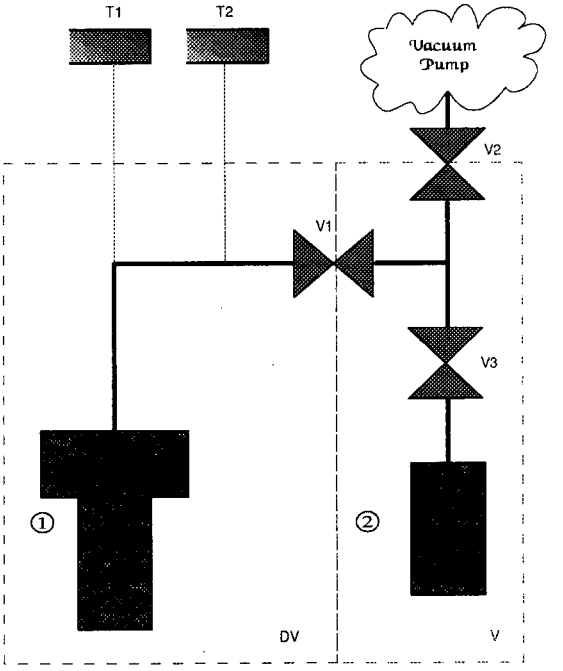

Figure 5: Experimental apparatus.

All is inside an oven, fully insulated. Data on pressure and temperature are recorded by a Data Logger.

The maximum reachable temperature is 250 °C, limited by the valves and cables; the pressure/temperature transducer is certified only below 230 °C. The main operating parameters are collected in the following table:

Item	*Description*
Sample Holder (1)	This is the container of the cutting; the mass of the rock sample is 300 g. The Dead Volume (DV) is 1.50E-4 m^3.
Expansion Volume (2)	The total volume of the expansion chamber (V), with piping and valves is 1.145E-4 m^3.
Valve V1	This is the valve which separates the Dead Volume (DV) and the expansion one (V). It is opened for expansion, with valve V2 closed.
Valve V2	This is used after each expansion step, with V1 closed, in order to evacuate the volume (V).
Valve V3	Not used in operation.
Transducer T1	This is a thermoresistence (class A IEC 751: ±0.5°C at 200°C), giving the internal sample temperature: it is inside the rock.
Transducer T2	This carries Pressure and Temperature coupled signals, which are used for the experimental measurement; the precision is ±0.18% span (2.5 Mpa), i.e. 4.5 KPa.

The work of [Shang, 1994[2]] has demonstrated the equivalence of measurement of core samples or cutting, as shown in Figure 6.

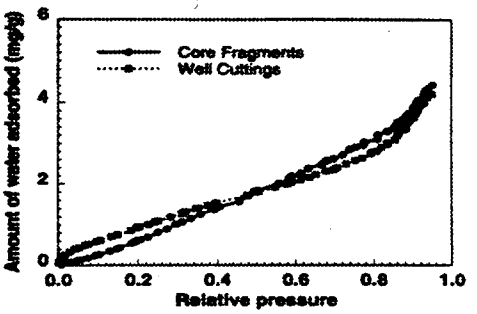

Figure 6: Comparison between core and cuttings.

Using cuttings the experimental procedure is speeded up, due to the smaller equilibrium times.

3.2. Experimental procedure

Preliminary, the Dead Volume was measured using helium expansion between DV and the volume V; the Dead Volume is the free volume in the core holder, including tubing and pore volume, excluding only the rock. First of all, the sample is fully water saturated; and afterwards a vacuum is made inside the circuit. Then, the temperature rises until the desired value is reached (for instance 180 °C); and the pressure is monitored, with venting of the excess water. When an equilibrium is reached at super-heated conditions, approximately after 24 hours, the valve V2 is opened and the vapour fills the second part of the apparatus; the pressure will decrease as in Figure 7.

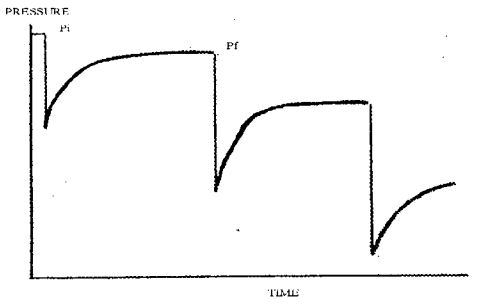

Figure 7: Pressure transient (theoretical).

The steady state pressure (after 2-3 hours) has higher values than the isothermal expansion at a constant number of moles, because of the desorbed water from the sample.

From the pressure difference between the iso-moles value and the actual one, it is possible to determine the mass (in mg) of desorbed water per gram of rock, at the final relative pressure, from the following simple equations:

M_i= Initial mass of steam in the Dead Volume;

P_i= Initial pressure of steam in the Dead Volume (measured);

P_f= Final pressure of steam after expansion (measured);

P_f^0= Final pressure at a constant number of moles (no desorbed water);

DELTA is the amount of desorbed moles of water from the rock sample.

$$M_i = \frac{P_i * DV}{Z * R * T}$$

$$P_f^0 = \frac{Z * M_{i*} * R * T}{(DV + V)}$$

$$P_f = P_f^0 + \frac{Z * R * T * DELTA}{(DV + V)}$$

The final ratio ADS (in mg of water per grams of rock) is given by

$$ADS = \frac{DELTA * 18}{Rock\_Mass}$$

Due to the volumes and the precision of the pressure transducer, the minimum desorbed water which it is possible to measure is roughly **0.05** mg/g.

4. Conclusion

The apparatus for the ENEL desorption experiment is able to measure the isotherms for rock samples of relative big size (~300 grams), from 140°C to 240°C; our goal is the measurement at 180°C, 200°C and 220°C of different samples, in order to estimate an average reservoir desorption curve.

Comparaison with Geyser samples are also in schedule.

5. References

R. Bertani, G. Cappetti (1995): "Numerical simulation of the Monteverdi zone (western border of the Larderello geothermal field", *Proceedings of the World Geothermal Congress*, Florence, Italy, 18-31 May 1995 (in press).

M.J. Economides, F.G. Miller (1985): "The effect of Adsorption Phenomena in the evaluation of Vapour Dominated Geothermal Reservoirs", *Geothermics* vol. 14, No. 1, pp.3-27.

J.W. Hornbrook, R.N. Horne (1994): "The effect of adsorption on injection into geothermal reservoir", *Proceedings of Nineteenth Annual Workshop on Geothermal Reservoir Engineering*, Stanford University, Stanford, CA, January 18-20, 1994.

J.W. Pritchett (1992): STAR User's Manual, S-Cubed, SSS-TR-92-13366; see also J.W. Pritchett (1994): "STAR-A General Purpose Geothermal Reservoir Simulator", *Geothermal Resource Council Bulletin*, vol. 23, No. 4 - April 1994, pp. 139-141.

S. Shang, R. N. Horne and H. J. Ramey Jr. (1994[1]): "Experimental Study of Water Vapour Adsorption on Geothermal Reservoir Rocks", and "Water Vapour Adsorption on Geothermal Reservoir Rocks", submitted to *Geothermics*.

S. Shang, R. N. Horne and H. J. Ramey Jr (1994[2]): "Measurament of surface area and water adsorption capacity of the geyser rocks.", *Proceedings of Nineteenth Annual Workshop on Geothermal Reservoir Engineering*, Stanford University, Stanford, CA, January 18-20, 1994.

PROCEEDINGS, Twentieth Workshop on Geothermal Reservoir Engineering
Stanford University, Stanford, California, January 24-26 1995
SGP-TR-150

HDR RESERVOIR ANALYSIS INCORPORATING ACOUSTIC EMISSION DATA

J. Willis-Richards[1], K. Watanabe[2], T. Yamaguchi[3], Y Sato[4] and S. Takasugi[5]

1 Dept. of Resources Engineering, Tohoku University, Sendai 980, Japan
2 Research Institute for Fracture Technology, Tohoku University, Sendai 980, JAPAN
3 National Institute for Resources and Environment, 16-3 Onogawa, Tsukuba-shi, Ibaraki, 305, JAPAN
4 NEDO, Geothermal Energy Dept., Sunshine 60, Higashi-Ikebukoro 3-1-1, Toshima, Tokyo 170, Japan
5 Geothermal Energy Research and Development Co., Ltd., Kyodo Bldg., 11-7 Kabuto-cho, Nihonbashi, Chuo-ku, Tokyo 103, Japan

ABSTRACT

A set of models of HDR systems is presented which attempts to explain the formation and operation of HDR systems using only the in-situ properties of the fractured rock mass, the earth stress field, the engineering intervention applied by way of stimulation and the relative positions and pressures of the well(s).

A statistical and rock mechanics description of fractures in low permeability rocks provides the basis for modeling of stimulation, circulation and water loss in HDR systems. The model uses a large number of parameters, chiefly simple directly measurable quantities, describing the rock mass and fracture system.

The effect of stimulation (raised fluid pressure allowing slip) on fracture apertures is calculated, and the volume of rock affected per volume of fluid pumped estimated. The total rock volume affected by stimulation is equated with the rock volume containing the associated AE (microseismicity). The aperture and compliance properties of the stimulated fractures are used to estimate impedance and flow within the reservoir. Fluid loss from the boundary of the stimulated volume is treated using radial leak-off with pressure-dependent permeability.

The model is applied to HDR stimulation and circulation experiments carried out at Rosemanowes, UK (1983-1989) and at Hijiori, Japan (1986-1991).

INTRODUCTION

The linked models of stimulation, circulation and water loss presented here use simple rock mechanics applied to a population of (circular) fractures in an attempt to reach an understanding of the creation and operation of HDR systems. Worldwide HDR experiments and other field observations over the past 15 years (CSM Associates, 1992) suggest:

- The rock mass is subject to anisotropic, remotely generated lithospheric stresses
- Fracture lengths can often be described by fractal distributions
- The in situ permeability of the natural fracture systems in crystalline basements selected for HDR experiments is generally 1 - 100 μD (e.g. Clauser, 1992). Circulation through such systems, unmodified, would have unacceptably high impedance and water losses
- High pressure fluid injection, by reducing the normal stress on fractures, enables slip to take place. In strong rocks slipping at low normal stress this generally leads to a significant increase in fracture aperture and permeability. A small fraction of the slip is unstable and causes AE, which may be located, typically appearing as structured ellipsoidal clouds
- The ratio of the permeability within the stimulated volume (AE cloud) to that outside it is high, generally several orders of magnitude
- It appears to be difficult to create extensive new fractures in anisotropically stressed and pre-fractured crystalline rock
- The position of recovery wells in relation to the injection well, fracture orientations and the earth stresses exerts a strong effect on production. Optimal positioning has yet to be determined
- Steady state water losses increase more than linearly with reservoir mean pressure

These considerations suggest that "first principles" models should contain the following elements:

- Description of fracture lengths, orientations, compliance and shear behavior; the rock elastic properties; the in-situ fluid pressure and stresses.

- A treatment of stimulation which describes the resulting fracture aperture distribution and makes predictions that can be verified against AE locations

- A treatment of circulation which uses the stimulated fracture properties and their geometry in relation to the wells, the earth stresses and the pressure distribution

- A treatment of water loss from the margins of the stimulated region

For HDR application, the complexity of explicit 3-D geometric fracture representations and the computational demands of coupled flow solvers are disproportionate to our knowledge of the actual geometry of the fracture system, which, in any case, we believe to be "well connected".

The objectives of the models presented here are to predict field production, impedance and water loss data from experimental or hypothetical HDR systems with the minimum of model calibration involving input parameters that can not be measured, at least in principle, in the field or laboratory.

ROCK MASS DESCRIPTION

Fracture orientation data is gathered from borehole wall images or core. For each visible fracture, the orientation and length of observed fracture should be recorded. Fracture orientation can be simulated by resampling the observed data set, using the length of fracture observed as a "weight" thereby removing any geometric observational censoring of the fracture network without recourse to analytic corrections. The fracture density, at the resolved fracture length scale, can be estimated directly as the total recovered fracture area divided by the core volume.

Fracture lengths, at the scale of interest for HDR circulation (> about 2m), are typically unmeasurable for HDR reservoirs. This is potentially a very serious problem, since the proportion of longer fractures determines the ease with which large shear displacements, and hence large apertures, may be created. Main et al. (1990) state that much of the current observation of trace lengths in outcrop for quasi-stable fracture systems suggest that the length distributions are characteristically fractal, with fractal dimension (D_L) close to 1.0.

A first order approximate simulation of a fracture network can, therefore, be made knowing only the fracture orientation distribution and the fracture density (e.g. Watanabe and Takahashi, 1995). Whilst the models used here do not simulate the fracture network explicitly, they make use of both the fracture density and the fracture length distribution. A default value for D_L of 2.0 for fracture radii (equivalent to an D_L of 1.0 for outcrop trace length distribution) is used.

Fracture in-situ apertures, closure and shear behavior can be obtained from laboratory experiment carried out on core specimens or on samples of outcropping analog fractures. Their effects on stimulation and circulation, as expressed through the model, are not dependent on the fine detail of the chosen constitutive laws, but a clear distinction can be drawn between weak or strong asperities, and rough or smooth fractures.

Water loss from an HDR system is dependent on the far field in-situ permeability, usually at hydrostatic pressures. There also appears to be a scale effect, with higher permeability observed at increasingly larger scales up to about 100m. Permeability should be measured from low pressure injections into long open hole lengths and with large radii of investigation (both > 100m). Even when careful measurements are made, considerable uncertainty, perhaps up to nearly an order of magnitude, may still remain. In as much as the in situ permeability is uncertain, so are predictions of water loss.

Rock elastic properties may be measured from core specimens or from logs.

Calculation of the response of the fractures to fluid injection requires knowledge of the in situ stresses. One principal axis of the stress tensor is assumed to be normal to the earth's surface, and its magnitude given by the weight of overburden (but see Cornet and Burlet, 1992). The orientation of the remaining axes may be determined from borehole breakouts, drilling induced fracture orientation, differential strain curve analysis (i.e. microcrack orientation) or hydraulic fracturing. Where tress directions are coherent over wide areas, a good estimate of the maximum principal stress direction can be found in the world stress map (Zoback, 1992).

The stress magnitudes are also needed. If direct estimates of the magnitude of σ_{min} (usually one of the horizontal stresses in deep HDR sites) from hydraulic fracturing or ISIP analysis are not available then indirect indicators should be used. These may include the pressure at which AE are first induced, or analysis of microseismic focal mechanisms.

STIMULATION MODEL

HDR stimulation is the creation of irreversible increases in fracture aperture by high pressure fluid injection through shear movement of rough fracture surfaces in stressed rock. Since the apertures produced during stimulation are high (of order 1 mm), the stimulation volume is considered be at a single uniform pressure and bounded by a narrow region in which much active shear is taking place and across which pressures drop rapidly to hydrostatic. The effects of stimulation on an individual fracture can be calculated by:

1. Assessing frictional stability using a simple Coulomb friction law
2. Noting that shear stiffness is proportional to the fracture radius and so calculating the amount of slip
3. Calculating the increase in aperture that results

By noting the increase in aperture of many fractures and knowing the fracture density, the ratio of the volume of fluid injected to the volume of rock affected can be calculated. this is termed the ***rock / fluid ratio*** (RFR), see Willis-Richards (1995) for details of the calculations involved.

An estimate of the RFR is necessary to correctly calculate

the "backstress" terms. Any one of a number of analytical solutions available for the stresses imposed by the expansion of a flattish ellipsoid in an elastic medium (e.g. Eshelby, 1957) may be used.

The stimulation model produces a collection of stimulated fractures, each defined by its orientation, length, and shear displacement. The RFR estimate can be compared with the volume of the microseismic cloud generated divided by the volume of fluid injected. Typical RFR ratios can vary from about 2000:1 for high pressure injection into rough fractures with high stress anisotropy (σ_1-σ_3) and hence high potential for fracture opening by shear dilation, to 30,000:1 or more for lower pressure injections that are just able to cause widespread shear movement.

Stimulation design objectives are to minimize the pressure used and hence the fluid volume required, whilst at the same time ensuring that the reservoir created has low enough impedance. Low impedance ensures a low mean reservoir operating pressure and hence minimizes far field fluid losses, as well as reducing parasitic pumping requirements. Excessive pressure during stimulation increases costs through the higher fluid volume requirement and possibly through the need to use gel rather than water. Too much fluid pumped leads to too large a stimulated volume, which results in high far field losses.

The critical operationally controllable parameter for HDR stimulation, therefore, is the pressure. Changes in flow rate will have little effect on resulting apertures unless the change in treatment pressure is significant, but may expand the stimulated volume until the injection rate balances far field losses.

In the case of a seismogenic circulation, which is a "progressive stimulation", the critical pressure is a mean reservoir pressure, approximately determined as a weighted average of injection and recovery well pressures.

CIRCULATION MODEL

The stimulated fractures are the main resource from which a picture of the circulation is drawn. Since we seek to avoid a complex 3-D simulation of the fracture network, simple geometric combinations of fractures which reflect flow paths across the reservoir are sought. A single such flow path can be envisaged as the series of fractures traced by fluid crossing the reservoir.

A large number of flow paths are simulated, and the fracture area and impedance of each calculated. The total fracture area to simulate, the total flow and the resulting flow-area distribution can be assessed by comparison with suitably analyzed field data from a well studied reservoir, such as the Rosemanowes Phase 2B system. Agreement validates the flow path generation method, at least for the particular reservoir used for calibration.

The model assumes that if the flow-area distribution for the Rosemanowes Phase 2B reservoir, deduced from tracer and thermal draw down data by Nicol and Robinson (1990), Table 1, can be matched by the flow path generator chosen, then useful results can be obtained for other sites when the total fracture area is suitably scaled by the well separation. Naturally, other fracture orientations, stresses and well geometries will automatically generate other flow-area distributions; but these should be appropriate for the sites in question if the flow path generator chosen is sensible.

Table 1: Reservoir flow / area distribution determined by Nicol and Robinson (1990) for the Rosemanowes RH12 - RH15 Phase 2B reservoir as 4 flow paths

Flow path area (m^2)	Flow %	Cumulative area %	Cumulative flow %
7400	15.1	2.6	15.1
40400	34.2	16.6	49.3
130300	39.6	61.7	88.9
110500	11.1	100.0	100.0

It turns out (fortuitously?) that the simplest possible flow path geometry, that of overlapping fractures in series, figure 1, can generate suitable flow-area distributions.

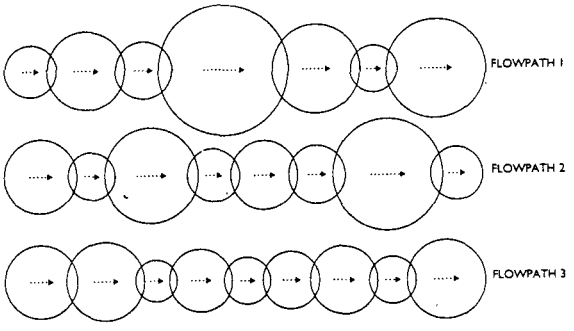

Fig. 1. Conceptual model of reservoir made up of a number of linear flow paths

Two parameters, fracture path tortuosity (T_{path}) and the ratio of total simulated fracture area to reservoir flowing fracture area, are available for customizing the fit to the Rosemanowes Phase 2B data. A good fit is achieved with $T_{path} \approx$ 1.3 and fracture area ratio 2.5, figure 2. The fit obtained to the experimental cumulative area / cumulative flow curve for the Rosemanowes reservoir means that the flow model should similarly be able to reproduce the tracer and thermal draw down results, were these aspects to be included.

The model can be simply, but approximately, adapted to multiple well configurations, provided that each set of flow paths is treated independently i.e. there is no flow interference between paths.

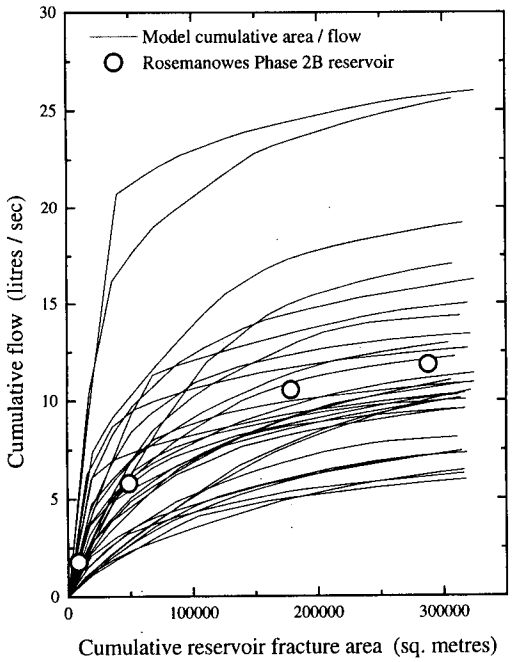

Fig. 2 30 realizations of the flow model for the Phase 2B circulation. Flow paths sorted in order of flow density and plotted as cumulative flow against cumulative fracture area. Field data from Nicol and Robinson (1991).

Results quoted below are the mean of 100 realizations of the flow paths concerned. The variance of individual well production flow is, as might be expected, quite high, but the relative magnitudes of production from the different wells are generally preserved.

WATER LOSS MODEL

Circulation takes place towards the center of a stimulated volume of high permeability. Fluid loss, on the other hand, is leak off from the margins of this volume and is controlled by the in-situ permeability and its response to fluid pressure change in the sub-seismogenic pressure range. Fluid losses are not a function of the injection or recovery flow rates as such, but rather of the mean reservoir pressure seen at the margin of the stimulated volume and of it's surface area. The injection and recovery pressures, weighted by their flow rates, are used to estimate the mean reservoir pressure, somewhat after the manner of Brown (1994).

At sub-seismogenic fluid pressures, permeability changes will be most strongly controlled by the response to changes in effective stress of the most compliant fractures. Such fractures are those sub-parallel to the maximum principal stress i.e. with the minimum normal stresses. Typical fracture compliance curves can be measured or otherwise estimated from generic data. The cube of the ratio of fracture apertures at some fluid pressure P and at the in-situ fluid pressure can thus be used to calculate the change in permeability with pressure (the "cubic" flow law implicitly assumed).

An aperture compliance law, together with the measured in situ permeability and an equivalent radius for the stimulated volume, lets us calculate the water loss for a given pressure drop by numerical integration from the edge of the stimulated region outwards. This simple model, which has a reasonable physical and geometric basis, gives the commonly observed super-linear relationship between mean reservoir pressure and water loss.

Extra fluid losses can also take place during "steady state" circulation if AE events are being produced. The process is identical with that during stimulation. A significant fraction of the high water losses experienced during seismogenic circulation at various sites can be ascribed to this mechanism. Quantitative examination of the importance of this mechanism is possible using the stimulation and water loss models together. The great expansion of the stimulated volume accompanying circulation AE will result in a permanent increase in the water loss rate from the reservoir, even when the mean reservoir pressure is reduced to sub-seismogenic levels.

The water loss model is incorporated within the circulation model, but may be used in isolation if required.

APPLICATION TO PHASE 2A AND 2B CIRCULATION EXPERIMENTS, ROSEMANOWES, CORNWALL, UK

The Phase 2B (1985-1989) circulation from well RH12 to well RH15 over a distance of 190m took place within a small volume of rock (~10^7 m^3), stimulated by a viscous fluid injection (~12-14 MPa, 5500m^3) in 1985 (Richards et al., 1994). However, this reservoir was contained within a much larger (~$6x10^8$ m^3) stimulated volume created during Phase 2A (1983) by a prolonged seismogenic circulation between wells RH12 and RH11 at injection pressures of about 8 - 12 MPa. A total of about 10^5 m^3 of water was lost creating this microseismic cloud, a water to rock ratio of about 6000:1 without correction for aseismic leakoff to the far field.

Fracture orientations are simulated by resampling the BHTV database, a fracture D_L of 1 is assumed. Stresses were measured by hydraulic fracturing and a number of other methods (Pine et. al, 1990)

Phase 2A

For the Phase 2A "seismogenic circulation" a mean reservoir pressure in the range 6 to 10 MPa is investigated. Table 2 shows the range of RFR to be expected for these injection pressures and the water losses from the margins of the seismic cloud, using a far field permeability of 20μ D. A self consistent picture of fluid loss and stimulation emerges for a mean reservoir pressure of about 8 MPa, consistent with typical recoveries of about 30 - 40% at the higher injection pressures.

Table 2: Phase 2A "circulation - stimulation" water budget and rock/fluid ratios (RFR)

Average reservoir pressure MPa	Maximum fluid loss rate l/sec	Estimated total fluid loss m^3	RFR observed adjusted for fluid loss	RFR calculated
6	5.6	22000	7700	19000
7	7.5	29000	8500	13000
8	10.0	39000	9800	9200
9	13.3	52000	12500	6800

The Phase 2A circulation took place within a more restricted rock volume created by the RT2A046 - RT2A051 stimulations at pressures of about 11 - 12 MPa. Using this stimulation pressure to create a file of stimulated joints as input, the circulation model suggests appropriate flow rates and recoveries of about 75% for RH12 - RH11 circulation, provided that the circulation was aseismic. This is consistent with the relatively high recovery rates for the low injection pressure circulations during Phase 2A. The high Phase 2A water losses appear to be due to the continuous AE expansion of the stimulated volume, creating void space by shear dilation, combined with increased potential for marginal water loss as the stimulated volume expanded. A much improved Phase 2A reservoir could have been created by proppant placement around the recovery well, reducing the mean reservoir pressure to sub-seismogenic values at acceptable injection rates.

Phase 2B

The RT2B022 viscous gel stimulation determined the inter well fracture apertures for the Phase 2B circulation. Well head pressures of 14.4 MPa suggest formation treatment pressures of about 12 MPa. This stimulation took place from RH15, ensuring that the highest pressures were seen by the fractures near the production well. The observed RFR inferred from AE locations, was about 2000:1. The actual RFR was likely to have been somewhat greater due to leadoff into the Phase 2A stimulated volume. For a 12 MPa stimulation the predicted RFR is 3400:1.

Using this stimulation pressure to describe the circulation fracture apertures, the predicted injection and fluid loss rates are shown in Figure 3, together with field data from Phase 2B. The simulated flow area was 288,000m^2, as calculated by Nicol and Robinson. As was the case in Phase 2A, the actual injection rates and water loss increase markedly when AE start, at mean reservoir pressures of about 6 MPa. The improved production well treatment and more favorable production flow path direction, reduced the impedance and thereby lowered the mean reservoir pressure for a given injection flow rate. The improved recovery and impedance thus allowed high recoveries to persist to higher injection pressures and much higher injection flow rates.

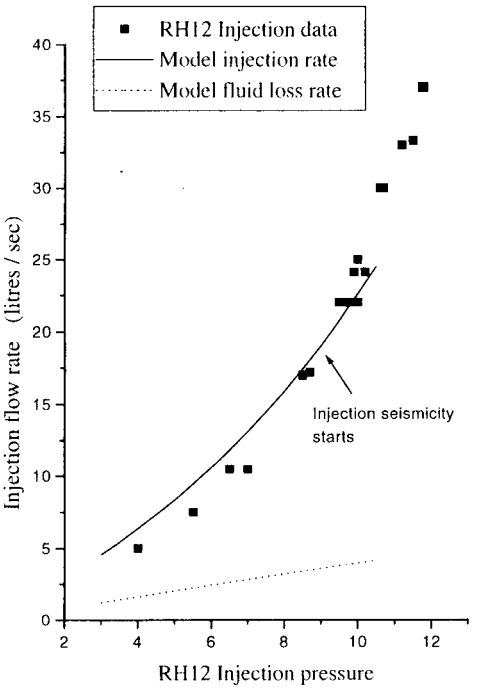

Fig 3. Model injectivity, water loss and actual injectivity data for the RH12-15 Phase 2B (1985-1989) circulation at Rosemanowes.

These quantitative estimations of rock mass response and fluid flow at Rosemanowes are only possible given suitable values of the "unmeasurable" input parameters (total simulated flow path area, mean flow path tortuosity). The values used, however, are reasonable and are carried forward for use with the Hijiori reservoir below.

The concepts within the model allow a synthesis of stimulation, fluid loss, seismicity and circulation for the Phase 2A and 2B experiments at Rosemanowes that has hitherto been lacking.

APPLICATION TO THE HIJIORI HDR PROJECT, YAMAGATA PREFECTURE, JAPAN

HDR experiments have taken place at Hijiori in a shallow (1800m) reservoir since 1985 (Matsunaga et al., 1990; NEDO, 1987-1992; CSM Associates, 1992). Stimulation was from the injection well (SKG-2) and recovery from up to three wells (HDR-1, HDR-2 and HDR-3) which were progressively added to the system. Experimentation on this "shallow" reservoir culminated in 1991 with a three month circulation test using all three production wells.

Fracture orientations for modeling were simulated by re-sampling 229 measurements made on core from well HDR-3, figure 4.

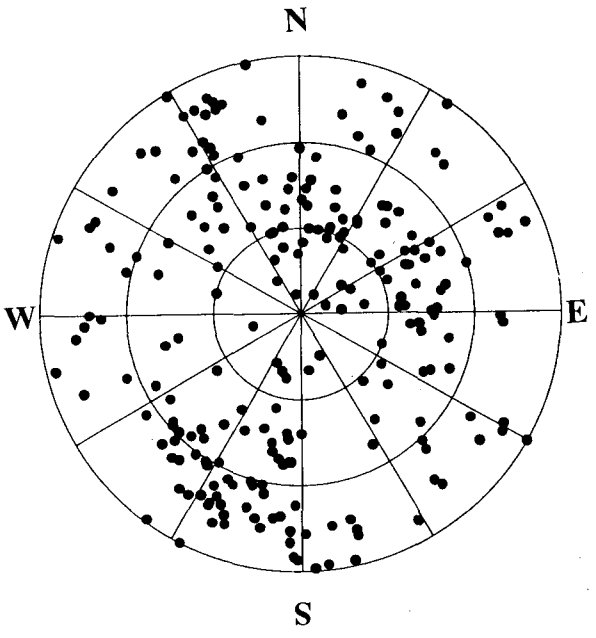

Fig. 4. Polar plot of normals to fractures measured in oriented core recovered from well HDR-3.

The stress data are somewhat ambiguous, but information includes DSCA measurements on core, ISIP and pressure / flow histories, AE focal mechanisms and observation of the minimum fluid injection pressure required to cause AE. The far field permeability has not been determined at low injection pressures, but appears to be higher than that at Rosemanowes; the modeling reported here uses a value of 60μD.

The history of experimentation can be divided into 4 parts:

1. Early stimulations 1985 - 1988
2. Exp. 8505 seismogenic circulation
3. Exp. 8902 seismogenic circulation
4. Exp. 9102 aseismic circulation

Early stimulations

A total of about 3500m^3 of water was injected into SKG-2 at well head pressures of up to about 15 MPa. Allowing for depressurizations and reinflations, the effective pumped volume was probably about 2500m^3, and estimated friction losses suggest formation treatment at about 13 MPa for which an RFR of 2600:1 is calculated. The volume of the AE cloud created was about 9 x 10^6 m^3 (NEDO, 1988, p20) giving an observed RFR of about 3600:1. Fluid loss estimates, based on the compliant fracture model described above, suggest aseismic leakoff during the stimulation of 10 - 20 liters /sec, about 15 - 30% of the mean fluid injection rate and consistent with the two estimates of the RFR. The fracture properties determined by these stimulations are used to calculate subsequent circulation performance.

Exp. 8502 seismogenic circulation

13600m^3 of water was injected into SKG-2 over 14 days at a rate of 16.7 l/sec and well head pressures of 5.5 to 6.1 MPa. About 35% was recovered from HDR-1. 70 AE were located, defining a cloud of about 60 x 10^6 m^3.

The stimulation and water loss models suggest an RFR of about 25000:1 and water losses of up to 16 l/sec when the AE cloud is fully developed. It appears likely that the majority of the actual water loss took place aseismically at the margins of the growing AE cloud, and that only about 2000m^3 of the 10000m^3 total water loss was due to shear dilation.

The circulation model, when applied within this extended AE cloud and using a total reservoir fracture area of 10000m^2, suggests recovery of about 30% from HDR-1 with total injection of about 15 l/sec, both very close to the actual figures.

Exp. 8805 seismogenic circulation

46000m^3 of water were injected into SKG-2 over 29 days at a rate of 18 l/sec and well head pressures of 4.5 to 5.0 MPa. Over 400 AE events were recorded, defining a cloud of about 250 x 10^6 m^3 (NEDO, 1989, p55). Despite both HDR-1 and HDR-2 being allowed to flow, total recovery was still only about 34%, about 8% from HDR-1 and 26% from HDR-2 (NEDO, 1991, p13).

The stimulation and water loss models suggest an RFR of 65000:1 and water losses of up to about 12 l/sec when the AE cloud is fully developed. Thus, of the 26000m^3 of water loss, about 3000 - 4000 m^3 was due to shear dilation, the remainder, about 9 l/sec leaking off into the formation aseismically.

The circulation model, adapted to two wells with a total reservoir fracture area of 25000m^2 contained within the newly extended AE volume, predicts about 45 - 50% total recovery split, in the ratio 1:4 between HDR-1 and HDR-2. Total injection flow is about 20% overestimated. The higher production from HDR-2 is due to a better alignment with respect to SKG-2 and the joint and stress orientations (achieved through using the AE cloud as a drilling target) which allows more direct communication via large aperture fractures.

The failure to improve recovery was due to the expansion of the AE cloud, water losses being caused by both active shear dilation and the increase in surface area.

Exp. 9102 aseismic circulation

90000m^3 of water was injected over 3 months at about 18 l/sec and well head pressures of 3.0 to 4.0 MPa. No AE were detected. A total recovery of about 75% was obtained, distributed in the ratio of about 1:2:2 between HDR-1, HDR-2 and HDR-3 respectively.

The water loss model, applied within the 250 x 10^6 m^3 AE cloud created by Exp. 8902, gives a water loss rate of 5.5 l/sec using the weighted mean reservoir pressure, close to the actual loss rate of just over 4 l/sec. The circulation

model gives predicted recovery rates in the ratio 2:10:7 from HDR-1, HDR-2 and HDR-3 with total recovery of about 70%, figure 5.

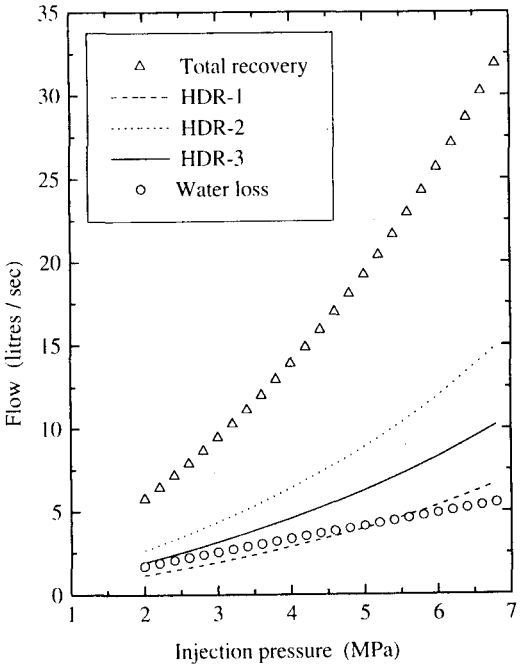

Fig. 5 Model recovery and water loss for the Hijiori 1800m reservoir circulated from SKG-2 to HDR-1, HDR-2 and HDR-3 at different injection pressures

During this test, pairs of production wells were shut in and the injection pressure and remaining recovery flow rate allowed to rise. Only the test with HDR-2 under production appeared to reach a near steady state flow (up 40%) with constant production well-head pressure. The circulation model with HDR-2 alone producing gives a 10% increase in recovery from that well. It is likely that the remaining 30% increase in recovery actually obtained comes from flow to HDR-2 in paths previously directed towards HDR-1 and HDR-3.

DISCUSSION

The results obtained for Hijiori appear reasonable and utilize the same values for flow path tortuosity and the ratio of total fracture area to reservoir fracture area as was employed for Rosemanowes.

The remaining major uncertainty is the appropriate form of the functional relationship between well separation and total reservoir fracture area. For Rosemanowes we know that a well separation (S) of 188m leads to a total fracture area resolvably involved in heat transfer (A) of about 288,000m^2. For Hijiori the individual well production results reported above were obtained with the total fracture areas and separations in Table 3, using the positions of the major flow exits / entries to define S:

Table 3 Well separation / area values used for the modeling hydraulic performance at Hijiori.

Well pair	S (m)	A (m^2)
SKG-2 to HDR-1	43	10000
SKG-2 to HDR-2	52	20000
SKG-2 to HDR-3	86	90000

Figure 5 shows the apparently linear relationship between the well separation and the successful model reservoir fracture areas for Rosemanowes and Hijiori.

However, useful heat extraction capacity will depend on the flux density distribution in the few best flow paths and not just on the total area. For example the SKG-2 to HDR-3 heat extraction during Exp. 9102 was modeled by Tenma et al. (1994) with a heat transfer area of less than 10000m^2. This is not necessarily inconsistent with the model presented here in which 50% of the flow is frequently associated with 10% of the total area (this is because the model has to generate many "poor" flow paths to find the good ones).

The circulation model used here, whilst capable of generating a good match when the total fracture area is known, is clearly as yet deficient and improved methods are being sought.

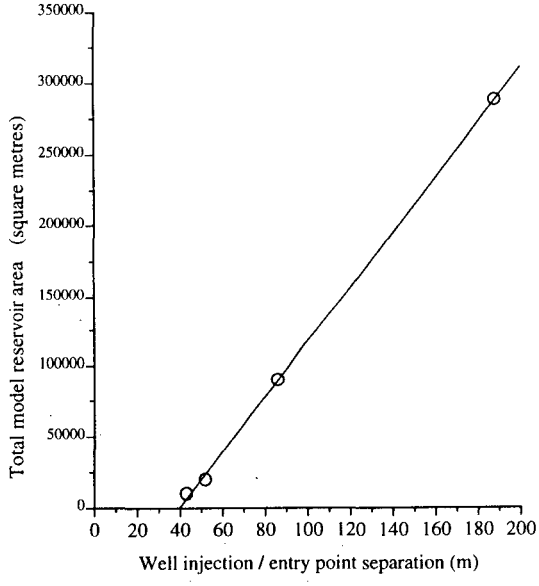

Fig. 6 Tentative relationship between total model reservoir area (A) and well separation (S); A = 1940.S - 77000

Implicit within the stimulation model is the identification of AE with some small fraction of the total fracture shear taking place. The predicted shear movement causes dilation, creating void space equal to the volume of

injected fluid minus the calculated leak off. From this it follows that AE density, if simply related to total shear displacement / area product, is necessarily a good measure of the fluid flow as well as pressure distribution. Were this argument to fail, and aseismic leakoff along "invisible" yet highly permeable features was important, then the predicted and observed RFR's would fail to agree.

CONCLUSIONS

Since the fracture networks at most HDR research sites in crystalline basement appear to be well connected, it should be possible to make simple numerical models which avoid the complexity and CPU demands associated with an explicit representation of 3-D fracture systems. The models used here are a first step in this direction.

The rock mass descriptive properties which seem to most strongly affect the outcome of HDR stimulation and circulation are identified together with simple methods for their quantification. The small range of fractal dimension exhibited by natural fracture systems greatly reduces the uncertainty at a point where direct underground observations are lacking.

A simple model of shear and shear dilation of single circular fractures is developed as the basis for the description of rock mass stimulation in terms of a rock to fluid ratio (RFR) and the set of apertures of the fractures that result. Good matches to field data for experiments at Rosemanowes, UK and Hijiori, Japan are found.

AE recorded during stimulation are likely to be good predictors of fluid flow paths as well as pressure transmission due to the necessity of significant fluid input to fill the associated shear dilation void space.

Circulation is described by an "in-series" connection of fractures between injection and recovery wells, but a method for adequately predicting the total area of fracture connecting two wells is required. Reasonable descriptions of flow / area partitioning and injectivity curves are easily made, but further developments of this aspect of the model will be made.

Water loss from the margins of the high permeability stimulated volume is calculated using fracture compliance to generate a pressure dependent permeability. Significant water loss by shear dilation during seismogenic circulation is also identified and quantified.

Three important operational lessons emerge. Firstly, stimulation of too large a volume of rock will result in high marginal water losses without useful increase in heat extraction capability. Secondly, increase in the stimulated volume by seismogenic circulation progressively increases marginal water losses without improving inter-well impedance and should be avoided. Thirdly, a good basis exists for associating AE clouds with fluid flow. This enables the use of AE for well targeting with greater confidence.

ACKNOWLEDGMENTS

J. Willis-Richards acknowledges with gratitude Prof. H. Takahashi of the Research Institute for Fracture Technology, Tohoku University and Prof. K. Nakatsuka of the Dept. of Resources Engineering, Tohoku University for funding his studies in Japan in 1994/5 whilst on sabbatical leave from CSM Associates Ltd., Penryn, Cornwall, U.K.

The work reported in this paper has been possible only as the result of collaboration between the staff of many different organizations sponsored by both the Ministry of Education (Monbusho) and by the Ministry of International Trade and Industry (MITI).

REFERENCES

Brown D.W. (1994) How to achieve a four fold productivity increase at Fenton Hill. Geothermal Resources Council Transactions, Vol. 18, p 405-408, October 1994.

Cornet F.H. and Burlet D. (1992) Stress Field Determinations in France by Hydraulic Tests in Boreholes. Journal of Geophysical Research, Vol. 97 (B8), p 11,829-11,849, July 1992.

Clauser C. (1992) Permeability of crystalline rocks. **EOS**, Vol. 73(21), p 233 et seq.

CSM Associates (1992) Review of HDR Projects. Authors: A.J. Jupe, J. Willis-Richards and J.D. Nichols. Report prepared for AEA Technology, IR03/06, unpublished. 1992.

Eshelby J.D. (1957) The determination of the elastic field of an ellipsoidal inclusion, and related problems. Proc. of the Royal Soc. of London, series A, 241, p 376 et seq.

Main I.G., Meredith P.G., Sammonds P.R. and Jones C. (1990) Influence of fractal flaw distributions on rock deformation in the brittle field. Deformation Mechanisms, Rheology and Tectonics, Geological Society Special Publication, 54, p 81-96, 1990.

Matsunaga, I. Hiwaki N., Echigoya H. and Okubo S. (1990) Recent progress in Hot Dry Rock project at Hijiori, Japan. Proceedings of the 12th New Zealand geothermal workshop, 1990.

NEDO (1987-1992) Financial Year Summary Reports of Hot Dry Rock Geothermal Power Project in Japan. Geothermal Energy Department, New Energy and Industrial Technology Development Organization, Tokyo.

Nicol D.A.C. and Robinson B.A. (1990) Modeling the heat extraction from Rosemanowes HDR reservoir. Geothermics, Vol. 19(3), p 247-257, 1990.

Pine R.J., Jupe A.J. and Tunbridge L. (1990) An evaluation of in situ stress measurements affecting different volumes of rock in the Carnmenellis granite. International Society for Rock Mechanics Workshop on Scale Effects in Rock Masses, Loen, Norway, June 1990.

Richards H.G., Parker R.H., Green A.S.P.G., Jones R.H., Nicholls J.D.M., Nicol D.A.C., Randall M.M., Richards S., Stewart R.C. and Willis-Richards J. (1994) The performance and characteristics of the experimental Hot Dry Rock geothermal reservoir at Rosemanowes, Cornwall (1985-1988). Geothermics, Vol. 23(2) , p 73-109, 1994.

Watanabe K. and Takahashi H. (1995) Fractal geometry characterization of geothermal reservoir fracture network. Journal of Geophysical Research, 1995 (in press).

Willis-Richards J. (1995) Assessment of HDR reservoir stimulation and performance using simple stochastic models. Geothermics, 1995 (submitted).

Zoback M.L. (1992) First- and second-order patterns of stress in the lithosphere: The world stress map project. Journal of Geophysical Research, Vol. 97(B2), p 11,703-11,728, 1992.

PROCEEDINGS, Twentieth Workshop on Geothermal Reservoir Engineering
Stanford University, Stanford, California, January 24-26 1995
SGP-TR-150

CHEMICAL WATER/ROCK INTERACTION UNDER RESERVOIR CONDITION

K. Watanabe[1], K. Tanifuji[1], H. Takahashi[1],
Y. Wang[2], N. Yamasaki[3] and K. Nakatsuka[2]

1 Research Institute for Fracture Technology, Faculty of Engineering, Tohoku Univ., Sendai 980, JAPAN
2 Department of Resources Engineering, Faculty of Engineering, Tohoku Univ., Sendai 980, JAPAN
3 The Research Laboratory of Hydrothermal Chemistry, Faculty of Science, Kochi Univ., Kochi 780, JAPAN

ABSTRACT

A simple model is proposed for water/rock interaction in rock fractures through which geothermal water flows. Water/rock interaction experiments were carried out at high temperature and pressure (200~350 °C, 18 MPa) in order to obtain basic solubility and reaction rate data. Based on the experimental data, changes of idealized fracture apertures with time are calculated numerically. The results of the calculations show that the precipitation from water can lead to plugging of the fractures under certain conditions. Finally, the results are compared with the experimental data.

INTRODUCTION

Recently geothermal energy extraction from the crust via Hot Dry Rock (HDR) (Tester, 1989; Robinson and Pendergrass, 1989) or Hot Wet Rock (HWR) (Takahashi and Hashida, 1992) systems have received much attention. Thermal energy is extracted by circulating water through artificial and/or natural underground fracture networks.

Because the fractures in such systems are filled with geothermal water, it is necessary to examine the effect of chemical interaction between water and rock on water circulation. Water temperature and its change through the flow path is one of the most important variables for chemical interactions such as dissolution and precipitation. Few published sources are available for rock dissolution. Hashida and Takahashi (1983) performed dissolution experiments using granite. On the other hand, there are many report about the dissolution behavior of quartz, one of commonest rock forming minerals (Kennedy, 1950; Kitahara, 1960; Rimsted et al., 1980). They show that the solubility of quartz has a maximum value at around 320 °C, and thereafter decreases with increasing temperature.

In this paper, a simple model of water/rock interaction in a one-dimensional fracture is developed. In order to obtain the basic parameters for this model, granite dissolution experiments at high temperatures and high pressure are performed with batch and one-through autoclaves. The solubility of granite at several temperatures is obtained from the batch autoclave experiment, and the reaction rates are obtained from the one-through autoclave experiment. The influence of temperature on water/rock interaction is discussed. Based on the experimental results, the changes of fracture aperture caused by rock dissolution and precipitation are modeled numerically. Finally, these numerical results are compared with the experimental results from a tube-reactor autoclave which is constructed to simulate water flow in rock fractures.

WATER/ROCK INTERACTION MODEL

Chemical interactions between rock and water have not yet been fully described, and therefore, there is no well established set of equations which describe rock/water interactions. In this paper we assumed that the rock dissolution can be expressed by following equation :

$$\frac{\partial C}{\partial t} = \frac{S}{M} \cdot K(T) \cdot \{C^{\infty}(T) - C\} \qquad (1)$$

where C is concentration of rock and t is time. M is amount of water involved in the reaction, and S is the water/rock contact area. K is the dissolution rate constant and C^{∞} is the solubility of rock, and both values are functions of temperature, T. Equation 1 is the key equation for the water/rock interaction model presented in this paper.

Although the apertures of natural fractures are unlikely to be spatially uniform, we assume that water flow can be approximated by that in a parallel-sided fracture with a uniform aperture as shown in Fig. 1.

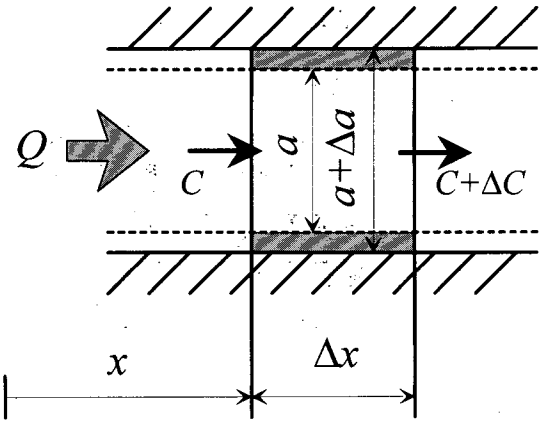

Fig. 1 The model of rock dissolution in a fracture.

Consider a small length, Δx at the point x at time t, with fracture aperture $a(x,t)$ as shown in Fig. 1, the mass balance of water/rock interaction is expressed as :

$$\rho_R \cdot \Delta x \cdot \Delta a(x,t) = \Delta C(x,t) \cdot \rho_W \cdot Q \cdot \Delta t \qquad (2)$$

where ρ_R and ρ_W are the densities of rock and water. Q is water flux through the fracture. Letting $\Delta t \rightarrow 0$ and $\Delta x \rightarrow 0$, equation 2 can be transformed to the following equation which expresses the rate of the aperture change along the fracture.

$$\frac{\partial a(x,t)}{\partial t} = \frac{\rho_W \cdot Q}{\rho_R} \cdot \frac{\partial C(x,t)}{\partial x} \qquad (3)$$

Considering the temperature at this point as $T(x,t)$, according to equation 1, the change of concentration, $\Delta C(x,t)$ is calculated as :

$$\Delta C(x,t) = \frac{2 \cdot \Delta x}{\rho_W \cdot Q \cdot \Delta t} \cdot K(T(x,t)) \cdot \left\{C^{\infty}(T(x,t)) - C(x,t)\right\} \cdot \Delta t \qquad (4)$$

Letting $\Delta x \rightarrow 0$, equation 4 can be transformed to the following equation which express the concentration along the fracture.

$$\frac{\partial C(x,t)}{\partial x} = \frac{2}{\rho_W \cdot Q} \cdot K(T(x,t)) \cdot \left\{C^{\infty}(T(x,t)) - C(x,t)\right\} \qquad (5)$$

Combining equations 3 and 5 :

$$\frac{\partial a(x,t)}{\partial t} = \frac{2}{\rho_R} \cdot K(T(x,t)) \cdot \left\{C^{\infty}(T(x,t)) - C(x,t)\right\} \qquad (6)$$

Equation 6 expresses the rate of fracture aperture change with time, and the fracture aperture at any position and any time can be calculated using this equation. However, in order to use equation 6 in numerical analysis, the solubility, C^{∞} and the dissolution rate constant, K have to be measured as functions of temperature.

THE SOLUBILITY OF GRANITE

The reaction processes between water and granite are very complicated due to its composition. It is therefore impossible to determine a solubility for granite sensuo stricto. Therefore the "apparent solubility" has been assumed to be the solubility of granite, as explained in following discussion.

The granite used in this study comes from Fukusima, Japan, and the mineral composition is shown in Table 1.

Mineral	Quartz	Orthoclase	Albite	Anorthosite	Biotite
Formula	SiO2	KAlSi3O8	NaAlSi3O8	CaAl2Si2O8	Omission
Vol. %	37 %	23 %	24 %	10 %	6 %

Table 1. Mineral composition of Fukushima granite.

Specimens are cut into small plates whose sizes are 45 mm x 40 mm x 5 mm, polished by 1500 mesh sand paper, and washed in acetone to remove cutter oil. Fig. 2 illustrates the batch type autoclave and specimen holder. This autoclave can be operated at temperatures up to 350 °C and pressures up to 20 MPa.

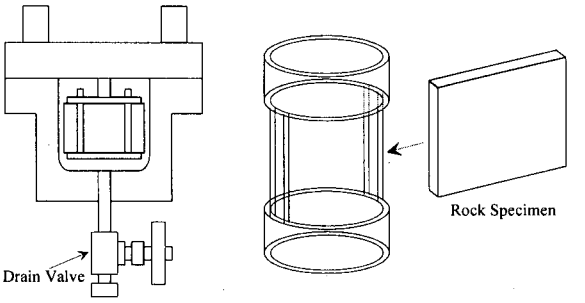

Fig. 2 Batch autoclave. Rock specimens are fixed by the specimen holder, and located in the middle of the autoclave.

Experiments were carried for several run times at temperatures of 200 °C, 250 °C, 300 °C, 330 °C and 350 °C, at a pressure of 18 MPa. After each run, the reacted water was extracted through the drain valve without cooling the autoclave. The specimens were weighed before and after the experiment to calculate the weight loss. In this study, the "granite" concentration in the reacted water was determined from the weight loss of specimens, not from solution analysis.

Figure 3 shows the relationship between time and weight loss expressed as a concentration in the fluid for each temperature.

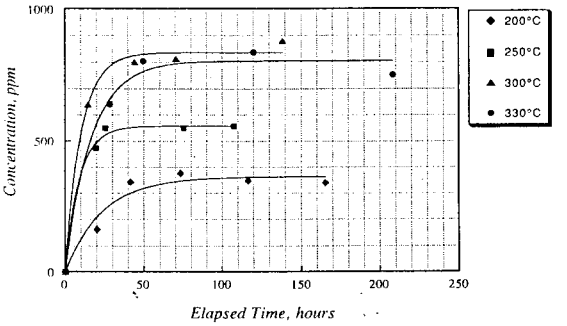

Fig. 3 The weight loss with time caused by dissolution.

Due to precipitation on the inside of autoclave, it was impossible to measure the concentration for the experiments at 350 °C. The results for 350 °C are not shown in Fig. 3. Because the saturated vapor pressure of water at 350 °C is close to 18 MPa, and the precipitation occurred in an air layer, the precipitation may have caused by boiling of the water.

As mentioned before, the strict solubility of granite can not be determined because it is almost impossible to know all the reactions between water and rock. In this paper,

however, we introduce apparent solubility as a tentative solubility for granite. We have already assumed that the interaction between water and rock was governed by equation 1. Integrating equation 1 with time, t, and appling the condition, C=0 when t=0, the equation to express the relationship between the run time and the concentration is obtained as follows for these experiments.

$$C(t) = C^{\infty}(T) \cdot \left\{ 1 - \exp\left(-\frac{S}{\rho_W \cdot V} \cdot K(T) \cdot t \right) \right\} \qquad (7)$$

In equation 7, S is the total reaction interface which is assumed to be equal to geometrical surface area in this study, and V is the volume of water in the autoclave. The unknown values in equation 7 are $C^{\infty}(T)$ and $K(T)$. By fitting equation 7 to the experimental results using a least squares method, both the "apparent solubility", $C^{\infty}(T)$ and the dissolution rate constant, $K(T)$ have been determined in this study. Each fitting curve is shown in Fig. 3. The "apparent solubility" is defined as the solubility of granite in this study. Fig. 4 shows the solubility of granite for each temperature obtained from these experiments. The solubility of quartz measured by Kennedy (1950) and Kitahara (1960) are also shown in Fig. 4.

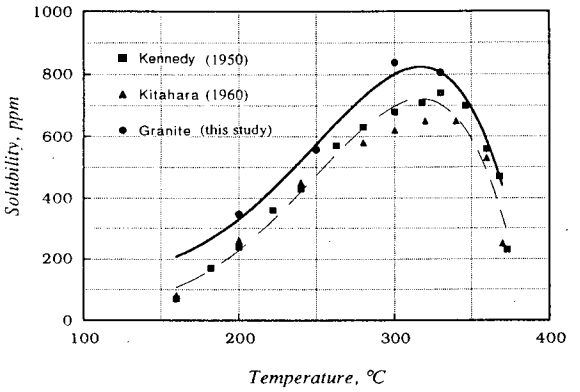

Fig. 4 The "granite" solubility as a function of temperature. The solid curve is used for numerical analysis. The solubility of quartz is also shown.

Although the dissolution rate constants, $K(T)$, for each temperature was measured by these experiments, these values may have large errors caused during heat up time of the autoclave. We, therefore, performed another set of experiments to measure $K(T)$ using the one-through autoclave as discussed next session.

THE DISSOLUTION RATE CONSTANT FOR GRANITE

Granite dissolution experiments in circulating water were performed using one-through autoclave as shown in Fig. 5.

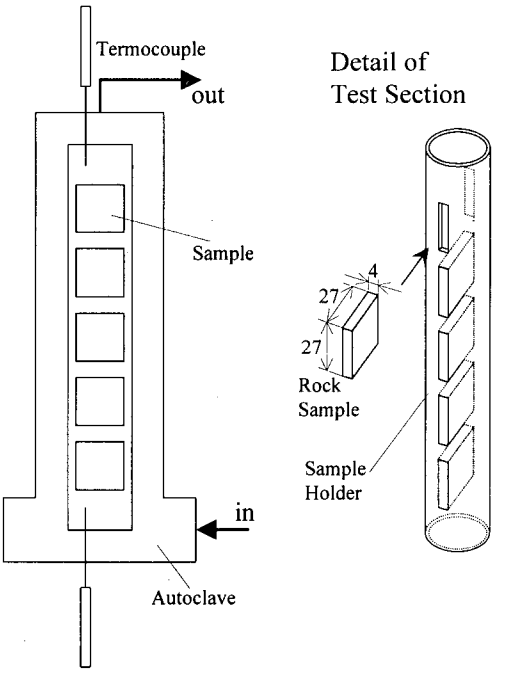

Fig. 5 One-through autoclave. Five rock specimens are set in the holder.

The major difference between this autoclave and the batch autoclave is that fresh water is continuously supplied to the autoclave by a high pressure pump. The experimental conditions are the same as previous section, that is, temperatures are 200 °C, 250 °C, 300 °C, 330 °C and 350 °C and the pressure is 18 MPa. The water flow rate was 1.0×10^{-2} m^3/h, sufficient to keep the "granite" concentration in the water to a very low value. The weight losses of the specimens were calculated in the same way as described in the previous section. Fig. 6 summarizes the results of these experiments for each temperature and run time.

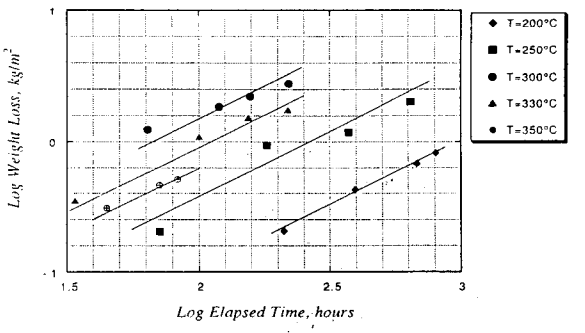

Fig. 6 The weight loss of rock specimens. Solid lines are the best fit lines when the reaction rate is assumed to be constant during experiments.

The reaction rate must change somewhat with time, because of the changes of reaction condition, such as total area of reaction surface. In this study, however, we assumed that the reaction rate did not change with time and that the weight losses should be proportional to the run time. Based on this assumption, straight line fits were obtained as shown in Fig. 6. These lines show the rate of weight loss with time.

In these experiments, the amount of fresh water being supplied continuously into the autoclave is large enough to assume that the concentration in the autoclave is almost equal to zero. Therefore, equation 1 can be eritten as :

$$\frac{\partial C}{\partial t} = \frac{S}{\rho_W \cdot Q} \cdot K(T) \cdot C^{\infty}(T) \qquad (8)$$

The weigh loss per unit area, ΔW can be calculated by following equation, according to mass balance.

$$\Delta W = \Delta C \cdot \rho_W \cdot Q / S \qquad (9)$$

Therefore :

$$\frac{\partial W}{\partial t} = \frac{\rho_W \cdot Q}{S} \cdot \frac{\partial C}{\partial t} = K(T) \cdot C^{\infty}(T) \qquad (10)$$

The left side of equation 10 is the rate of weight loss which we have measured by these experiments. The solubility of granite, $C^{\infty}(T)$, was measured in previous section. Therefore, the dissolution rate constant, $K(T)$, can be calculated based on equation 10. Fig. 7 shows $K(T)$ for each temperature, and the fitting curve in Fig. 7 is used for the following numerical analysis.

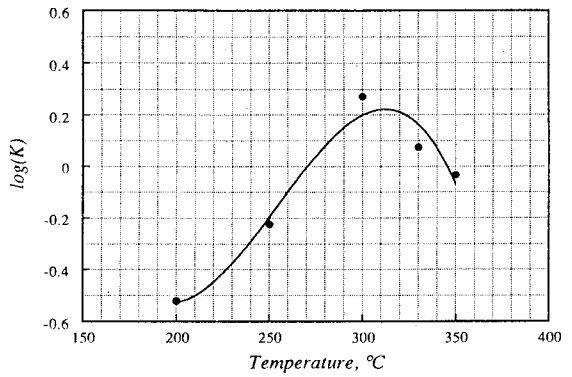

Fig. 7 The relationship between the dissolution rate constant and temperature. Solid curve is used for the numerical analysis.

ANALYSIS OF FRACTURE APERTURE CHANGE

In order to estimate the changes of the fracture apertures in geothermal reservoirs, the one-dimensional water flow model as shown in Fig. 8 has been introduced. In this model, it is assumed that the injection water is saturated with rock and rock precipitation occurs instantaneously when the concentration exceeds the solubility.

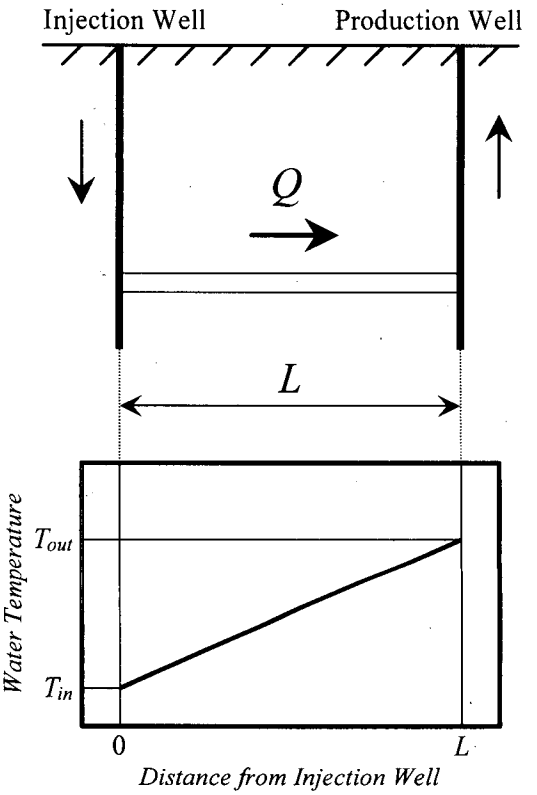

Fig. 8 A model of one-dimensional water flow through a fracture. The water temperature increases linearly with the distance from the Injection well.

In this model, water flow occurs only through the parallel-sided fracture, and the water temperature increases linearly through the fracture as shown also in Fig. 8. The water temperature at inlet and outlet are expressed by T_{in} and T_{out} respectively. The distance between the injection well and the production well was set to be 200 m. Four examples with different condition as follows have been examined.

Ex. 1 : T_{in}=200 °C, T_{out}=300 °C, Q=10 m^2/h
Ex. 2 : T_{in}=250 °C, T_{out}=350 °C, Q=10 m^2/h
Ex. 3 : T_{in}=200 °C, T_{out}=300 °C, Q=100 m^2/h
Ex. 4 : T_{in}=250 °C, T_{out}=350 °C, Q=100 m^2/h

The analytical result of the concentration change through the fracture for the Ex. 1 is shown by solid line in Fig. 9 (a). The dashed line expresses the saturation solubility at each point, i. e., each temperature along the fracture. Fig. 9 (b) shows the changes of fracture aperture after 2, 4, 6, 8 and 10 years. The corresponding results for Ex. 2, Ex. 3 and Ex. 4 are shown in Fig. 10, Fig. 11, and Fig. 12 respectively.

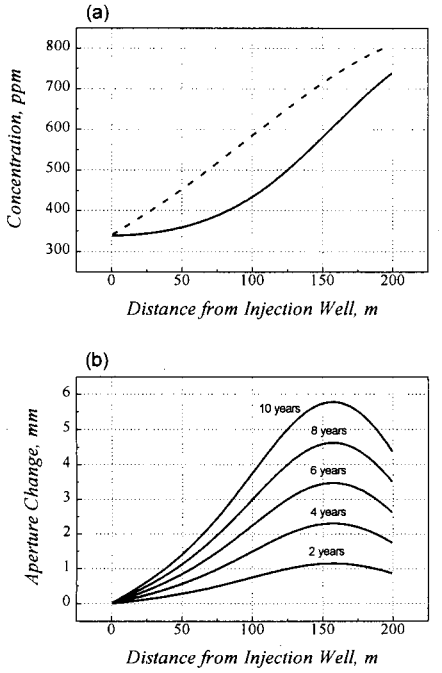

Fig. 9 The change of concentration and fracture aperture along the fracture for Ex. 1. The concentration never reached saturation, therefore, precipitation did not occur at any point.

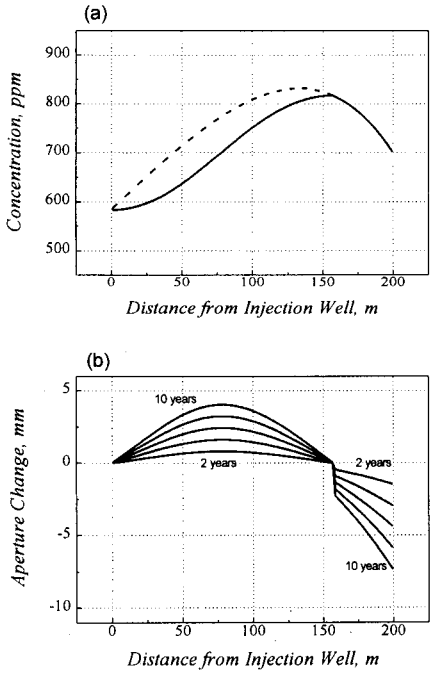

Fig. 10 The change of concentration and fracture aperture along the fracture for Ex. 2. The concentration reached saturation, and precipitation occurred at certain point.

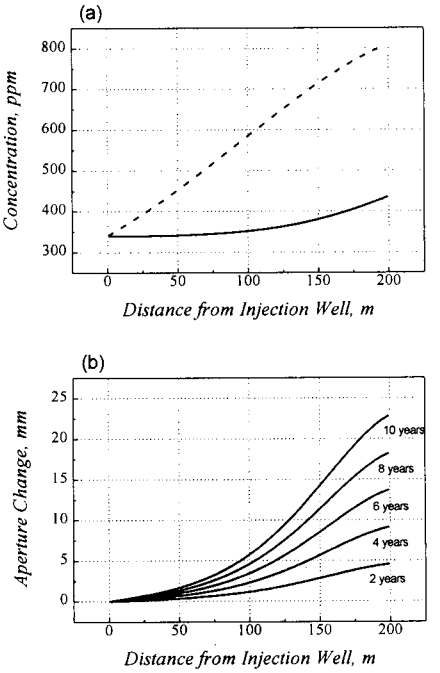

Fig. 11 The change of concentration and fracture aperture along the fracture for Ex. 3. The water flux is fast enough not to make a large change in the concentration.

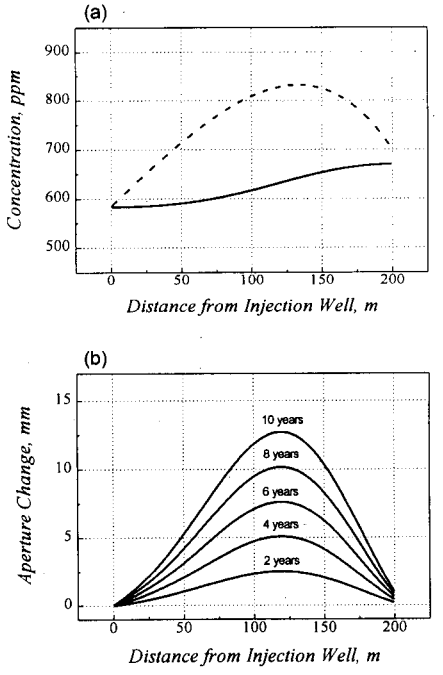

Fig. 12 The change of concentration and fracture aperture along the fracture for Ex. 4. The water flux is fast enough to prevent the precipitation.

In Ex. 1, the solubility increases along the fracture and the concentration never reached the solubility. This allowed only dissolution and results in widening the fracture aperture. In Ex. 2, on the other hand, the concentration reached saturation and precipitation occurred from this point. The water flux used for Ex. 3 and Ex. 4, Q=100 m^2/h, is large enough to prevent the concentration along the fracture increasing significantly. Even in Ex. 4, where temperature condition was same as Ex. 2, precipitation did not occur at any point.

COMPARISON WITH EXPERIMENTAL DATA

To help verify the numerical results, we have developed the tube-reactor type autoclave as shown in Fig. 13. This autoclave makes it possible to simulate water flow in a fracture using cylindrical rock specimens. Five separate heaters are attached along the 1 m long tube, and several kind of temperature gradient can be set. In order to examine the precipitation behavior suggested in the previous section, the experimental temperate was selected to be around 320 °C. Two experiments with different water flow rate (0.5 mm^3/s and 5 mm^3/s) were performed. The number of cylindrical specimens used for each run was 50. The water temperatures were set 250 °C, 300 °C, 330 °C, 350 °C and 340 °C at each heater point from the inlet. The last heater was set lower to prevent the output water boiling.

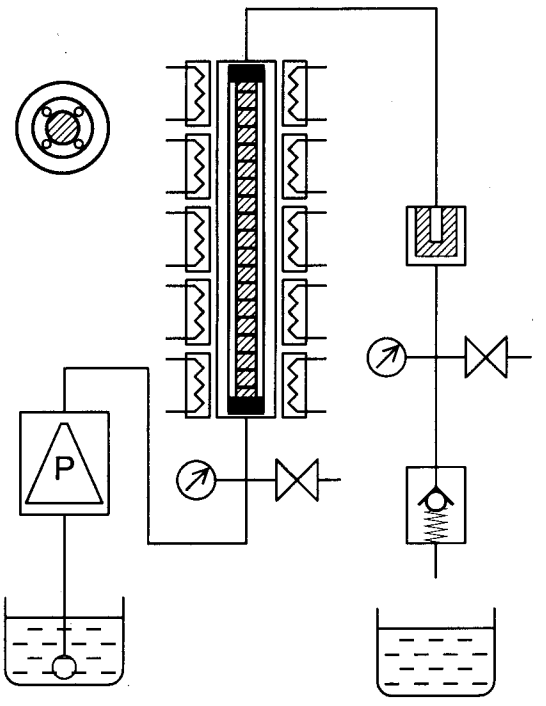

Fig. 13 Tube-reactor autoclave. Temperature gradient can be introduced along the flow path using five heaters.

Figure 14 (a) shows the weight changes of the specimens along flow path measured from the experiment with Q=0.5 mm^3/s. The weight of some specimens increased due to precipitation. This lappened at the point where the temperature exceeded 320 °C, as same as the numerical analysis. Fig. 14 (b) shows the concentration profile calculated from weight loss of specimens, and the solid line is the solubility of granite for each point. A region of over-saturation was found. This means that the precipitation rate constant should be also considered in order to inprove the numerical model presented here.

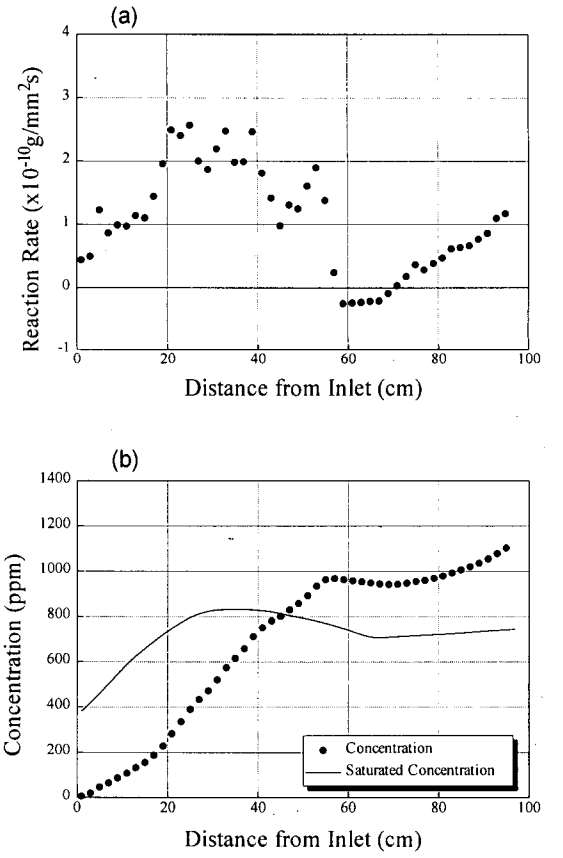

Fig. 14 The reaction rate and the calculated concentration along flow path obtained from the experiment for Q=0.5 mm^3/s. Rock precipitation occurred around the point of 60 cm from inlet. The water was over saturated from the point of 45 cm from inlet.

Figure 15 shows the results for the experiment with Q=5 mm^3/s. In this experiment, no specimen increases its weight and the concentration never reached asturation. However, the dissolution rate decreased from the point where temperature exceeded 320 °C.

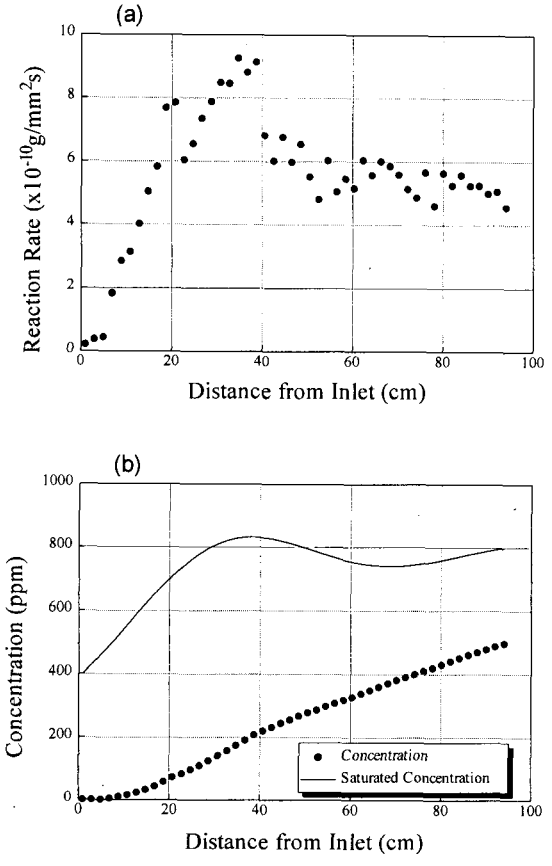

Fig. 15 The reaction rate and the calculated concentration along flow path obtained from the experiment for Q=5.0 mm^3/s. Water flux was sufficiently high that the saturation concentration was never reached, and no precipitation could not take place.

CONCLUSIONS

The solubility of granite may be dominated by quartz, and its sensitivity to temperature was similar to that of quartz. Fractures in geothermal reservoirs may be subjected to various chemical problems depending on temperature, flow rate and other parameters. The analytical and experimental results in this study suggest that rock precipitation can occur and may result in the plugging of the fractures in geothermal energy extraction systems whose reservoir temperatures exceed 300 °C.

Although, in this study, precipitation was assumed to occur at the point where the concentration exceeds the solubility, experimental results suggest that rock supersaturation persist for some time. This implies that the precipitation rate constant should also be measured in future work.

ACKNOWLEDGMENT

A part of this work presented here was supported by Ministry of Education, Science and Culture under Grant-in-Aid for Scientific Research on Priority Areas entitled "Fractal Fracture Mechanics and Advanced Geothermal Energy Extraction System Design," Grant No. 05232101, 05232102 and 05232104.

REFERENCES

Hashida, T. and Takahashi, H. (1983) "Dissolution Behavior of Granite under Simulated Geothermal Reservoir Conditions," 4th International Symposium Water-Rock Interaction, Extended Abstracts, pp. 172-174.

Kennedy, G. C. (1950) "A Portion of the System Silica-Water," Econ. Geol. Vol. 45, pp. 629-253.

Kitahara, S. (1960) "The Solubility of Quartz in Water at High Temperatures and High Pressures," The Review of Physical Chemistry of Japan, Vol. 30-2.

Rimsted, J. D. and Barnes, H. L. (1980) "The Kinetics of Silica-Water Reaction," Geochimica et Cosmochimica Acta, Vol. 44, pp. 1683-1699.

Robinson, B. A. and Pendergrass, J. (1989) "A Combined Heat Transfer and Quartz Dissolution/Deposition Model for A Hot Dry Rock Geothermal Reservoir," Proceeding of 14th Workshop on Geothermal Reservoir Engineering, Stanford University.

Takahashi, H. and Hashida, T. (1992) "New Project for Hot Wet Rock Geothermal Reservoir Design Concept," Proceedings of the 17th Workshop on Geothermal Reservoir Engineering, Stanford University, Vol. 17, pp. 39-44 (SGP-TR-141).

Tester, J. W., Brown, D. W. and Potter, R. M. (1989) "Hot Dry Rock Geothermal Energy - A New Energy Agenda for the 21st Century," Los Alamos National Laboratory report LA-11514-MS.

PROCEEDINGS, Twentieth Workshop on Geothermal Reservoir Engineering
Stanford University, Stanford, California, January 24-26 1995
SGP-TR-150

FUTURE TARGET FOR GEOTHERMAL DEVELOPMENT - FRACTAL FRACTURE MECHANICS AND ITS APPLICATION TO CONCEPTUAL HDR RESERVOIR DESIGN -

Hideaki Takahashi, Kimio Watanabe and Toshiyuki Hashida

Research Institute for Fracture Technology, Faculty of Engineering
Tohoku University, Sendai 980, JAPAN

ABSTRACT

A concept of "Fractal Fracture Mechanics" for HDR (Hot Dry Rock) geothermal reservoir design has been developed as an extension of conventional rock fracture mechanics. It is suggested that this concept is successfully applicable to characterize and model subsurface fracture network in HDR geothermal reservoir.
Furthermore, this modeling procedure makes it possible to evaluate the thermal energy output from the fractal HDR reservoir and its life performance, and to understand the fractal multiple cracking behavior during the hydraulic fracturing.

INTRODUCTION

Since a half century design concept and procedure of pressure vessel and piping system like boiler or nuclear and chemical reactor for energy conversion engineering has been developed as an accumulated and integrated technology system, where there have existed a lot of inventions and improvement in the fields of important basic research area, for example, combustion technology, heat transfer, and material science and engineering.

Nowadays, in fact, the standard design procedure for a power plant boiler of 500 MW has been established as ASME Boiler and Pressure Vessel Design Code. As illustrated in Fig. 1 (a), when the design specification of a power plant is determined, then the conceptual design and engineering details such as type of boiler, area of heat exchanging surface and etc., can be selected, and consequently design engineers can estimate a cost and time schedule for the whole construction.
In geothermal engineering, on the other hand, there has not been established a reasonable basic design procedure for the thermal output from the earth's crust. In another word, there is no standard design procedure for "Geothermal Underground Boiler". Until now, the thermal output and life time of a geothermal power plant is determined only from well logging data obtained for the reservoir concerned. As shown already in Fig. 1 (b), the most important key technologies to establish "Geothermal Boiler Technology" is a design procedure of heat exchange surface in the underground and its life performance estimation. The majority of currently operating geothermal power plants in the world heavily rely on natural geothermal fluid stored in the existing subsurface fracture network.

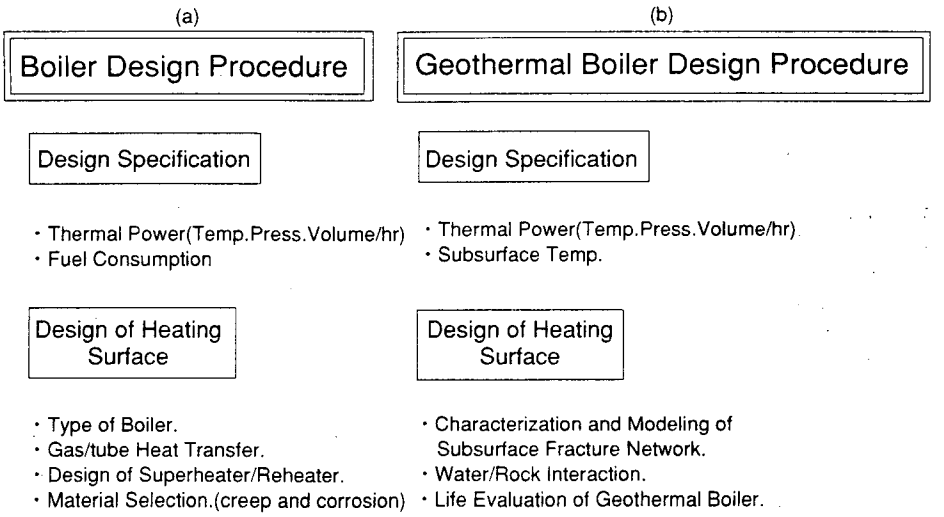

Fig. 1 Comparison of design procedures for conventional boiler and geothermal subsurface boiler.

Therefore thermal output is limited because of the locality, and the potential thermal energy from the surrounding areas is typically not fully utilized and remains unexplored. Here, the basic idea of HDR (Hot Dry Rock) can be applied to extract those potential thermal energy of surrounding areas in the conventional geothermal field, where a name of "HWR (Hot Wet Rock)" was proposed and this HWR system refers to the combined natural and artificial crack network (Takahashi and Hashida, 1992). The research target is directed towards enhancing the geothermal power of existing reservoir. This paper describes a future R&D and target for HDR or combined HDR-HWR geothermal reservoir engineering in next decay, where a contribution of "Fractal Fracture Mechanics" to the geothermal reservoir design is demonstrated and the basic research items to be solved are also discussed.

NEED OF QUANTITATIVE CHARACTERIZATION OF SUBSURFACE FRACTURE NETWORK FOR GEOTHERMAL RESERVOIR

Since 20 years HDR geothermal energy extraction technology has been developed as one of the most attractive energy conversion systems. Although several HDR field experiments demonstrated the strong potential for energy production from the crust, no HDR power plant is realized yet, because hot water circulation systems are still not fully understood and consequently HDR reservoir could not be designed in the engineering base.

Hence, the key technologies for the future HDR development are summarized as follows :

(1) Characterization of fracture networks in a subsurface and their modeling for the HDR reservoir design.
(2) Evaluation of water permeation through the fracture networks and design of the circulation systems.
(3) Evaluation of heat and mass transfer and their change during HDR life time.
(4) Mechanical response of fractal fracture network during hydraulic fracturing stimulation and service operation.

Among those key technologies mentioned above, it is first of all important that three-dimensional fracture network systems in the crust are fully understood and modeled reasonably based on the geological background.

Geometrical similarity of the fracture patterns has been reported often in the literature, where various fractures from the microscopic grain-size fracture (~1 mm) to macroscopic fault-size fracture (~1 km) were described and characterized. Recently strong attention has been paid on "fractal geometry" to explain and characterize those fracture patterns.

Although as described previously, no HDR power plant is available, there are many conventional geothermal power plants in the world. Their thermal outputs per unit power station are limited c/a 30~50 MW, on average, to prevent thermal draw down and keep long life performance.

Figure 2 shows an illustrative sketch of the future research and development target not only for the traditional geothermal energy extraction but also for the HDR reservoir design.

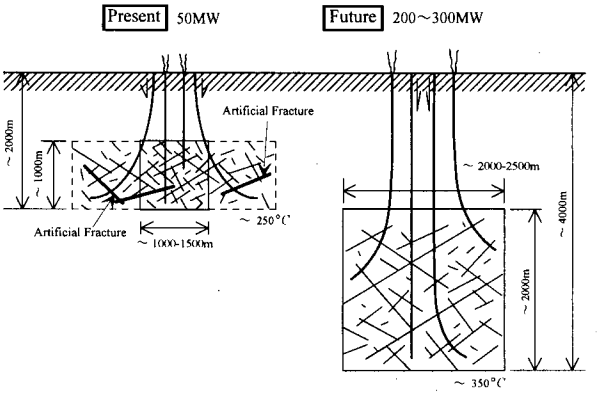

Fig. 2 Future target for geothermal energy extraction from HDR/HWR reservoir making use of subsurface fracture networks.

It is understood that thermal output of 30~50 MW seems to be the optimal energy output from a 1 km cube of rock of ~250°C temperature. Next-generation HDR energy extraction from deep crust provides us the potential for large capacity power plants (~300 MW). An image of our future HDR reservoir is illustrated also in Fig. 2, where the depth of well attains 4~5 km, and rock temperature ~350°C. The size of the HDR reservoir is a 2 km cube. After we can understand the fracture networks, water circulation and thermal output within a 1 km cube quantitatively and it can be modeled by use of simple methodology, a scale-up to 2 km cube HDR reservoir is easily achieved. In Fig. 2 there are illustrated two-dimensional fracture network systems by which the water circulation from inlet well to production well and energy extraction could be made.

FRACTAL FRACTURE NETWORK RESERVOIR MODEL

Recently, Watanabe and Takahashi (1995) proposed a two-dimensional modeling technique for subsurface fracture networks on the basis of "fractal geometry" as a new procedure for modeling geothermal energy extraction system. This procedure makes it possible to characterize geothermal reserves by parameters measured from field data such as core sampling. This two-dimensional model can be easily extended to three-dimensional model as described as following.

There is essentially no information available concerning the three-dimensional shape of subsurface fractures. In this paper, therefore, we assume the subsurface fractures to

be penny-shaped as in the analysis by Koldith (1993) and Willis-Richards et al. (1995), and the diameter distribution to be fractal in which the relation between fracture length, r and the number of fractures, N whose lengths are equal to or larger than r can be expressed by the following fractal equation :

$$N = C \cdot r^{-D} \qquad (1)$$

where C is a constant and D is a fractal dimension.
Figure 3 shows the concept of the three-dimensional fracture network model, and a schematic of the fracture network water circulation system. The network is generated by distributing a fractal size distribution of penny-shaped fractures with random orientations to random positions in the cube. In order to simplify and generalize the discussion, the area and the fractures are normalized by the size of cubic.

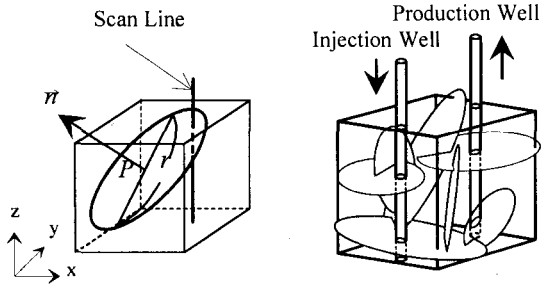

Fig. 3 General concept of the individual fracture generation for the three-dimensional fracture network model and a schematic of the fracture network water circulation model.

In this normalized model, the total number of fractures is expressed by the symbol n, and the ith (i=1,2,...,n) fracture is characterized by the following three parameters: mid-point of the fracture, p_i; normal to the fracture plane : $\vec{n}_i$; and diameter of the fracture : r_i. Similarly, fracture network patterns are characterized by the following three parameters : the total number of fractures, n; fractal dimension, D; and fracture density parameter, C. In this paper, these parameters are determined as follows.

Mid-point of the fracture, p_i. It is assumed that the fractures do not interact to form clusters, so the x, y and z co-ordinates of the point p_i are determined by using random numbers lying between 0 and 1.

Normal to the fracture plane, $\vec{n}_i$. The distribution of $\vec{n}_i$ often appears to be random, but observations of fractures in borehole cores and in the field commonly show that fracture sets have preferred orientations. Therefore, if it is possible to obtain the preferred orientations, $\vec{n}_i$ must be determined to have the same tendency as that of the field data. In this study, however, only a random distribution of normal to the fracture plane is used.

Diameter of the fracture, r_i. Since the diameter distribution of the fractures is governed by fractal geometry, the distribution of values of r_i must satisfy equation (1). In order to satisfy equation (1), r_i is determined by the following formula :

$$r_i = (C / i)^{1/D} \qquad (2)$$

Total number of fractures, n. Theoretically, if we were to consider very small fractures whose lengths approach zero, then n would approach infinity. However, very small fractures cannot be observed, and the minimum fracture size which can be observed is dependent upon the resolution of the measuring instrument. In this paper, r_{min} is defined as the smallest length of fracture which must be considered for the analysis. Although we do not discuss the details here, pre-calculation has shown that fractures with normalized lengths smaller than 0.1 exert only a very small influence on the permeability. So, we have set the value of r_{min} as 0.1, and the smallest value of i which satisfies $r_i > r_{min}$ is accepted as the value of n.

Fractal dimension, D. Although some fault systems have been investigated and their fractal dimensions calculated by the box-counting method, the fractal dimensions required for equation (1) are not available. As described above, Main et al. (1990) have reported the relationship between the fracture length and the number of fractures at four different scale fault systems and shown that the fractal dimensions of all fault systems are almost equal to 1. Because geothermal energy extraction systems often make use of natural fault systems in the reservoir for water flow paths, it is reasonable to adapt the same value obtained by Main et al. (1990) to geothermal reservoir models. Theoretically a three-dimensional fractal dimension must be 2.0 to get a fractal distribution of fracture lengths with D=1.0 on the section areas of the three-dimensional model proposed here. So, the fractal dimension of the three-dimensional fracture network model is assumed to be 2.0 in this present work.

Fracture density parameter, C. Once the total number of fractures and their fractal dimension are determined, then the fracture network models can be described simply by parameter C alone. In this study, parameter C is used as the model comparison parameter. For actual geothermal sites, it is also possible to estimate the value of parameter C based on field data. It is relatively easy to measure the number of fractures per unit length that are observed on core material that samples a borehole interval of interest. If we then consider a borehole as a scan-line of a subsurface fracture network as shown in Figure 3, it is possible to predict the number of fractures observed per unit length of core m by the following equation :

$$m = \overline{\sin\theta_i} \cdot \left\{ \int_{r_{min}}^{1} \pi \cdot \left(\frac{r}{2}\right)^2 \cdot \left(-\frac{dN(r)}{dr}\right) dr + C \right\} \qquad (3)$$

where $\overline{\sin\theta_i}$ is the average sin of all the angles of fractures from horizontal, θ_i. From equation (3), the parameter C

can be calculated according to :

$$C = \frac{4m}{\sin\theta_i \cdot \left\{9\pi \cdot \left(1 - r_{\min}^{0.2}\right) + 1\right\}} \qquad (4)$$

CONCEPTUAL HDR RESERVOIR DESIGN PROCEDURE BASED ON FRACTAL FRACTURE MECHANICS

Figure 4 illustrates a basic concept of "Fractal Fracture Mechanics", where three essential parameters, crack distribution, crustal stress data and fracture toughness of rocks are interrelated each other as a fracture mechanics parameter.

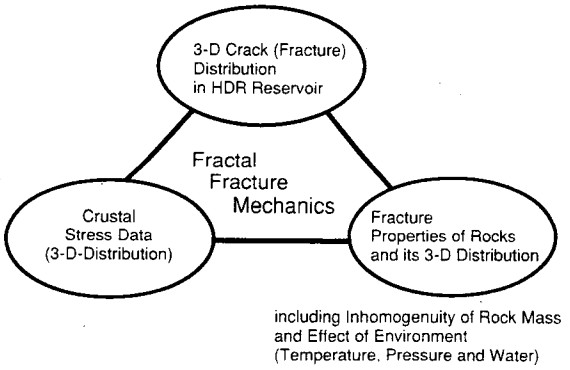

Fig. 4 Concept of fractal fracture mechanics with three essential geophysical parameter.

Because, in the previous section described above, there is no quantitative information of three-dimensional information of subsurface fracture network, a simple three dimensional model for HDR reservoir was proposed by use of circular shaped fracture (Watanabe and Takahashi, 1993, 1995). Figure 5 is an example of R&D program of a conceptual HDR reservoir design procedure based on "Fractal Fracture Mechanics". This design flow chart presents a fundamental step of the Fractal Fracture Mechanics applied to HDR reservoir modeling by use of core sample information. Until now this design procedure is not yet established as the whole system technology. However, the conventional fracture mechanics can be used as a fundamental tool and be modified for subsurface application. In the conventional fracture mechanics, a single crack problem is a typical one, while there are naturally created multiple cracks (fractures) within HDR reservoir. Therefore it is strongly needed to develop a standard procedure to characterize three-dimensional crack system in the reservoir from borehole data such as core sample or BHTV. When the fracture network is known, then fluid flow and heat transfer analysis can be made even for the complicated fracture system as mentioned later.

EVALUATION OF THERMAL OUTPUT FROM THREE-DIMENSIONAL FRACTAL HDR RESERVOIR AND ITS LIFE PERFORMANCE

Single Fracture and Permeable Zone Models

In the first instance, it is important to estimate geothermal energy extraction performances from the single fracture and permeable zone models since these will provide respectively the lower and upper bounds of the reservoir performance due to the total area of heat exchange surface.

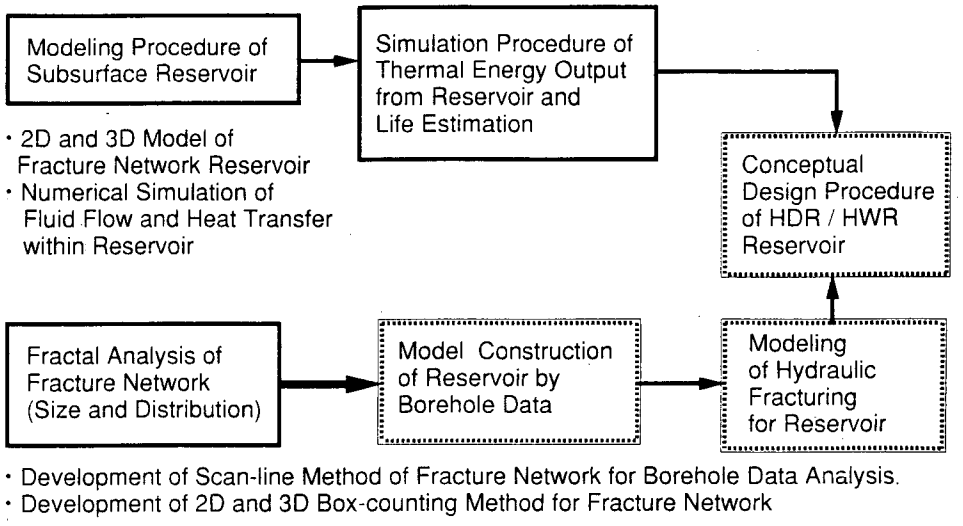

Fig. 5 An example of R&D program for establishing the conceptual design procedure of HDR reservoir based on fractal fracture mechanics.

Figure 6 illustrates the three-dimensional single fracture and permeable zone models used in this study. In the single fracture model, water flow occurs only through one fracture which connects the injection well and the production well as shown in Fig. 6. The permeable zone model is considered as an equivalent of the fracture network model in which fractures fill the volume uniformly. These two models are the ideal examples of the fracture network model.

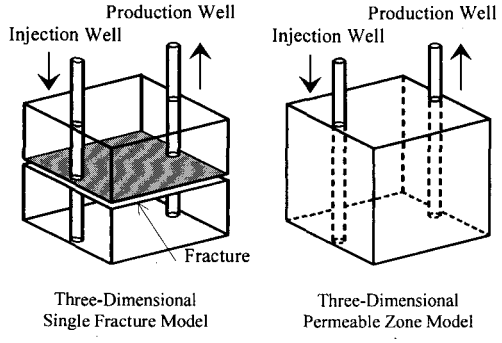

Fig. 6 Three-dimensional single fracture and permeable zone models.

Water Flow Model

Assuming that the density of water is constant at every point and temperature within the model reservoir volume, the water flow through the permeable volume can be expressed by :

$$k_x \cdot \frac{d^2P}{dx^2} + k_y \cdot \frac{d^2P}{dy^2} + k_z \cdot \frac{d^2P}{dz^2} = 0 \qquad (5)$$

where P is the water pressure, and k_X, k_Y and k_Z represent the permeability in the x, y and z directions. For numerical calculations, the volume of interest is divided into a mesh of small elements. In this paper, the local permeability is given between elements in the mesh where fractures intersect element interfaces as shown in Fig. 7.

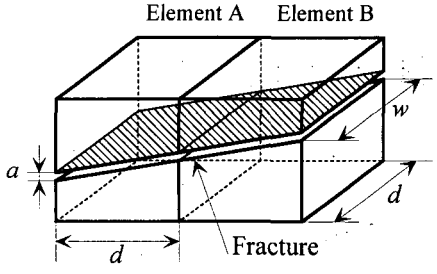

Fig. 7 Definition of local permeability between elements where a fracture intersects the boundary.

Although the apertures of natural fractures are not spatially uniform and an "effective" aperture should therefore be calculated, we have assumed that water flow can be approximated by that in a parallel-sided fracture with some constant effective aperture. According to the cubic flow law, the quantity of water flowing between elements, q_i, can be expressed by :

$$q_i = \alpha \cdot w \cdot a^3 \cdot \Delta P / d \qquad (i = x, y, x) \qquad (6)$$

where a and w express the aperture and the width of fracture intersecting the element interface, and ΔP is the difference in fluid pressure between the two elements. d is the element size and α is a constant.

In this model, the local permeability between elements is defined as :

$$k_i = u_i \Big/ \left(\frac{\Delta P}{d}\right) = \left(\frac{q_i}{d^2}\right) \Big/ \left(\frac{\Delta P}{d}\right) = \alpha \cdot \frac{w \cdot a^3}{d^2} \qquad (7)$$

where u_i is the water velocity, and i symbolizes the directions x, y and z. The effective aperture of fractures is assumed to be proportional to the fracture lengths according to :

$$a = \beta \cdot r \qquad (8)$$

therefore :

$$k_i = \gamma \cdot w \cdot r^3 \qquad (\gamma = \alpha \cdot \beta^3 / d^2) \qquad (9)$$

where β *and* γ are constants.

In this study, the local permeability is alsó normalized to the permeability of the whole mesh by the following equation :

$$k_i^* = \frac{\gamma \cdot w \cdot r^3}{\gamma \cdot d \cdot L^3} = \frac{w \cdot r^3}{d \cdot L^3} \qquad (10)$$

Thermal Transfer Model

The model used to calculate the thermal transfer is shown in Fig. 8. In Fig. 8, the dotted line indicates the adiabatic thermal boundary for the calculation of thermal transfer, and LE represents the distance to the thermal boundary. LE is determined by a theoretical calculation of the one-dimensional heat transfer rate to be the minimum distance for approximately zero temperature change over the time scale of interest.

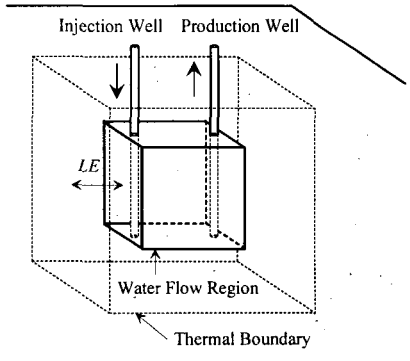

Fig. 8 Thermal transfer model. The solid lines express the water flow region where no water flows occur. The dotted lines express the adiabatic thermal boundary.

The following equation is used for the calculation of thermal transfer :

$$C_R \cdot \rho_R \cdot \frac{\partial T}{\partial t} + C_W \cdot \rho_W \cdot \left(u_x \cdot \frac{\partial T}{\partial x} + u_y \cdot \frac{\partial T}{\partial y} + u_z \cdot \frac{\partial T}{\partial z} \right) = \lambda \cdot \left(\frac{\partial^2 T}{\partial x^2} + \frac{\partial^2 T}{\partial y^2} + \frac{\partial^2 T}{\partial z^2} \right) \quad (11)$$

where T is the temperature of the rock (equal to the temperature of the water in this calculation) and t is time. λ is the thermal conductivity of the rock. C_R and C_W are respectively the specific heats of the rock and the water, ρ_R and ρ_W are respectively the densities of the rock and the water, and u_x, u_y and u_z are the water velocities in each direction. Normalized value of temperature, T^*, time, t^*, water velocity, u_x^*, u_y^*, u_z^* and quantity of circulating water, Q^* are defined as follows :

$$T^* = \frac{T - T_0}{T_\infty - T_0} \quad (12), \qquad t^* = \frac{\lambda \cdot t}{C_R \cdot \rho_R \cdot L^2} \quad (13)$$

$$u_i^* = \frac{L \cdot C_W \cdot \rho_W \cdot u_i}{\lambda} \quad (14), \qquad Q^* = \frac{C_W \cdot \rho_W \cdot Q}{L \cdot \lambda} \quad (15)$$

where T_∞ and T_0 define the initial temperatures of the rock mass and the water in the injection well, respectively. Q is the quantity of circulating water.

Changes in Thermal Output with Time

The thermal energy output profile is the most important parameter for performance estimation. Hence, We define the normalized thermal energy output E^* as :

$$E^* = Q^* \cdot T^* \quad (16)$$

Figure 9 shows the changes in E^* with time for each reservoir model. The thermal energy change for a single water quantity of Q^*=100 has been used to compare the performance of each model. Three fracture network models with different fracture densities (C=2.0, C=4.0, C=6.0) have been used. Because our fracture network model is generated using random numbers, each profile of thermal energy output is obtained from the average value of 20 trials with different random seeds.

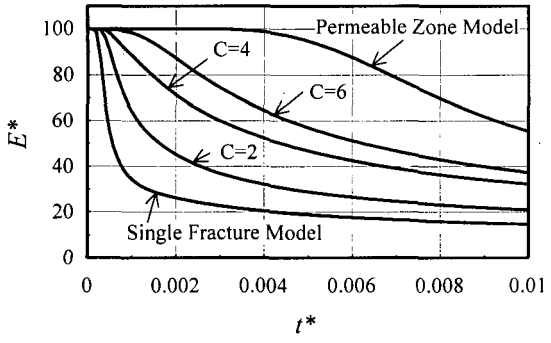

Fig. 9 Changes in the thermal energy outputs for the single fracture and permeable zone models, and the variants of the fracture network model.

OPTIMUM DESIGN AND POTENTIAL ANALYSIS

Design Optimization of Energy Extraction

For economically effective energy extraction, the optimum design of HDR systems must be discussed. Although there are many factors to be considered for the optimum system design, here, we use only the normalized optimum quantity of circulating water Q^* as the optimization parameter. Because the temperature of a geothermal reservoir decreases with heat energy extraction, it is necessary to define the normalized reservoir life, t_{life}^*. In this study, the normalized temperature threshold of production water, T_{th}^* is used to determine t_{life}^* as shown in Fig. 10.

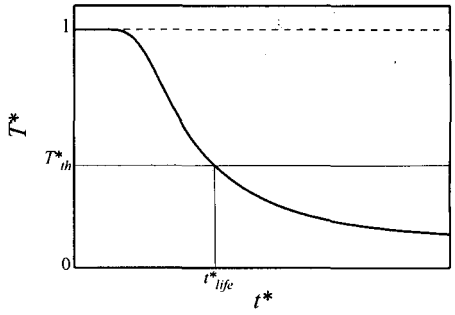

Fig. 10 Definition of the normalized reservoir life.

T_{th}^* is the lowest temperature at which economical energy production is possible. As we saw in the previous section, the normalized temperature of production water decreases as fracture density, quantity of circulating water and time all increase. The reservoir life, t_{life}^* is defined as the point where the normalized temperature of production water reaches T_{th}^*, as also shown in Fig. 10. Once T_{th}^* is fixed, and the fracture density is obtained, t_{life}^* can be predicted as a function of Q^* as shown in Fig. 11.

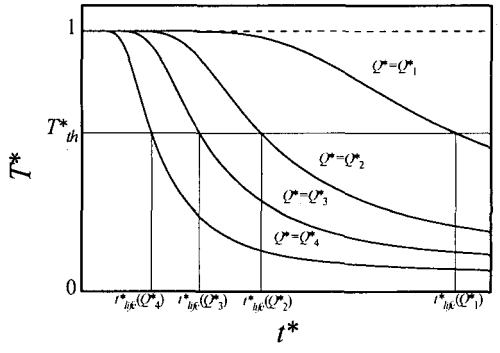

Fig. 11 The relationship between the reservoir life and the quantity of circulation water.

For optimized systems, t_{life}^* should be equal to the design life. It is possible to set the value of T_{th}^* to be equivalent to the design life by controlling Q^*. In this study, the optimum design requires us to find the value of Q^* which

give the same value of t_{life}* as the design life, and this value of Q* for each system is defined as the normalized optimum quantity of circulating water, Q^*_{opt}. Fig. 12 shows the relationship between Q^*_{opt} and t_{life}* for T_{th}*=0.5, and it is found that the relationship is linear in log-log space.

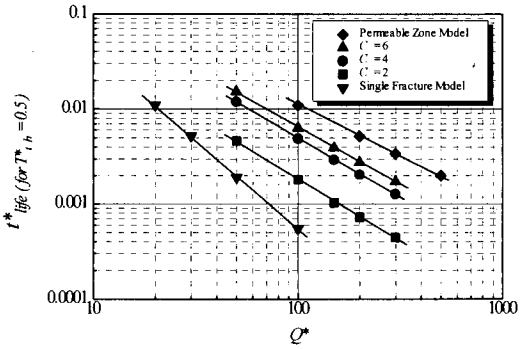

Fig. 12 The normalized optimum design curve. Each line shows the optimum quantity of circulating water for the reservoir life (design life).

Potential of Energy Extraction from HDR

To estimate the potential of HDR systems, a numerical analysis of energy extraction from optimized HDR systems, i. e., those with an optimized quantity of circulation water, has been performed. Fig. 13 shows the relationship between reservoir size and maximum energy output transformed from normalized values using following conditions and the thermal properties.

Initial temperature of rock mass : $200°C$
Temperature of injection water : $100°C$
T_{th}* : $150°C$, t_{life}* : 20 years
$\lambda = 2.40\ W/m \cdot K$
$C_R = 1.20 \times 10^3\ J/K \cdot kg$, $\rho_R = 2.26 \times 10^3\ kg/m^3$
$C_W = 4.48 \times 10^3\ J/K \cdot kg$, $\rho_W = 8.68 \times 10^2\ kg/m^3$

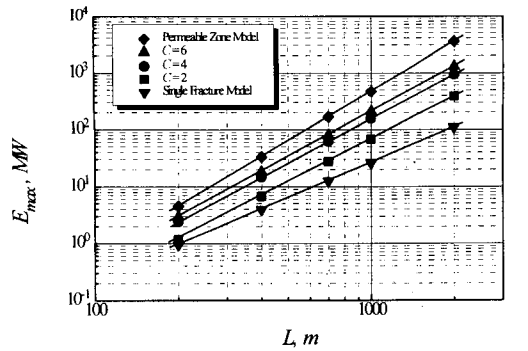

Fig. 13 The maximum thermal energy output from HDR with the optimum quantity of circulation water.

From Fig. 13 it can be predicted that a 2km x 2km x 2km HDR reservoir which has a relatively high fracture density (C=4.0) can produce more than 300 MW under optimized operational conditions. This shows the great potential of HDR geothermal energy extraction as a new energy production technique.

FRACTAL FRACTURE MECHANICS MODEL OF HYDRAULIC FRACTURING

In this section, outline of a numerical simulation model is presented which was used to study the crack pattern induced by hydraulic fracturing in a fractured rock mass in two dimensions, and some preliminary results are given.

The model employs the Fluid Rock Interaction Program (FRIP)(Cundall, 1983; Markland, 1992), but a beam model is built into the simulation code so that the growth behavior of newly created crack by hydraulic fracturing can be simulated in addition to the stimulation of pre-existing cracks in the fractured rock mass. The model consists of a regular grid of elastic blocks separated by weak planes. An elastic beam network is constructed on the grid model such that two neighboring grids are bridged by the elastic beam. The beams are rigidly connected at the center of the grid. The elastic beam represents the cohesive strength of the weak plane in which the fluid flow occurs. The fluid flow in the weak plane is allowed to occur when the tensile stress in the beam reaches the fracture strength of the rock. The elastic modulus and the cross sectional dimensions of the elastic beams are selected to simulate the elastic properties of the rock.

In order to simulate the pre-existing cracks in rock masses, the cohesive strength along the weak plane is set to be zero; namely the elastic beam across the pre-existing cracks is broken before fluid injection is applied. A population of pre-existing cracks varying in size and orientation is generated stochastically. A fractal distribution is assumed for the crack size, and the crack orientation and location is assumed to be random.

Numerical simulations were conducted to examine the effects of the density of the pre-existing cracks and the fractal dimension on the hydraulically induced crack pattern. The initial crack densities used in the simulations were 5, 7.5, 10, 15 and 20 %, and the fractal dimensions for the crack size were 1.0, 1.4 and 1.8. In order to characterize the size of the stimulated reservoir, the number of the stimulated cracks , i.e. the broken beams within the square grid model were counted. The relationship between the number of the stimulated cracks and the initial crack parameters is shown in Fig. 14 along with typical crack patterns obtained by the above procedure on a square grid model 50 x 50 with a free external boundary. The dimensions of the grids are 0.1 m x 0.1 m. The incompressible fluid is injected at the center of the grid model. The thick line indicated in the grid

model shows the stimulated reservoir. It appears that the number of the stimulated cracks (total flow area) primarily depends on the initial crack density.

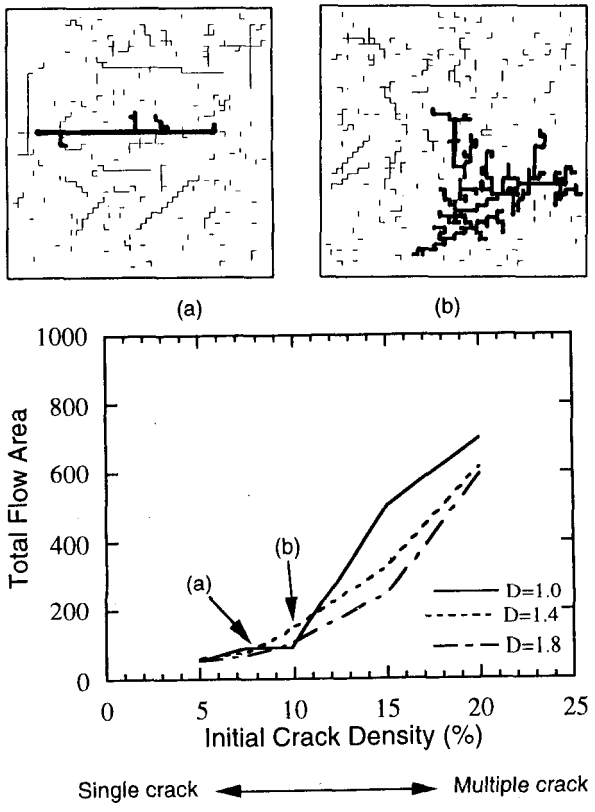

Fig. 14 Transition of the hydraulically induced crack pattern

Furthermore, it is shown that the crack pattern transition from a single crack to the multiple crack type reservoir occurs approximately above the initial crack density of 10 %. Information regarding the initial crack density can be obtained from a borehole survey. Thus, it may be possible to predict the reservoir type using the present hydraulic fracturing model combined with such field data. There has been reported the very similar crack patterns created by hydraulic fracture simulation (Herrmann et al., 1993). More rigorous three-dimensional simulation model which allows for the pressure gradient in the crack and the growth of shear dilation along pre-existing cracks is currently being developed at Tohoku University.

CONCLUDING REMARKS

With special reference to fracture network in the HDR/HWR geothermal reservoir, the concept of "Fractal Fracture Mechanics" was proposed to develop a conceptual design procedure for the geothermal boiler.
In order to establish this concept, the further development of both fundamental methodology and careful accumulation of field examples would facilitate during next 10 years.

ACKNOWLEDGMENTS

Recently the keyword "Fractal Fracture Mechanics" has been also proposed by Dr P.G. Meredith (UCL, London) and Prof. I. G. Main (Univ. of Edinburgh) in United Kingdom. Authors would like to acknowledge them for JSPS-British Council collaboration research project on "Fractal Fracture Mechanics" (1992-94).

REFERENCES

Cundall, P. A. (1983), "Fluid-Rock Interaction Program (FRIP) : Computer Model of HDR Reservoir," Phase 2 Group IV Part 2 Report, CSM Geothermal Energy Project.

Herrmann, H., Poliakov, N. B. and Tzschichholz, F. (1993), "Engineering Applications of Fractal : Examples from Soil and Rock Mechanics," Proceedings of Symposium on Fractals in Science and Engineering, Tokyo.

Koldith, K. and Diersch, H. (1993), "Quasi-steady-state Strategy for Numerical Simulation of Geothermal Circulation in Hot Dry Rock Fractures," International Journal of Non-Linear Mechanics, Vol. 28, No. 4, pp. 467-481.

Main, I. G., Peacock, S. and Meredith, P. G. (1990), "Scattering Attenuation and Fractal Geometry of Fracture System," Pure and Applied Geophysics, Vol. 133, pp. 283-304.

Markland, J. T. (1992), "Modelling and Design of HDR Reservoir Creation," Camborne School of Mines Geothermal Energy Project Report 3A-5.

Takahashi, H. and Hashida, T. (1992) "New Project for Hot Wet Rock Geothermal Reservoir Design Concept," Proceedings of the 17th Workshop on Geothermal Reservoir Engineering, Stanford University, Vol. 17, pp. 39-44 (SGP-TR-141).

Watanabe, K. and Takahashi, H. (1993) "Fractal Characterization of Subsurface Fracture Network for Geothermal Energy Extraction System," Proceedings of the 18th Workshop on Geothermal Reservoir Engineering, Stanford University, Vol. 18, pp. 119-124.

Watanabe, K. and Takahashi, H. (1995) "Fractal Geometry Characterization of Geothermal Reservoir Fracture Networks," Journal of Geophysical Research, in press.

Willis-Richards, J., Watanabe, K., Yamaguchi, T., Sato, Y and Takasugi, S. (1995) "HDR Reservoir Analysis Incorporating Acoustic Emission Data," To be presented in this workshop.

PROCEEDINGS, Twentieth Workshop on Geothermal Reservoir Engineering
Stanford University, Stanford, California, January 24-26 1995
SGP-TR-150

STUDY OF DESORPTION IN A VAPOR DOMINATED RESERVOIR WITH FRACTAL GEOMETRY

Monica Tudor, Roland N. Horne, Thomas A. Hewett

Petroleum Engineering Department
Stanford University, Stanford CA 94305-2220

ABSTRACT

This paper is an attempt to model well decline in a vapor dominated reservoir with fractal geometry. The fractal network of fractures is treated as a continuum with characteristic anomalous diffusion of pressure. A numerical solver is used to obtain the solution of the partial differential equation including adsorption in the fractal storage space. The decline of the reservoir is found to obey the empirical hyperbolic type relation when adsorption is not present. Desorption does not change the signature of the flow rate decline but shifts it on the time/flow rate axis. Only three out of six model parameters can be estimated from field data, due to the linear correlation between parameters. An application to real well data from The Geysers field is presented together with the estimated reservoir, fractal space and adsorption parameters. Desorption dominated flow is still a questionable approximation for flow in fractal objects.

INTRODUCTION

Classical modeling approaches available in the literature for describing fractured reservoirs are based either on discrete deterministic and/or statistical fracture geometry information or on a lumped parameter multiple (usually dual) continuum approach. In many cases, however, the discrete fracture network approach is bound to fail due to the prohibitively large number of fracture parameters required by the model. This is the case with The Geysers geothermal field for which studies of the fracturing patterns have concluded that it can only be characterized as "effectively random" (Beall and Box, 1989).

At the other extreme, the continuum approach, usually involving the presence of double continua with different storage parameters coexisting in a Euclidean space with dimension D=2 or 1, offers little flexibility for characterization at the reservoir scale. The implicit assumption embedded in these models is that there exists a typical scale at which the variation of reservoir parameters is bounded, in other words that there exists a Representative Elementary Volume (REV).

Alternatively, fractal geometry of fracture networks provides a promising framework for a realistic reservoir model unconstrained by the requirement of REVs and without ruling out the possibility of using the continuum approach. Fractal geometry is characterized by self-similarity over all scales: zooming in a fractal object results in deterministic and/or statistically identical copies of the whole. This repetitivity determines on one hand the degree to which a fractal object fills the embedding space, or in other words the mass fractal dimension D and on the other hand the connectivity of the object, expressed by its spectral dimension. The discontinuous character of a fractal object, as opposed to the perfectly connected embedding Euclidean space, renders functions defined on it nondifferentiable. Thus the very idea of a partial differential equation written for flow in fractals would not be justified unless the properties of the medium were replaced by analytical equivalents. Following the model developed by O'Shaughnessy and Procaccia (1985) for diffusion on fractals, Chang and Yortsos (1990) have established the differential equation which governs flow in a fractal network of fractures. The solution of the welltest problem presented by them illustrates the phenomenon of anomalous diffusion typical for fractal geometry.

Often natural fracture systems have been successfully described within the framework of fractal geometry. Sammis et al. (1991) studied graywacke outcrop fracture patterns at Geysers and found that the scaling re-

lationship characteristic to fractal objects is applicable over a span of scale of two orders of magnitude. An interesting application of fractal analysis to pressure transients in the Geysers field was shown by Acuna et al. (1992) who found that the mass fractal dimension could range between 1.2 and more than 2.0. According to them this type of analysis is more likely to give a plausible explanation for pressure transients than an alternative single finite conductivity fracture model. To our knowledge, no attempt has been made to date to interpret reservoir decline data using the fractal network of fractures model. Studies of well decline at Geysers have usually used the semiempirical Fetkovich method.

It has been suggested that adsorption is a plausible storage mechanism in vapor dominated reservoirs (Nghiem and Ramey, 1991). Measurements of adsorption on cores from Geysers have shown that adsorbed water completely saturates micropores in the reservoir rock (Shang at al., 1993). However, the numerical model set up by Hornbrook (1994) to compute the pressure response to production in a one-dimensional reservoir where adsorption was modeled by Langmuir isotherms has shown very small adsorption effects at late times.

The objective of this paper is to analyze the adsorption effects on reservoir decline when fluid flow takes place in a fractal network of fractures. The partial differential equation established for pressure diffusion and incorporating an adsorption source term is solved using a numerical solver. Following the theoretical analysis of the results, the application of the model to specific well decline data from The Geysers gives an estimate of the model parameters and allows for an evaluation of the present approach.

MATHEMATICAL MODEL

The physical model considered consists of a fracture network embedded in the Euclidean rock matrix, considered to be impermeable. Traditionally the storage and flow properties of the porous medium included in the mathematical model are porosity and permeability, respectively. In a fractal object neither porosity nor permeability have a constant value across the model. Both porosity and permeability are considered to decrease with the Euclidean distance, r, from the well in a power law fashion (Chang and Yortsos, 1988):

$$porosity: \quad \phi = \frac{aV_s}{B} r^{D-d} \tag{1}$$

$$permeability: \quad k = \frac{aV_s}{B} m r^{D-d-\theta} \tag{2}$$

where a is a constant characteristic of the fractal object expressing the number of sites per fractal mass (dimension L^{-D}), V_s the volume of each site assumed constant across the fractal object (dimension L^3), B a geometric constant (of dimension L^{3-D}) which describes the appropriate symmetry ($B = A, 2\pi h, 4\pi$ for rectilinear, cylindrical and spherical symmetry, respectively, where A and h represent cross-sectional area and reservoir thickness respectively), m is a parameter akin to permeability which expresses connectivity and flow conductance, D is the mass fractal dimension, d is the dimension of the embedding Euclidean space and θ is a parameter related to the spectral dimension of the fractal network (O'Shaughnessy and Procaccia, 1985). Note that for a Euclidean fracture network: $D = d$ and $\theta = 0$. In this case the two relations above reduce to:

$$B\phi = aV_s \tag{3}$$

$$m = \frac{k}{\phi} \tag{4}$$

The partial differential equation describing diffusion on a fractal network of fractures has been derived by Chang and Yortsos (1988). The nondimensional form of this equation and the associated dimensionless group is:

$$(r_D)^\theta \frac{\partial p_D}{\partial t_D} = \frac{\beta}{r_D} \frac{\partial p_D}{\partial r_D} + \frac{\partial^2 p_D}{\partial {r_D}^2} \tag{5}$$

$$r_D = \frac{r}{r_D}; \; t_D = \frac{t}{t\star}; \; p_D = \frac{{p_i}^2 - p^2}{{p_i}^2} \tag{6}$$

$$with \quad t\star = \frac{\overline{c_f \mu} {r_w}^{\theta+2}}{m} \tag{7}$$

where r_w is the well radius and p_i the initial reservoir pressure. The choice for this nondimensionalization of the pressure was determined by the fact that for the purposes of a well decline analysis the boundary condition at the well is usually prescribed (constant/variable) pressure.

Two important observations should be made with respect to this equation: 1) nowhere in Eqn. (5) does the embedding Euclidean space dimension appear and 2) the anomalous diffusion phenomenon is captured by the power law relation between the diffusivity and radial distance.

The addition of a new term representing the desorption of water in the fracture network as a source at

each site in the fractal object will bring the partial differential equation to the desired form for studying the adsorption effects on the fluid flow. In order to derive the adsorption source term we will consider the Langmuir isotherm model for the mass X of water adsorbed in a unit volume of rock:

$$X\left(\frac{p}{p_s}\right) = d\frac{c\left(\frac{p}{p_s}\right)}{1+(c-1)\left(\frac{p}{p_s}\right)} \tag{8}$$

where d is the magnitude factor which determines the maximum amount adsorbed at $p = p_s$, c is a shape factor which determines the rate at which desorption occurs and p_s represents the saturation pressure at initial reservoir temperature, hereafter considered equal to the initial pressure in the reservoir. Let V be the volume of rock available for adsorption in a cylinder of radius r. If the space available for adsorption has a mass fractal dimension, Z then:

$$V = V_a r^Z \tag{9}$$

where V_a is a geometric factor of dimension L^{3-Z}. Total adsorbed mass in the cylinder of radius r is, therefore:

$$A_t = dcV_a\frac{\left(\frac{p}{p_s}\right)}{1+(c-1)\left(\frac{p}{p_s}\right)}r^Z\rho_R \tag{10}$$

where ρ_R represents the rock density. The dimensional form of the adsorption source term can be obtained by differentiating A_t with respect to r and t:

$$Q_A = (Z+1)\,r^{Z-1}dcV_a\frac{p_s}{2p\left(p_s+(c-1)\,p\right)^2}\frac{\partial\left(p^2\right)}{\partial t}\rho_R \tag{11}$$

Expressing p in terms of the nondimensional p_D:

$$p = p_i\sqrt{1-p_D};\quad \frac{\partial\left(p^2\right)}{\partial t_D} = -{p_i}^2\frac{\partial p_D}{\partial t_D} \tag{12}$$

and using the assumption that the reservoir was initially at saturation conditions, $p_i = p_s$, after normalization we obtain:

$$Q_A = A{r_D}^{\alpha}F\left(p_D\right)\frac{\partial p_D}{\partial t_D} \tag{13}$$

with constant A given by:

$$A = \frac{(Z+1)\,dcV_a m\rho_R}{2\overline{\mu c_f}\rho_s {r_w}^{D+\theta-Z+2}\left(aV_s\right)} \tag{14}$$

where ρ_s is the density of saturated vapour, exponent α is $Z-D$ and the pressure function F is given by:

$$F\left(p_D\right) = \frac{1}{\sqrt{1-p_D}\left(1+(c-1)\sqrt{1-p_D}\right)^2} \tag{15}$$

Note that $F(p_D) > 0$ for any value of the shape factor $c > 0$ and any p_D in $(0,1)$. Also note that large values for this term can be expected when the dimensionless pressure is small: $p_D \to 0$ (which occurs at the beginning of the drawdown) and the shape factor has a small value: $c \to 0$ (favorable for desorption). Reasonable estimates of parameter A are of the order of 10^3.

The partial differential equation including desorption effects becomes:

$$\frac{\partial p_D}{\partial t_D}\left[{r_D}^{\theta}+A{r_D}^{\alpha}F\left(p_D\right)\right] = \frac{\beta}{r_D}\frac{\partial p_D}{\partial t_D}+\frac{\partial^2 p_D}{\partial {r_D}^2} \tag{16}$$

It can be assumed that the dimension of the storage space coincides with the dimension of the adsorption space: $D = Z$.

A numerical solver based on the method of lines was used to solve Eqn. (16) for prescribed wellbore pressure and infinite acting outer boundary conditions. The solution, represented with cubic Hermite polynomials, is presented in the next section.

RESULTS AND DISCUSSION

The solution of the equation of flow in a fractal network of fractures was computed first for the case where the adsorption term was neglected ($A = 0$). The results are presented in terms of dimensionless flow rate vs. dimensionless time in Fig. 1. As expected, they reduce to the well-known solutions for one-, two- and three-dimensional cases, when the flow space has a Euclidean geometry. The distinct feature of the solution for $D < 2$ is a practically constant log-log slope at late time:

$$log\ q = a\ log\ t + b \tag{17}$$

$$or\quad q = B\,t^a \tag{18}$$

where a and $B = 10^b$ are constants related to the model parameters: D and θ. Differentiating relation

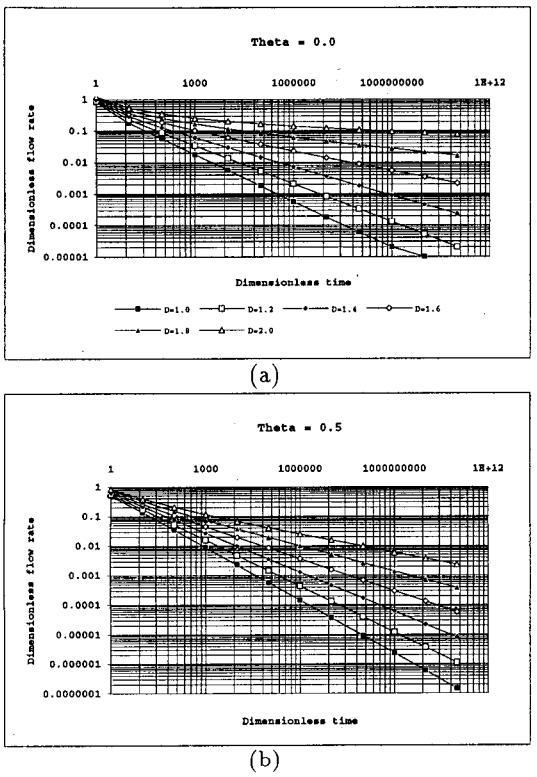

Figure 1: Well decline with no adsorption, (a) $\theta = 0.0$ and (b) $\theta = 0.5$

(18) with respect to time and replacing time t with the power $1/a$ of the flow rate q divided by the constant B we obtain:

$$\frac{dq}{dt} = \frac{a}{B^{1-\frac{1}{a}}} q^{1-\frac{1}{a}} \tag{19}$$

The generic form of (19):

$$\frac{dq}{dt} = C\ q^h \tag{20}$$

is known as the general empirical hyperbolic decline relationship and has been used in specific forms to analyze the decline of wells at The Geysers.

A sensitivity analysis was conducted for the two model parameters involved: mass fractal dimension D and the spectral dimension dependent parameter θ. The results, presented as a graph of the log-log slope of flow rate - time relation versus D and θ respectively (Fig. 2) shows that the solution is more sensitive to the mass fractal dimension D than to the parameter θ, specially at lower values of D (closer to 1.0). Also, Fig.

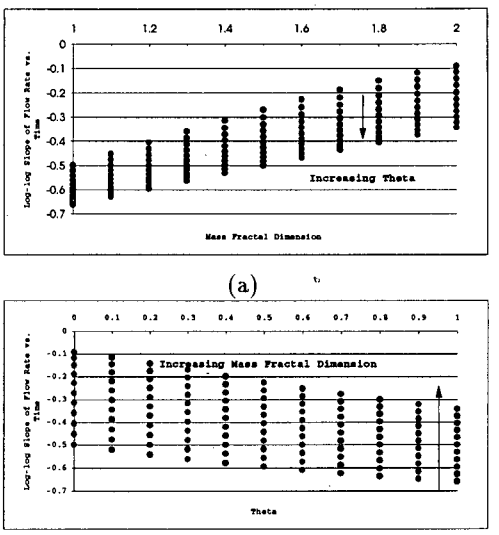

Figure 2: Effects of fractal parameters on the log-log slope of the well decline (a) Mass fractal dimension effect (b) Effect of parameter θ

3 clearly shows that D and θ are linearly correlated.

The next step was to compute the solution for the case where adsorption was present. For this a fractal geometry with parameters $D = 1.9$, $\theta = 0.25$ was considered (in agreement with the results obtained by Acuna et al., 1992, in one of the wells at The Geysers), a dimensionless adsorption parameter between 1 and 100 and an adsorption curve shape coefficient ranging between 0.01 and 10. Fig. 4a) shows the effects of increasing the dimensionless adsorption coefficient. It can be seen that beyond a threshold value of A (10 for this set of parameters) the decline curves start with a plateau

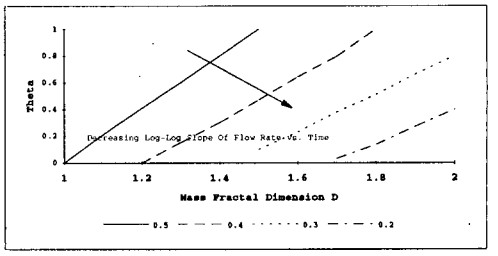

Figure 3: Linear correlation of fractal parameters

value corresponding to a maximum flow rate that can be sustained by the specific geometry of the reservoir. Although the ratio of the flow rates sustained by the reservoir for different dimensionless adsorption coefficients decreases with time, the curves remain distinct during the entire time span examined. The adsorption curve shape coefficient c has practically the same influence as A on the decline curve (curves in Fig. 4b) were obtained for $A = 1000$). The maximum sustainable flow rate was obtained for $c = 1$, which is exactly the value which divides the interval of possible values of c into two classes: the adsorption favorable class ($c > 1$) and the desorption favourable class ($c < 1$). For values of adsorption coefficients in excess of the threshold values the reservoir can be characterized as desorption dominated.

Examining the radius r_i at which interference can be noted (r for which $p_{wf} = 0.01$) it can be seen from Fig. 5a) and 5b) that a power law relation between r_i and the two adsorption coefficients A and θ is applicable. The value of r_i itself for desorption dominated flow is extremely low: $r_i < 300 r_w$ at $t_d = 10^9$, which lays a question mark on the validity of the assumption that pressure can be approximated by its smooth envelope at such small radii.

APPLICATION TO FIELD DATA ON WELL DECLINE

The parameters of the model which have to be estimated from field data are: $q\star$ and $t\star$, the flow rate and time normalizing constants, D and θ, the fractal object parameters and A and c, the adsorption coefficients. However, not all these parameters are independent of one another.

We have seen already from Fig. 3 that the fractal object parameters are not independent. Also, overall both adsorption parameters, A and c, have the effect of shifting the decline curve in time, therefore being correlated with the normalizing time constant. This is of consequence in analyzing field data and estimating reservoir parameters, causing the problem to be poorly constrained.

Another aspect important in estimating the reservoir parameters is that the boundary condition at the well may be very important for the 'signature' of the decline curve. An illustration of the effect of changing the level of the well pressure is given in Fig. 6. The case where p_{wf} is changed from 0.3 to 1.0 within a period of time spanning two orders of magnitude, although less likely to be encountered in practice, shows that the shape of the pressure decline curve can be dis-

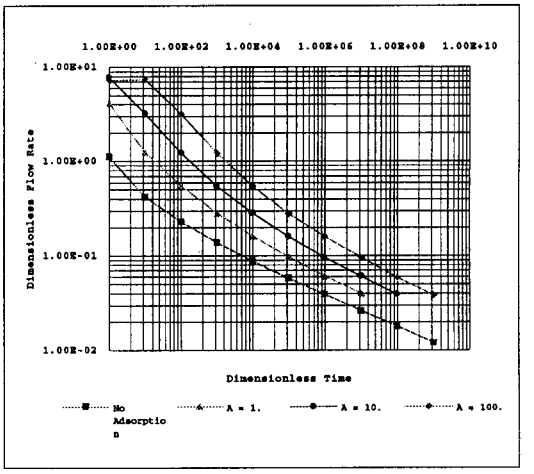

(a)

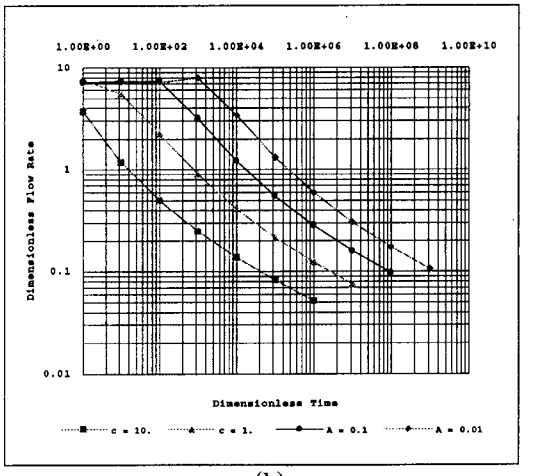

(b)

Figure 4: Effects of adsorption parameters on well decline (a) c=0.01 and variable A and (b) A=1000 and variable c

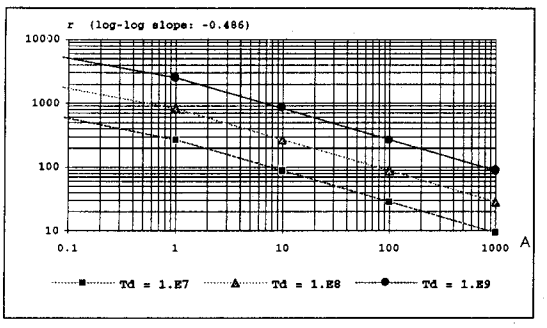

(a)

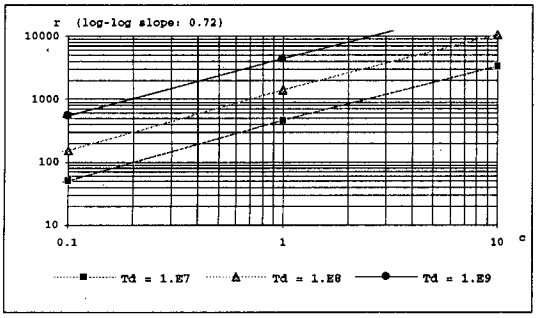

(b)

Figure 5: Interference radius (a) vs. adsorption parameter A and (b) vs. adsorption parameter c

torted sufficiently to make a simple type-curve match with type curves computed for constant wellbore pressure impractical. Therefore an automated model fitting using the appropriate boundary conditions is required.

Finally, we can set as a target for an automated type-curve matching program the estimation of 3 out of 6 parameters. As an illustration of the application of the model to real field data we have tried to estimate the reservoir parameters for well LF 425 of Unit 12, Geysers geothermal field. The parameters to be estimated were: $q*$, D, A. The bottomhole corrected pressure was computed using Goyal's method (1986) and used in defining the boundary condition at the well for the partial differential equation. For the short part of the decline data the parameters that were used as input to the program were: $\theta = 0.1$, $t* = 0.19$, $c = 0.1$, and the parameters resulting from the automated evaluation were: $D = 1.15$, $q* = 12.5$, $A = 2137$. This set of parameters is by no means unique. It belongs to an entire family of correlated parameter sets. For instance the data could have been modeled with $D = 1.45$ and $\theta = 0.55$.

In spite of the underdetermination of the model it can,

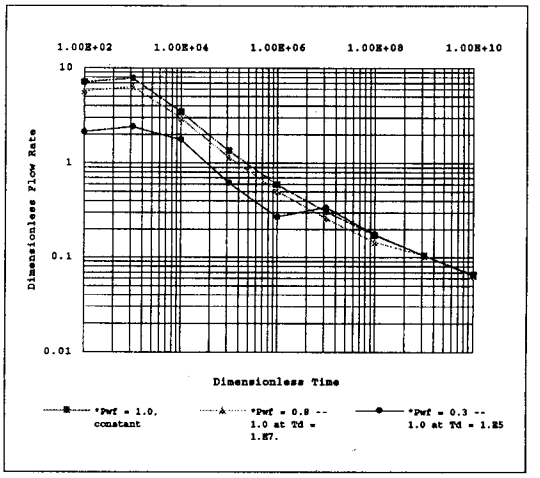

Figure 6: Effects of changing the bottomhole pressure

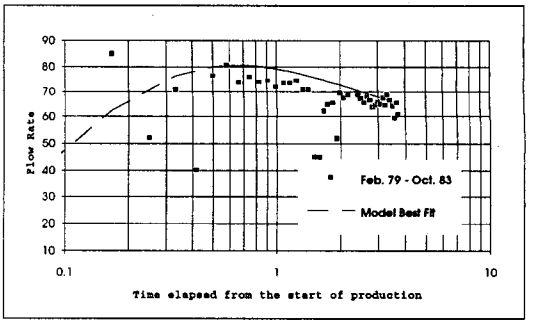

Figure 7: Model fitting to decline data from well LF State 425, The Geysers

nevertheless be used to predict future decline in wells.

CONCLUSIONS

The characteristics of flow denoted by 'anomalous diffusion' are determined by a power law relation of diffusivity and Euclidean radius. Models of flow in a fractal network of fractures require two additional parameters: D, the mass fractal dimension, associated with the storage properties of the reservoir and θ, a parameter representative for the spectral dimension of the fractal object, associated with the permeability field. Since adsorption is determined by the vapor pressure lowering phenomenon it can be assumed that the same mass fractal dimension of the storage space can be applied to the adsorption space.

Flow rate decline in a fractal reservoir without adsorption obeys the general relation for hyperbolic decline. The signature of the flow rate decline in the presence of adsorption does not change significantly at late times. However, at early times a constant maximum attainable flow rate develops when threshold values of the adsorption coefficients A and c are exceeded and desorption becomes dominant. Model results show that when desorption dominantes interference effects may be completely eliminated. A question mark remains as to whether the assumption of a good approximation of the actually nondifferentiable pressure function defined on a discontinuous fractal space is the smooth envelope anymore.

Parameters akin to storage properties: adsorption coefficients A and c and the invariant part of the diffusivity are strongly correlated and thus difficult to estimate from field data on flow rate decline. Reservoir response is less sensitive to the spectral dimension related parameter θ than to the mass fractal dimension D. Estimation of a range of (D,θ) values is possible using real well decline data. Due to the correlation of model parameters a set of maximum three independent parameters out of six can be obtained by automated type curve matching. The model was successfully tested on a well from The Geysers geothermal field.

AKNOWLEDGEMENTS

The authors thank the Department of Energy, Geothermal Division, who provided partial funding for this research through contract DE-FG07-90ID12934, and the Stanford Center for Reservoir Forecasting (SCRF) who also provided partial funding.

REFERENCES

Acuna, J.A., and Y.C. Yortsos (1991), "Numerical Construction and Flow Simulation in Networks of Fractures Using Fractal Geometry", presented at the SPE Annual Technical Conference, Dallas, TX.

Acuna, J.A., I. Ershaghi, and Y.C. Yortsos (1992), "Fractal Analysis of Pressure Transients in The Geysers Geothermal Field", presented at the 17th Annual Workshop on Geothermal Reservoir Engineering, Stanford University, Stanford, CA.

Beall, J.J., and W.T. Box Jr. (1989), "The Nature of Steam Bearing Fractures in The South Geysers Reservoir, Geothermal Resources Council Transactions, vol.13, pp. 441-448.

Chang, J.,and Y.C. Yortsos (1990), "Pressure-Transient Analysis of Fractal Reservoirs",SPE Formation Evaluation, **289** , pp. 631-643.

Cuong, P.N., and H.J. Ramey Jr. (1991), "One Dimensional Steam Flow in Porous Media Under Desorption", GRC Monograph on The Geysers Geothermal Field, Spec. Rep. no. 17.

Goyal, K.P. (1986), "A Note on Downhole Pressure in a Flowing or Static Steam Well", courtesy of UNOCAL.

Hewett, T.A. (1986), "Fractal Distributions of Reservoir Heterogeneityand Their Influence on Fluid Transport", SPE paper 15386 presented at 61st Annual Technical Conference and Exhibition of SPE, New Orleans, LA Oct. 5-8.

Hornbrook, J.W., and R.N. Horne (1994), "The Effects of Adsorption on Injection Into Geothermal Reservoirs", presented at 19th Workshop on Geothermal Reservoir Engineering, Stanford, CA, Jan. 18-20.

O'Shaughnessy, B., and I. Procaccia (1985), "Diffusion on Fractals", Phys. Rev. A (Nov. 1985), **32** , pp. 3073-3083.

Sammis, C.G., L.J. An, I. Ershaghi (1991), "Fractal Patterns in Graywacke Outcrops at The Geysers Geothermal Field", presented at 16th Workshop on Geothermal Reservoir Engineering, Stanford, CA, Jan. 23-25.

Shang, S., R.N. Horne, H.J. Ramey Jr. (1993), "Experimental Study of Water Vapor Adsorption on Geothermal Reservoir Rocks", Stanford Geothermal Program Technical Report, Dec.

PROCEEDINGS, Twentieth Workshop on Geothermal Reservoir Engineering
Stanford University, Stanford, California, January 24-26 1995
SGP-TR-150

INSTABILITIES DURING LIQUID MIGRATION INTO SUPERHEATED HYDROTHERMAL SYSTEMS

Shaun D. Fitzgerald & Andrew W. Woods

Institute of Theoretical Geophysics,
Departments of Applied Mathematics & Theoretical Physics,
Cambridge.

ABSTRACT

Hydrothermal systems typically consist of hot permeable rock which contains either liquid or liquid and saturated steam within the voids. These systems vent fluids at the surface through hot springs, fumaroles, mud pools, steaming ground and geysers. They are simultaneously recharged as meteoric water percolates through the surrounding rock or through the active injection of water at various geothermal reservoirs. In a number of geothermal reservoirs from which significant amounts of hot fluid have been extracted and passed through turbines, superheated regions of vapour have developed. As liquid migrates through a superheated region of a hydrothermal system, some of the liquid vaporizes at a migrating liquid-vapour interface. Using simple physical arguments, and analogue laboratory experiments we show that, under the influence of gravity, the liquid-vapour interface may become unstable and break up into fingers.

1 INTRODUCTION

For several decades fluids have been extracted from two-phase geothermal reservoirs for power generation. Important reservoirs include The Geysers, California and Larderello, Italy. As a result of the depletion of fluids that has arisen (Kerr 1991), the pressures within such reservoirs have decreased and some regions of the systems have become superheated. As reservoir pressures fall, the rate of supply of steam has been observed to decrease by as much as 50% per year (Enedy *et al.* 1993). In a number of reservoirs, cold fluid has been injected in order to recharge the system through the vaporisation of a fraction of this water as it migrates through the hot rock (Enedy, Enedy & Maney 1991; Enedy *et al.* 1993). In order to evaluate the efficiency of such reinjection programmes, the fundamental controls upon the rate of vaporisation of an advancing liquid front must be determined.

Pruess *et al.* (1987a) have shown that as liquid is injected at a steady rate from a vertical well, a relatively cold liquid-saturated region develops around the well. This region is separated from the hot superheated vapour in the far field by a migrating liquid-vapour interface. As the rock is invaded by cold water it cools and the thermal energy released is used to vaporize a fraction of the water. New vapour is thus formed at the liquid-vapour interface. Woods & Fitzgerald (1993) extended the work of Pruess *et al.* (1987a) by considering injection in various geometries and presenting analytical solutions for the long-time behaviour of the system. The results of both of these studies indicated that if liquid is injected from a vertical well then the total rate of vapour production increases with injection rate although the fraction vaporizing actually decreases. Figure 1 shows the relationship between the mass injection rate and the mass fraction of liquid which vaporises in a two dimensional injection geometry, as presented by Woods and Fitzgerald (1993).

Most studies of liquid injection into superheated geothermal systems have implicitly assumed that the migrating liquid-vapour interface is planar. However, such interfaces may become unstable and break up into fingers if a sufficient fraction of the water vaporizes. In this paper we build upon these preliminary results (Fitzgerald and Woods 1994) by assessing the important and sometimes dominant effects of gravity. Our analysis and analogue laboratory experiments provide important constraints upon models of vapour generation in superheated reservoirs. Our results are also of broader interest for understanding the dynamic state of geothermal systems. We also apply our results to interpret the effects of reinjection in the Geysers reservoir California, and the Lardarello field, Italy.

As well as being of major importance to the geothermal industry, our stability analysis may also lead to new insights into the formation of precious ore deposits (Cline, Bodnar & Rimstidt 1992) and also the intensity of fumarolic activity associated with crater lakes (Brown *et al.* 1989; Hurst & Dibble 1981).

After discussing the different structures of geothermal reservoirs, we present a physical discussion of the instability of a liquid-vapour interface, focusing upon the role of gravity in (de-)stabilising the interface, and identifying an upper bound upon the stability of the interface. We then present some new analogue labo-

ratory experiments, which identify the development of this instability. Finally, we discuss the implications of our results to various geothermal reservoirs, and contrast our results with earlier models of reinjection.

2 MODELLING OF HYDROTHERMAL SYSTEMS

Hydrothermal systems are commonly thought to exist in a dynamic state in which fluid circulates within fractured, porous rock (Cathles 1977; Donaldson 1962; Dunn & Hardee 1981; Hurst & Dibble 1981; Parmentier & Schedl 1981; Grant, Donaldson & Bixley 1982; Wohletz & Heiken 1992). The pores and fractures of the systems are saturated with water or water and vapour. Typically one phase is continuous and to good approximation this determines the distribution of pressure within the system (Pruess & Narasimhan 1982). In the case of a two-phase system, if the distribution of pressure is similar to that of a liquid-filled (vapour-filled) system then the system is described as liquid-dominated (vapour-dominated).

The influence of the fractures upon the fluid flows within the reservoirs is highly dependent upon the relative resistance to flow within the fractures and porous matrix. The relative resistance to flow is dependent upon the fracture apertures, the permeability of the porous matrix and the spacing of the fractures. In many reservoirs, such as Kawah Kamojang in Indonesia (Wohletz & Heiken 1992), The Geysers in California, Larderello in Italy, Ahuachapan in El Salvador and Kawerau in New Zealand (Grant, Donaldson & Bixley 1982), the bulk of the fluid flows are believed to occur within the fractures. The flow of fluid in certain other reservoirs, such as the East Mesa reservoir in California is, in contrast, primarily within the porous matrix (Grant, Donaldson & Bixley 1982). Effects of the fractures upon the fluid flow within geothermal reservoirs are often inferred from detailed measurements of pressure and temperature within wells used for the extraction or injection of fluid (Fradkin *et al.* 1981; Goyal & Box 1990; Axelsson & Bodvarsson 1987). In many reservoirs such data suggests that the fracturing is highly pervasive (Wohletz & Heiken 1992) and that the heat and mass transfer occur over lengthscales of the same order as or larger than the interwell spacing. Therefore, for modelling purposes the rock may be treated as a homogeneous continuum with a uniform network of interconnected pores through which fluid may flow (Cathles 1977; Elder 1981; Pruess *et al.* 1987a). The volume flux per unit area $\mathbf{u}$ may then be related to the interstitial velocity $\mathbf{v}$ by

$$\mathbf{u} = \phi \mathbf{v} \tag{2.1}$$

where ϕ is the void fraction (Bear 1972; Phillips 1991). In many situations of interest the fluid velocities through a geothermal reservoir are sufficiently low that viscous frictional forces are much greater than the inertial forces so that the interstitial Reynolds number, $R = \rho v d/\mu$ is small, $R \ll 1$ (Rubin & Schweitzer 1972; Pruess *et al.* 1987a); ρ represents the density of the fluid, μ the dynamic viscosity, d a typical pore size, and v the interstitial speed. The volume flux per unit area $\mathbf{u}$ is then given by Darcy's Law

$$\mu \mathbf{u} = -k(\nabla P - \rho \mathbf{g}) \tag{2.2}$$

where ∇P is the applied pressure gradient, $\mathbf{g}$ is the gravitational acceleration and k is the permeability (Bear 1972; Rubin & Schweitzer 1972; Dullien 1992). For liquid flow through porous rocks of typical pore size $d \sim 10^{-5}$ m and liquid density 10^3 kg/m^3, the condition $R \ll 1$ is valid for interstitial speeds $v \leq 10^{-3}$ m/s.

If the fluid velocities v and the typical grain size D are sufficiently small then the timescale for fluid and solid to thermally equilibrate, D^2/κ, is much shorter than the timescale for the advection of heat across a grain, D/v, and the medium becomes locally isothermal. Thus for a grain size of 0.5 mm, the condition for local thermal equilibrium is the same as that for low Reynolds number flows, $v \leq 10^{-3}$ m/s since typically the thermal diffusivity of rock $\kappa \sim 2 \times 10^{-6}$ m^2/s.

In the following analysis, we therefore assume that the rock may be modelled as an isotropic porous medium in which Darcy's law (2.2) is valid and in which the rock and fluid are in local thermal equilibrium. In this case we may adopt the results of Woods and Fitzgerald (1993), shown in figure 1 herein, which describes the mass fraction which vaporises as a function of the mass flow rate of liquid injected into the reservoir.

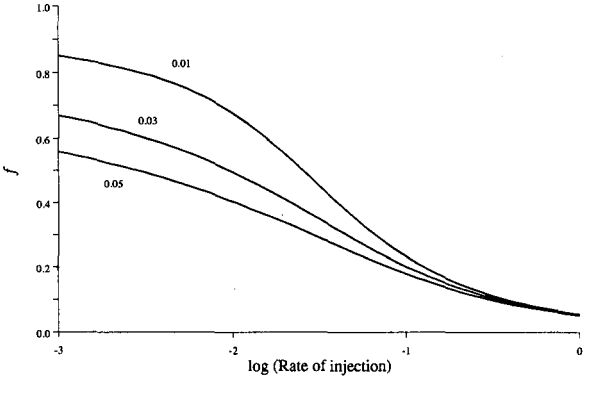

Figure 1 Mass fraction vaporising f as a function of dimensionless flow rate taken from Woods and Fitzgerald 1993. Curves are shown for 3 different porosities as labelled.

3 THE STABILITY OF A MIGRATING INTERFACE

We now present a simple physical argument to determine whether a vaporising liquid interface is stable. This simple analysis identifies the fundamental process by which an interface may become unstable, and provides a lower bound on the mass fraction which may vaporise without destabilising the interface.

The interface between two regions of fluid migrating through a porous medium can become unstable if the magnitude of the pressure gradient increases across the interface in the direction of the flow (Saffman and Taylor 1958; Homsy 1987). If liquid migrates towards a vaporising interface with Darcy velocity u, then the pressure gradient on the liquid side of the interface has the form

$$\frac{dp}{dz} = \rho_l g - \frac{\mu_l}{k} u \tag{3.1}$$

where g is the component of the gravitational acceleration in the directon of the flow, z, ρ_l is the liquid density and μ_l the liquid viscosity. If a fraction f of this liquid vaporises, then the mass flux of vapour ahead of the interface is $\rho_l f u$. Therefore, the velocity of the vapour ahead of the interface is

$$u_v = \frac{\rho_l}{\rho_v} f u \tag{3.2}$$

where ρ_v is the vapour density and the pressure gradient in the vapour region is

$$\frac{dp}{dz} = \rho_v g - \frac{\mu_v}{k}\frac{\rho_l}{\rho_v} f u \tag{3.3}$$

where μ_v is the vapour viscosity.

The pressure gradient therefore decreases (magnitude increases) in the direction of the flow across the interface whenever

$$(\rho_l - \rho_v) g > \frac{u}{k}(\mu_l - \mu_v f \frac{\rho_l}{\rho_v}) \tag{3.4}$$

Since the vapour density is much less than the liquid density, the left hand side of this expression is positive whenever the liquid overlies the vapour; such a configuration is therefore gravitationally unstable. Conversely, if the vapour overlies the liquid, then the system is gravitationally stable. The right hand side of (3.4) is positive whenever

$$\frac{\mu_l \rho_v}{\mu_v \rho_l} > f \tag{3.5}$$

In this case, the magnitude of the pressure gradient associated with the viscous stresses decreases in the direction of the flow, tending to stabilise the interface. The quantity $\frac{\mu_l \rho_v}{\mu_v \rho_l}$ has a value of the order 0.1-0.2 for a water-vapour system. Therefore expression (3.5) applies and the viscous pressure forces are stabilising whenever the mass fraction of liquid which vaporises, f, is sufficiently small

$$f < 0.1 - 0.2 \tag{3.6}$$

Otherwise the viscous pressure forces tends to destabilise the interface, as in the classical Saffman-Taylor instability (Saffman and Taylor 1958).

This result may at first appear surprising, since the relatively dense liquid is migrating into a region of less dense vapour; however, whenever, the mass fraction of liquid which vaporises is of order 0.1-1.0, the mass flux of vapour is comparable to the mass flux of liquid, and therefore the speed of the vapour is much greater than the speed of the liquid. Since the density ratio ρ_l/ρ_v is greater than the viscosity ratio μ_l/μ_v, this situation can then lead to an adverse viscous pressure gradient in the direction of flow.

For simplicity, let us introduce the dimensionless parameters

$$S = \frac{k \rho_l g}{\mu_l u} \tag{3.7}$$

and

$$F = f \frac{\mu_v \rho_l}{\mu_l \rho_v} - 1 \tag{3.8}$$

which denote the magnitude of the gravitational and viscous destabilisation of the interface. (Negative values correspond to a stabilising effect). If we assume that $\rho_v \ll \rho_l$, as is typically the case, then instability may be possible, (3.4), whenever

$$S + F > 0 \tag{3.9}$$

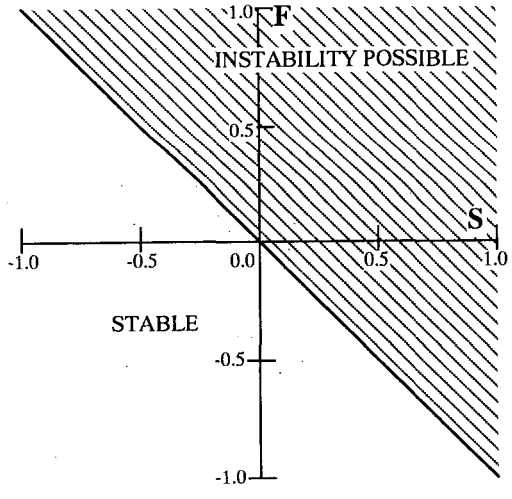

Figure 2 Schematic diagram of the various possible regimes in which a geothermal system may exist. If $S+F > 0$ then the interface may become unstable.

This expression identifies six possible stability regimes, as shown pictorially in figure 2. Two of the most interesting regimes are the cases in which (i) $S > 0$ and $F < 0$, $S + F < 0$, in which case the viscous pressure force can stabilise a gravitationally unstable situation; and (ii) $S < 0$ and $F > 0$, $S + F > 0$, in which case the viscous pressure forces may destabilise a gravitationally stable interface. Case (i) only develops when a small fraction of the descending liquid front vaporises, while case (ii) only develops when a large fraction of an ascending liquid front vaporises. Fitzgerald and Woods (1994) described the simpler system in which $g = 0$ and hence $S = 0$; this corresponds to the x-axis of figure 2.

Equation (3.9) provides a simple lower bound on the condition for instability of the vaporizing interface. In a more detailed analysis Fitzgerald & Woods (1994) have shown that in the absence of gravity long wavelength perturbations to a migrating liquid-vapour interface could be stabilized as a consequence of the compressibility of the vapour. In essence, newly formed vapour accumulates ahead of the interface, building up the pressure and suppressing the formation of an advancing perturbation on the interface. Also, short wavelength disturbances can be stabilized through the action of thermal diffusion. As a result, only perturbations of intermediate wavelength are unstable, and so perturbations of these wavelengths will grow on the interface.

4 EXPERIMENTS ON INSTABILITY

We have conducted a series of analogue laboratory experiments to examine conditions under which a migrating liquid-vapour interface becomes unstable. We injected liquid ether into packed beds of pre-heated sand, and recorded the evolution of the interface. Liquid ether was injected both from above and from below into a perspex vessel, of cross-sectional area 100cm^2, and depth 40cm. The flow regime was recorded by video, and the mass fraction vaporising was calculated by comparing the mass supply rate with the observed rate of ascent of the interface. In the case of injection from below, from section 3, we expect that the liquid-vapour interface will remain stable. This is indeed the case, as may be seen in the photograph in figure 3(a). In our analogue experiments, the packed bed of sand was sufficiently fine-grained that the liquid and ether remained in thermal equilibrium. Thus, for a given descent speed and conditions under which the interface remains planar, the mass fraction vaporising follows the model of Pruess *et al.* (1987) and Woods and Fitzgerald (1993)

$$f = \frac{(1-\phi)\rho_s C_{ps}(T_s - T_b)}{(1-\phi)\rho_s C_{ps}(T_s - T_b) + \phi\rho_l(C_{pv}(T_s - T_b) + L)} \qquad (4.1)$$

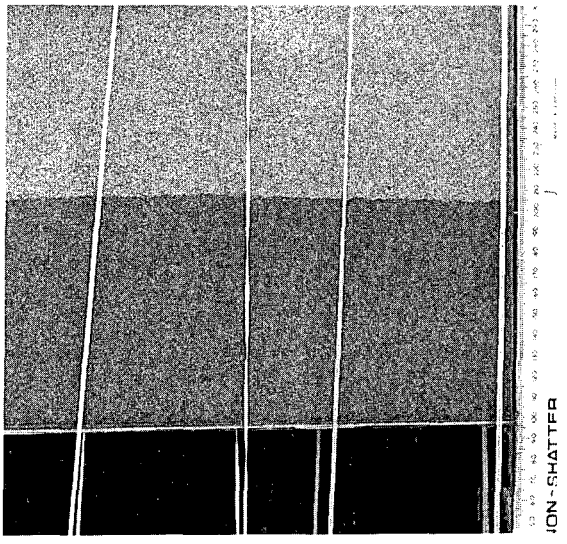

Figure 3 (a) Photograph of an ascending liquid-vapour interface. Liquid ether is supplied from below into a sand layer of approximately 50° C. The photograph shown was taken from an experiment conducted in a sand chamber of internal horizontal dimensions 30 cm by 1 cm. Although heat losses in this particular experiment were considerably greater than those conducted using the main apparatus described in the text, the morphology of the ascending interface was essentially the same in all experiments. The dark zone is the liquid-saturated region and the lighter zone the vapour-filled one.

as shown in figure 4, where C_p denotes specific heat capacity, T corresponds to temperature, L the latent heat of vaporisation, subscript s a property of the sand/rock, subscripts l and v correspond to properties of the liquid and vapour, and subscripts h and b to conditions in the hot superheated region and at the boiling temperature respectively. In the figure, we include theoretical predictions for the mass fraction vaporising in porous layers of porosity 0.4, 0.45 and 0.5, which represent bounds for the porosity in our laboratory experiments. The data were collected from a series of experiments in which the initial temperature of the sand bed was varied. The boiling point of ether is ~34° C.

When the liquid ether was injected downwards from above, the liquid-vapour interface became unstable, as suggested by the analysis shown in figure 2. The development of this instability is shown in the sequence of experiments in figure 3(b). The instability leads to the advance of non-linear fingers of liquid into the vapour zone, thereby significantly changing the vaporisation process from that predicted by equation (4.1). Indeed, we found that a broad two phase saturated zone devel-

ops as the interface descends, in contrast to the sharp interface which forms with an ascending interface.

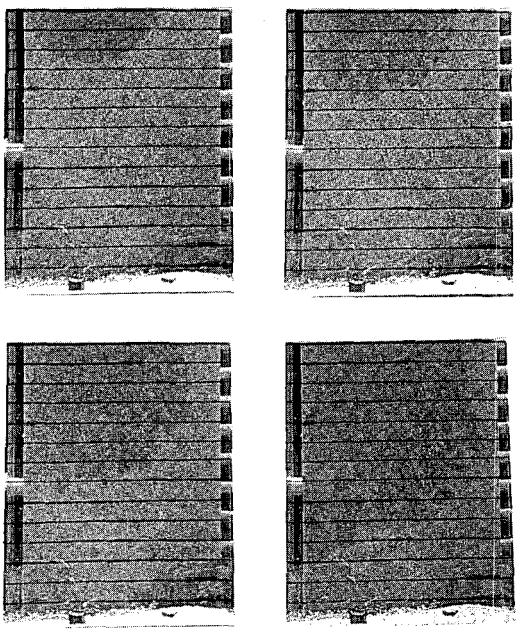

Figure 3(b) Sequence of four photographs of a descending liquid-vapour interface. Liquid ether is supplied from above into a sand layer of approximately 90° C. Photographs were taken at times 1, 3, 7 and 11 s after onset of the experiment. Fingers of liquid ether are observed to form and grow ahead of the uniformly liquid-saturated region. The dark zone is the liquid-saturated region and the lighter zone the vapour-filled one.

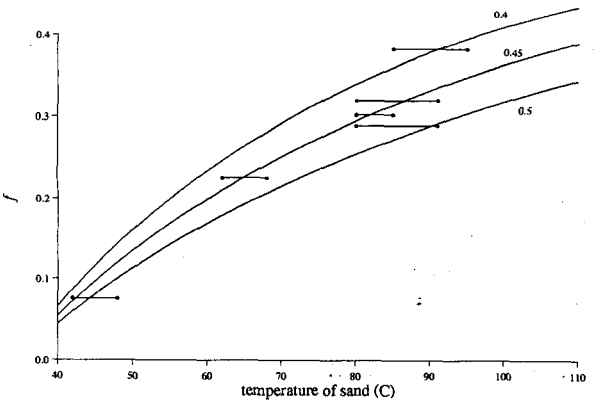

Figure 4 Mass fraction vaporising f as a function of sand temperature. Three curves are given representing the theoretical values for sand porosities of 0.4, 0.45 and 0.5 as indicated on the figure.

5 APPLICATIONS

The results of this analysis identify dynamic situations in which liquid zones may overlie and migrate into vapour-filled regions of rock. Although our model is very simple, and is based upon a number of simplifying assumptions, it is of interest to examine the consequences of our model, noting the rather severe restictions upon its applicability to a heterogeneous fractured reservoir.

For example, 22 years ago, in well SB10 at the Geysers reservoir, at points deeper than 350 m, the pressure gradient became significantly less than liquid-static, where the temperature was about 240° C and pressure about 30 bar (Truesdell & White 1973; White, Muffler & Truesdell 1971). Furthermore, below this point the fluid became more superheated. The well data of Enedy, Enedy & Maney (1991) and that of Enedy (1987) suggests that the permeability in the reservoir lies in the range $10^{-15} - 10^{-13} m^2$. Therefore, in the regions of lowest permeability, the simple analysis of section 3, combined with the relationship between the mass fraction vaporising and the injection rate (Woods and Fitzgerald 1993), predicts that the liquid-vapour interface would be stable for liquid velocities greater than about 2 m per year.

As a result of the net extraction of fluids from the Geysers reservoir, the pressures within the system have fallen (Kerr 1991) and values of 10 bar are now measured in various sections of the field (Enedy *et al.* 1993). This has increased the effective superheat of the reservoir. As a result, a greater fraction of the liquid may vaporize at a migrating liquid-vapour interface. For present conditions at The Geysers, we deduce that according to our analysis, a migrating liquid-vapour interface would be stable for liquid velocities greater than about 2.5 m per year in the regions of lowest permeability.

Conditions in various sections of the Larderello field in Italy are somewhat hotter. Temperatures of 300° C at pressures of around 30 bar are observed, (Pruess *et al.* 1987b), although we note temperatures as great as 394° C have been reported for the San Pompeo well (Truesdell 1991). The permeability variation within the field derived from well data indicates that values lie between $1 - 250 \times 10^{-16} m^2$ and hence our model predicts a migrating liquid-vapour interface is stable in the regions of lowest permeability for liquid velocities greater than about 0.2 m per year.

6 CONCLUSIONS

We have developed a simple model describing how liquid can migrate through a superheated geothermal reservoir. We have identified that if the liquid velocity is

too low then the destabilizing force produced by gravity will exceed the resistance to motion within the liquid zone and consequently, the interface will become unstable. We have also identified that if the fraction of liquid which vaporizes is too high then the pressure gradient within the vapour region can exceed that in the liquid zone, thereby leading to instability at the interface. We have also demonstrated this instability with some analogue laboratory experiments in which large non-linear fingers develop.

7 REFERENCES

Axelsson, G. & Bodvarsson, G. 1987 Analysis of production data from fractured liquid dominated geothermal reservoirs in Iceland. *Trans. Geoth. Res. Counc.* **11**, 573–580.

Bear, J. 1972 *Dynamics of Fluids in Porous Media.* Dover.

Brown, G., Rymer, H., Dowden, J., Kapadia, P., Stevenson, D., Barquero, J. & Morales, L.D. 1989 Energy budget analysis for Poás crater lake: implications for predicting volcanic activity. *Nature* **339**, 370–373.

Cathles, L.M. 1977 An analysis of the cooling of intrusives by ground-water convection which includes boiling. *Econ. Geol.* **72**, 804–826.

Cline, J.S., Bodnar, R.J. & Rimstidt, J.D. 1992 Numerical simulation of fluid flow and silica transport and deposition in boiling hydrothermal solutions: application to epithermal gold deposits. *J. Geophys. Res.* **97**(B6), 9085–9103.

Donaldson, I.G. 1962 Temperature gradients in the upper layers of the earth's crust due to convective water flows. *J. Geophys. Res.* **67**, 3449–3459.

Dullien, F.A.L. 1992 *Porous Media Fluid Transport and Pore Structure.* Academic.

Dunn, J.C. & Hardee, H.C. 1981 Superconvecting geothermal zones. *J. Volcanol. Geoth. Res.* **11**, 189–201.

Elder, J. 1981 *Geothermal Systems.* Academic.

Enedy, S. 1987 Applying flowrate type curves to Geysers steam wells. *Proc. Stanford Geoth. Workshop* **12**, 29–36.

Enedy, S., Enedy, K. & Maney, J. 1991 Reservoir response to injection in the southeast Geysers. *Proc. Stanford Geoth. Workshop* **16**.

Enedy, S.L., Smith, J.L., Yarter, R.E., Jones, S.M. & Cavote, P.E. 1993 Impact of injection on reservoir performance in the NCPA steam field at the Geysers. *Proc. Stanford Geoth. Workshop* **18**.

Fitzgerald, S.D. & Woods, A.W. 1994 The instability of a vaporization front in a hot porous rock. *Nature* **367**, 450–453.

Fradkin, L.J., Sorey, M.J. & McNabb, A. 1981 On identification and validation of some geothermal models. *Water Resour. Res.* **17**(4), 929–936.

Goyal, K.P. & Box, W.T. 1990 Reservoir response to production: Castle Rock Springs Area, East Geysers, California, USA. *Proc. Stanford Geoth. Workshop* **15**, 103–112.

Grant, M.A., Donaldson, I.G. & Bixley, P.F. 1982 *Geothermal Reservoir Engineering.* Academic.

Homsy, G.M. 1987 Viscous fingering in porous media. *Ann. Rev. Fluid Mech.* **19**, 271–311.

Hurst, A.W. & Dibble, R.R. 1981 Bathymetry, heat output and convection in Ruapehu crater lake, New Zealand. *J. Volcan. Geoth., Res.* **9**(1), 215–236.

Kerr, R.A. 1991 Geothermal tragedy of the commons. *Science* **253**, 134–135.

Parmentier, E.M. & Schedl, A. 1981 Thermal aureoles of igneous intrusions: some possible indications of hydrothermal convective cooling. *J. Geol.* **89**, 1–22.

Phillips, O.M. 1991 *Flow and Reactions in Permeable Rocks.* Cambridge.

Pruess, K., Calore, C., Celati, R. & Wu, Y.S. 1987a An analytical solution for heat transfer at a boiling front moving through a porous medium. *Int. J. Heat Mass Transfer* **30**(12), 2595–2602.

Pruess, K., Celati, R., Calore, C. & Cappetti, G. 1987b On fluid and heat transfer in deep zones of vapour-dominated geothermal reservoirs. *Proc. Stanford Geoth. Workshop* **12**, 89–96.

Pruess, K. & Narasimhan, T.N. 1982 On fluid reserves and the production of superheated steam from fractured, vapour-dominated geothermal reservoirs. *J. Geophys. Res.* **87**, 9329–9339.

Rubin, A. & Schweitzer, S. 1972 Heat transfer in porous

media with phase change. *Int. J. Heat Mass Transfer* **15**, 43–60.

Saffman, P.G. & Taylor, G.I. 1958 The penetration of a fluid into a porous medium or Hele-Shaw cell containing a more viscous liquid. *Proc. R. Soc. A* **245**, 312-329.

Truesdell, A.H. 1991 The genesis of vapour-dominated geothermal reservoirs with high-temperature zones. *Proc. Stanford Geoth. Workshop* **16**.

Truesdell, A.H. & White, D.E. 1973 Production of superheated steam from vapour-dominated geothermal reservoirs. *Geothermics* **2**, 154–173.

White, D.E., Muffler, L.J.P. & Truesdell, A.H. 1971 Vapour-dominated hydrothermal systems compared with hot-water systems. *Econ. Geol.* **66**, 75–97.

Wohletz, K. & Heiken, G. 1992 *Volcanology and Geothermal Energy.* California.

Woods, A.W. & Fitzgerald, S.D. 1993 The vaporization of a liquid front moving through a hot porous rock. *J. Fluid Mech.* **251**, 563–579.

PROCEEDINGS, Twentieth Workshop on Geothermal Reservoir Engineering
Stanford University, Stanford, California, January 24-26 1995
SGP-TR-150

NUMERICAL MODELING OF BOILING DUE TO PRODUCTION IN A FRACTURED RESERVOIR AND ITS FIELD APPLICATION

Yusaku Yano and Tsuneo Ishido

Geological Survey of Japan
1-1-3 Higashi, Tsukuba
305 Japan

ABSTRACT

Numerical simulations were carried out to characterize the behaviors of fractured reservoirs under production which causes in-situ boiling. A radial flow model with a single production well, and a two-dimensional geothermal reservoir model with several production and injection wells were used to study the two-phase reservoir behavior. The behavior can be characterized mainly by the parameters such as the fracture spacing and matrix permeability. However, heterogeneous distribution of the steam saturation in the fracture and matrix regions brings about another complicated feature to problems of fractured two-phase reservoirs.

INTRODUCTION

"MINC" method (Pruess and Narasimhan, 1985) is usually used for numerical simulation of fractured reservoirs. Pritchett and Garg (1990) made a classification of numerical treatments for fractured reservoirs, based on a spherical, zero-dimensional MINC model. In the classification, the time required for pressure equilibrium to be reached between the fracture zone and the matrix block (τ_{pe}), and the time required for temperature equilibrium to be reached due to heat conduction acting alone (τ_{hc}) are the basic parameters for choosing a suitable numerical treatment including MINC method and porous medium assumption.

If τ_{pe} is short enough compared with the time of interest, the pressures within the rock matrix is in equilibrium with fracture zone. In this case, porous medium assumption can be used for numerical treatment. This case is also divided into two cases, one is with high permeability rock matrix, and the other is with low permeability rock matrix. In the former case, τ_{pe} is short enough compared with τ_{hc}, so that complete porous medium assumption can be applied. In the latter case, τ_{pe} is comparable with or greater than τ_{hc}, so the effect of heat conduction appears depending on the matrix permeability k_m.

If τ_{pe} is greater than the time of interest, the pressures within the rock matrix cannot reach to equilibrium with fracture zone within the time. In this case, MINC method should be used to represent transient flow between rock matrix and fracture zone. In this case, however, if τ_{pe} is short enough compared with τ_{hc}, there is no heat conduction effect, and models with the same k_m/λ^2 (λ is the fracture spacing) behave the same way.

Using above classification of Pritchett and Garg(1990), judgement for choosing numerical method can be made quantitatively, considering the time of interest, compressibility (two-phase or single-phase), rock matrix permeability, and fracture spacing.

However, in the real geothermal application, existence of "global flow", which is not present in the above zero-dimensional model, makes reservoir behavior much more complicated. In this paper, numerical simulation studies to assess the influence of the global flow on the behavior of two-phase fractured reservoirs are discussed.

PRODUCTION INDUCED BOILING IN A RADIAL FLOW MODEL

Reservoir behavior associated with production and injection has a much shorter time scale compared with natural state problems, and sometimes it cannot be treated by a "porous medium" assumption. In many geothermal reservoirs, boiling of fluids occurs in formations near production wells, due to production induced pressure decrease. Two-phase fluid compressibility is larger than that of single phase fluid by three orders of magnitude, and it often makes τ_{pe} long enough to be comparable with τ_{hc}.

At first, we studied two-phase reservoir behavior using a radial flow model with production from a horizontal formation where fractures are distributed homogeneously. The parameters of the model are listed in Table 1. The initial condition of the reservoir is a saturated liquid at 300°C. Production calculations were performed for an interval of 10^7 seconds (4 months).

The fluid and heat flow between the fracture and country rock (matrix), and within the matrix region is controlled by the fracture spacing and matrix permeability. Here, we consider nine different cases of fractured reservoirs, by the combination of three different fracture spacings and three different matrix permeabilities. "Global" permeability and porosity for all cases are the same as those of the reference "porous medium" case.

Table 2 shows τ_{pe} and τ_{pc} for the nine cases. Within the calculation time of 10^7 seconds, all cases H, which have the highest matrix permeability, and all cases M, which have an intermediate matrix permeability, reach to the pressure equilibrium. On the other hand, case 10L, which has the lowest matrix permeability and the largest fracture spacing, cannot reach to the pressure equilibrium. For cases H, the heat conduction effect is slower than the pressure relaxation. For cases M, they have the same time scale. And for cases L, the heat conduction effect comes faster than the pressure relaxation.

Figure 1 shows numerical representation of the fractured reservoirs by MINC method. Numerical blocks which represent fractures are interconnected, and global flow can only passes through fracture blocks. Numerical blocks which represent matrix regions exchange heat and mass with the adjacent fracture blocks. The flow into the interior of matrix region is expressed by the connection of separated numerical blocks (shells).

The calculations were performed using the STAR general-purpose geothermal reservoir simulator (Pritchett, 1989). In the "MINC" medium representation on the sub-grid scale, the STAR simulator idealizes a "typical" block of matrix as a sphere, surrounded by a concentric spherical shell of high-permeability material representing the fracture zone. In the present calculations, the matrix region was subdivided into 6 concentric spherical shells for numerical purposes (for explanation of the MINC representation employed in the STAR code, see e.g. Pritchett and Garg, 1990).

Figure 2 shows the calculated pressure change in the well block. The pressure change of the "porous medium" case, which is shown as a straight line on the semi-log plot, represents the "global" permeability-thickness and storativity of the reservoir. For the "fractured reservoir" cases, the calculated results are largely affected by the matrix permeability, and also there are some differences in the pressure changes

Table 1. Model parameters used for the numerical simulation of a production test with in-situ boiling.

RESERVOIR GEOMETRY
- Horizontal layer : Thickness = 100 m
- Numerical blocks: divided by distance from the production well. Distance between the well center and block boundary = r(i); r(1)=0.1 m, $\Delta r(i+1) = \Delta r(i) \times 1.3$, r(max) = r(40) = 12,039 m

ROCK PROPERTIES
- (1) Common properties
  - Rock grain heat capacity = 1000 J/kg°C
  - Rock grain thermal conductivity = 2.5 W/m°C
  - Rock grain density = 2700 kg/m^3
- (2) Well block
  - Porous medium
  - Porosity = 0.99
  - Permeability = 10^{-10} m^2
- (3) Reservoir blocks (porous medium or fractured)
  - Total porosity = 0.05
  - Global permeability = 10^{-13} m^2
  - Fracture volume ratio to total volume = 0.1
  - Porosity of fracture = 0.1

INITIAL CONDITIONS
- Temperature: 300 °C
- Pressure: 8.5927 MPa (saturation pressure for 300°C)

PRODUCTION
- 31.416 kg/sec for 10^7 sec (about 4 month)

Table 2. Times (in seconds) required for pressure equilibrium (τ_{pe}) and temperature equilibrium (τ_{hc}) of the nine cases for numerical simulation of in-situ boiling.

fracture spacing (m) / rock matrix permeability (md)	1	√10	10
0.1	(1H) $\tau_{pe}=10^4$ $\tau_{hc}=10^5$	(3H) $\tau_{pe}=10^5$ $\tau_{hc}=10^6$	(10H) $\tau_{pe}=10^6$ $\tau_{hc}=10^7$
0.01	(1M) $\tau_{pe}=10^5$ $\tau_{hc}=10^5$	(3M) $\tau_{pe}=10^6$ $\tau_{hc}=10^6$	(10M) $\tau_{pe}=10^7$ $\tau_{hc}=10^7$
0.001	(1L) $\tau_{pe}=10^6$ $\tau_{hc}=10^5$	(3L) $\tau_{pe}=10^7$ $\tau_{hc}=10^6$	(10L) $\tau_{pe}=10^8$ $\tau_{hc}=10^7$

among cases of the same matrix permeability but of different fracture spacings.

For cases H, pressure equilibrium time is short compared with the calculation time, and the time scale for heat conduction effect is larger than the pressure equilibrium time by one order of magnitude. In these cases, the results had been expected to be the same as the "porous reservoir" case on the basis of the criterion proposed by Pritchett and Garg (1990). However, the calculated results for cases H (Figure 2) are different from the "porous reservoir" result. The pressures of cases H are larger at each time than the "porous" model, although the lines of pressure change are almost parallel to the "porous" result. This difference seems to be caused by the existence of "global" flow which is not present in the zero-dimensional model.

In order to understand the cause of this difference, we checked steam saturations of the fracture and the matrix regions. At 10^5 seconds (about one day) from the beginning of production, the steam saturation in the fracture of the numerical block next to the well block is 0.16. At this time, the steam saturation of the matrix is 0.65 for every shell. Although the pressure and temperature are in equilibrium, large difference of steam saturations between

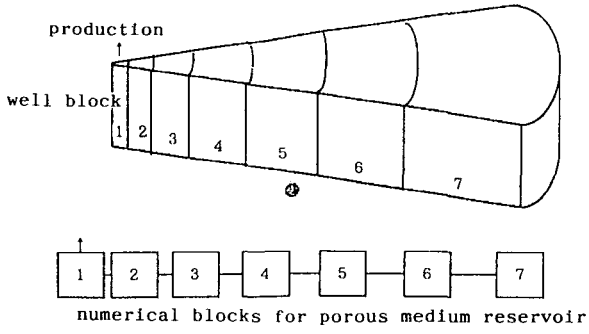

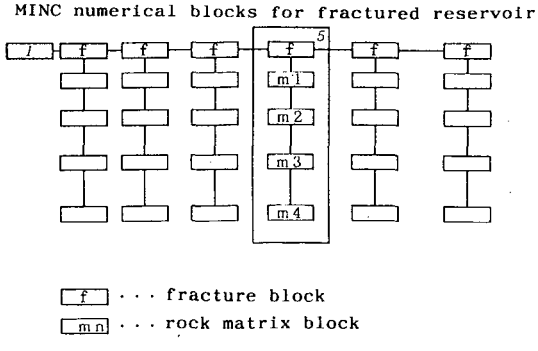

Fig. 1. Numerical block configurations for the production test. Fracture blocks are connected in the "MINC" model for global flow representation.

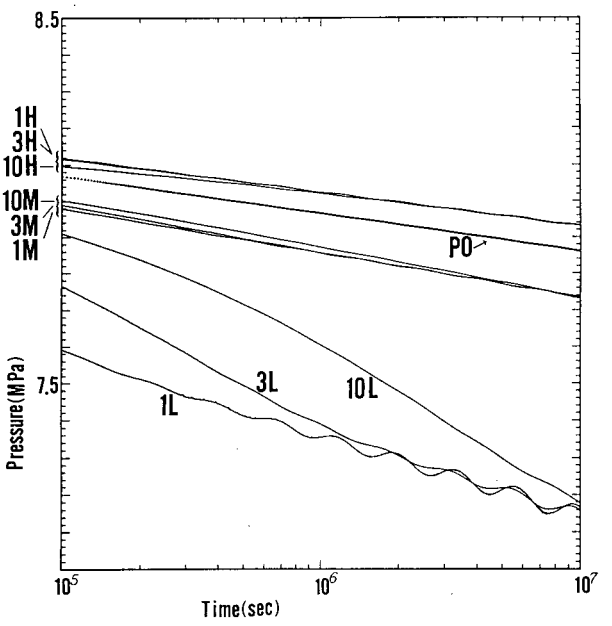

Fig. 2. Pressure transients of the well block in a production test with in-situ boiling. Results are shown for nine different fractured reservoir cases and a "porous" reservoir case.

the fracture and matrix exists. This is because the matrix region only supplies fluid to the fracture and becomes highly steam saturated, while the fracture gets fluid from the matrix and also from the global flow through fractures. These different steam saturations lead to different flow conditions through relative permeability difference.

In our numerical calculation, we used a X-type relative permeability function with residual saturations of water and steam of 0.3 and 0.05 respectively. On the basis of this function, the relative permeability of water is 0.77 and that of steam is 0.12 in the fracture, and these control global flow condition in the reservoir. On the other hand, the steam saturation in the same numerical block of the "porous medium" reservoir is 0.23. In this case, the relative permeabilities of water and steam are 0.67 and 0.19 respectively. Considering total mass flux for a constant pressure gradient, the global flow through the fracture zone will have a larger flux rate than the "porous medium" reservoir of the same global permeability. This higher mobility of cases H makes the pressure decrease smaller than the "porous" reservoir.

The pressure of case 10H is a little lower than cases 1H and 3H at early times. This is because only case 10H has not attained pressure equilibrium at these times.

Pressure decreases of all of cases M and L are larger than the "porous" case as seen in Figure 2. The time constant of temperature relaxation in the matrix region is shorter than the pressure time constant for cases L, and they are comparable for cases M. At time scales before reaching pressure equilibrium between the fracture and matrix, the temperature is lower in the fracture than in the matrix under the two-phase conditions. For cases L and M, rapid heat conduction takes place in these short time scales due to short τ_{hc}. This facilitates the increase in steam saturation in the fracture zone, leading to lower global flow mobility. As a consequence, the pressure decrease at the well block becomes larger than the "porous medium" case.

The time constant τ_{hc} is 10^6 seconds for cases 3L and 3M, and 10^7 seconds for cases 10L and 10M. As seen in Figure 2, after 10^6 (10^7) seconds of production , case 3L (10L), and case 3M (10M) behave as the same way as case 1L and case 1M respectively.

The pressure fluctuations of cases 1L and 3L seen in Figure 2 are caused by jumps of boiling front over finite distance corresponding to the size of numerical blocks, and has no physical meaning.

As we have mentioned above, the reservoir behavior with global flow is more complicated than that without global flow, mainly because of heterogeneous distribution of steam saturation between the fracture and matrix regions. The present result is thought to be useful when we analyze the complicated behaviors of production-induced boiling in fractured reservoirs.

PRODUCTION FROM A TWO-DIMENSIONAL GEOTHERMAL RESERVOIR

In this section, we use a mathematical reservoir model of one of geothermal fields in Japan for production simulation. However, allocations of production and injection wells, production rates, and production conditions including wellhead pressures used in this paper are all just hypothetical.

Figure 3 shows the computational grid blocks of the vertical two-dimensional reservoir model (thickness is 500m). High permeability (100 md) reservoir (A) is formed along a large fault zone, and

is covered by a low permeability caprock (D). Hot water is fed from the deep conduit (E) into the reservoir, and flow out through the horizontal conduit (B), surrounding rocks (C), and a permeable passage (F) through the caprock to the surface. In the permeable passage and in most of the upper part of the reservoir, a two-phase zone with high steam saturations is developed under the natural state conditions.

Three hypothetical production wells and several injection wells are set in the model as shown in the figure. Production calculations were done for 30 years. Constant steam flowrate to produce 10MW of electricity was assumed. A fixed separator pressure of 5 bars was used, and all separated liquid water and small amount of steam condensate were reinjected. For the calculations, the newest version of STAR geothermal reservoir simulator (Pritchett, 1993) was used.

A "porous" medium reservoir model (Case P) and two "MINC-type fractured reservoir" models (Case F30 and F100) were applied to the production calculation, using the same boundary conditions and geologic structures, and global permeabilities. The fracture spacing and matrix permeability are 30m and 0.001 md respectively in Case F30, and 100m and 0.01 md respectively in Case F100. (The matrix region was subdivided into 4 shells in both cases.) The time constant of pressure equilibrium, τ_{pe} is about 30 years under the two-phase conditions for both cases. Due to the difference of fracture spacings, they have different time constants of temperature equilibrium, τ_{he}. In Case F30, τ_{he} is about 3 years, and in Case F100, τ_{he} is about 30 years.

Figure 4 shows the total fluid production rate of the three cases. Since the steam flowrate is fixed, the total fluid production rate (water and steam) required by the power station will change with time, and is inversely correlated with the average produced fluid enthalpy (the steam saturation in the blocks of production feedpoints). Figure 5 shows the steam saturation in a block centrally located in the production zone. For the "fractured reservoir" cases, the steam saturations of the fracture and the center of matrix region are both shown. Figure 6 shows temperature changes of the same production block for the three cases. Since, in two-phase flow, fluid pressures and temperatures lie along the saturation curve for steam/water mixtures, the pressure changes of the production block can be seen from Figure 6.

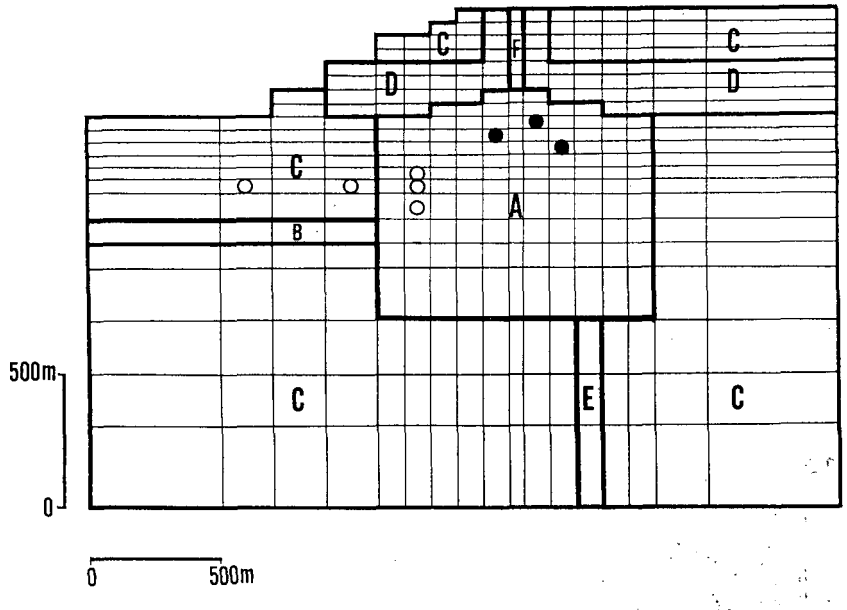

Fig. 3. Computational grid block used in the numerical simulation of production from a vertical two-dimensional geothermal reservoir model. Letters A to F represent geologic formations enclosed by bold lines. The symbol ● represents production feed points and the symbol ○ represents injection feed points.

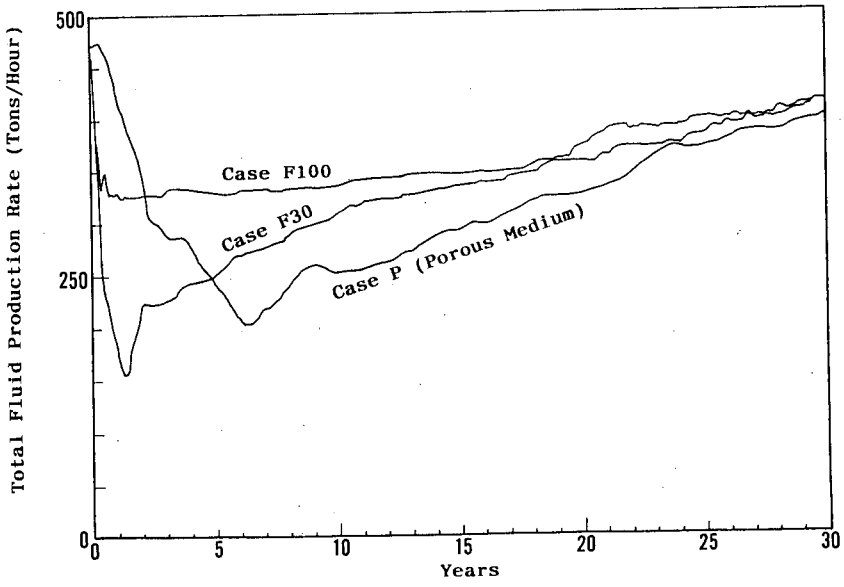

Fig. 4. Change in total fluid production rate versus time.

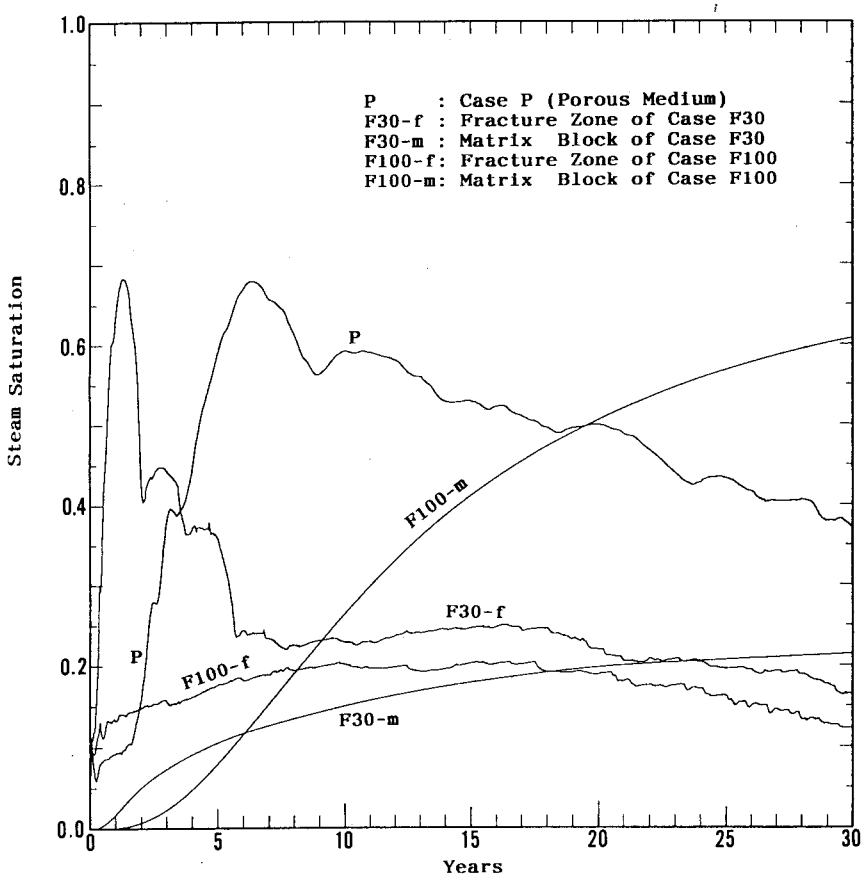

Fig. 5. Change in steam saturation versus time in the grid block of the middle elevation production feedpoint.

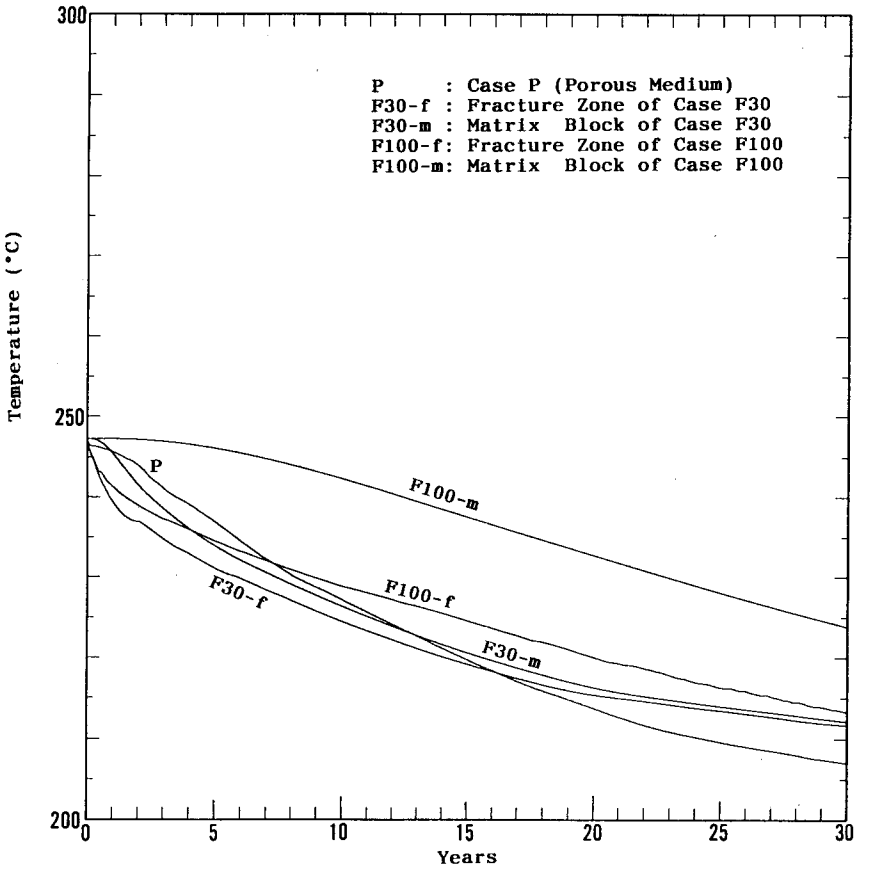

Fig. 6. Change in temperature versus time in the same grid block as Figure 5.

At early times (up to 1-2 years), the temperature (and pressure) decrease is larger for "fractured reservoir" cases than for "porous medium" case (Figure 6), even though the total production rate is lower for the "fractured reservoir" cases as seen in Figure 4. This behavior is consistent with the results for the "radial flow" model described in the previous section. Considering the relationship among τ_{pe}, τ_{hc} and the time of interest, Case F30 and F100 correspond to Case 3L and 10M in the previous section respectively. The same explanation as that described in the previous section can be applied to understand the early time behaviors of the "fractured reservoirs" shown in Figures 4 to 6. Due to the large τ_{pe}, the pressure in the fracture decreases faster than the "porous medium" case. The steam saturation in the fracture zone rises very quickly due to the rapid heat conduction effect for Case F30. This brings about reduction in the global flow mobility and facilitates the pressure decrease.

The histories of total fluid production rate at early times are largely different among the three cases considered here (Figure 4). It should be noted that rapid decrease in the total production rate is present at early stages for the fractured two-phase reservoirs.

After 1-2 years of operation, low-enthalpy fluid inflow from the reinjection zone is probably involved for "fractured reservoir" cases. The "cold front" travels faster with increasing fracture spacing, so the steam saturation in the fracture does not show any significant increase for Case F100 (100 m fracture spacing) as seen in Figure 5. In Case F30 (30 m fracture spacing), the influence of the low-enthalpy fluid starts to appear about 1.5 years and suppress the steam saturation in the fracture.

REFERENCES

Pritchett, J. W. (1989) Star user's manual. S-Cubed Report SSS-TR-89-10242.

Pritchett, J. W. and Garg, S. K. (1990) On similitude, heat conduction, and two-

phase flow in fractured porous media. Proc. Fifteenth Workshop on Geothermal Reservoir Engineering, Stanford University.

Pritchett, J. W. (1993) Star user's manual. S-Cubed Report SSS-TR-92-13366.

Pruess, K. and Narasimhan, T. N. (1985) A practical method for modeling fluid and heat flow in fractured porous media. SPE Journal, Feb., 14-26.

PROCEEDINGS, Twentieth Workshop on Geothermal Reservoir Engineering
Stanford University, Stanford, California, January 24-26 1995
SGP-TR-150

THERMODYNAMIC TRANSIENT BEHAVIOR OF A GEOTHERMAL FRACTURE

Ascencio,F. (1), Samaniego,F. (2), Cinco-Ley,H. (2), Rivera,J. (2)
(1) Escuela de Ingeniería Mecánica. Universidad Michoacana.
Edificio W, Ciudad Universitaria. Morelia, Mich., México. CP 58060
(2) Universidad Nacional de México.

ABSTRACT

This paper presents a space integrated zero dimensional model that describes the thermodynamic behavior of a geothermal fracture undergoing exploitation. The main assumptions involved are: fluid and energy entering the fracture come from the surrounding matrix, fracture of infinite conductivity, and that the steam and water phases are gravitationally segregated and in thermodynamic equilibrium. The nonlinear equations of mass and energy conservation are numerically solved. A sensitivity analysis on the main parameters that affect this problem was carried out. Water recharge is described by a linear infinite aquifer, and heat flow from the matrix to the fluid was also considered by means of a linear infinite system. The behavior of the system is clearly described for conditions of exploitation in the steam, in the water, or mixed completion in both steam and water zones.

INTRODUCTION

The main aim of reservoir engineering is to determine the optimum exploitation conditions of a reservoir. Currently mathematical modeling plays a very important role in accomplishing this task. In a general sense these models consists of a set of nonlinear partial differential equations, relating the conservation of mass and energy. The use of reservoir simulation would allow the consideration of all production schemes considered as viable; thus, after proper economic analysis the optimum exploitation procedure for the reservoir can be determined.

Historically there have been two types of models used to predict the behavior of a reservoir; the zero dimensional models (ZDM) and the distributed parameters models (DPM). Zero dimensional models consider that rock and fluid properties are uniform and independent of the position in the reservoir. Two approaches for the consideration of these ZDM models have been presented in the literature. The first uses the classical visualization of the integrated material balance equation (Shilthius, 1936; Craft and Hawkins, 1959; Whiting and Ramey, 1969; Brigham and Morrow, 1977; Brigham and Neri, 1980; Grant, 1977; Sorey and Fradkin, 1979; Castanier et al., 1980). The second approach uses a space integrated version of the partial differential equations of the distributed parameters models. These type of models have been previously described in the petroleum engineering literature (Muskat, 1945; Raghavan, 1994). In the application of these models to geothermal reservoir engineering, time is the independent variable and the model is composed of ordinary differential equations for the mass conservation of vapor and water, and for energy conservation.

The complex distributed parameters models (Brownell et al., 1977; Garg et al., 1975; Garg and Pritchet, 1977; Faust and Mercer, 1979,a,b; Pruess 1983, 1987, 1988) consider the spatial and time distribution of the formation and fluid properties. The equations for the conservation of mass and energy are discretized in space and time and are numerically solved.

The purpose of this paper is to present a space integrated zero dimensional model (SIZDM), for the description of the thermodynamic behavior of a geothermal fracture undergoing exploitation. The main assumptions involved are: recharge fluid enters the fracture through the original liquid level, energy entering the fracture comes from the surrounding matrix, fracture of infinite conductivity, and that the vapor and water phases are gravitationally segregated and in thermodynamic equilibrium.

MATHEMATICAL MODEL

We consider an infinite conductivity geothermal fracture (ICGF), with gravity segregated steam and water in thermodynamic equilibrium, as shown in Fig. 1. Applying the principles of mass and energy balances we obtain the following set of differential equations:

Mass conservation:

$$\phi_f bL\frac{d}{dt}(\rho_w z_l + \rho_s(z_t - z_l)) = w_r - w_{wp} - w_{sp} \quad (1)$$

The water recharge w_r term in Eq. 1 represents the natural recharge to the fracture, which can be expressed through the convolution integral given by Eq. 2:

$$w_r = \int_0^t \frac{\partial \Delta p(\tau)}{\partial \tau} w_1(t-\tau)d\tau \quad (2)$$

In Eq. 2 w_1 represents the influence function for the recharge system, or in other words is a unit pressure drop water recharge response. Considering a linear recharge system, the influence function is given by Eq. 3 (Miller, 1962; Nabor and Barham, 1964):

$$w_1 = \phi_r \rho_r b z_{l,t=0}\ c_t\sqrt{\frac{k}{\pi\phi_r\mu_r c_t t}} \quad (3)$$

Energy conservation:

$$\phi_f bL\frac{d}{dt}(\frac{(1-\phi_f)}{\phi_f}\rho_{sR}c_{sR}z_t T + \rho_w u_w z_l + \rho_s u_s(z_t - z_l))$$

$$= w_r h_r - w_{wp}h_w - w_{sp}h_s + q \quad (4)$$

Eq. 4 assumes that within the fracture thermodynamic equilibrium prevails between the steam, water, and the rock.

Similary to the previous discussion on recharge mass flow, the heat rate toward the fracture q can be expressed by Eq. 5:

$$q = \int_0^t \frac{\partial \Delta T(\tau)}{\partial \tau} q_1(t-\tau)d\tau \quad (5)$$

Considering that this rate comes through the two fracture faces, under linear flow conditions, the heat influence function is given by Eq. 6 (Carslaw and Jaeger, 1959):

$$q_1 = 2z_t L\sqrt{\frac{\rho_R c_R \kappa_R}{\pi t}} \quad (6)$$

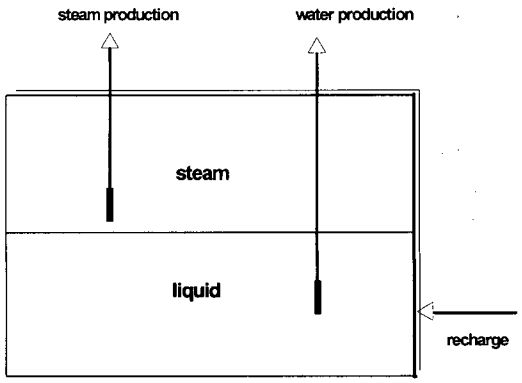

Fig. 1. Infinite conductivity geothermal fracture (ICGF).

NUMERICAL SOLUTION

The nonlinear system of equations given by expressions 1 and 4 was solved through an iterative numerical procedure, briefly described as follows:

1. The fracture temperature in an unknown integration Δt time step decreases in $\Delta T = T_i - T_{i-1}$, where i refers to the time level. Thus, in accordance to this consideration, the thermodynamic properties of the steam and water phases at saturation conditions can be determined. It is considered that T_0 and p_0 are the temperature and pressure of the fracture at initial conditions.

2. Eqs. 1 and 4 are discretized on time and solved for the unknowns liquid level $z_{l,i}^k$ and the time step Δt_i^k, where k is the iteration level.

$$a_m z_{l,i}^k - b_m \Delta t_i^k = c_m \tag{7}$$

$$a_e z_{l,i}^k - b_e \Delta t_i^k = c_e \tag{8}$$

The coefficient in these Eqs. 7 and 8 are defined by the following expressions:

$a_m = \rho_{w,i} - \rho_{s,i}$;

$a_e = \rho_{w,i} u_{w,i} - \rho_{s,i} u_{s,i}$;

$b_m = -(w_{wp} + w_{sp})/\phi_f bL$;

$b_e = -(w_{wp}\bar{h}_w + w_{sp}\bar{h}_s)/\phi_f bL$;

$c_m = (\rho_{w,i-1} - \rho_{s,i-1}) z_{l,i-1} + (\rho_{s,i-1} - \rho_{s,i}) z_t + w_r \Delta t_i^{k-1}/\phi_f bL$;

$c_e = (\rho_{w,i-1} u_{w,i-1} - \rho_{s,i-1} u_{s,i-1}) z_{l,i-1} +$
$(\rho_{s,i-1} u_{s,i-1} - \rho_{s,i} u_{s,i}) z_t + \frac{(1-\phi_f)}{\phi_f} \rho_{sR} z_t c_{sR} \cdot$
$\Delta T_i + (w_r h_r + q) \Delta t_i^{k-1}/\phi_f bL$;

where $\bar{h}_w$ and $\bar{h}_s$ are the average enthalpies within a time step for the water and steam phases, respectively.

The water recharge w_r and the heat rate towards the fracture q, can be evaluated following the discretization procedure of the convolution integrals presented by Eqs. 9 and 10:

$$w_r(t_i) = \sum_{j=1}^{j=i} \Delta p_j \cdot w_1(\Delta t_i^k + t_{i-1} - t_{j-1}) \tag{9}$$

$$q(t_i) = \sum_{j=1}^{j=i} \Delta T_j \cdot q_1(\Delta t_i^k + t_{i-1} - t_{j-1}) \tag{10}$$

3. Once the following convergence criteria are met

$$|\Delta t_i^k - \Delta t_i^{k-1}| < Tol, \text{ and}$$

$$|z_{l,i}^k - z_{l,i}^{k-1}| < Tol.$$

The new time level t_i is calculated through Eq. 11:

$$t_i = t_{i-1} + \Delta t_i^k. \tag{11}$$

Next the control returns to step 1 of this algorithm and a new time step calculation is started.

After the second time step ($i \geq 3$) the convergence of the algorithm can be speeded up taking into account the results of the two previous time steps. Thus, Eq. 12 can be used for the Δt evaluation at the first iteration level ($k = 0$)

$$\Delta t_i^{k=0} = \left(\frac{t_{i-1} - t_{i-2}}{t_{i-2} - t_{i-3}}\right) \cdot (t_{i-1} - t_{i-2}) \tag{12}$$

The following criteria were taken for the production of water and/or steam from the fracture:

1. The turbine admission steam rate $w_{s\ adm}$, is considered to be equal to the steam mass production w_{sp} from the fracture steam zone:

$$w_{sp} = w_{s\ adm} \tag{13}$$

2. Fluid production from the water zone w_{wp} occurs under isoenthalpic conditions, resulting in a mixture (water and steam) enthalpy at vapor pressure turbine admission $p_{s\ adm}$, being equal to that of water at fracture pressure (or temperature) conditions h_w. Under this assumption the mixture quality at the surface can be expressed as follows:

$$x = \frac{h_w - h_{w\ adm}}{h_{fg\ adm}} \tag{14}$$

where $h_{w\ adm}$ is the water specific enthalpy at turbine admission steam pressure, and $h_{fg\ adm}$ is the latent heat of vaporization.

This study considers a constant turbine admission steam mass rate, $w_{s\ adm}$; thus the water mass production from the fracture can be expressed by Eq. 15:

$$w_{wp} = w_{s\ adm}/x \tag{15}$$

3. For the case of simultaneous mass production from the steam and water zones through a single well, Eqs. 16 and 17 express the steam w_{sp} and water production w_{wp}:

$$w_{sp} = f_s w_{s\ adm} \tag{16}$$

$$w_{wp} = f_w\left(\frac{w_{s\ adm} - w_{sp}}{x}\right) \tag{17}$$

where f_s and f_w are the liner length fractions in contact with the steam and water phases, respectively.

PRODUCTION CONDITIONS

It is important to keep in mind that the results of this study to be next presented, were obtained considering a simplified visualization of the system geothermal fracture-recharge-matrix heat source, previously described in relation to Fig. 1.

Table 1 presents the basic data used for the numerical modeling of the ICGF system of this work. As it has been stated, the production conditions considered are of constant turbine admission steam mass rate $w_{s\ adm}$, fixed for our forthcoming results at 1 kg/s. The simulations to be discussed are grouped in accordance to the three main physical possibilities that can be present in the field, when dealing with a gas cap reservoir (Grant and Glover, 1984), Fig. 1:

1. Production from the water zone.
2. Production from the steam zone.
3. Mixed production from both zones.

DISCUSSION OF RESULTS

With regard to case 1 for conditions of the well producing from the steam zone, results are presented in Figs. 2-5. Fig. 2 shows the temperature and pressure variation versus time, observing a decrease of approximately 9.5 $°C$ for a production time of 1300 days. At this time the water level in the fracture reduced to zero, as indicated in Fig. 3. Fig. 4 presents the variation of the recharge mass flow to the fracture versus time; it can be observed that in spite of the high aquifer permeability of 50 Darcys, recharge rates are low in relation to total mass production, in the order of 10 percent. Fig. 5 indicates that the main providing mass source to the steam cap is the evaporation of the water zone, ocurring at its contact with the steam, Fig. 1, with an approximately constant 80 percent of the total production during the considered exploitation period. This finding explains the linear decrease versus time of the water level shown in Fig. 3.

Figs. 6-8 present the results obtained for producing conditions in the water zone. It can be noticed that the producing life of the fracture is substantially reduced, to 215 days. This is due to the fact that a greater mass production from the fracture is needed to provide the specified turbine admission rate of 1 kg/s.

Figs. 9 and 10 show the fracture behavior corresponding to case 3 of mixed production from the steam cap and water zone, through a liner open between the 350-400 m fracture height. These graphycal results clearly show two different behaviors of the ICGF, that occur at short and large production times, which correspond to previously discussed cases 1 and 2 with regard to Figs. 2-5 and 6-8, respectively.

Sensitivity studies were also carried out for some of the main parameters that enter into the equations that describe this flow problem. For instance, with regard to the aquifer permeability the values considered were 50,100 and 500 Darcys, resulting in temperature variations essentially coincident. The effect of the thermal conductivity of the matrix surrounding the fracture is presented in Fig. 11, for values of this parameter of 0.0005, 0.0010 and 0.0020 $W/m\ °C$. It can be noticed that its effect is very important, and as expected, increasing the thermal conductivity results in grater heat rates and smaller temperature drops.

One point that deserves discussion is that related to the importance of the steam cap expansion in the thermodynamic behavior of a fracture undergoing exploitation. This significance can be observed when comparing the temperature and pressure behavior versus time for cases 1 and 2, shown in Figs. 2 and 6, observing in the latter results corresponding to production from the liquid zone, a minimum pressure drop due to the high compressibility of steam, that contributes significantly to the pressure support of the system.

TABLE 1. PARAMETERS USED IN THE SIMULATION.

Fracture:	
z_t, (m)	700
L, (m)	900
b, (m)	0.3
Initial conditions:	
T, $(\ °C)$	250
z_l, (m)	500
Rock:	
$\rho_R = \rho_{sR}$, (kg/m^3)	2650
$c_R = c_{sR}$, $(kJ/kg\ °C)$	1
$\kappa_R = \kappa_{sR}$, $(W/m\ °C)$	0.001
Aquifer:	
T_r, $(\ °C)$	250
ϕ,$(\ )$	0.20
k, $(Darcy)$	50
c_t, $(1/Pa)$	1.2e-9
Production:	
$w_{s\ adm}$, (kg/s)	1
$p_{s\ adm}$, (MPa)	0.8

CONCLUSIONS

The main purpose of this paper has been to present results obtained from a numerical solution to a space integrated zero dimensional model (SIZDM), for the description of the thermodynamic behavior of a geothermal fracture undergoing exploitation. The motivation of this work came after identifying the need for a better understanding of the behavior of wells producing from main fractures, in geothermal reservoirs.

From the results of this study, the following conclusions can be made:

1. A SIZDM is presented for the thermodynamic behavior description of a geothermal fracture.
2. The nonlinear equations of mass and energy conservation were numerically solved.
3. The system's behavior is described for exploitation conditions in the steam, in the water, or in both zones.
4. The main providing mass source to the steam cap is the evaporation of the water zone.
5. For producing conditions in the water zone the producing life of the fracture is substantially reduced.
6. The effect of the matrix thermal conductivity on the heat rates is very important.
7. The steam cap expansion has a great significance in the thermodynamic behavior of a fracture.

NOMENCLATURE

b = fracture thickness (m)
c = specific heat $(J/kg\ ^\circ C)$
c_t = aquifer total compressibility $(1/Pa)$
L = length of fracture (m)
h = specific enthalpy (J/kg)
$\bar{h}$ = average specific enthalpy (J/kg)
k = permeability (m^2)
κ = thermal conductivity $(W/m\ ^\circ C)$
p = pressure (Pa)
q = heat rate toward the fracture (J/s)
q_1 = influence function $(J/s\ ^\circ C)$
t = time (s)
T = temperature $(\ ^\circ C)$
u = specific internal energy (J/kg)
x = mixture quality (fraction)
z_l = liquid level refered to the fracture base (m)
z_t = fracture height (m)
$z_{l,t=0}$ = height of the initial steam-water level (m)
w = production (kg/s)
w_1 = influence function (kg/sPa)
Δt = time step (s)
Δp = pressure drop $(= p_i - p_{i-1})$ (MPa)
ΔT = temperature drop $(= T_i - T_{i-1})$ $(\ ^\circ C)$
ρ = density (kg/m^3)
ϕ = porosity (fraction)

Subscripts:

adm= turbine admission
f = fracture
i = time level
l = liquid
p = production
r = recharge
R = rock
s = steam
sR = solids in the fracture
w = water
1 = influence function

superscripts:

k = iteration level

REFERENCES

Brigham,W.E., and Morrow,C.B. (1977):*P/z Behaviour for Geothermal Steam Reservoirs.* Soc. Pet. Eng. J. **17**(5), pp 407-412.

Brigham, W.E. and Neri, G. (1980): *A Depletion Model for the Gabbro Zone (Northern Part of Larderello Field).* Proc., Second DOE-ENEL Workshop Cooperative Research Geothermal Energy, Berkeley, CA, pp 434-463.

Brownell, D.H., Garg, S.K. and Pritchett, J.W. (1977): *Governing Equations for Gothermal Reservoirs.* Water Resources Research, **13**(6), pp 929-935.

Carslaw, H.S. and Jaeger, J.C. (1959): *Conduction of Heat in Solids.* Oxford University Press, Oxford, England.

Castanier,L.M., Sanyal, S.K. and Brigham, W.E. (1980): *A Practical Analytical Model for Geothermal Reservoir Simulation.* Paper SPE 8887, SPE California Regional Meeting, Los Angeles, CA.

Craft, B.C. and Hawkins, M.F. Jr (1959): *Applied Petroleum Reservoir Engineering.* Prentice-Hall, Inc. New Jersey.

Faust, C.R. and Mercer, J.W. (1979a): *Geothermal Reservoir Simulation, 1. Mathematical Models for Liquid and Vapor Dominated Hydrothermal Systems.* Water Resources Research, **15**(1), pp 23-30.

Faust, C.R. and Mercer, J.W. (1979b): *Geothermal Reservoir Simulation, 2. Mathematical Models for Liquid and Vapor Dominated Hydrothermal Systems.* Water Resources Research, **15**(1), pp 31-46.

Garg, S.K, Pritchett, J.W. and Brownell,D.H. (1975): *Transport of Mass and Energy in Porous Media.* Presented at Second United Nations Symposium on the Development and Use of Geothermal Resources, San Francisco, California, May 20-29.

Garg, S.K., Pritchett, J.W. (1977) : *On Pressure-Work, Viscous Dissipation and the Energy Balance Relation for Geothermal Reservoirs.* Advances in Water Resources, **1**(1), pp 41-47.

Grant, M.A (1977): *Broadlans: A Gas-Dominated Field.* Geothermics, **6**(1), pp 9-29.

Grant, M.A., Donaldson, I.G. and Bixley,P.F. (1982): *Geothermal Reservoir Engineering.* Academic Press, New York.

Muskat,M. (1945):*The Production Histories of Oil Producing Gas-Drive Reservoirs.* Jour. of Applied Physics (March), pp 147-159.

Miller, F.G. (1962): *Theory of Unsteady-State Influx of Water in Linear Reservoir.* Journal of Institute of Petroleum, **48**, pp 365- 379

Nabor, G.W. and Barham, R.H. (1964): *Linear Aquifer Behavior.* May, Jour. Pet. Tech., Trans., AIME, **231**, pp 561-563.

Pruess, K. (1983): *Development of the General Purpose Simulator MULKOM.* Annual Report 1982, Earth Sciences Division, report LBL- 15500, Lawrence Berkeley Laboratory.

Pruess, K. (1987): *TOUGH User's Guide.* Nuclear Regulatory Commission, Report NUREG/CR 4644.

Pruess, K. (1988): *SHAFT, MULKOM, THOUGH: A Set of Numerical Simulators for Multiphase Fluid and Heat Flow.* Geotermia, Revista Mexicana de Geoenergía, 4(1), pp 185-202.

Raghavan,R. (1994):*Well Test Analysis.* Prentice Hall, Englewood Cliffs, New Jersey.

Schilthuis, R.J. (1936): *Active Oil and Reservoir Energy.* Trans., AIME, **118**, pp 33-52.

Sorey, M.L. and Fradkin, L.J. (1979):*Validation and Comparison of Different Models of the Wairakei Geothermal Reservoir.* Fifth Workshop Geothermal Reservoir Engineering, Stanford University, Stanford, CA, pp 215-220.

Whiting,R.L. and Ramey,H.J. Jr. (1969): *Application of Material and Energy Balances to Geothermal Steam Production.* Jour. of Pet. Tech., July,**21**(7),pp 893-900.

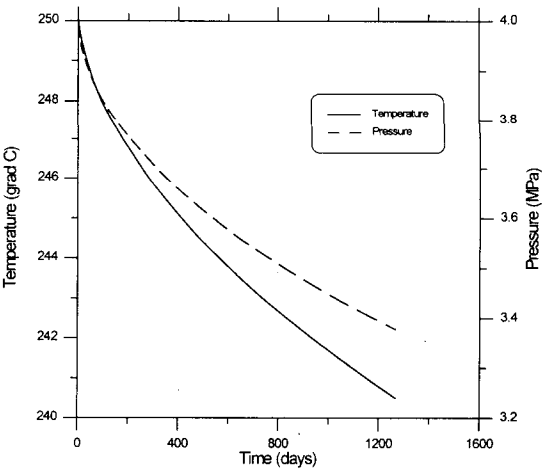

Fig. 2. Temperature and pressure behavior versus time; production from the steam zone.

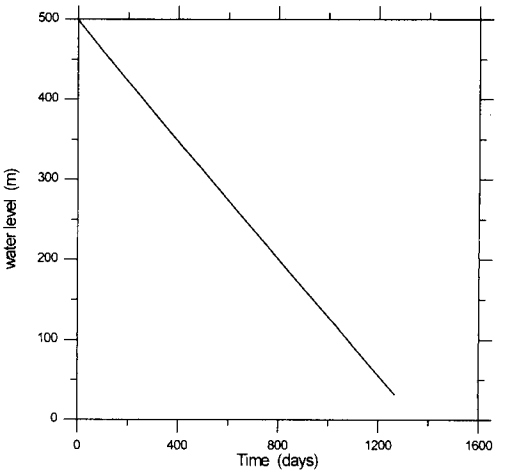

Fig. 3. Water level behavior versus time; production from the steam zone.

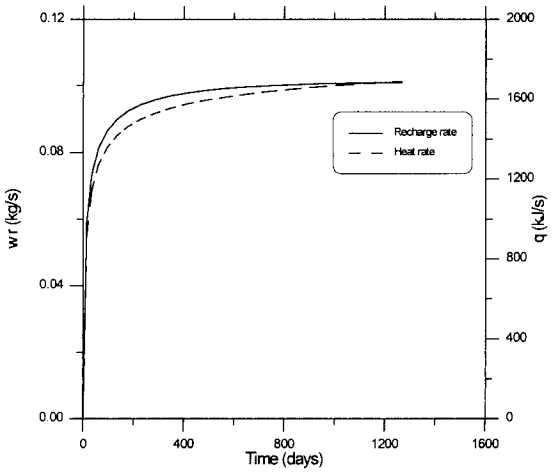

Fig. 4. Water recharge rate and heat rate toward the fracture; production from the steam zone.

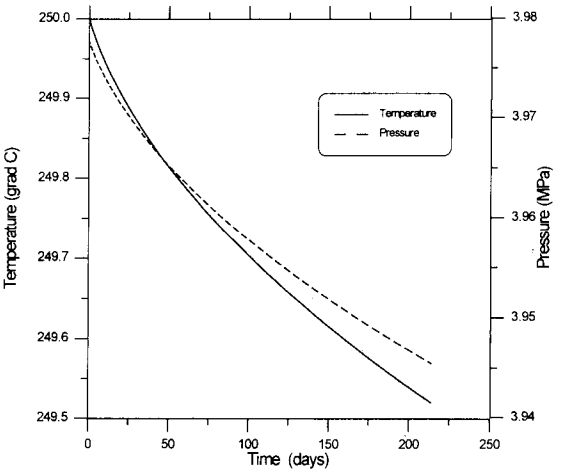

Fig. 6. Temperature and pressure behavior versus time; production from the water zone.

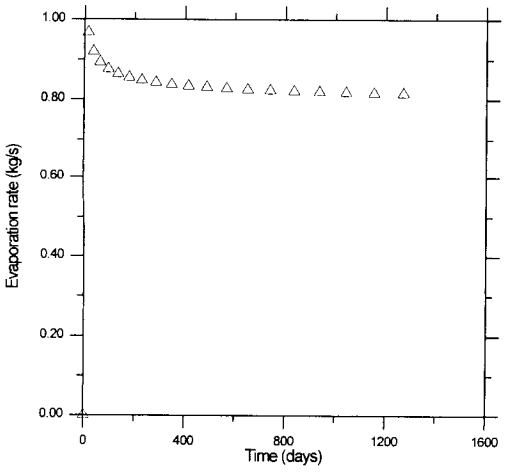

Fig. 5. Evaporation rate of the water zone; production from the steam zone.

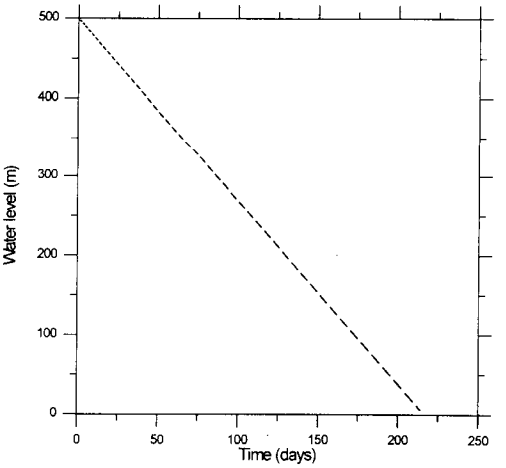

Fig. 7. Water level behavior versus time; production from the water zone.

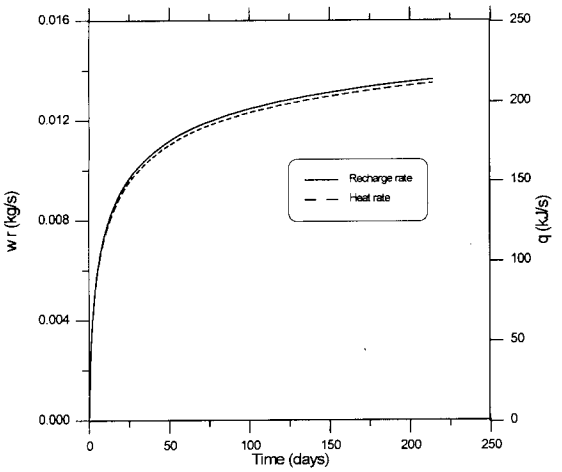

Fig. 8. Water recharge rate and heat rate toward the fracture; production from the water zone.

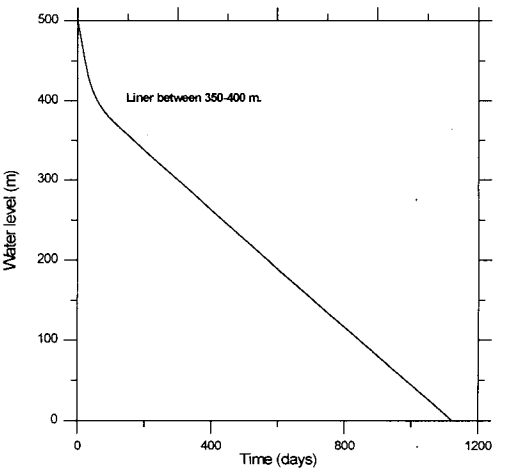

Fig. 10. Water level behavior versus time; mixed production.

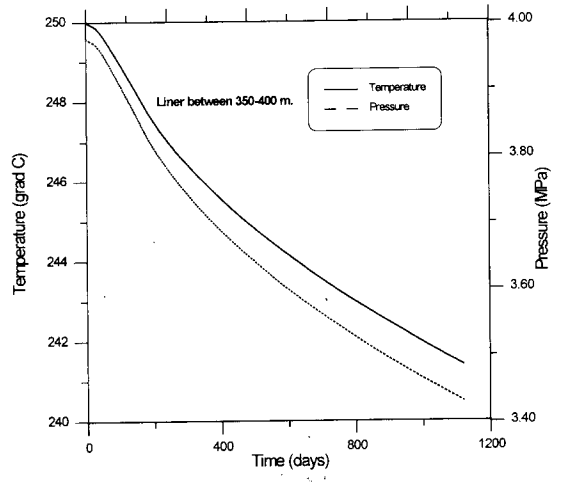

Fig. 9. Temperature and pressure behavior versus time; mixed production.

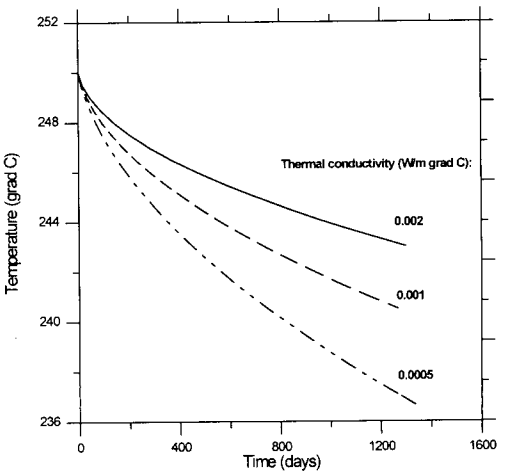

Fig. 11. Effect of the thermal conductivity; production from the steam zone.

PROCEEDINGS, Twentieth Workshop on Geothermal Reservoir Engineering
Stanford University, Stanford, California, January 24-26 1995
SGP-TR-150

USING A HOT DRY ROCK GEOTHERMAL RESERVOIR FOR LOAD FOLLOWING

Donald Brown and Robert DuTeau

Los Alamos National Laboratory
Earth and Environmental Sciences Division
Los Alamos, New Mexico 87545

ABSTRACT

Field measurements and modeling have shown the potential for using a Hot Dry Rock (HDR) geothermal reservoir for electric ***load following***: either with Power-Peaking from a base-load operating condition, or for Pumped Storage of off-peak electric energy with a very significant thermal augmentation of the stored mechanical energy during periods of power production. For the base-load with power-peaking mode of operation, an HDR reservoir appears capable of producing over twice its nominal power output for short -- 2 to 4 hour -- periods of time. In this mode of operation, the reservoir normally would be produced under a high-backpressure condition with the HDR reservoir region near the production well highly inflated. Upon demand, the production backpressure would be sharply reduced, surging the production flow.

Alternatively, for Pumped Storage, the reservoir would be operated in a cyclic mode, with production shut-in during off-peak hours. When the produced thermal energy of such a pumped-storage system is considered, an HDR reservoir would be capable of returning considerably more energy to the surface during the production phase than would have been consumed in inflating the reservoir during the off-peak storage phase. Pumped Storage reservoir operation was actually demonstrated experimentally during a brief series of cyclic reservoir tests at the end of the Long-Term Flow Test (LTFT) of the HDR reservoir at Fenton Hill, NM in May 1993.

The analytical tool used in these investigations has been the transient finite element model of the an HDR reservoir called GEOCRACK, which is being developed by Professor Dan Swenson and his students at Kansas State University. This discrete-element representation of a jointed rock mass has recently been validated for transient operations using the set of cyclic reservoir operating data obtained at the end of the LTFT.

INTRODUCTION

The subjects of Power Peaking and Pumped Storage Energy Production, which would offer electric utilities flexibility in load management when using engineered Hot Dry Rock (HDR) geothermal systems, are very timely as concerns the commercialization of HDR geothermal technology. This is because one or the other of these load following concepts may provide an initial "niche" market application which would allow HDR geothermal energy to become economically competitive earlier in the commercial demonstration phase, before HDR technology would have had sufficient time for the anticipated engineering refinements that will be necessary to make HDR power generation an accepted option in the presently very competitive electric power marketplace. In both of these applications, one would use the large fluid capacitance of a highly pressurized HDR reservoir to store and then rapidly produce energy. The resulting flexibility offered by these engineered HDR systems may be the ultimate key to the development of HDR geothermal energy as a commercial reality.

The first concept is that of on-demand power peaking using an HDR geothermal system. In this concept, the HDR reservoir would be continuously produced in a high-backpressure base-load operating mode with the ability -- and flexibility -- to almost instantaneously double the power output by dropping the production backpressure to a much lower level. In practice, this might be accomplished by reducing the backpressure from a base-load level of 3000 psi to 700 psi in less than a minute, effecting a very significant increase in the production flow rate, as well as an increase in the produced geofluid temperature, as the inflated portion of the reservoir surrounding the production wellbore is rapidly vented.

The second concept is that of using an HDR reservoir for pumped storage and power peaking as follows: The reservoir would be shut-in and pressurized with an electrically driven pump during off-peak hours, inflating the reservoir with fluid and storing mechanical energy through the elastic compression of the rock comprising the HDR reservoir region. Then, the reservoir would be partially vented during the subsequent period of peak power demand, returning the previously stored mechanical energy in the form of a much larger amount of thermal energy. This augmented energy production, with the mechanical energy being returned as thermal energy, obviously results from the increase in the enthalpy of the injected fluid as heat is extracted from the HDR reservoir during the storage phase of the cycle. This recovered thermal energy, during the production phase of the cycle, would then be converted to electrical energy in a conventional geothermal power plant.

In this "pumped-storage" mode of operation, an HDR reservoir is capable of returning to the surface significantly more thermal energy than was stored as mechanical energy during the hours of off-peak pressurization. This behavior is not unlike that of a heat pump, which is capable of providing several times its electric power input as space heat during winter months.

This study represents only a first analysis of these two HDR load-following concepts. A more definitive study must await a comprehensive experimental data set supported by further numerical modeling. The presently available data is from a 3-day sequence of cyclic flow experiments performed in May 1993, at the end of the Long-Term Flow Test (LTFT) of the Fenton Hill HDR reservoir. The modeling results presented here will allow us to better define and plan the sequence of HDR production flow experiments planned for the summer of 1995.

ADVANTAGES AND DISADVANTAGES OF THESE TWO METHODS OF LOAD FOLLOWING

Advantages of operating an HDR system in a high-backpressure base-load mode with the option of power peaking:

- This mode of operation would add significantly to the flexibility of an HDR-based geothermal power plant.
- The revenue potential would be increased due to the doubling of the power output during periods of peak demand and the premium price paid for peaking power.
- Injection pumping costs during high-backpressure base-load operation would be reduced because elevated production pressures would, with proper surface-system design, significantly reduce the pumping power required for any given injection pressure.

Disadvantages:

- The base-load power production at a backpressure of 3000 psi would be only about 60% of that at 1400 psi.
- Production wellhead equipment would be subjected to marked pressure fluctuations.
- A more complicated power plant design would be required, with more injection pumping capacity and with attendant increased capital costs to accommodate the doubling of the production thermal power output during the relatively short periods of enhanced production.

Advantages of Cyclic Reservoir Operation Associated with Pumped Storage:

- During the production portion of the cycle, significantly more power would be generated than during comparable base-load operation, partially compensating for the reduced period of power production.
- Heat removal from the less-fluid-accessible portions of the reservoir volume would be enhanced.
- Cyclic operation would reduce the tendency for reservoir flow short-circuiting.

Disadvantages:

- This method of operation could adversely affect power plant and wellhead equipment due to pressure *and* temperature fluctuations.
- The capital investment in the power plant, wells and reservoir would be underutilized. However, enhanced reservoir power production and peaking-power revenue would at least partially compensate for lost revenue duing shut-in periods.
- Borehole heat losses would be accentuated since the production well(s) would be shut-in for up to 16 hours per day. This would have the effect of markedly reducing the surface production temperature for the first few hours of each production interval, as discussed later. An insulated production tubing string would reduce these heat losses, but at an added cost.
- To best utilize the pumped-storage aspect of this mode of operation, it would be most advantageous if the reservoir were produced open-loop, with the fluid stored above ground for later reinjection. However, this would add to the overall capital costs and would result in the evolution of some of the gas dissolved in the geofluid and the precipitation of minerals during the time of storage.

MODEL REPLICATION OF EXPERIMENTAL CYCLIC RESERVOIR PERFORMANCE

The GEOCRACK model was first validated against the cyclic reservoir performance measured near the the end of the Long Term Flow Test in May 1993. The injection and production pressure profiles for these three cycles are shown in Figure 1 while the corresponding injection and production flow rates are shown in Figure 2. It should be noted that because freezing nighttime temperatures were still anticipated at Fenton Hill

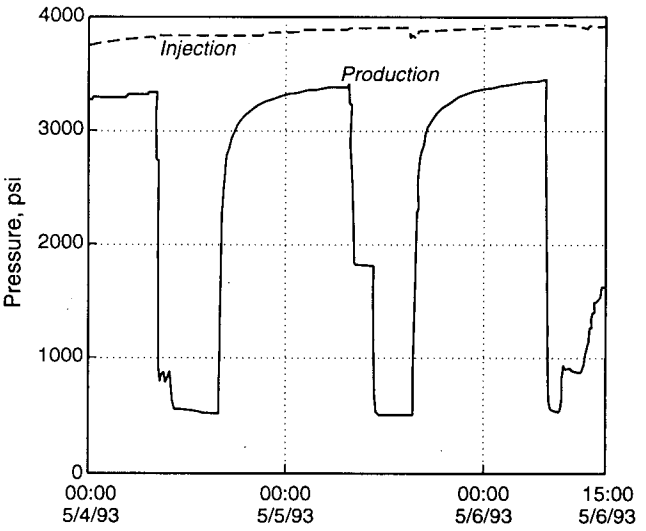

Figure 1. Injection and Production Pressure Profiles During the 3-Day Cyclic Flow Experiment in Early May, 1993.

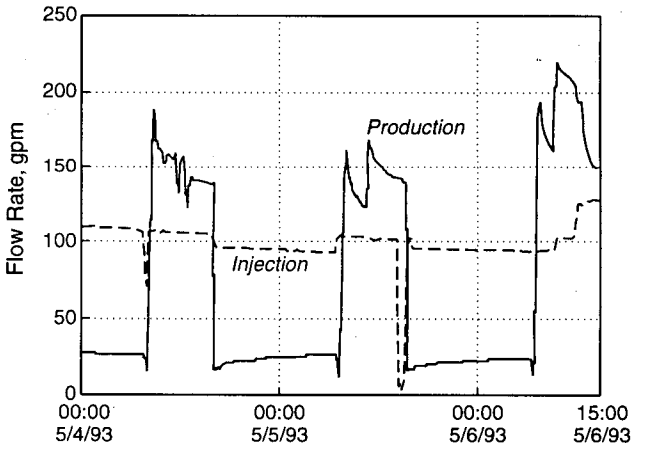

Figure 2. Injection and Production Flow Rate Profiles During the 3-Day Cyclic Flow Experiment.

during May, a small (about 25 gpm) production flow was maintained during each 16-hour overnight production "shut-in" to prevent damage to the air-cooled heat exchanger.

Analysis efforts were concentrated on the second cycle which began the morning of May 5 (at the first sharp drop in production backpressure) because this cycle contained all the necessary components for an adequate model validation:

- Two unique levels of production backpressure during the 8-hour production interval: 1800 psi and 500 psi,
- A 16-hour period of reservoir inflation while the production well was nearly shut-in and,
- A near-constant injection pressure of 3900 psi.

As shown in Figure 2, the most significant feature regarding production enhancement is that the *average* flow rate during the second 8-hour production interval was about 145 gpm. This flow rate is about 60% greater than the previous steady-state production flow rate of 90 gpm measured two weeks earlier at the end of the second phase of the Long-Term Flow Test (Brown, 1994a).

Figure 3 shows the production temperature variation during these three one-day cycles. The initial production temperature of only 107°C (225°F) at the beginning of the first 8-hour production interval shows the significant cooling effect resulting from having shut-in production for the previous 13 days. At the beginning of the next two intervals, the geofluid production temperature is still depressed, but not as much as for the first cycle. For the second and third cycles, the initial geofluid temperature was in the range of 130°C (260 to 270°F) compared to the 184°C (363°F) geofluid production temperature near the end of the second phase of the LTFT in April 1993 (Brown, 1994a). These temperatures clearly show the effects of wellbore cooling during the preceding 16-hour shut-ins. This reduced geofluid temperature for the first 3 to 4 hours of each production interval points up an obvious disadvantage with this mode of reservoir operation which, however, could be mitigated by using an insulated production tubing string.

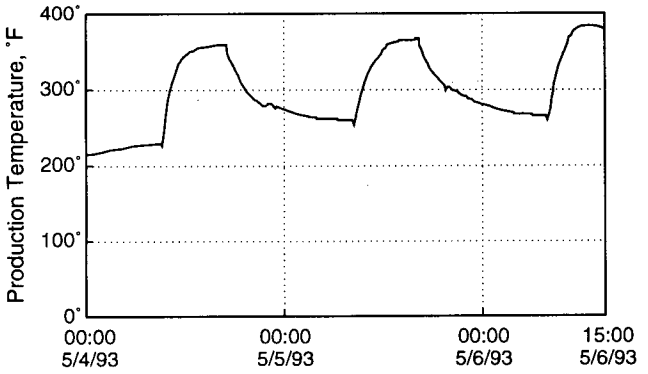

Figure 3. Production Temperature Variation During the 3-Day Cyclic Flow Experiment.

MODELING RESULTS

Replication of Actual Cyclic Reservoir Behavior

The behavior of the Phase II HDR reservoir during transient operations has been modeled with the finite-element coupled fluid-flow and deformation portion of the GEOCRACK model. In particular, the reservoir behavior during the second 24-hour cycle shown in Figures 1 and 2 (from 08:00 on May 5 through 08:00 on May 6) has been simulated with GEOCRACK. As shown in these two figures, there were essentially two phases to this second cycle which can be represented as follows: A two-stage high-rate production interval starting at 08:00 on May 5 and lasting 8 hours, followed by a low-production/very-high-backpressure phase lasting 16 hours.

The model input parameters and results for the simulation of the second cycle are shown in Figure 4. It should be noted that the initial half-day "lead-in" period shown in this figure was used to establish the array of converged steady-state solutions throughout the reservoir region before the sharp transient drop in the production backpressure at 0.5 days. For the entire period modeled, a constant injection pressure of 3700 psi (25.5 MPa) and the time-varying production backpressure profile shown in Figure 4 were used as model inputs. For the 8-hour high-production phase, two stepwise decreases in the production backpressure, from an initial value of 3500 psi (24.2 MPa), were specified: first to 1800 psi (12.5 MPa) for 3 hours and then to 500 psi (3.5 MPa) for the next 5 hours. For the subsequent 16-hour phase of this cycle, a very rapid increase in the production backpressure from 500 psi to 2980 psi (20.5 MPa) was specified, followed by a much more gradual approach to a near-constant backpressure of 3500 psi (24.2 MPa) by the end of 16 hours.

Figure 4 also presents the principal outputs from the model simulation of the cyclic behavior of the reservoir for an 8-hour high-production-rate phase followed by a 16-hour near shut-in phase -- the temporal variation of the production flow including a constant production flow rate of 25 gpm for the second 16-hour phase. When compared to the measured production flow behavior during the second cycle as shown in Figure 2, the high degree of replication by the GEOCRACK model is evident.

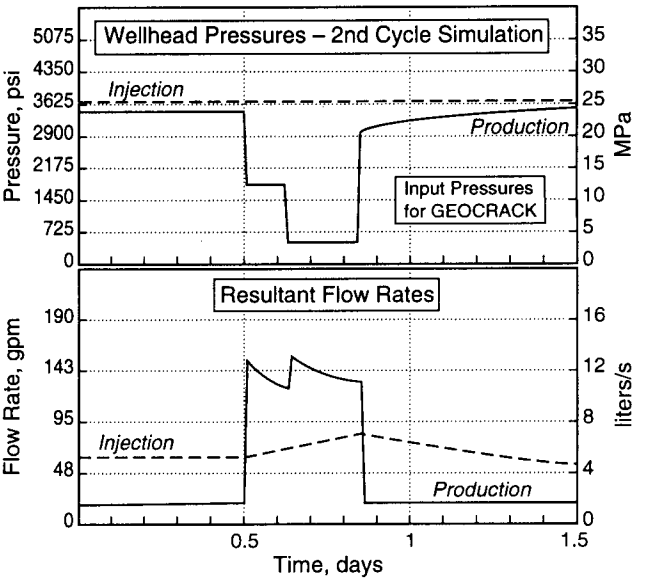

Figure 4. Modeling Results for the Second Cycle of the Cyclic Flow Experiment.

CYCLIC RESERVOIR OPERATION ASSOCIATED WITH POSITIVE-GAIN PUMPED STORAGE

The actual behavior of the Fenton Hill reservoir under an 8-hour on and 16-hour off mode of cyclic production has already been experimentally determined. This behavior is best represented by the second production cycle starting May 5, 1993 as discussed above. During continuous commercial operation of such an HDR load-following system, it would be anticipated that a very similar approach would be taken: a high production rate during daytime hours followed by a near shut-in condition during off-peak hours. To minimize the effects of thermal transients on the production piping and to prevent freezing during winter operations, it would be anticipated that a modest production flow would be maintained during the "shut-in" periods, as was used at Fenton Hill. Thus, the measured behavior as shown in Figures 1, 2, and 3 as well as the modeling results shown in Figure 4 can be used to better understand cyclic HDR system operation associated with a positive-gain pumped storage mode of reservoir operation.

A first observation is that the amount of mechanical energy stored during 16 hours of reservoir inflation is small compared to the electrical energy generated during the 8 hours of high-production flow. For a combined 2-well injection rate of 272 gpm at 5200 psi (Brown, 1994b), only 10 MW-hours of mechanical energy would be stored during the 16-hour reservoir inflation (shut-in) phase. During the 8-hour production phase,

however, up to 40 MW-hours of electrical energy could be produced, representing a net gain of a factor of 4 over the stored mechanical energy. This number was derived as follows from the previously reported 20 MW(th) potential power output from the Fenton Hill Reservoir when using a 2-production-well system (Brown, 1994b):

Average production flow enhancement for 8 hours = 1.6 (145 gpm/90 gpm)

Peaking power production = 1.6 x 20 = 32 MW(th)

Using a net 16% power conversion efficiency for a geofluid production temperature of about 210°C (410°F), and with no injection pumping losses, the peaking electrical power generation would be about 5 MW for 8 hours, or 40 MW-hours of electrical energy -- 4 times the stored mechanical energy.

A second observation is that if the Fenton Hill reservoir were to be operated in this load-following mode for 8 hours a day, one would need to sell this peaking power for at least twice the base-load rate to produce the same revenue as continuous base-load operation (assuming other plant costs were comparable).

However, the absence of flow short-circuiting, the enhanced thermal recovery from the entire reservoir region, and the fact that the reservoir would experience only half the draw-down (or, conversely, twice the lifetime) when compared to base-load operation may add to the desirability of this cyclic mode of reservoir operation.

Operation in a High-Backpressure Base-Load Mode with the Capability for Power Peaking

Operation of the Fenton Hill reservoir in a high-backpressure base-load mode of operation, with periodic flow surging to approximate the system response to a peaking power demand, has also been simulated with the GEOCRACK model. Steady-state reservoir operating conditions as measured during the LTFT and the two higher backpressure portions of the Interim Flow Test (Brown, 1994a) were used to determine reservoir flow parameters and boundary conditions. However, the model had to be adjusted in the far-field region to account for the significantly larger capacitance of the Phase II reservoir than had previously been replicated by the GEOCRACK model. The simulations were performed as if the HDR system were being operated in flow control, with the backpressure being continuously adjusted to produce a constant elevated flow rate during periods of peak power demand. These periods of enhanced power production were assumed to be for either 4 or 8 hours each day.

Figure 5 shows the predicted behavior of the Fenton Hill HDR system operated in a high-backpressure mode, with 4-hour power surges each day produced by significantly reducing the production backpressure from a 3000 psi baseline level. This figure shows the specified production flow parameters: 63.5 gpm (4 l/s) for 20 hours and then 127 gpm (8 l/s) for the next 4 hours. Using a flow control system to produce a constant power output by controlling the production backpressure, the base-load flow rate was easily doubled during the 4-hour period of peak power demand. It should be noted that since the production backpressure only dropped to 1820 psi (12.5 MPa) during this period of enhanced power production, the overall system performance could be further improved in either of two ways: By reducing the backpressure level during base-load operation, the base-load power output could be increased and the minimum backpressure would still not drop below the desired 500 to 700 psi level during the period of flow surging. Alternatively, the production flow rate could be increased by more than a factor of 2 during peaking operations, increasing the power output and still not dropping below the 500 psi back-pressure limit after 4 hours of enhanced production.

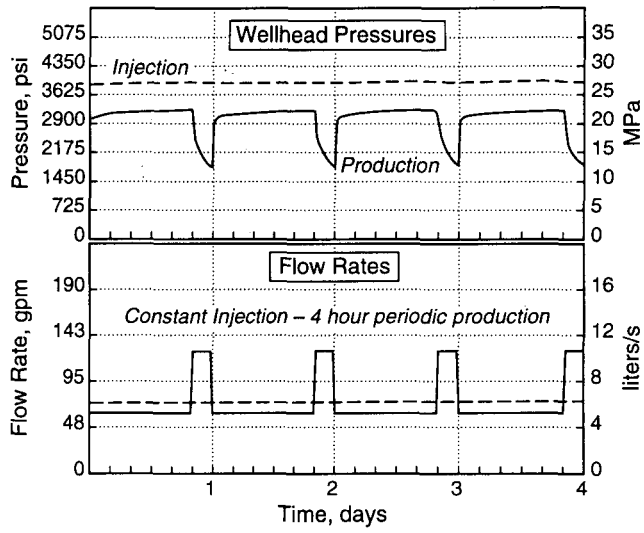

Figure 5. Simulated Reservoir Behavior for High-Backpressure Base-Load Operation with 4 Hours of Low-Pressure Production Every 24 Hours.

Figure 6 presents the results from simulating a similar peaking-power mode of reservoir operation, but with an 8-hour high-rate production interval rather that the 4-hour period discussed above. In order to produce the same level of enhanced power production for 8 hours instead of 4 hours, it was necessary to increase the mean injection pressure by 300 psi, to 4250 psi (29.3 MPa). As a consequence, the base-load production flow rate increased from 63.4 gpm (4 l/s) to 85.6 gpm (5.4 l/s), resulting in only a 48% gain in power during the period of enhanced power production, but now from a considerably higher initial power level.

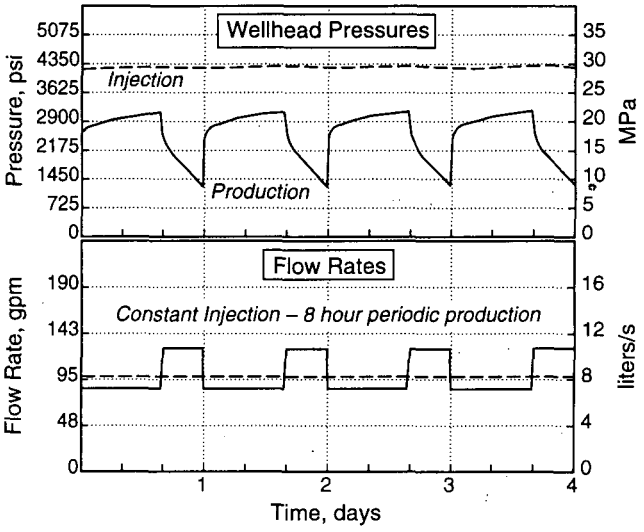

Figure 6. Simulated Reservoir Behavior for High-Backpressure Base-Load Operation with 8 Hours of Low-Pressure Production Every 24 Hours.

Hopefully, questions regarding how best to operate an HDR reservoir in a base-load mode with extended power surges will be answered experimentally during the reservoir flow testing planned for the summer of 1995.

DISCUSSION AND CONCLUSIONS

These preliminary experimental and modeling results suggest that load-following methods of HDR reservoir operation could be very attractive from a commercial power-production standpoint.

The HDR load-following concept which maintains the system in a high-backpressure base-load operating condition except for periods of peak demand, when the reservoir is produced in a rapid venting mode with at least twice the power output for 4-hour intervals, appears to offer the most attractive method of load following.

However, positive-gain pumped storage using an HDR reservoir appears to offer several advantages over conventional pumped storage concepts now being used by the electric utility industry -- the principal one being an energy output several times greater than the off-peak energy storage.

As now planned, the initial results obtained from this study will be confirmed during the summer of 1995 when a sequence of cyclic flow tests will be performed in association with additional numerical modeling using a model with a more detailed representation of the jointed rock region in the vicinity of the production wellbore. This region of the model is the most important for modeling cyclic reservoir production, since a significant fraction of the produced fluid will have been stored in the pressure-dilated region within 100 m or so of the production wellbore prior to each low-backpressure production interval.

References

Brown, D. W. (1994a), Summary of Recent Flow Testing of the Fenton Hill HDR Reservoir, Proceedings, 19th Workshop on Geothermal Reservoir Engineering, Jan. 18-20, 1994, Stanford University, Stanford, CA p. 113-116.

Brown, D. W. (1994b), How to Achieve a Four-Fold Productivity Increase at Fenton Hill, Trans. Geothermal Resources Council, 18 p. 405-408, Oct. 1994.

TWENTIETH ANNUAL WORKSHOP ON GEOTHERMAL RESERVOIR ENGINEERING STANFORD UNIVERSITY

Participants List

Michael C. Adams
University of Utah Research Institute
391 Chipeta Way, Suite A
Salt Lake City, UT 84108
Tel.: 801-584-4435, Fax: 801-584-4453

Chitoshi Akasaka
Electric Power Development Co.
15-1 Ginza 6-chome Chuo-ku
Tokyo 104, Japan
Tel.: 81-3-3546-2221, Fax: 81-3-3546-1685

Willis Ambusso
Stanford Geothermal Program
Green Earth Sciences Bldg, Rm 65
Stanford, CA 94305-2220
Tel.: 415-723-9219, Fax: 415-725-2099
E-Mail: ambusso@pangea.stanford.edu

David N. Anderson
Geothermal Resources Council
P.O. Box 1350
Davis, CA 95617
Tel.: 916-758-2360

Fernando Ascencio-Cendejas
Univ. Michoacana de San Nicholas de Hidalgo
Escuela de Ingenieria Mecanica
Edif. "W" Planta Alta
Ciudad Universitaria
Morelia, Mich., Mexico
Tel.: 43-15-68-69, Fax: 43-15-68-69

Benjamin Barker
UNOCAL Geothermal
3576 Unocal Place
Santa Rosa, CA 95403
Tel.: 707-545-7600, Fax: 707-545-8746

Ruggero Bertani
ENEL-DPT/VDTG
Via Andrea Pisano, 120
Pisa 56100, Italy
Tel.: 39-50-53-5705, Fax: 39-50-533290

Steve Bjornstad
Naval Air Weapons Station
Geothermal Program Office, 823G00D/C8306
China Lake, CA 93555
Tel.: 619-939-4048, Fax: 619-939-2449

Kit Bloomfield
Pacific Gas & Electric
P.O. Box 456
Healdsburg, CA 95448
Tel.: 707-431-6235, Fax: 707-431-6197

Greg N. Boitnott
New England Research Inc.
76 Olcott Drive
White River Junction, VT 05001
Tel.: 802-296-2401, Fax: 802-296-8333

Brian P. Bonner
Lawrence Livermore National Lab
L-201, Box 808
Livermore, CA 94550
Tel.: 510-422-7080, Fax: 501-423-1057

William T. Box
Calpine Corporation
1160 N Dutton
Santa Rosa, CA 95406-1279
Tel.: 707-527-6700, Fax: 707-544-2422

Donald W. Brown
Los Alamos National Laboratory
P.O. Box 1663
Group EES-4, MS D443
Los Alamos, NM 87545
Tel.: 505-667-4318, Fax: 505-667-8487

Jim Combs
Geo Hills Associates
27790 Edgerton Road
Los Altos Hills, CA 94022-3212
Tel.: 415-941-5480, Fax: 415-941-5480

John R. Counsil
Engineering Consultant
1148 Shadyoak Place
Santa Rosa, CA 95404
Tel.: 707-538-2288

Douglas L. Crea
UNOCAL Geothermal
3576 Unocal Place
Santa Rosa, CA 95403-1774
Tel.: 707-545-7600, Fax: 707-545-8746

David V. Duchane
Los Alamos National Laboratory
EES-HDR
P.O. Box 1663, MS-D443
Los Alamos, NM 87545
Tel.: 505-667-9893, Fax: 505-667-8487

Steve Enedy
N.C.P.A.
P.O. Box 663
Middletown, CA 95461
Tel.: 707-987-3101, Fax: 707-987-2088

Shaun D. Fitzgerald
Stanford Geothermal Program
Green Earth Sciences Bldg, Rm 65
Stanford, CA 94305-2220
Tel.: 415-723-4744, Fax: 415-725-2099

Raymond Fortuna
U.S. Dept of Energy
EE-122
1000 Independence Ave, SW
Washington, DC 20585
Tel.: 202-586-1711, Fax: 202-586-8185

Robert O. Fournier
U.S. Geological Survey
345 Middlefield Rd., MS-910
Menlo Park, CA 94025
Tel.: 415-329-5205, Fax: 415-329-5203

D.H. Freeston
Univ. of Auckland, Geothermal Institute
Private Bag 92019
Auckland, New Zealand
Tel.: 64-9-373-7599, Fax: 64-9-373-7436

George Frye
Int'l. Geothermal Association
1 Cyclotron Rd., LBL 50E
Berkeley, CA 94720
E-Mail: igusec@lbl.gov

Hiroshi Fukagawa
Waseda University
Dept. of Mineral Resources Engr.
Ohkubo 3-4-1, Shinjuku-ku
Tokyo 169, Japan
Tel.: 81-3-3203-4141, Fax: 81-3-3200-2587

Sabodh K. Garg
S-Cubed
P.O. Box 1620
La Jolla, CA 92038-1620
Tel.: 619-587-8438, Fax: 619-755-0474

Colin Goranson
Consultant
1498 Aqua Vista Road
Richmond, CA 94805
Tel.: 510-234-0522, Fax: 510-234-5881

Keshav Goyal
Calpine Corporation
1160 North Dutton, #200
Santa Rosa, CA 95401
Tel.: 707-527-6700, Fax: 707-544-2422

Bill Guerard
California Dept. of Conservation
Div. of Oil, Gas & Geothermal Resources
801 K St., MS 20-20
Sacramento, CA 95814-3530
Tel.: 916-323-1777, Fax: 916-323-0424

Mohinder S. Gulati
UNOCAL Geothermal
P.O. Box 7600, Room 803
Los Angeles, CA 90051
Tel.: 213-977-7496, Fax: 213-977-6333

Teklu Hadgu
L.B.L., Earth Sciences Division
1 Cyclotron Road, Bldg. 50E
Berkeley, CA 94720-0001
Tel.: 510-486-6474, Fax: 510-486-5686

Richard Holt
Mesquite Group Inc.
P.O. Box 1283
Fullerton, CA 92632
Tel.: 714-738-8224, Fax: 714-525-2852

Roland N. Horne
Stanford Geothermal Program
Petroleum Engineering Dept.
Green Earth Sciences Bldg.
Stanford University
Stanford, CA 94305-2220
Tel.: 415-725-4744, Fax: 415-725-2099

Jeff Hulen
ESRI - University of Utah
391-C Chipeta Way
Salt Lake City, UT 84108
Tel.: 801-584-4446, Fax: 801-584-4453

Christy C. Hunter
California Dept. of Conservation
Div. of Oil, Gas & Geothermal Resources
485-B Broadway
El Centro, CA 92243
Tel.: 619-353-9900, Fax: 619-353-9594

Masami Hyodo
Geothermal Energy R & D Co.,Ltd
Kyodo Bldg, 11-7, Kabuto-cho
Nihonbashi, Chuo-ku
Tokyo 103, Japan
Tel.: 81-3-3666-5822, Fax: 81-3-3666-5289

William Irwin
Chevron Overseas Petroleum Inc.
PO Box 5046
San Ramon, CA 94583-0946
Tel.: 510-842-1616, Fax: 510-842-1275

Elizabeth Johnson
California Div. of Oil and Gas
801 K Street, MS 20-21
Sacramento, CA 95814
Tel.: 916-323-1786, Fax: 916-323-0424

Steve Jones
Northern California Power Agency
P.O. Box 666
Middletown, CA 95461
Tel.: 707-987-3101, Fax: 707-987-2088

Ann Kirkpatrick
Lawrence Berkeley Laboratory
Earth Sciences Div, Bldg 50E
1 Cyclotron Rd
Berkeley, CA 94720
Tel.: 510-486-6985, Fax: 510-486-5686

Christopher W. Klein
GeothermEx, Inc.
5221 Central Ave., Suite 201
Richmond, CA 94804
Tel.: 510-527-9876, Fax: 510-527-8164

Michael Krahmer
Caithness Resources
350 Indiana St, Ste. 510
Golden, CO 80401
Tel.: 303-279-5701, Fax: 303-279-3486

Michael Kramer
California Energy Commission
1516 9th St, MS-43
Sacramento, CA 95814
Tel.: 916-654-4599

Paul Kruger
Stanford University
Civil Engineering Dept.
Stanford, CA 94305
Tel.: 415-725-2382, Fax: 415-725-8662

Kok-Thye Lim
Stanford University
Dept of Petroleum Engineering
Stanford, CA 94305-2220
Tel.: 415-723-4744, Fax: 415-725-2099

Marcelo J. Lippmann
L.B.L., Earth Sciences Division
1 Cyclotron Road, Bldg. 50C
Berkeley, CA 94720-0001
Tel.: 510-486-5035, Fax: 510-486-5686

Sullivan Marsden
Stanford University
Dept of Petroleum Engineering
Green Earth Sciences Bldg, Rm 65
Stanford, CA 94305-2220
Tel.: 415-723-4744, Fax: 415-725-2099

Richard T. McCauley
Magma Operating Co.
551 W Main St, Ste. 3
Brawley, CA 92227
Tel.: 619-351-3060, Fax: 619-351-3039

James R. McNitt
GeothermEx, Inc.
5221 Central Ave., Suite 201
Richmond, CA 94804
Tel.: 510-527-9846, Fax: 510-527-8164

David Meade
U.S. Navy
Geothermal Program Office
China Lake, CA 93555
Tel.: 619-939-4057, Fax: 619-939-2449

Anthony J. Menzies
GeothermEx
5221 Central Avenue, No. 201
Richmond, CA 94804
Tel.: 510-527-9876, Fax: 510-527-8164

Frank Miller
Stanford Geothermal Program
Green Earth Sciences Bldg, Rm 65
Stanford, CA 94305-2220
Tel.: 415-723-2938, Fax: 415-725-2099

Antony Mossop
Stanford University
Geophysics Dept.
Mitchell Bldg.
Stanford, CA 94305
Tel.: 415-723-5485

Paul B. Mount, II
California State Lands Commission
200 Oceangate, 12th Floor
Long Beach, CA 90802
Tel.: 310-590-5201, Fax: 310-590-5995

Patrick Muffler
U.S.G.S.
345 Middlefield Road, MS-910
Menlo Park, CA 94025
Tel.: 415-329-5239, Fax: 415-329-5203
E-Mail: pmuffler@mojave.wr.usgs.gov

Dennis L. Nielson
ESRI - Univ. of Utah
391-C Chipeta Way
Salt Lake City, UT 84108
Tel.: 801-584-4438, Fax: 801-584-4453

Gerald Niimi
Thermasource, Inc.
725 Farmers Lane, #1
Santa Rosa, CA 95409
Tel.: 707-523-2960, Fax: 707-523-1029

Karen Norrell
Montana Tech. Univ.
610 So. Idaho
Butte, MT 59701
Tel.: 406-782-5929

Luis Ortega Pierres
Comision Federal de Electricidad
Laguna de Terminos 460
Col. Ventura Puente 58020
Morelia, Mich. C.P., 58290 Mexico
Tel.: 43-143970, Fax: 43-144735

Gudmundur Palmason
Orkustofnun
Grensasvegur 9
108 Reykjavik, Iceland
Tel.: 354-1-696000, Fax: 354-1-688896

Susan Petty
Black Mountain Technology
654 Glenmont Drive
Solano Beach, CA 92075
Tel.: 619-792-9055, Fax: 619-792-9055

John W. Pritchett
S-Cubed
P.O. Box 1620
La Jolla, CA 92038-1620
Tel.: 619-587-8440, Fax: 619-755-0474

Hector G. Puente
C.F.E. (Cerro Prieto)
P.O. Box 248
Calexico, CA 92231
Tel.: 65-53-6870, Fax: 65-53-6269

Marshall Reed
U.S. D.O.E., Geothermal Div., EE-122
1000 Independence Ave., S.W.
Washington, DC 20585
Tel.: 202-586-8076, Fax: 202-586-5124

Alex W. Reid, III
California State Land Commission
200 Oceangate, 12th Floor
Long Beach, CA 90802
Tel.: 310-590-5201, Fax: 310-590-5995

Joel Renner
INEL
Box 1625
Idaho Falls, ID 83415-3830
Tel.: 208-526-9824, Fax: 208-526-0969

Jose A. Rial
Univ. of North Carolina
Geology Dept., Mitchell Hall
CB #3315
Chapel Hill, NC 27514
Tel.: 919-966-4553, Fax: 919-966-4519

Peter Rose
ESRI - Univ. of Utah
391 Chipeta Way, Suite A
Salt Lake City, UT 84108
Tel.: 801-584-4430, Fax: 801-584-4453

John C. Rowley
Pajarito Enterprises
3 Jemez Ln.
Los ALamos, NM 82544
Tel.: 505-672-9770, Fax: 505-672-9770

Mohammad Sahimi
Univ. of Southern California
Dept. of Chemical Engineering
Los Angeles, CA 90089-1211
Tel.: 213-740-2064

Fernando Samaniego V.
University of Mexico
Division de Estudios de Posgrado
Facultad de Ingenieria, UNAM
04510 Mexico, D.F., Mexico
Tel.: 525-622-3017/550-8712
Fax: 525-616-1073

Subir K. Sanyal
GeothermEx, Inc.
5221 Central Avenue, Suite 201
Richmond, CA 94804
Tel.: 510-527-9876, Fax: 510-527-8164

Cengiz Satik
Stanford Geothermal Program
Dept of Petroleum Engineering
Stanford, CA 94305-2220
Tel.: 415-723-5377, Fax: 415-723-2099

Alexander Schriener, Jr.
Magma Power Company
551 W. Main, Suite 3
Brawley, CA 92227
Tel.: 619-351-3060, Fax: 619-351-3039

Ron Schroeder
Berkeley Group, Inc.
245 Gravatt Drive
Berkeley, CA 94705
Tel.: 510-883-0313, Fax: 510-883-0313

Shubo Shang
Stanford University
Dept of Petroleum Engineering
Stanford, CA 94305-2220
Tel.: 415-723-4744, Fax: 415-725-2099

Michael Shook
Idaho National Engineering Lab
P.O. Box 1625, MS-2107
Idaho Falls, ID 83415-2107
Tel.: 208-526-6945, Fax: 208-526-9822

Baljit Singh
UNOCAL
3576 Unocal Place
Santa Rosa, CA 95403
Tel.: 707-545-7600, Fax: 707-545-8746

Buck Sisson
INEL
Lockheed
PO Box 1625, MS-2107
Idaho Falls, ID 83415
Tel.: 208-526-1118, Fax: 208-526-0875

Estela M. Smith
Geothermal Resources Council
PO Box 1350
Davis, CA 95617-1350
Tel.: 916-758-2360

Supri Soengkono
Geothermal Inst., Univ. of Auckland
Private Bag 92019
Auckland, New Zealand
Tel.: 64-9-373-7599 x 8404
Fax: 64-9-373-7436

Mitchel A. Stark
UNOCAL
3576 Unocal Place
Santa Rosa, CA 95403
Tel.: 707-545-7600, Fax: 707-544-6855

Kenneth Stelling
CA Department of Conservation
Div. of Oil, Gas, and Geothermal Resources
50 D Street, Rm. 300
Santa Rosa, CA 95404
Tel.: 707-576-2385,, Fax: 707-576-2611

Deniz Sumnu
Stanford University
Dept. of Petroleum Engineering
Stanford, CA 94305-2220
Tel.: 415-723-4744, Fax: 415-725-2099

Hideaki Takahashi
Tohoku Univ.
Research Inst. for Fracture Technology
Aramaki-Aza-Aoba
Sendai/980, Japan
Tel.: 022-222-1800 x 4179
Fax: 022-225-2263

William Teplow
Trans-Pacific Geothermal Corp.
1901 Harrison St., Suite 1590
Oakland, CA 94612-3501
Tel.: 510-763-7812, Fax: 510-763-2504

Richard P. Thomas
California Dept. of Conservation
Div. of Oil, Gas, and Geothermal Resources
801 K. Street, MS 20-21
Sacramento, CA 95814-3530
Tel.: 916-323-1787, Fax: 916-323-0424

Alfred Truesdell
Entropy, Inc.
700 Hermosa Way
Menlo Park, CA 94025
Tel.: 415-322-6135, Fax: 415-324-4009

Monica Tudor
Stanford University
Dept. of Petroleum Engineering
Stanford, CA 94305-2220
Tel.: 415-725-5081, Fax: 415-725-2099

Ed Voge
UNOCAL, Geothermal Division
3576 Unocal Place
Santa Rosa, CA 95406
Tel.: 707-545-7600, Fax: 707-545-8748

Marina M. Voskanian
California State Lands Commission
200 Oceangate, 12th Floor
Long Beach, CA 90802
Tel.: 310-590-5201, Fax: 310-590-5995

Mark Walters
Engineering Consultant
1573 Manzanita Ave.
Santa Rosa, CA 95404
Tel.: 707-538-2705, Fax: 707-538-9206

Kimio Watanabe
Tohoku University
Research Inst. for Fracture Technology
Aramaki Aoba, Aoba-ku
Sendai 980, Japan
Tel.: 022-222-1800 x 4184
Fax: 022-225-2263

Colin F. Williams
U.S. Geological Survey
345 Middlefield Road, MS-923
Menlo Park, CA 94025
Tel.: 415-329-4881, Fax: 415-329-4876

J. Willis-Richards
Tohoku University
Research Inst for Fracture Technology
Aramaki Aoba, Aoba-ku
Sendai 980, Japan
Tel.: 81-22-216-8164, Fax: 81-22-225-2263

Yusaku Yano
Geological Survey of Japan
Geothermal Research Dept.
1-1-3 Higashi, Tsukuba
Ibaraki 305, Japan
Tel.: 81-298-54-3735, Fax: 81-298-52-0283

SUBJECT INDEX

AUTHOR INDEX